NASA Technical Memorandum 85674

Aileron Effectiveness for a Subsonic Transport Model With a High-Aspect-Ratio Supercritical Wing

Peter F. Jacobs

DECEMBER 1983

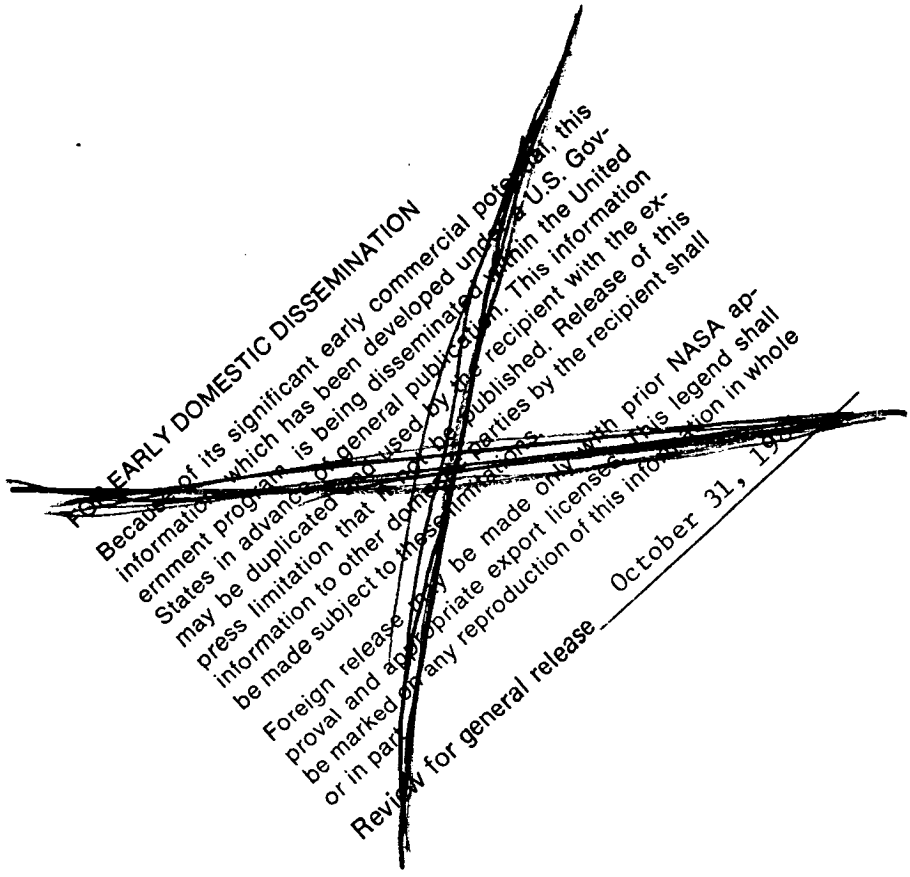

25th Anniversary
1958-1983

NASA

NASA Technical Memorandum 85674

Aileron Effectiveness for a Subsonic Transport Model With a High-Aspect-Ratio Supercritical Wing

Peter F. Jacobs
Langley Research Center
Hampton, Virginia

National Aeronautics
and Space Administration

**Scientific and Technical
Information Branch**

1983

SUMMARY

The purpose of this investigation was to determine aileron effectiveness for a subsonic energy-efficient transport (EET) model with a high-aspect-ratio supercritical wing. This investigation was conducted in the Langley 8-Foot Transonic Pressure Tunnel. Data were taken over a Mach number (M_∞) range of 0.30 to 0.86. The Reynolds number was 3.0×10^6 per foot for $M_\infty = 0.30$ and 5.0×10^6 per foot for the other Mach numbers. Data are presented for ailerons located at three positions along the wing span. The ailerons were designed as a preliminary active-control concept with gust-load alleviation, maneuver-load alleviation, and flutter-suppression systems. The data indicate a linear variation of rolling-moment coefficient with angle of attack for individual and multiple aileron deflections at Mach numbers up to 0.81. For Mach numbers greater than 0.81, the rolling-moment-coefficient data become nonlinear with increasing angle of attack. At Mach numbers near the design value ($M_\infty = 0.81$), increased aileron effectiveness resulted from aft transition locations, which produced relatively thin boundary layers (higher effective Reynolds number) and greater effective aileron deflections. Individual aileron deflections on the right wing panel produced only small effects on yawing-moment and side-force coefficients.

INTRODUCTION

Since the development of advanced-technology supercritical airfoils by the National Aeronautics and Space Administration, great strides have been made toward improving the cruise performance of future jet transport aircraft. Extensive theoretical studies and experimental wind-tunnel investigations have produced aerodynamically efficient transport wings which have higher lift-drag ratios, thicker airfoil sections, less sweep, and higher aspect ratios than the wings on current wide-body aircraft. The performance characteristics of these configurations have been documented in references 1 and 2; however, data on the effectiveness of lateral-control surfaces for these supercritical wings have not generally been available.

The purpose of this investigation was to determine aileron effectiveness for a high-aspect-ratio supercritical wing configuration. The control surfaces investigated were representative of a preliminary active-control technology concept with gust-load alleviation, maneuver-load alleviation, and flutter-suppression systems (ref. 3). These controls did not correspond directly to conventional aileron designs, either in size or location. It is anticipated, however, that this investigation will provide insight into the sizing of a more conventional set of ailerons for a high-aspect-ratio supercritical wing configuration.

SYMBOLS

Force and moment data presented in this paper have been reduced to conventional coefficient form based on the wing trapezoidal planform area (extended to the fuselage centerline). Longitudinal aerodynamic characteristics are referred to the stability-axis system, and lateral-directional aerodynamic characteristics are referred to the body-axis system. Moments are referenced to the quarter chord of the

mean geometric chord. All dimensional values are given in U.S. Customary Units. Symbols are defined as follows:

a_1, a_2, a_3 ailerons 1, 2, and 3, respectively (fig. 2)

b wing span, 52.97 in.

C_D drag coefficient, $\frac{\text{Drag}}{q_\infty S}$

C_L lift coefficient, $\frac{\text{Lift}}{q_\infty S}$

C_l rolling-moment coefficient, $\frac{\text{Rolling moment}}{q_\infty Sb}$

$C_{l_{\delta a_1}}, C_{l_{\delta a_2}}, C_{l_{\delta a_3}}$ control-effectiveness parameter for ailerons 1, 2, and 3, respectively, $\frac{\Delta C_l}{\Delta \delta a}$, per degree

C_m pitching-moment coefficient, $\frac{\text{Pitching moment}}{q_\infty S\bar{c}}$

C_n yawing-moment coefficient, $\frac{\text{Yawing moment}}{q_\infty Sb}$

C_Y side-force coefficient, $\frac{\text{Side force}}{q_\infty S}$

c local streamwise chord of wing, in.

$\bar{c}$ mean geometric chord of reference wing panel, 5.74 in.

M_∞ free-stream Mach number

q_∞ free-stream dynamic pressure, lb/ft^2

R Reynolds number per foot

S wing planform reference (trapezoidal) area, 1.988 ft^2

t/c local wing maximum thickness-to-chord ratio

x chordwise distance from wing leading edge, positive aft, in.

y spanwise distance from model centerline, in.

z vertical coordinate of airfoil, positive upward, in.

α angle of attack, deg

Δ incremental value

δ_a deflection angle of aileron, positive for trailing-edge down, deg

ε local wing incidence angle measured from fuselage waterline, positive for leading edge up, deg

η semispan station, $\frac{2y}{b}$

Subscripts:

1,2,3 ailerons 1, 2, and 3, respectively

EXPERIMENTAL APPARATUS AND PROCEDURES

Test Facility

This investigation was conducted in the Langley 8-Foot Transonic Pressure Tunnel (ref. 4). This facility is a continuous-flow, single-return tunnel with a rectangular, slotted test section. Tunnel controls allow independent variation of Mach number, density, stagnation temperature, and dew-point temperature. The test section is approximately 7.1 ft square (same cross-sectional area as that of a circle with an 8.0-ft diameter). The ceiling and floor are slotted axially and have an average openness ratio of 0.06. These features permit the test-section Mach number to be changed continuously throughout the transonic speed range. The stagnation pressure in the tunnel can be varied from a minimum of 0.25 atm (1 atm = 2116 lb/ft^2) at all Mach numbers to a maximum of approximately 2.00 atm at Mach numbers less than 0.40. At transonic Mach numbers, the maximum stagnation pressure that can be obtained is approximately 1.5 atm.

Model Description

Drawings of the model are shown in figures 1 and 2. A photograph of the model in the Langley 8-Foot Transonic Pressure Tunnel is shown in figure 3.

Fuselage.- The fuselage used in this investigation had a maximum diameter of 5.74 in. and was 49.56 in. long. The fuselage wetted area was approximately 5.63 ft^2. The fineness ratio of the fuselage (8.6) was typical of second-generation or wide-body jet transports. The lower surface of the wing was faired into the fuselage to produce a relatively flat bottom that extended from near the wing leading edge to approximately 6.0 in. aft of the trailing edge.

Wing.- The reduced-camber wing of reference 2 was used in this investigation. The wing had 5° of dihedral and 30° of sweep at the quarter chord. Based on the trapezoidal planform (extended to the fuselage centerline), the wing had a reference area of 1.988 ft^2, an aspect ratio of 9.80, and a taper ratio of 0.397. Twist and thickness distributions are shown in figures 4 and 5, respectively. Airfoil sections at several spanwise locations are shown in figure 6.

Ailerons.- An existing set of wing panels was modified for trailing-edge controls. The three ailerons represented a preliminary active-control design and were located on the right wing panel only. Details of the ailerons are shown in figure 2. Each aileron had angle brackets which produced deflections of 0°, ±5°, and ±10°. A plastic filler material prevented airflow through the gap between the wing and the

leading edges of the ailerons to simulate a sealed aileron configuration. The filler material was shaped to provide a smooth contour between the wing and ailerons.

Transition Strips

Boundary-layer transition strips were applied to the fuselage and the wing. These strips were comprised of a 0.10-in-wide band of carborundum grit set in a plastic adhesive. The grit was sized on the basis of reference 5.

A transition strip of No. 120 grit was applied to the fuselage 1 in. aft of the nose. The transition strip patterns on the wing are shown in figure 7. The transition strips on the wing were located rearward in an attempt to simulate a higher effective Reynolds number (ref. 6).

Measurements

Force and moment data were obtained by use of a six-component electrical strain-gauge balance housed within the fuselage cavity. Angle of attack was measured by an accelerometer that was also housed within the fuselage. Static pressures were measured in the model sting cavity by using differential-pressure transducers referenced to free-stream static pressures.

Corrections

The angle of attack of the model was corrected for flow angularity in the tunnel test section. This correction (approximately 0.1°) was obtained from upright and inverted tests of the basic wing configuration. The drag data have been adjusted to correspond to the condition of free-stream static pressure in the sting cavity. No Mach number correction was made for blockage effects, which were estimated to be negligible. Control-effectiveness-parameter values were computed using nominal control-deflection angles and were not corrected for control deflections under load.

Test Conditions

Throughout the entire test, stagnation temperature was maintained at 120°F, and the air was dried until the dew point was sufficiently low to prevent condensation effects. The test conditions for which data were taken are presented in the following table:

M_∞	α, deg	R, per foot	q_∞, lb/ft^2
0.30	-4 to 14	3.0×10^6	210
.60	-4 to 16	5.0	660
.70	-4 to 10	5.0	747
.77	-4 to 6	5.0	802
.81	-4 to 8	5.0	833
.84	-4 to 8	5.0	853
.86	-4 to 8	5.0	867

PRESENTATION OF RESULTS

The results of this investigation are presented in the figures, as indicated in the following table:

Aileron configuration			Figure numbers			
δa_1, deg	δa_2, deg	δa_3, deg	C_D vs C_L	C_L vs α	C_m vs C_L	C_l, C_n, and C_Y vs α
0	0	0	8	18	28	38
-10 to 10	0	0	9	19	29	39
0	-10 to 10	0	10	20	30	40
0	0	-10 to 10	11	21	31	41
-5	0	-5	12	22	32	42
5	0	-5	13	23	33	43
5	0	5	14	24	34	44
5	5	0	15	25	35	45
0	5	5	16	26	36	46
5	5	5	17	27	37	47

The variation of aileron-effectiveness parameter with Mach number is shown in figure 48.

DISCUSSION OF RESULTS

The purpose of this investigation was to determine aileron effectiveness for a subsonic EET model with a high-aspect-ratio supercritical wing. Since the ailerons were located on the right wing panel only, data for positive and negative deflections of each surface were summed in the calculation of the control-effectiveness values (i.e., on the basis of asymmetric control deflections $\Delta\delta a = \delta a_{down} - \delta a_{up}$).

Longitudinal Aerodynamic Characteristics

The static longitudinal aerodynamic characteristics of the model (figs. 8 to 37) are not representative of an actual aircraft because ailerons were located on the right wing panel only. The data are included and may be used judiciously, but they are considered of secondary importance to the lateral aerodynamic characteristics and will not be discussed.

Lateral-Control Characteristics

The static lateral aerodynamic data for the baseline configuration (no ailerons deflected) indicate a slight asymmetry of the model (fig. 38). The model asymmetry affects the absolute value of the baseline rolling-moment coefficient but has no effect on the calculation of the control-effectiveness parameter, which depends on increments in rolling-moment coefficient. Rolling-moment-coefficient values for the baseline configuration are positive for most angles up to stall and increase slightly

with Mach number. Poststall rolling-moment-coefficient values become very nonlinear for the baseline configuration at $M_\infty = 0.60$ (fig. 38(b)). This effect is probably caused by varying amounts of flow separation and aeroelastic deformation at the wing tip. A similar trend is shown for 5° and 10° deflections of the outboard aileron a_3 (fig. 41(b)). Positive deflections of a_3 increase the loading at the wing tip; however, the increased loading is partially offset by aeroelastic deformation of the wing (washout).

Data for individual aileron deflections (figs. 39 to 41) and multiple aileron deflections (figs. 42 to 47) indicate a linear variation of rolling-moment coefficient with angle of attack up to stall for Mach numbers up to and including the design Mach number ($M_\infty = 0.81$). For Mach numbers greater than 0.81, rolling-moment-coefficient values become nonlinear with increasing angle of attack, probably as a result of increased trailing-edge boundary-layer separation near the deflected ailerons. Aileron a_1 shows a control reversal anomaly in the rolling-moment data for Mach numbers of 0.84 and 0.86 (figs. 39(f) and 39(g)). This anomaly is probably caused by shock wave interaction between the wing and fuselage, since aileron a_1 is located approximately 0.2 in. from the fuselage. Rolling-moment data for multiple aileron deflections can be estimated by summing the data for individual deflections. The effect of individual aileron deflections (right wing panel) on yawing-moment and side-force coefficients is very small.

Aileron Effectiveness

For the Reynolds numbers of this test, aileron effectiveness is highly dependent on the transition location and growth rate of the boundary layer. Data in reference 7 indicate that thicker boundary layers (resulting from a forward movement of the transition strips) caused reduced aileron effectiveness. The thickening of the boundary layer on the ailerons may be considered as an effective reduction of the aileron deflection.

As previously stated, the transition strips for this investigation were located rearward to simulate a higher effective Reynolds number at near-cruise Mach numbers. However, the actual point of transition varies as a result of changes in chordwise pressure distribution with Mach number (ref. 8). For off-design conditions ($M_\infty < 0.70$), the supercritical wing of this investigation exhibits "peaky"-type chordwise surface pressure distributions. The adverse pressure gradient of this upper-surface pressure peak causes transition near the leading edge instead of at the transition strip location and results in a thicker boundary layer over the aft portion of the wing. As the Mach number approaches the design value ($M_\infty = 0.81$), the region of supersonic flow on the upper surface increases and forms a "plateau" in the pressure distributions at typical cruise lift coefficients. The plateau region is terminated by a relatively weak shock wave, which causes transition of the flow. The chordwise extent of the plateau region increases with Mach number and results in rearward movement of the transition point and relatively thin boundary layers (higher effective Reynolds number). At design cruise conditions, the plateau region on the wing upper surface extends from the leading edge to approximately 40 to 60 percent of the chord. However, the transition strip is normally located ahead of this point to prevent the formation of a laminar separation bubble at the base of the shock wave and to insure a precise and repeatable transition point.

The relatively thin boundary layers associated with aft movement of the transition point at cruise Mach numbers result in greater control effectiveness. This increase in control effectiveness is shown in figure 48, and the amount of the

increase is dependent on the local section wing loads. Aileron a_2, which has the largest product of area times moment arm and also has the highest section loads, shows the largest gain in control effectiveness. A combination of low section load and possible aeroelastic deformation (washout) causes the outboard aileron a_3 to show the least gain in effectiveness. The aileron-effectiveness values in figure 48 are nonlinear with increasing aileron deflection ($\Delta\delta a = 10°, 20°$) because of varying amounts of local flow separation. For Mach numbers greater than 0.83, strong shock waves produce boundary-layer separation, which drastically reduces the effectiveness of each of the control surfaces.

SUMMARY OF RESULTS

An investigation to determine aileron effectiveness for a subsonic energy-efficient transport (EET) model with a high-aspect-ratio supercritical wing was conducted in the Langley 8-Foot Transonic Pressure Tunnel. Data were taken over a Mach number (M_∞) range of 0.30 to 0.86. The Reynolds number was 3.0×10^6 per foot for $M_\infty = 0.30$ and 5.0×10^6 per foot for the other Mach numbers. The results of this investigation may be summarized as follows:

1. Individual and multiple aileron deflections produced a linear variation of rolling-moment coefficient with angle of attack up to the design Mach number of 0.81. For Mach numbers greater than 0.81, the rolling-moment-coefficient data become nonlinear with increasing angle of attack.

2. At Mach numbers near the design value ($M_\infty = 0.81$), increased aileron effectiveness resulted from aft transition locations, which produced relatively thin boundary layers (higher effective Reynolds number) and greater effective aileron deflections.

3. Individual aileron deflections on the right wing panel produced only small effects on yawing-moment and side-force coefficients.

Langley Research Center
National Aeronautics and Space Administration
Hampton, VA 23665
October 7, 1983

REFERENCES

1. Bartlett, Dennis W.: Wind-Tunnel Investigation of Several High Aspect-Ratio Supercritical Wing Configurations on a Wide-Body-Type Fuselage. NASA TM X-71996, 1977.

2. Bartlett, Dennis W.; and Patterson, James C., Jr.: NASA Supercritical-Wing Technology. NASA TM-78731, 1978.

3. Byrdsong, Thomas A.; and Brooks, Cuyler W., Jr.: Wind-Tunnel Investigation of Longitudinal and Lateral-Directional Stability and Control Characteristics of a 0.237-Scale Model of a Remotely Piloted Research Vehicle With a Thick, High-Aspect-Ratio Supercritical Wing. NASA TM-81790, 1980.

4. Schaefer, William T., Jr.: Characteristics of Major Active Wind Tunnels at the Langley Research Center. NASA TM X-1130, 1965.

5. Braslow, Albert L.; and Knox, Eugene C.: Simplified Method for Determination of Critical Height of Distributed Roughness Particles for Boundary-Layer Transition at Mach Numbers From 0 to 5. NACA TN 4363, 1958.

6. Blackwell, James A., Jr.: Preliminary Study of Effects of Reynolds Number and Boundary-Layer Transition Location on Shock-Induced Separation. NASA TN D-5003, 1969.

7. Anglin, Ernie L.; and Byrdsong, Thomas A.: Wing Flap-Type Control Effectiveness and Effects of Control Hinge Gap Seals for a Supercritical Wing. AIAA-82-0960, June 1982.

8. Whitcomb, Richard T.: Review of NASA Supercritical Airfoils. ICAS Paper No. 74-10, Aug. 1974.

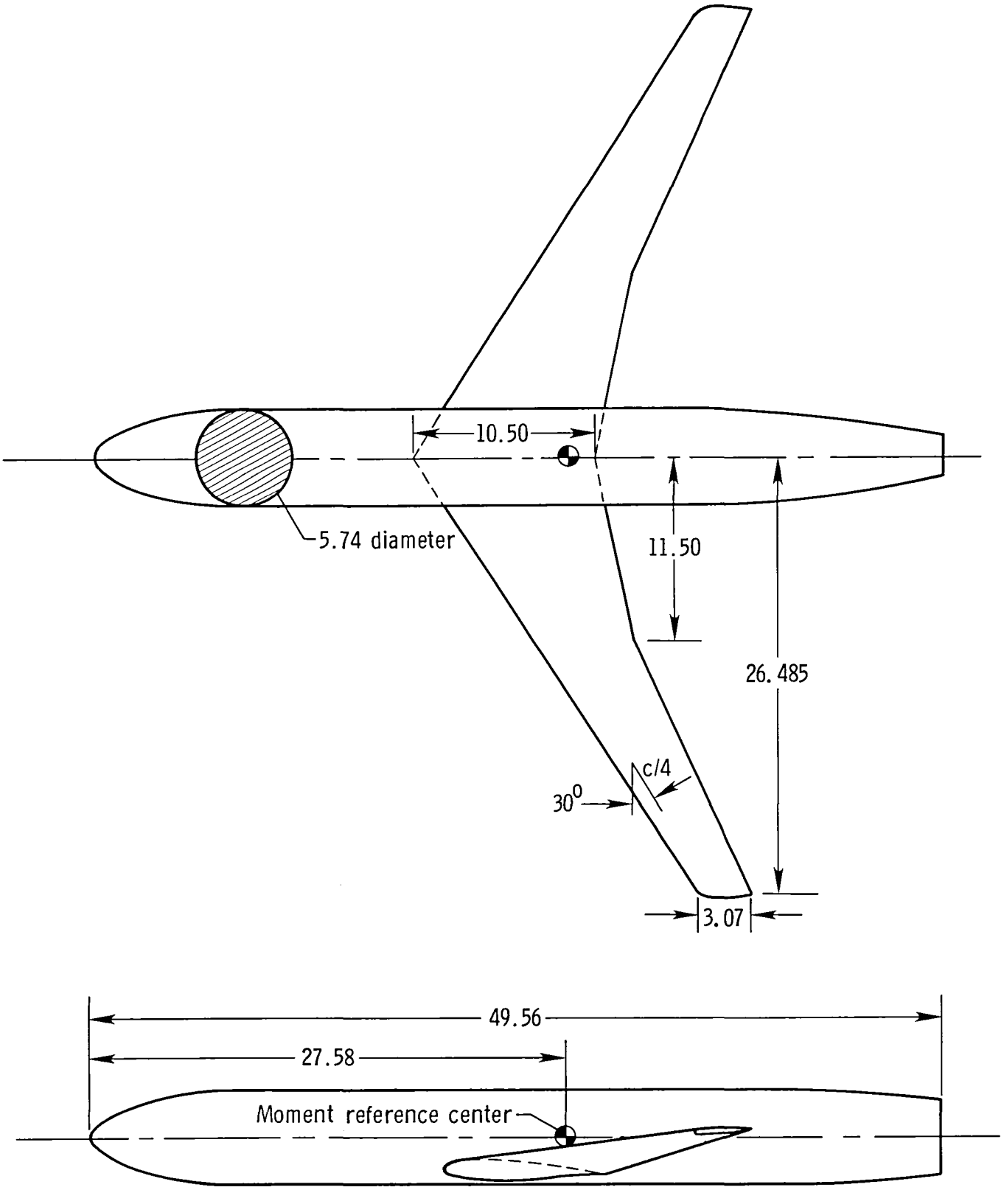

Figure 1.- Drawing of model. All dimensions are in inches.

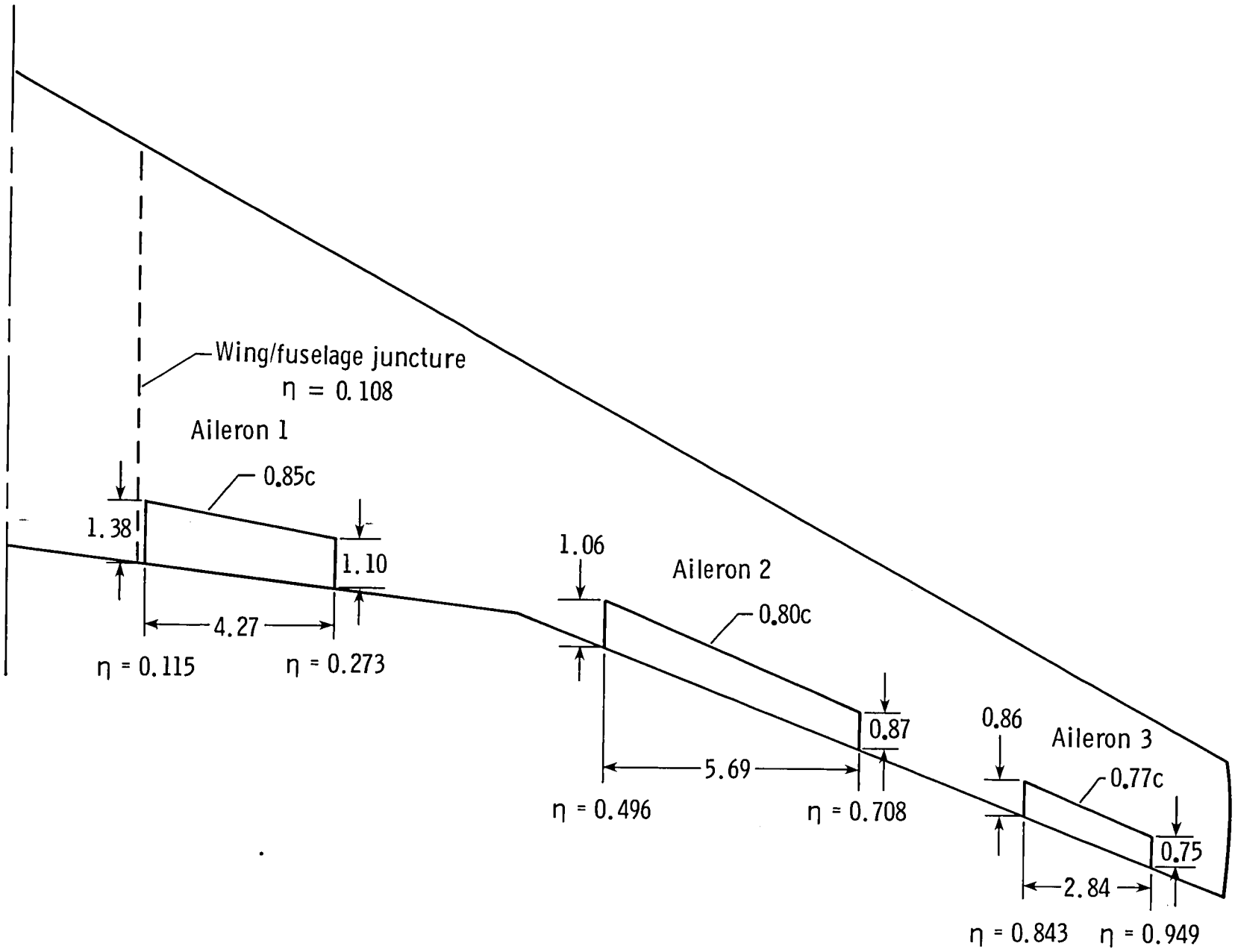

Figure 2.- Details of ailerons. All dimensions are in inches.

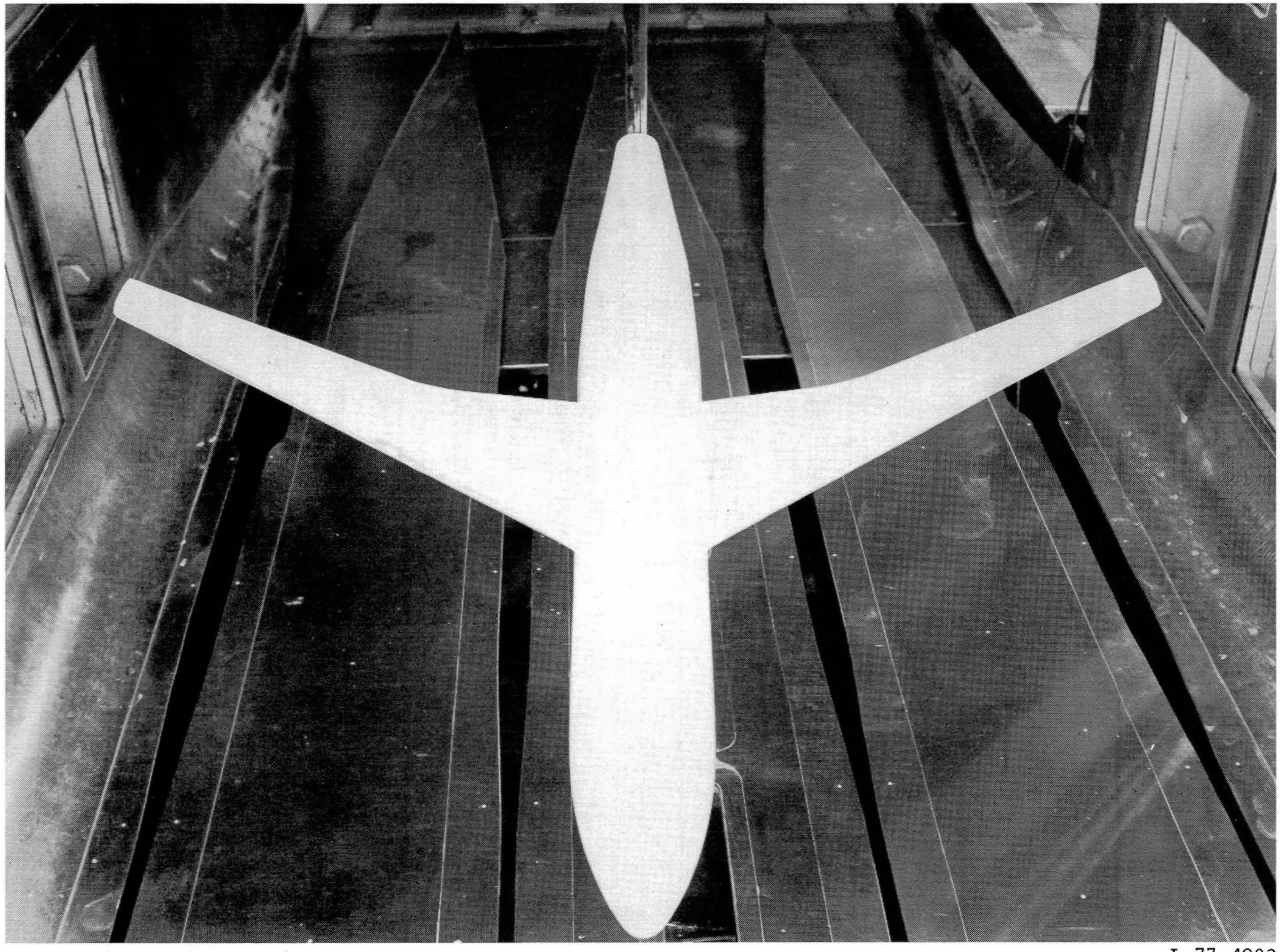

L-77-4903

Figure 3.- Photograph of model.

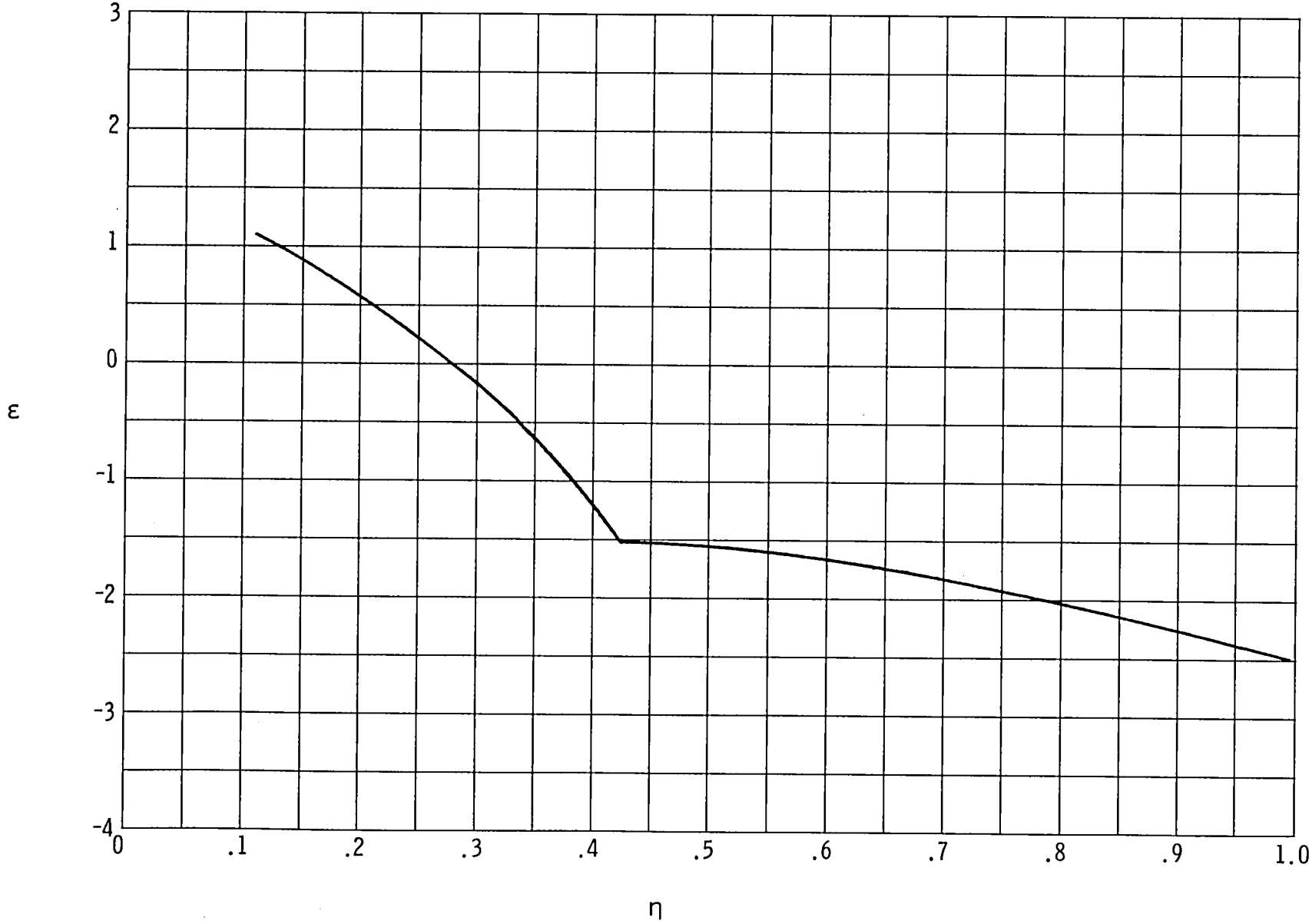

Figure 4.- Wing twist distribution.

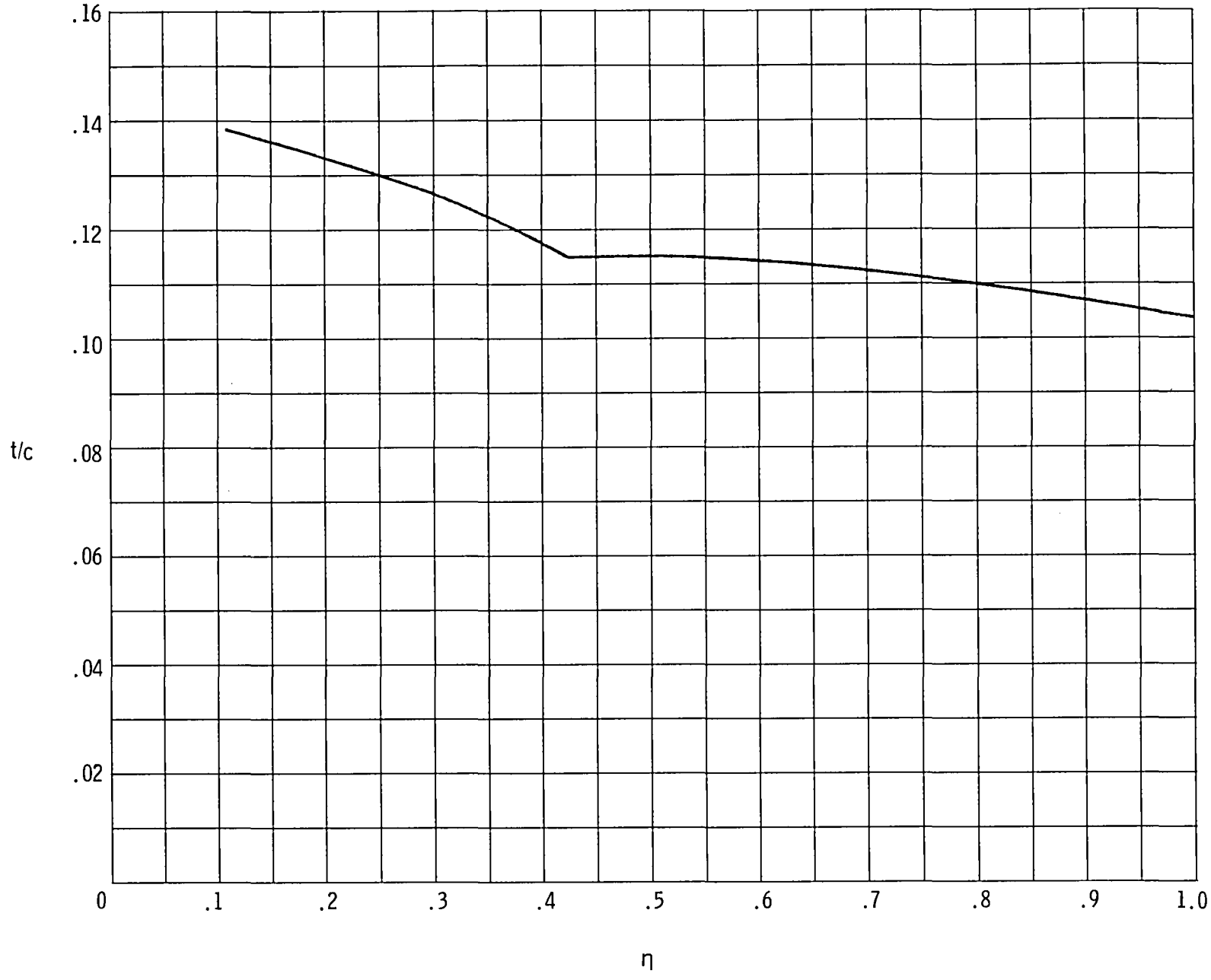

Figure 5.- Wing thickness distribution.

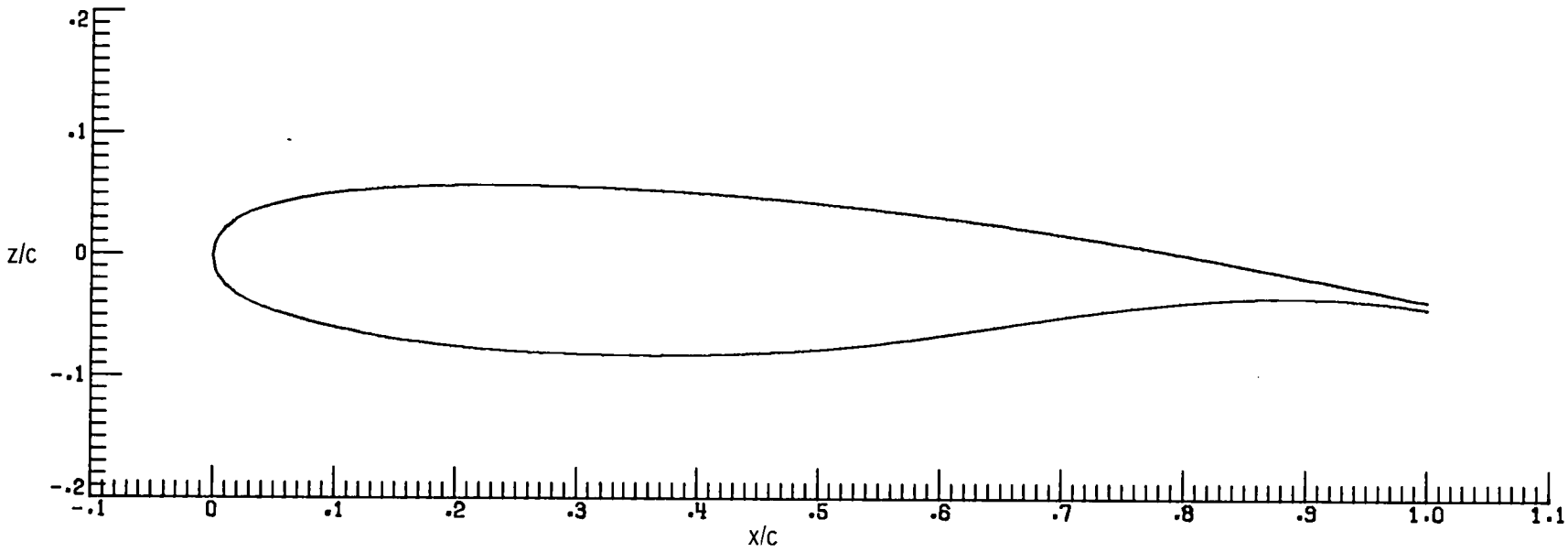

(a) $\eta = 0.122$.

Figure 6.- Wing airfoil sections.

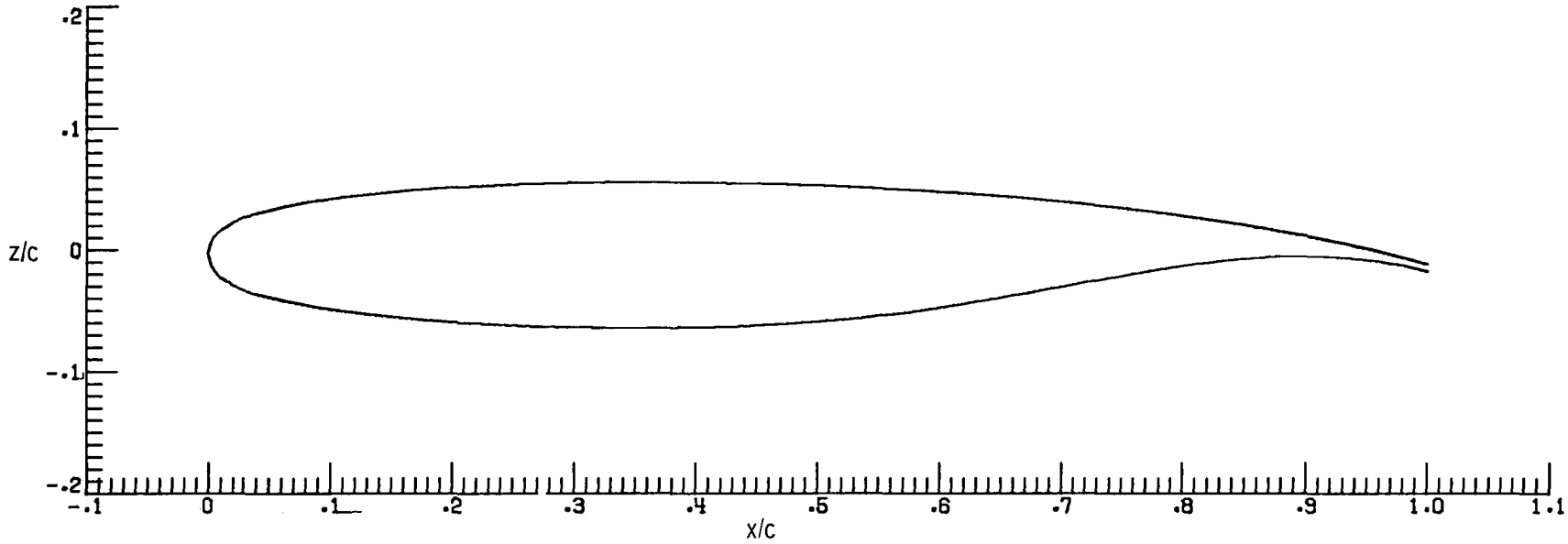

(b) $\eta = 0.376$.

Figure 6.- Continued.

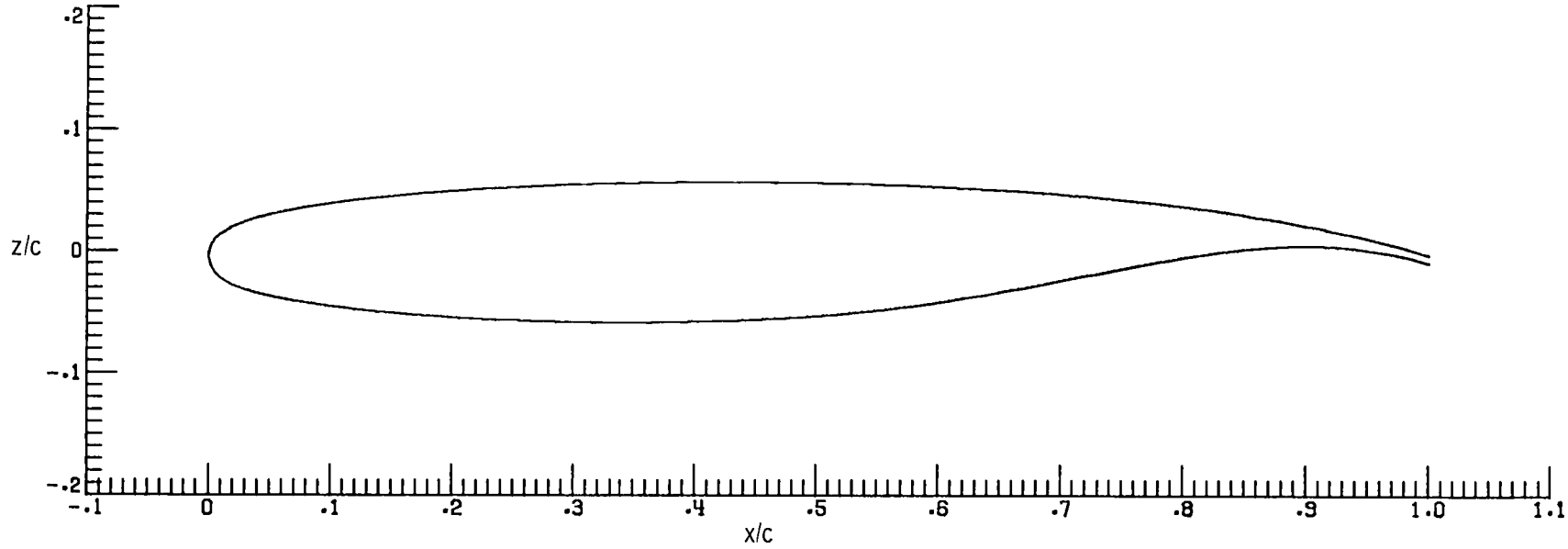

(c) $\eta = 0.425$.

Figure 6.- Continued.

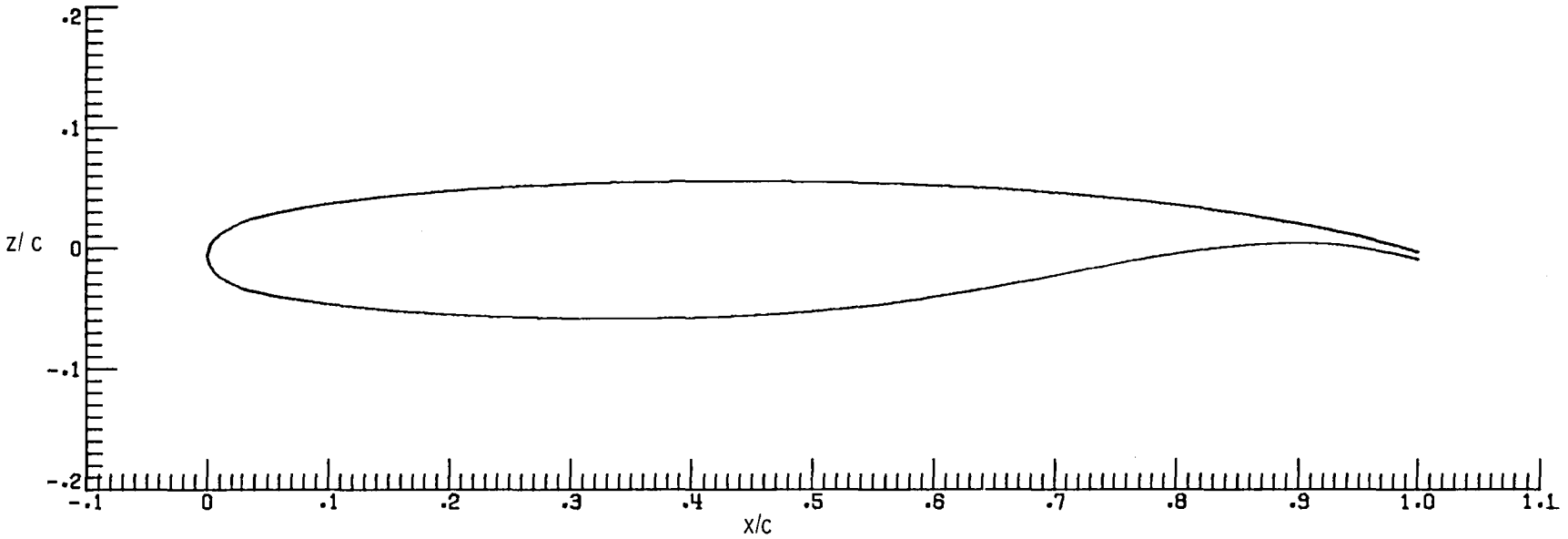

(d) $\eta = 0.639$.

Figure 6.- Continued.

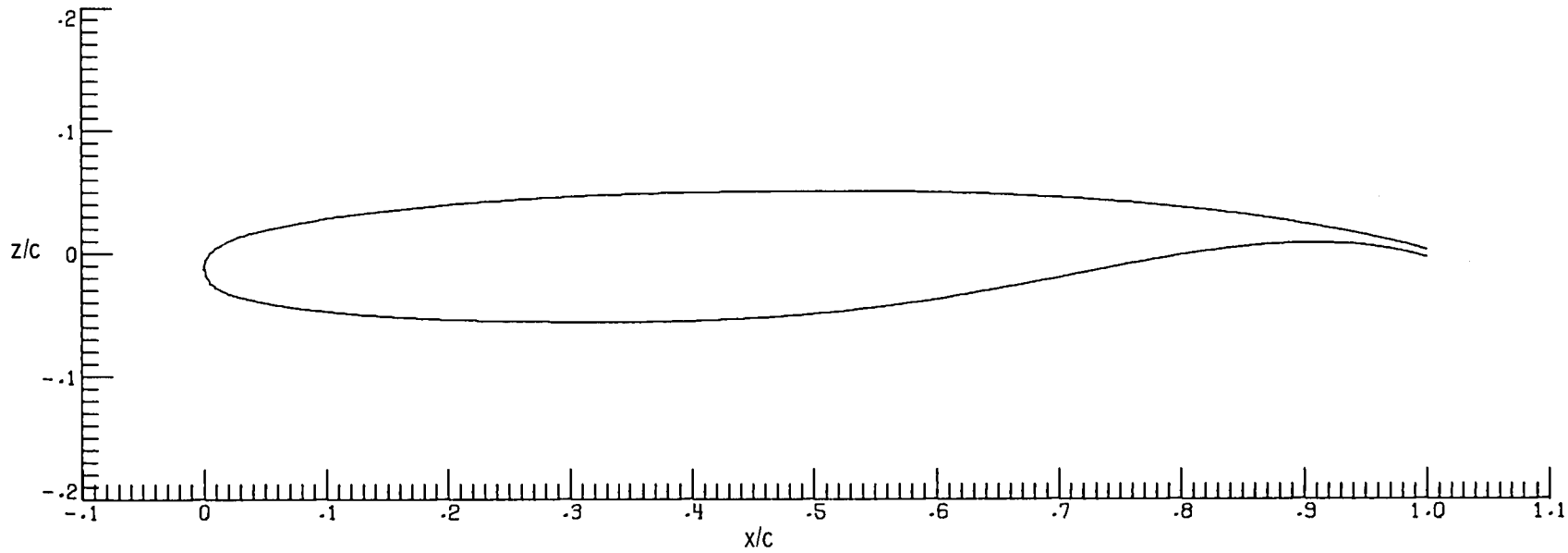

(e) $\eta = 0.962$.

Figure 6.- Concluded.

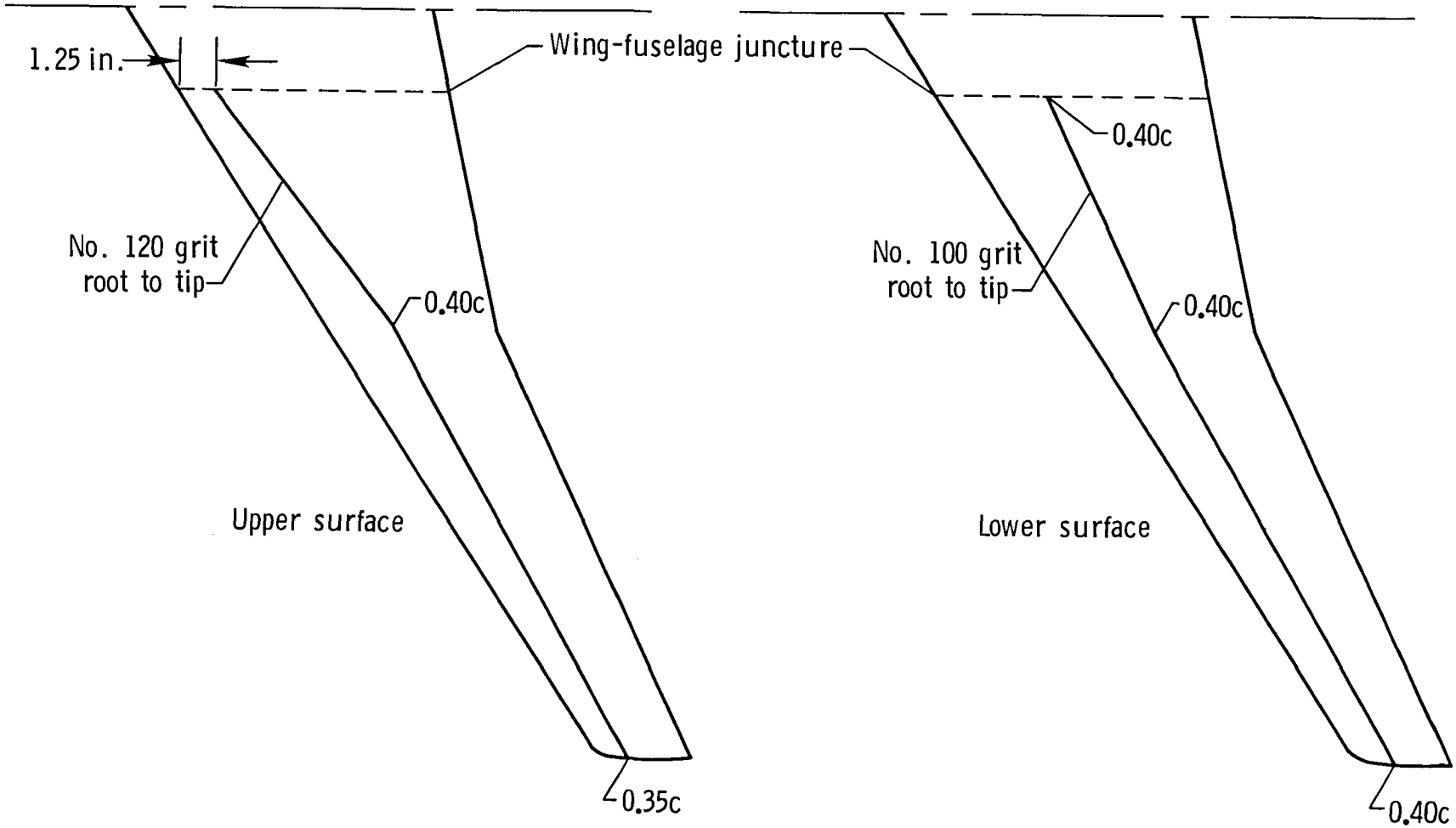

Figure 7.- Wing transition strip details.

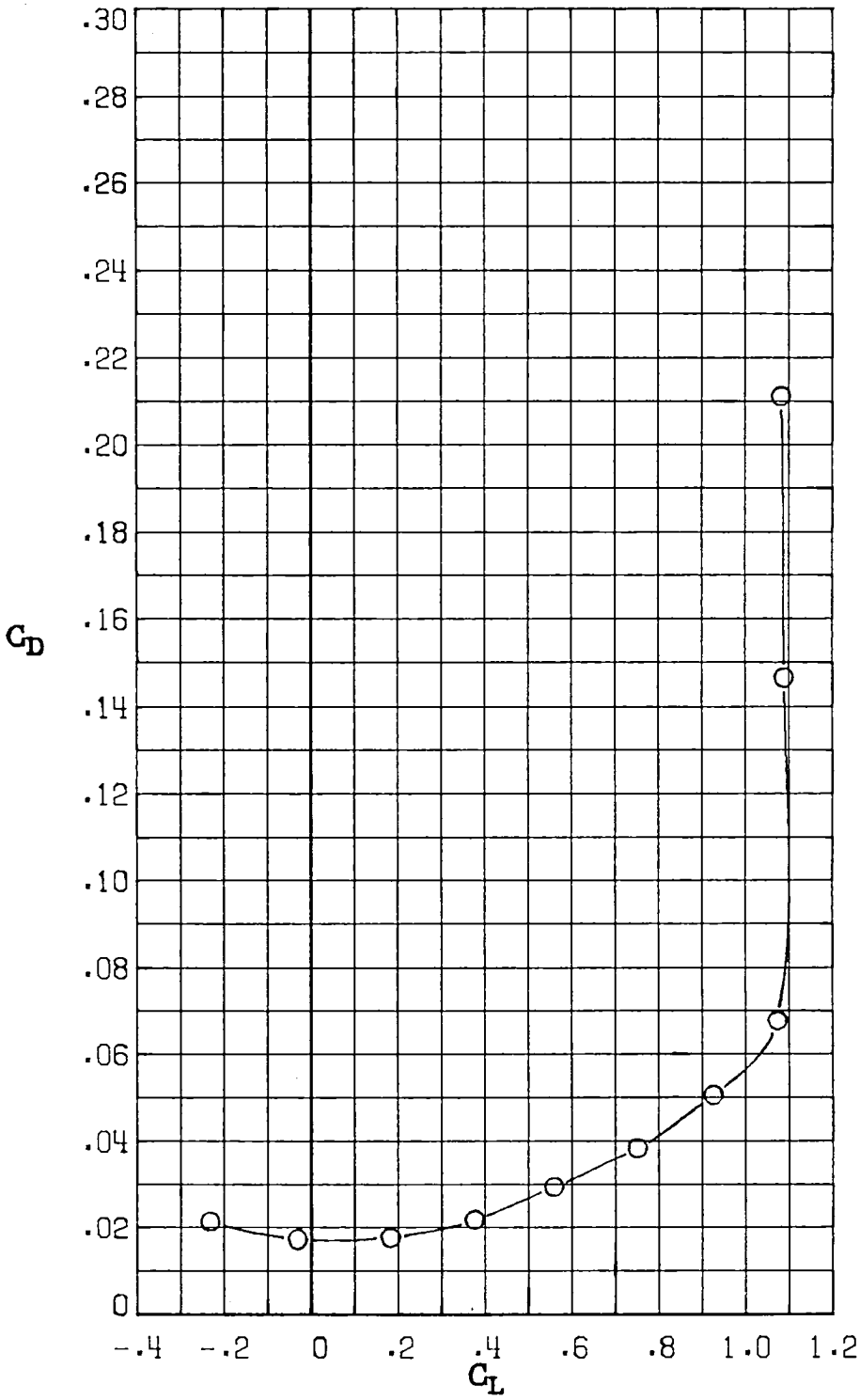

(a) $M_\infty = 0.30$.

Figure 8.- Variation of drag coefficient with lift coefficient for the baseline configuration ($\delta a_1 = 0°$; $\delta a_2 = 0°$; $\delta a_3 = 0°$).

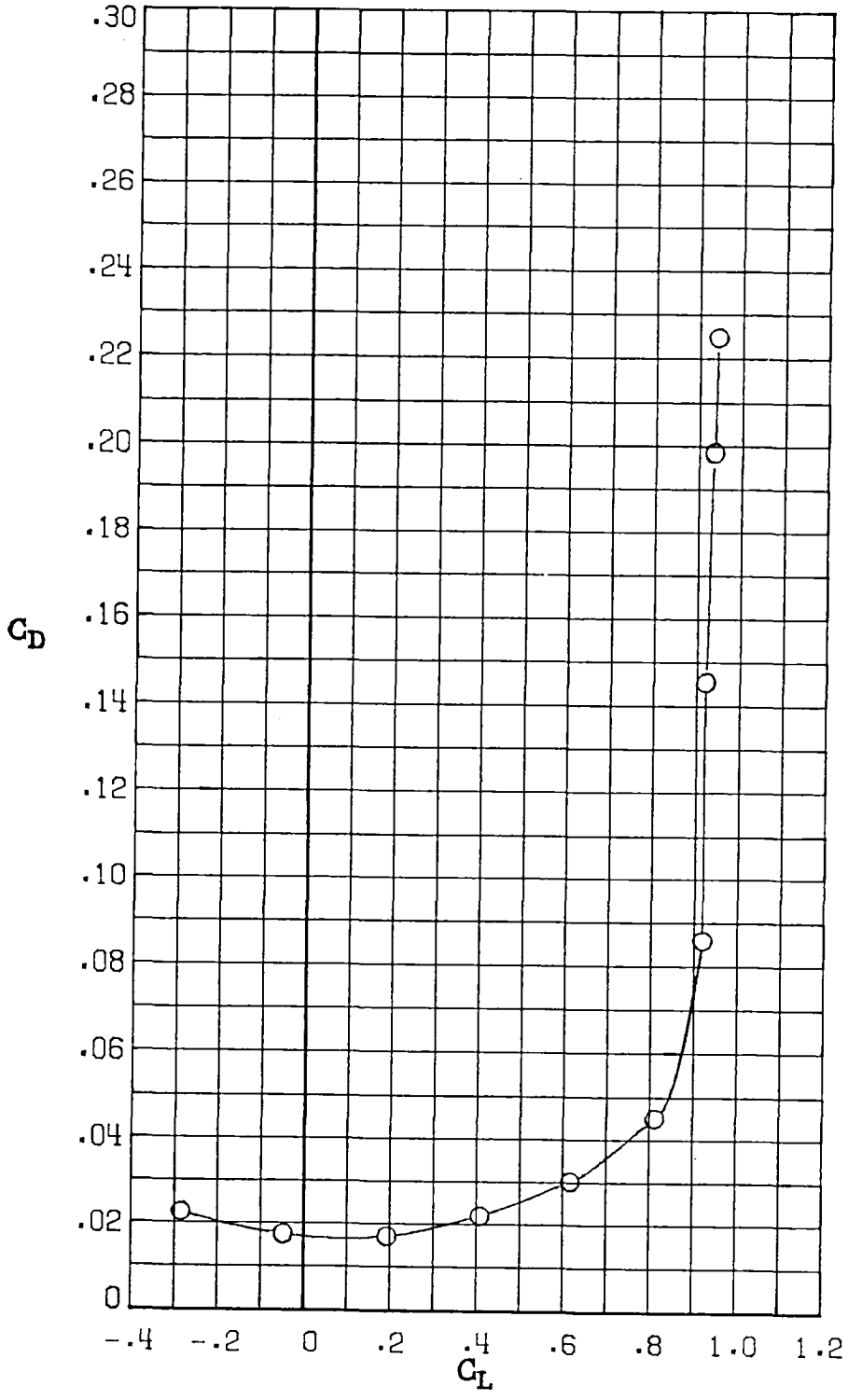

(b) $M_\infty = 0.60$.

Figure 8.- Continued.

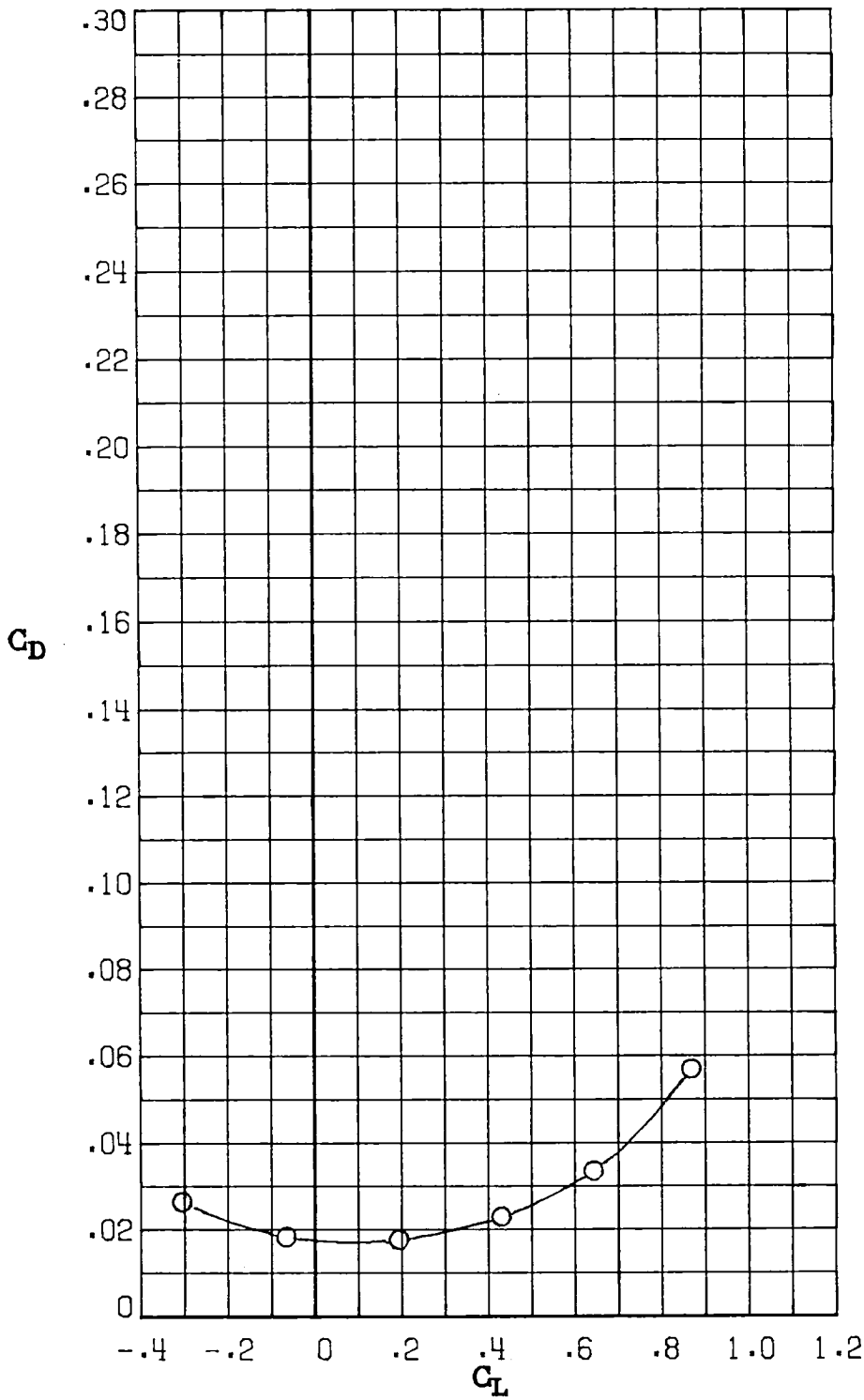

(c) $M_\infty = 0.70$.

Figure 8.- Continued.

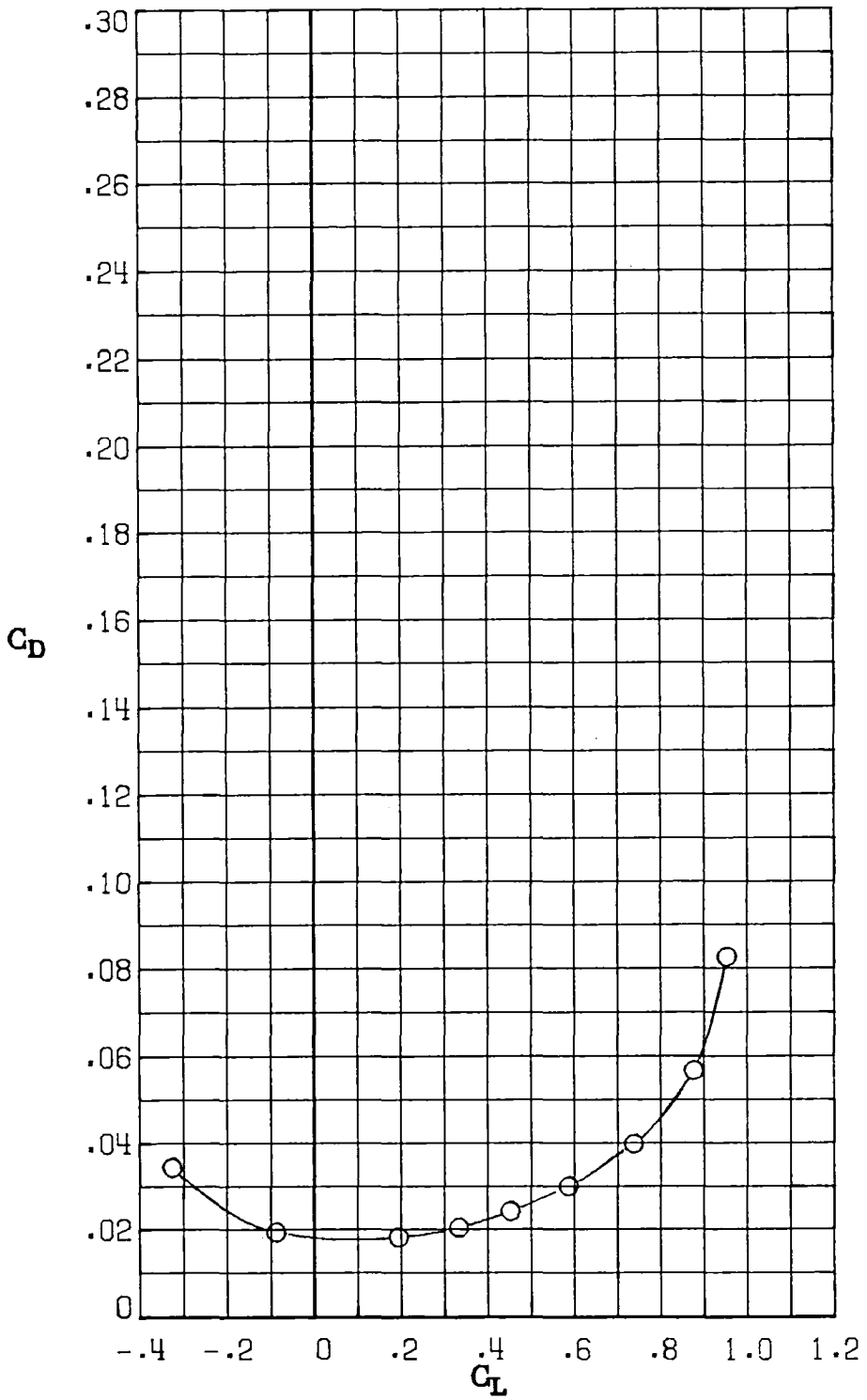

(d) $M_\infty = 0.77$.

Figure 8.- Continued.

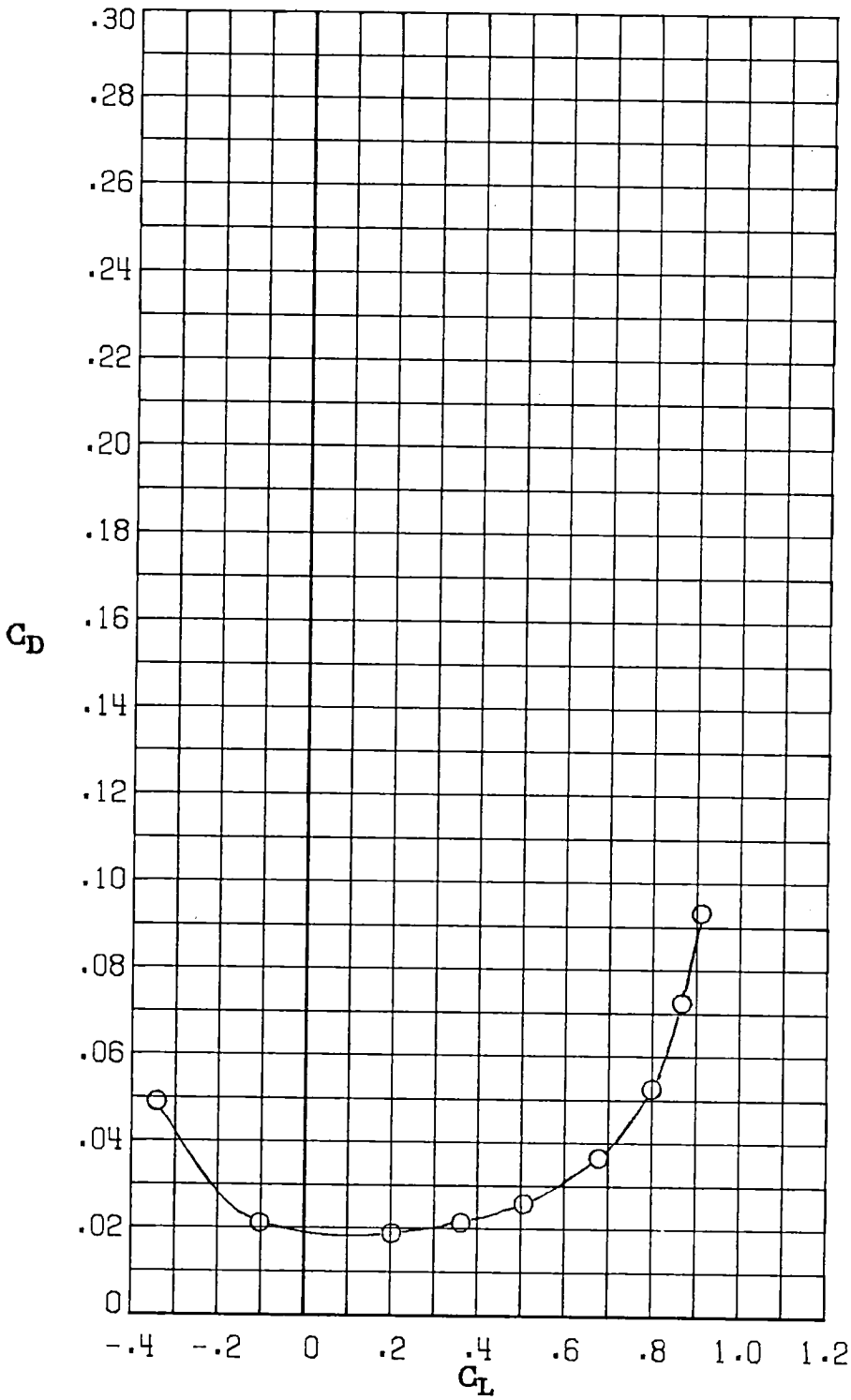

(e) $M_\infty = 0.81$.

Figure 8.- Continued.

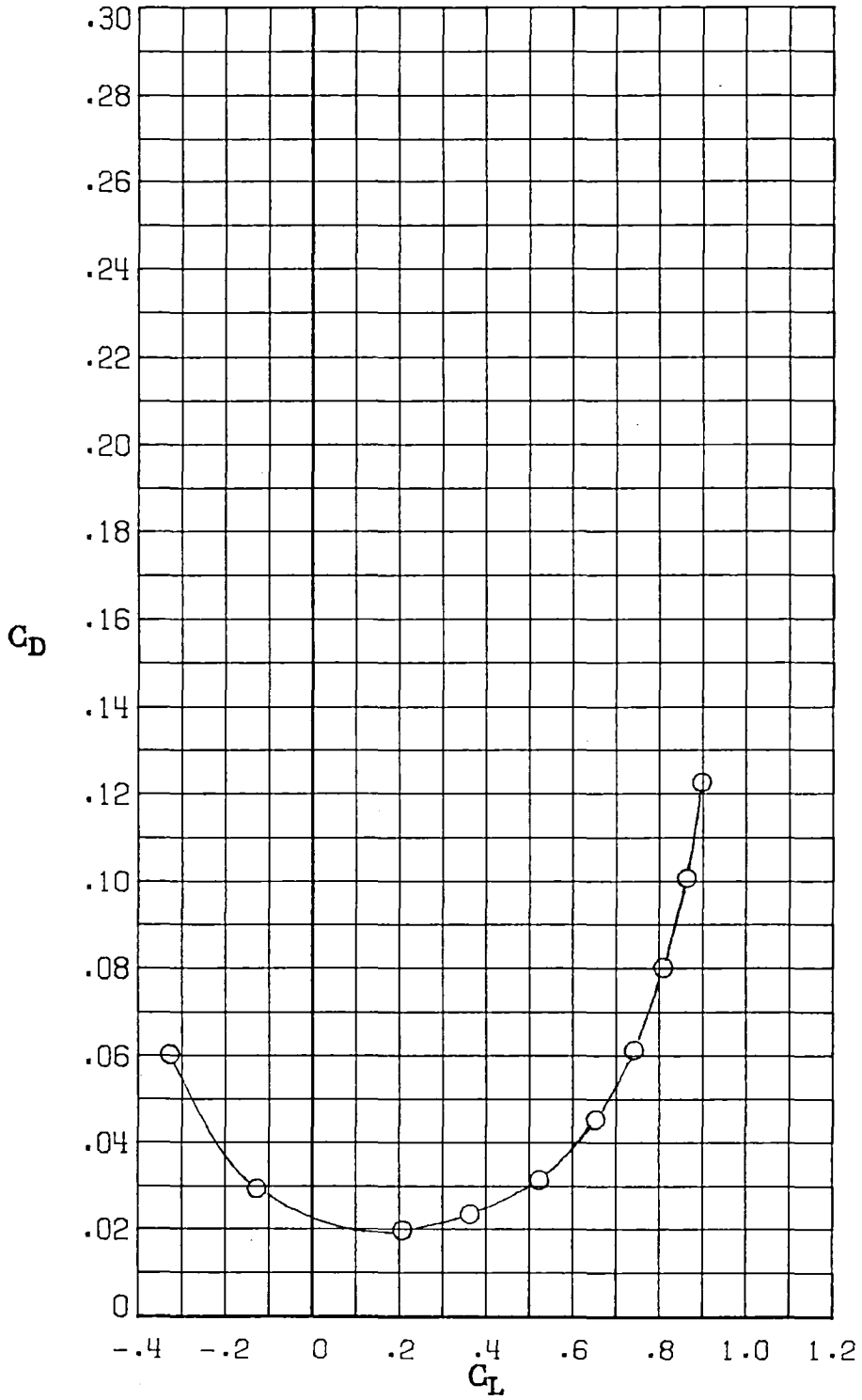

(f) $M_\infty = 0.84$.

Figure 8.- Continued.

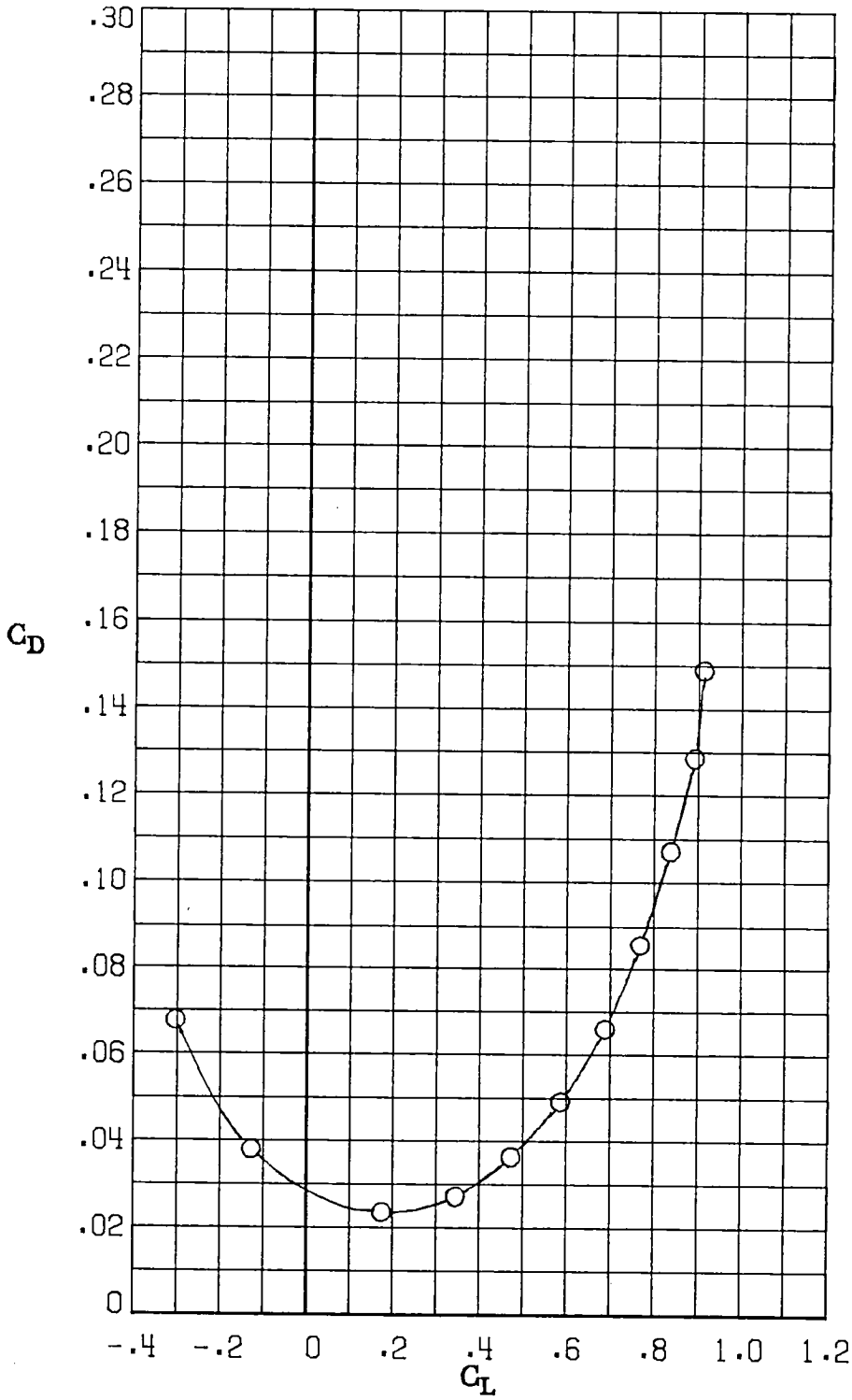

(g) $M_\infty = 0.86$.

Figure 8.- Concluded.

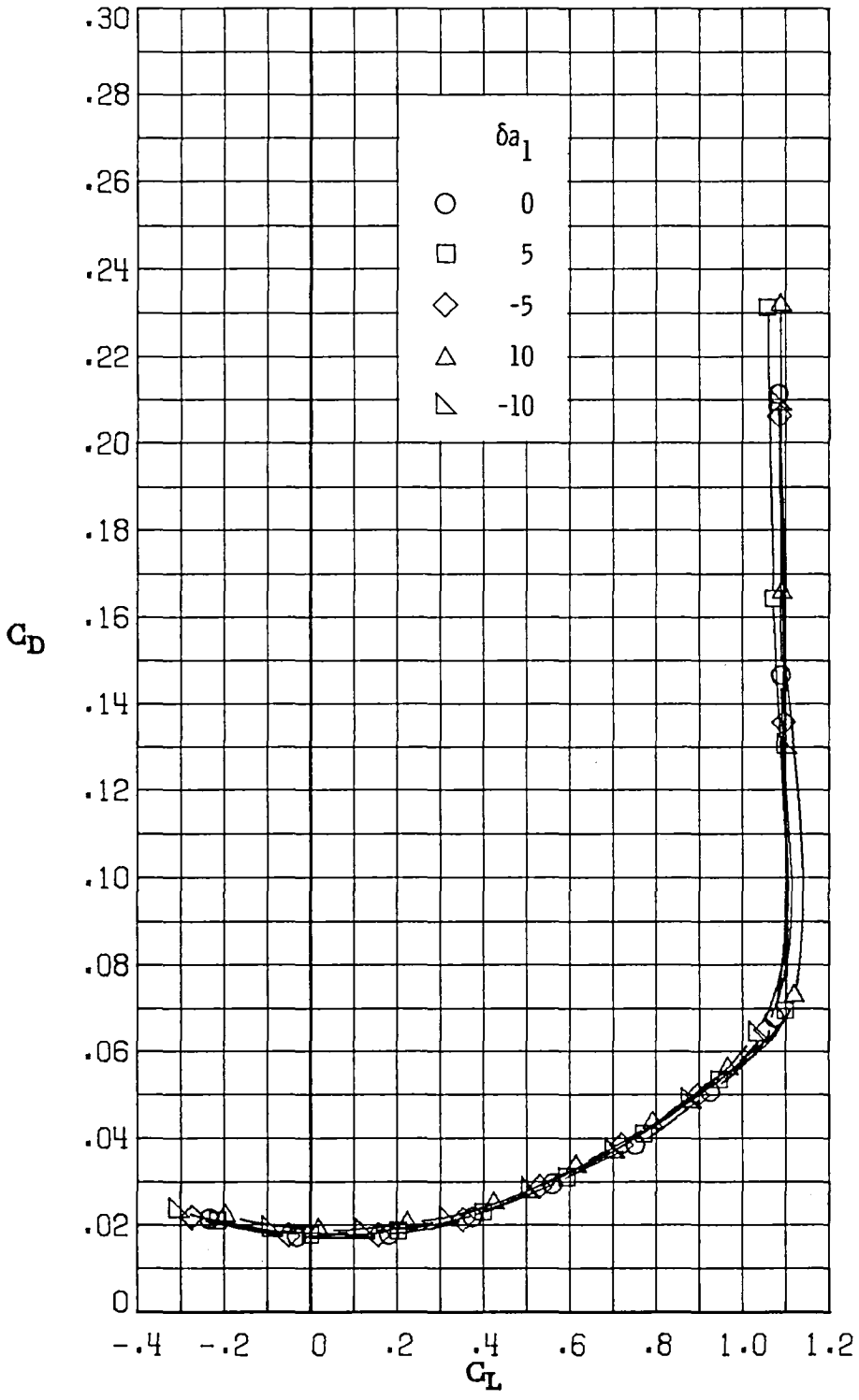

(a) $M_\infty = 0.30$.

Figure 9.- Variation of drag coefficient with lift coefficient for deflections of aileron 1 (δa_1 in degrees). $\delta a_2 = 0°$; $\delta a_3 = 0°$.

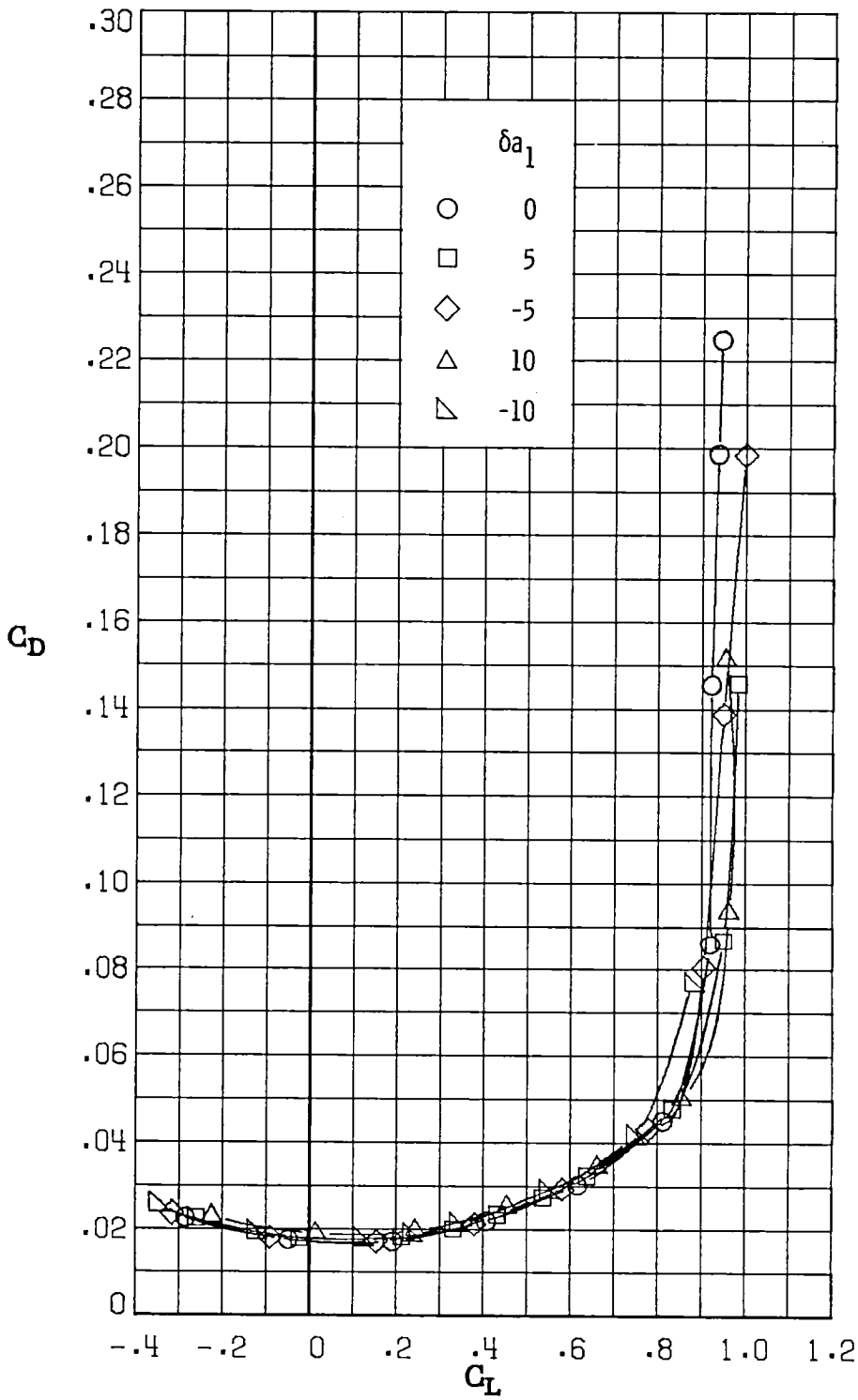

(b) $M_\infty = 0.60$.

Figure 9.- Continued.

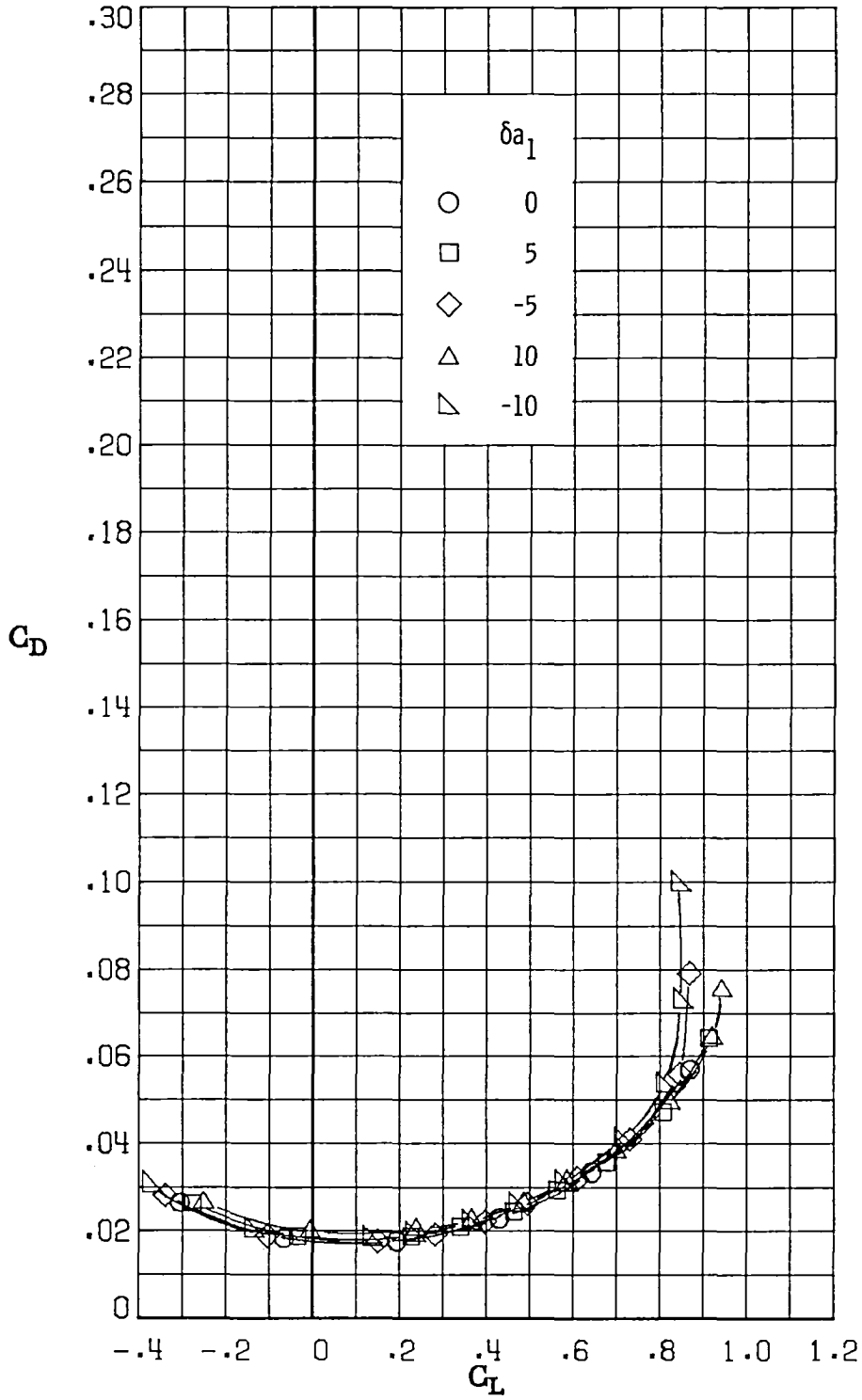

(c) $M_\infty = 0.70$.

Figure 9.- Continued.

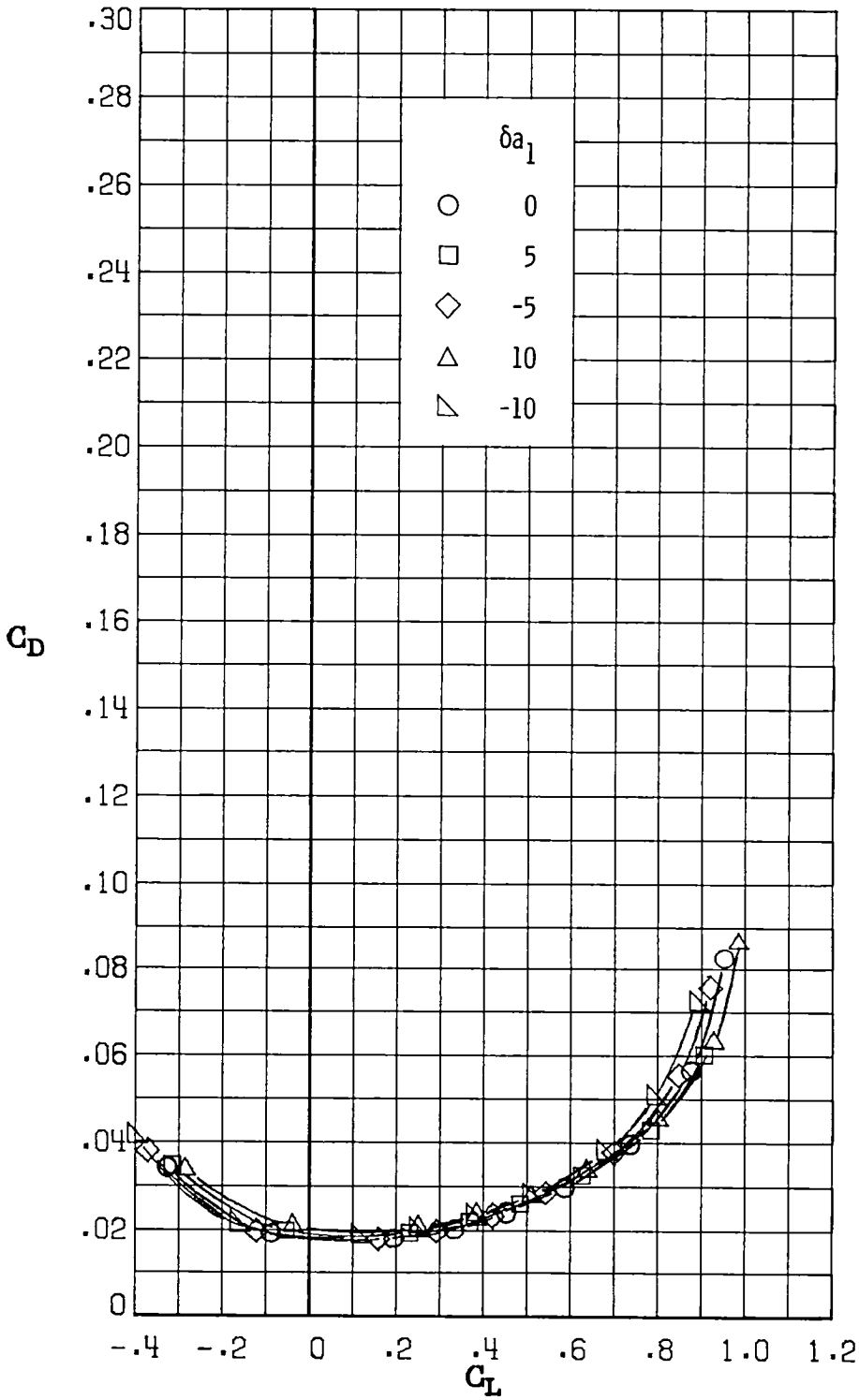

(d) $M_\infty = 0.77$.

Figure 9.- Continued.

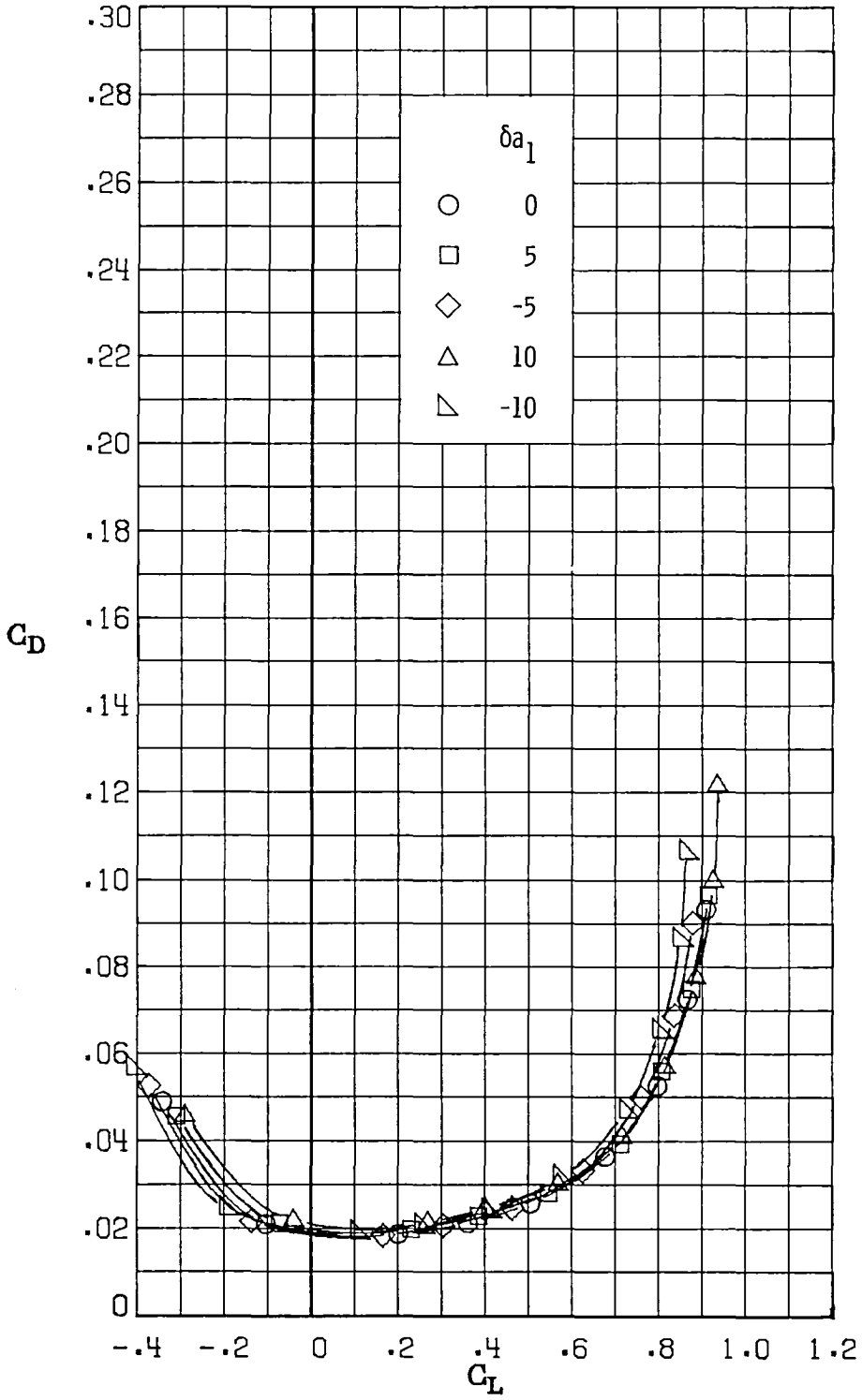

(e) $M_\infty = 0.81$.

Figure 9.- Continued.

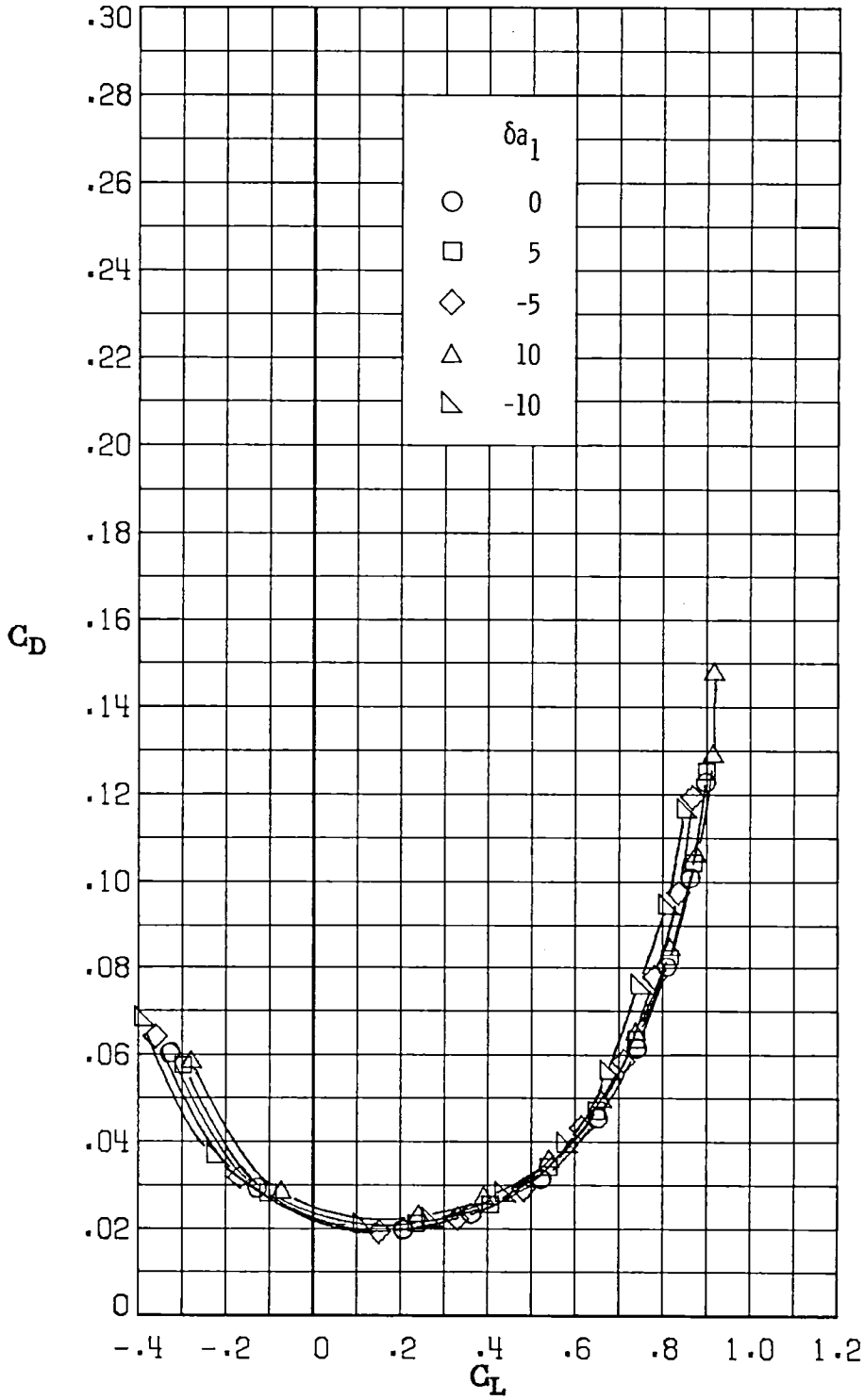

(f) $M_\infty = 0.84$.

Figure 9.- Continued.

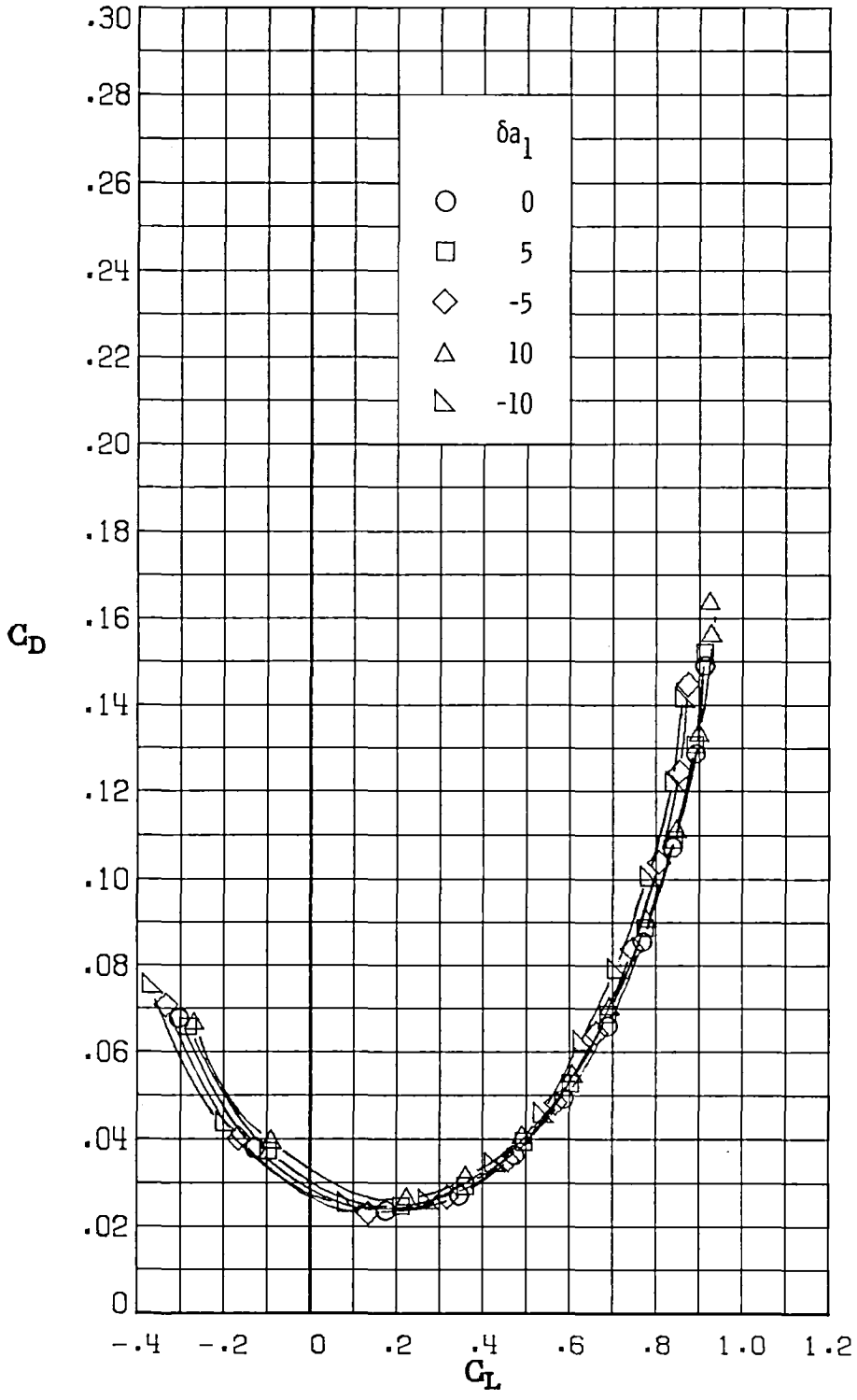

(g) $M_\infty = 0.86$.

Figure 9.- Concluded.

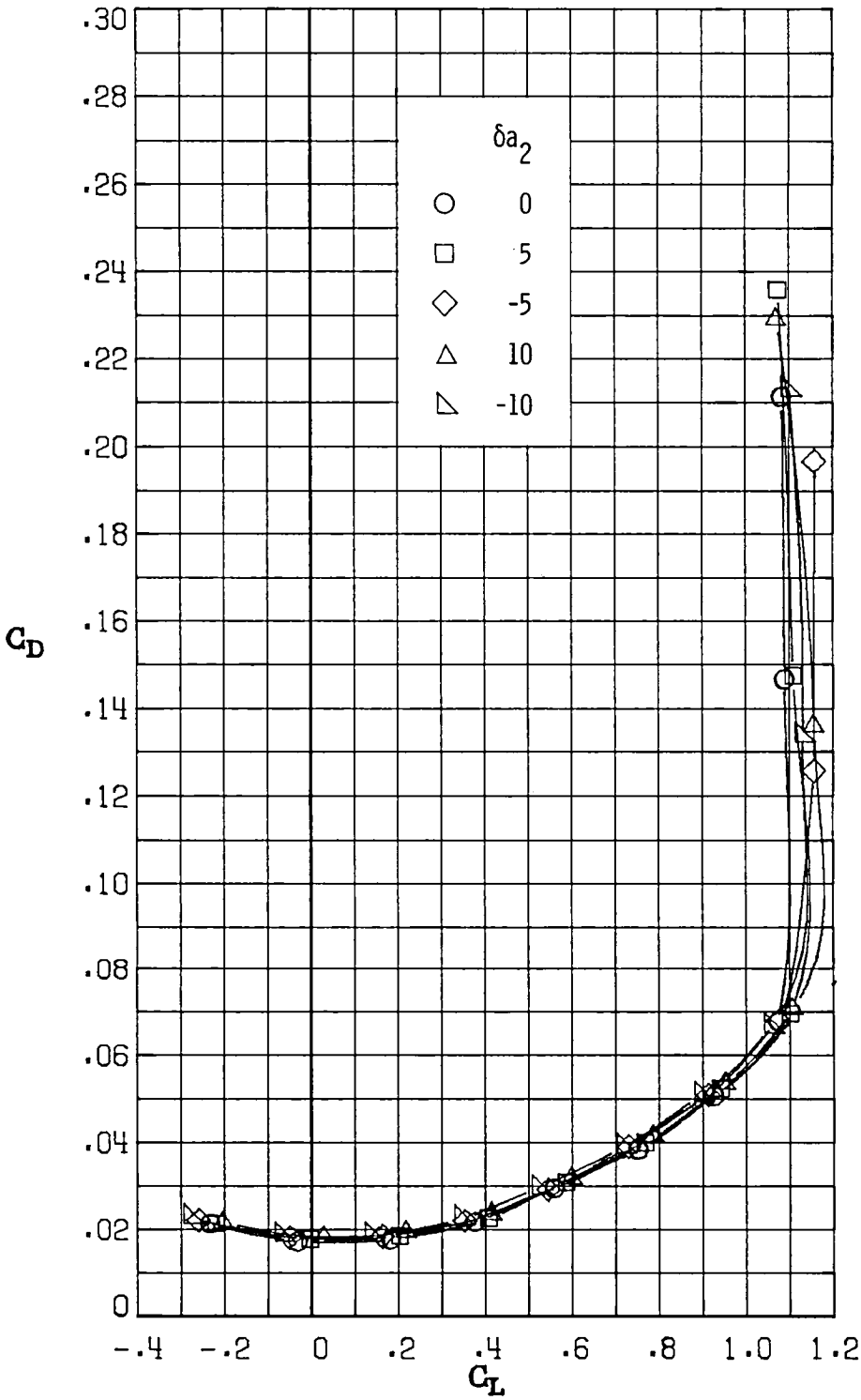

(a) $M_\infty = 0.30$.

Figure 10.- Variation of drag coefficient with lift coefficient for deflections of aileron (δa_2 in degrees). $\delta a_1 = 0°$; $\delta a_3 = 0°$.

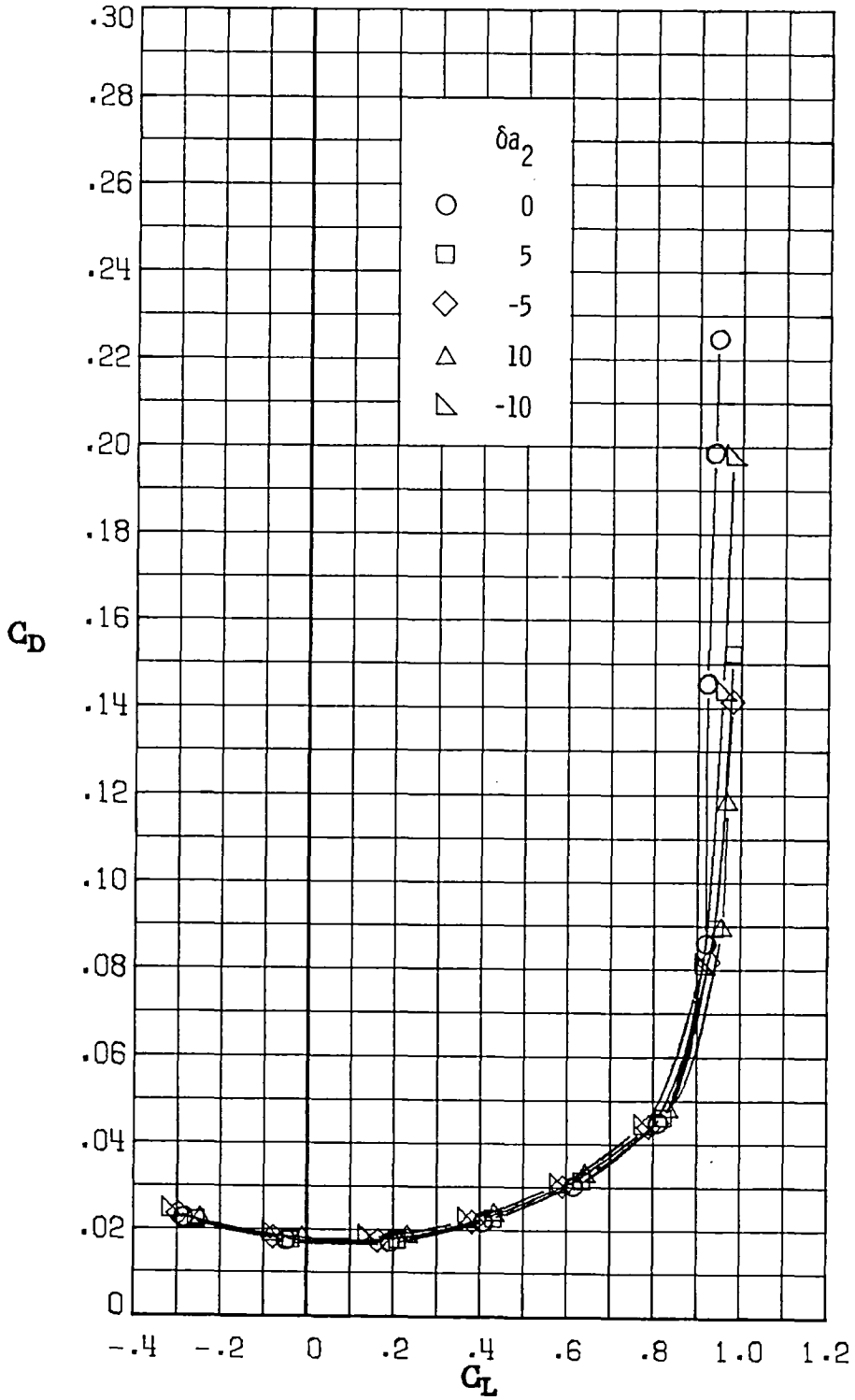

(b) $M_\infty = 0.60$.

Figure 10.- Continued.

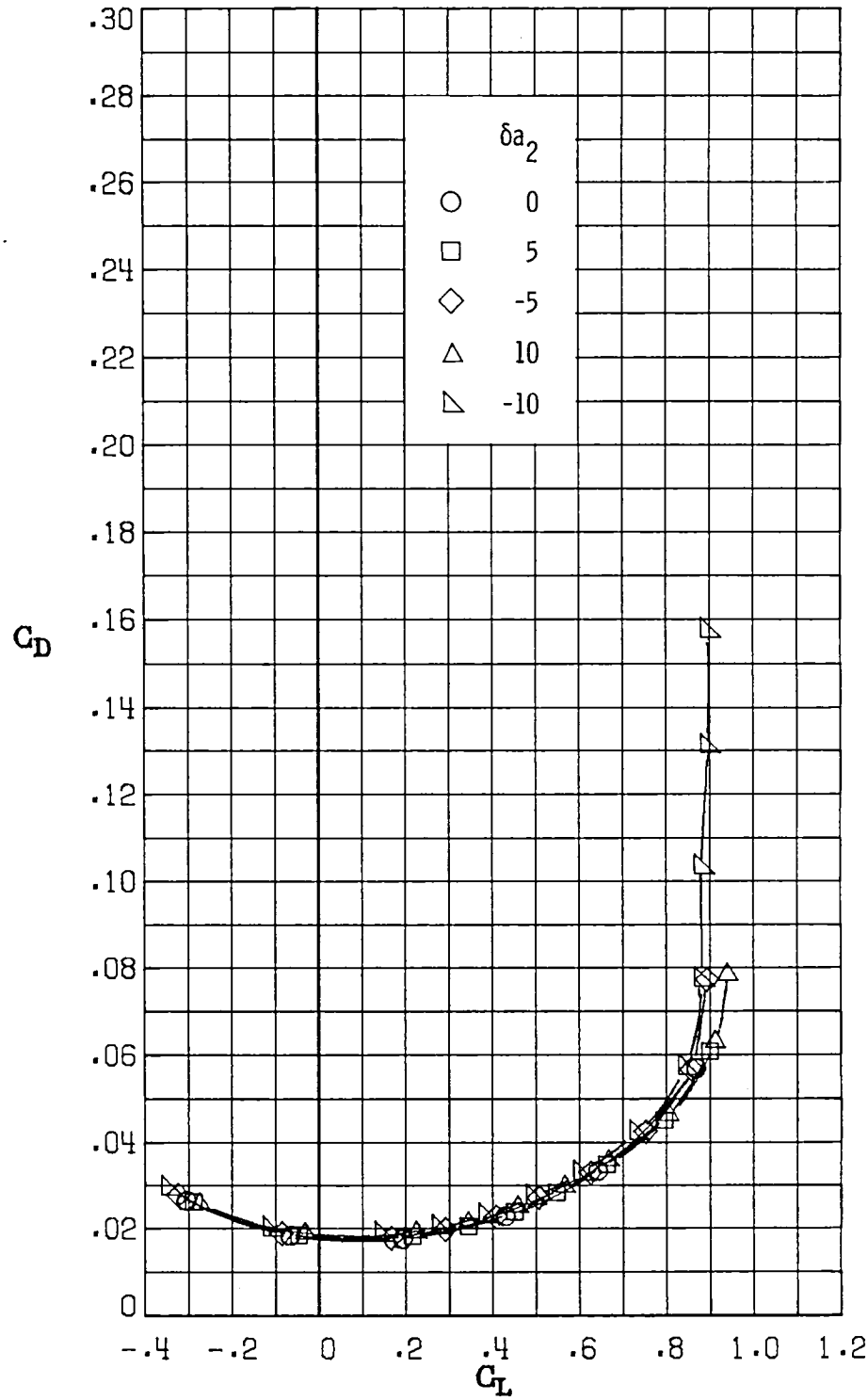

(c) $M_\infty = 0.70$.

Figure 10.- Continued.

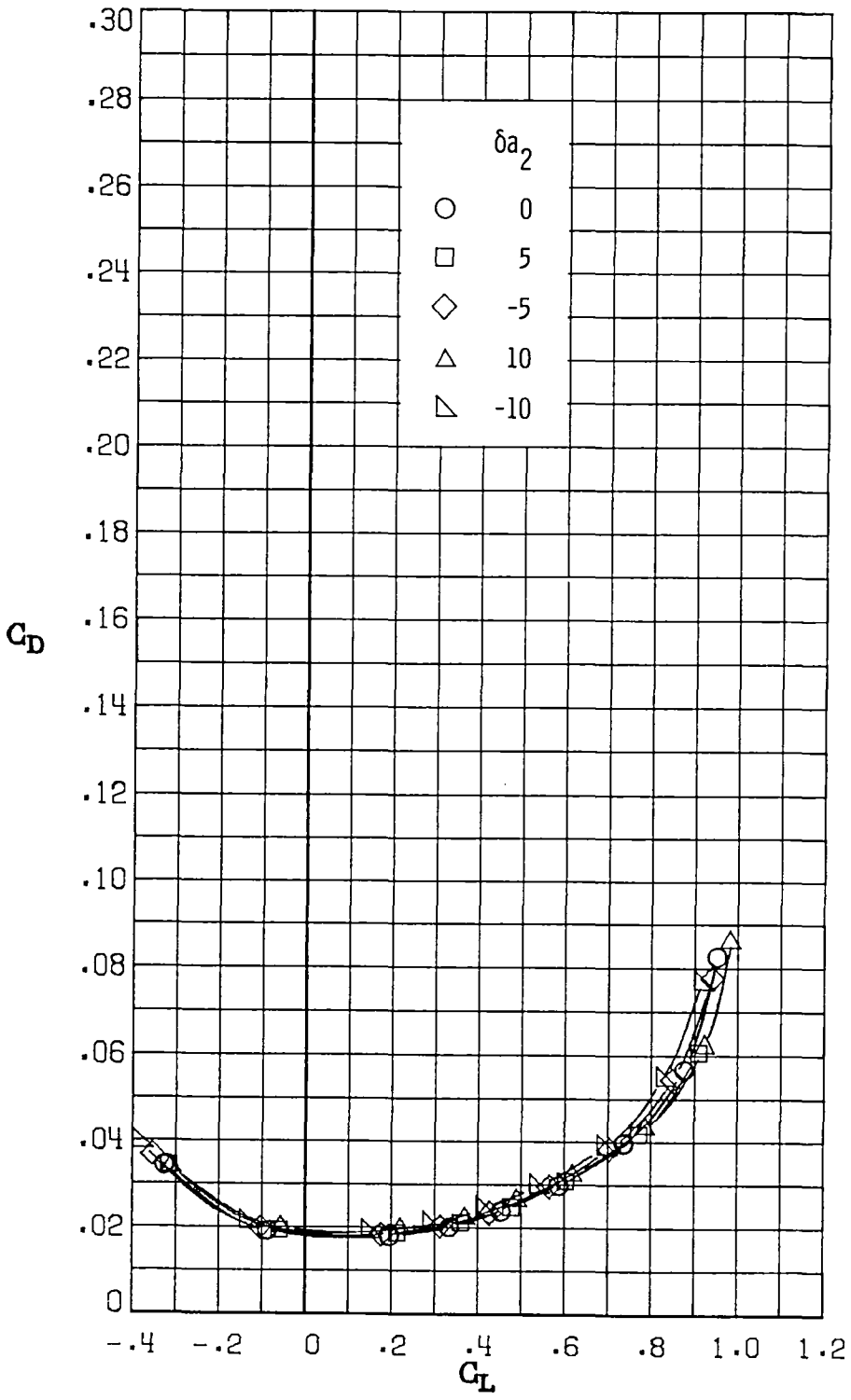

(d) $M_\infty = 0.77$.

Figure 10.- Continued.

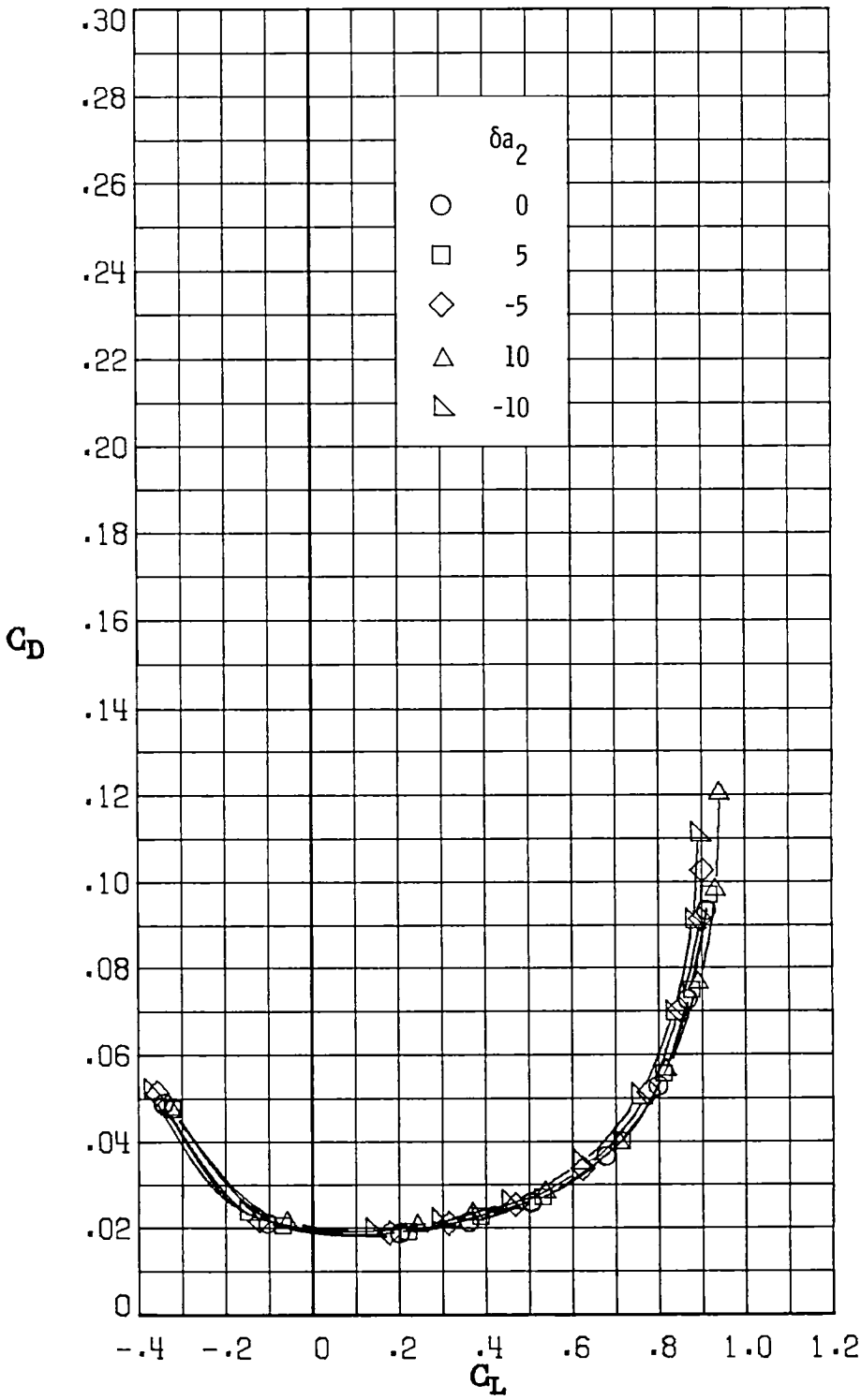

(e) $M_\infty = 0.81$.

Figure 10.- Continued.

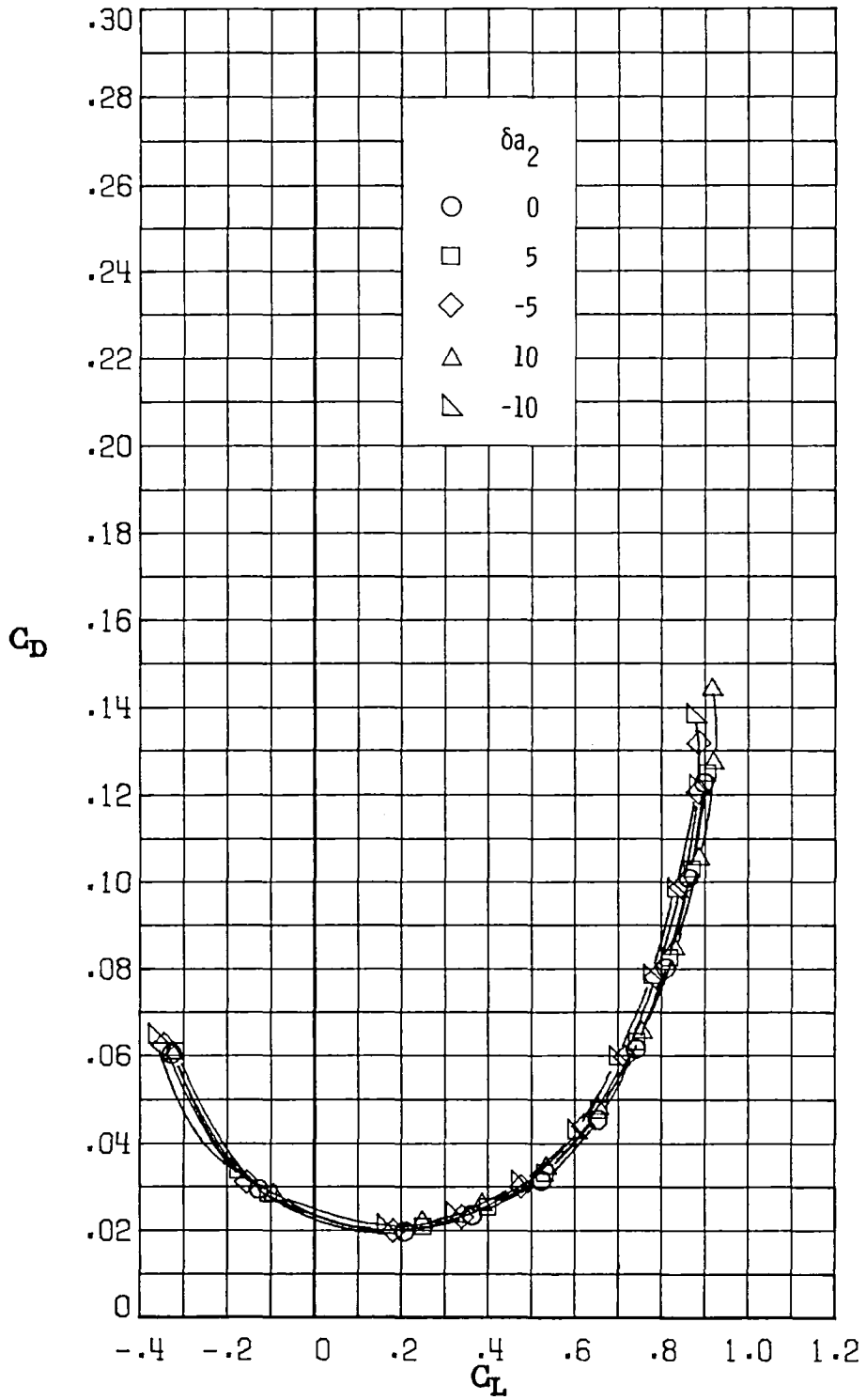

(f) $M_\infty = 0.84$.

Figure 10.- Continued.

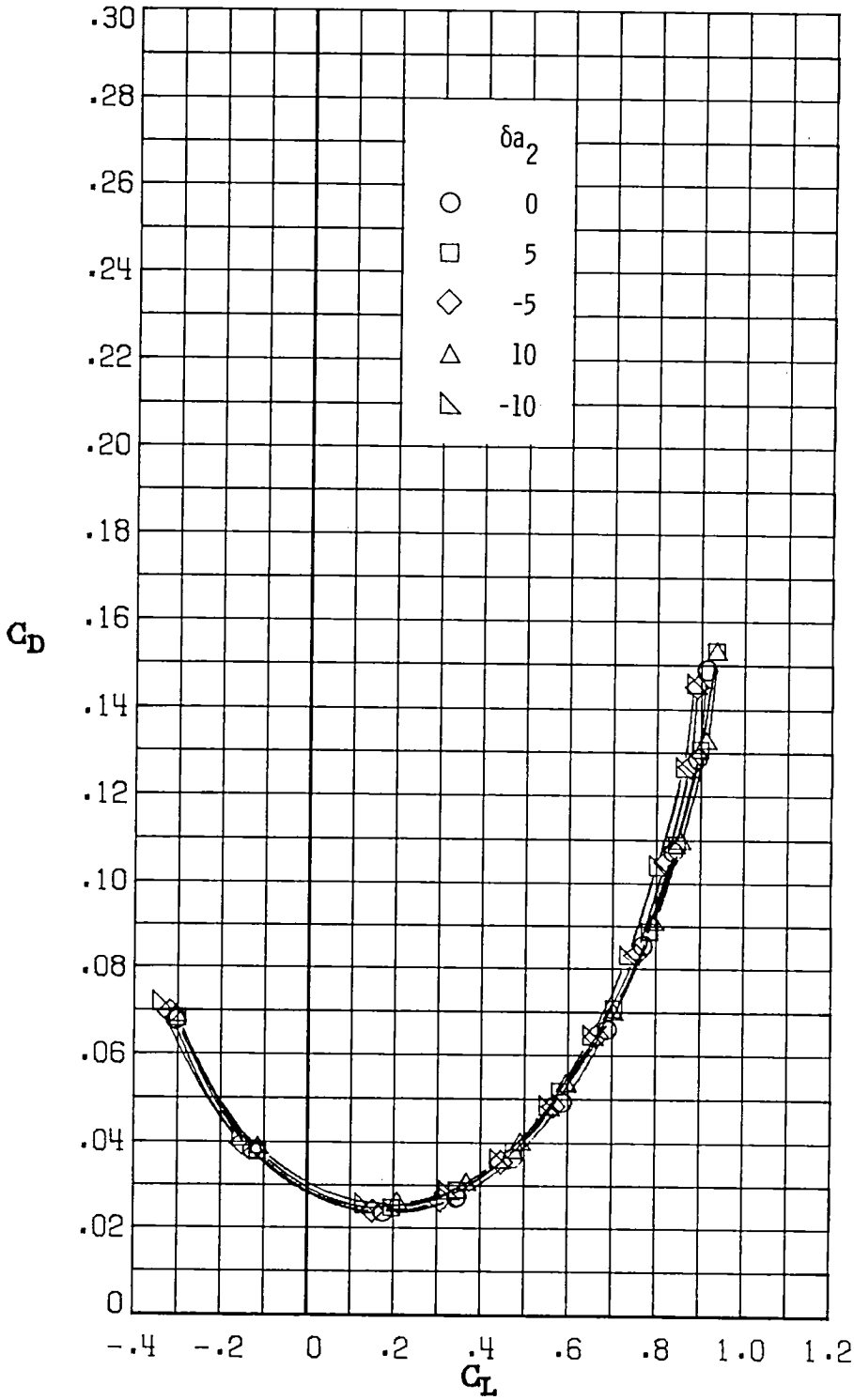

(g) $M_\infty = 0.86$.

Figure 10.- Concluded.

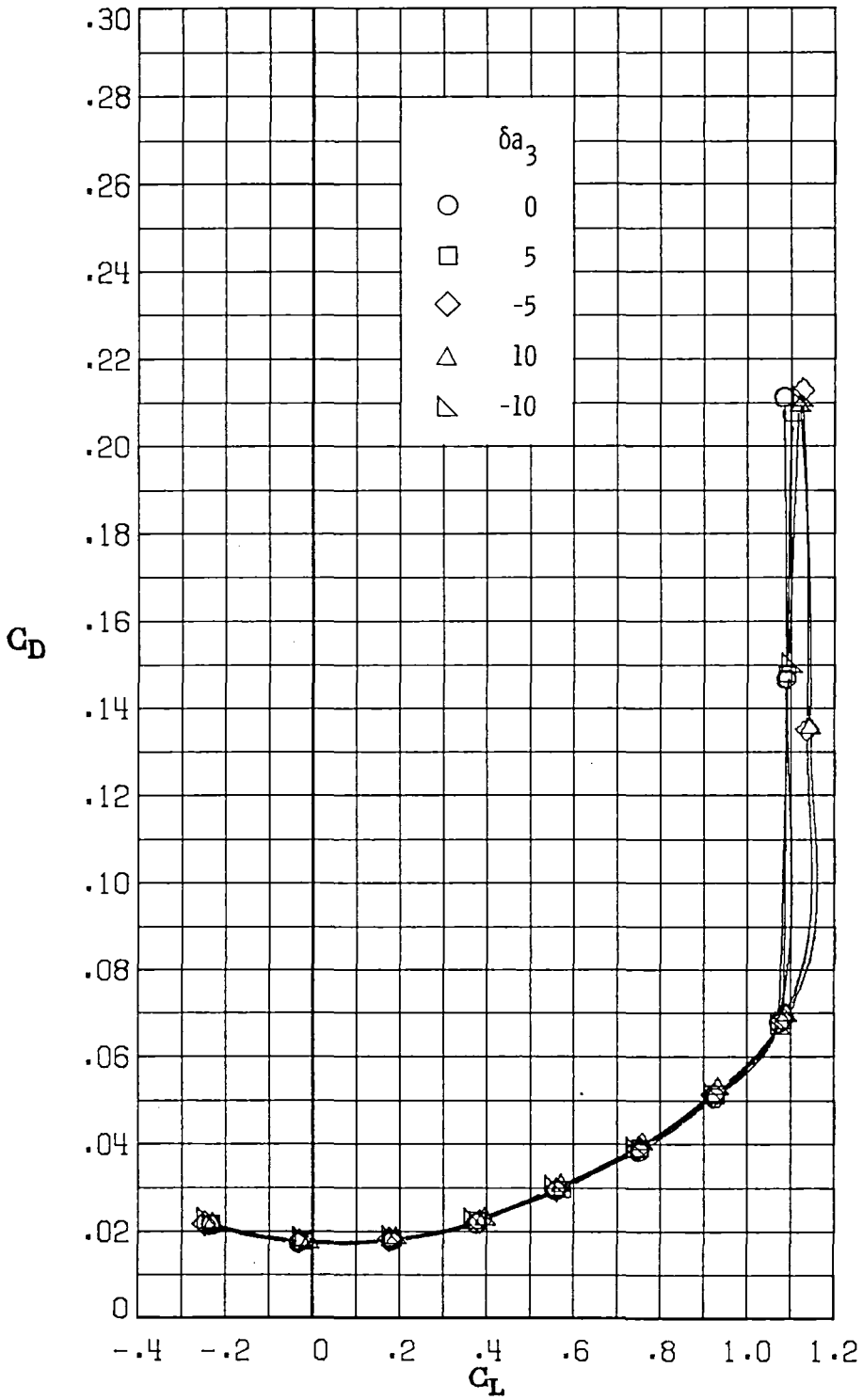

(a) $M_\infty = 0.30$.

Figure 11.- Variation of drag coefficient with lift coefficient for deflections of aileron 3 (δa_3 in degrees). $\delta a_1 = 0°$; $\delta a_2 = 0°$.

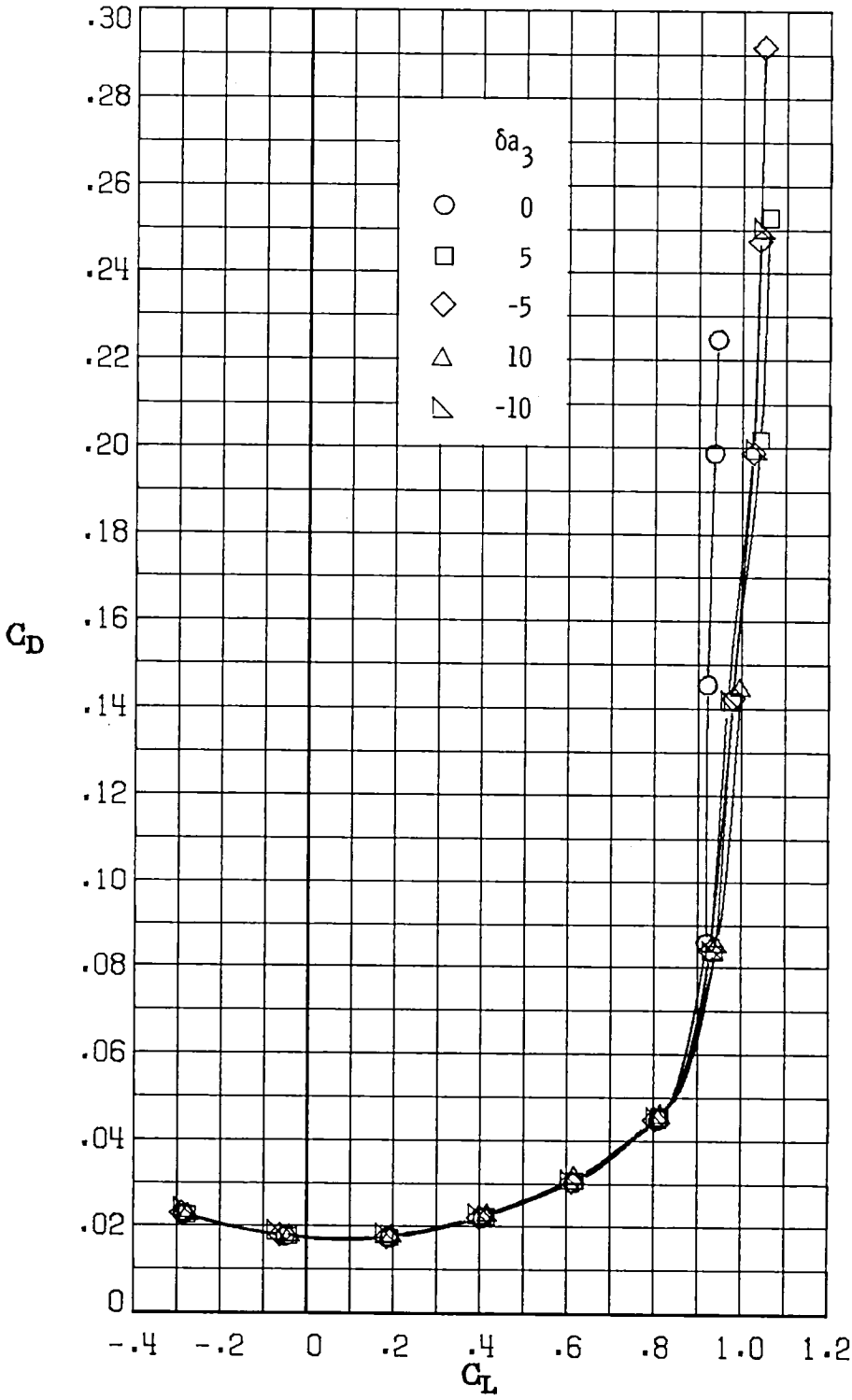

(b) $M_\infty = 0.60$.

Figure 11.- Continued.

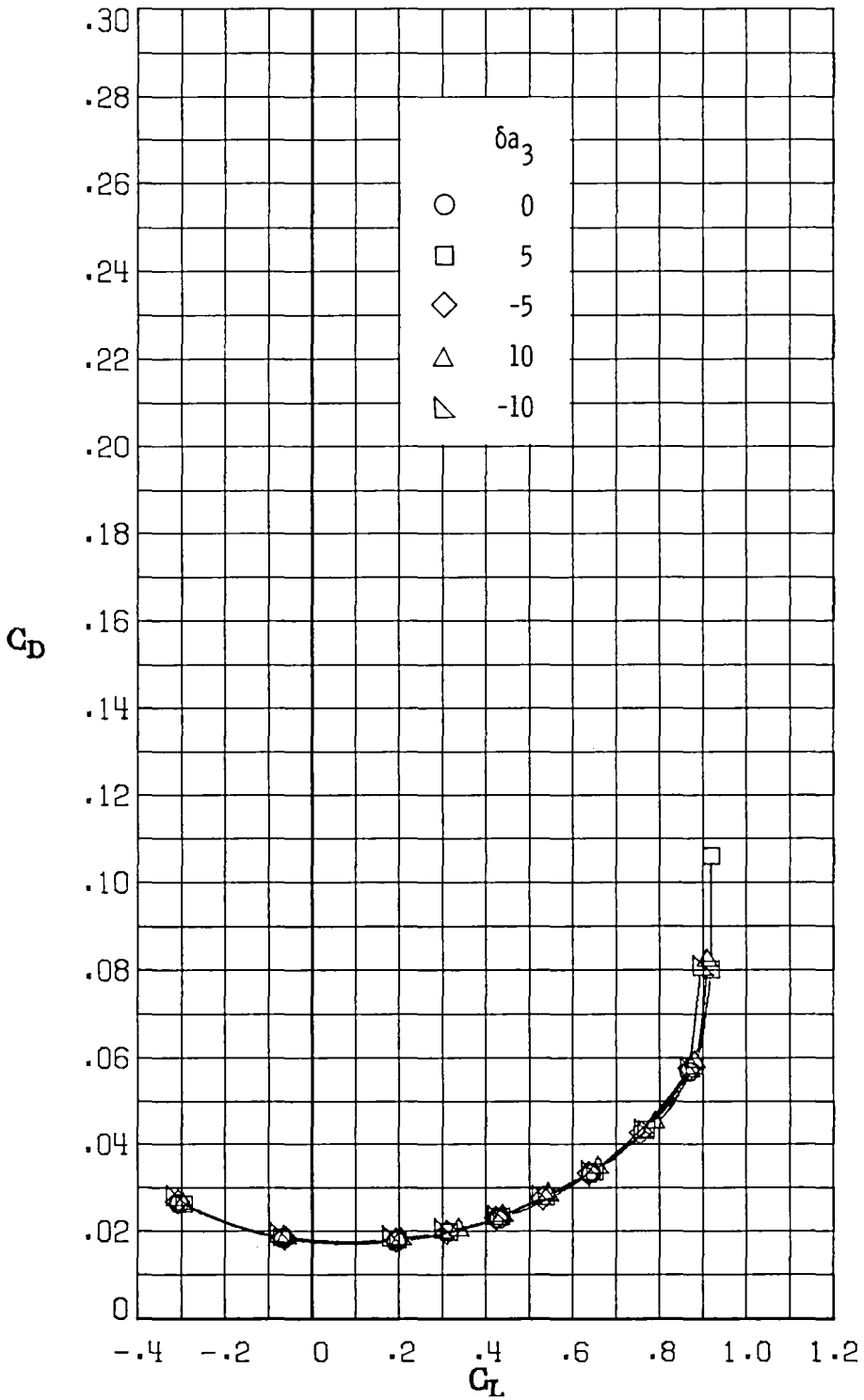

(c) $M_\infty = 0.70$.

Figure 11.- Continued.

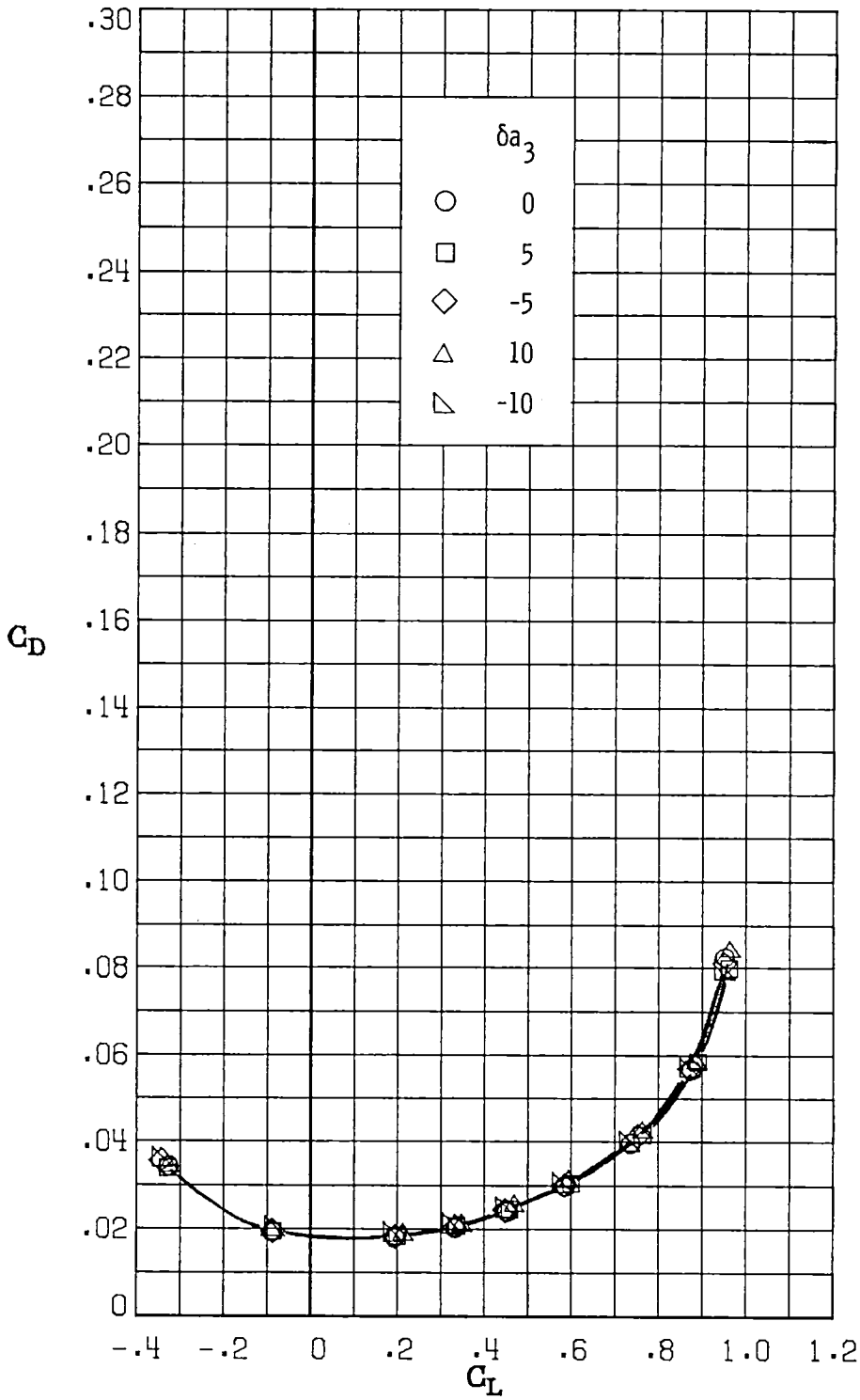

(d) $M_\infty = 0.77$.

Figure 11.- Continued.

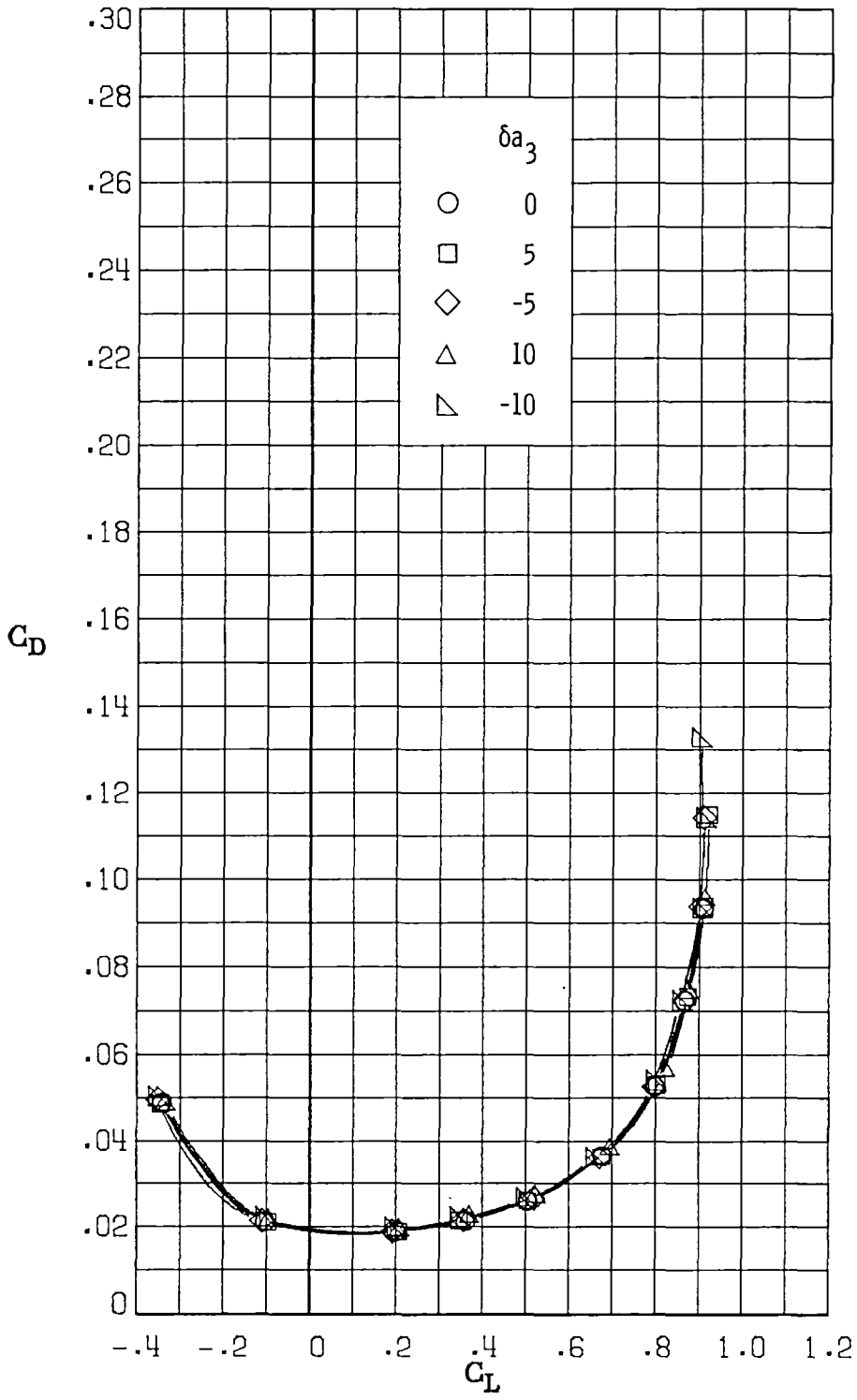

(e) $M_\infty = 0.81$.

Figure 11.- Continued.

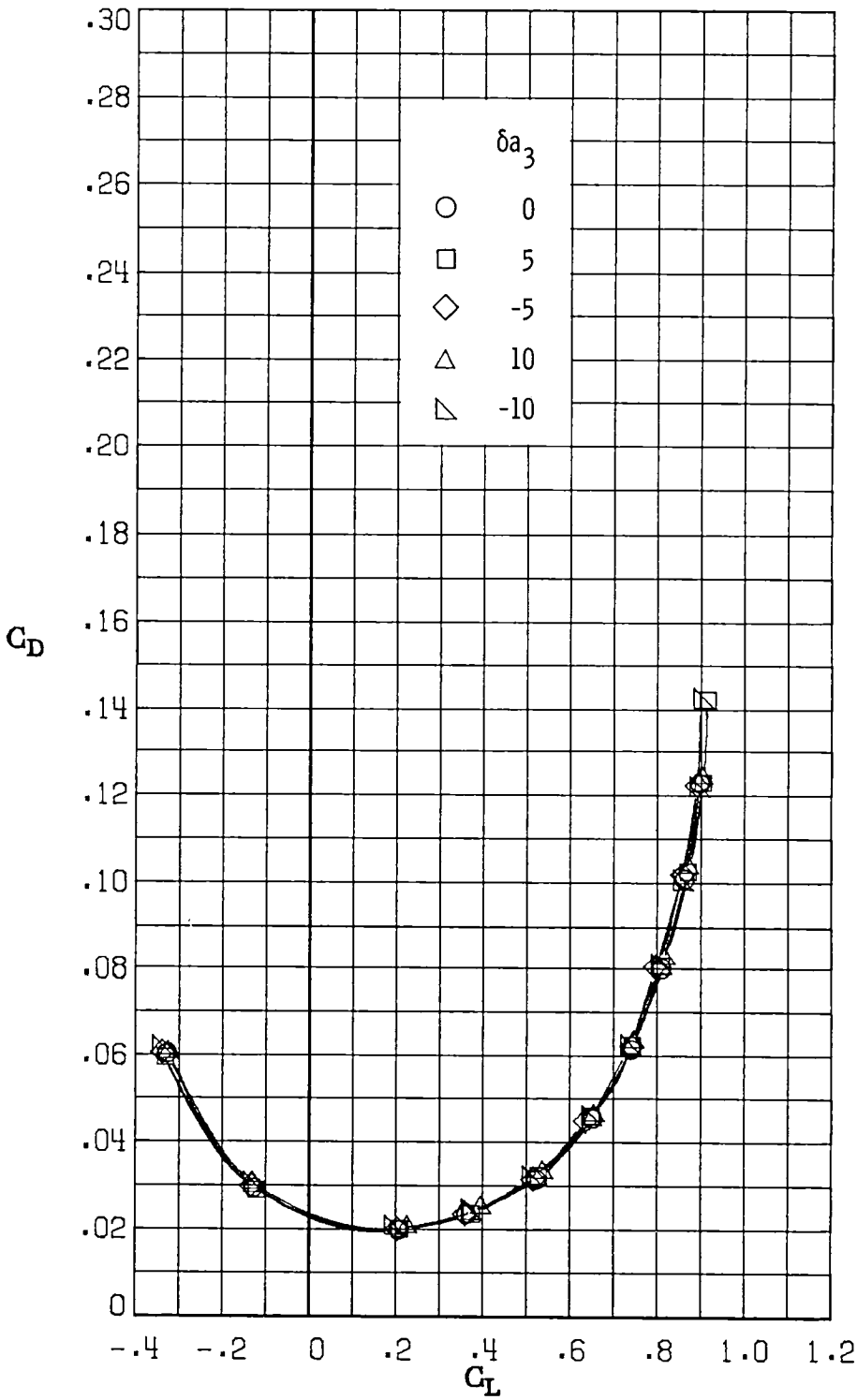

(f) $M_\infty = 0.84$.

Figure 11.- Continued.

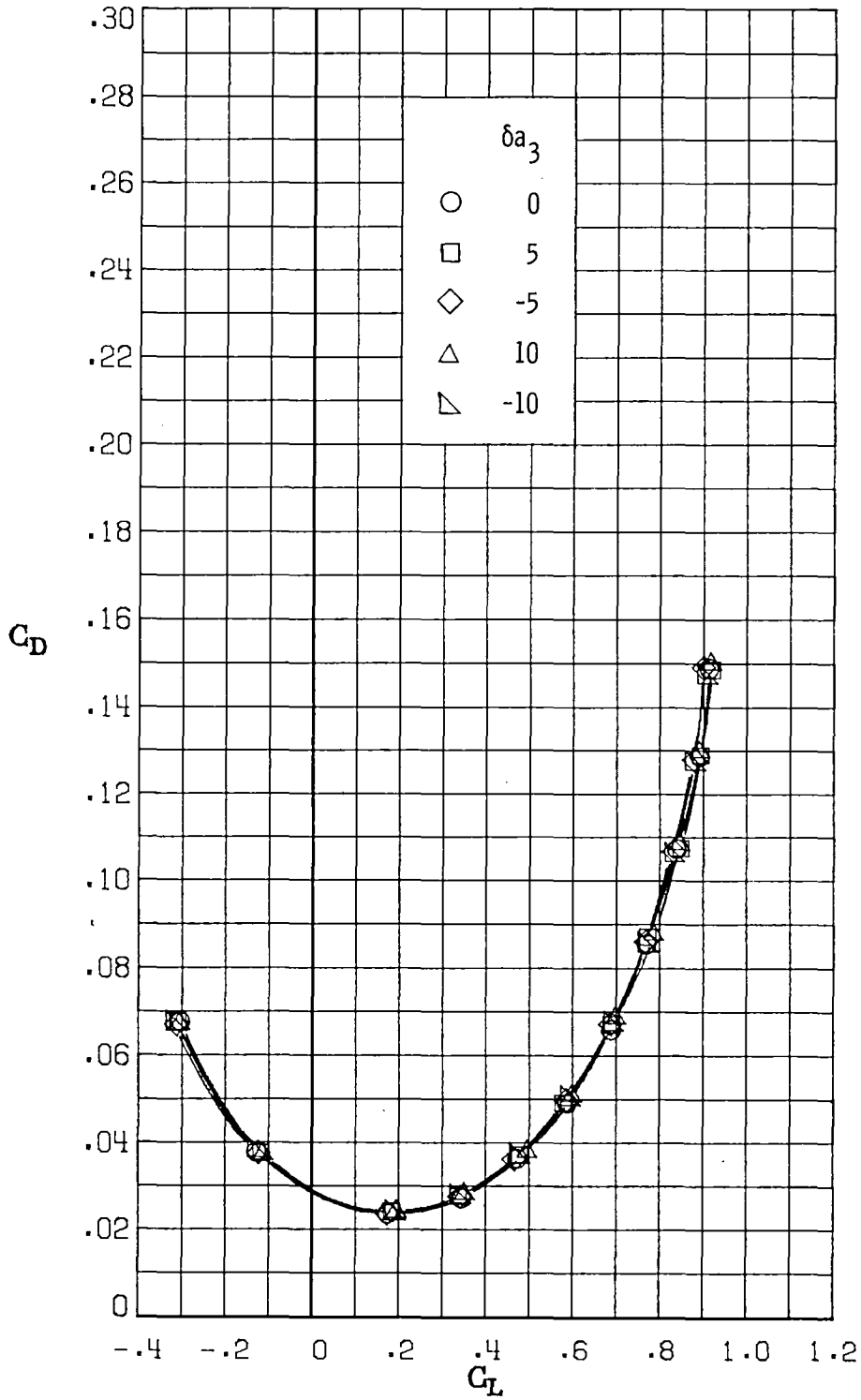

(g) $M_\infty = 0.86$.

Figure 11.- Concluded.

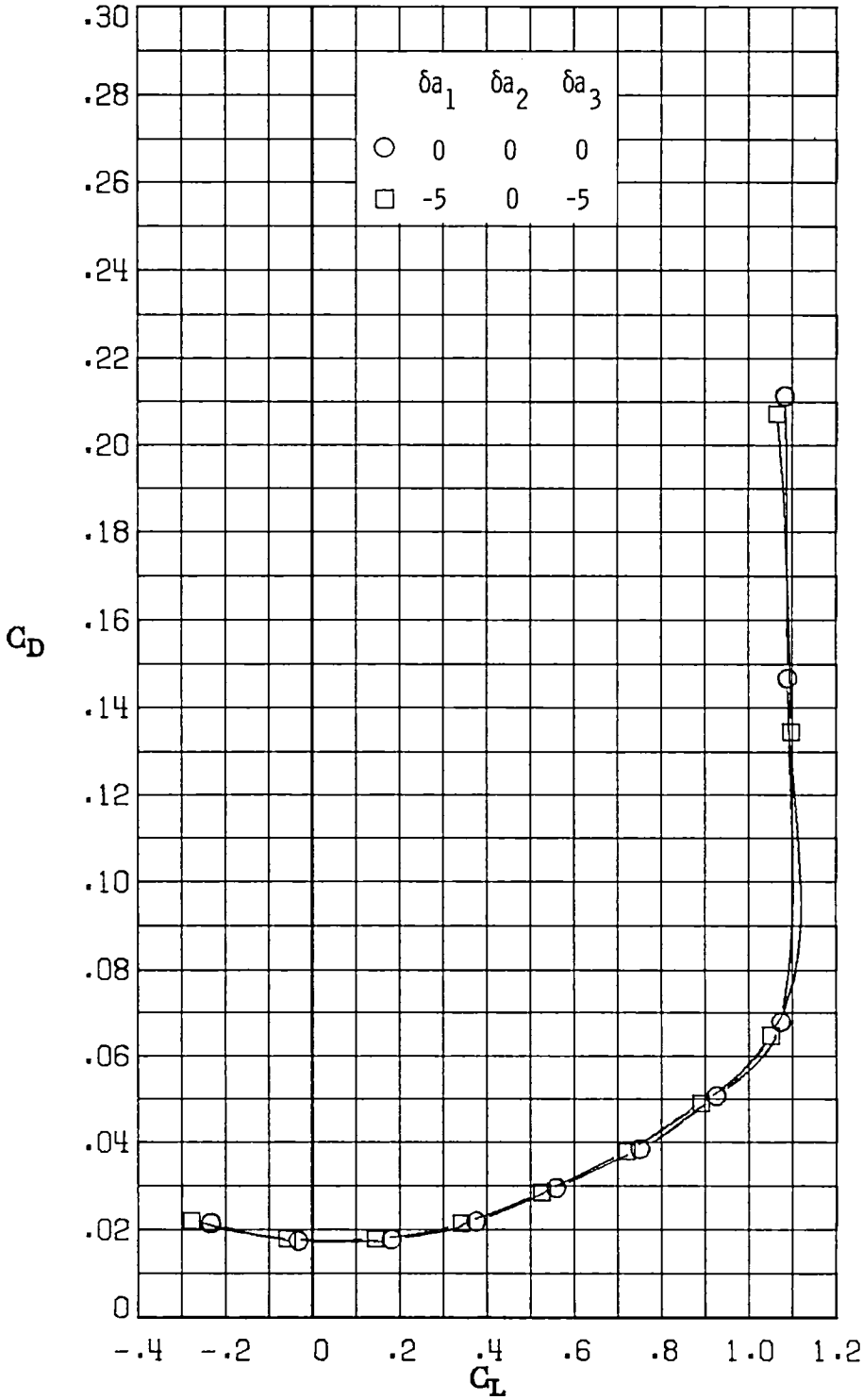

(a) $M_\infty = 0.30$.

Figure 12.- Variation of drag coefficient with lift coefficient for $\delta a_1 = -5°$, $\delta a_2 = 0°$, $\delta a_3 = -5°$.

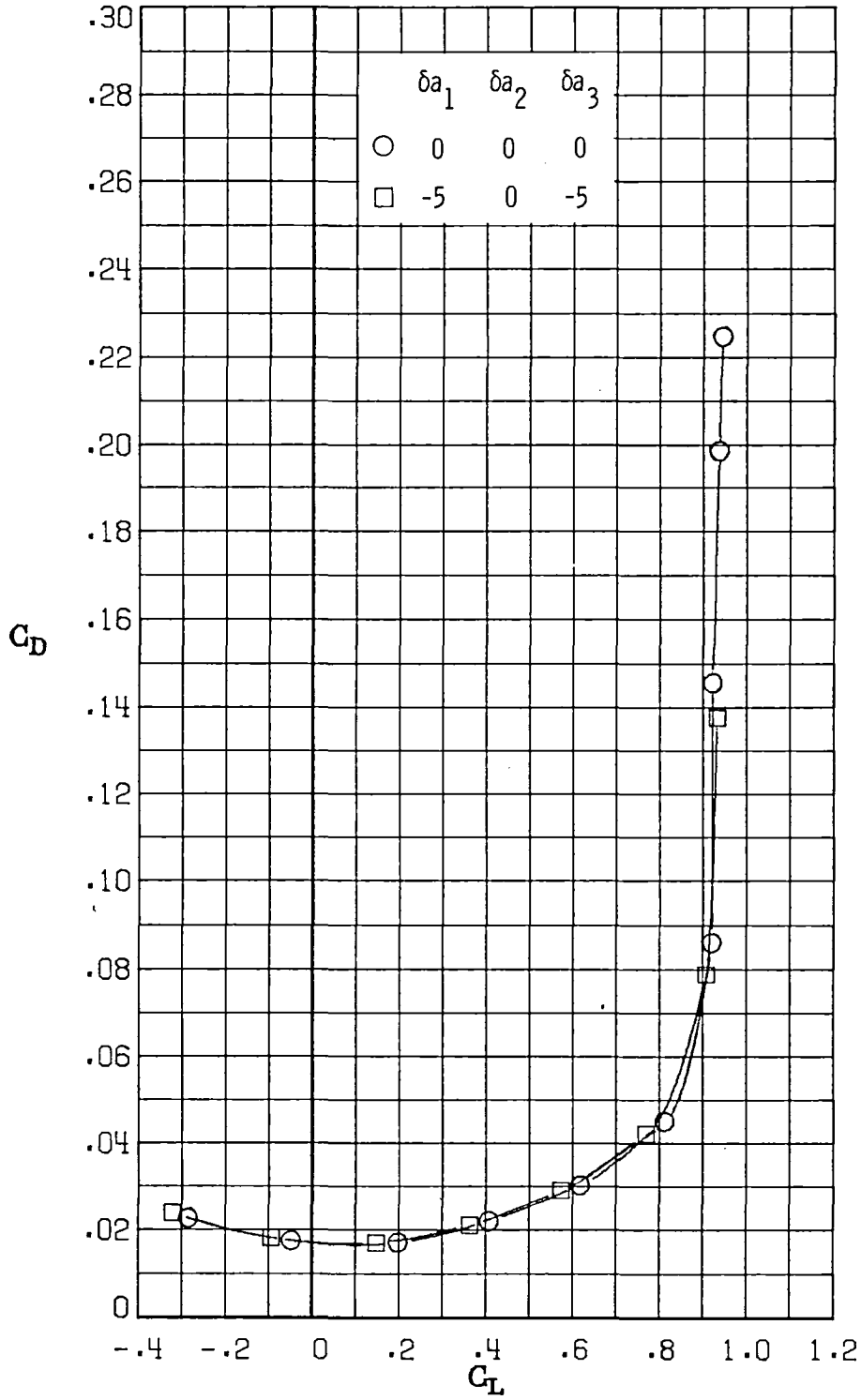

(b) $M_\infty = 0.60$.

Figure 12.- Continued.

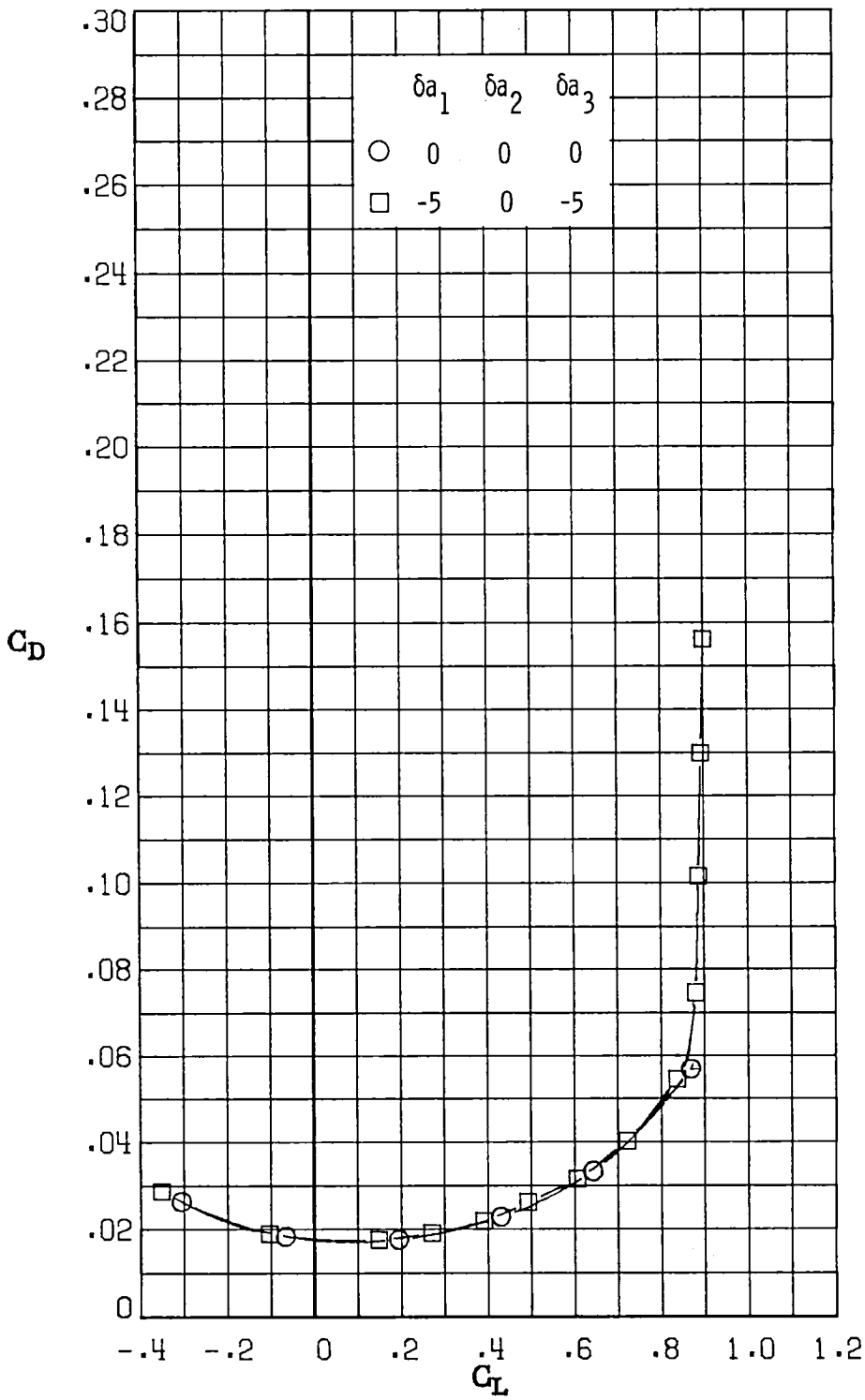

(c) $M_\infty = 0.70$.

Figure 12.- Continued.

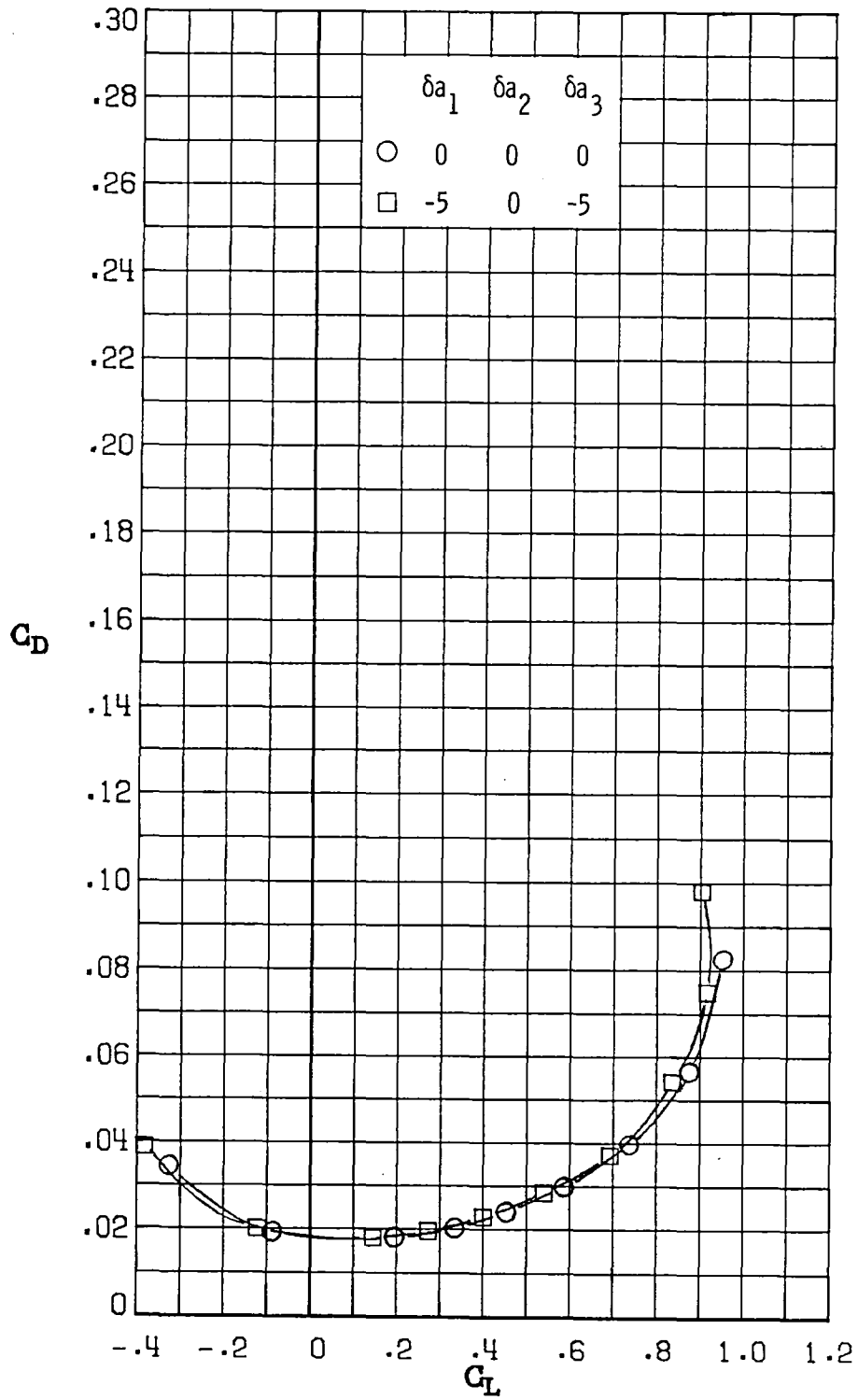

(d) $M_\infty = 0.77$.

Figure 12.- Continued.

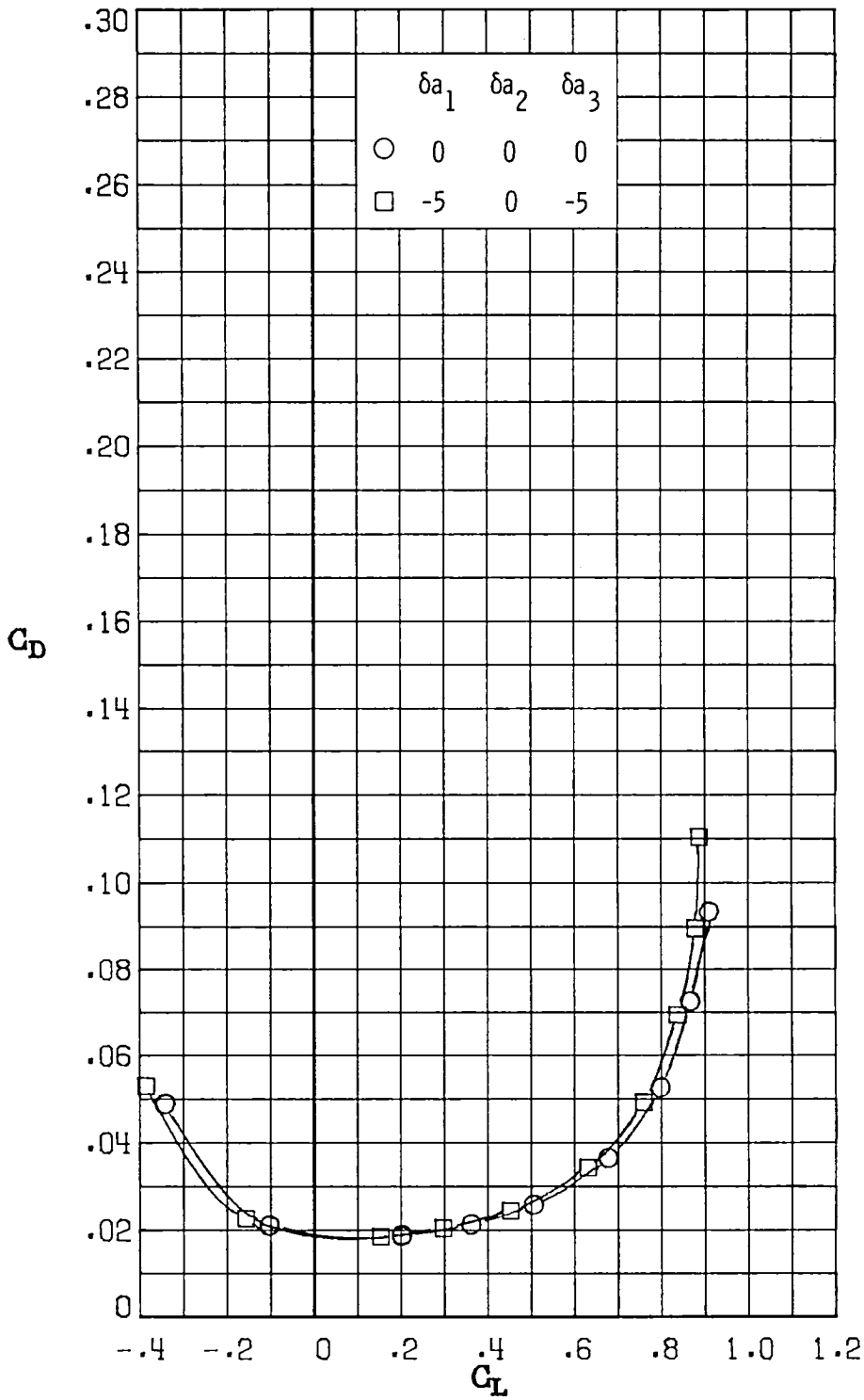

(e) $M_\infty = 0.81$.

Figure 12.- Continued.

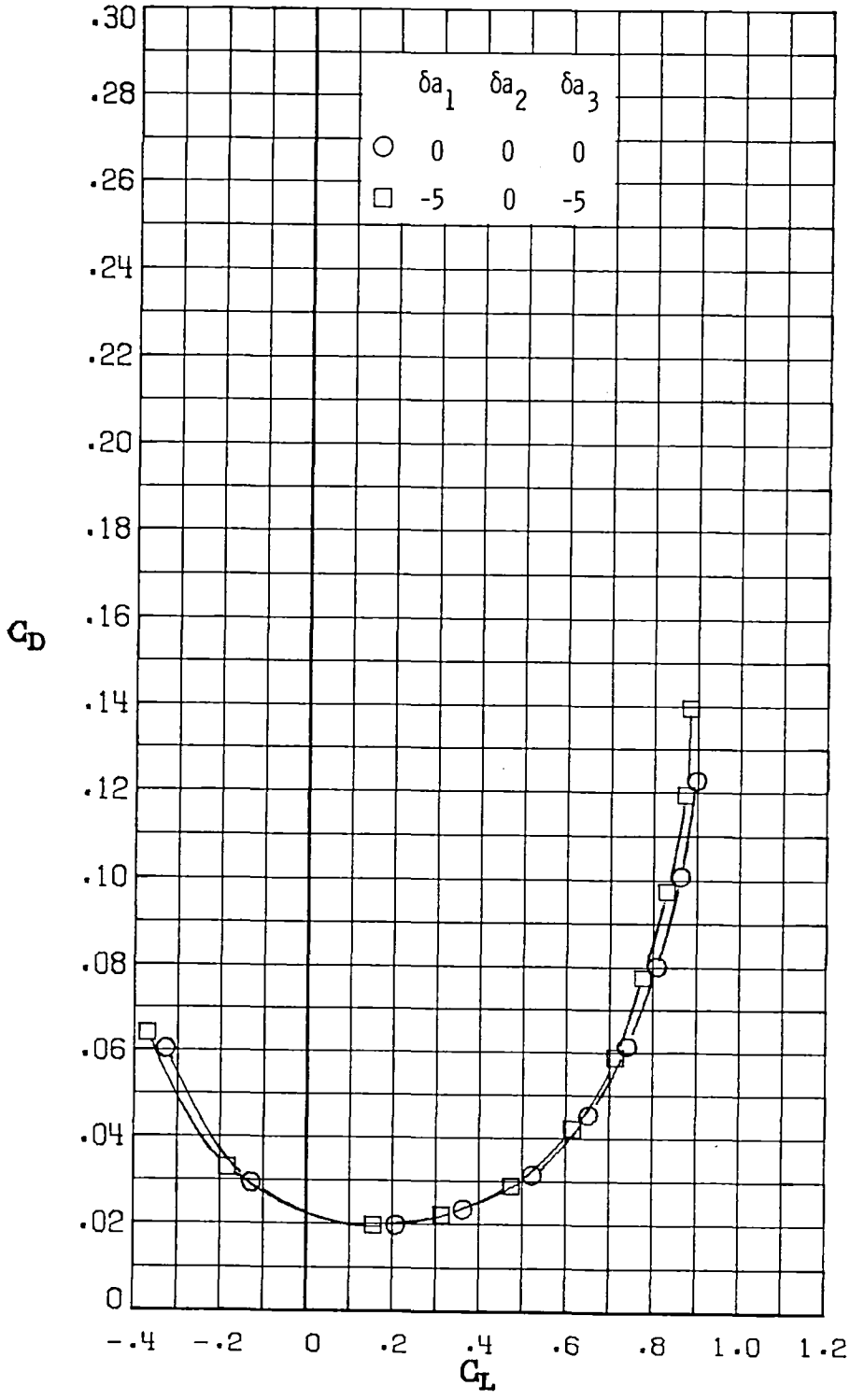

(f) $M_\infty = 0.84$.

Figure 12.- Continued.

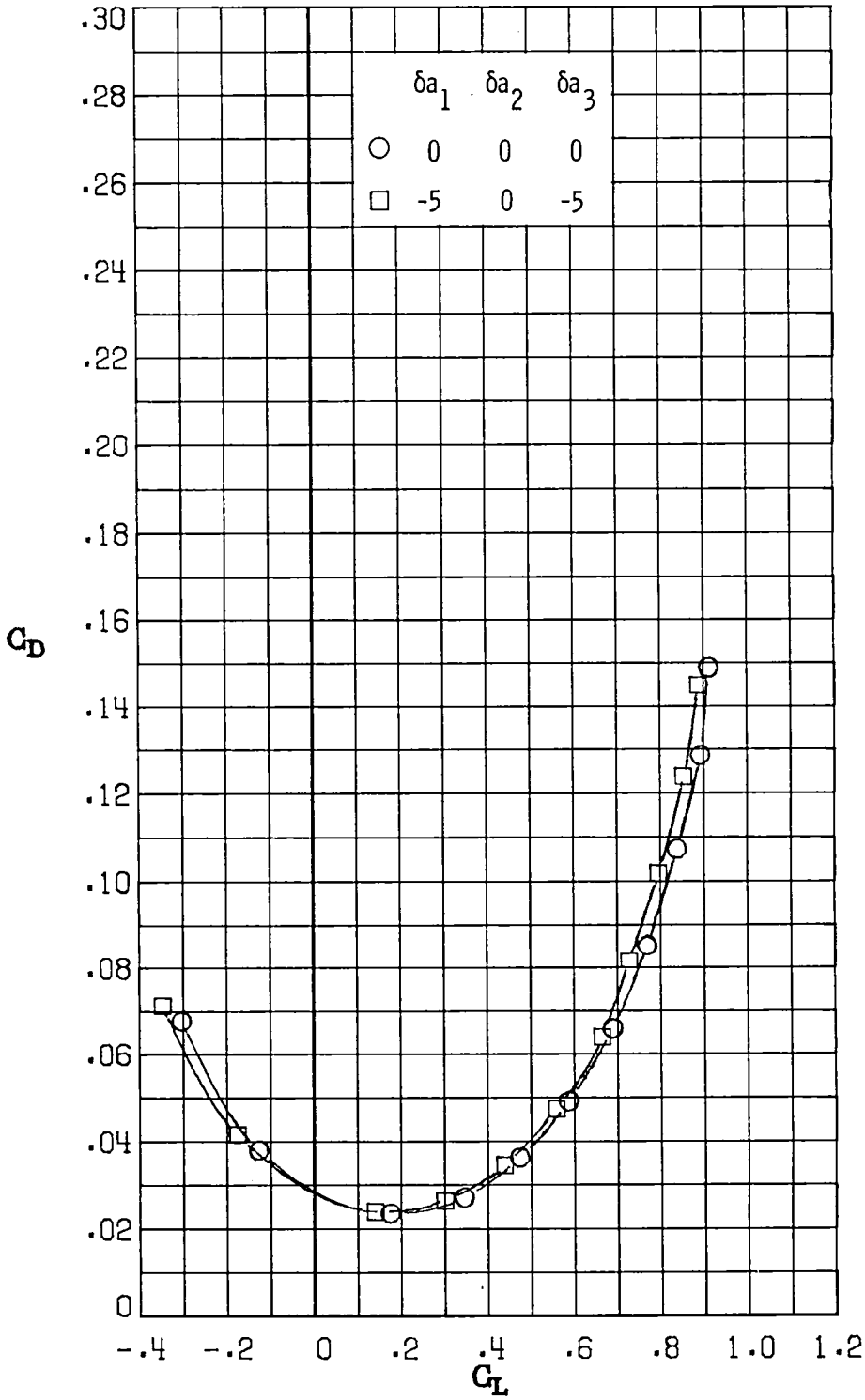

(g) $M_\infty = 0.86$.

Figure 12.- Concluded.

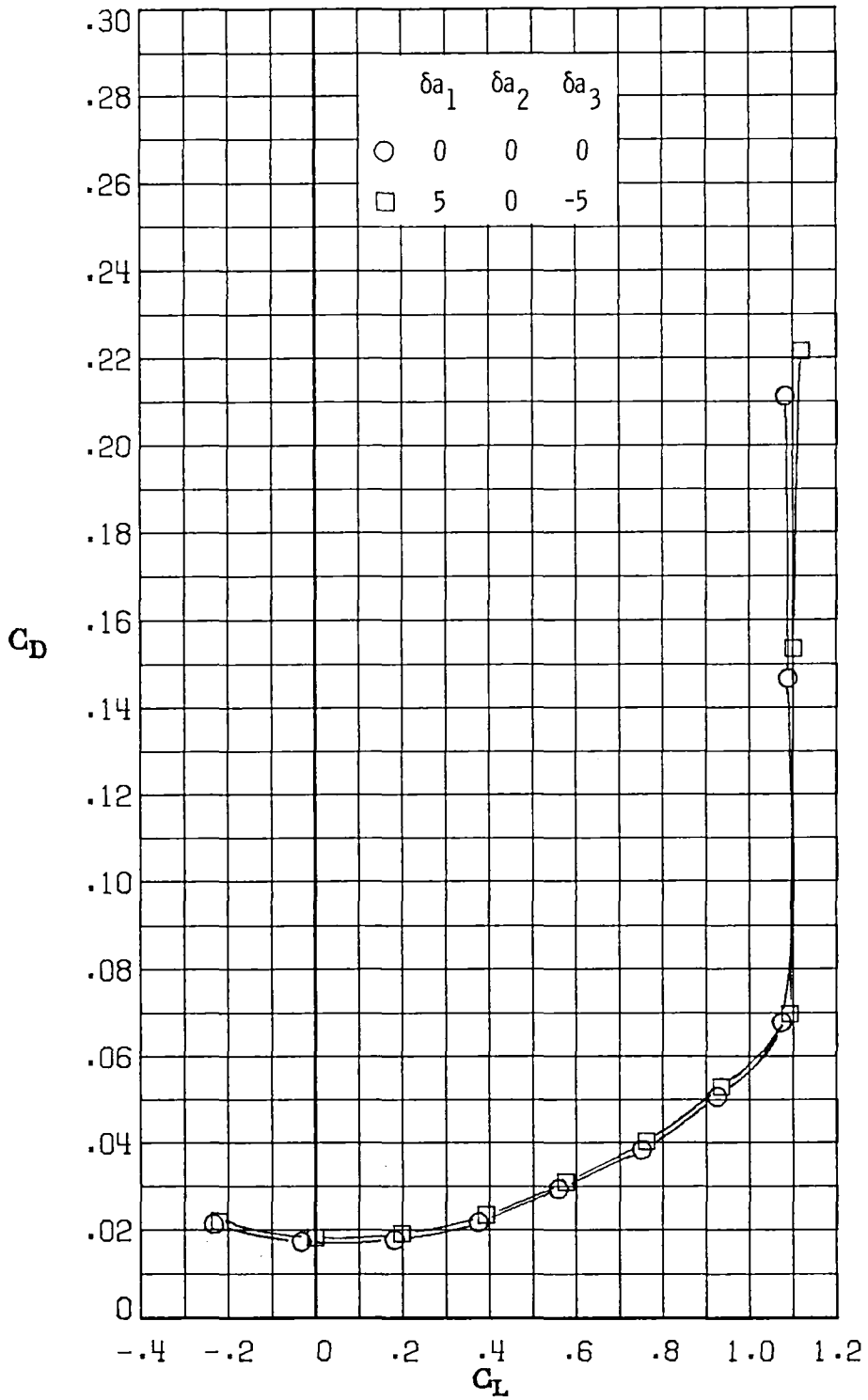

(a) $M_\infty = 0.30$.

Figure 13.- Variation of drag coefficient with lift coefficient for $\delta a_1 = 5°$, $\delta a_2 = 0°$, $\delta a_3 = -5°$.

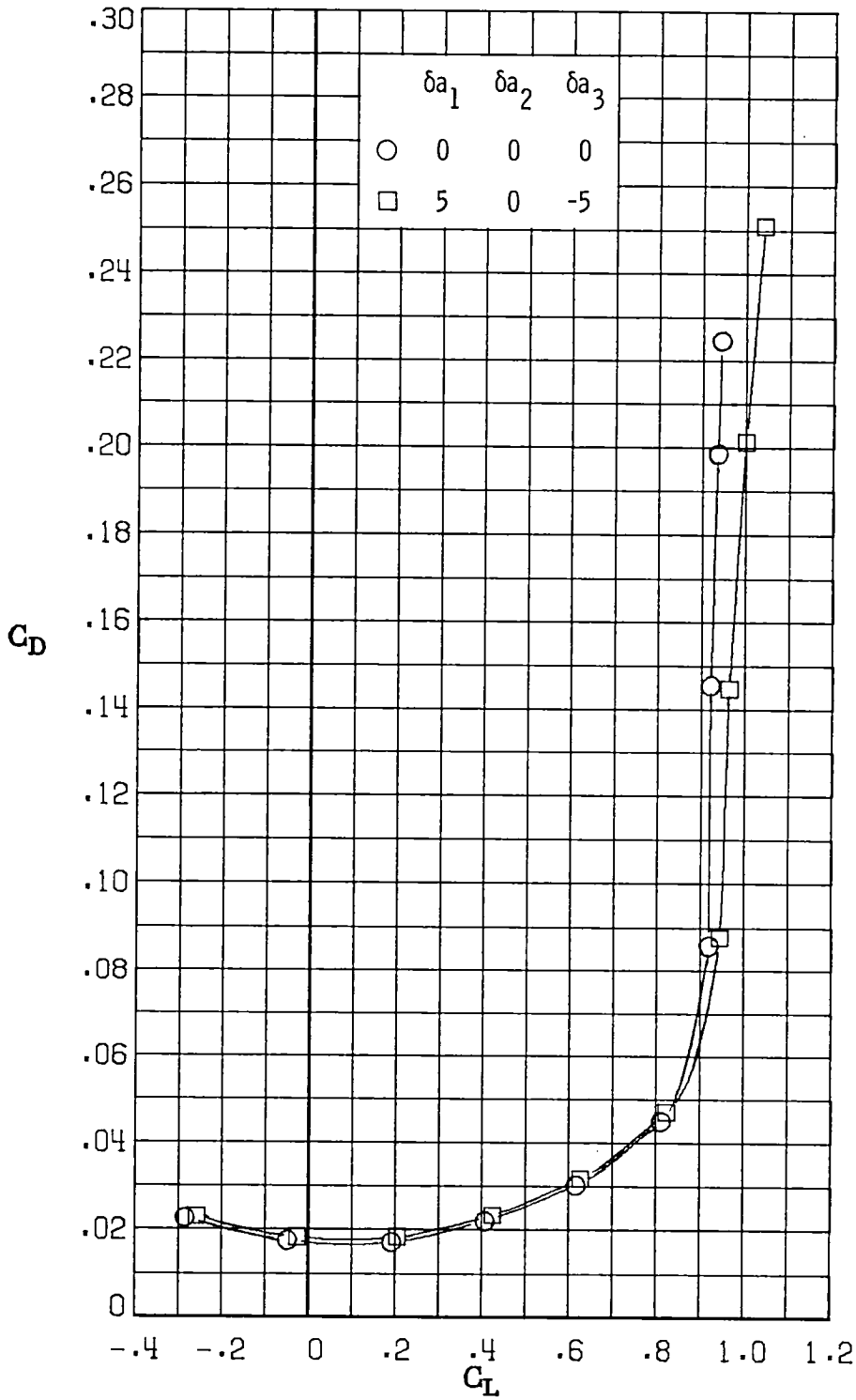

(b) $M_\infty = 0.60$.

Figure 13.- Continued.

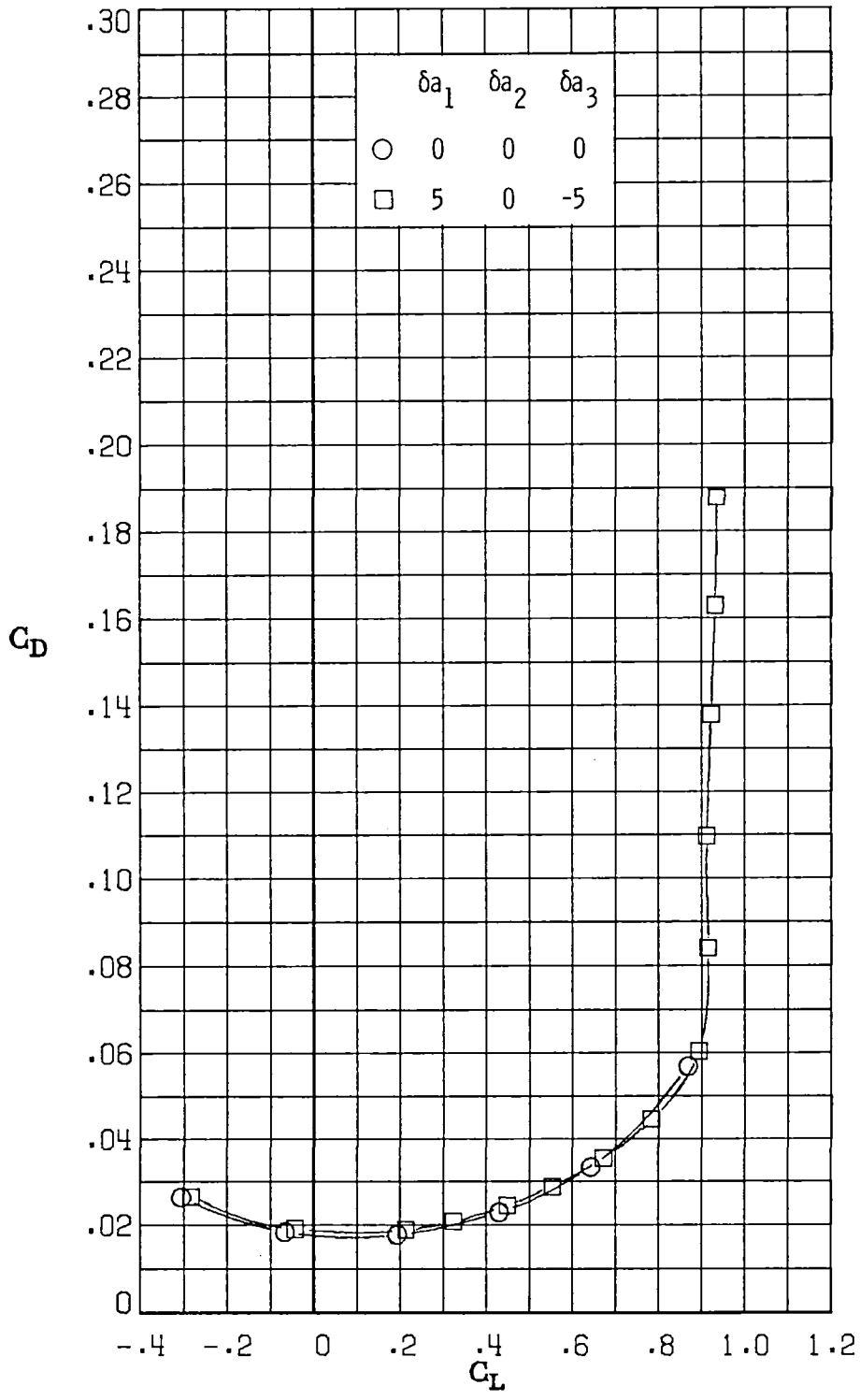

(c) $M_\infty = 0.70$.

Figure 13.- Continued.

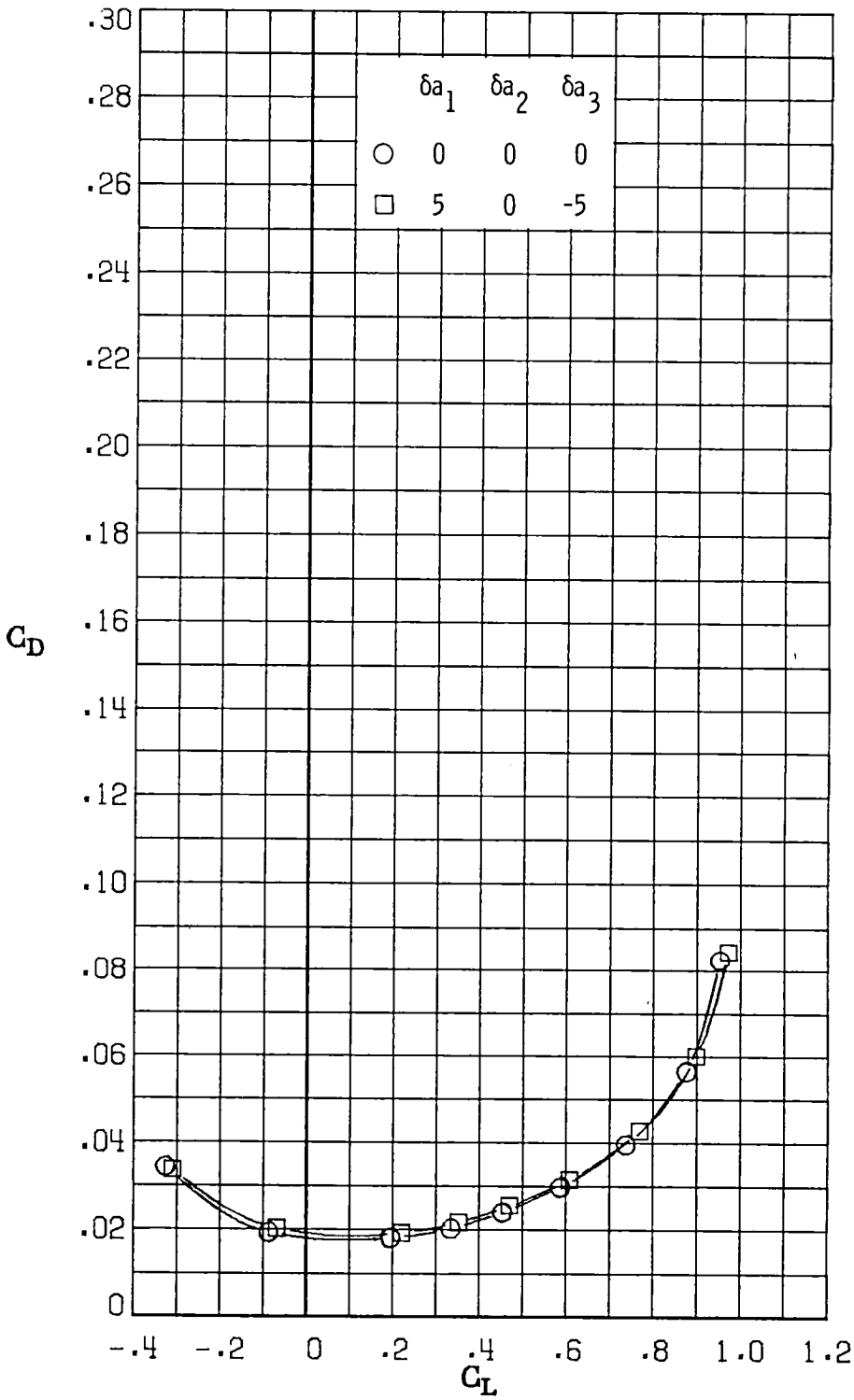

(d) $M_\infty = 0.77$.

Figure 13.- Continued.

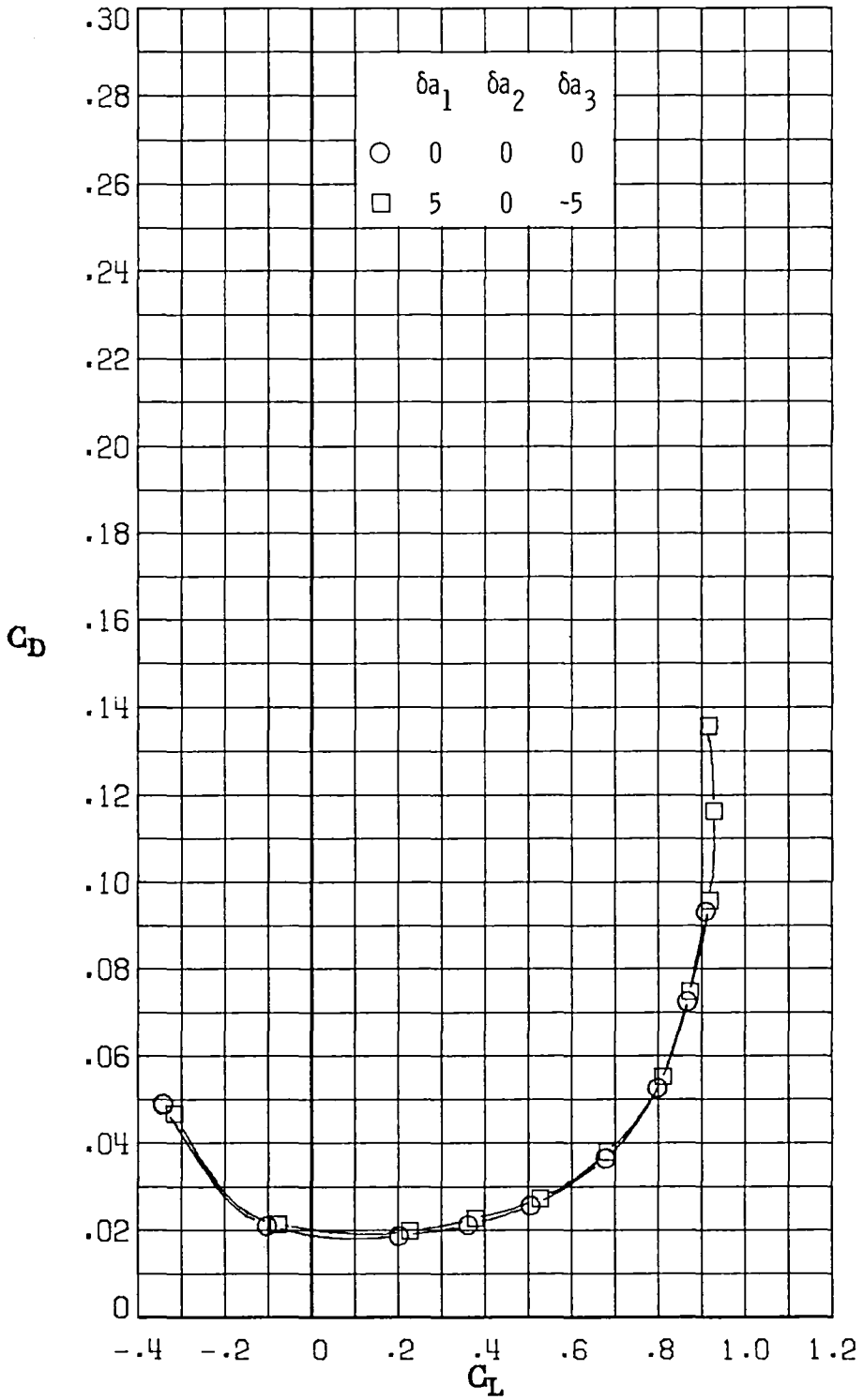

(e) $M_\infty = 0.81$.

Figure 13.- Continued.

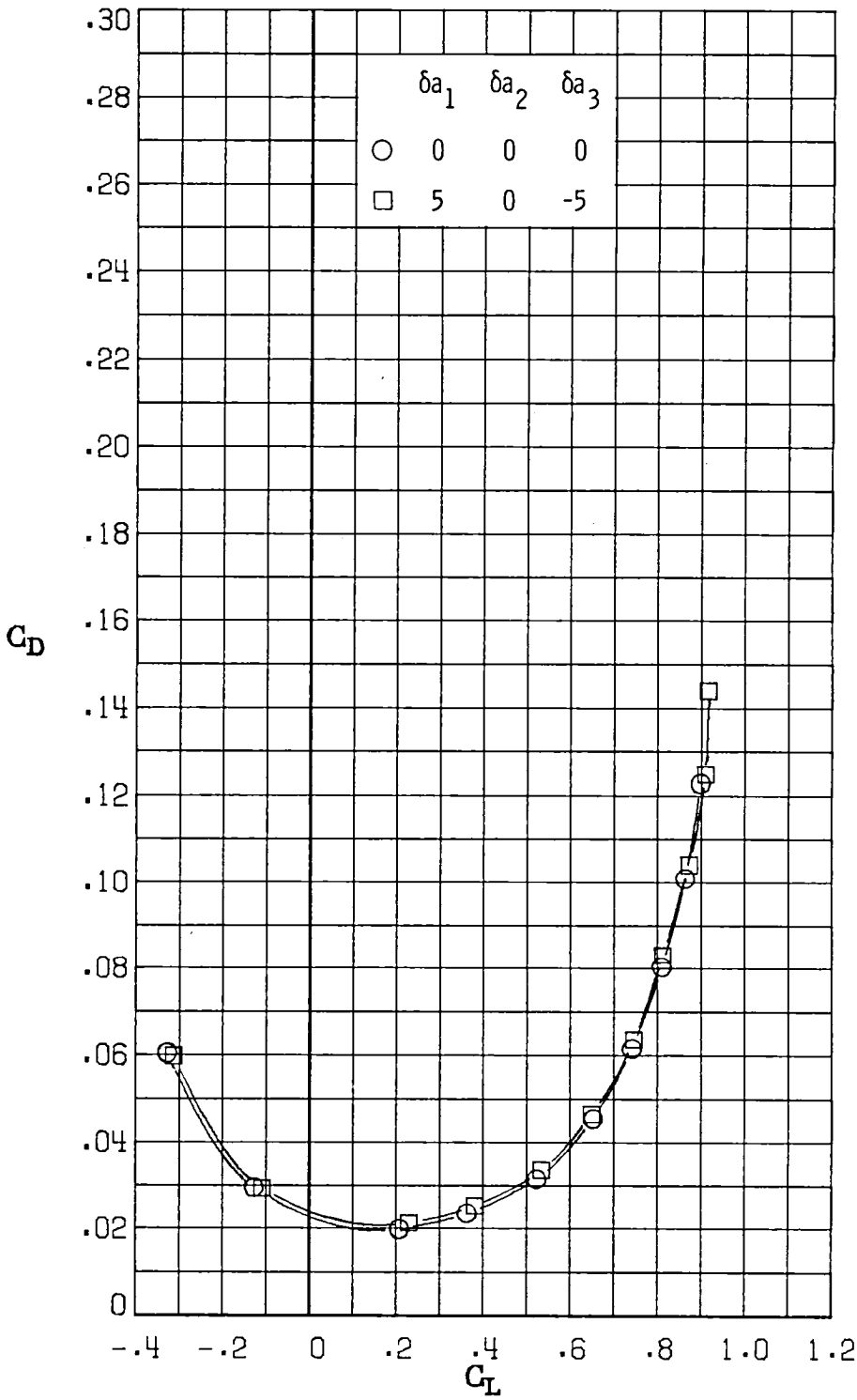

(f) $M_\infty = 0.84$.

Figure 13.- Continued.

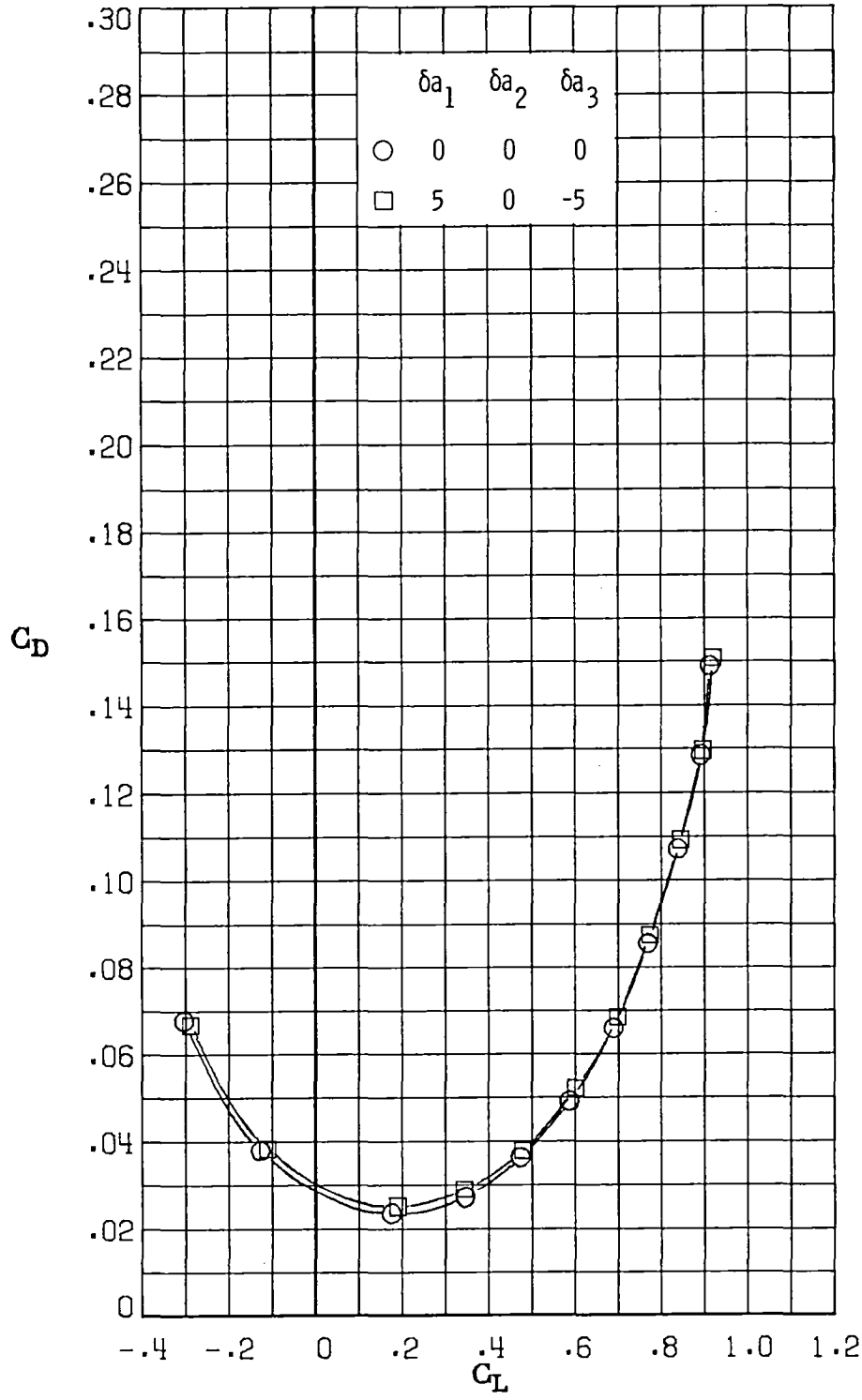

(g) $M_\infty = 0.86$.

Figure 13.- Concluded.

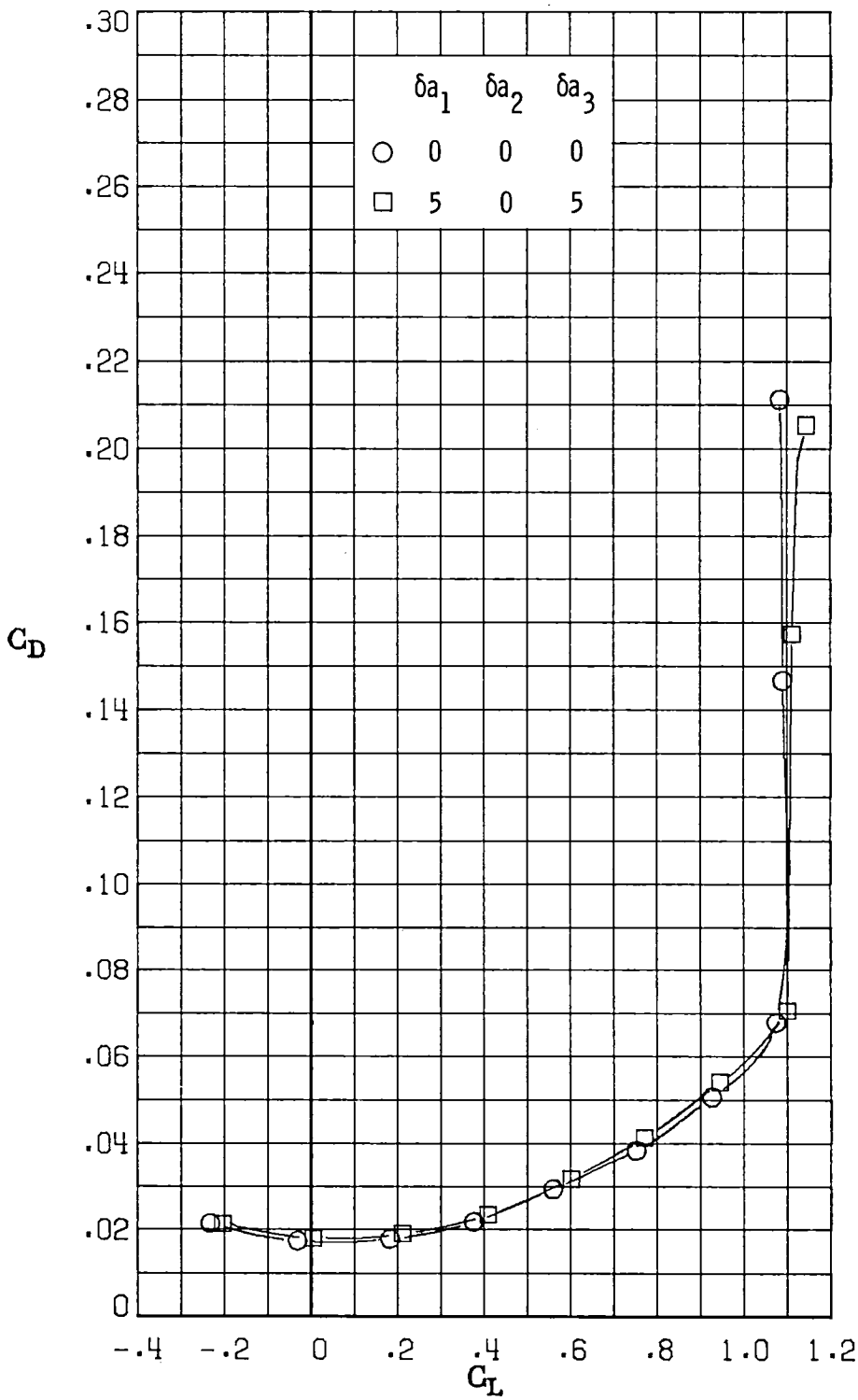

(a) $M_\infty = 0.30$.

Figure 14.- Variation of drag coefficient with lift coefficient for $\delta a_1 = 5°$, $\delta a_2 = 0°$, $\delta a_3 = 5°$.

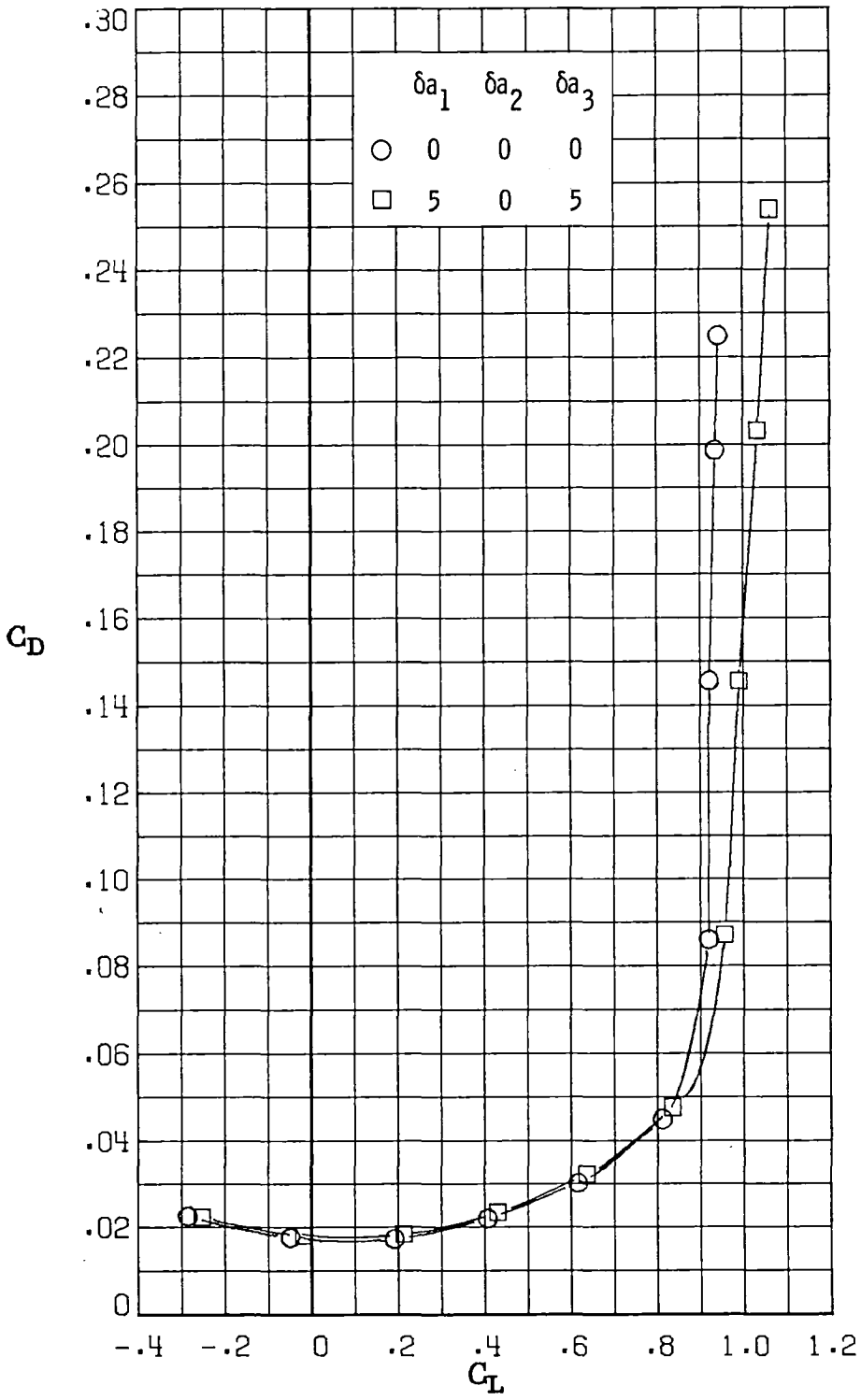

(b) $M_\infty = 0.60$.

Figure 14.- Continued.

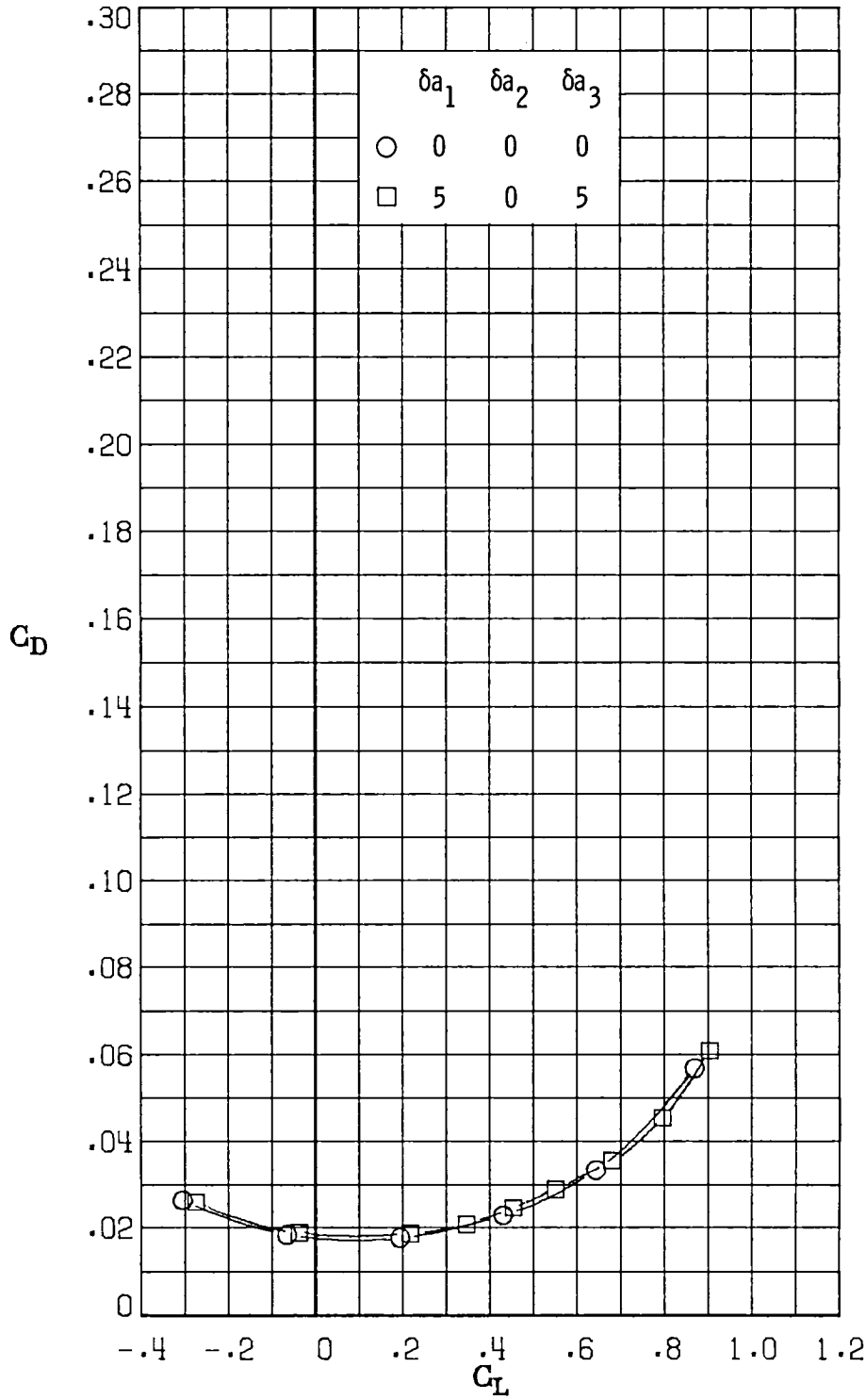

(c) $M_\infty = 0.70$.

Figure 14.- Continued.

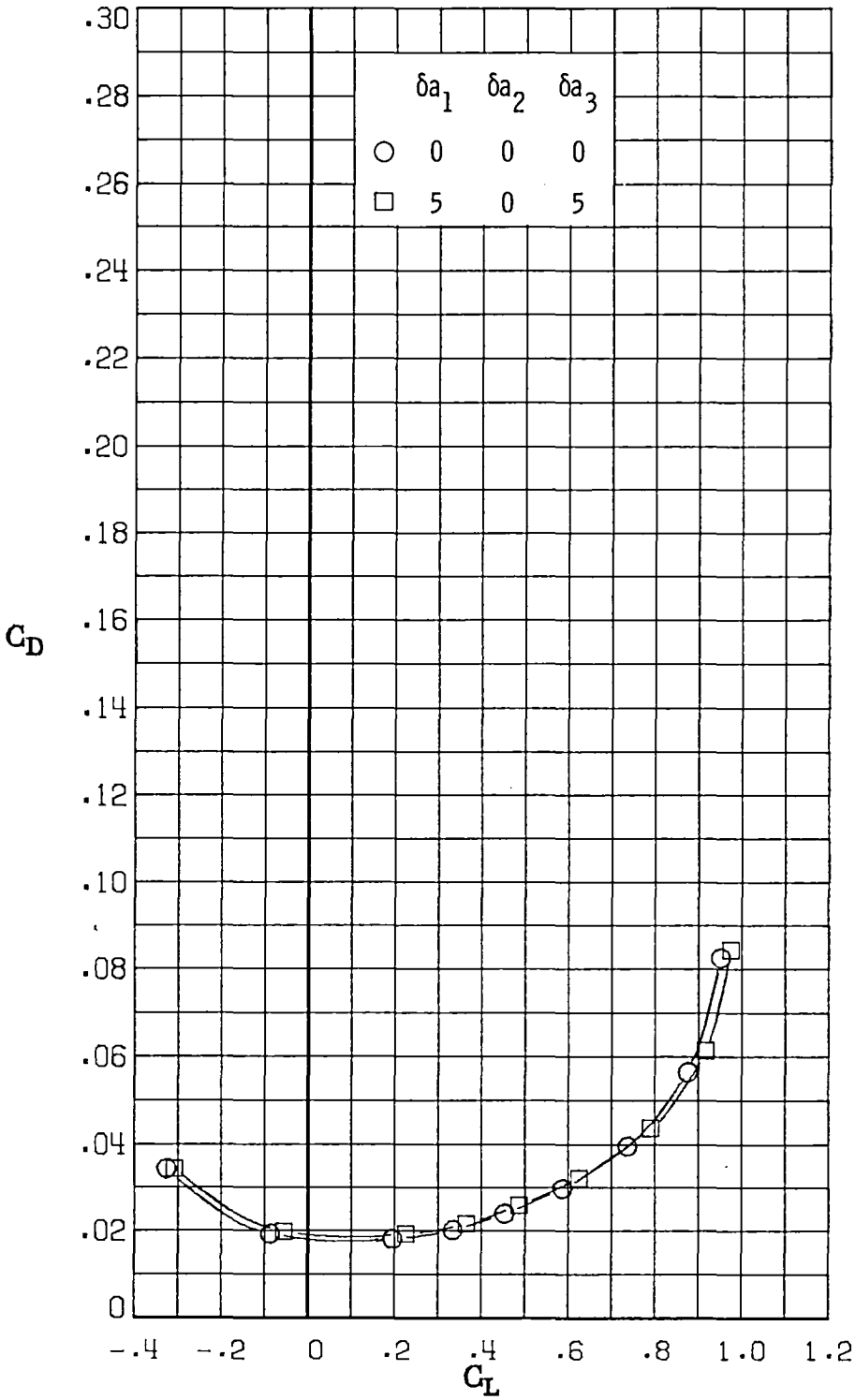

(d) $M_\infty = 0.77$.

Figure 14.- Continued.

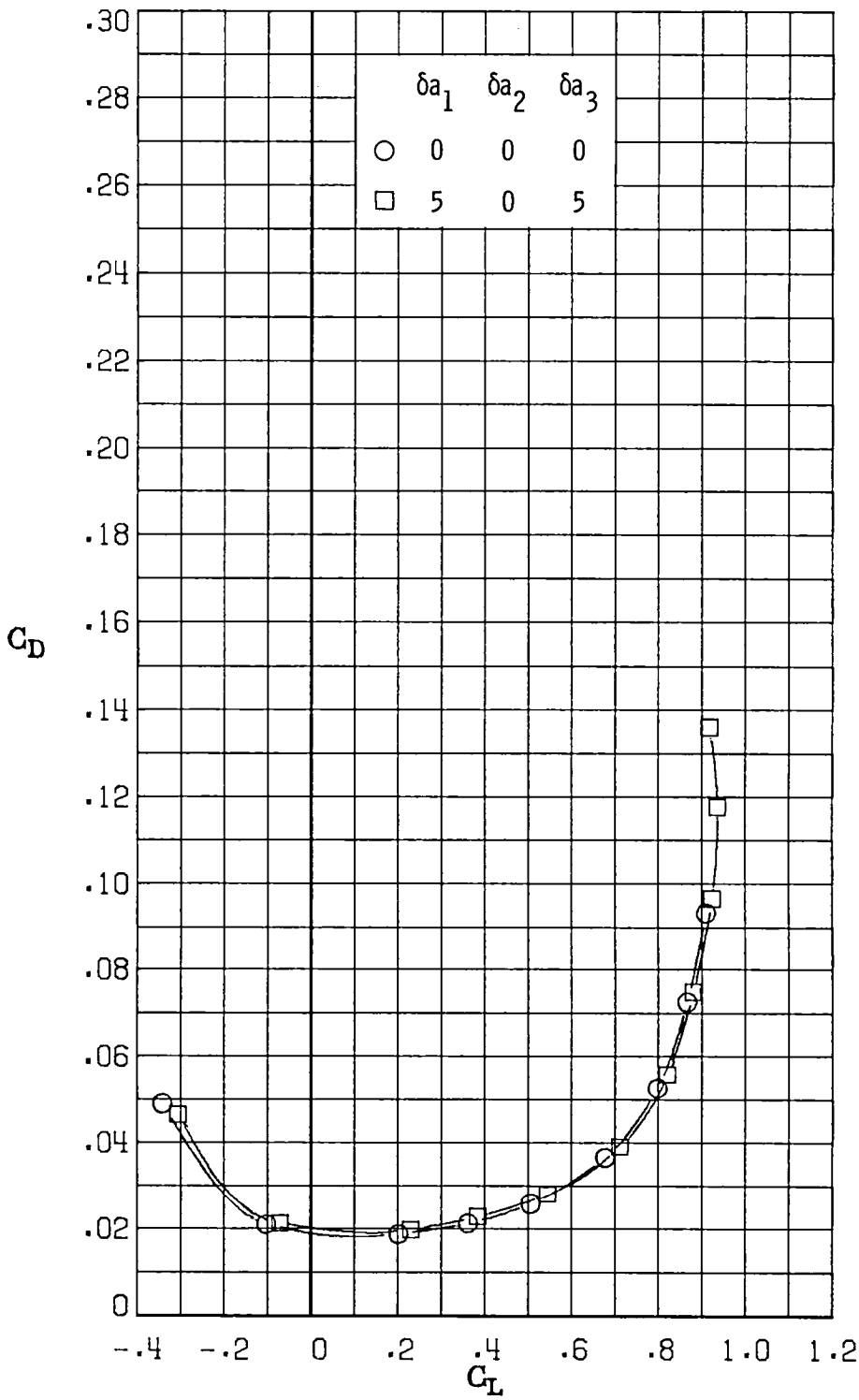

(e) $M_\infty = 0.81$.

Figure 14.- Continued.

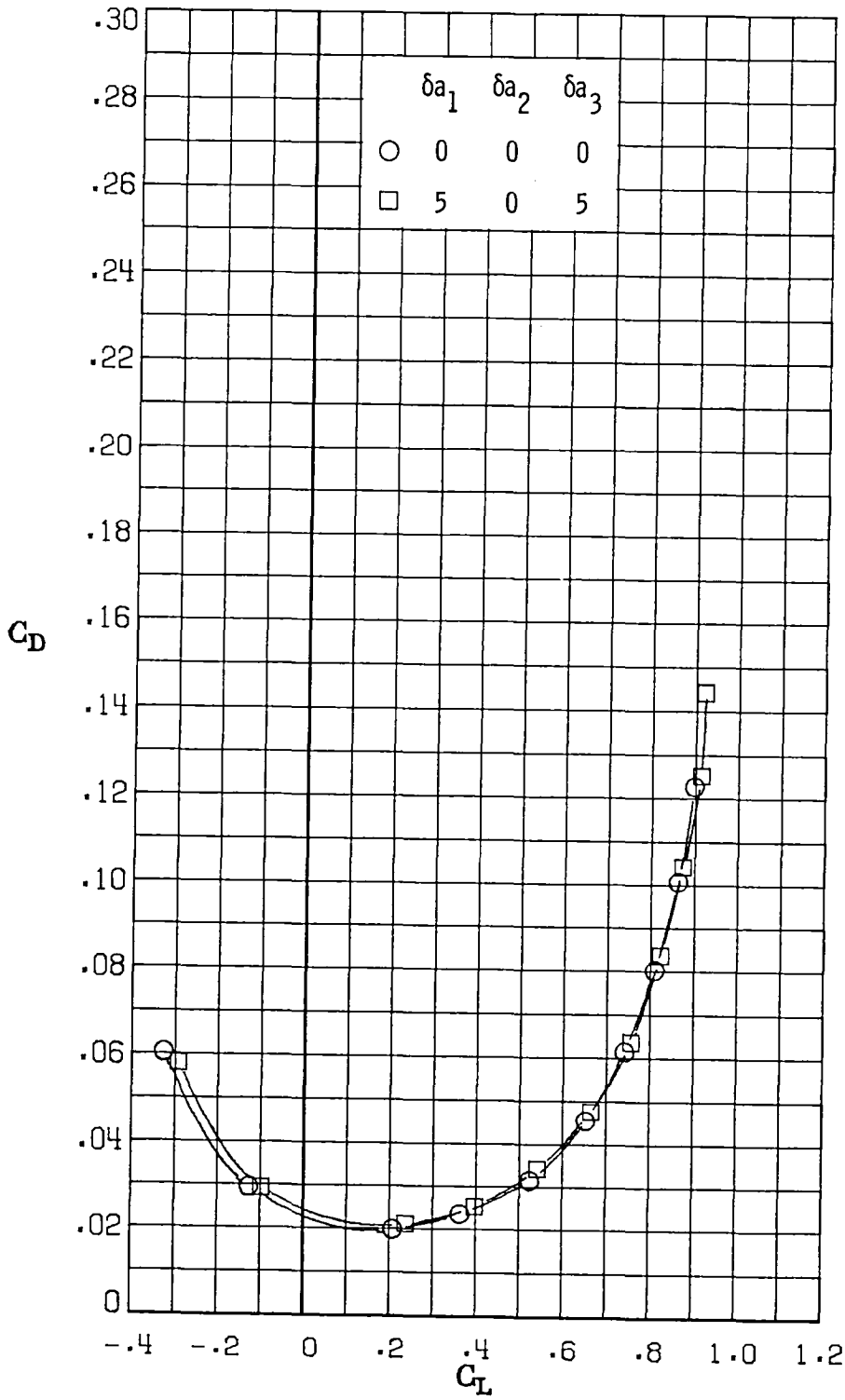

(f) $M_\infty = 0.84$.

Figure 14.- Continued.

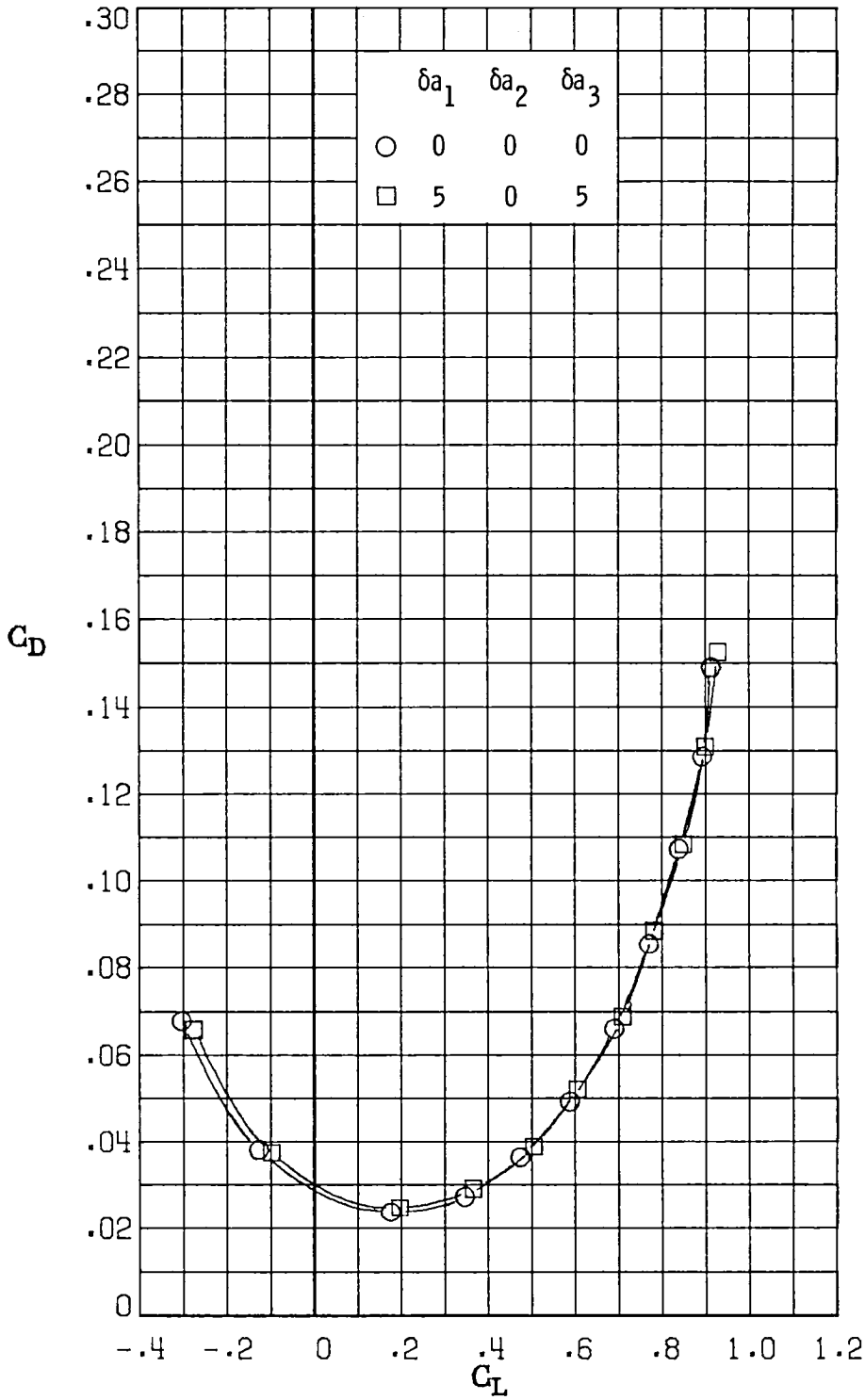

(g) $M_\infty = 0.86$.

Figure 14.- Concluded.

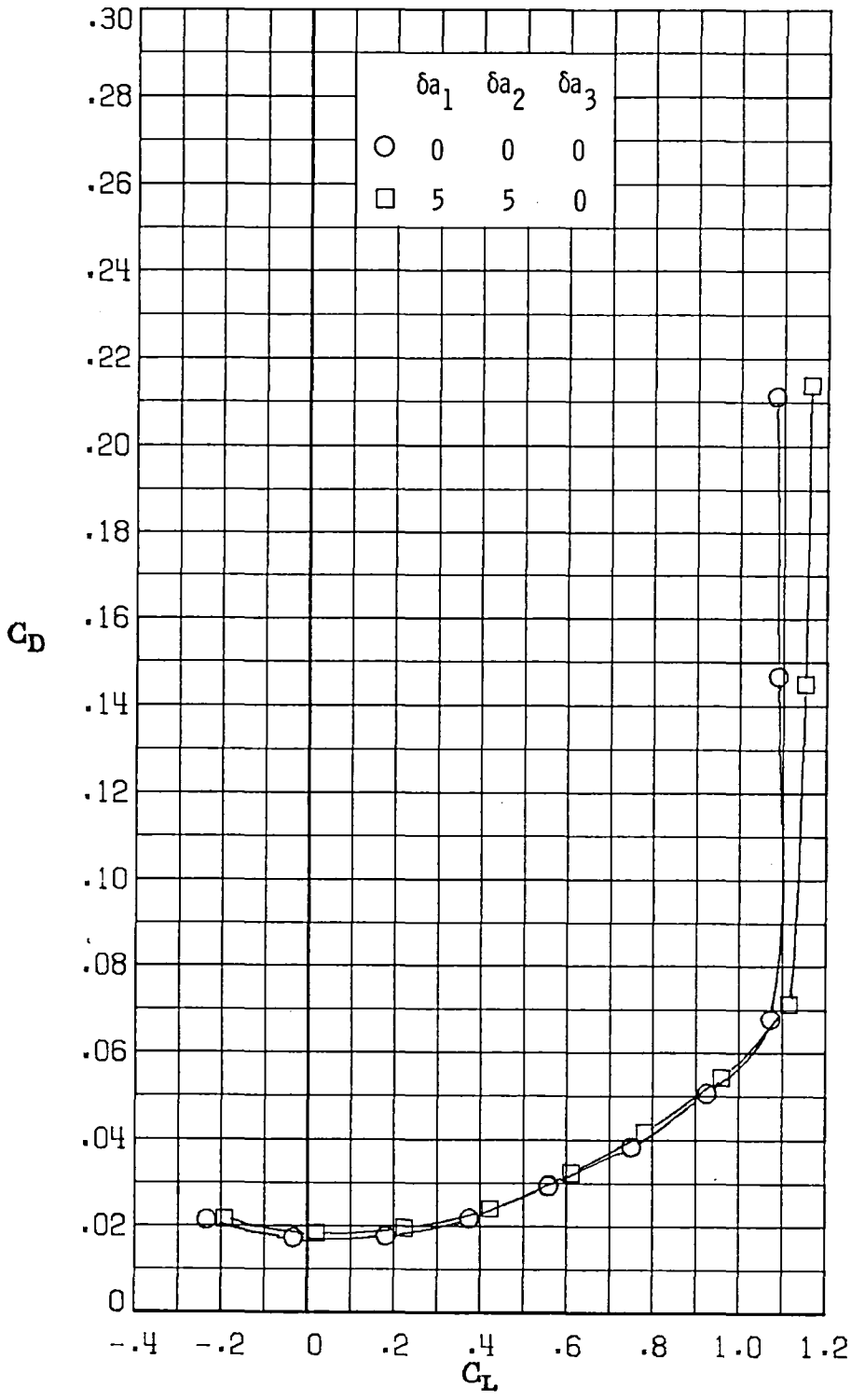

(a) $M_\infty = 0.30$.

Figure 15.- Variation of drag coefficient with lift coefficient for $\delta a_1 = 5°$, $\delta a_2 = 5°$, $\delta a_3 = 0°$.

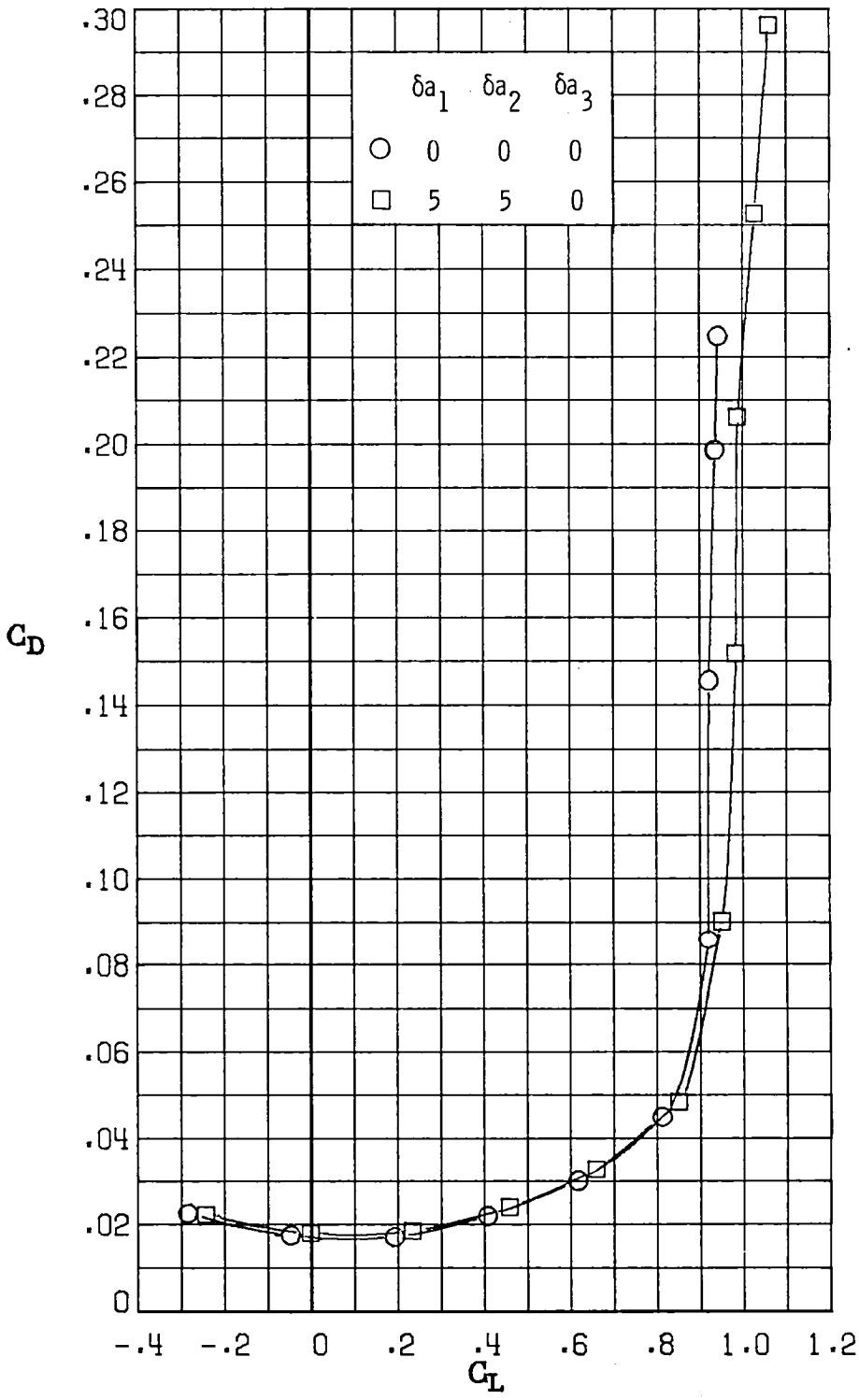

(b) $M_\infty = 0.60$.

Figure 15.- Continued.

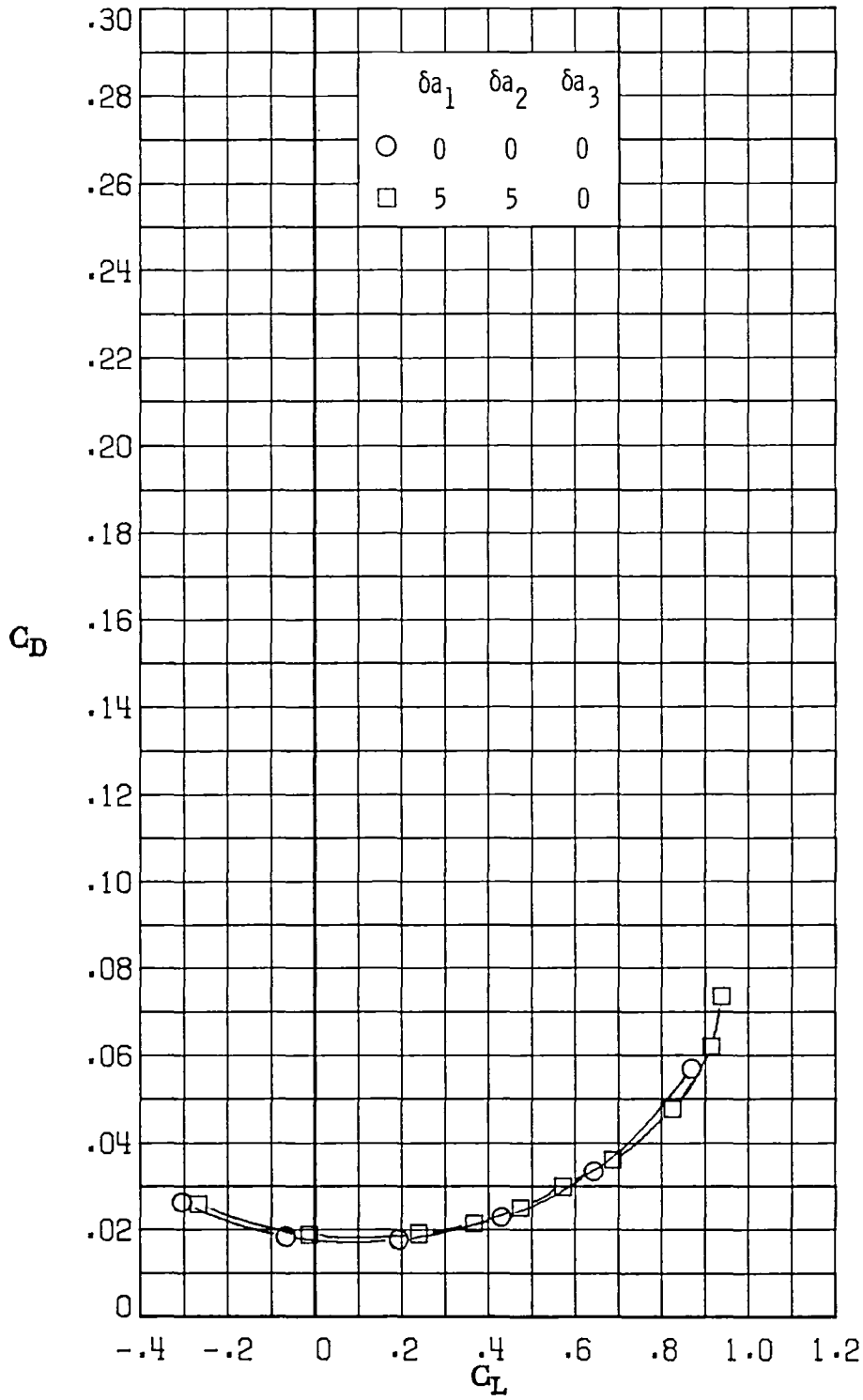

(c) $M_\infty = 0.70$.

Figure 15.- Continued.

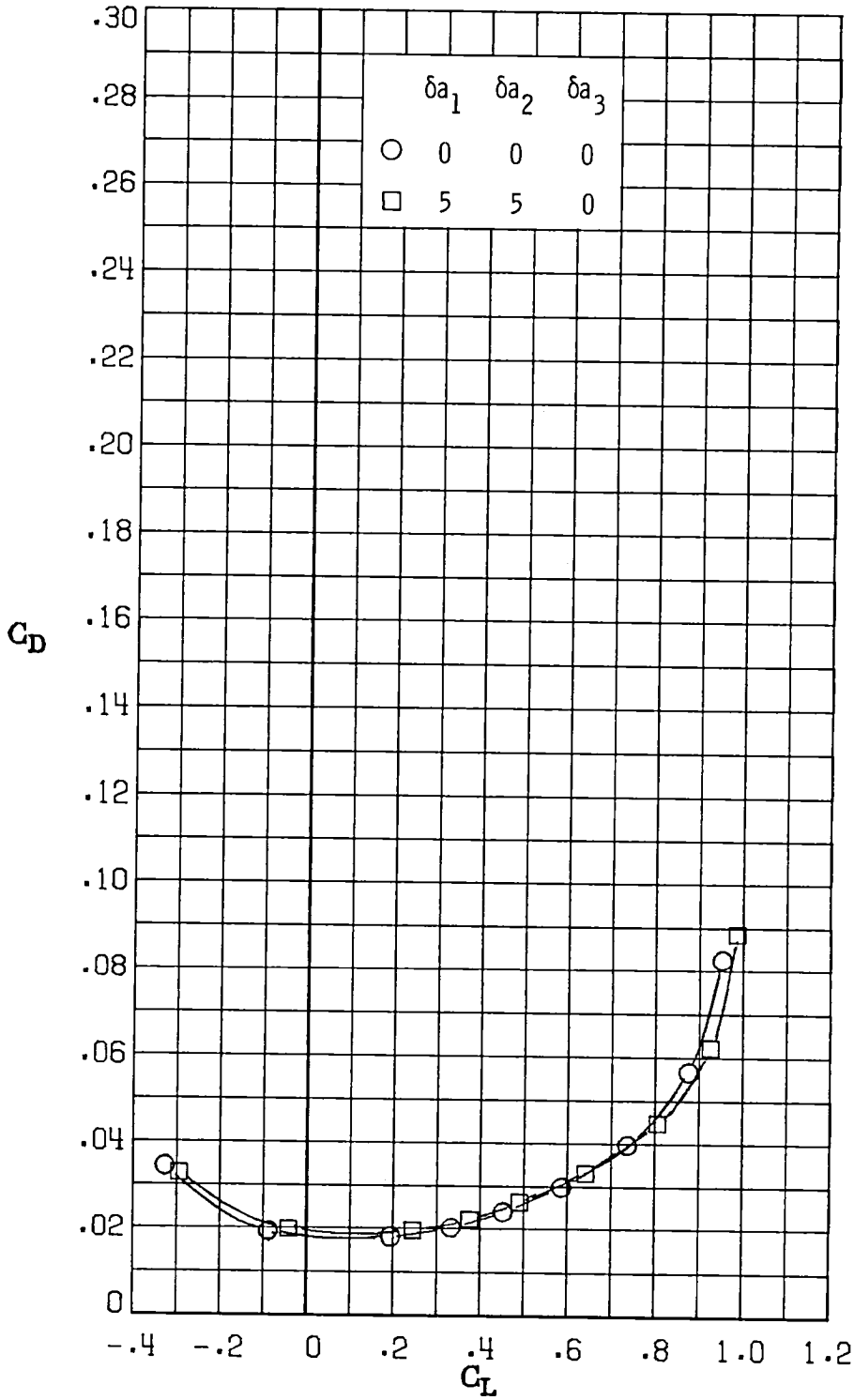

(d) $M_\infty = 0.77$.

Figure 15.- Continued.

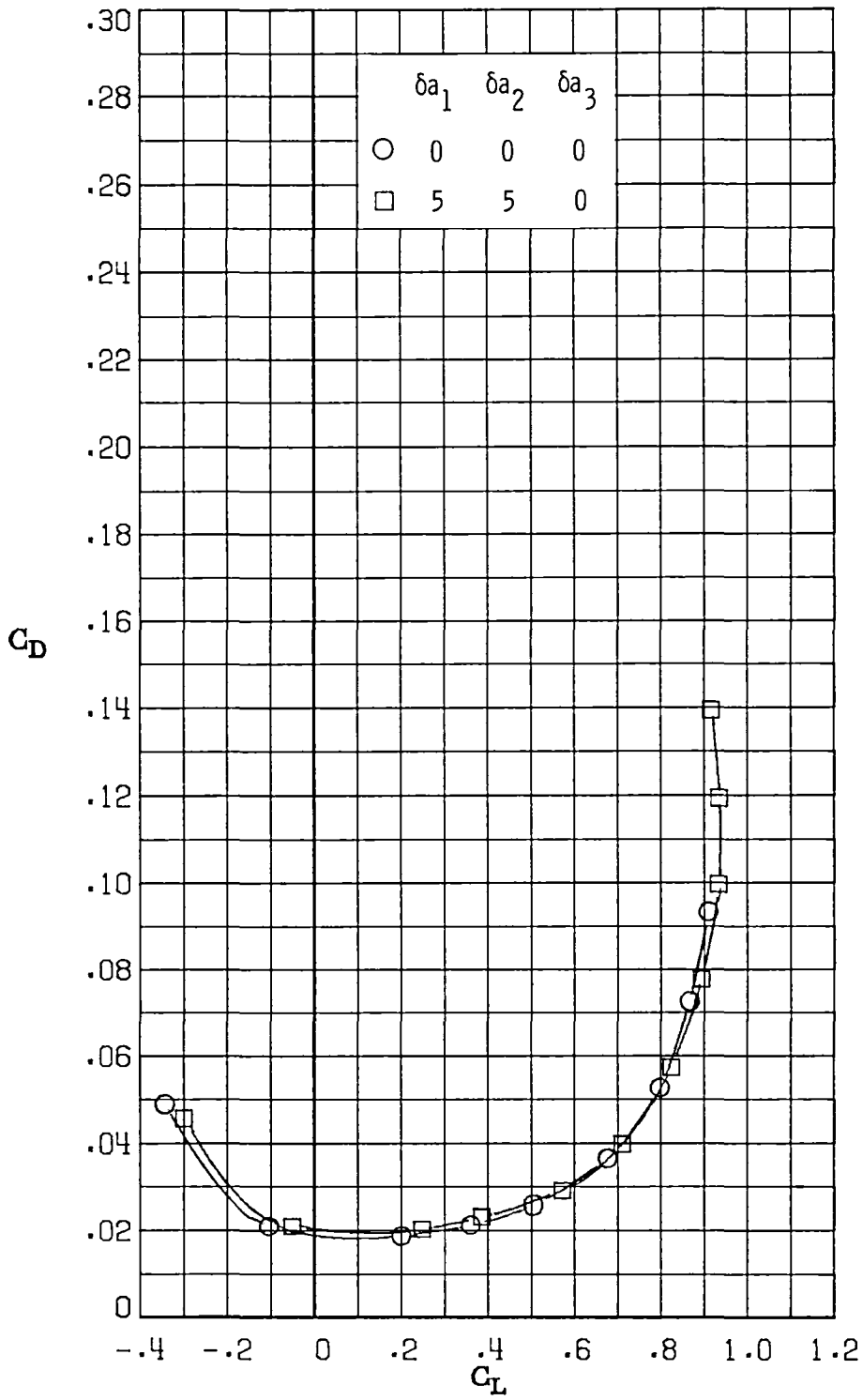

(e) $M_\infty = 0.81$.

Figure 15.- Continued.

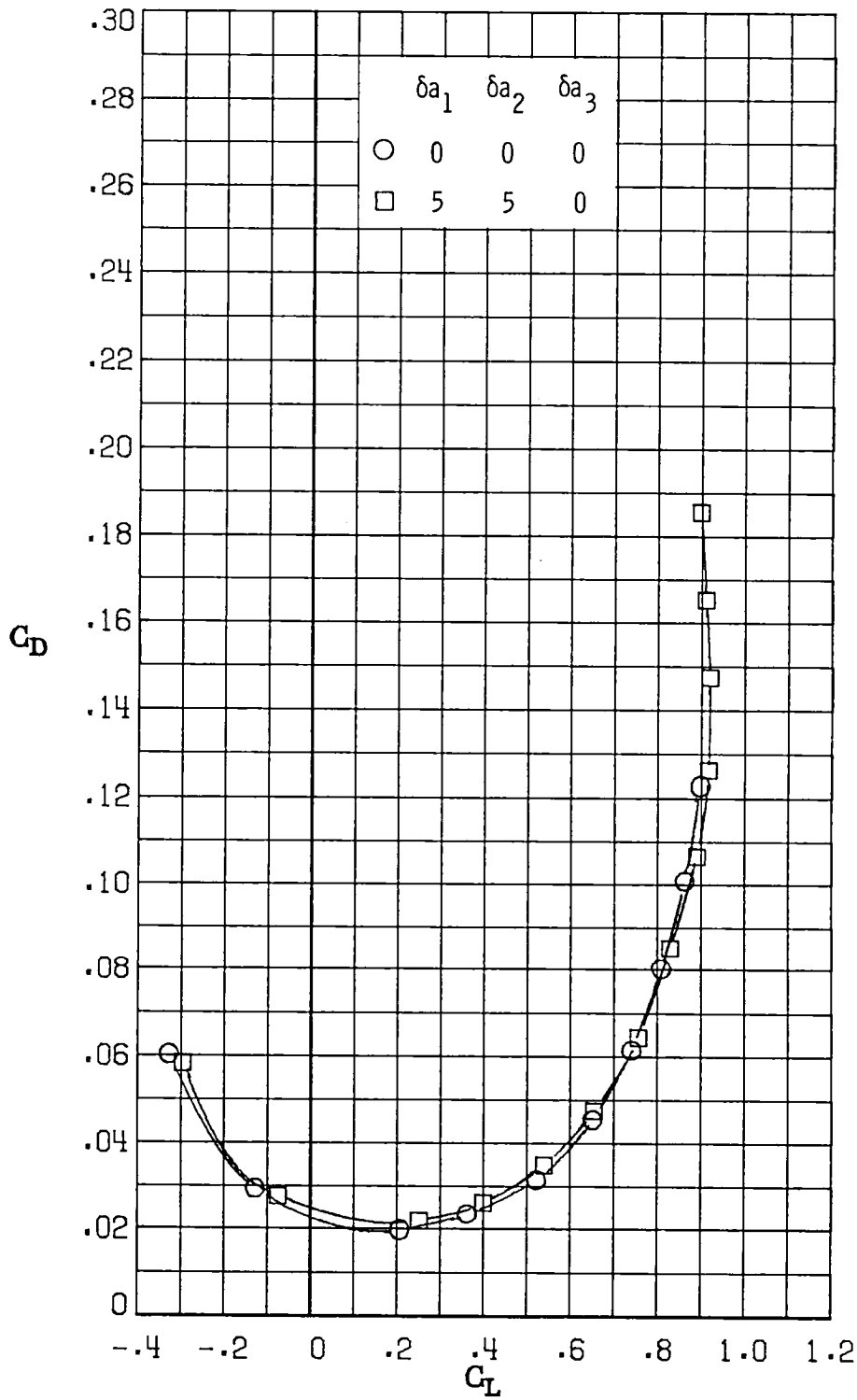

(f) $M_\infty = 0.84$.

Figure 15.- Continued.

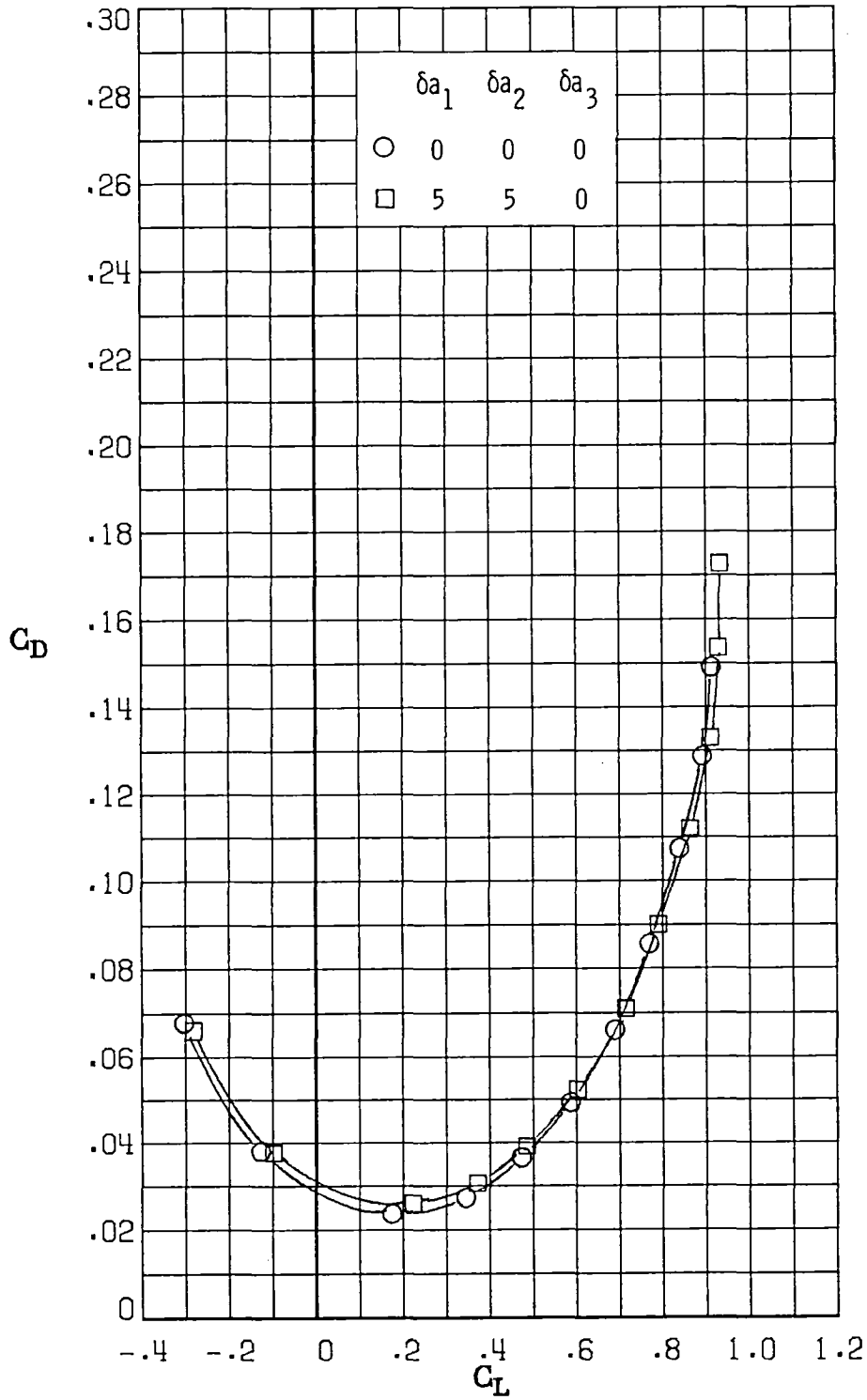

(g) $M_\infty = 0.86$.

Figure 15.- Concluded.

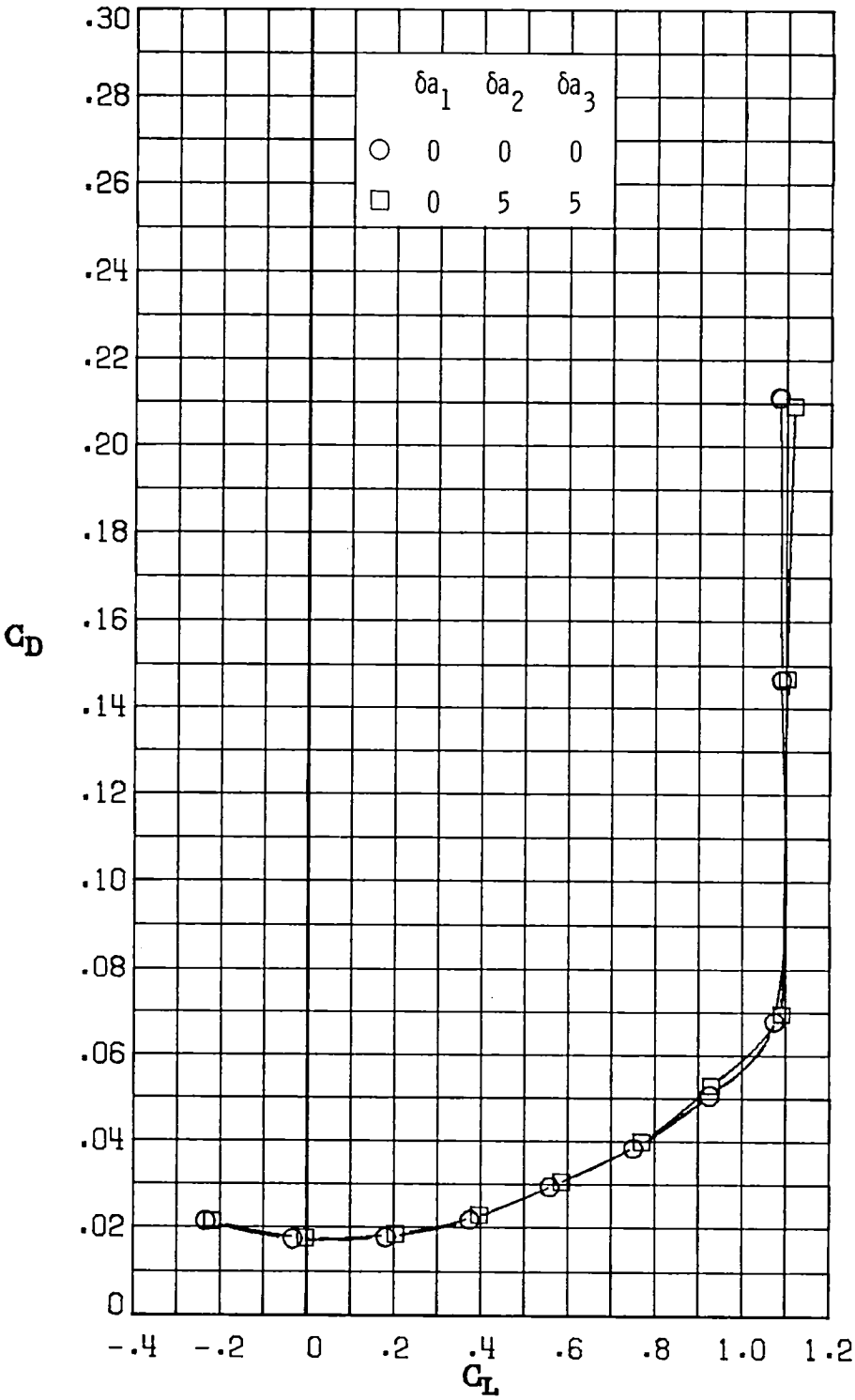

(a) $M_\infty = 0.30$.

Figure 16.- Variation of drag coefficient with lift coefficient for $\delta a_1 = 0°$, $\delta a_2 = 5°$, $\delta a_3 = 5°$.

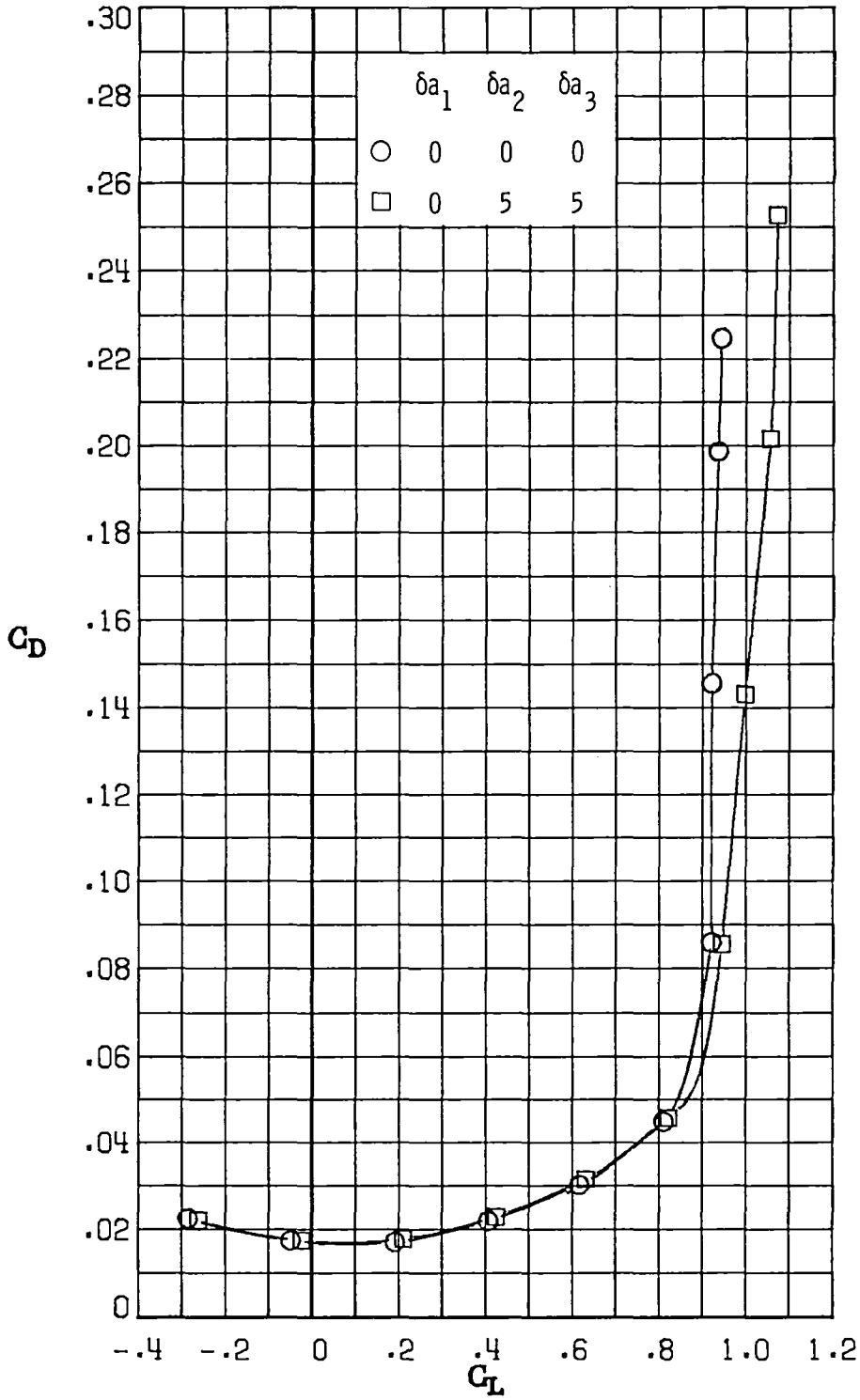

(b) $M_\infty = 0.60$.

Figure 16.- Continued.

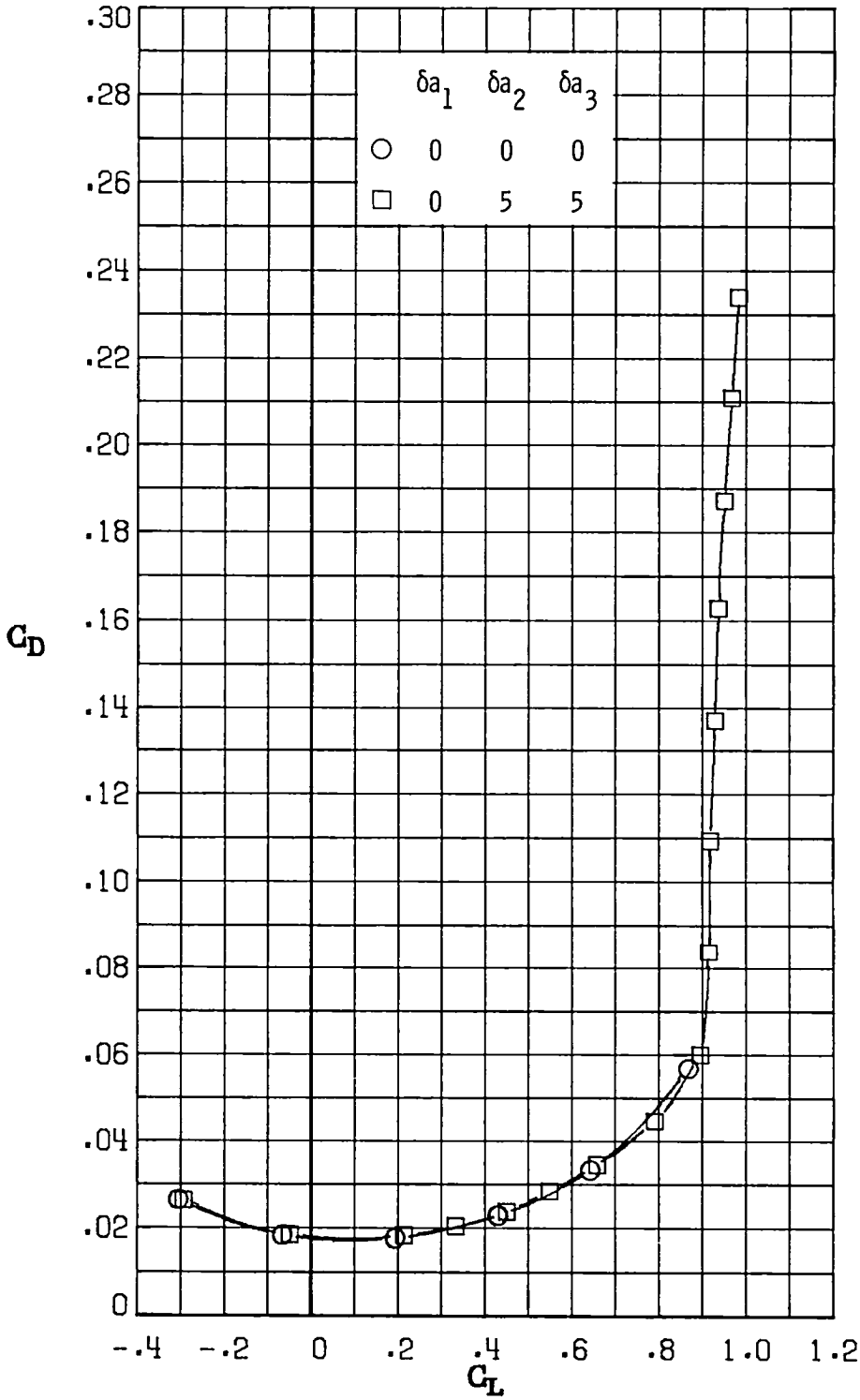

(c) $M_\infty = 0.70$.

Figure 16.- Continued.

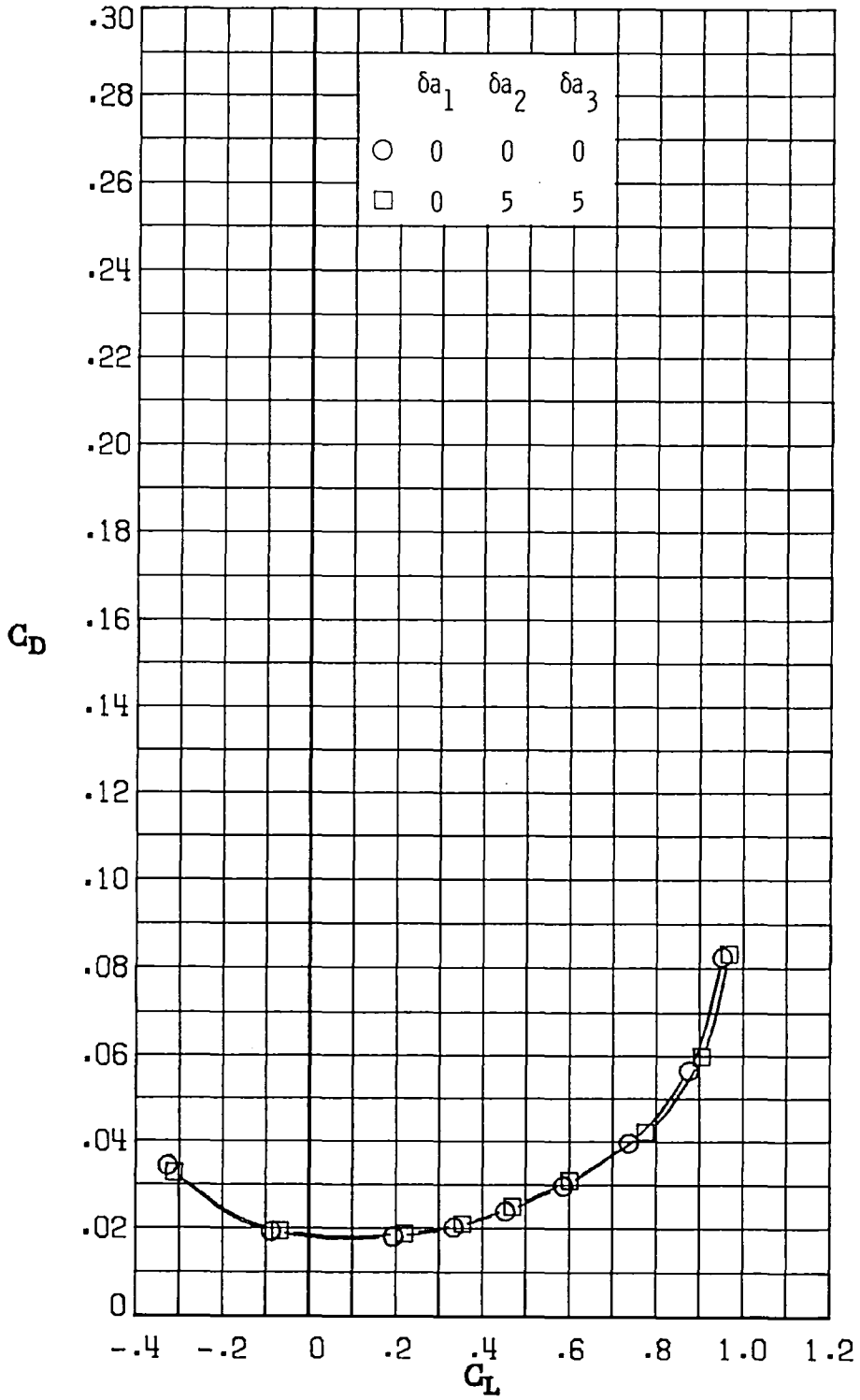

(d) $M_\infty = 0.77$.

Figure 16.- Continued.

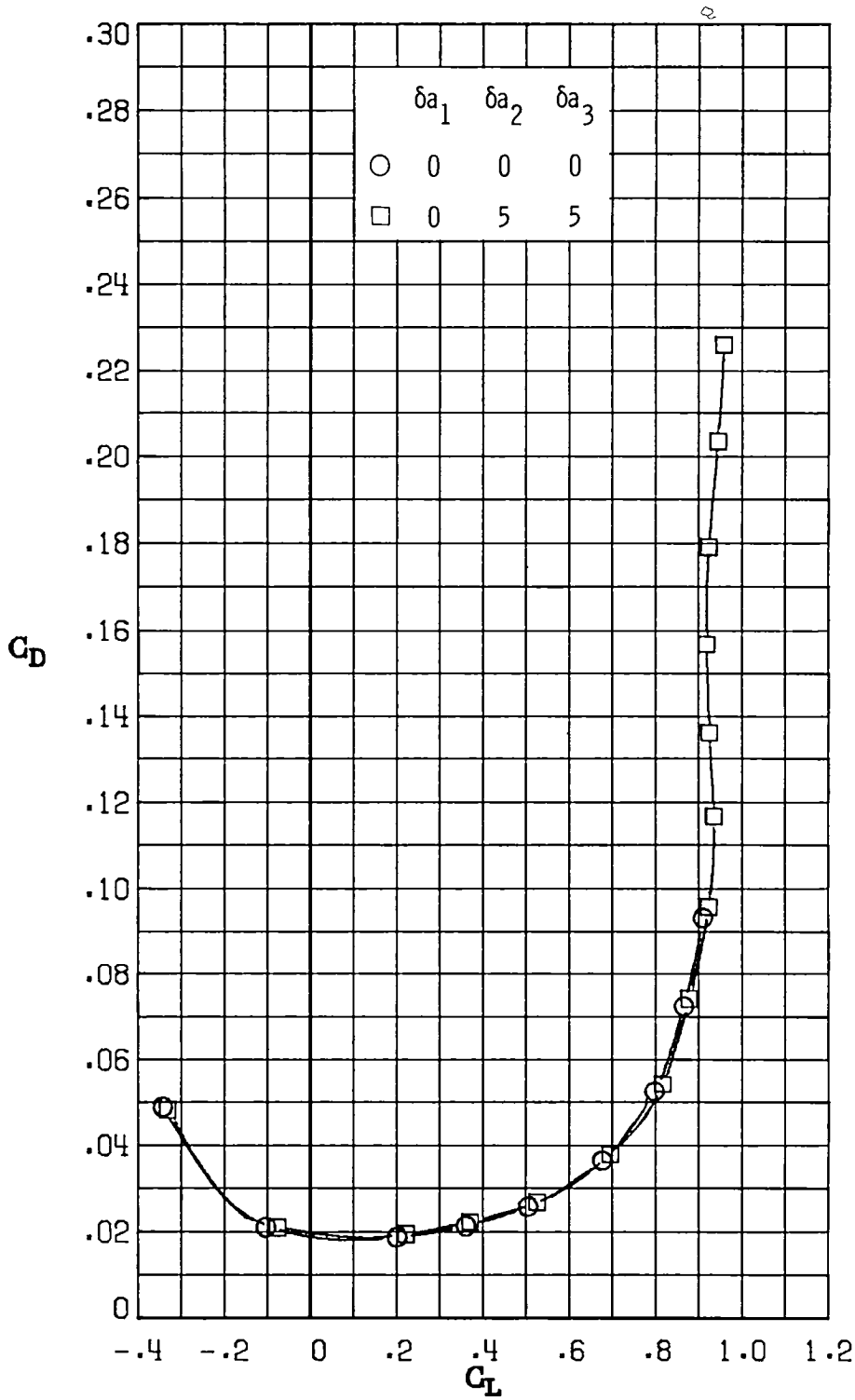

(e) $M_\infty = 0.81$.

Figure 16.- Continued.

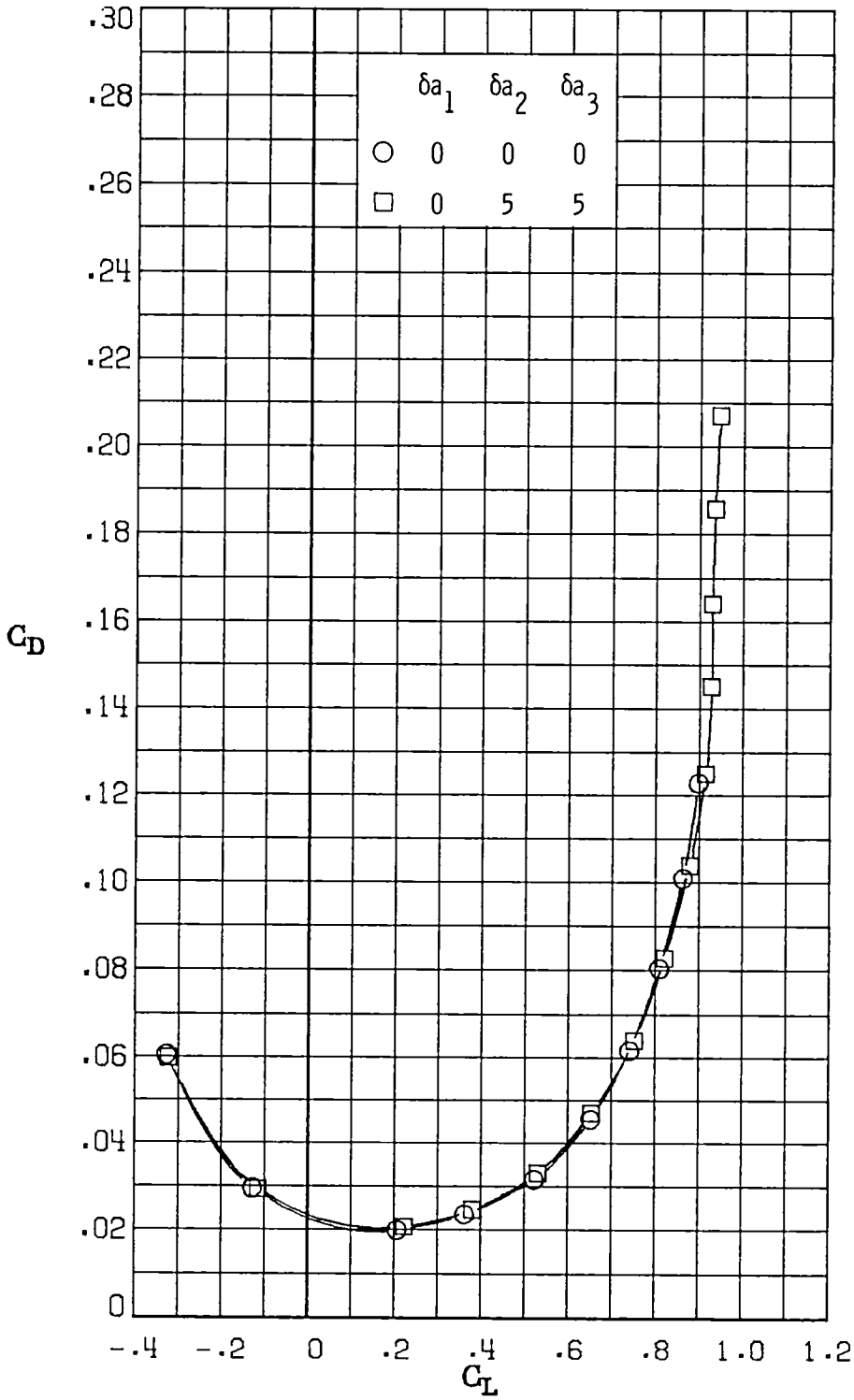

(f) $M_\infty = 0.84$.

Figure 16.- Continued.

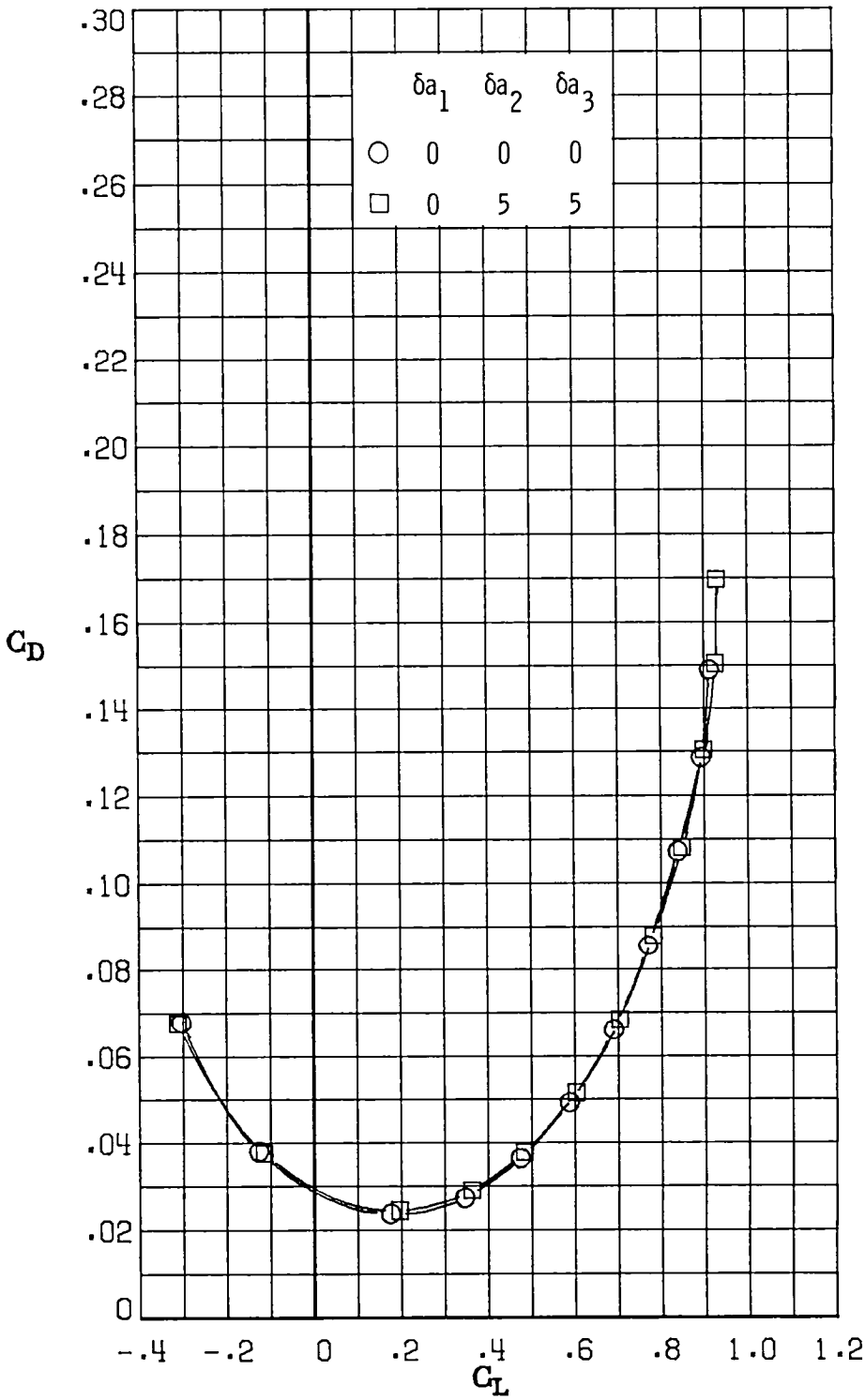

(g) $M_\infty = 0.86$.

Figure 16.- Concluded.

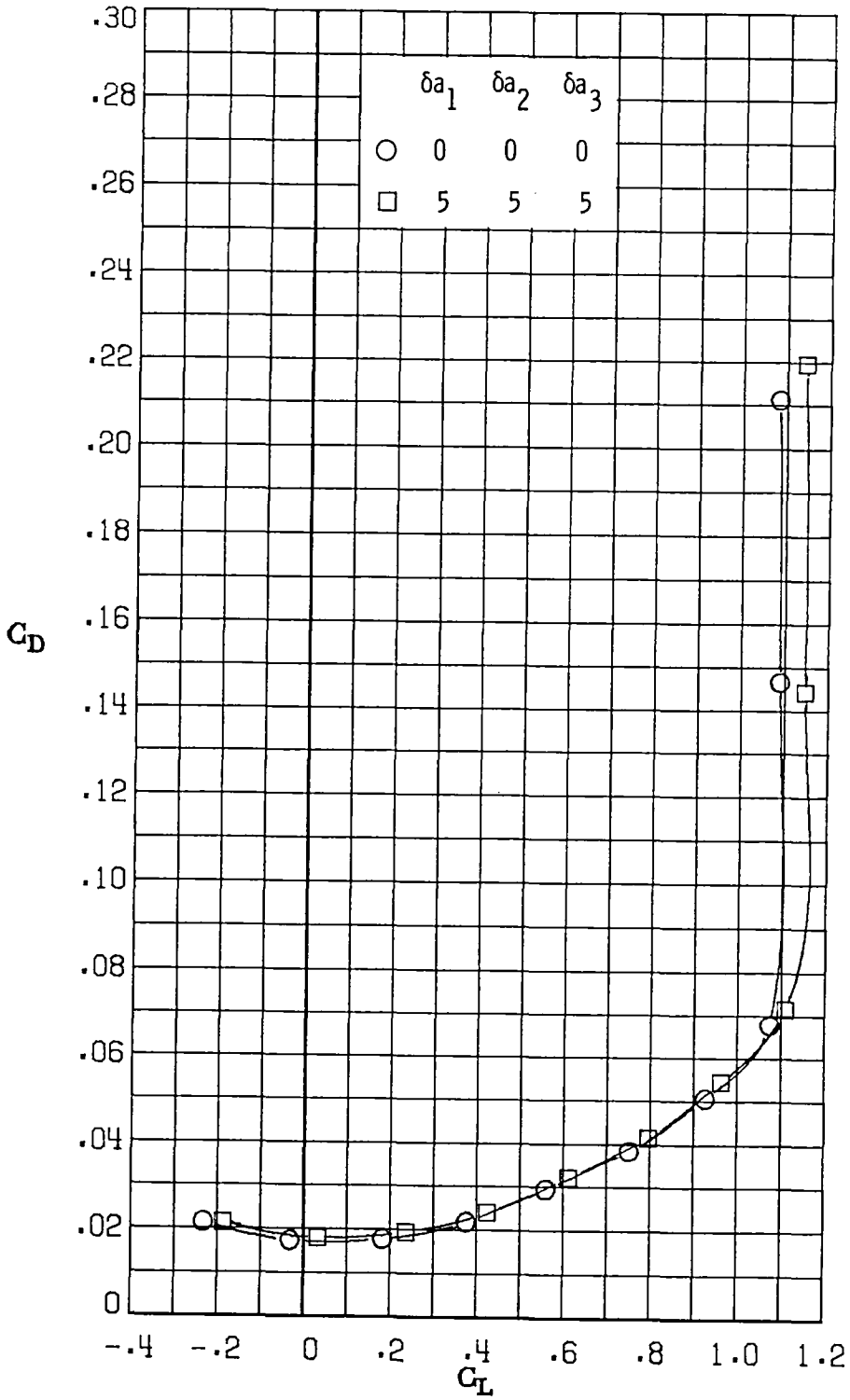

(a) $M_\infty = 0.30$.

Figure 17.- Variation of drag coefficient with lift coefficient for $\delta a_1 = 5°$, $\delta a_2 = 5°$, $\delta a_3 = 5°$.

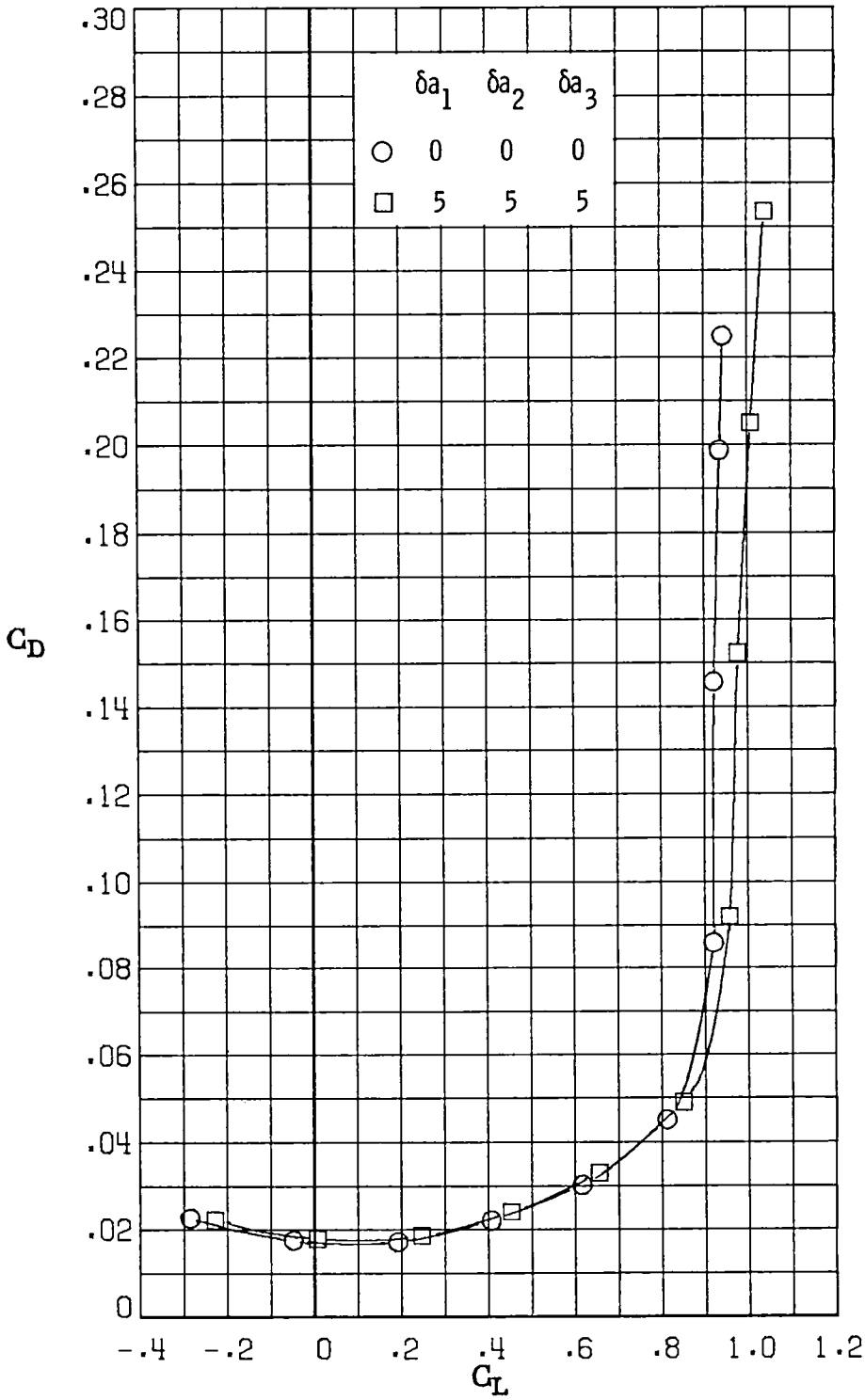

(b) $M_\infty = 0.60$.

Figure 17.- Continued.

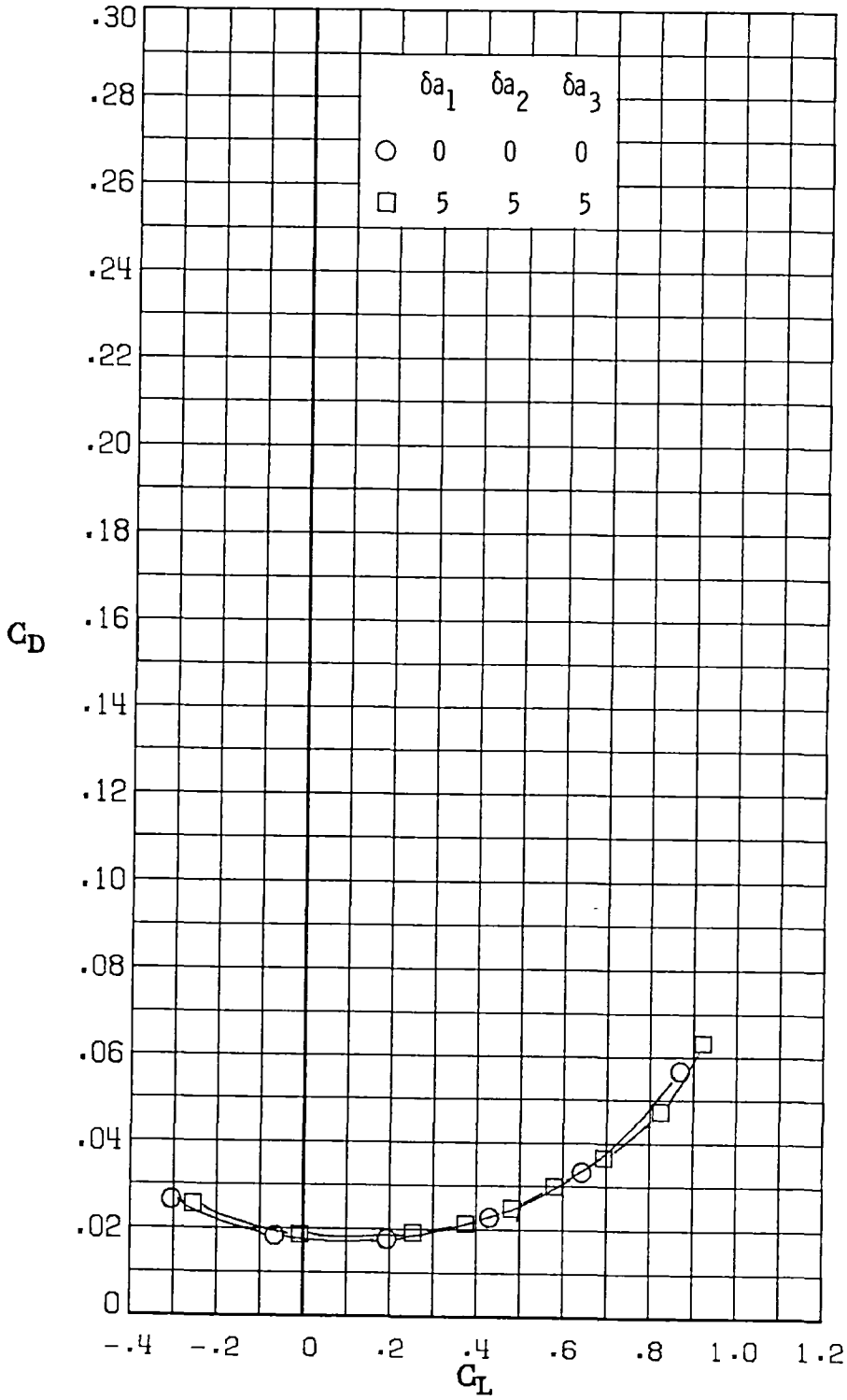

(c) $M_\infty = 0.70$.

Figure 17.- Continued.

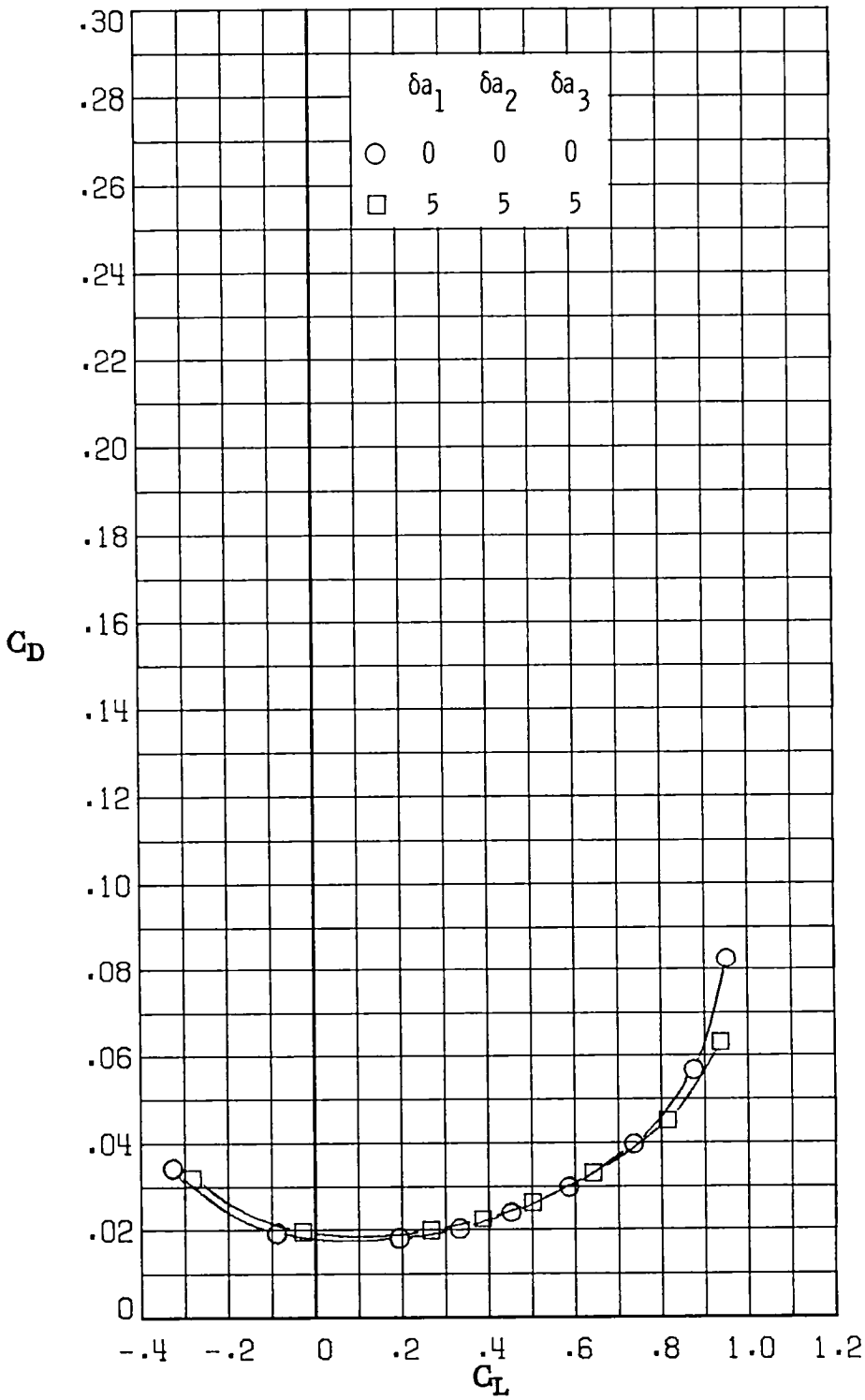

(d) $M_\infty = 0.77$.

Figure 17.- Continued.

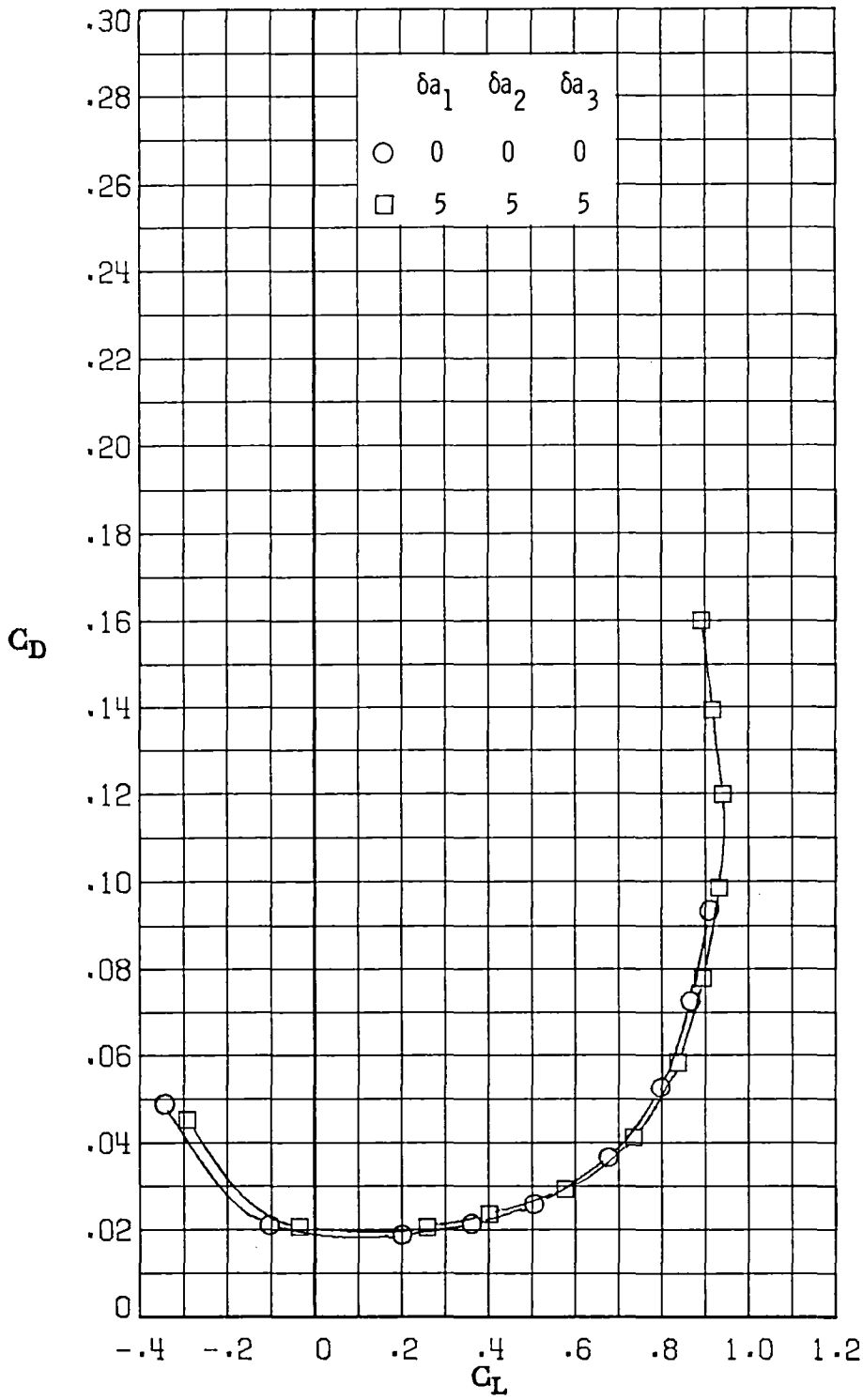

(e) $M_\infty = 0.81$.

Figure 17.- Continued.

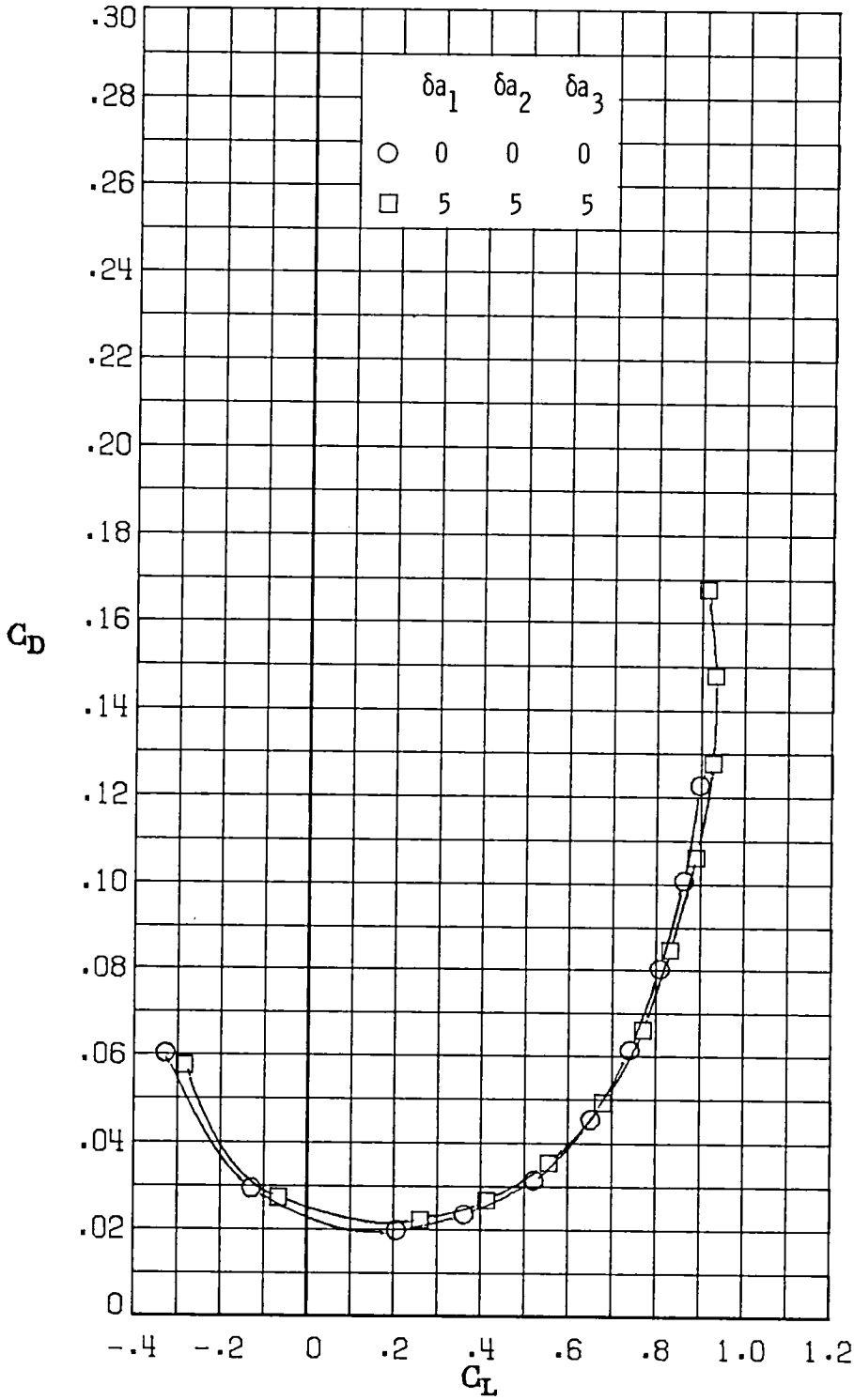

(f) $M_\infty = 0.84$.

Figure 17.- Continued.

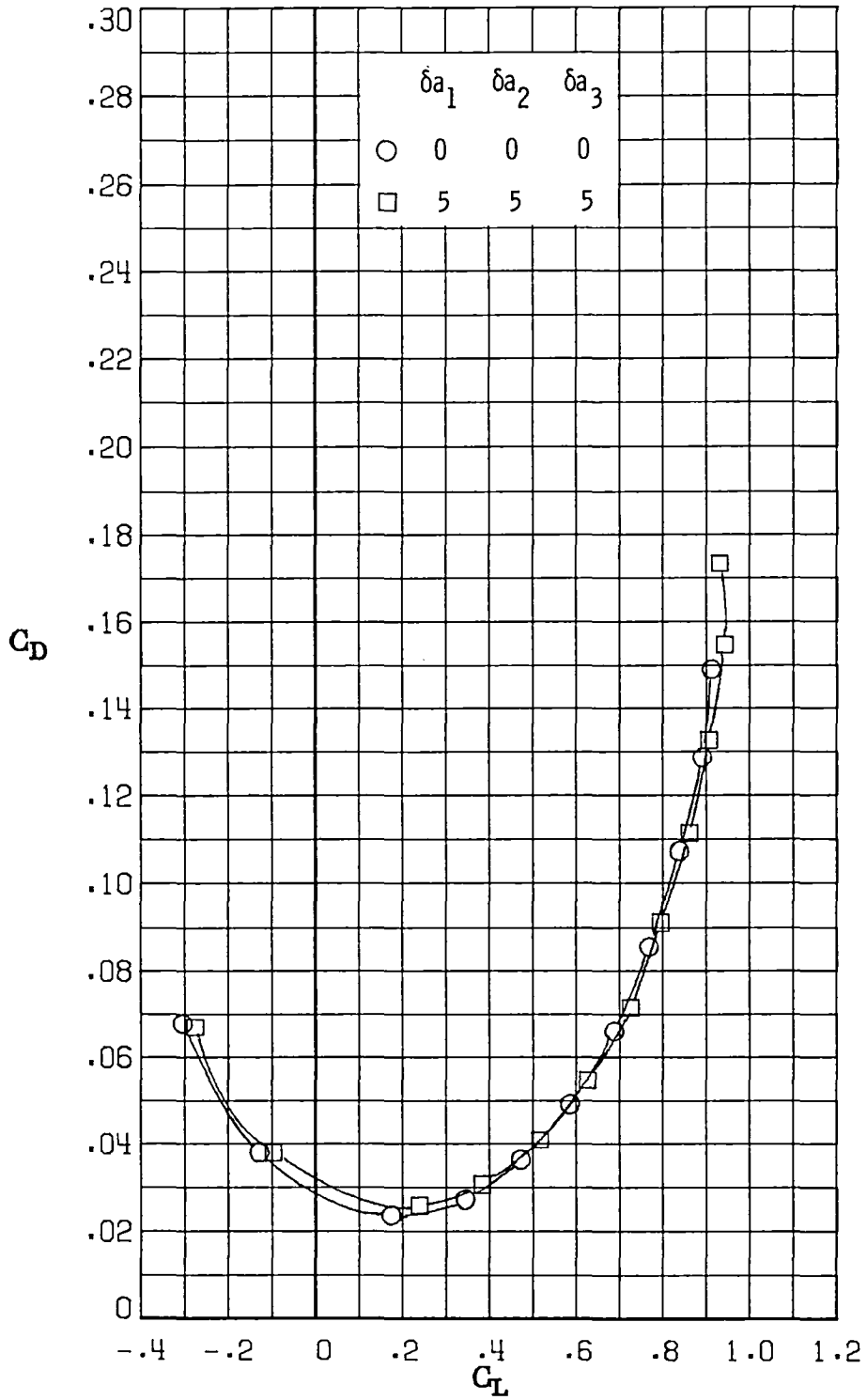

(g) $M_\infty = 0.86$.

Figure 17.- Concluded.

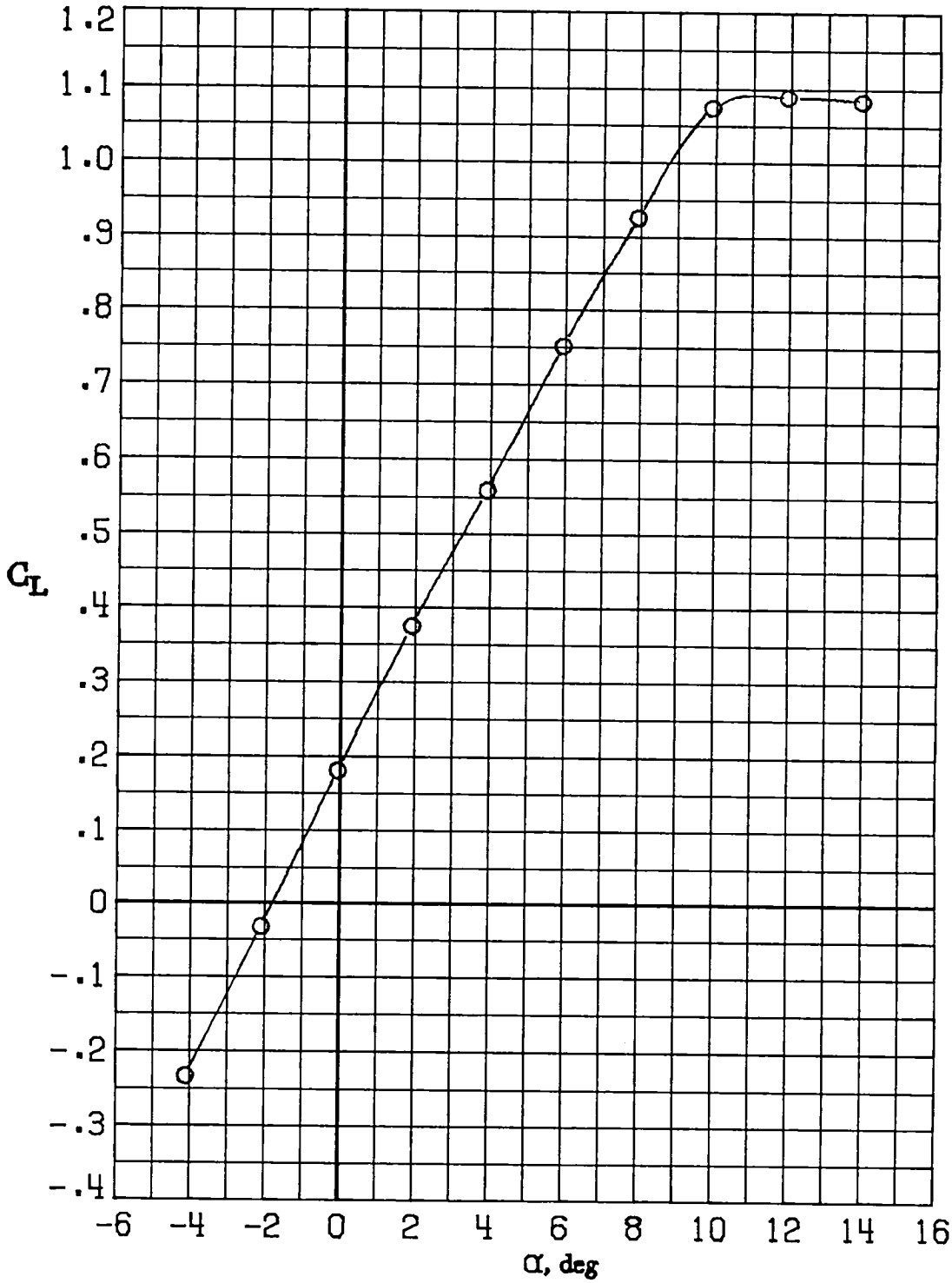

(a) $M_\infty = 0.30$.

Figure 18.- Variation of lift coefficient with angle of attack for the baseline configuration ($\delta a_1 = 0°$; $\delta a_2 = 0°$; $\delta a_3 = 0°$).

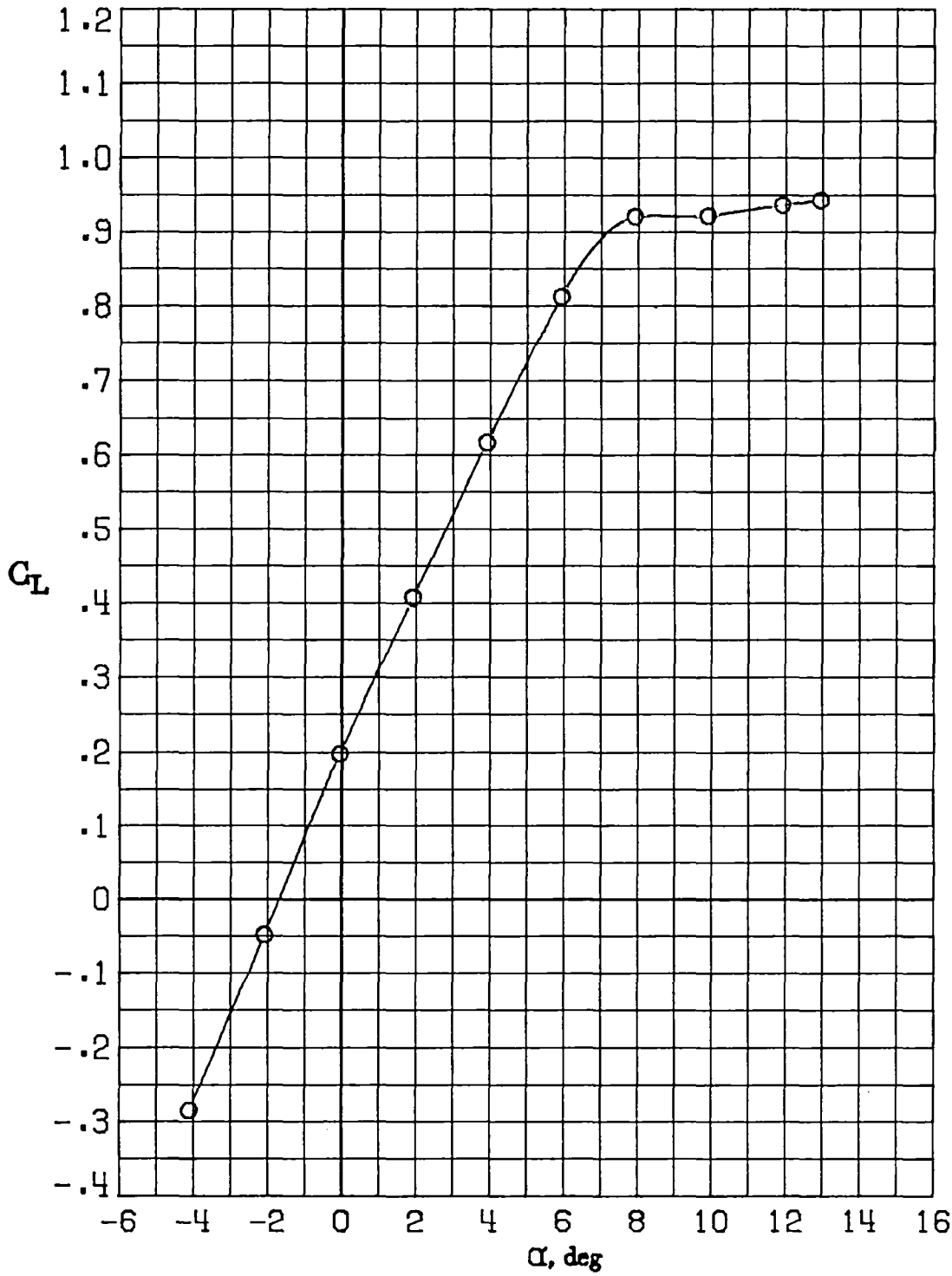

(b) $M_\infty = 0.60$.

Figure 18.- Continued.

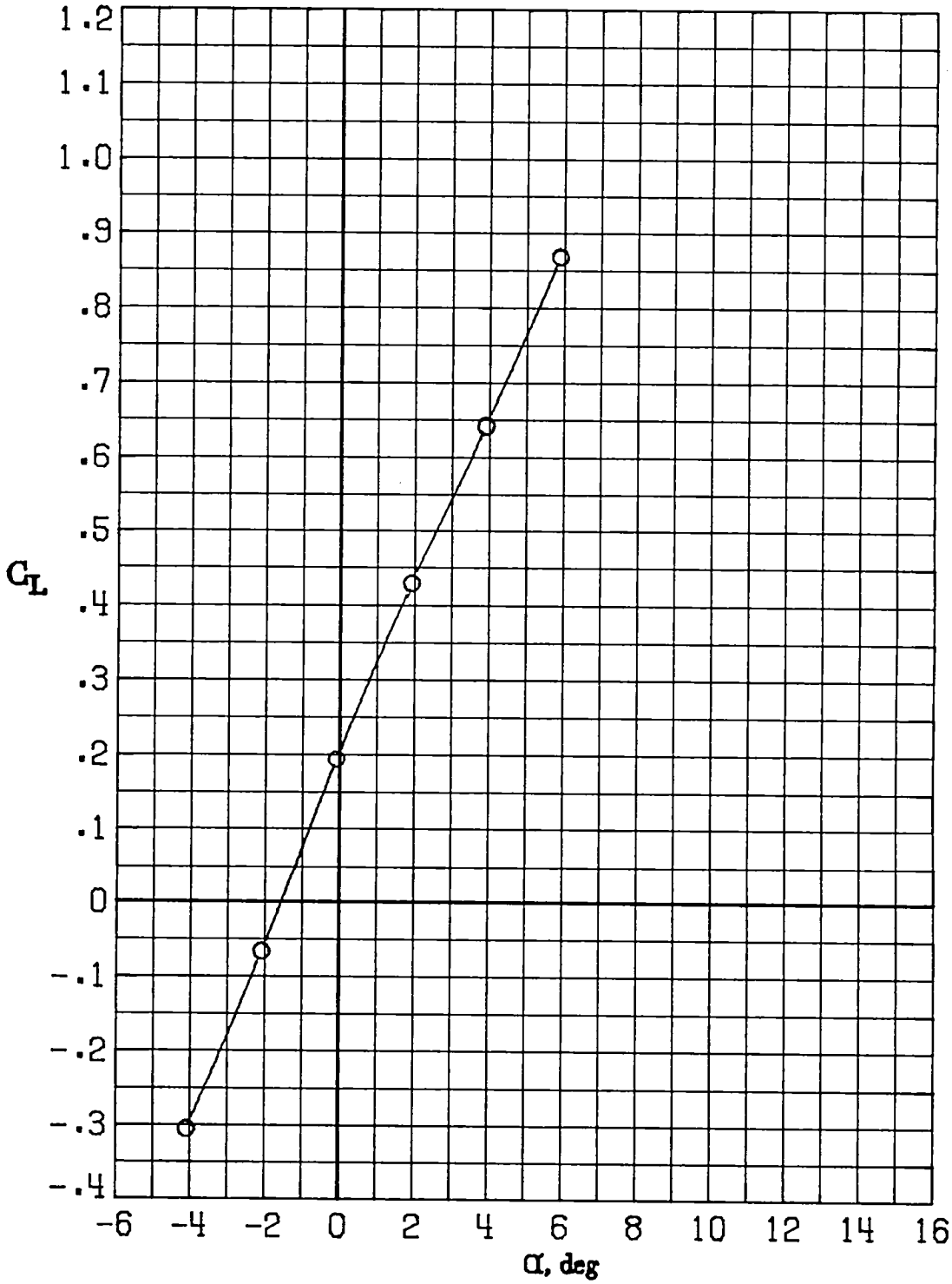

(c) $M_\infty = 0.70$.

Figure 18.- Continued.

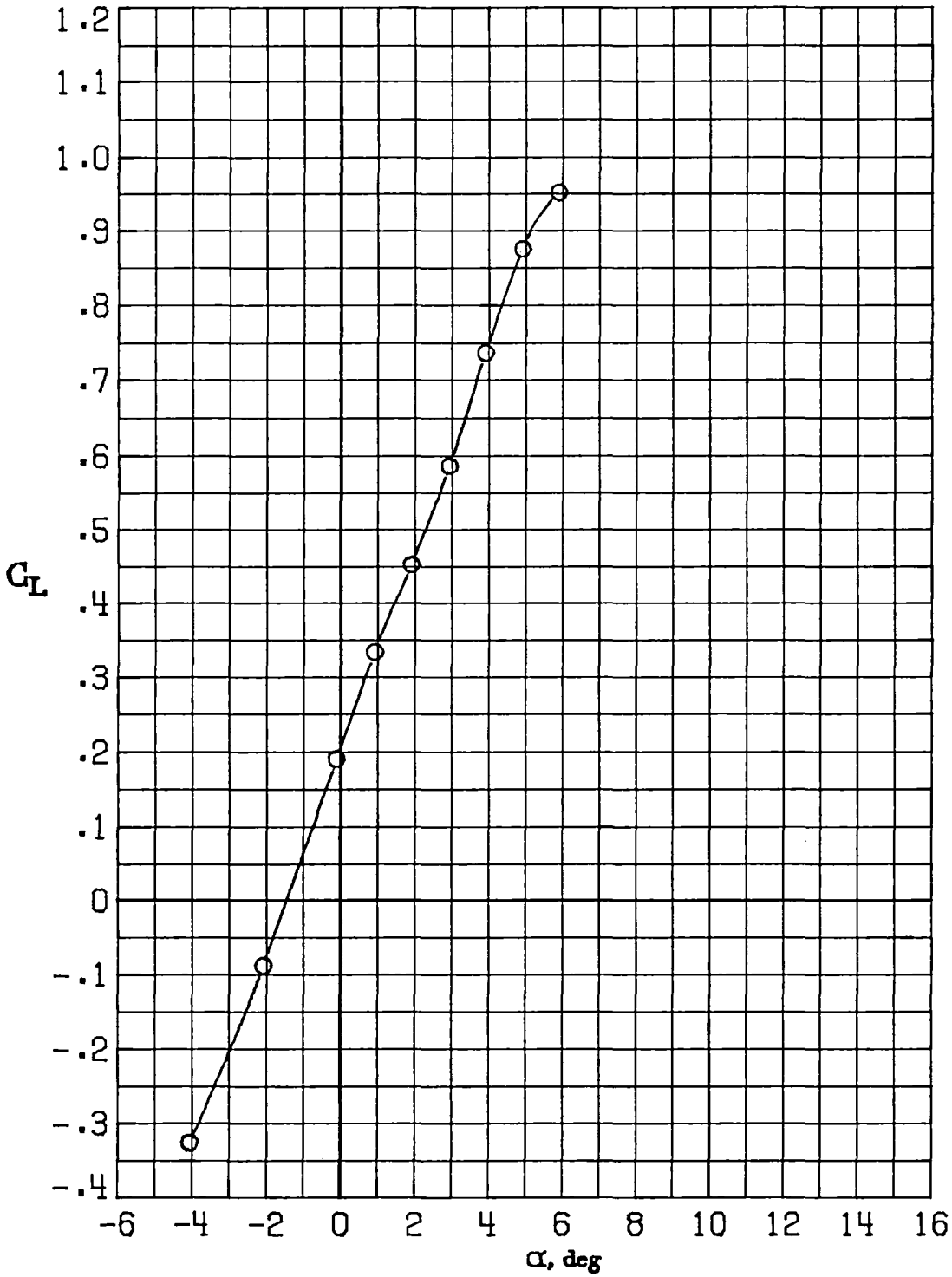

(d) $M_\infty = 0.77$.

Figure 18.- Continued.

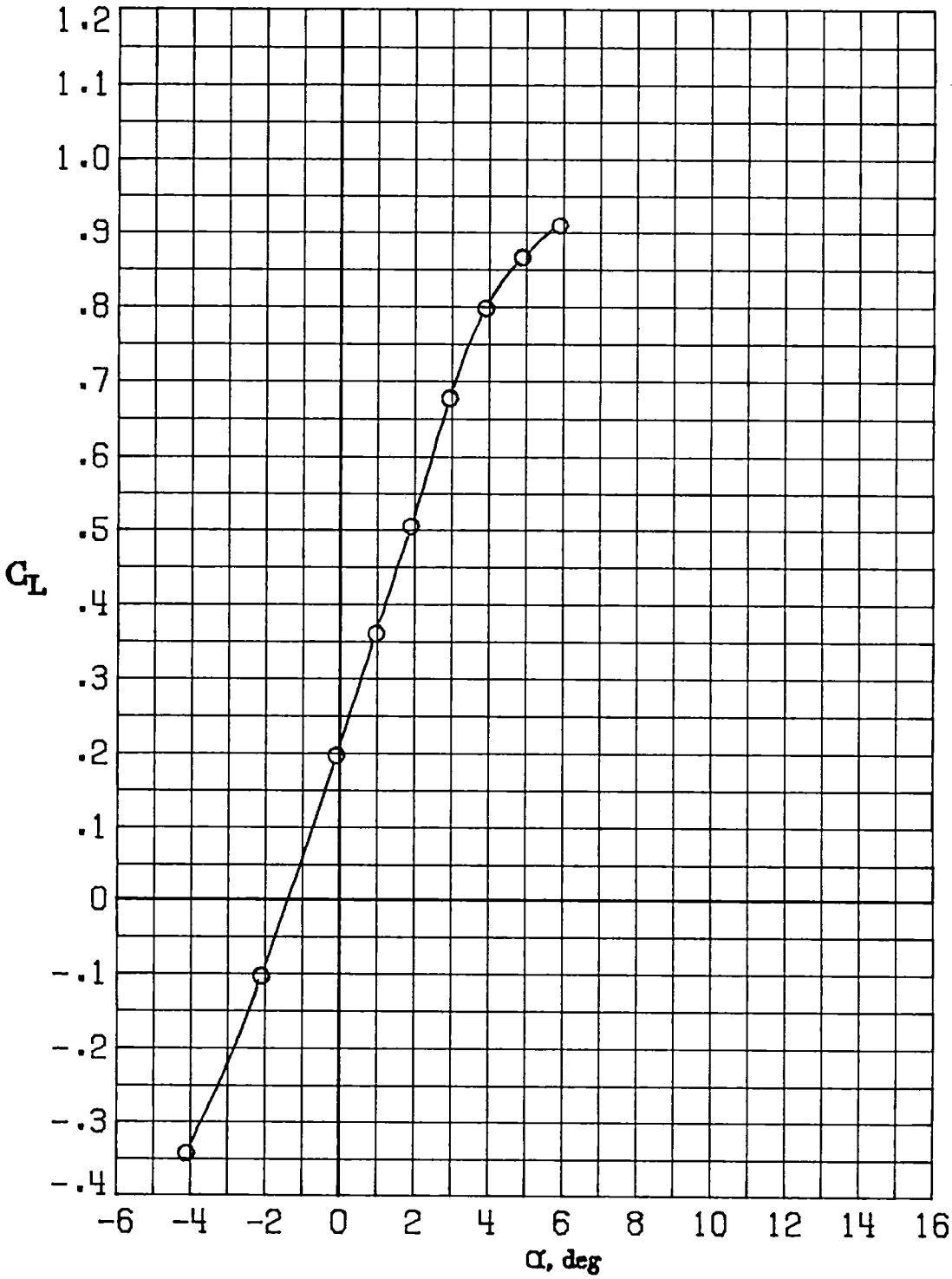

(e) $M_\infty = 0.81$.

Figure 18.- Continued.

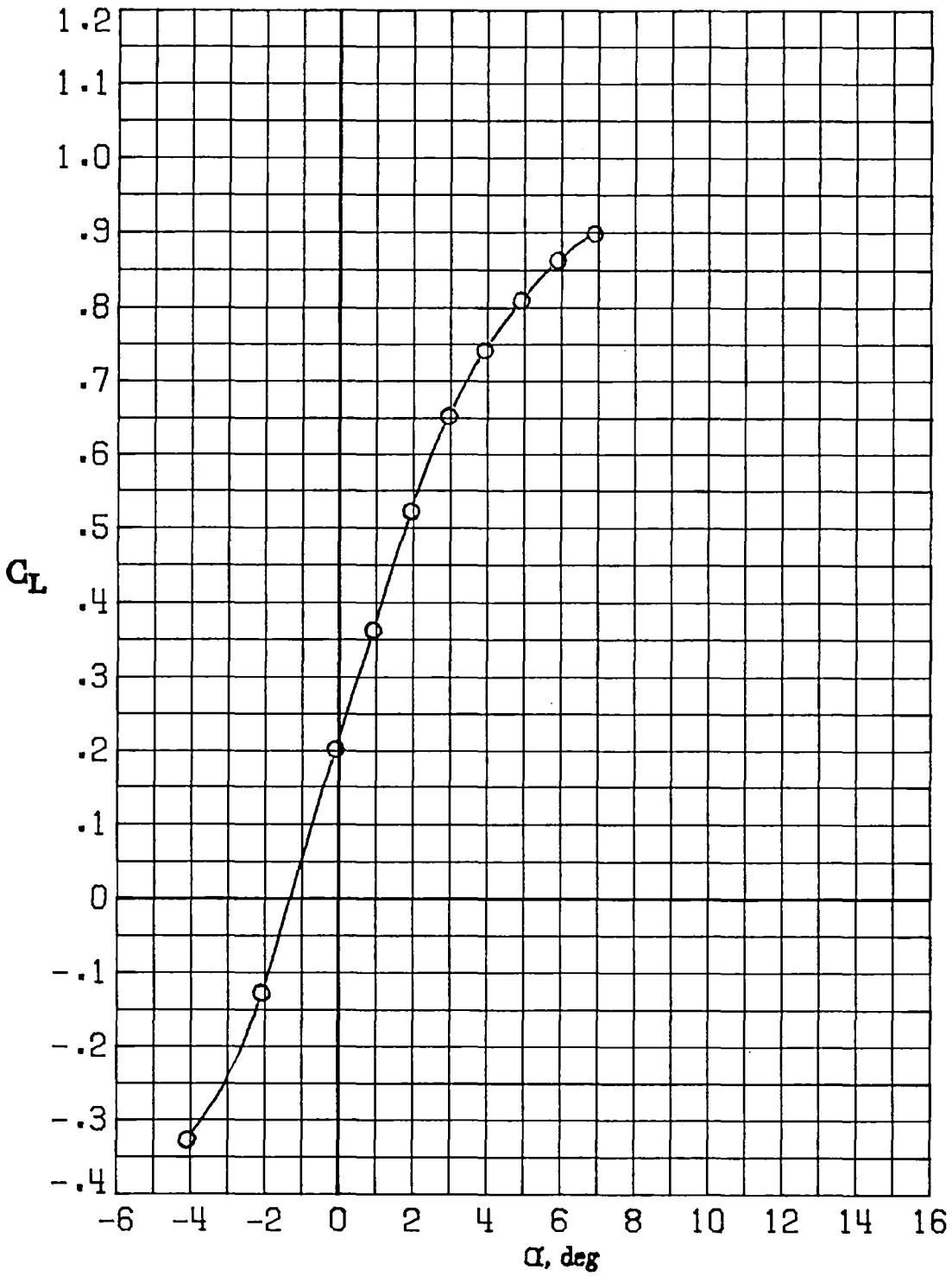

(f) $M_\infty = 0.84$.

Figure 18.- Continued.

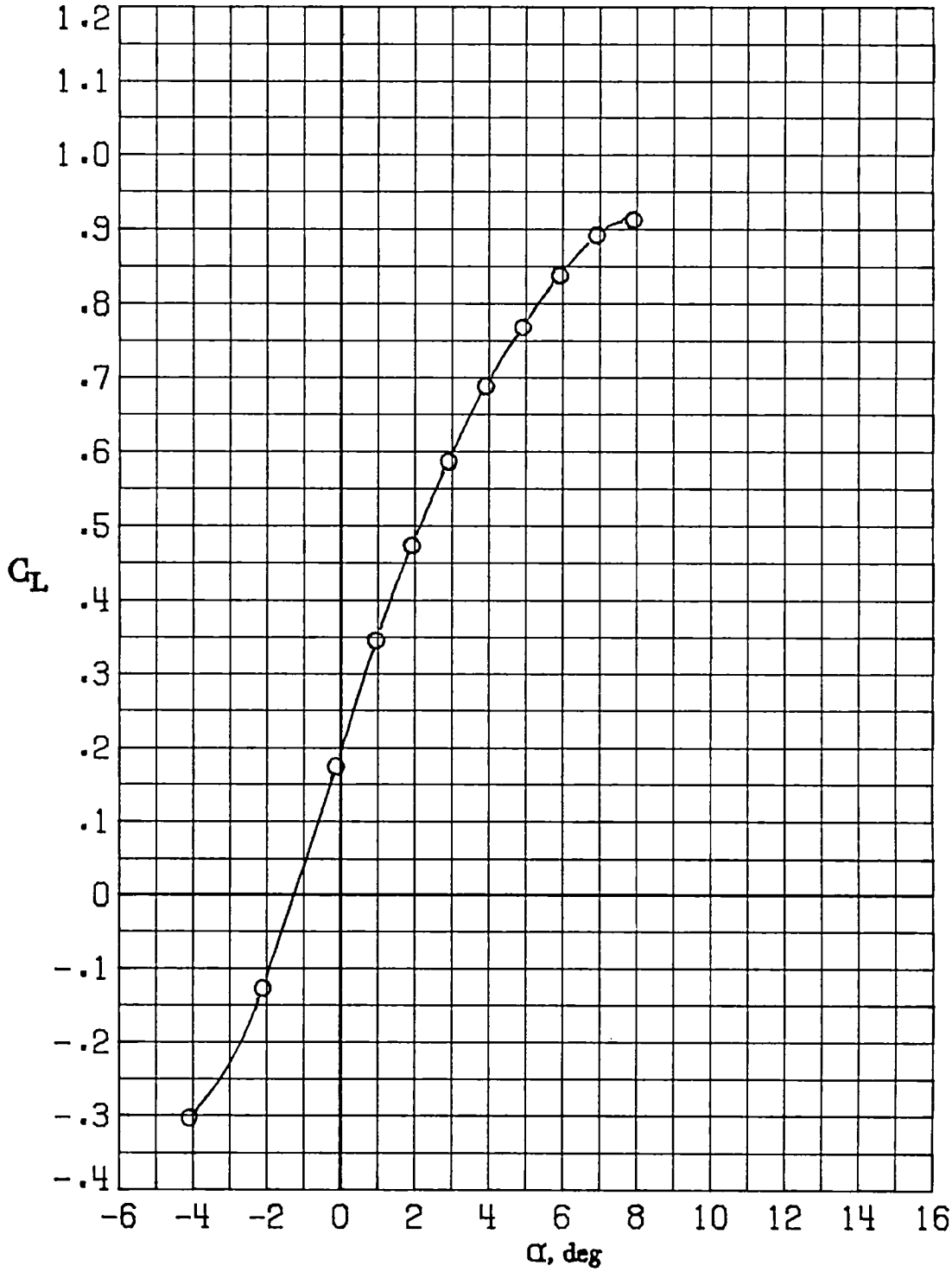

(g) $M_\infty = 0.86$.

Figure 18.- Concluded.

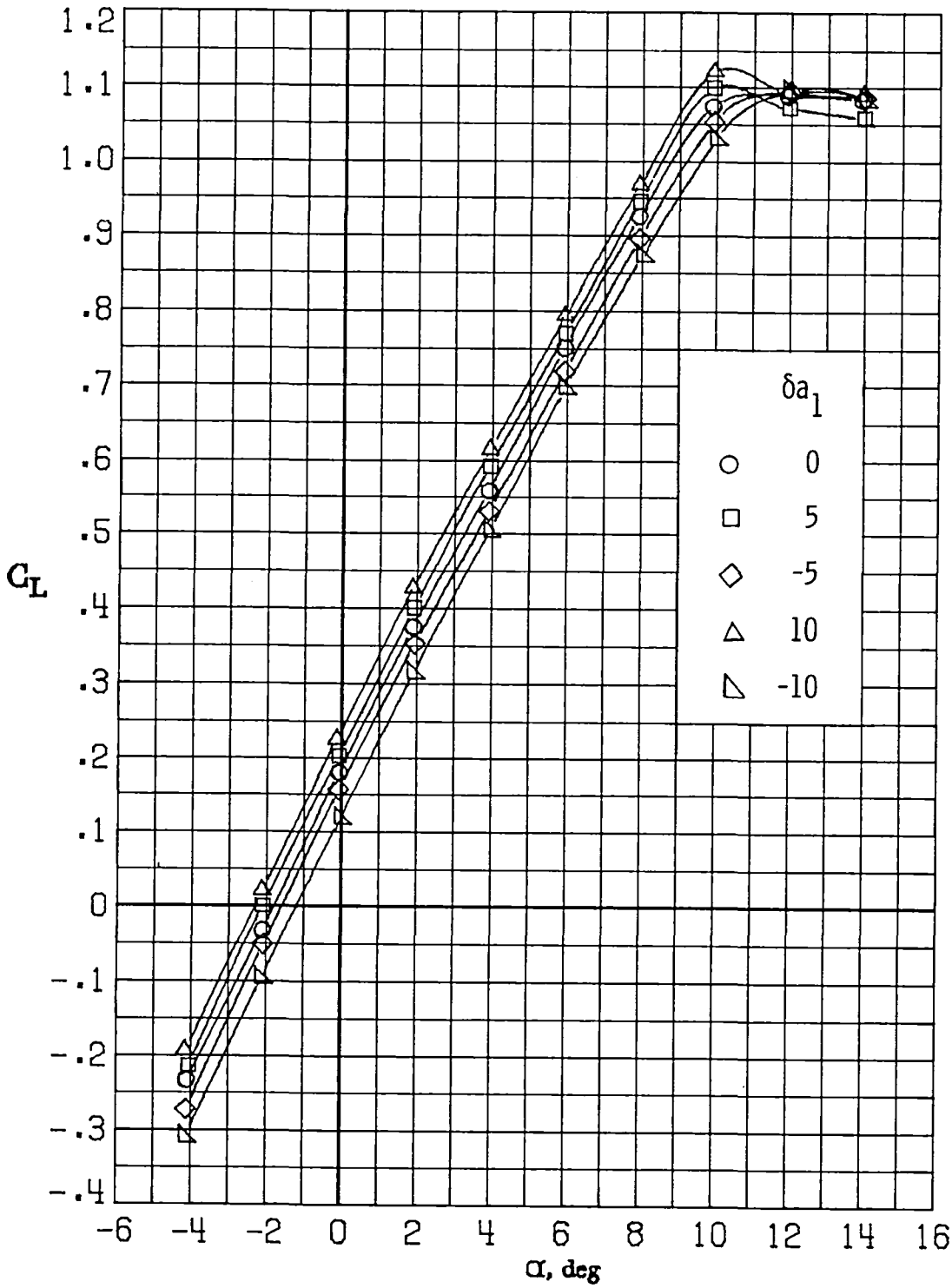

(a) $M_\infty = 0.30$.

Figure 19.- Variation of lift coefficient with angle of attack for deflections of aileron 1 (δa_1 in degrees). $\delta a_2 = 0°$; $\delta a_3 = 0°$.

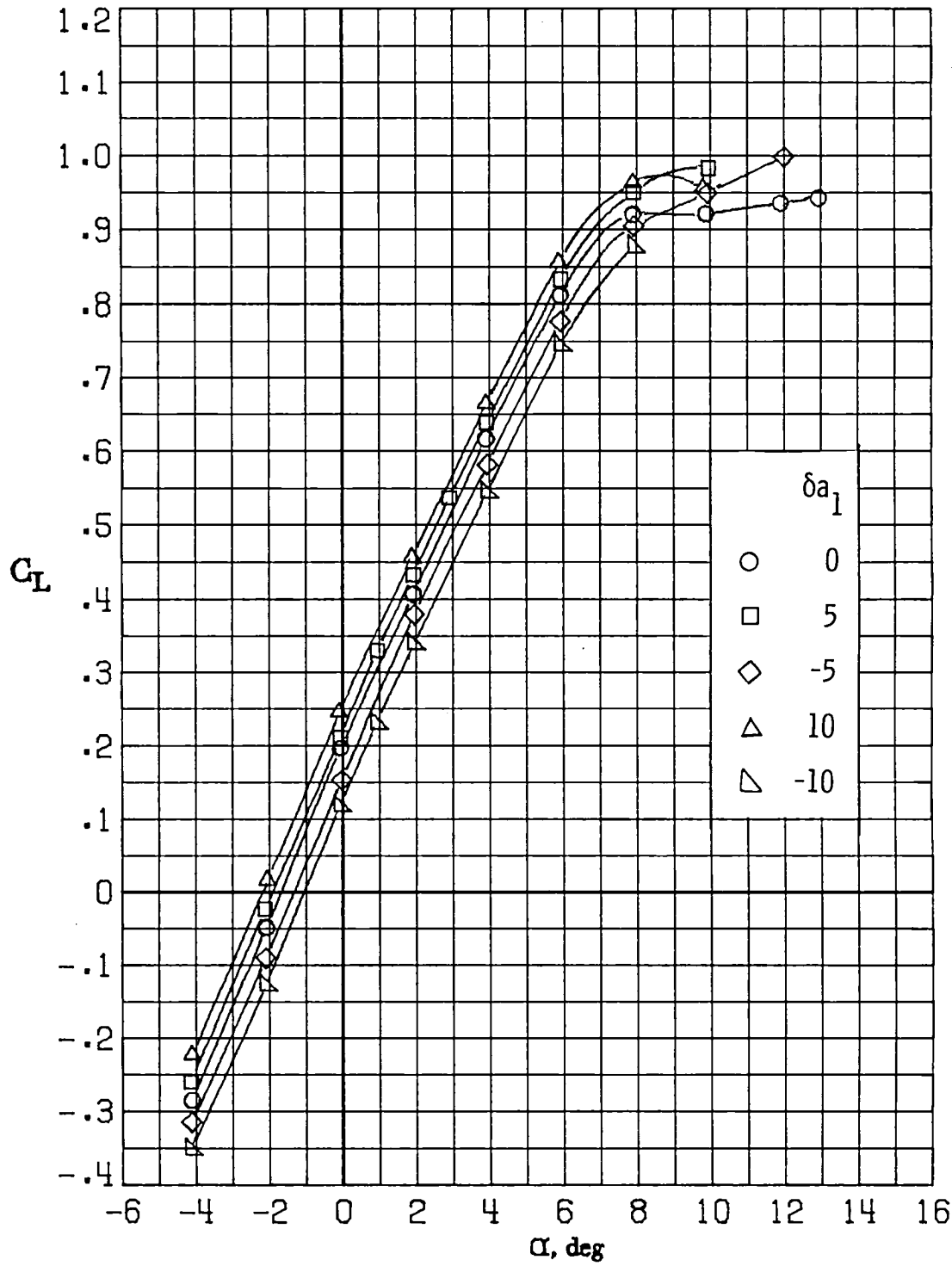

(b) $M_\infty = 0.60$.

Figure 19.- Continued.

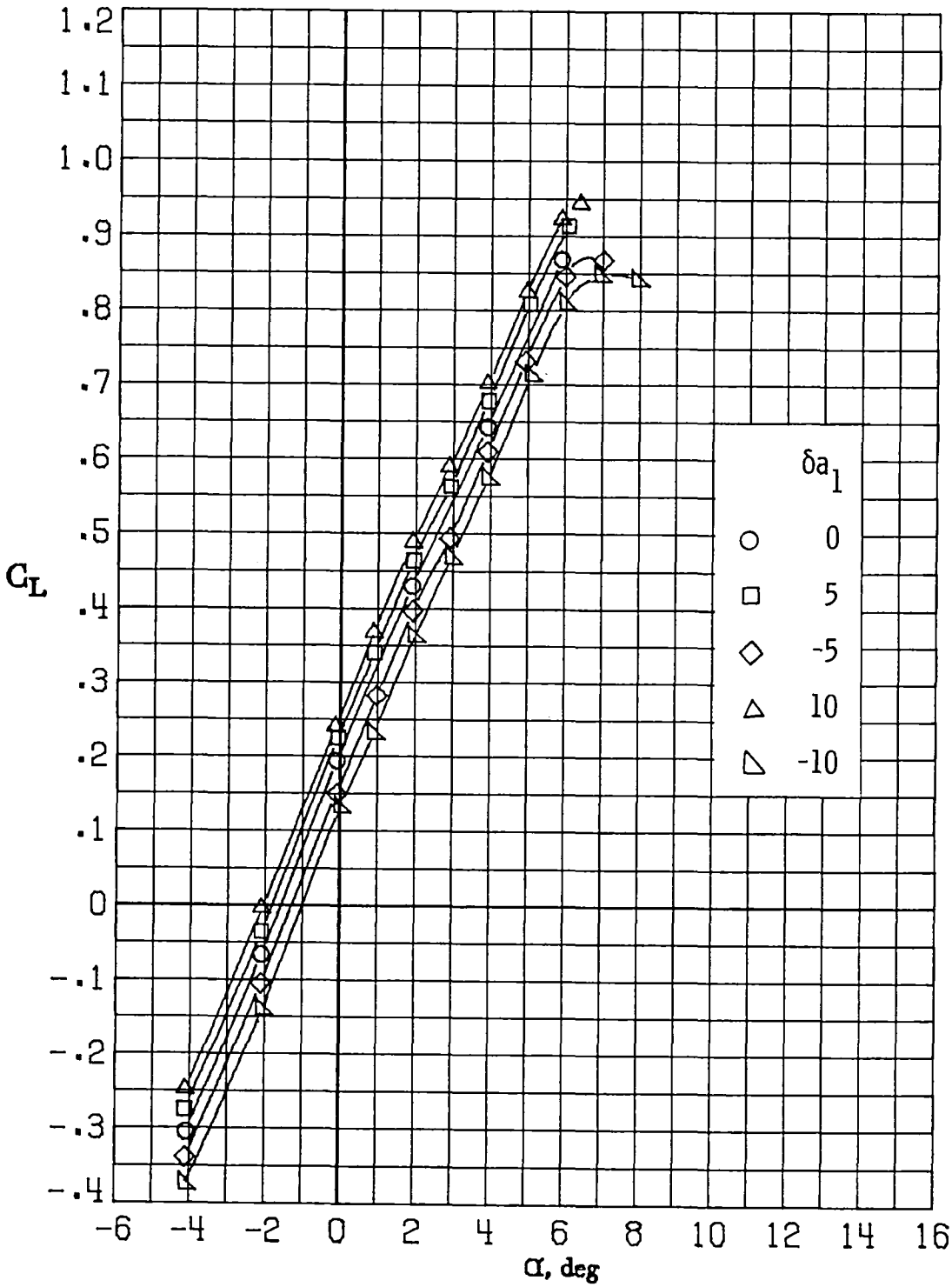

(c) $M_\infty = 0.70$.

Figure 19.- Continued.

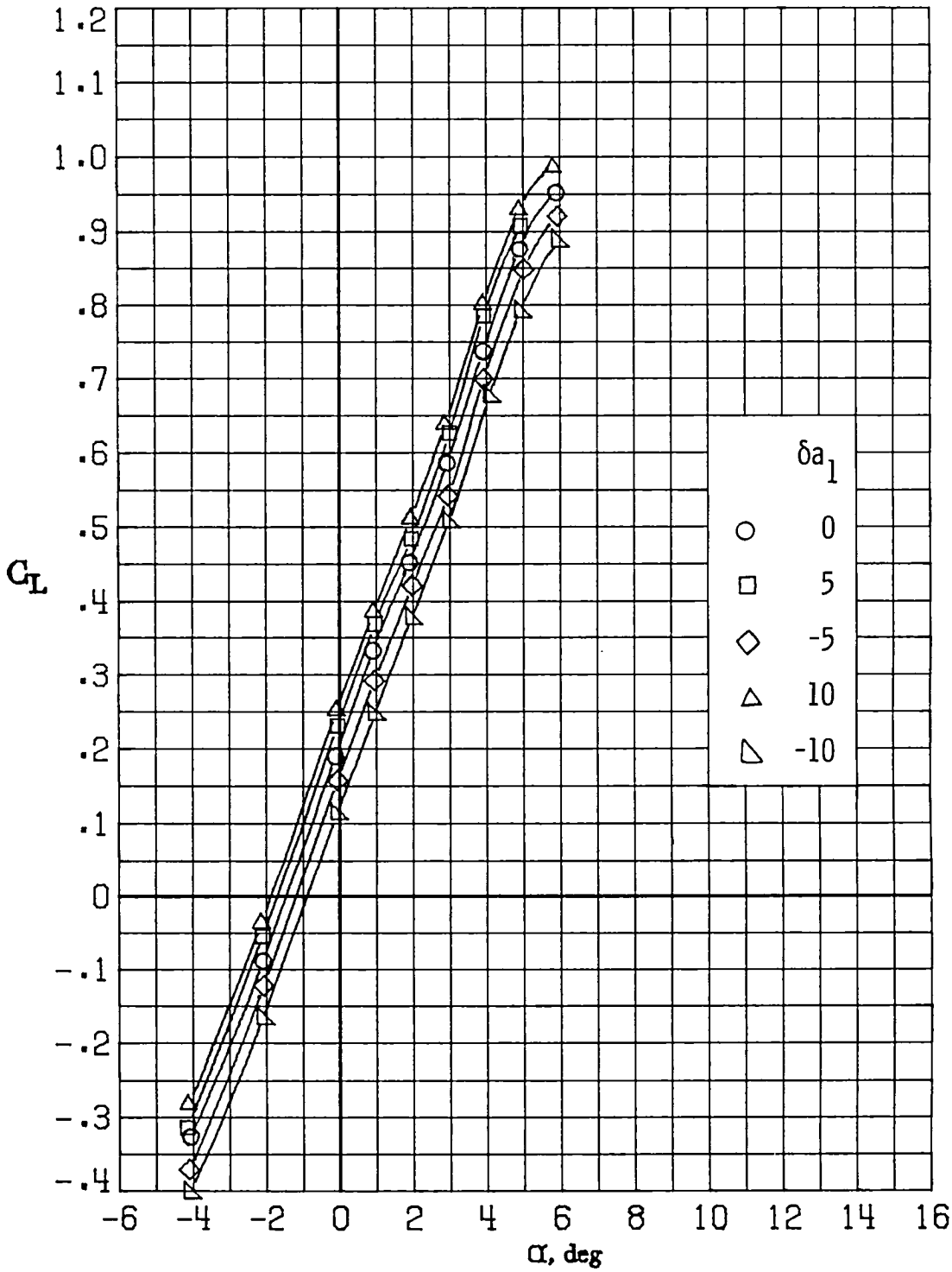

(d) $M_\infty = 0.77$.

Figure 19.- Continued.

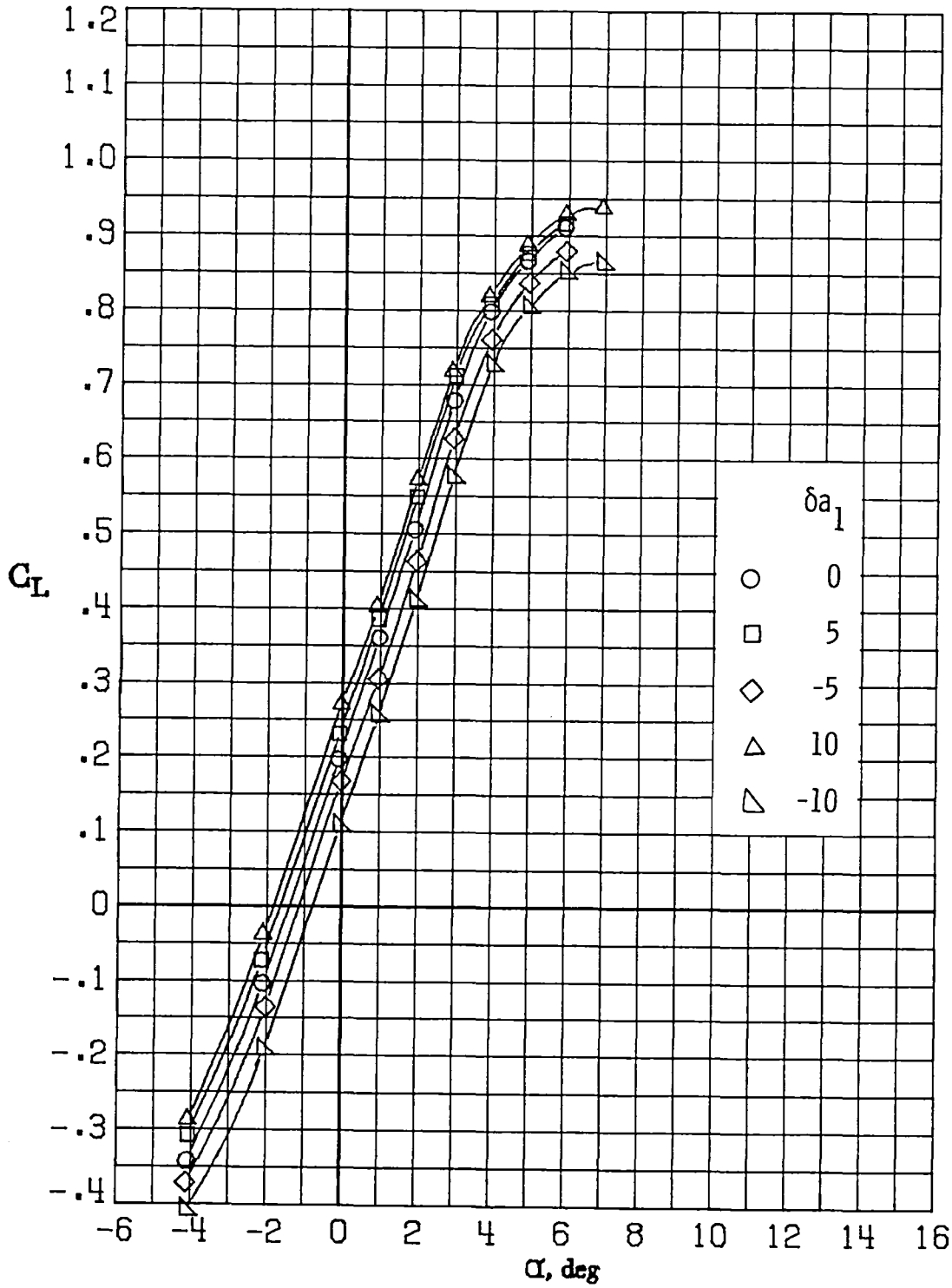

(e) $M_\infty = 0.81$.

Figure 19.- Continued.

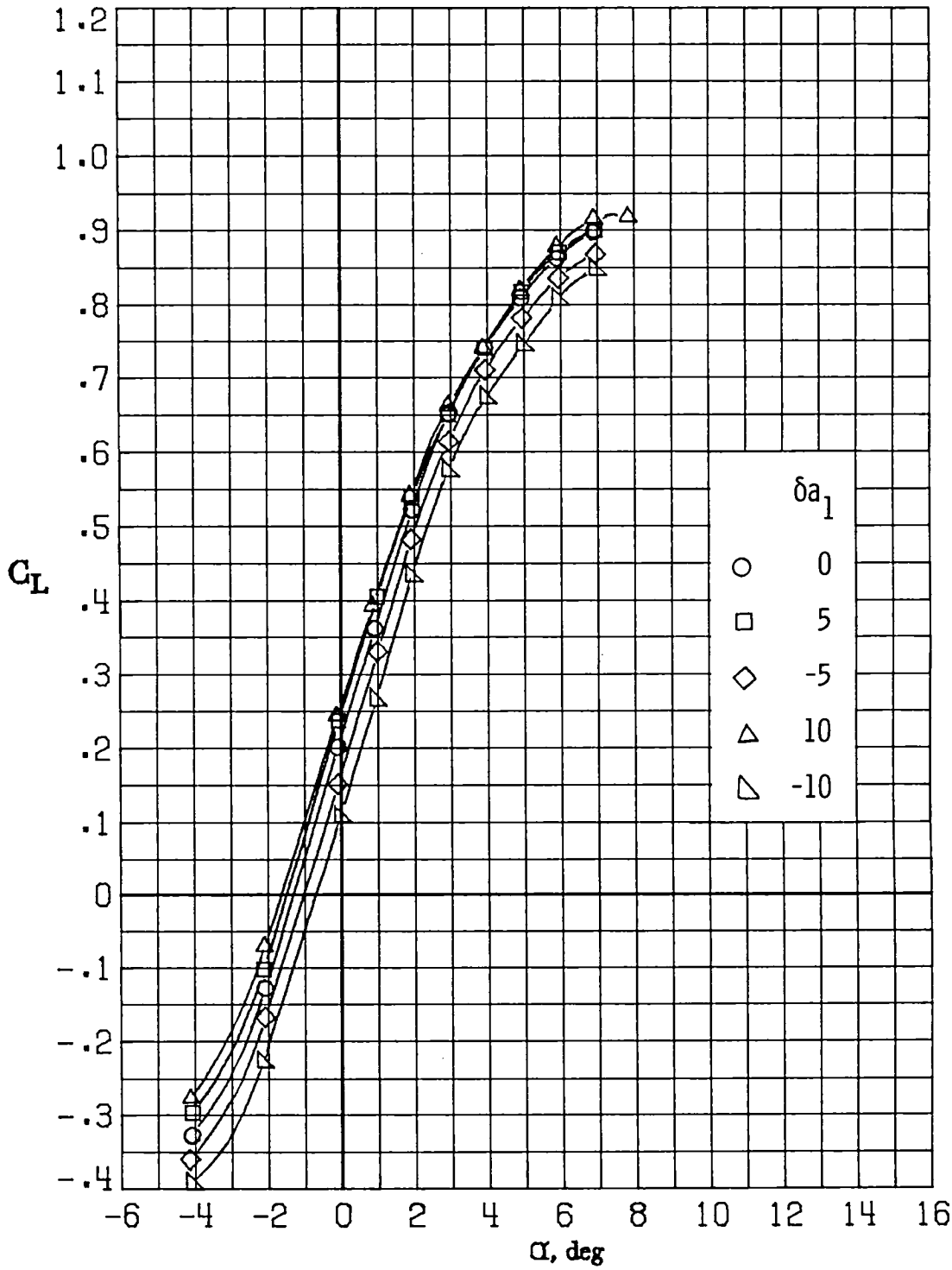

(f) $M_\infty = 0.84$.

Figure 19.- Continued.

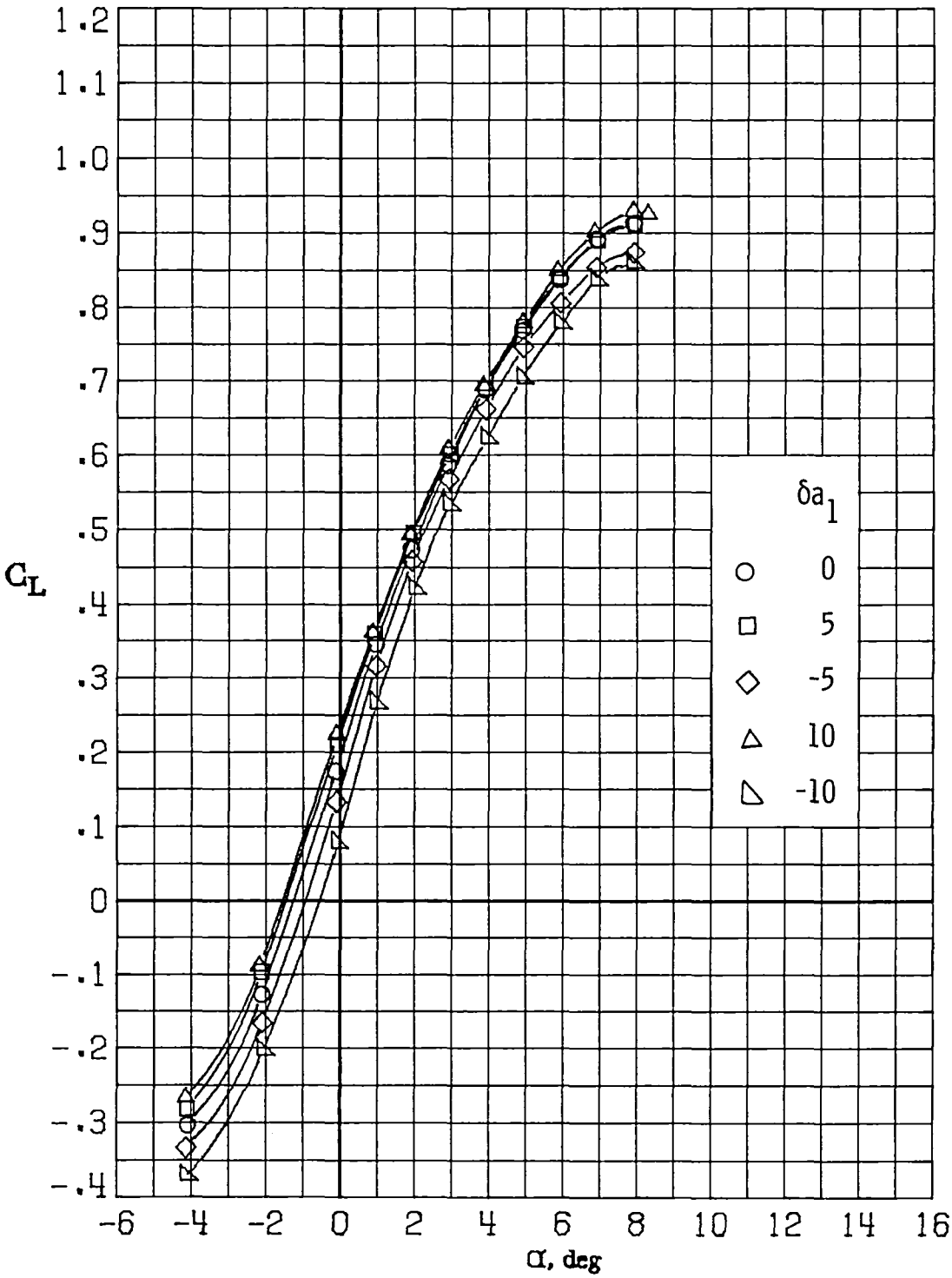

(g) $M_\infty = 0.86$.

Figure 19.- Concluded.

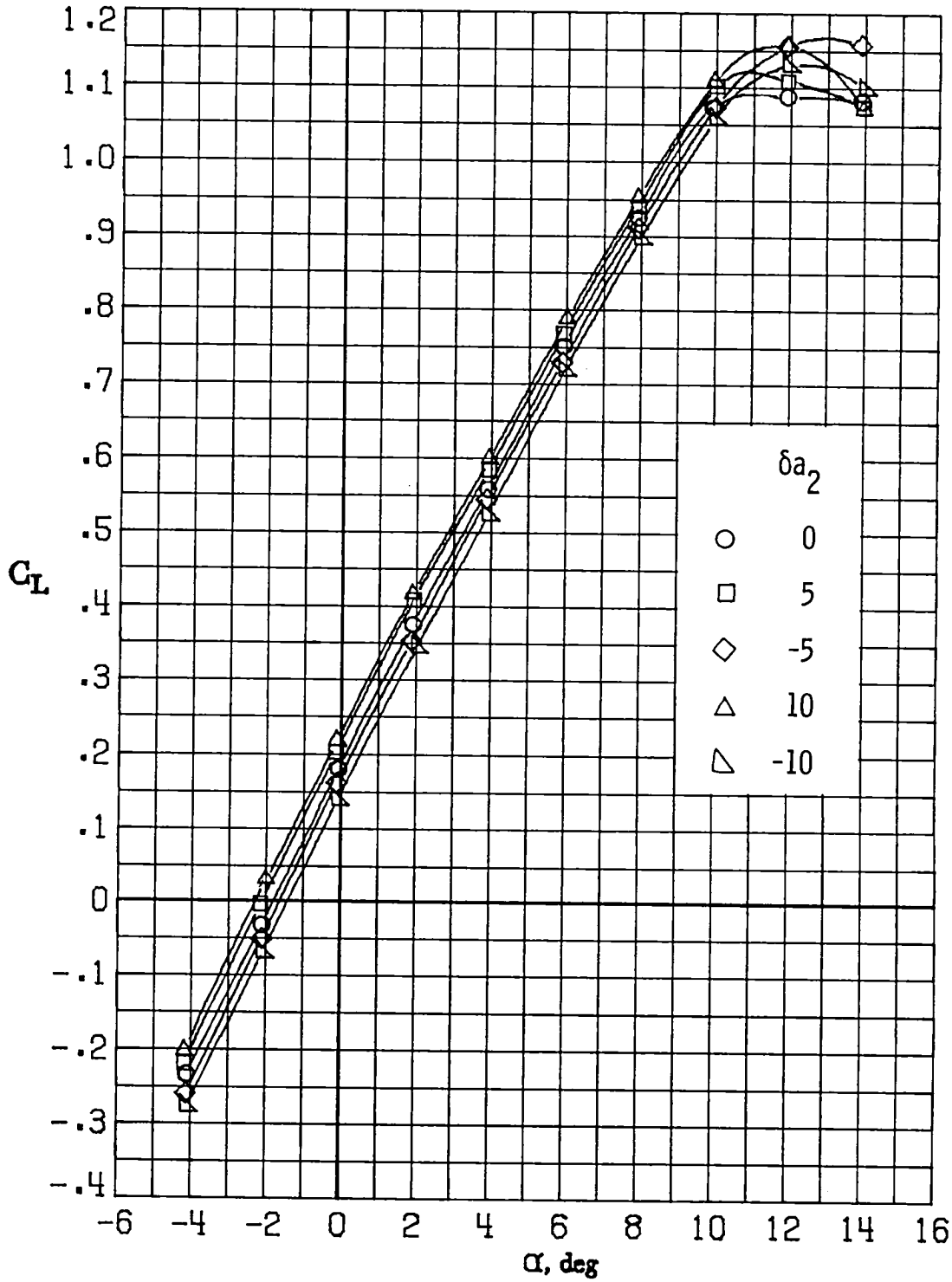

(a) $M_\infty = 0.30$.

Figure 20.- Variation of lift coefficient with angle of attack for deflections of aileron 2 (δa_2 in degrees). $\delta a_1 = 0°$; $\delta a_3 = 0°$.

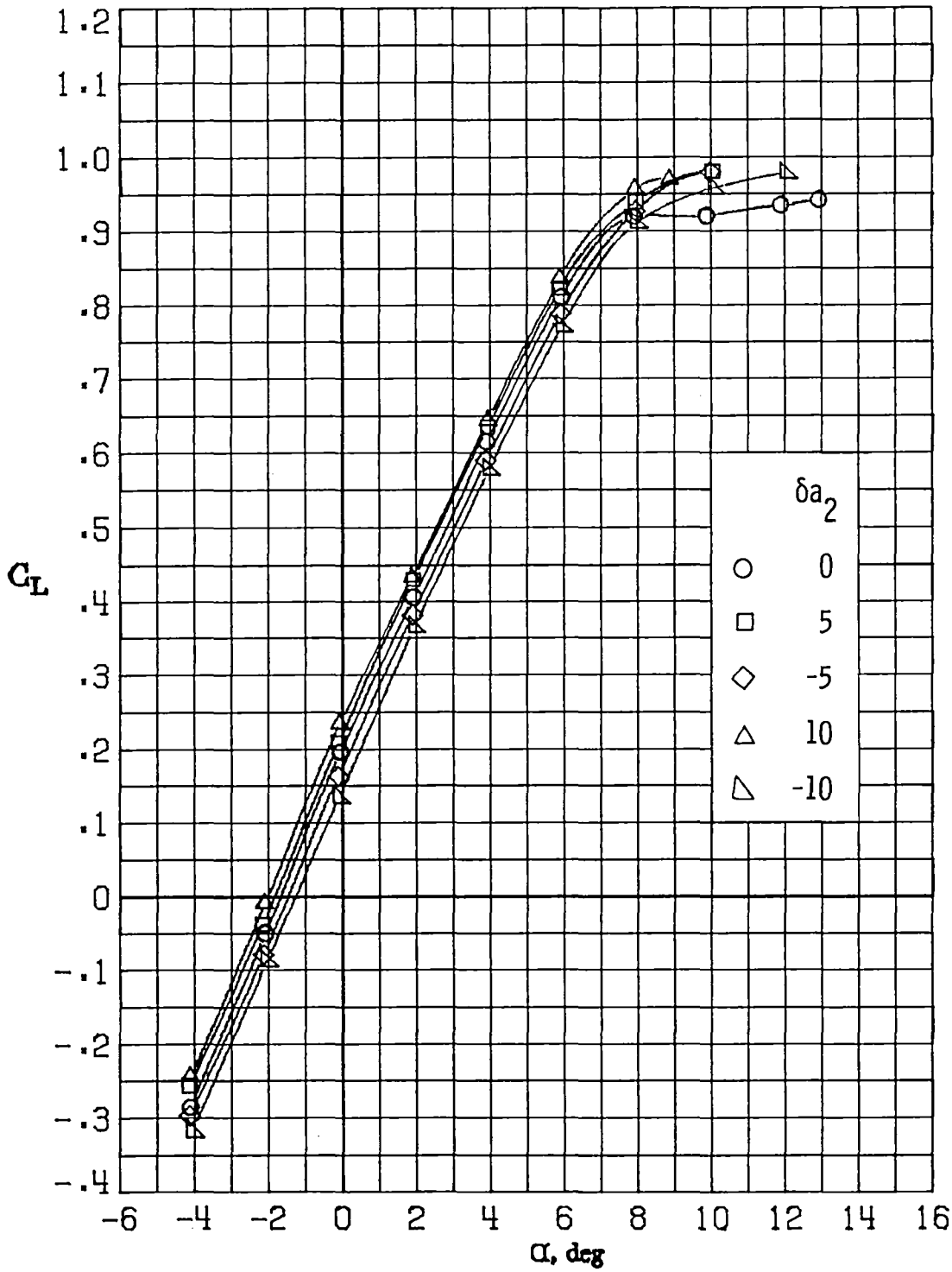

(b) $M_\infty = 0.60$.

Figure 20.- Continued.

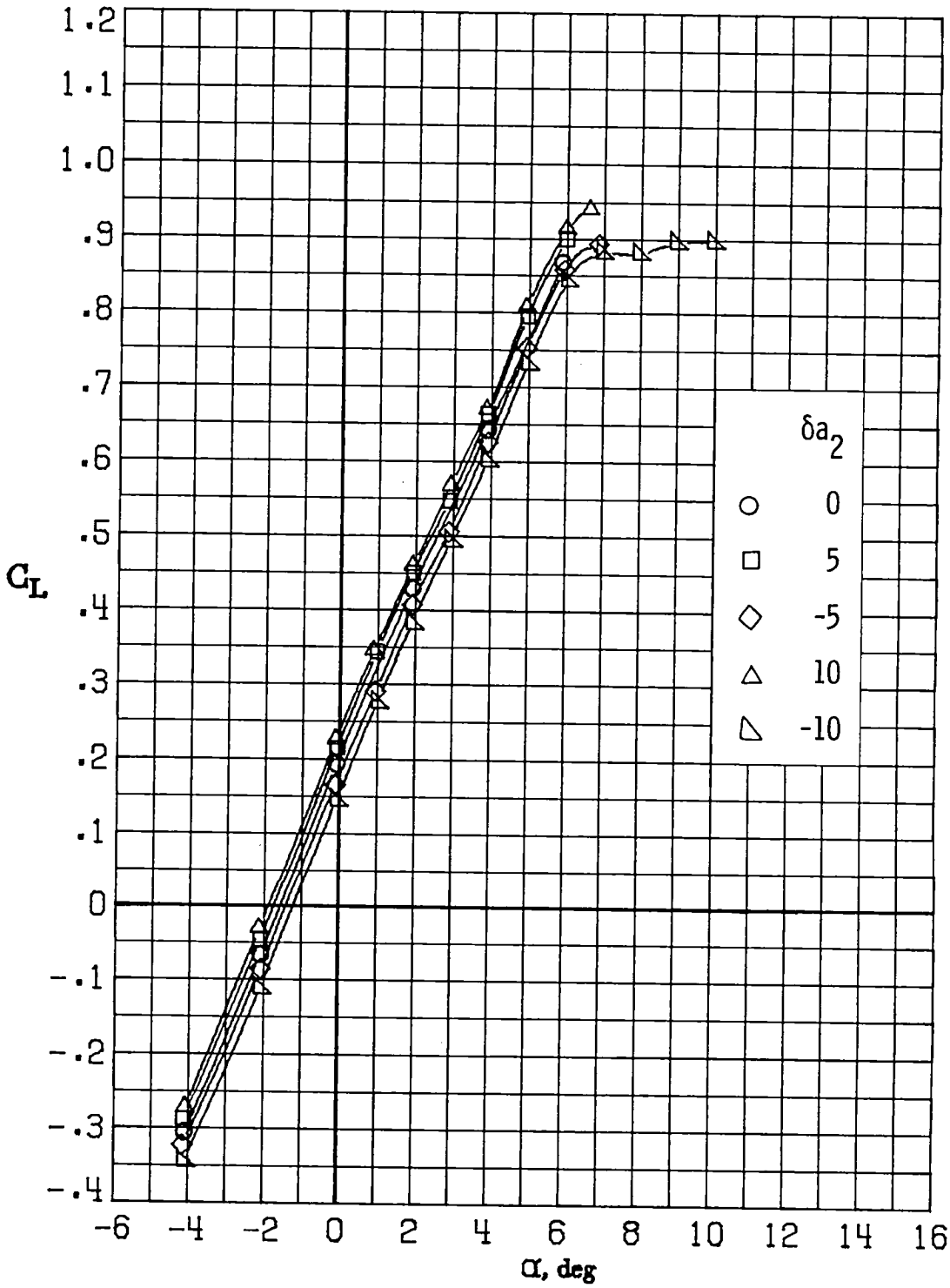

(c) $M_\infty = 0.70$.

Figure 20.- Continued.

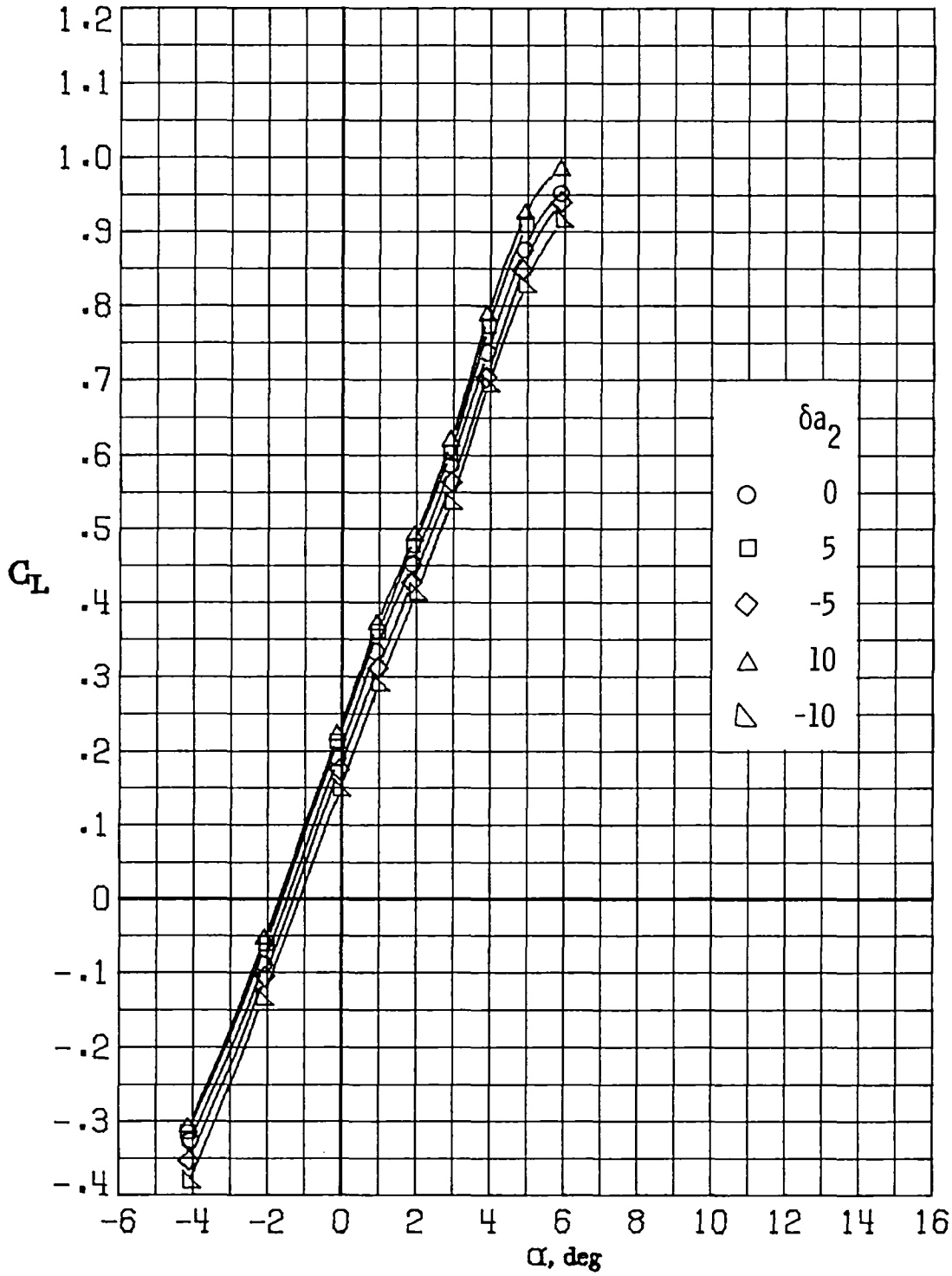

(d) $M_\infty = 0.77$.

Figure 20.- Continued.

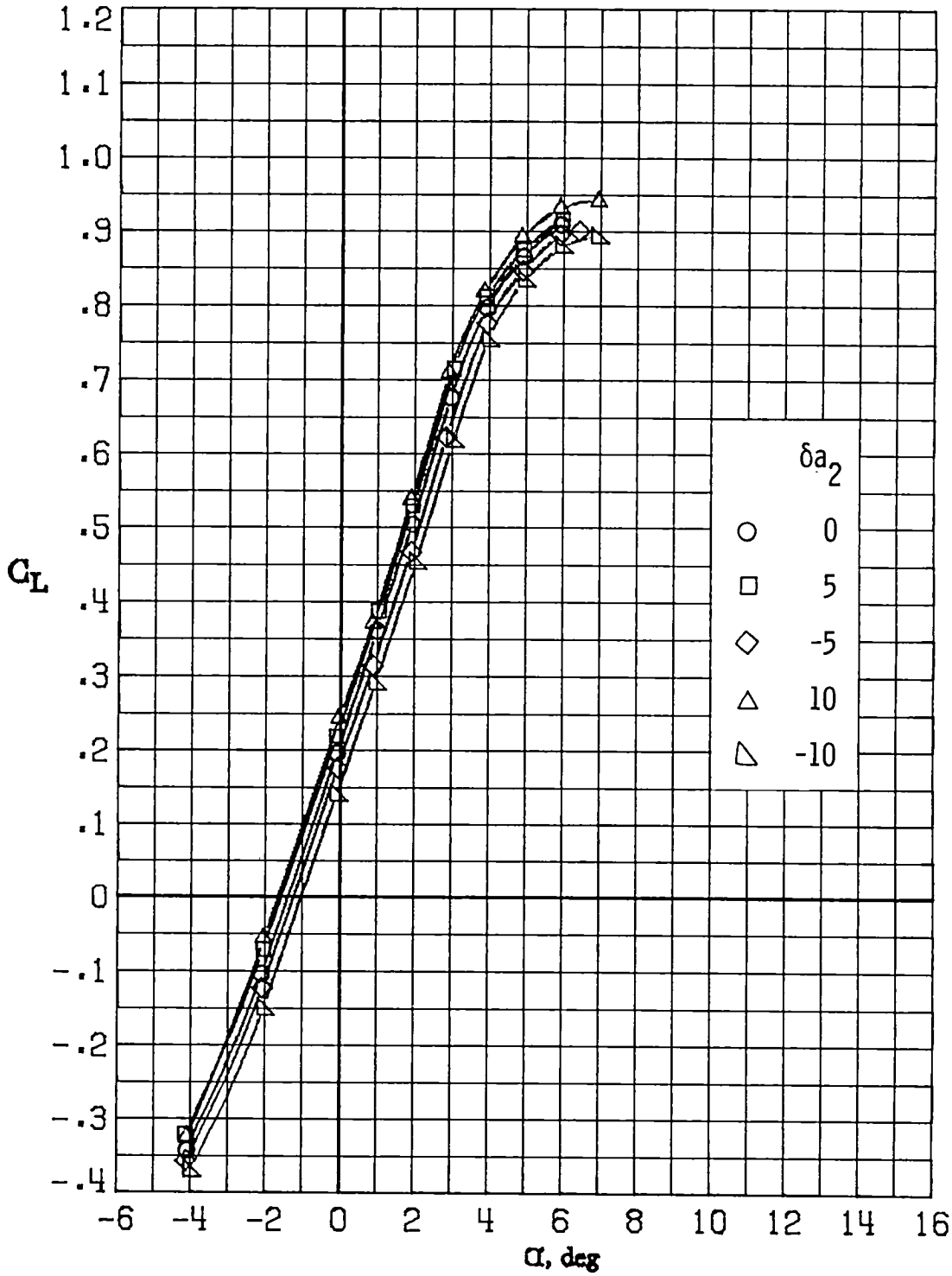

(e) $M_\infty = 0.81$.

Figure 20.- Continued.

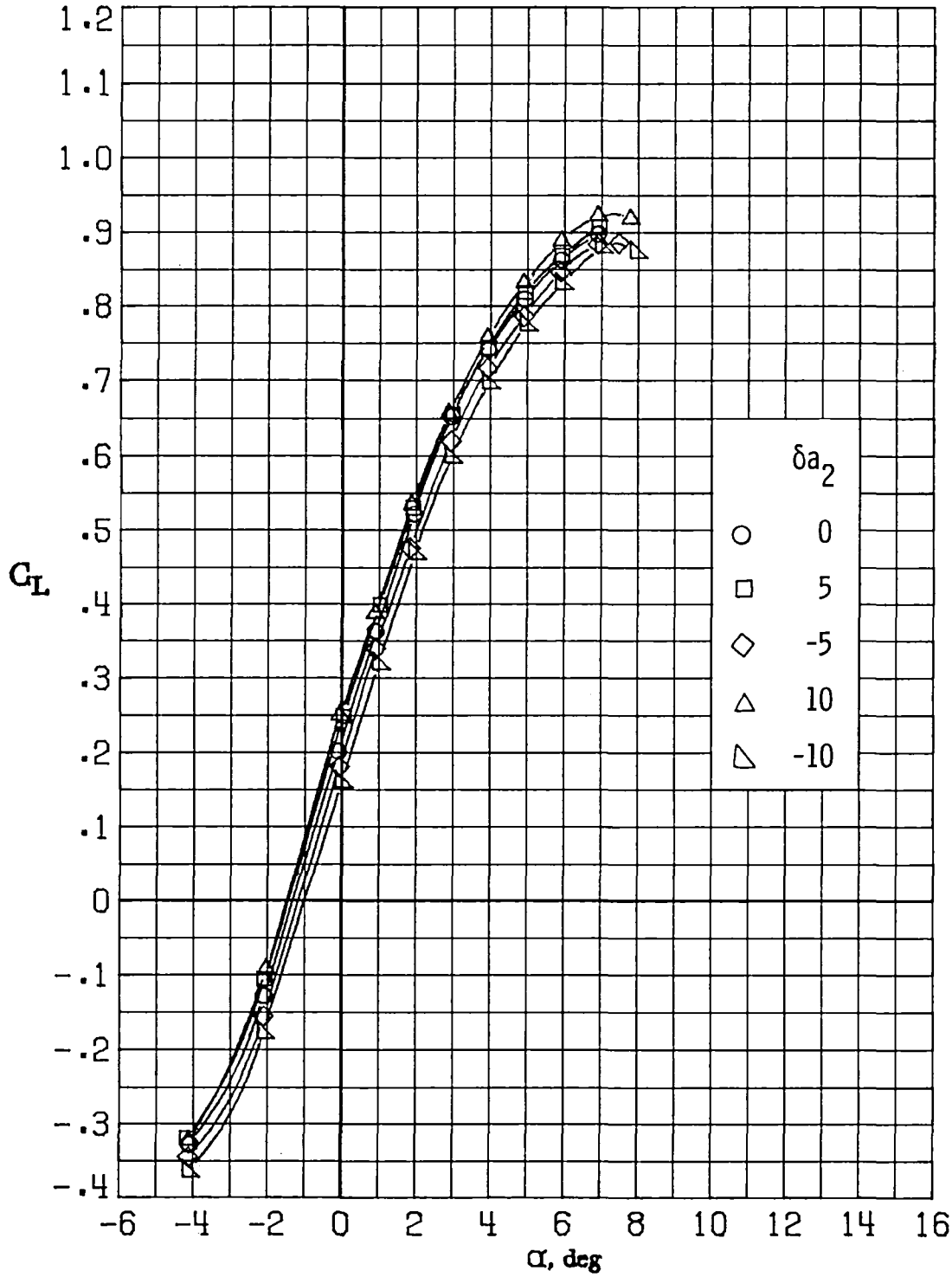

(f) $M_\infty = 0.84$.

Figure 20.- Continued.

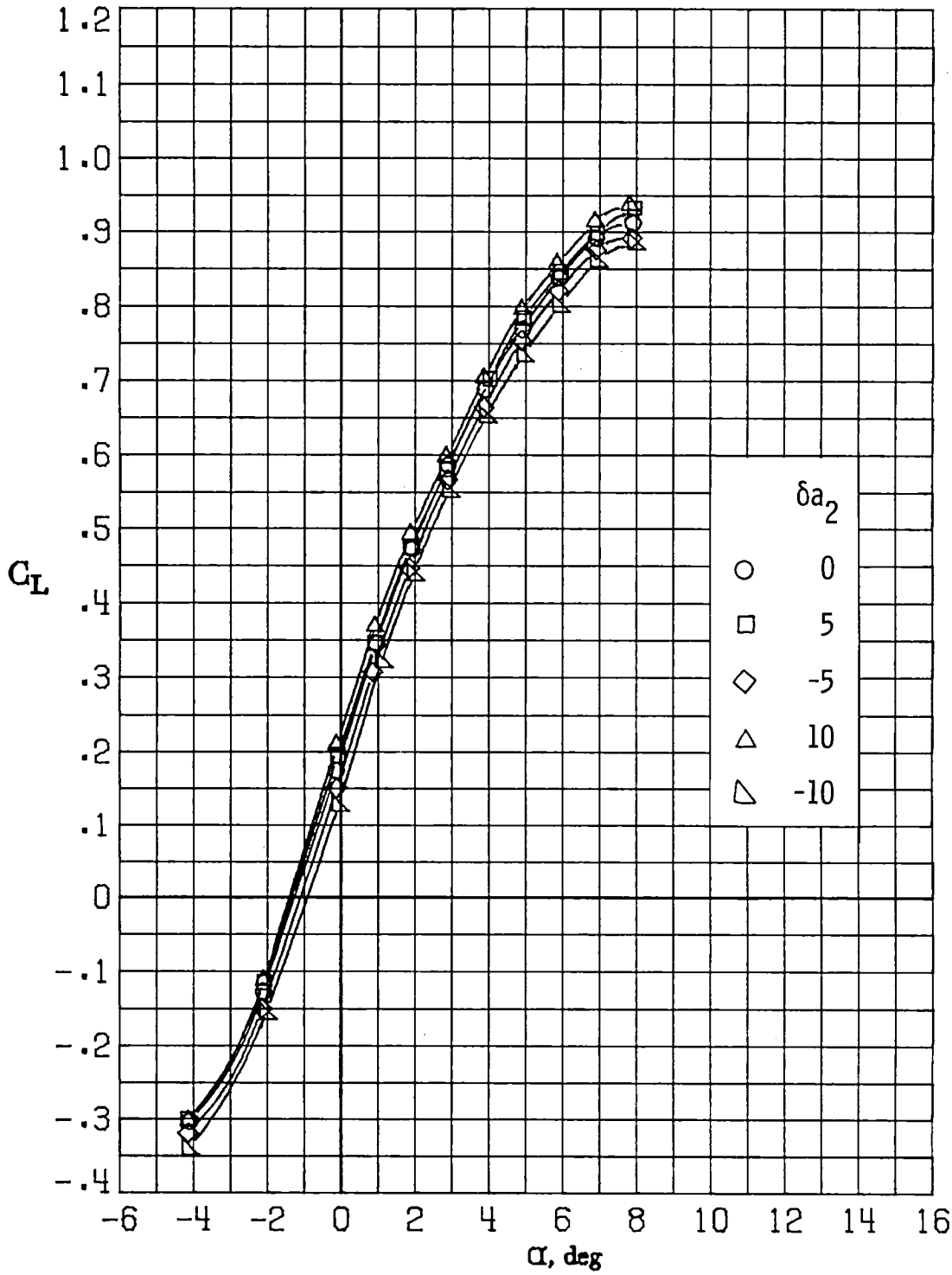

(g) $M_\infty = 0.86$.

Figure 20.- Concluded.

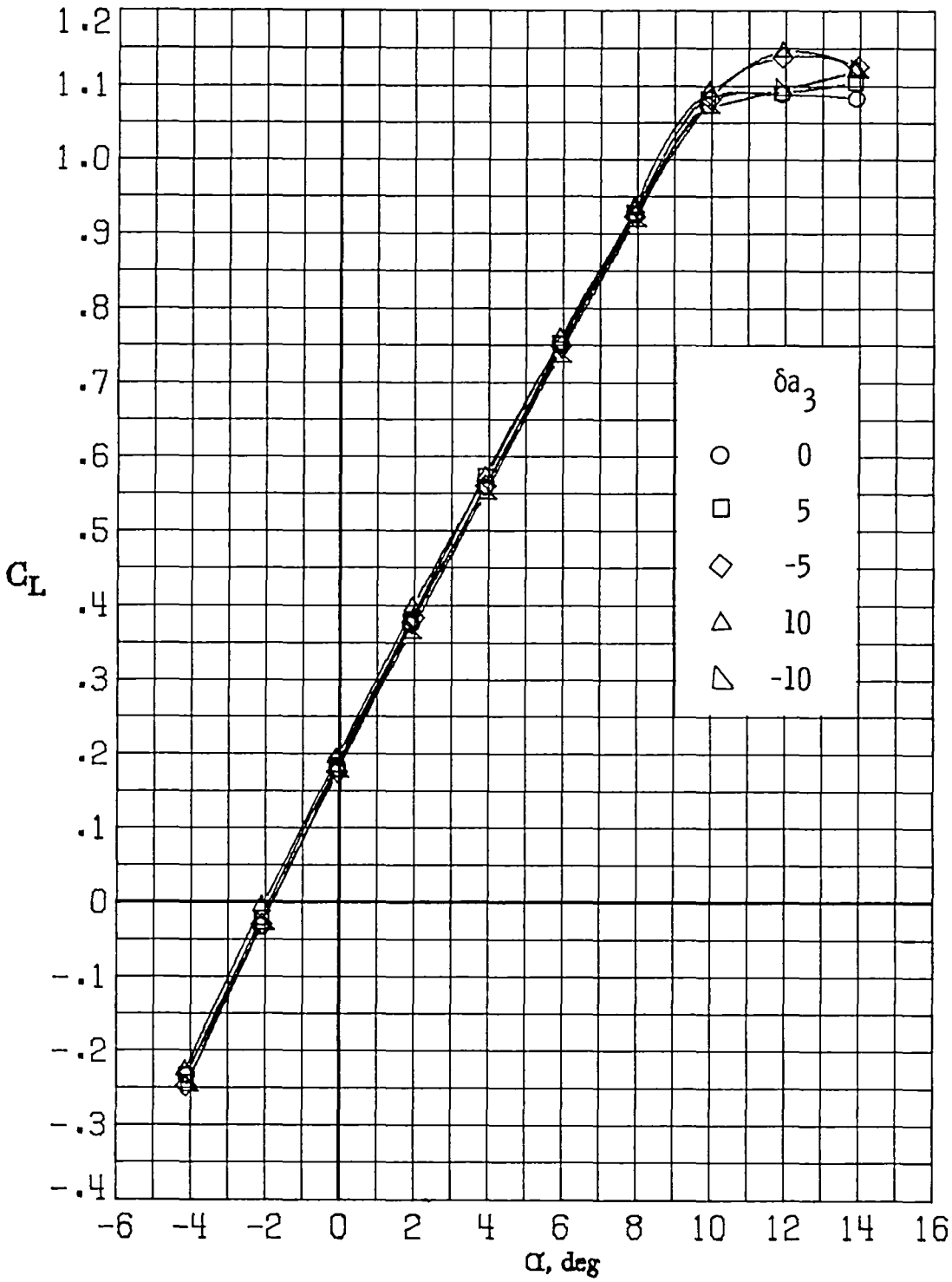

(a) $M_\infty = 0.30$.

Figure 21.- Variation of lift coefficient with angle of attack for deflections of aileron 3 (δa_3 in degrees). $\delta a_1 = 0°$; $\delta a_2 = 0°$.

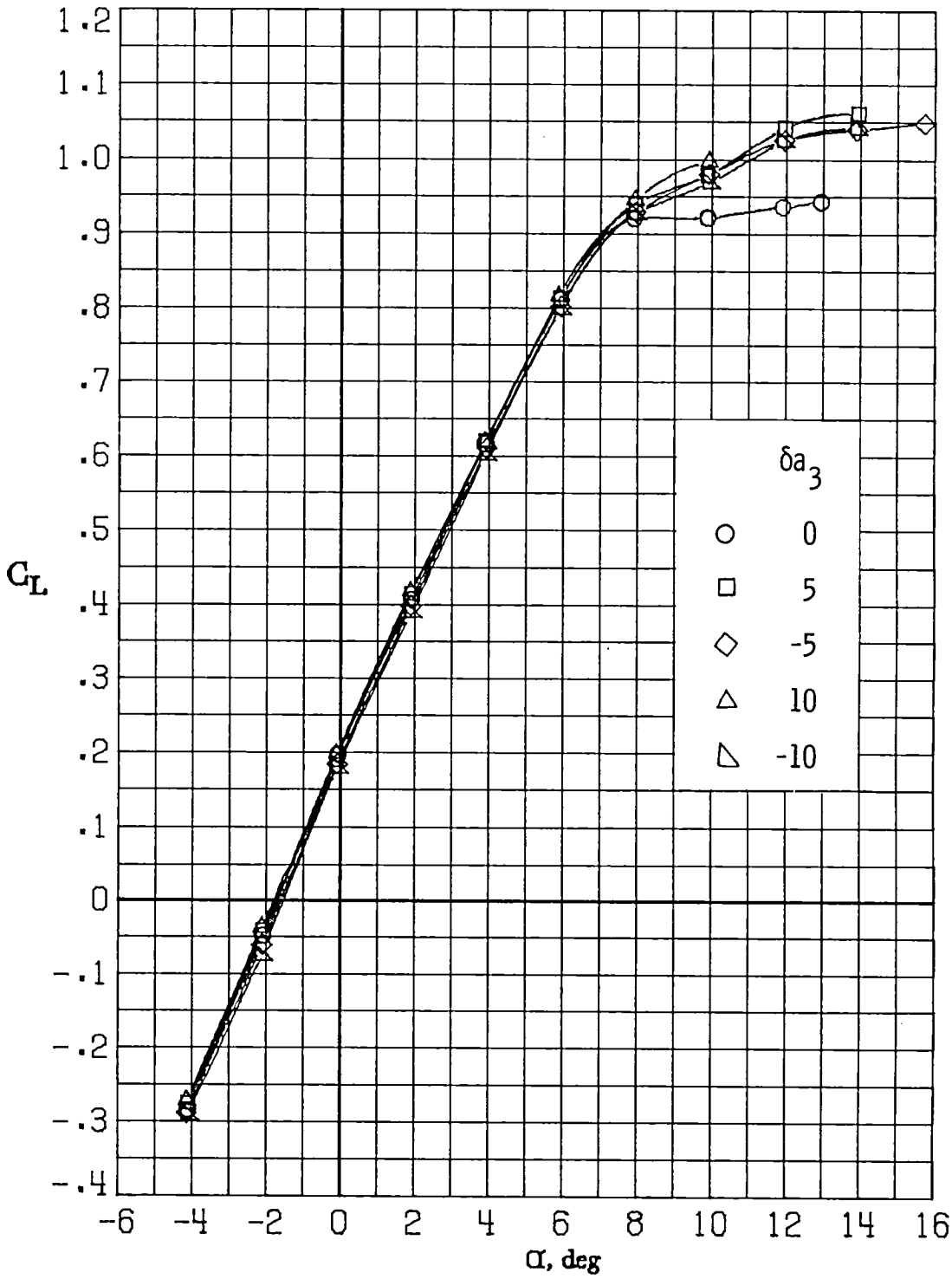

(b) $M_\infty = 0.60$.

Figure 21.- Continued.

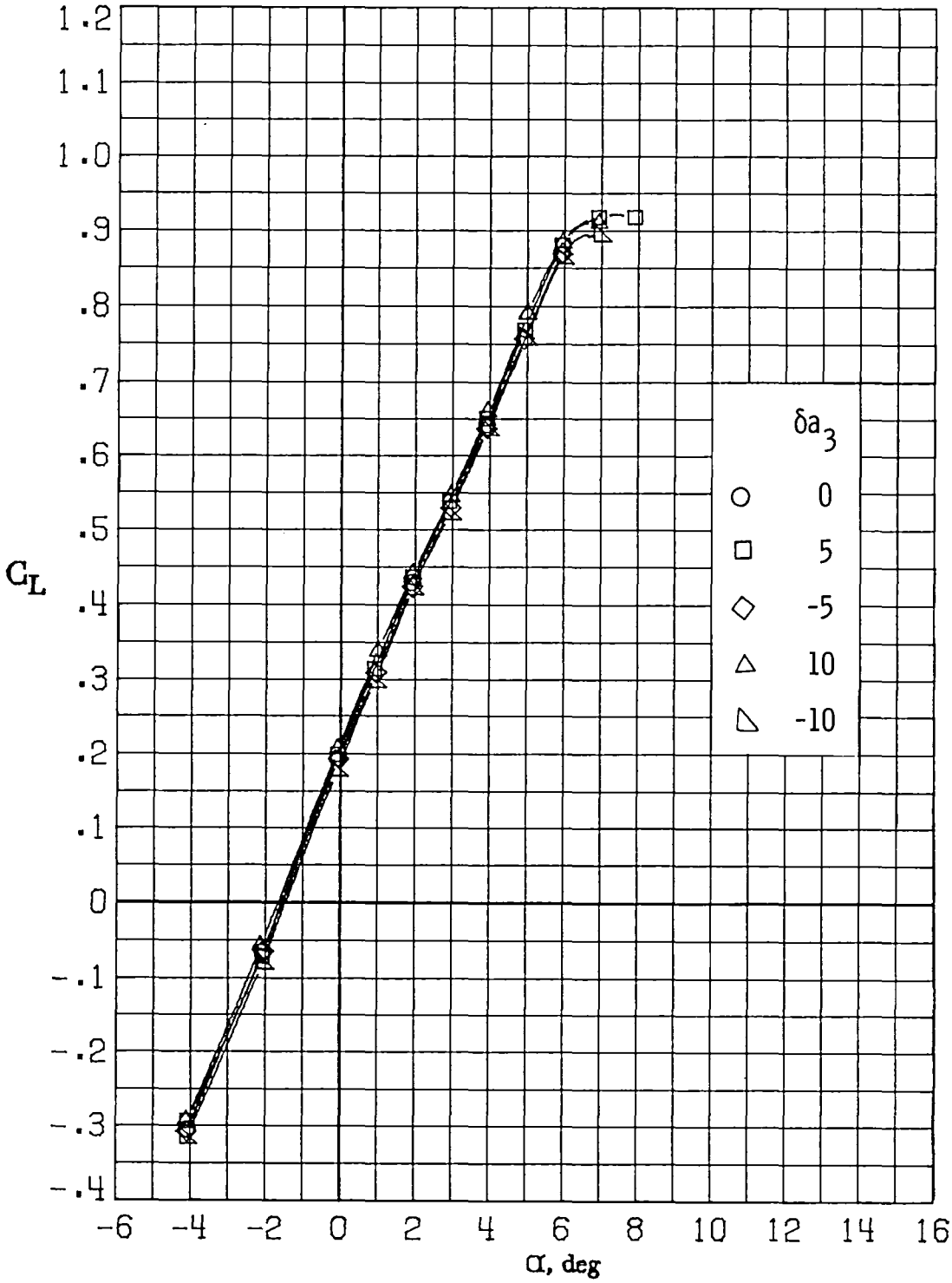

(c) $M_\infty = 0.70$.

Figure 21.- Continued.

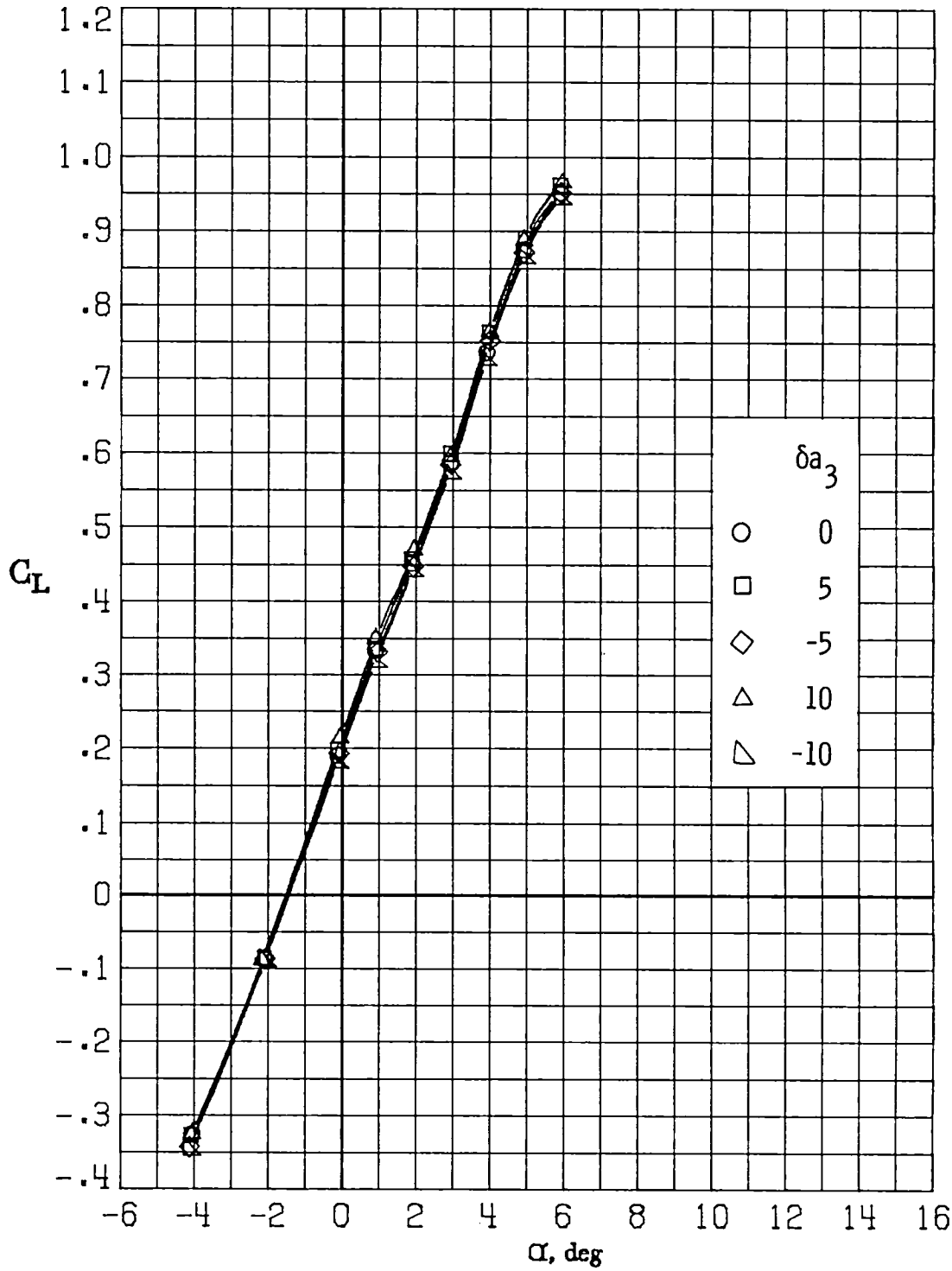

(d) $M_\infty = 0.77$.

Figure 21.- Continued.

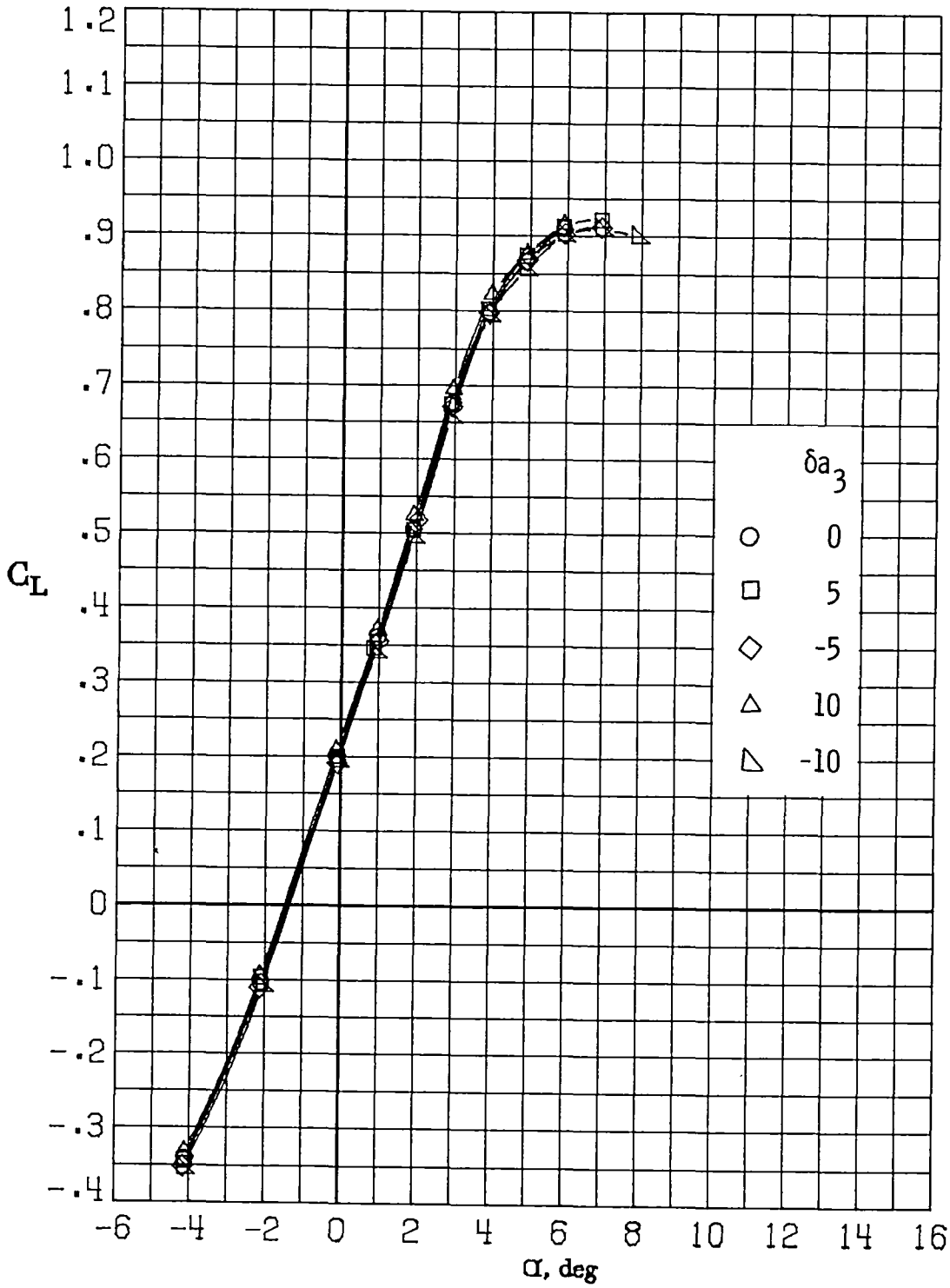

(e) $M_\infty = 0.81$.

Figure 21.- Continued.

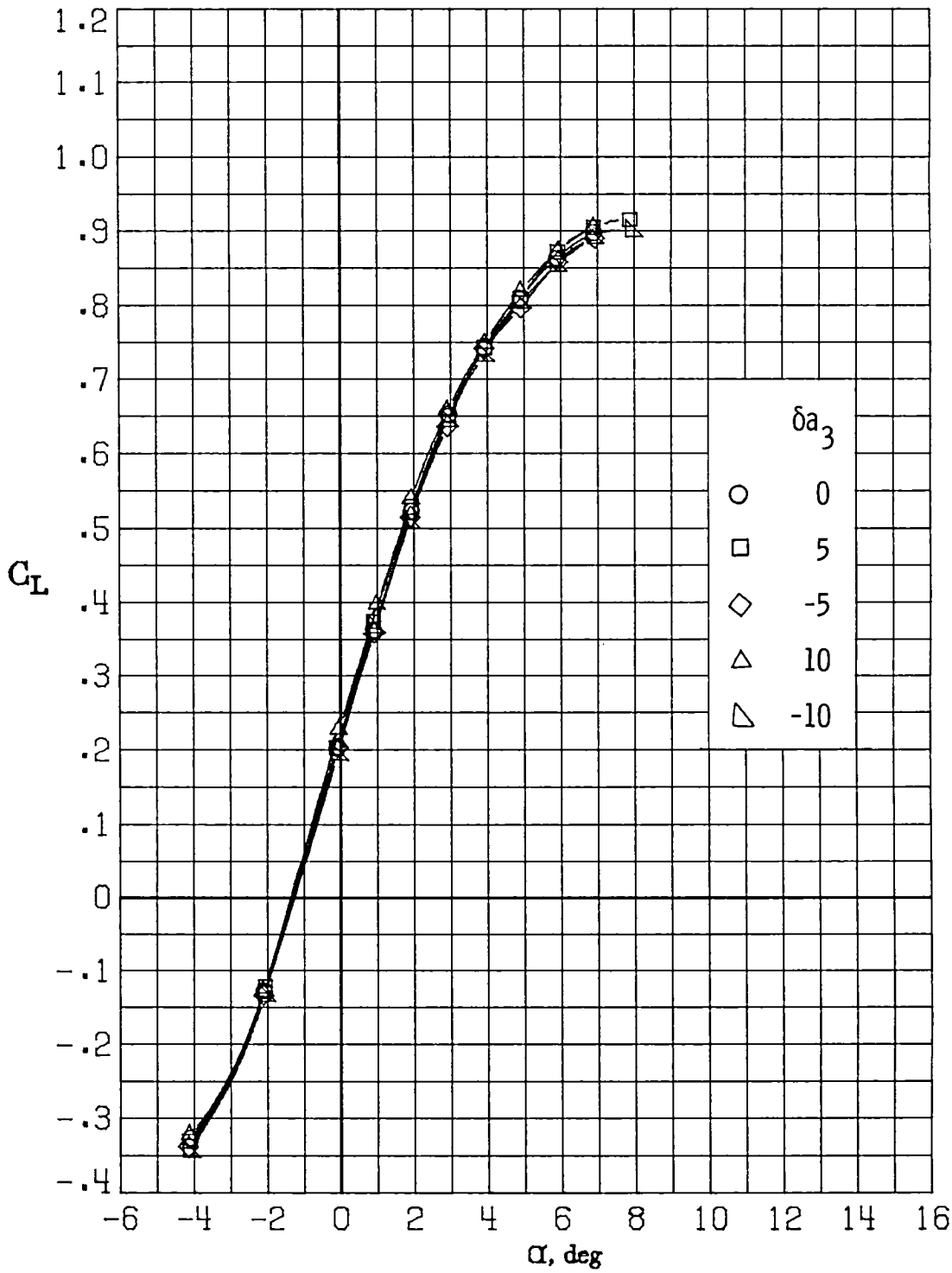

(f) $M_\infty = 0.84$.

Figure 21.- Continued.

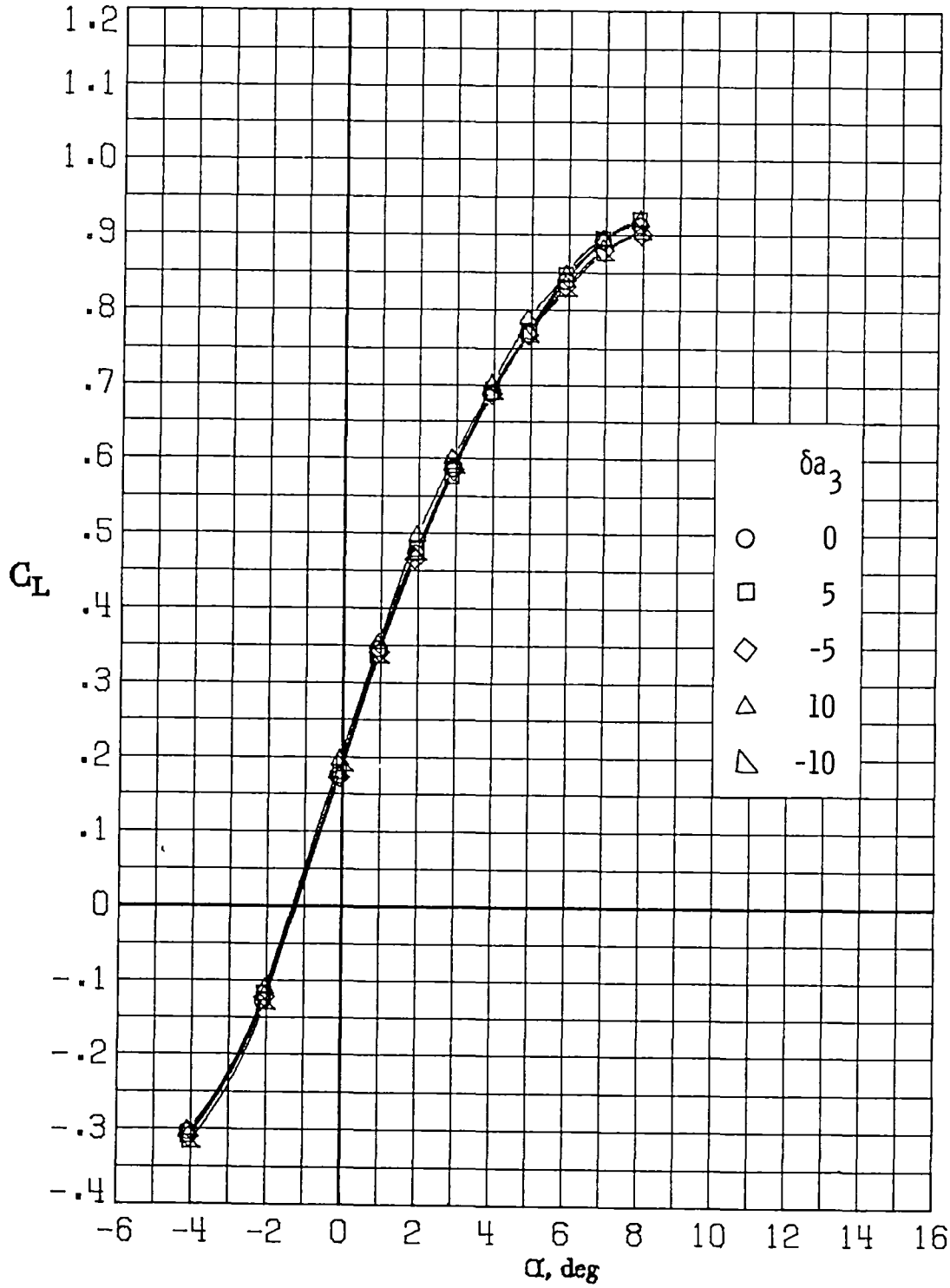

(g) $M_\infty = 0.86$.

Figure 21.- Concluded.

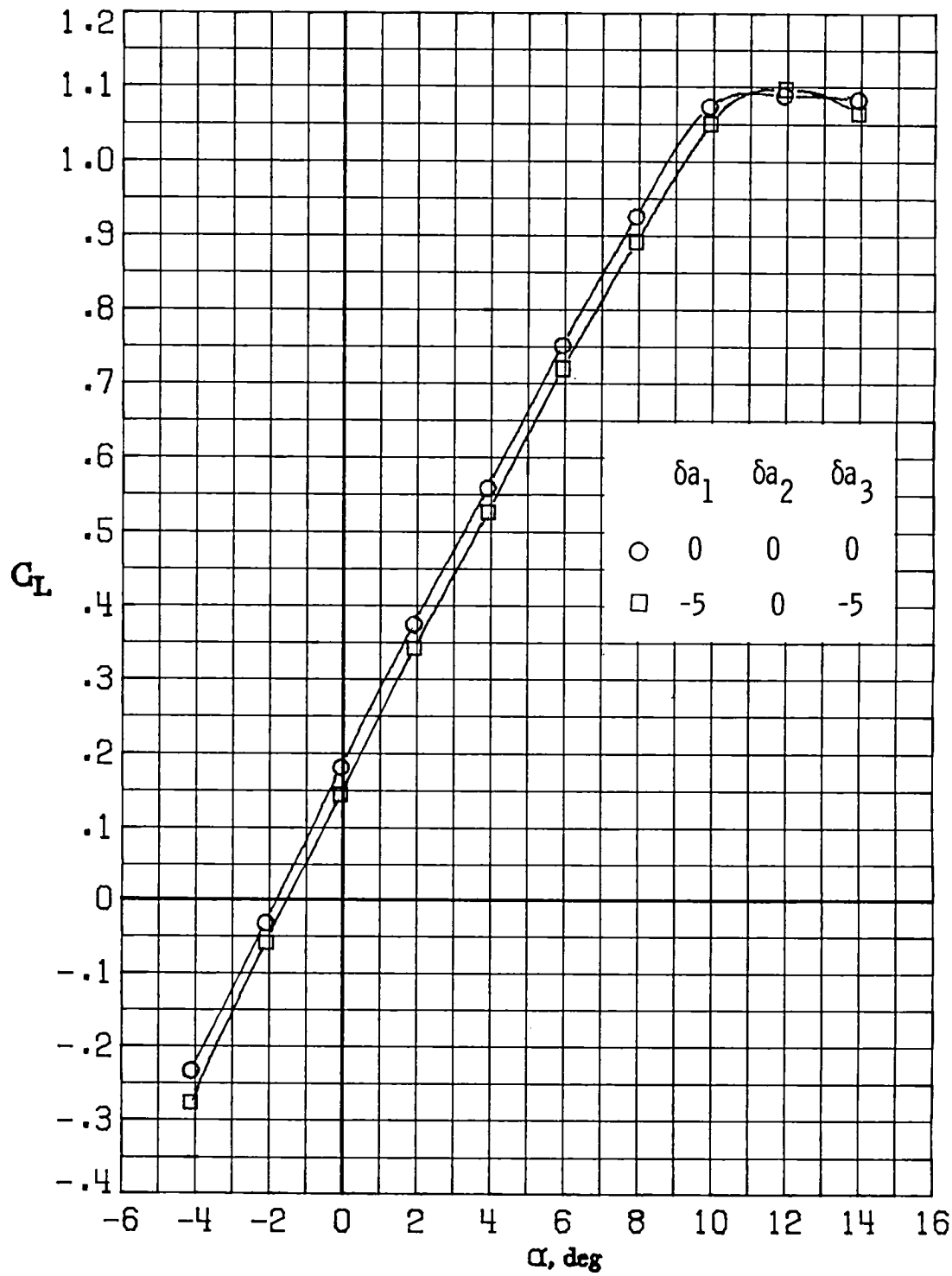

(a) $M_\infty = 0.30$.

Figure 22.- Variation of lift coefficient with angle of attack for $\delta a_1 = -5°$, $\delta a_2 = 0°$, $\delta a_3 = -5°$.

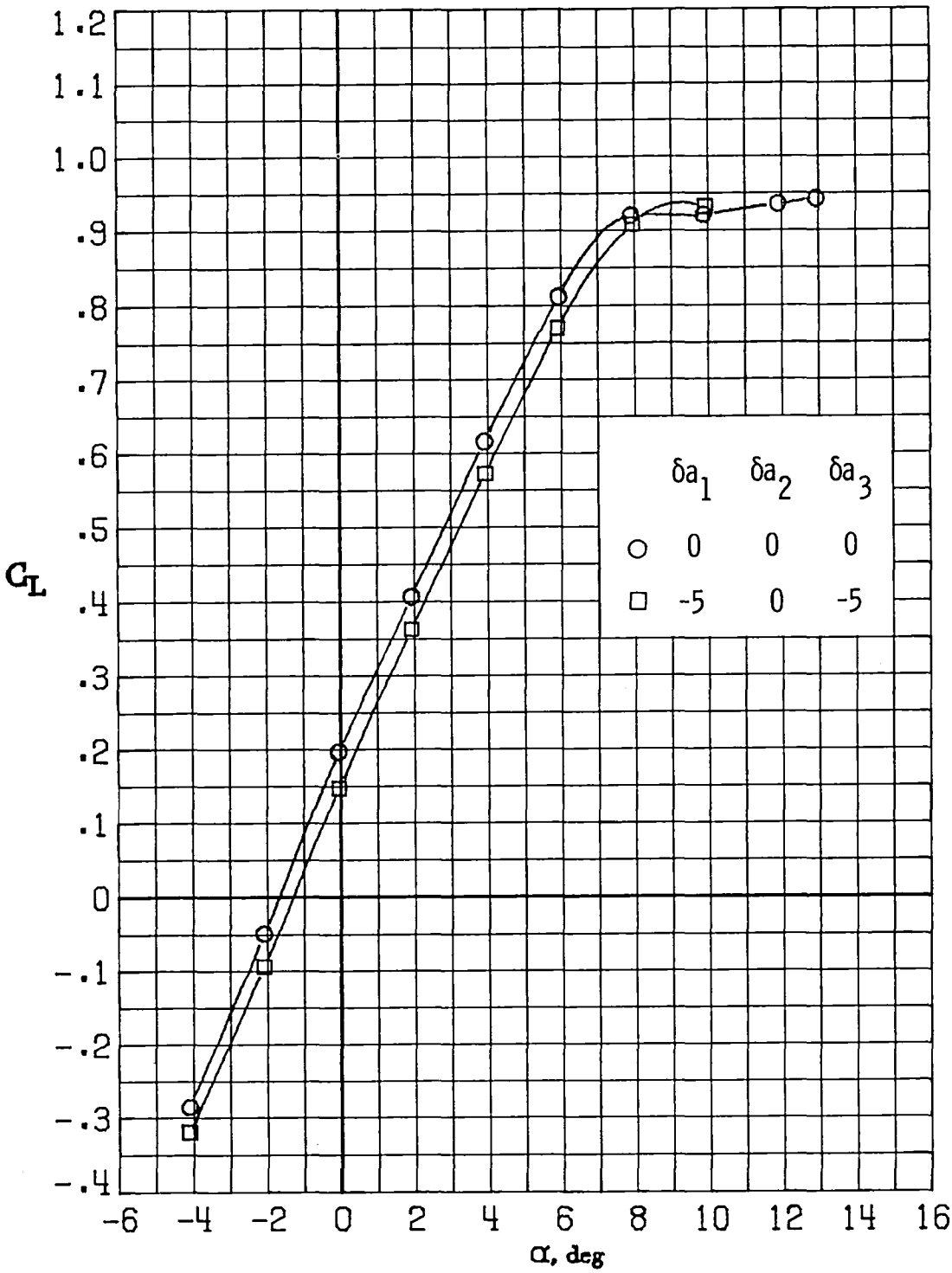

(b) $M_\infty = 0.60$.

Figure 22.- Continued.

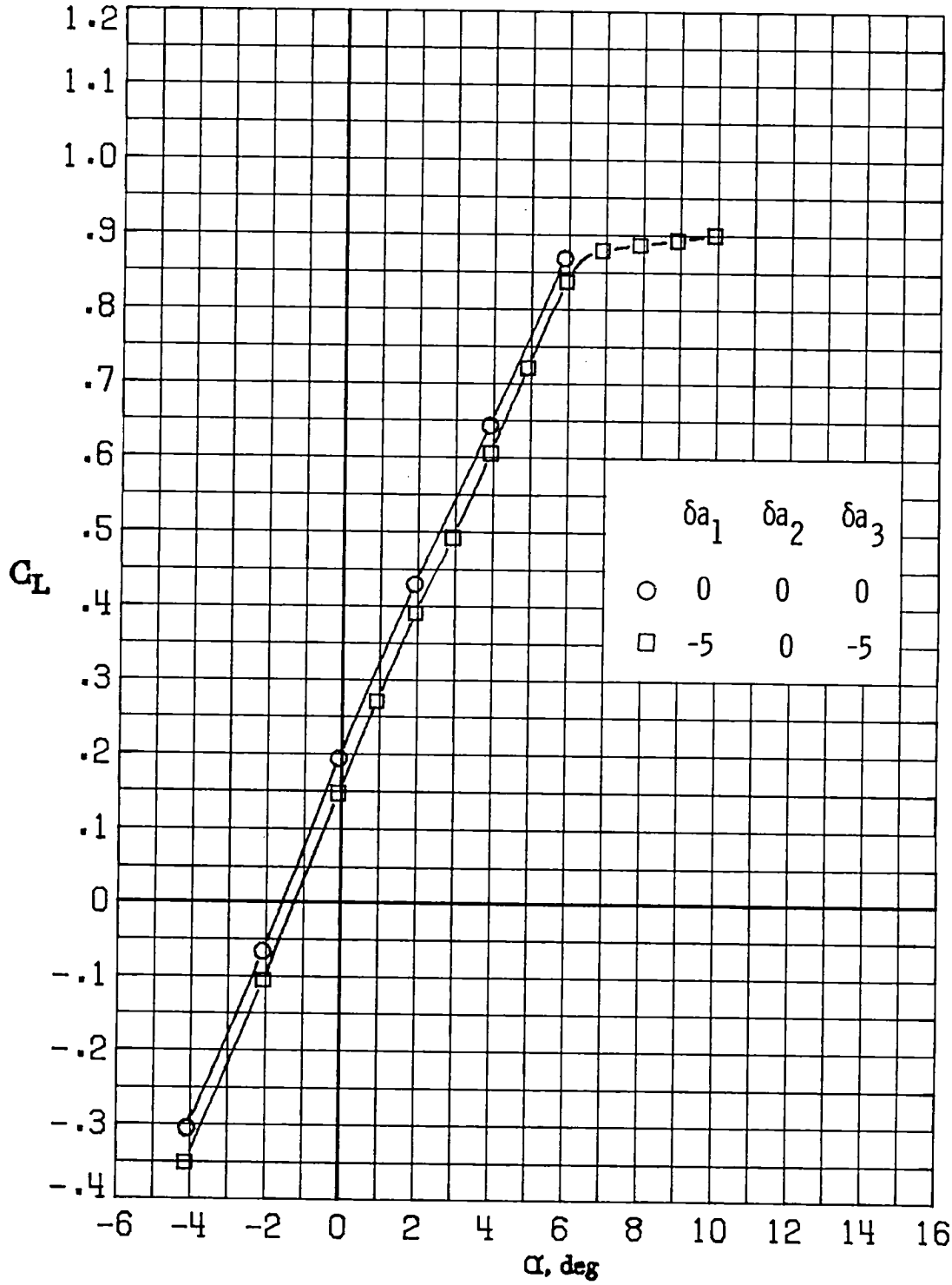

(c) $M_\infty = 0.70$.

Figure 22.- Continued.

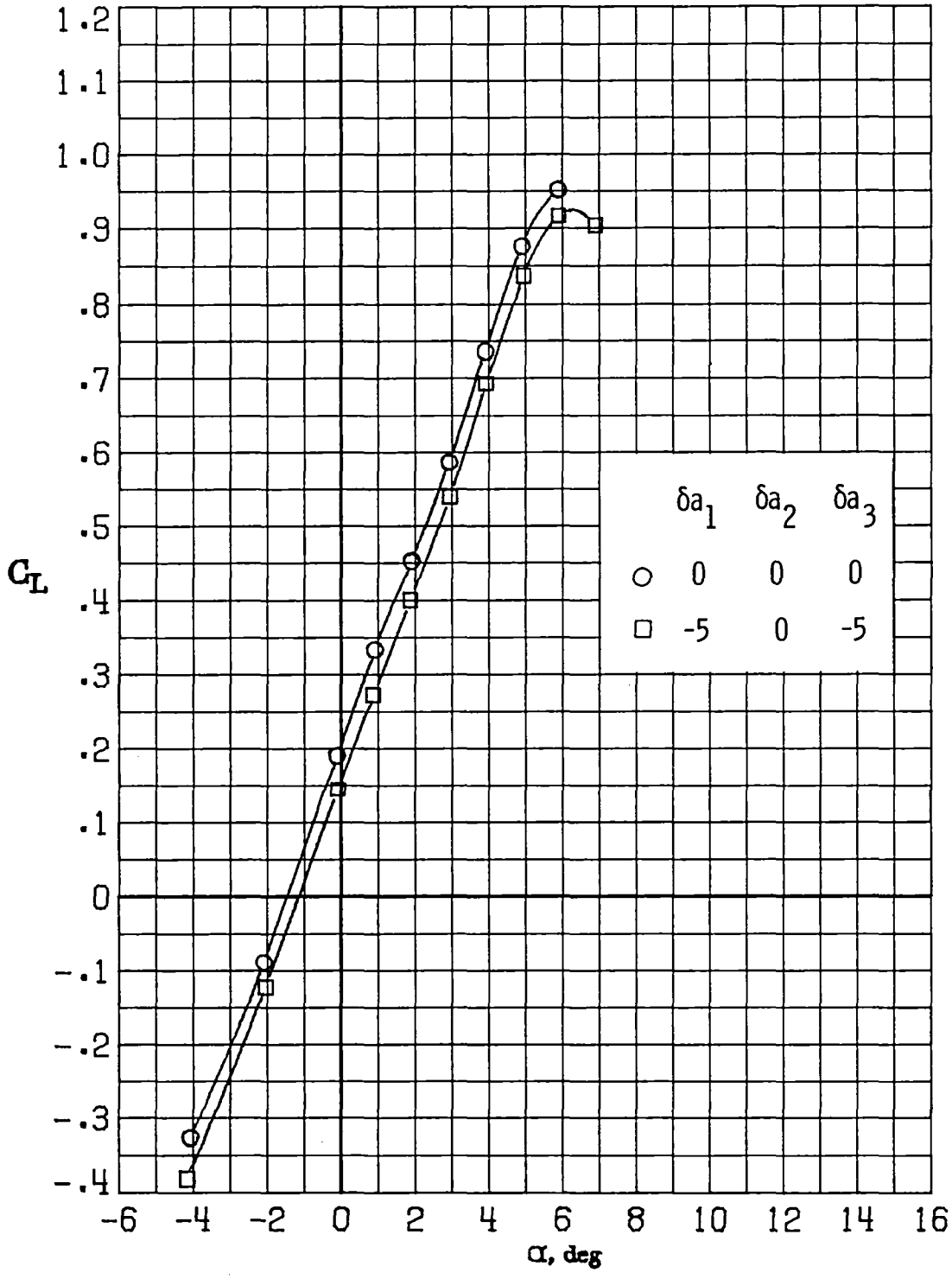

(d) $M_\infty = 0.77$.

Figure 22.- Continued.

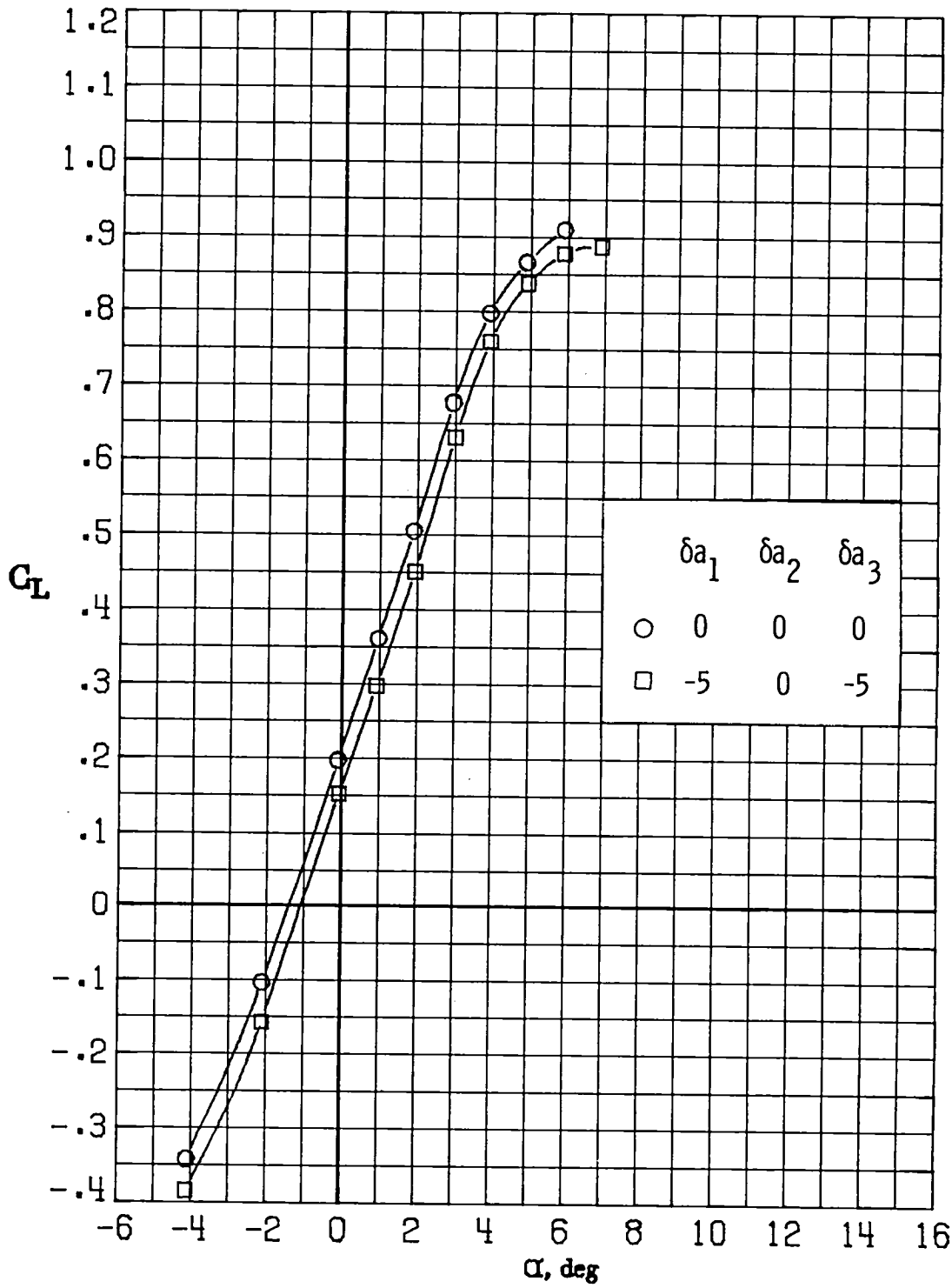

(e) $M_\infty = 0.81$.

Figure 22.- Continued.

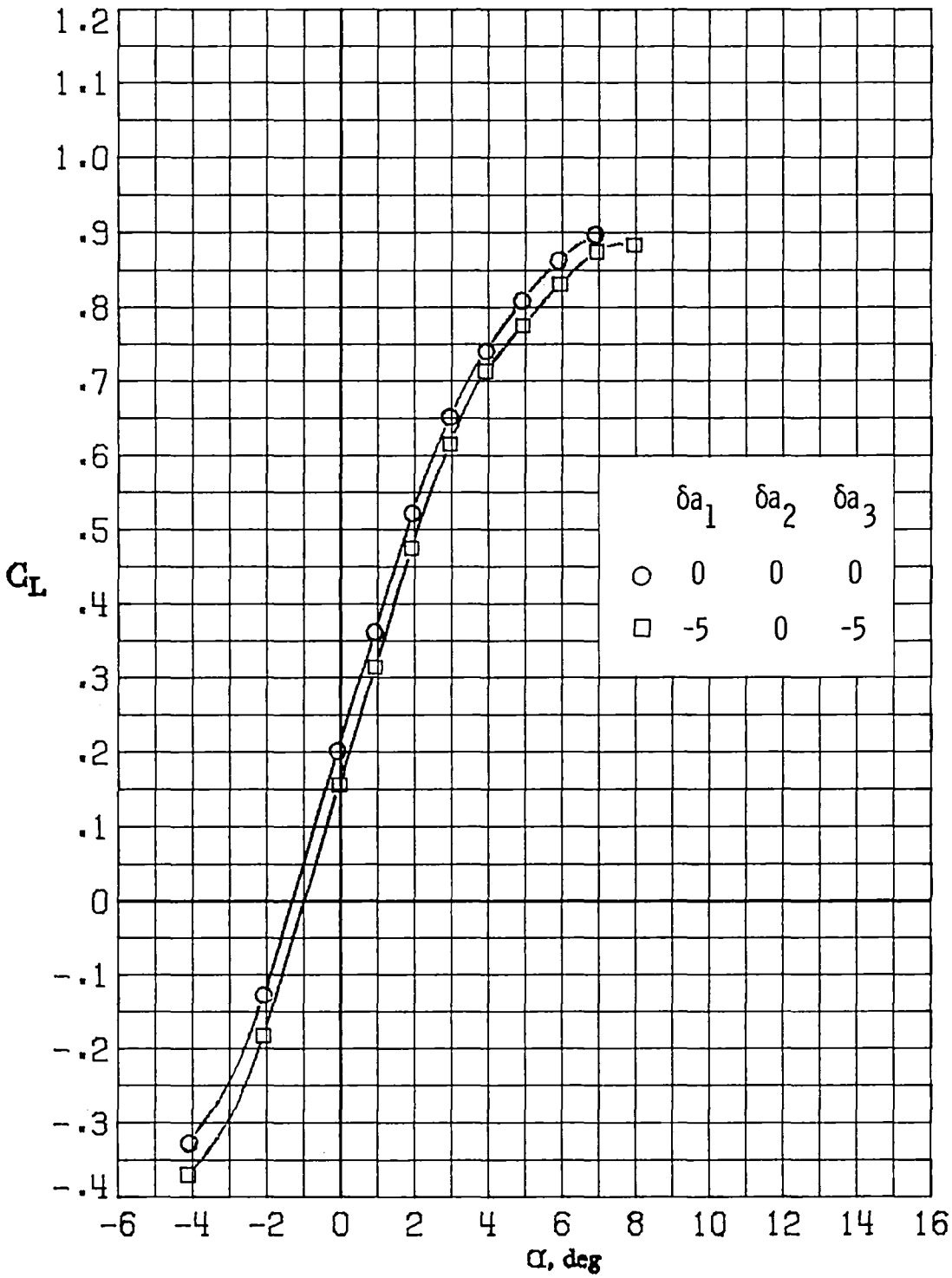

(f) $M_\infty = 0.84$.

Figure 22.- Continued.

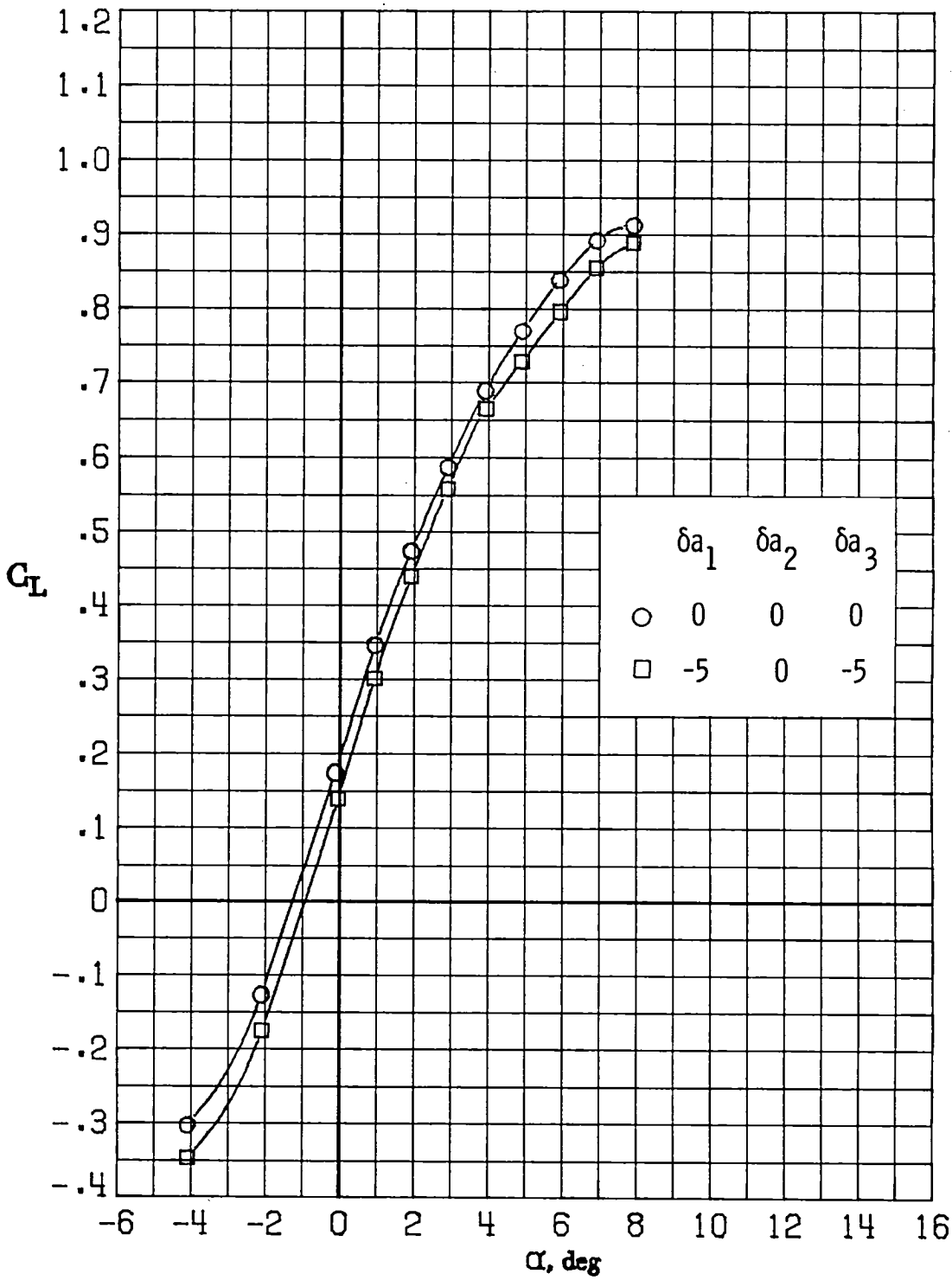

(g) $M_\infty = 0.86$.

Figure 22.- Concluded.

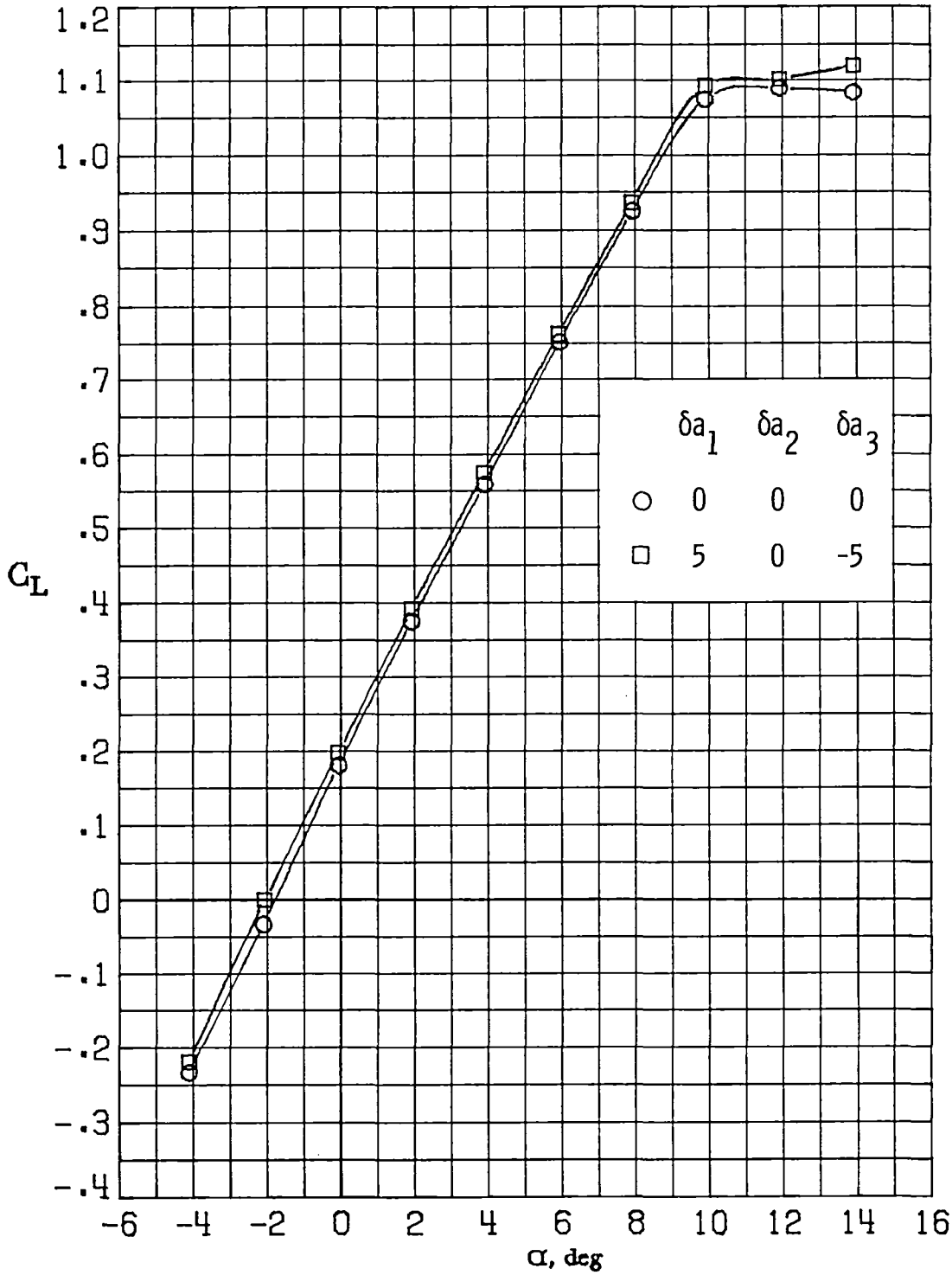

(a) $M_\infty = 0.30$.

Figure 23.- Variation of lift coefficient with angle of attack for $\delta a_1 = 5°$, $\delta a_2 = 0°$, $\delta a_3 = -5°$.

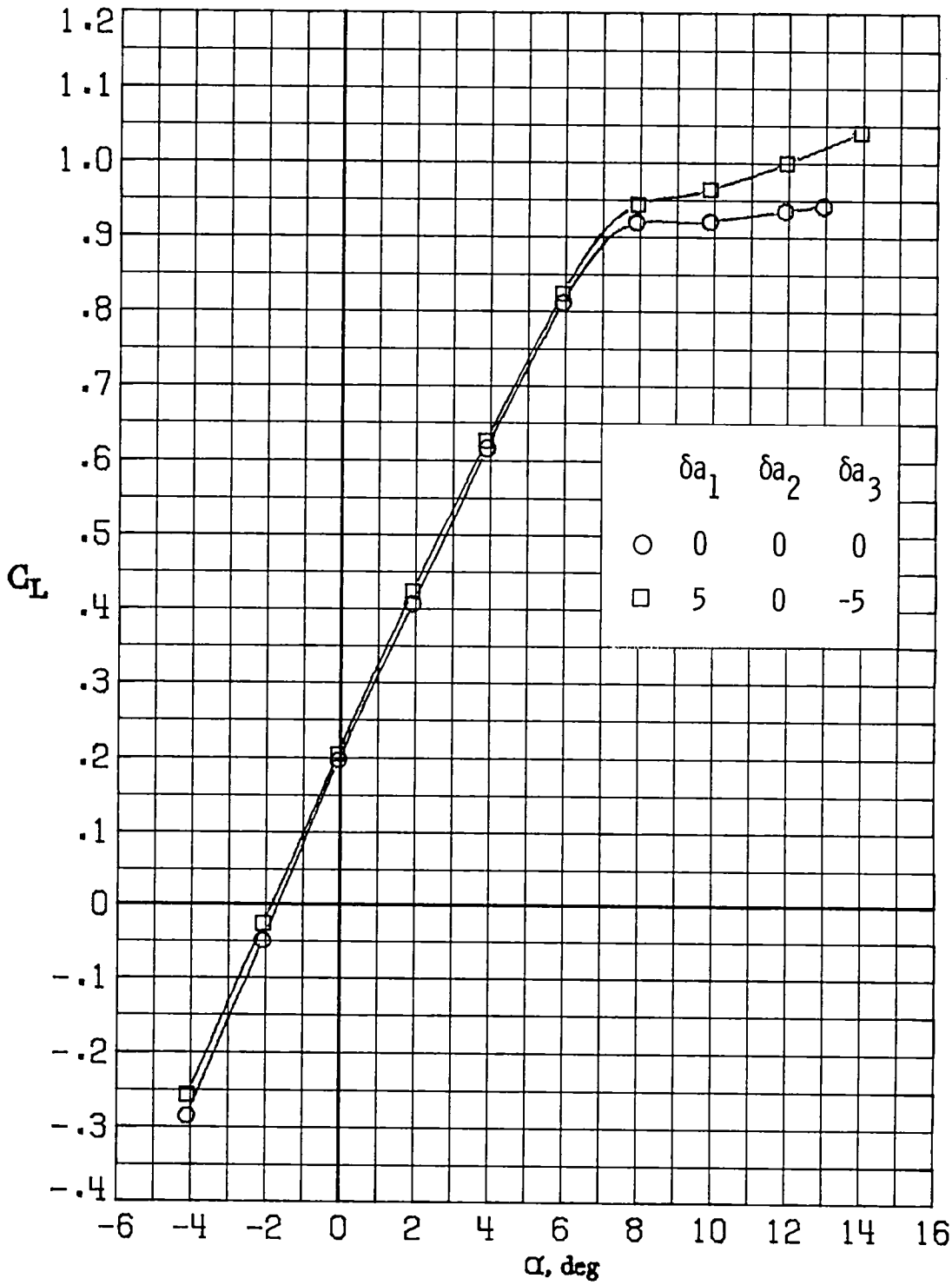

(b) $M_\infty = 0.60$.

Figure 23.- Continued.

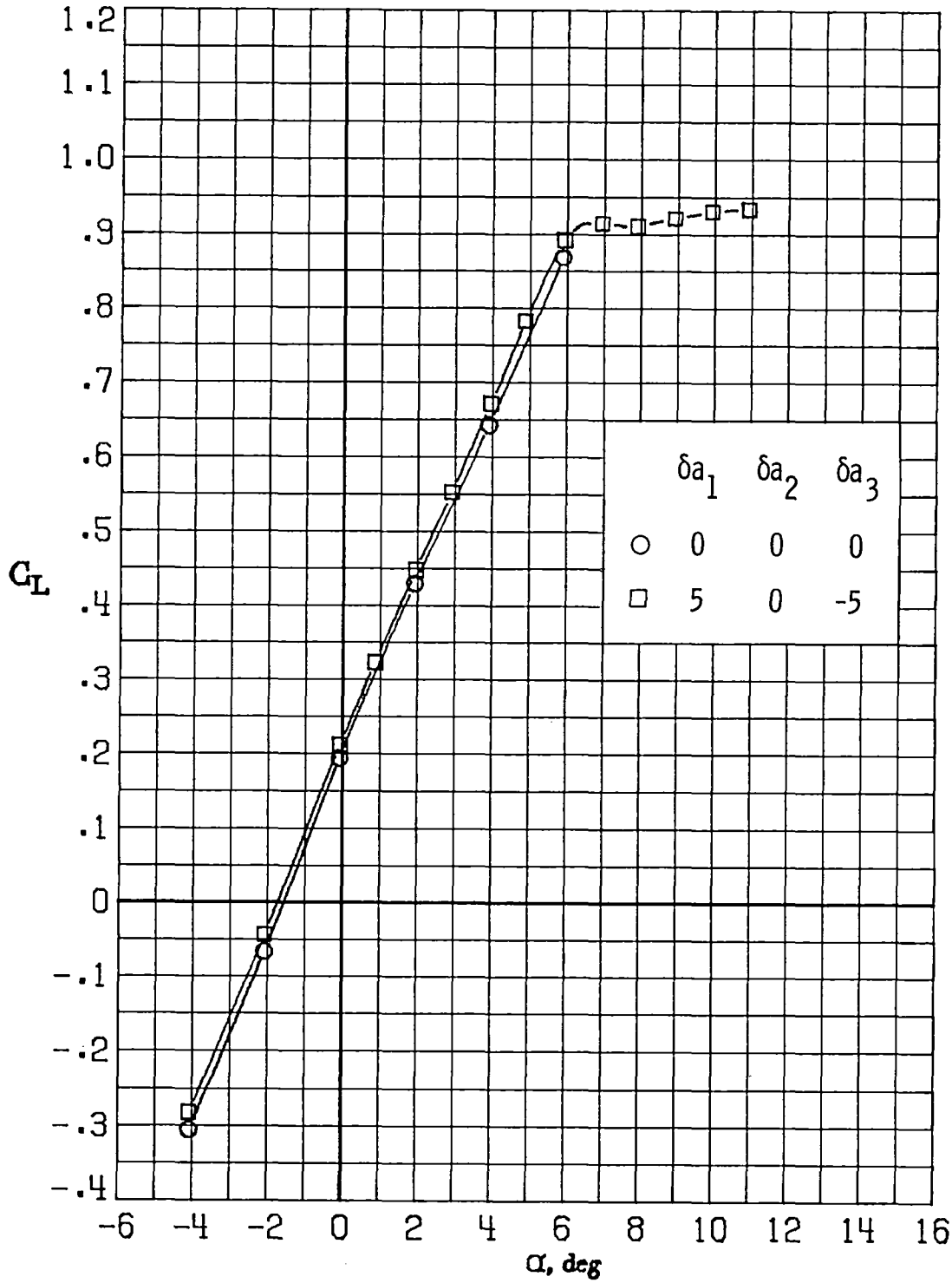

(c) $M_\infty = 0.70$.

Figure 23.- Continued.

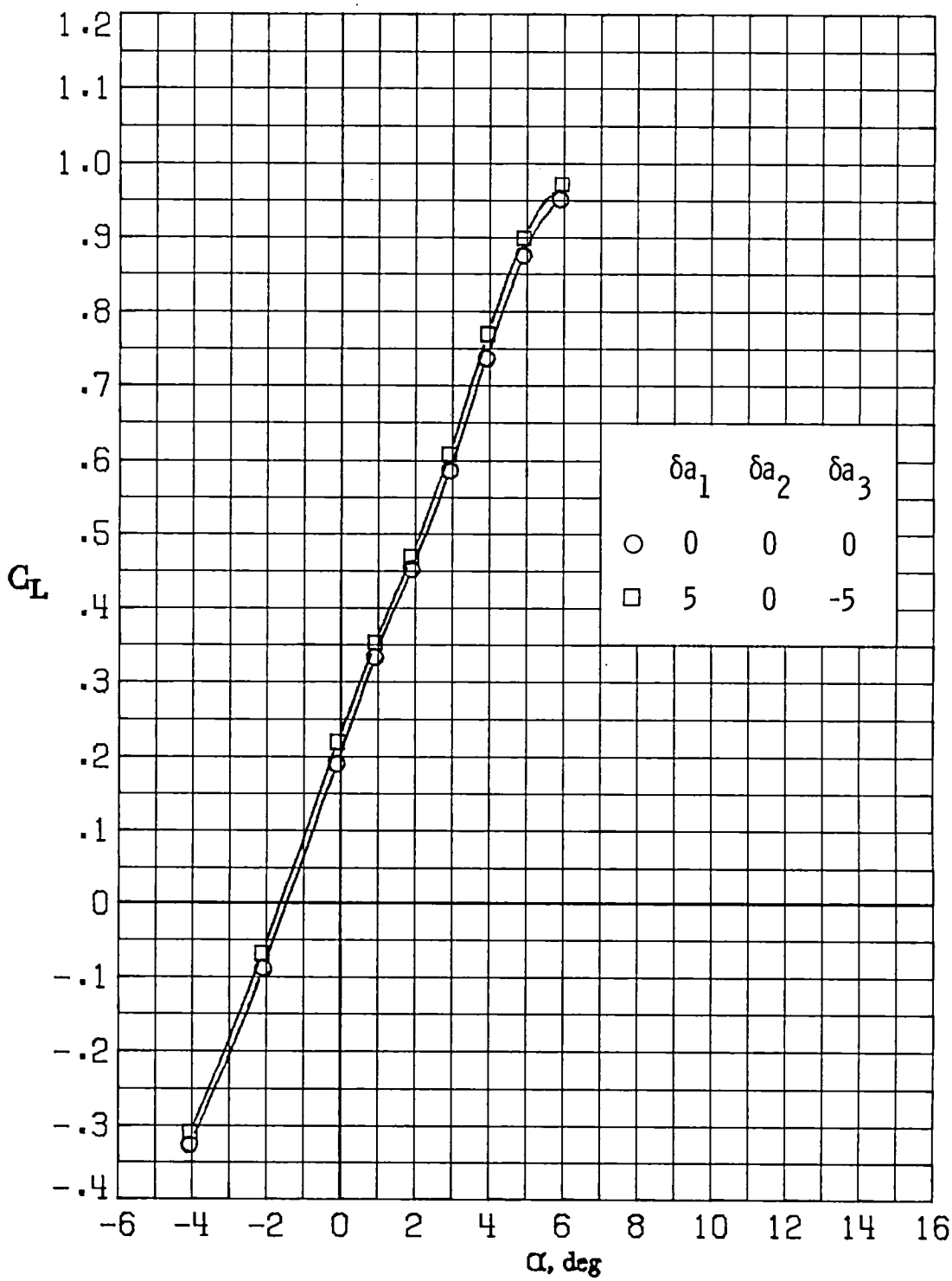

(d) $M_\infty = 0.77$.

Figure 23.- Continued.

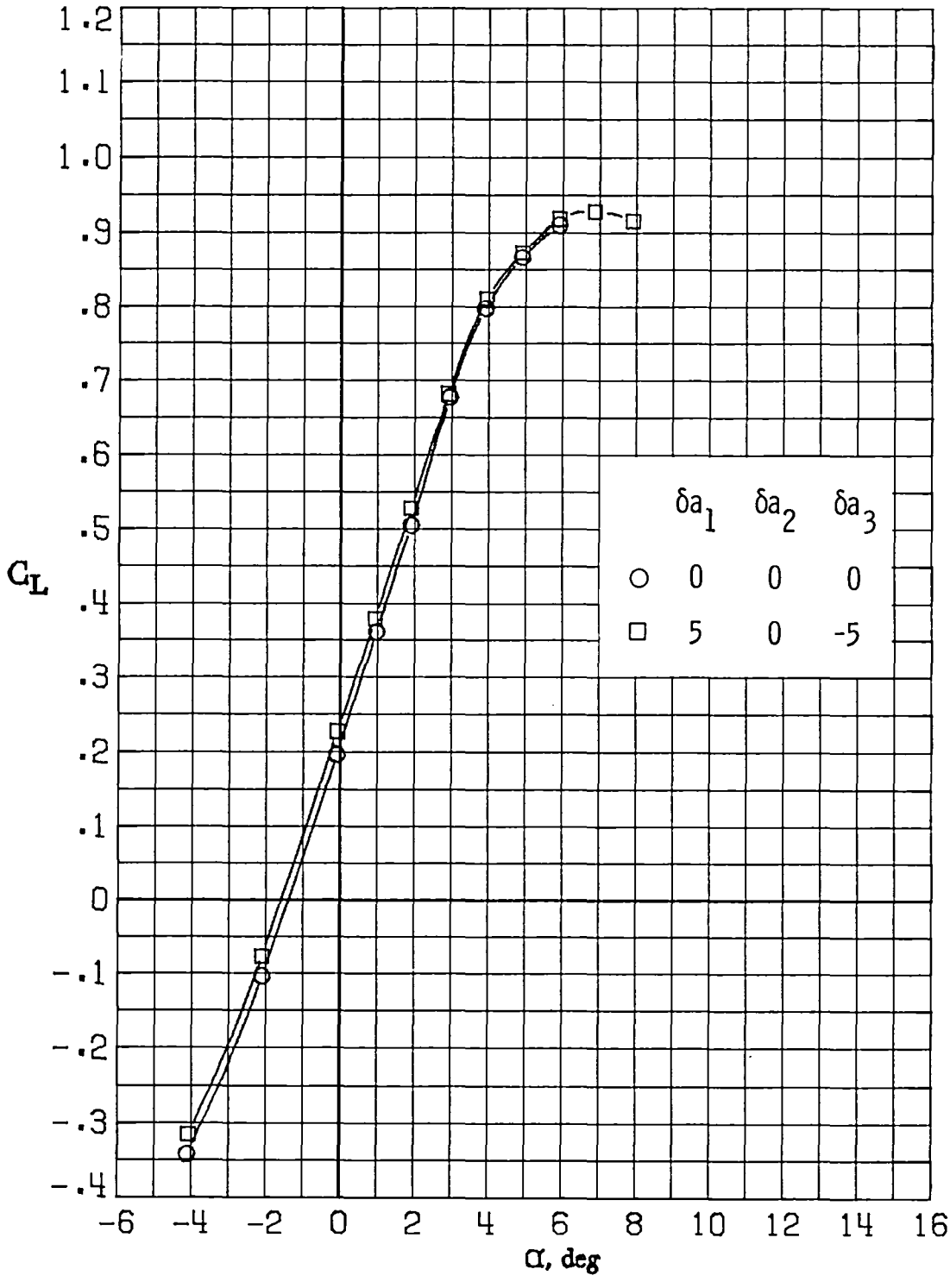

(e) $M_\infty = 0.81$.

Figure 23.- Continued.

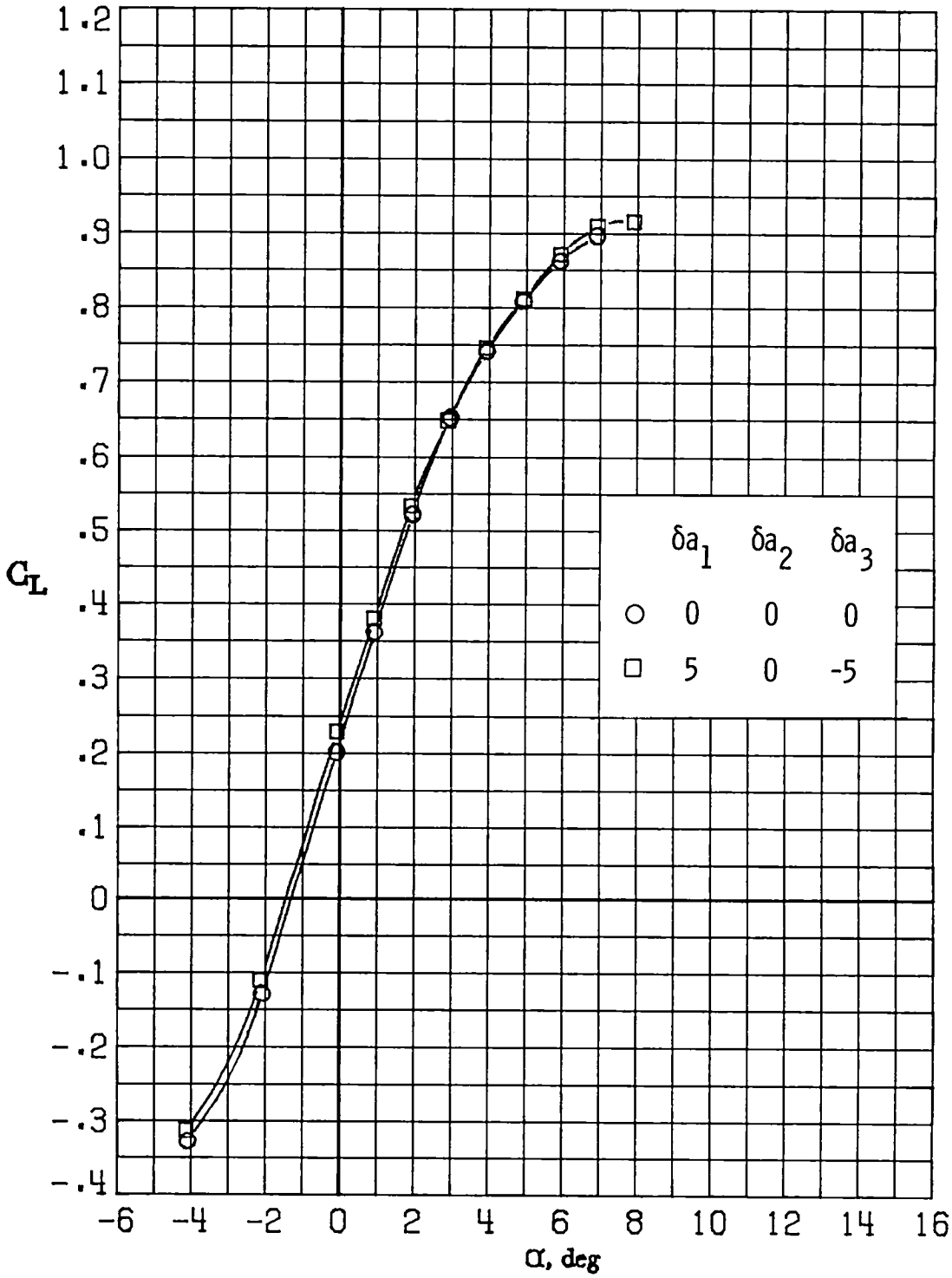

(f) $M_\infty = 0.84$.

Figure 23.- Continued.

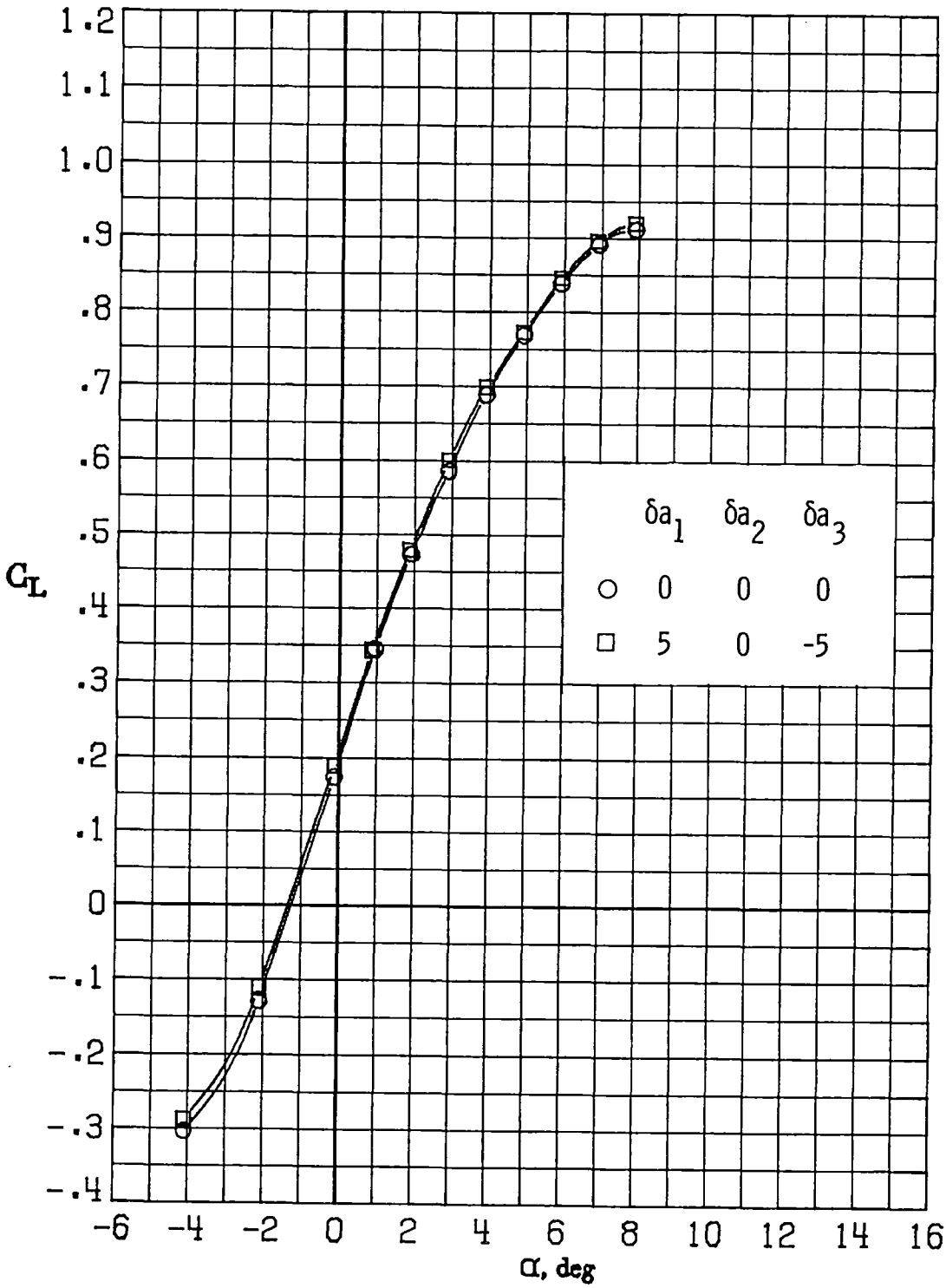

(g) $M_\infty = 0.86$.

Figure 23.- Concluded.

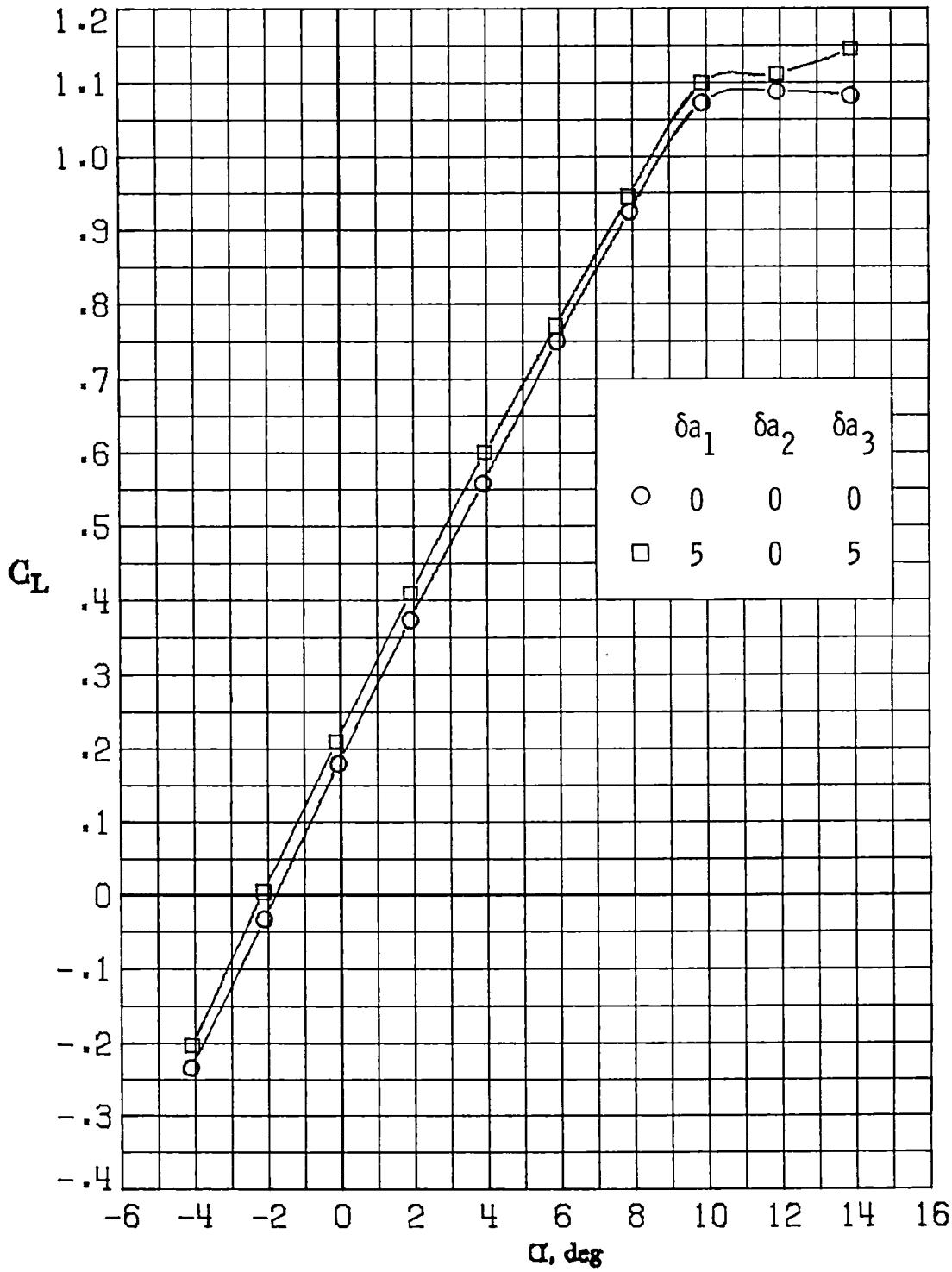

(a) $M_\infty = 0.30$.

Figure 24.- Variation of lift coefficient with angle of attack for $\delta a_1 = 5°$, $\delta a_2 = 0°$, $\delta a_3 = 5°$.

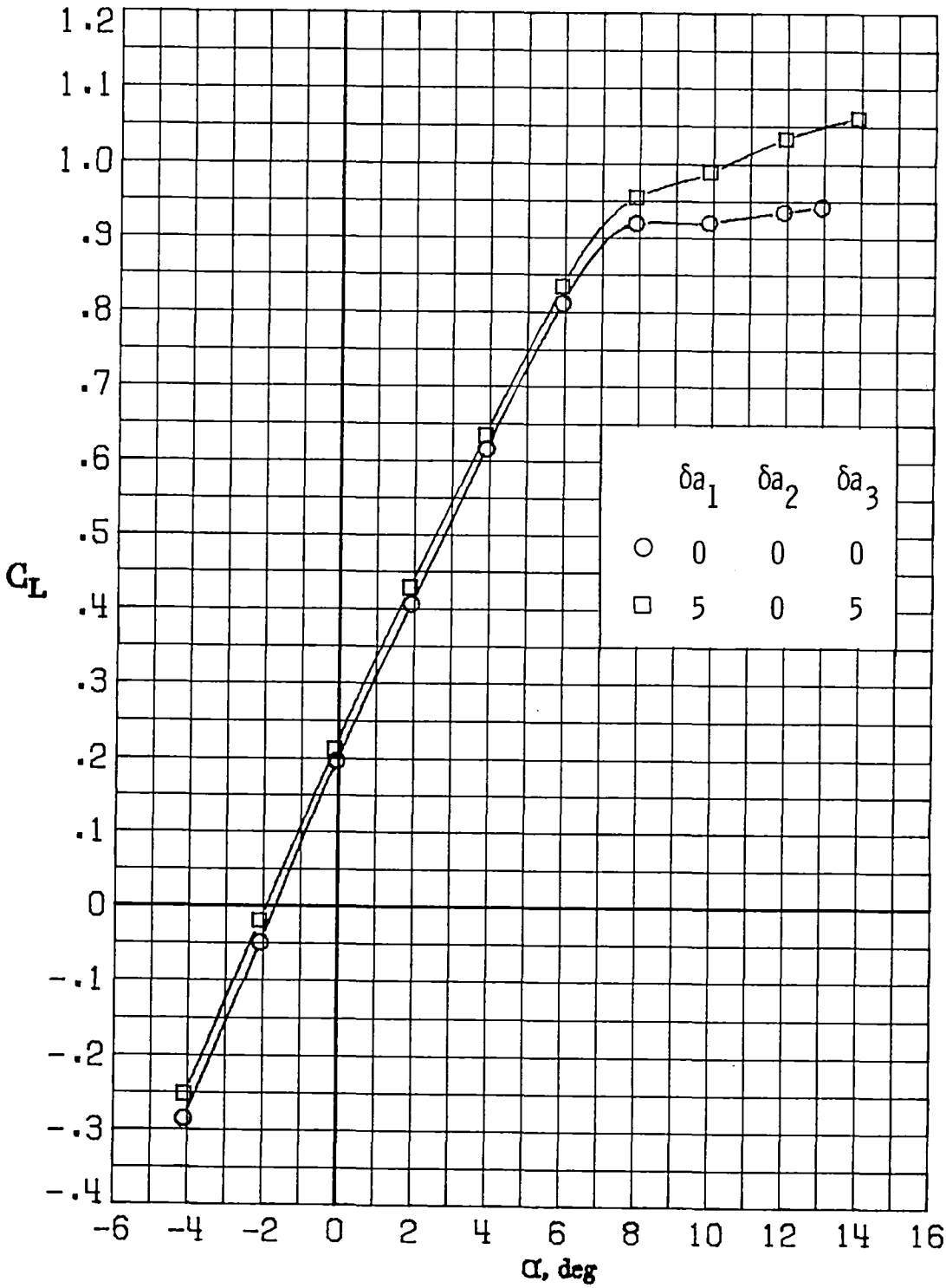

(b) $M_\infty = 0.60$.

Figure 24.- Continued.

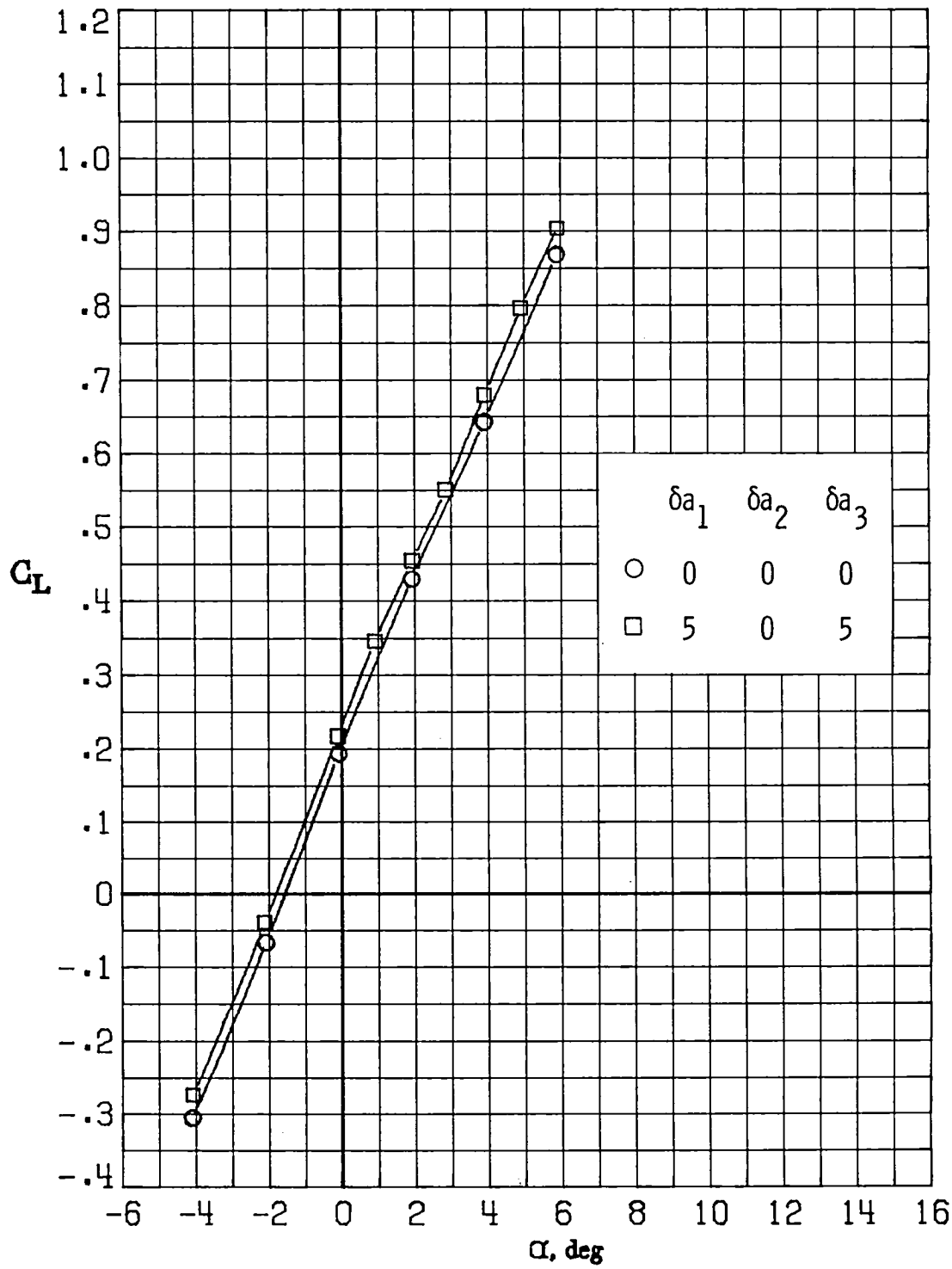

(c) $M_\infty = 0.70$.

Figure 24.- Continued.

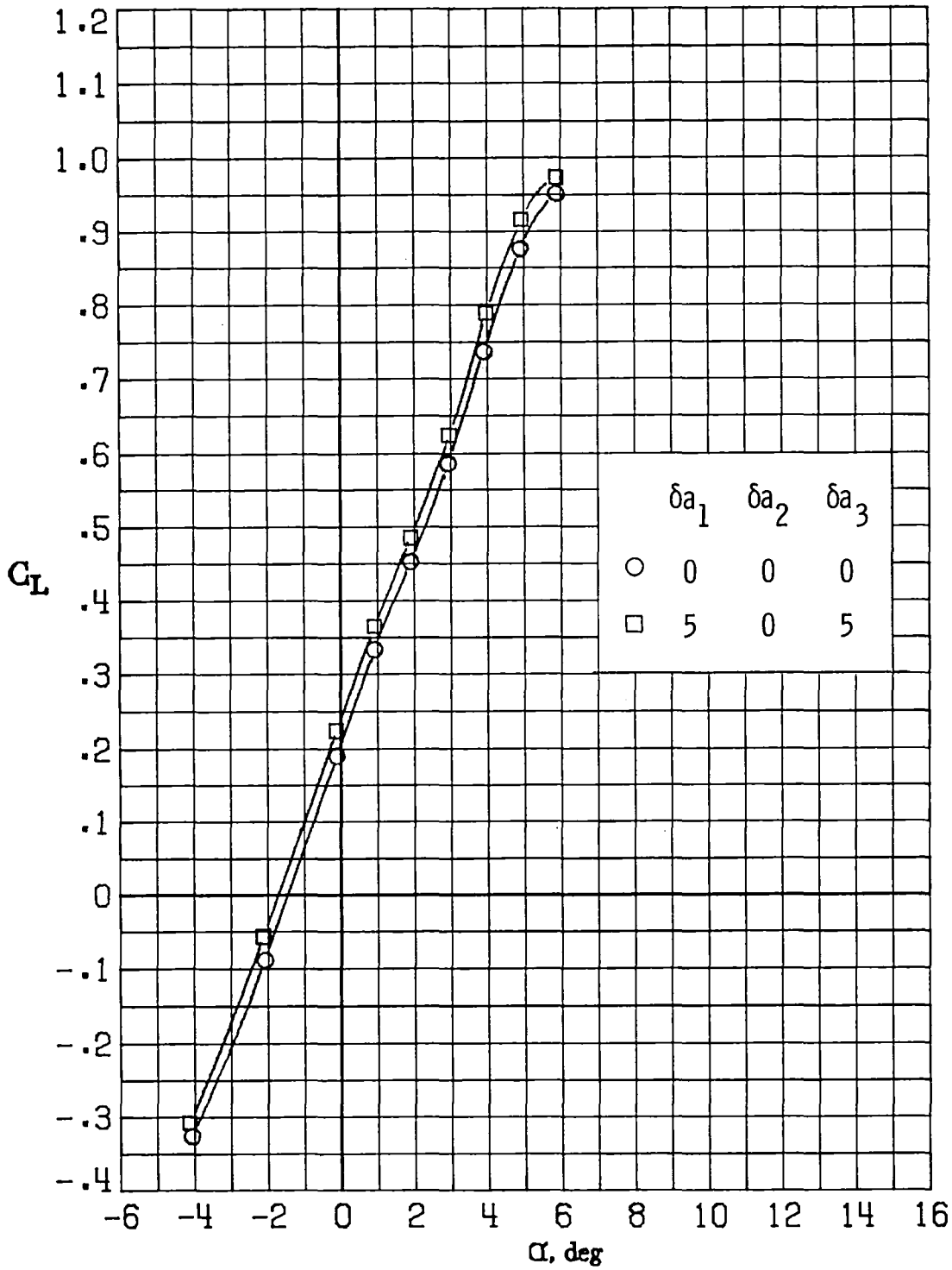

(d) $M_\infty = 0.77$.

Figure 24.- Continued.

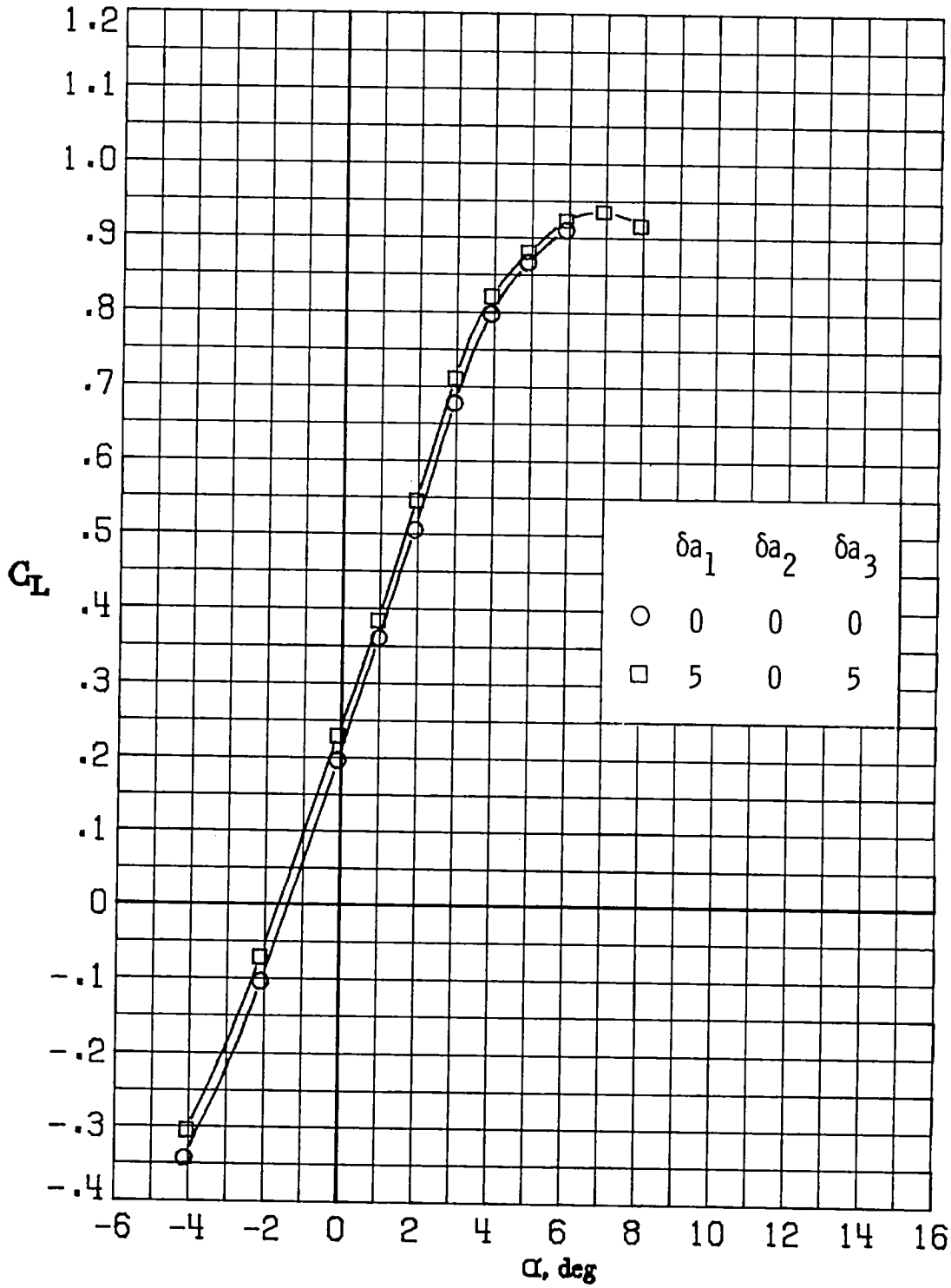

(e) $M_\infty = 0.81$.

Figure 24.- Continued.

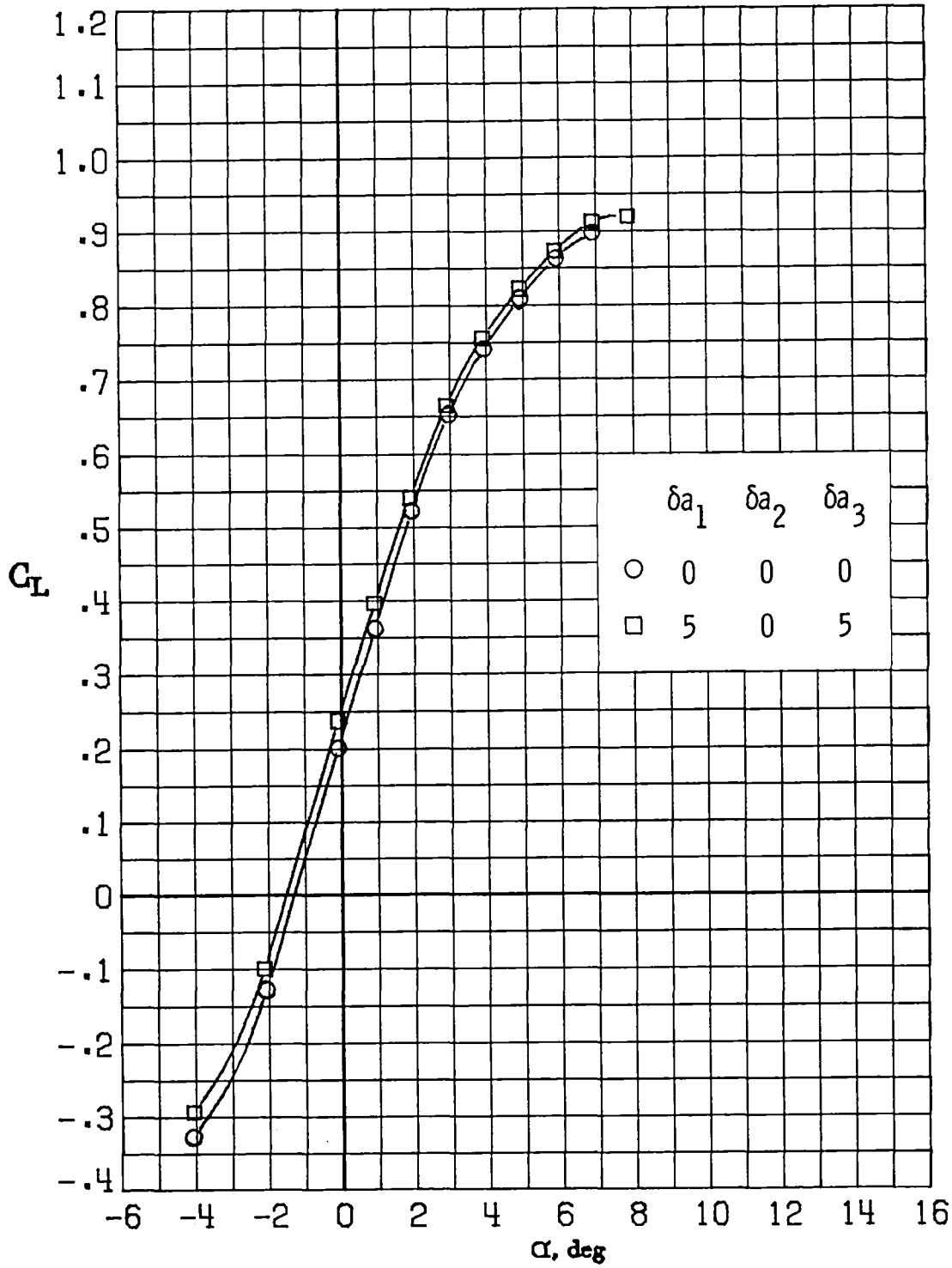

(f) $M_\infty = 0.84$.

Figure 24.- Continued.

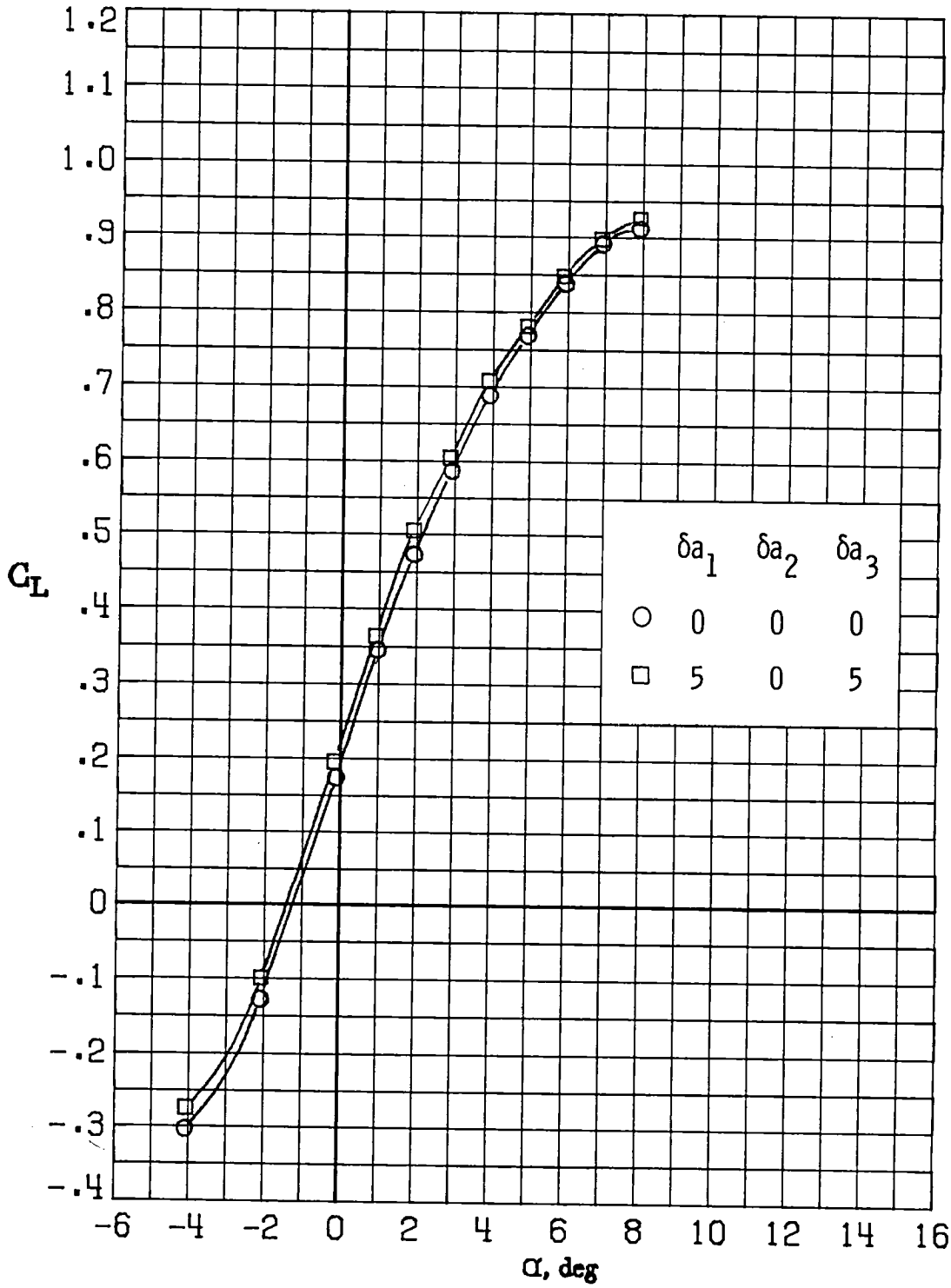

(g) $M_\infty = 0.86$.

Figure 24.- Concluded.

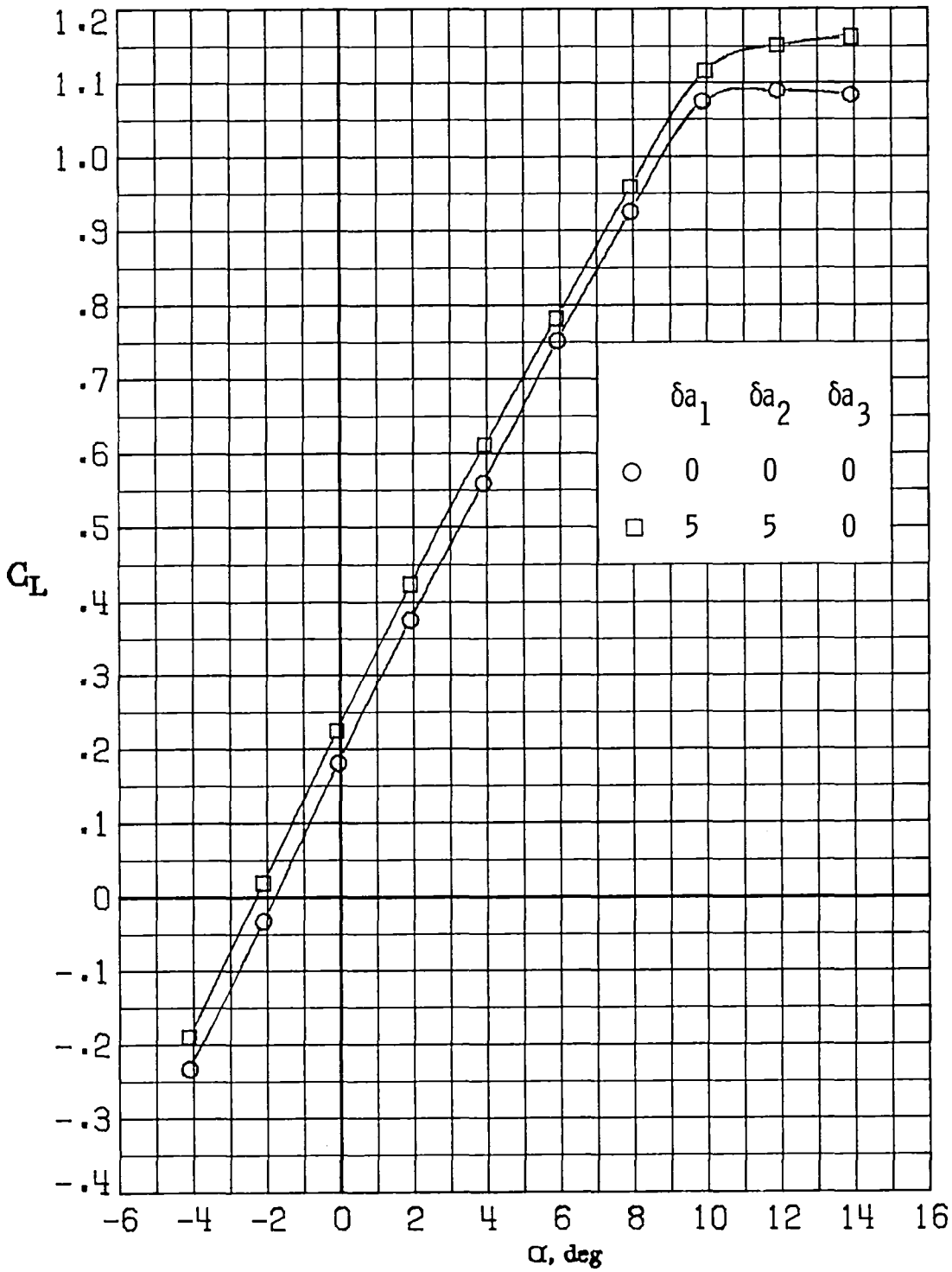

(a) $M_\infty = 0.30$.

Figure 25.- Variation of lift coefficient with angle of attack for $\delta a_1 = 5°$, $\delta a_2 = 5°$, $\delta a_3 = 0°$.

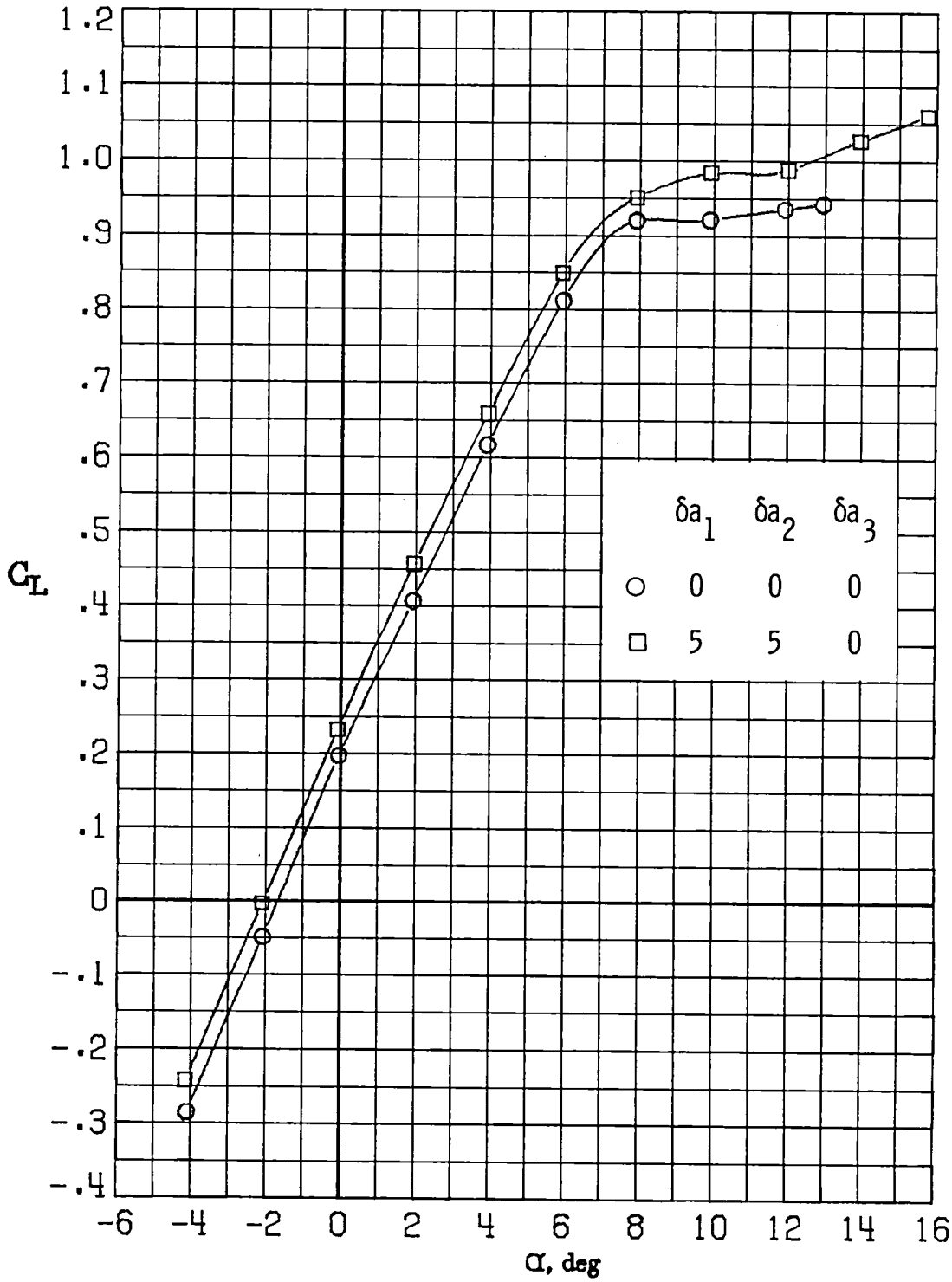

(b) $M_\infty = 0.60$.

Figure 25.- Continued.

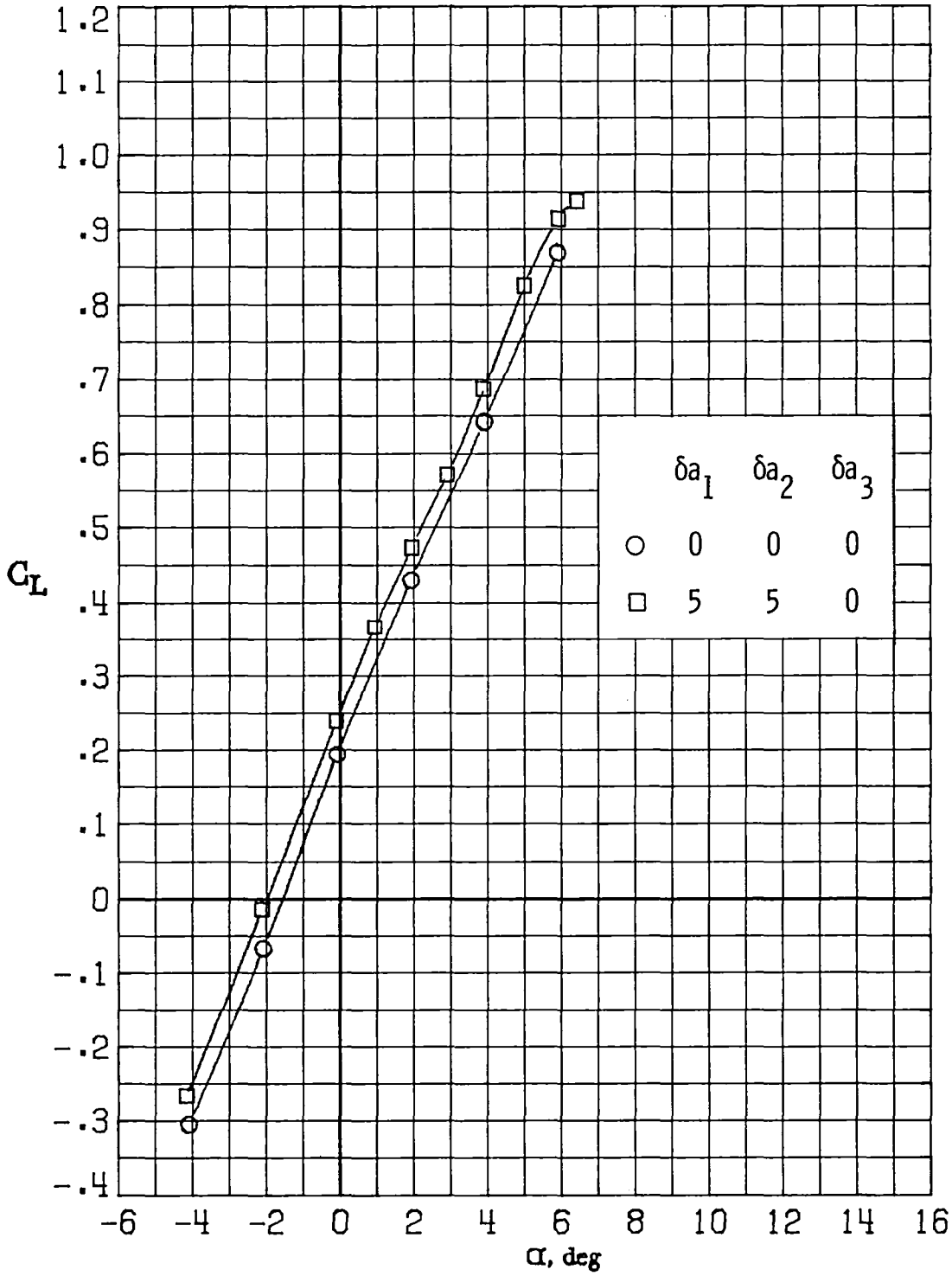

(c) $M_\infty = 0.70$.

Figure 25.- Continued.

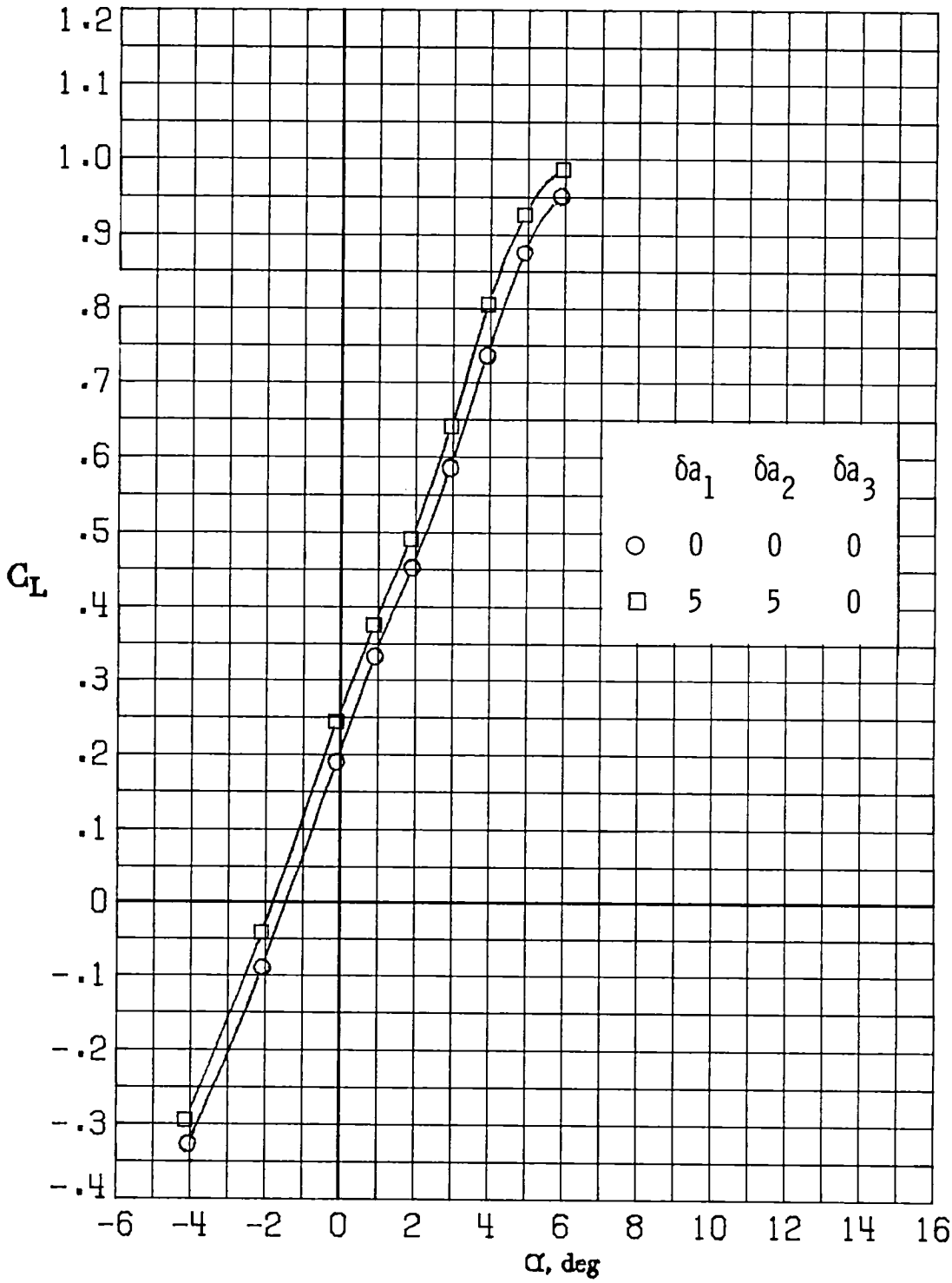

(d) $M_\infty = 0.77$.

Figure 25.- Continued.

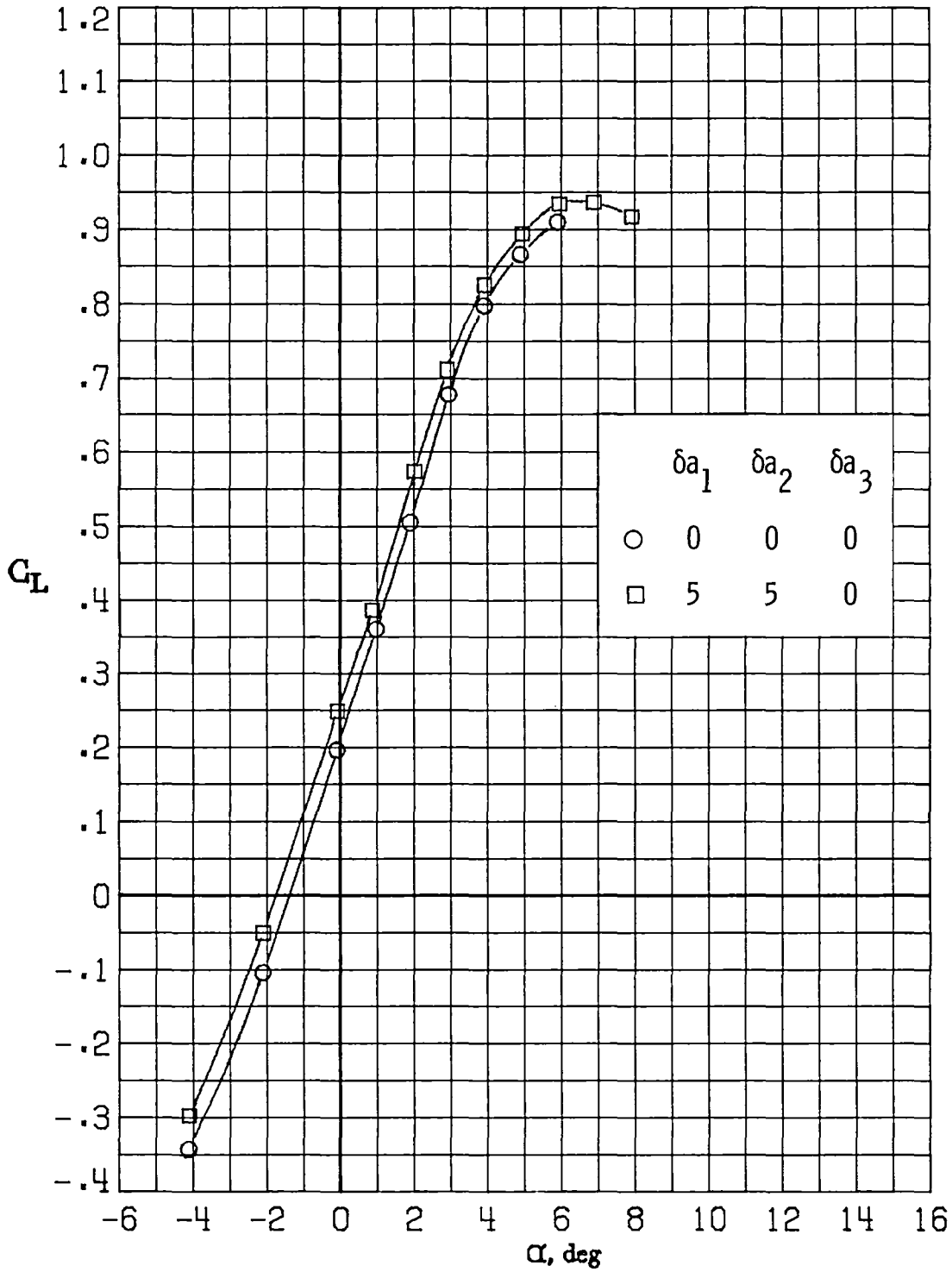

(e) $M_\infty = 0.81$.

Figure 25.- Continued.

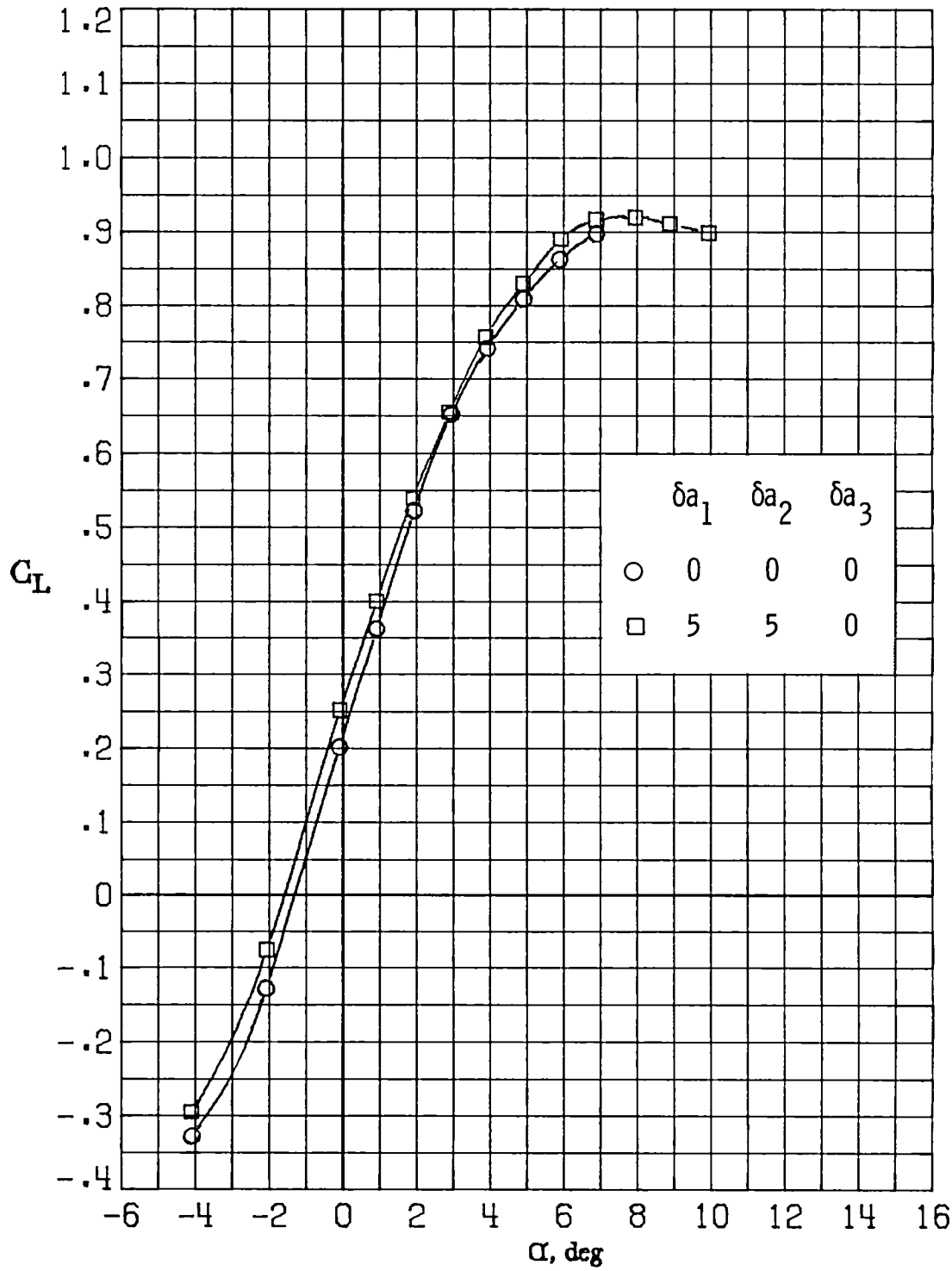

(f) $M_\infty = 0.84$.

Figure 25.- Continued.

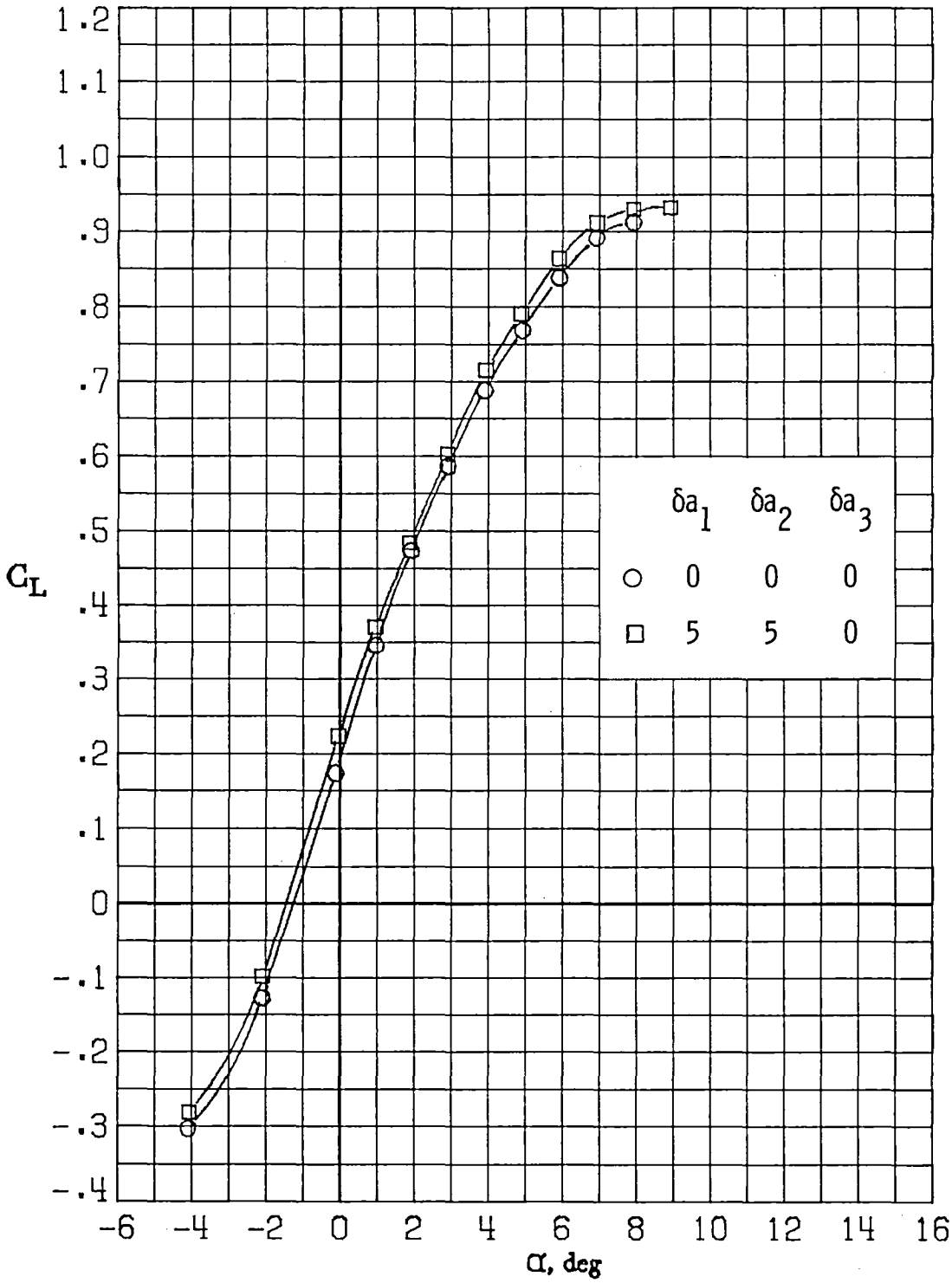

(g) $M_\infty = 0.86$.

Figure 25.- Concluded.

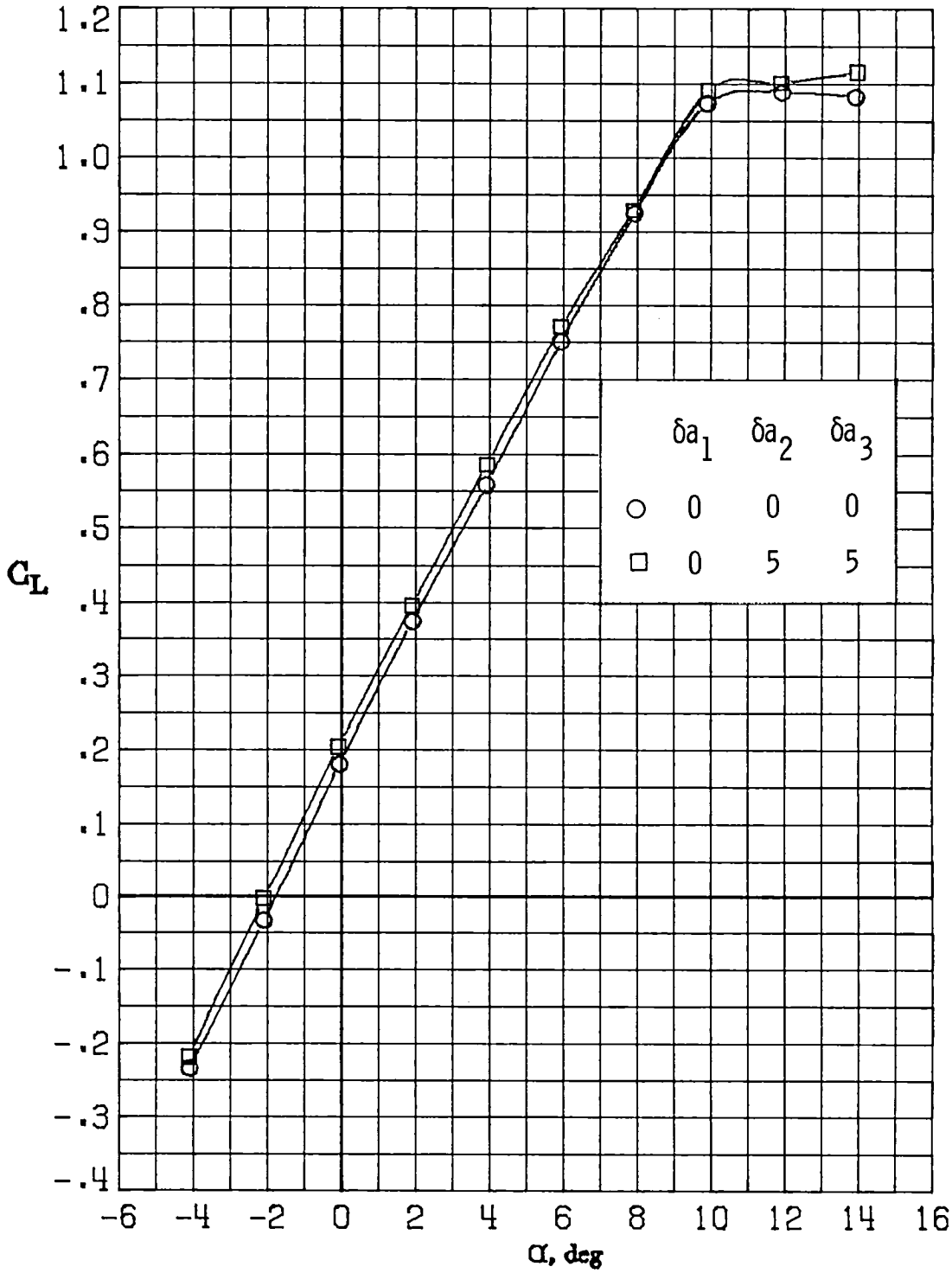

(a) $M_\infty = 0.30$.

Figure 26.- Variation of lift coefficient with angle of attack for $\delta a_1 = 0°$, $\delta a_2 = 5°$, $\delta a_3 = 5°$.

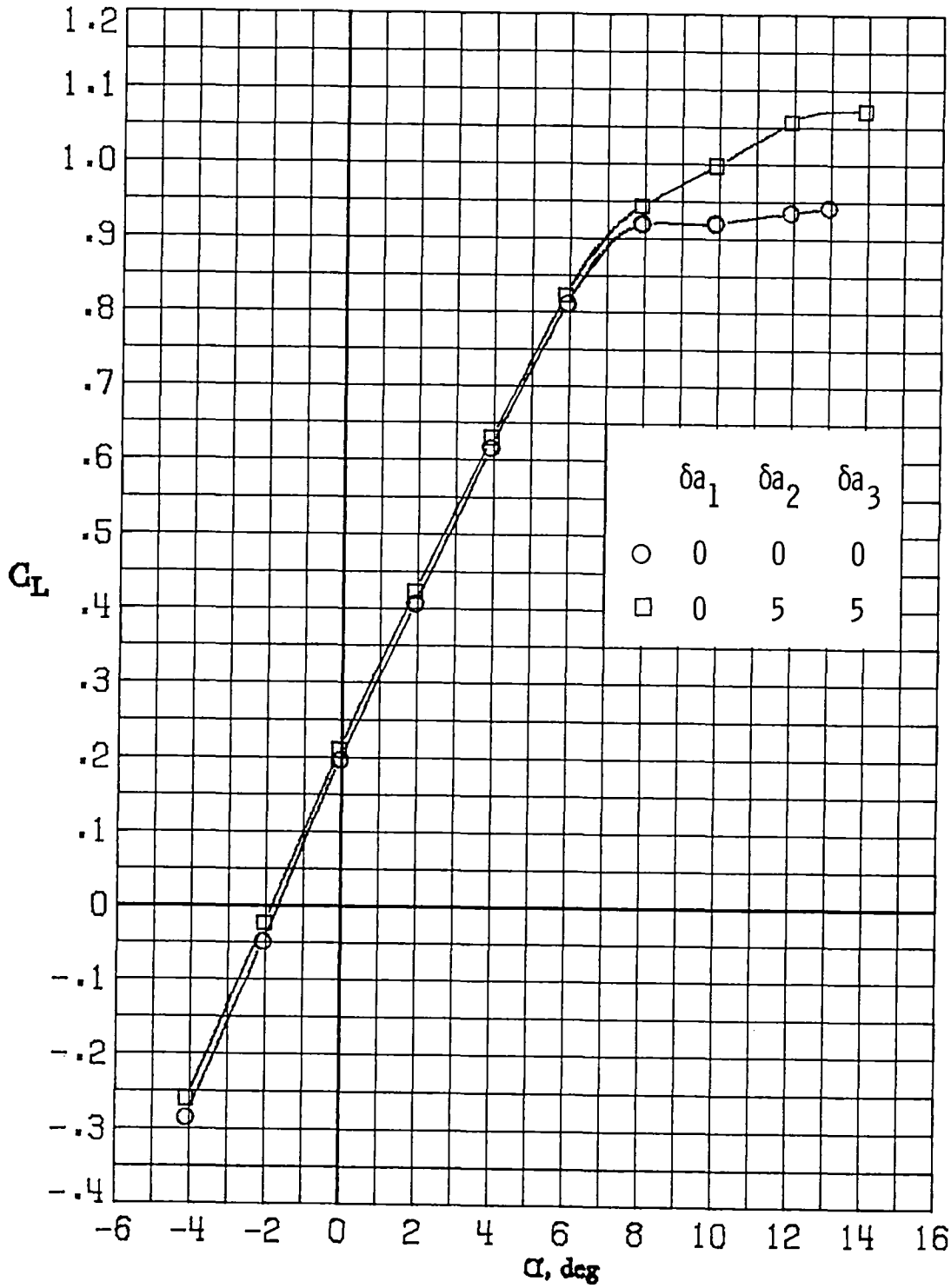

(b) $M_\infty = 0.60$.

Figure 26.- Continued.

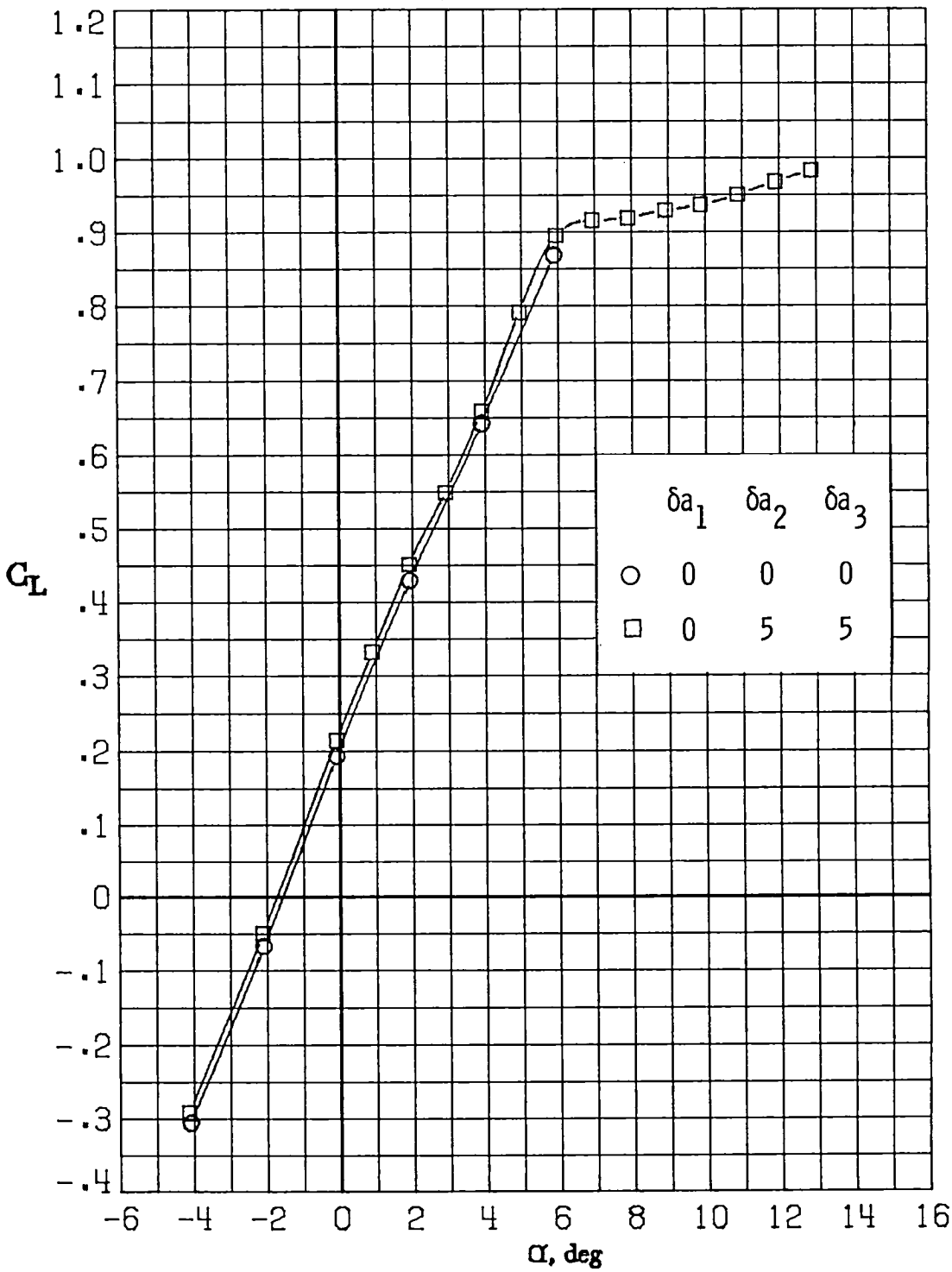

(c) $M_\infty = 0.70$.

Figure 26.- Continued.

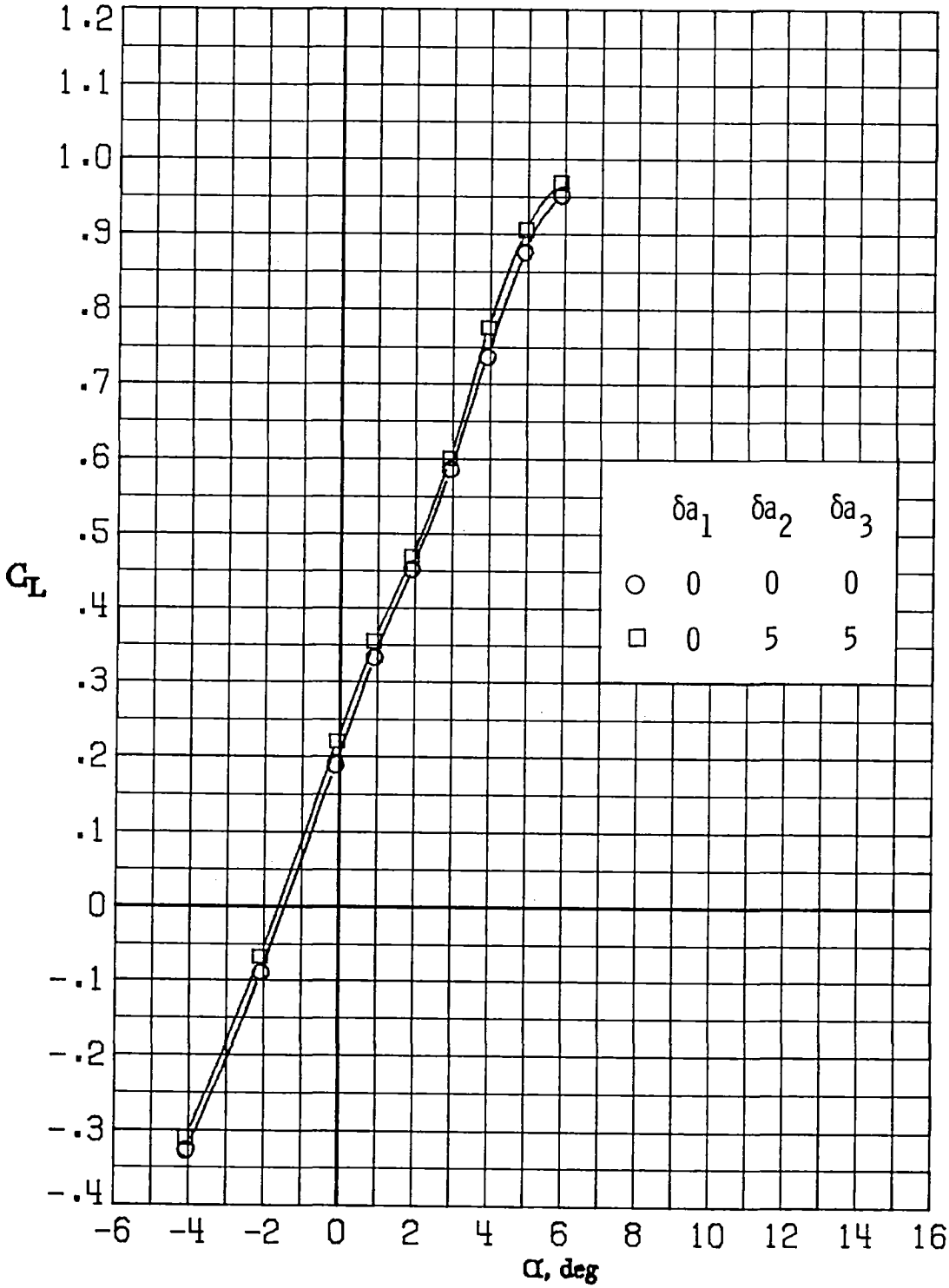

(d) $M_\infty = 0.77$.

Figure 26.- Continued.

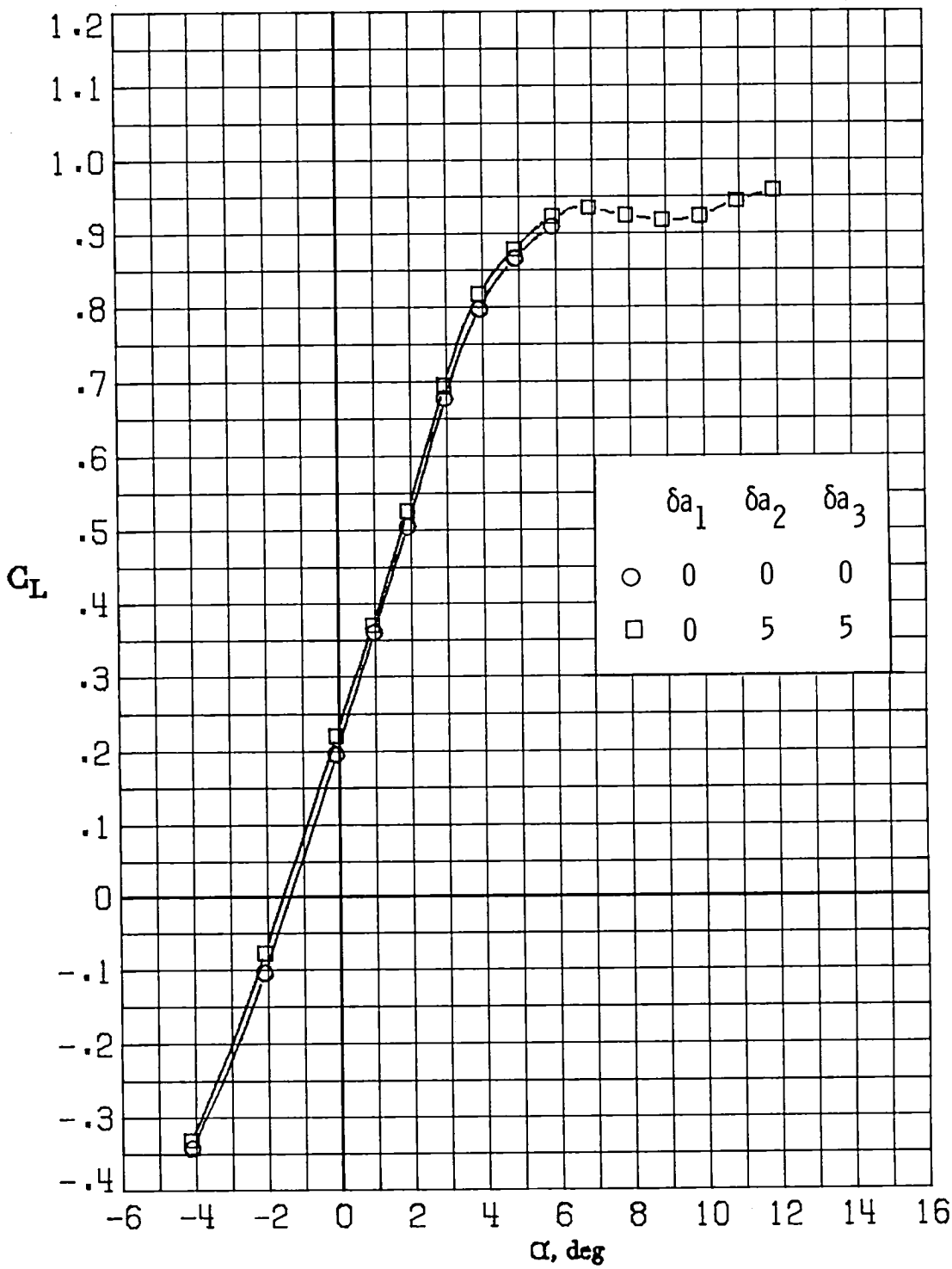

(e) $M_\infty = 0.81$.

Figure 26.- Continued.

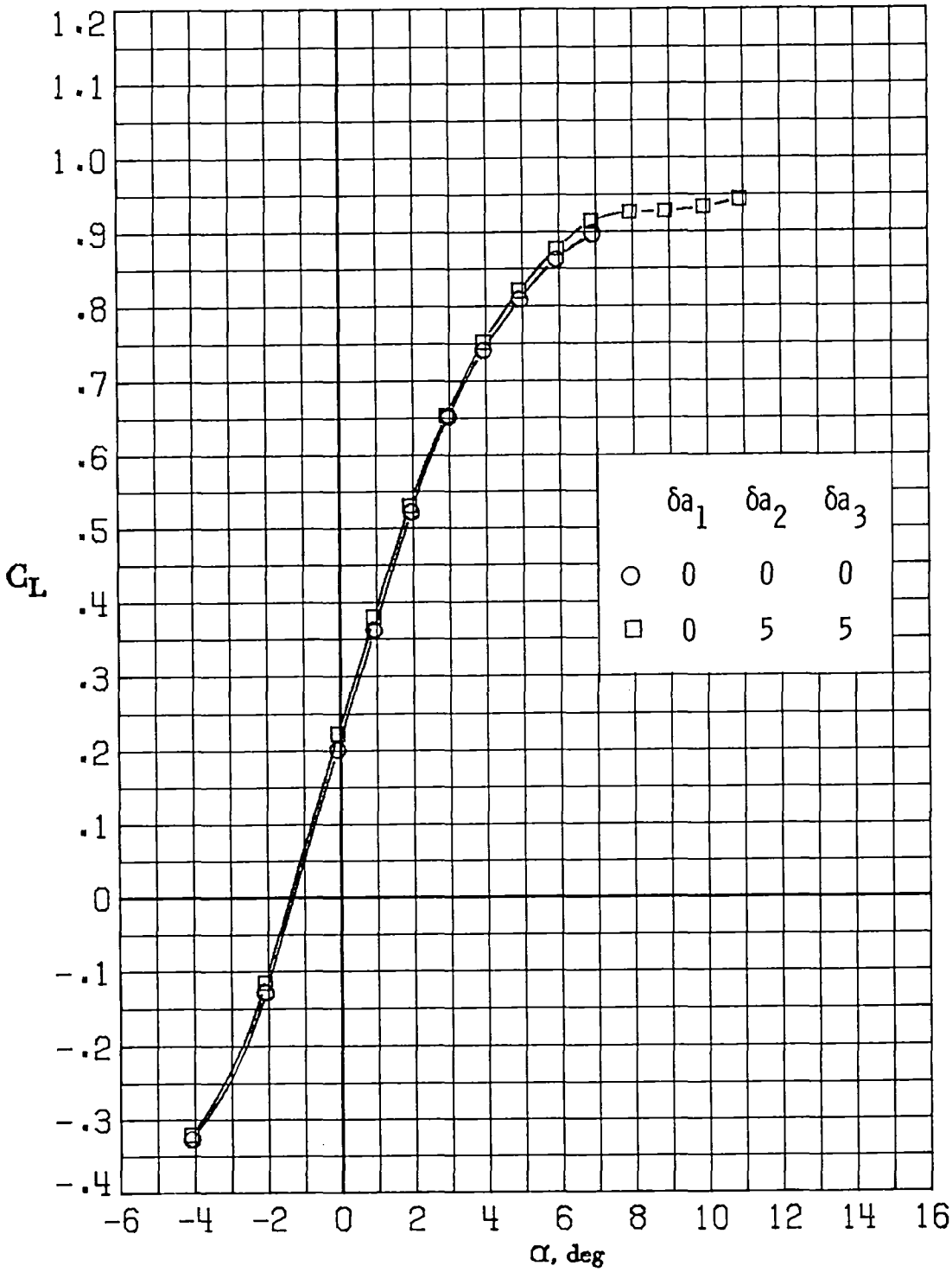

(f) $M_\infty = 0.84$.

Figure 26.- Continued.

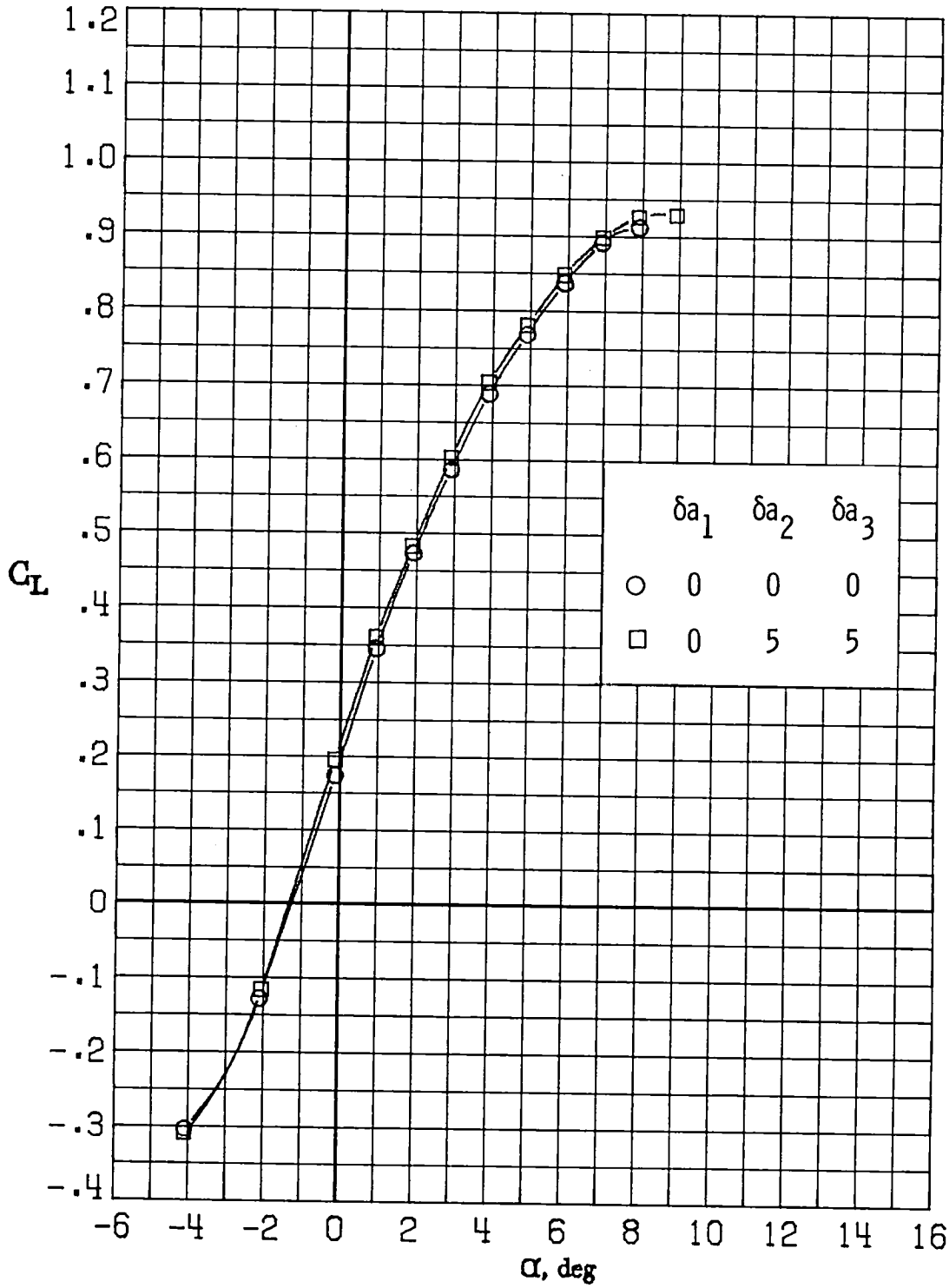

(g) $M_\infty = 0.86$.

Figure 26.- Concluded.

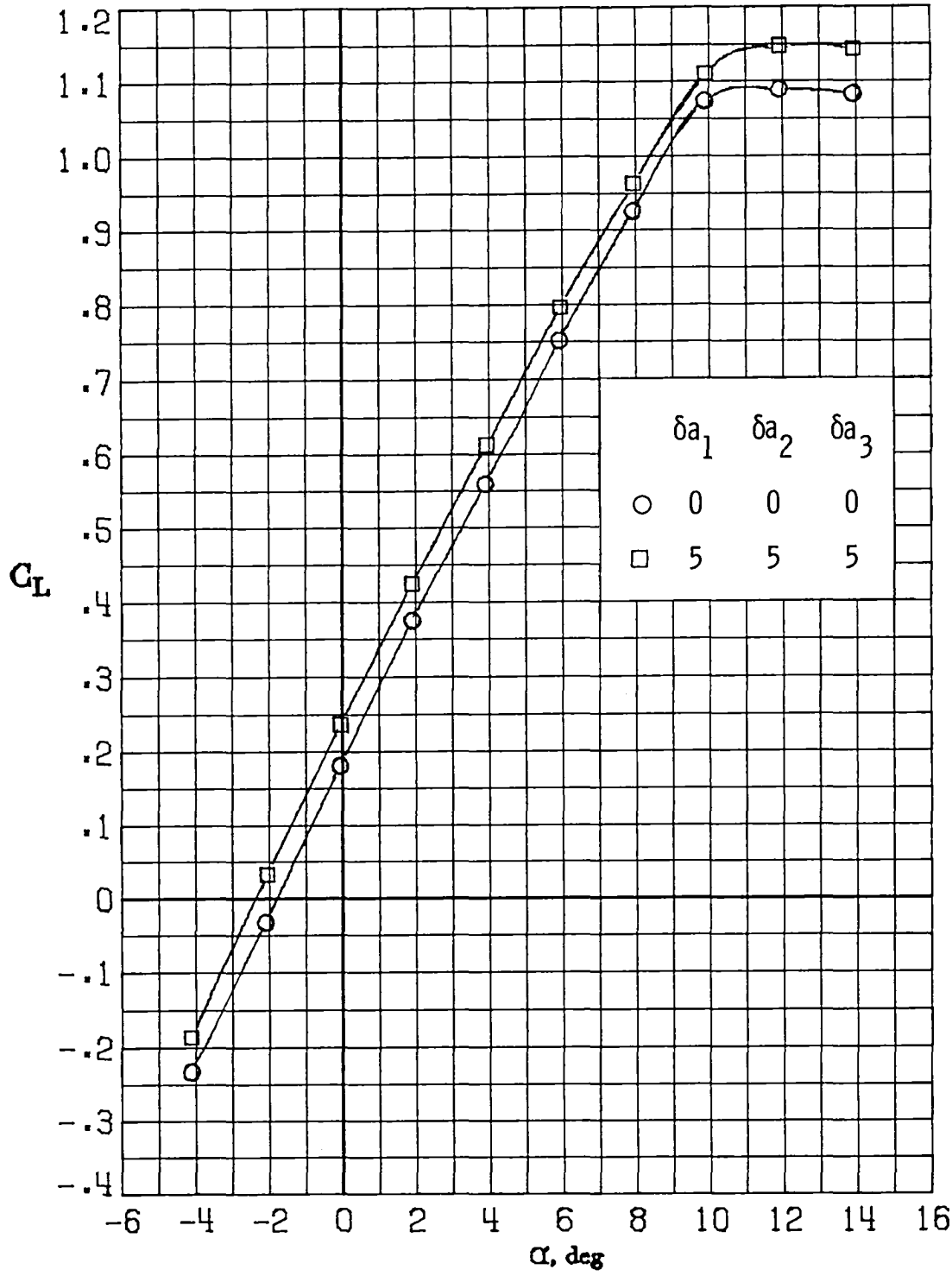

(a) $M_\infty = 0.30$.

Figure 27.- Variation of lift coefficient with angle of attack for $\delta a_1 = 5°$, $\delta a_2 = 5°$, $\delta a_3 = 5°$.

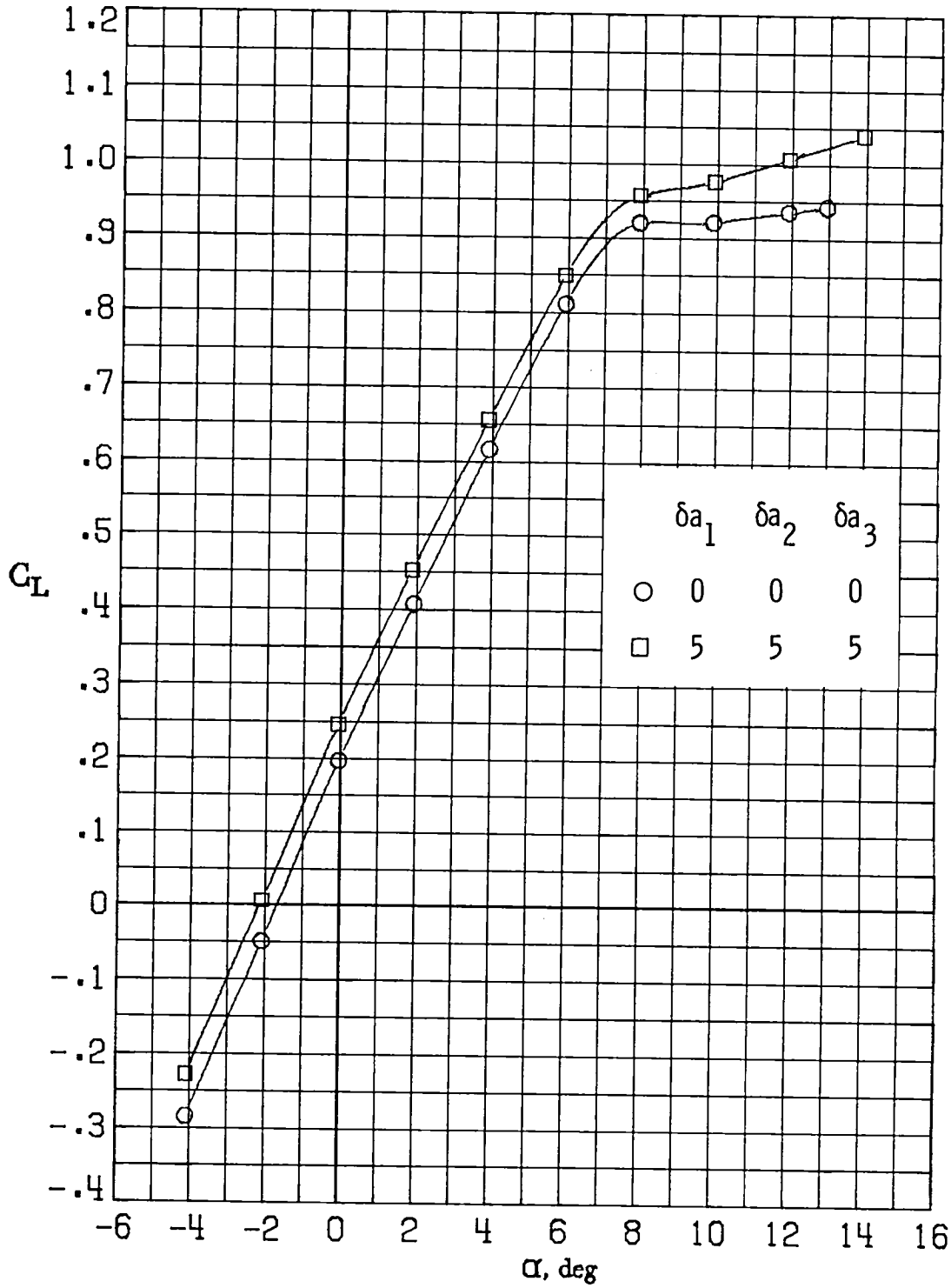

(b) $M_\infty = 0.60$.

Figure 27.- Continued.

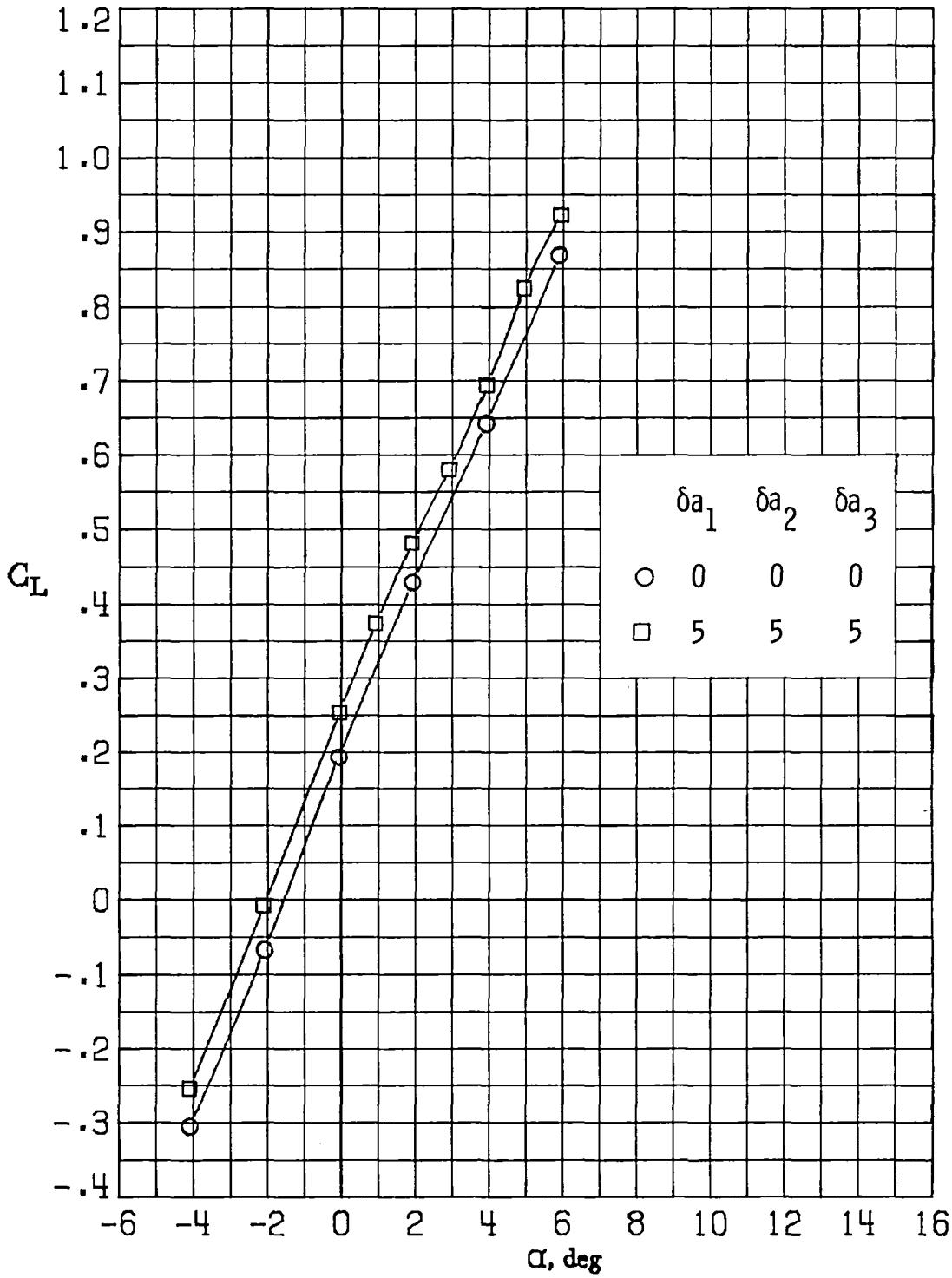

(c) $M_\infty = 0.70$.

Figure 27.- Continued.

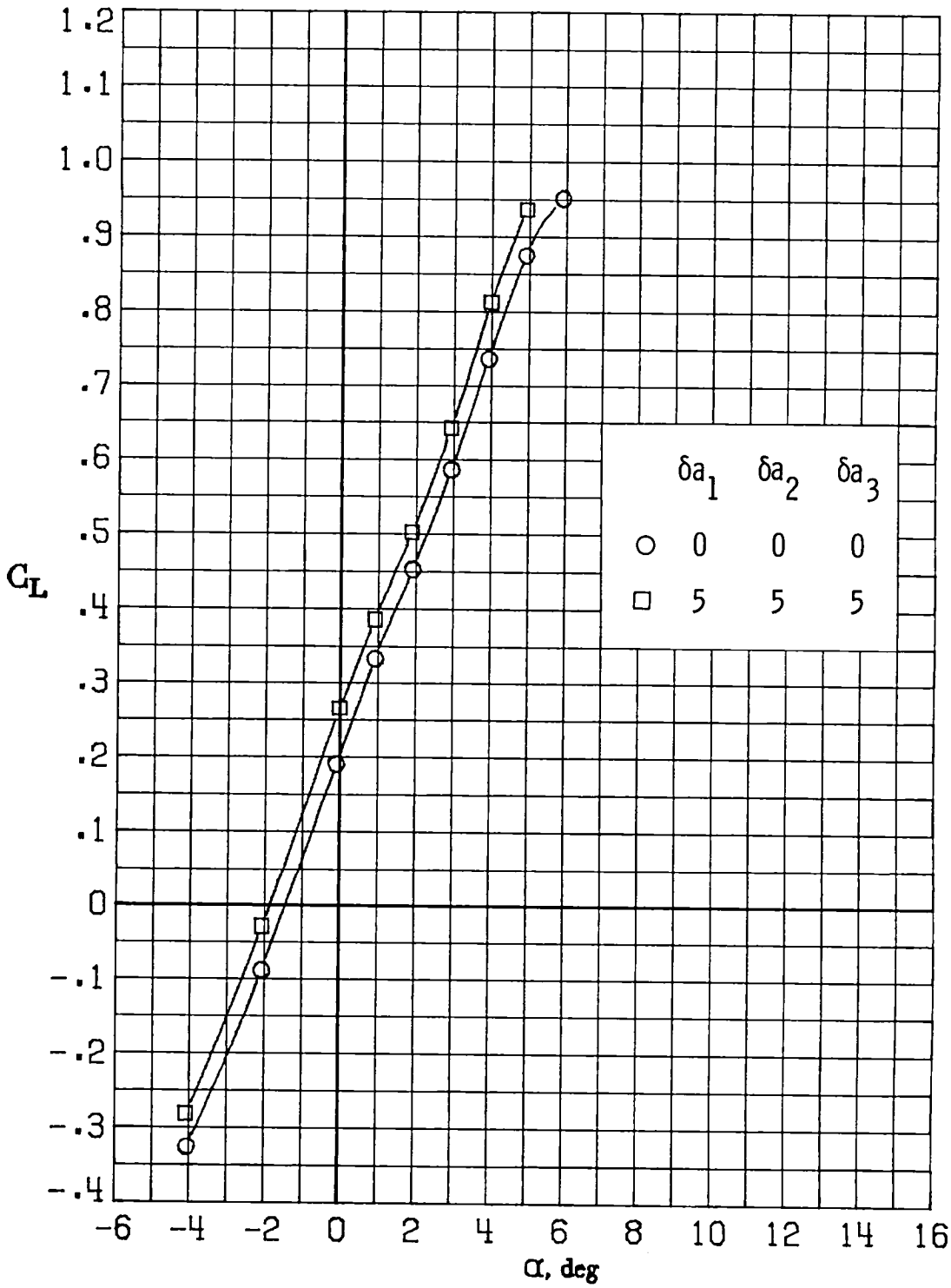

(d) $M_\infty = 0.77$.

Figure 27.- Continued.

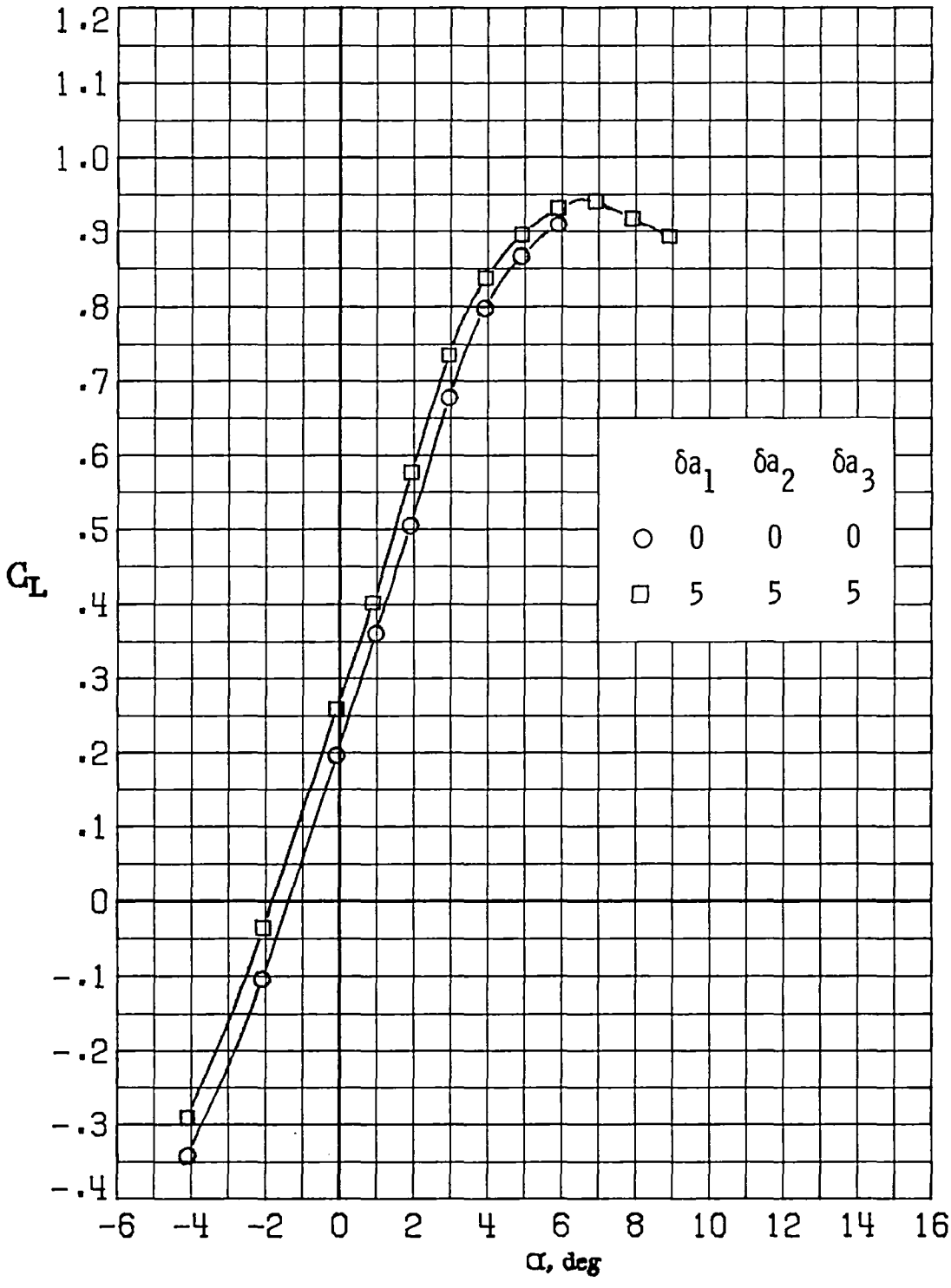

(e) $M_\infty = 0.81$.

Figure 27.- Continued.

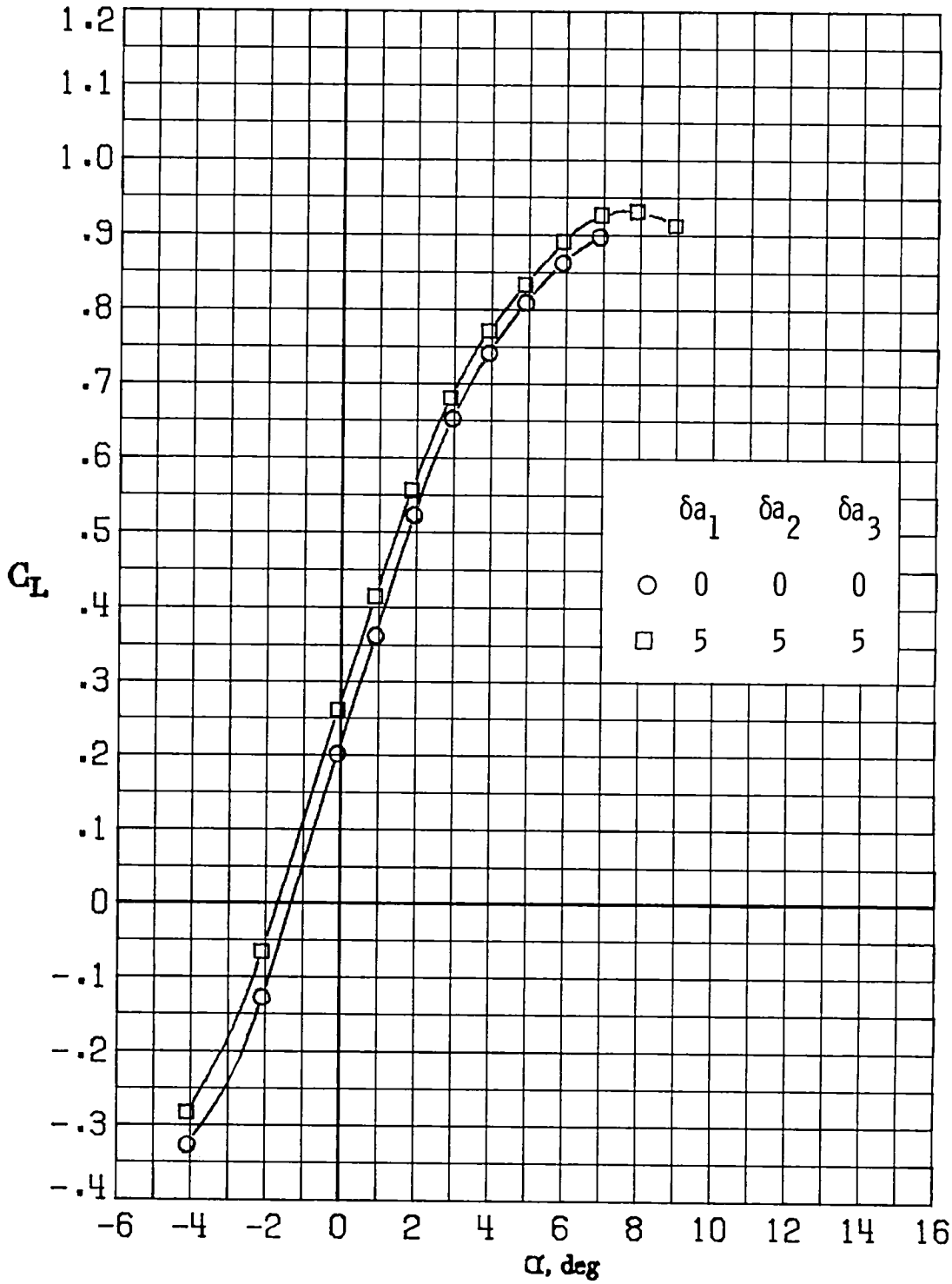

(f) $M_\infty = 0.84$.

Figure 27.- Continued.

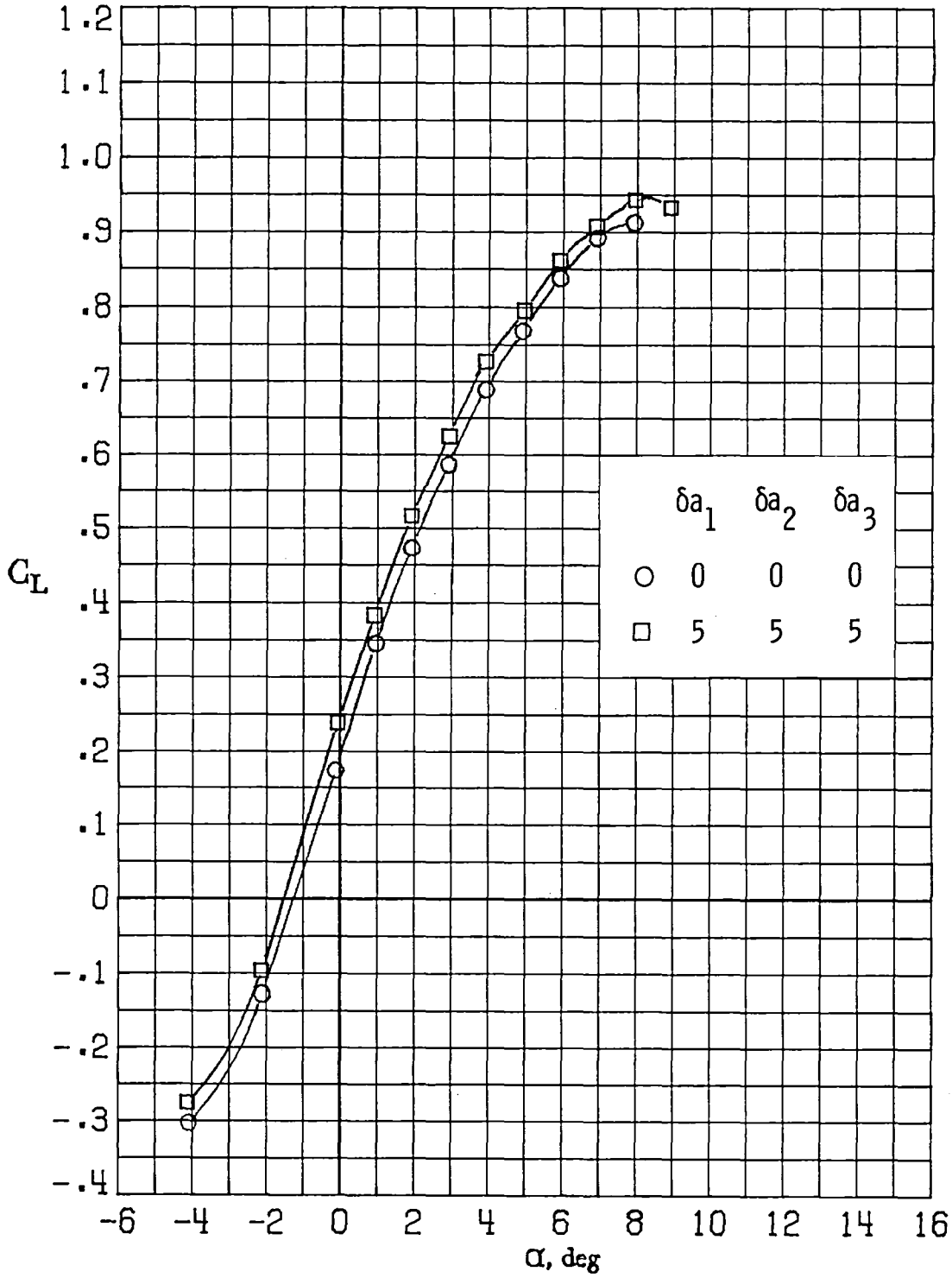

(g) $M_\infty = 0.86$.

Figure 27.- Concluded.

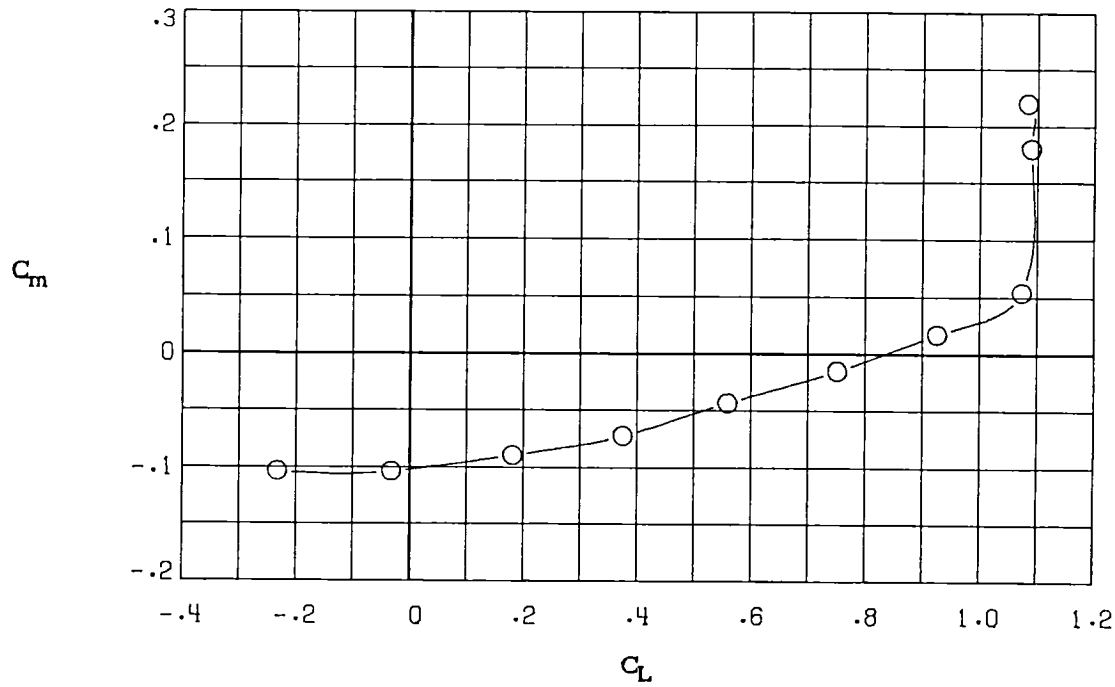

(a) $M_\infty = 0.30$.

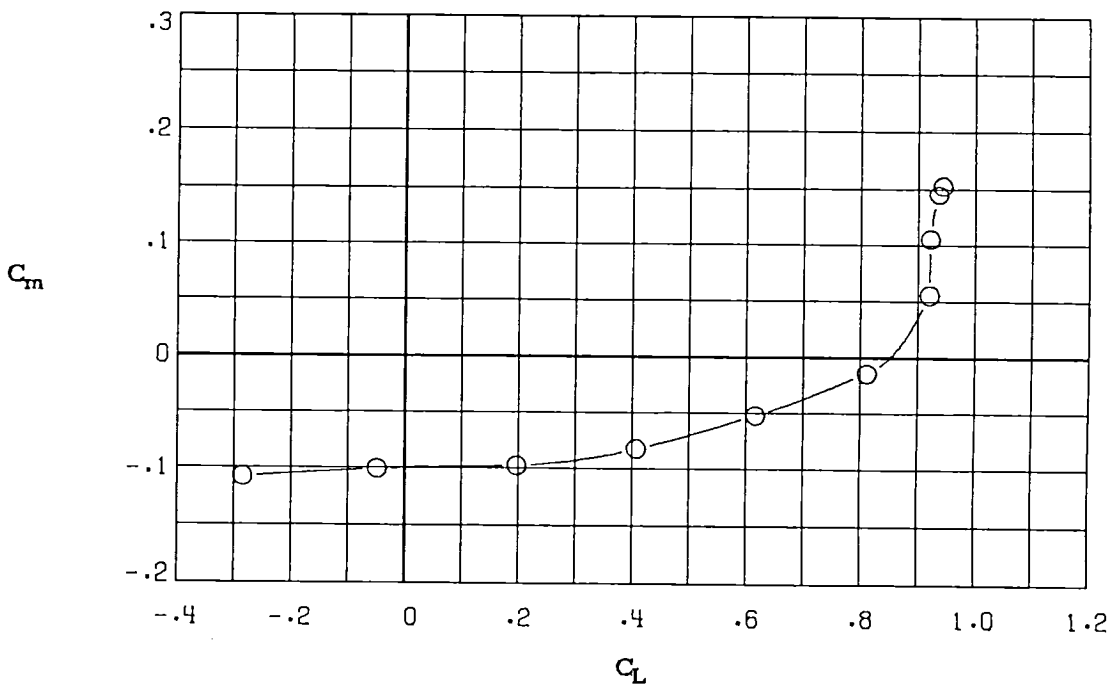

(b) $M_\infty = 0.60$.

Figure 28.- Variation of pitching-moment coefficient with lift coefficient for the baseline configuration ($\delta a_1 = 0°$; $\delta a_2 = 0°$; $\delta a_3 = 0°$).

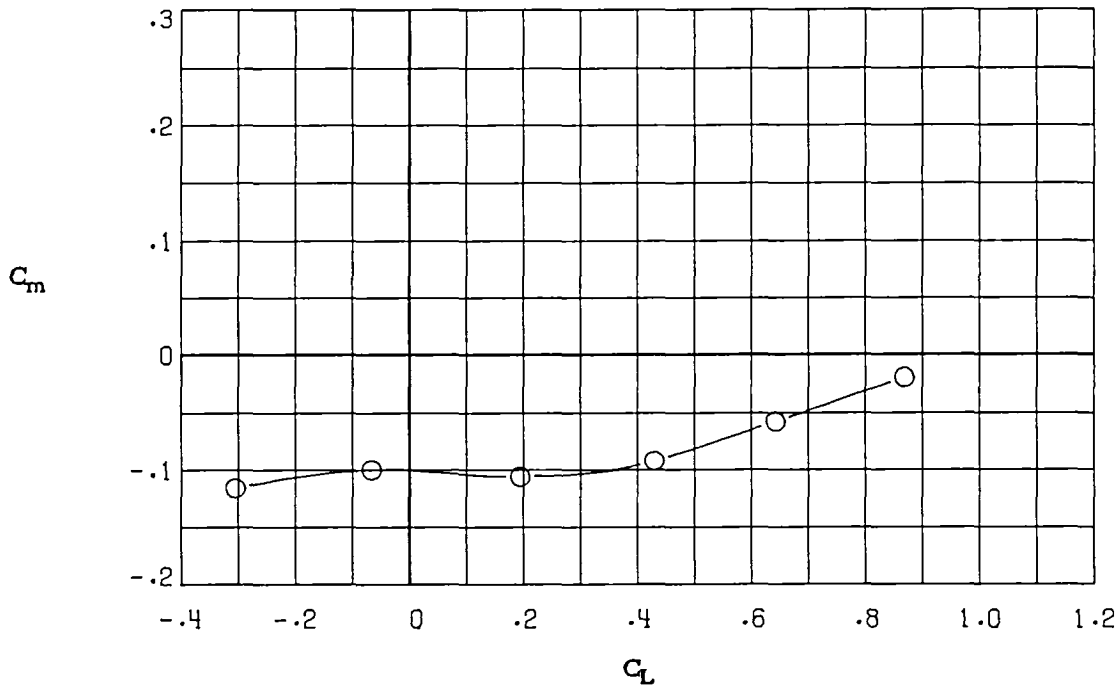

(c) $M_\infty = 0.70$.

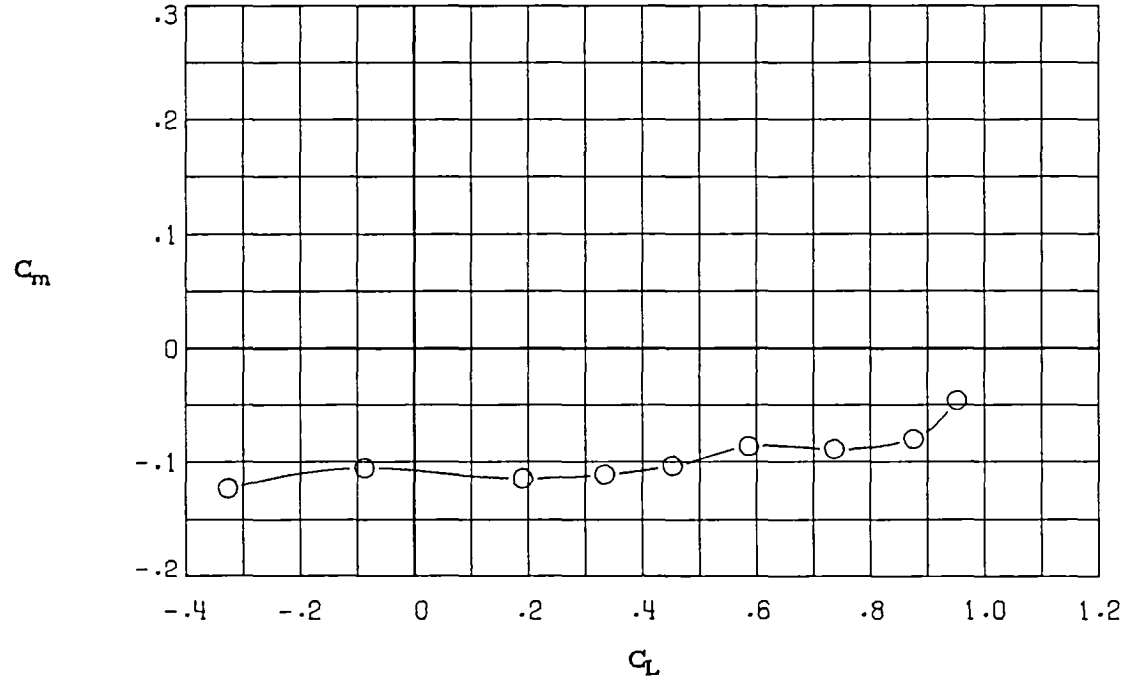

(d) $M_\infty = 0.77$.

Figure 28.- Continued.

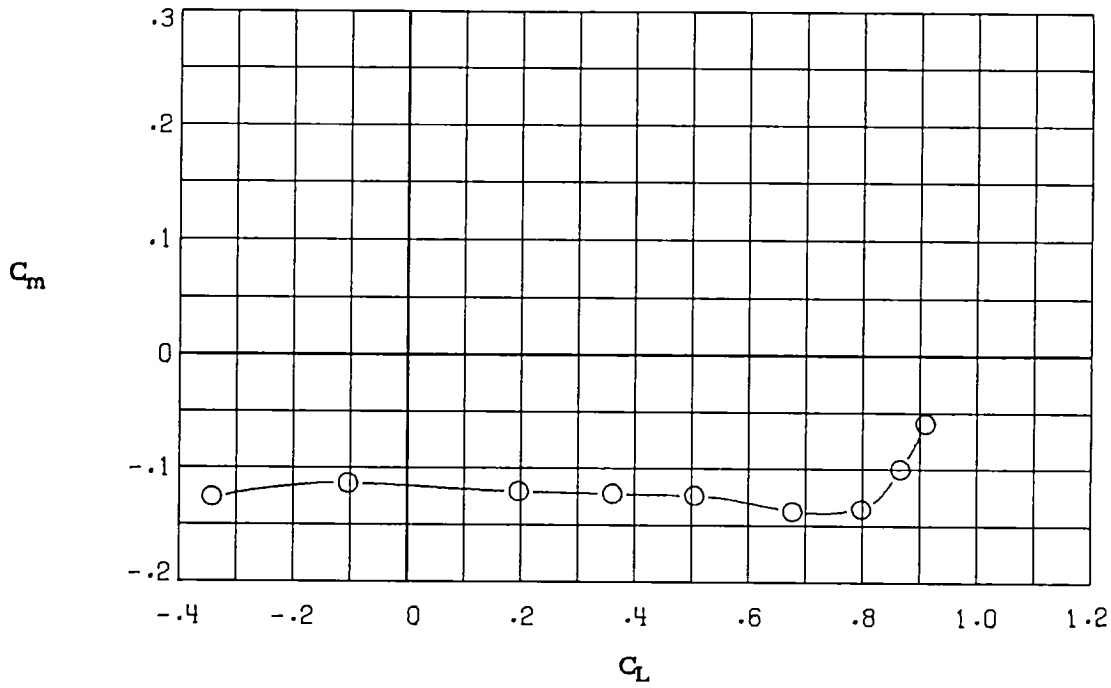

(e) $M_\infty = 0.81$.

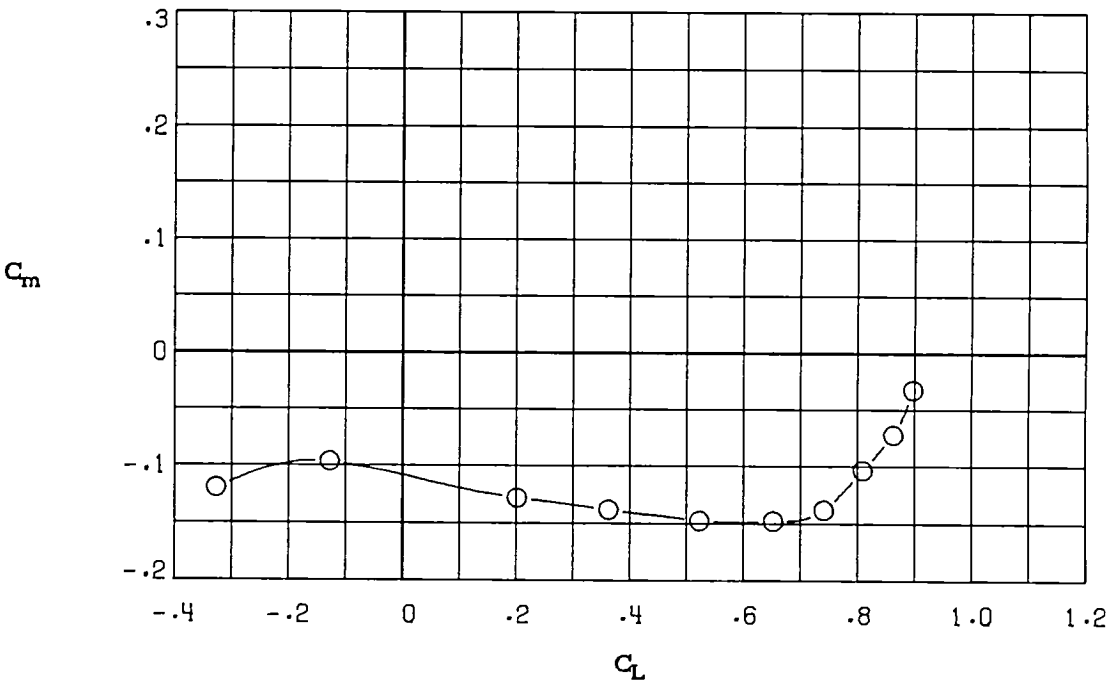

(f) $M_\infty = 0.84$.

Figure 28.- Continued.

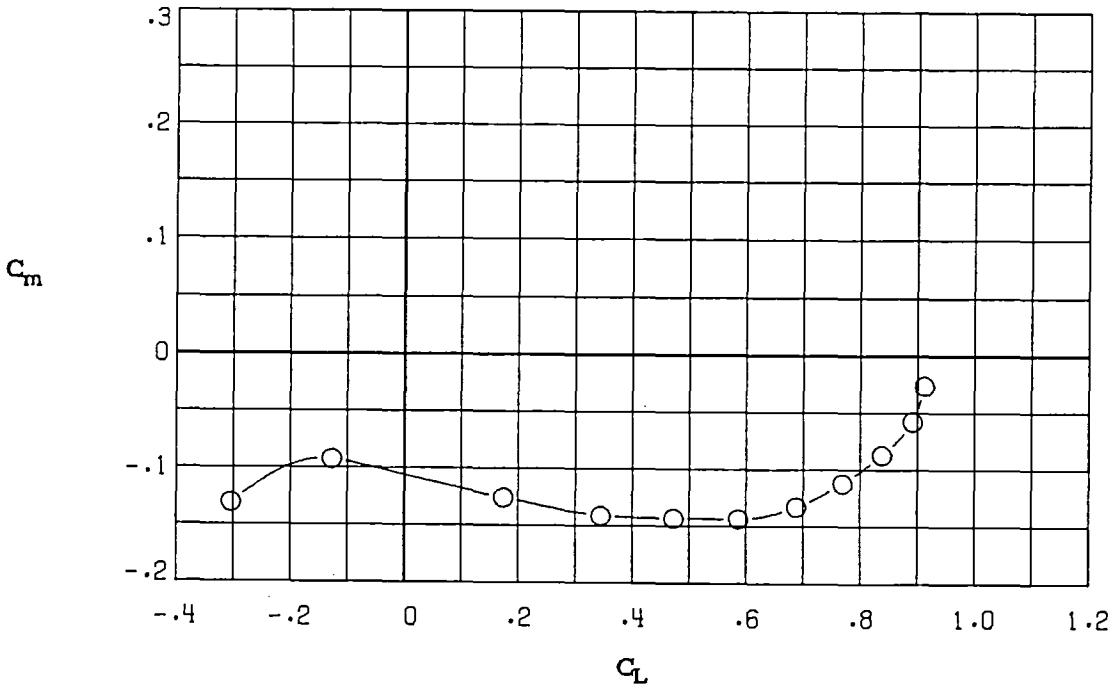

(g) $M_\infty = 0.86$.

Figure 28.- Concluded.

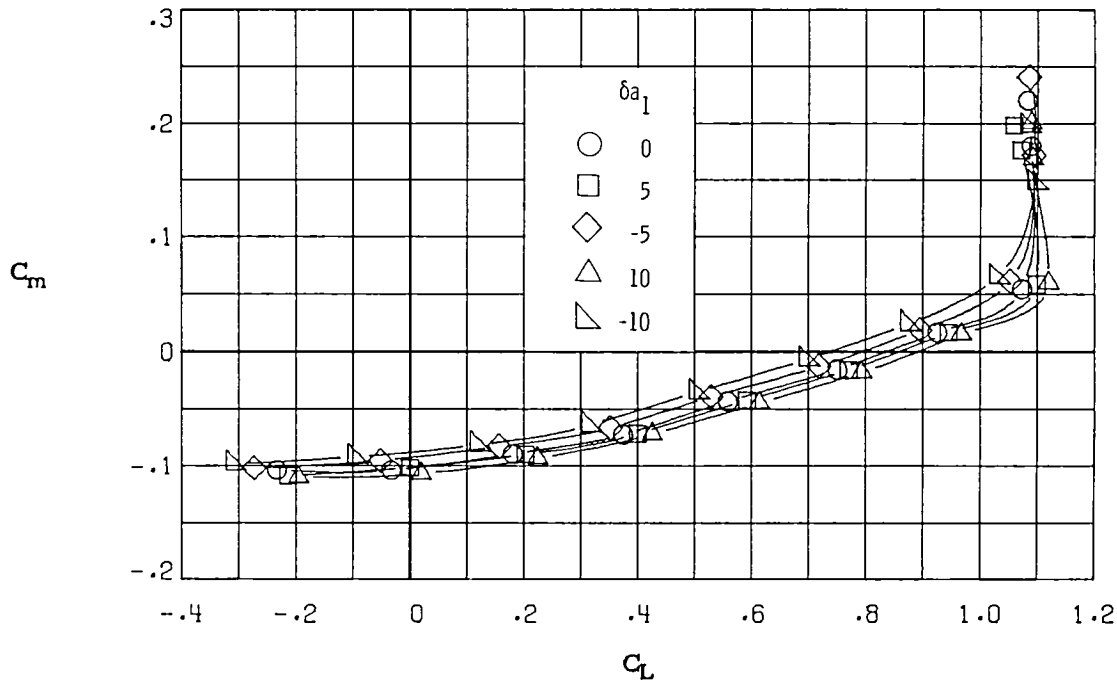

(a) $M_\infty = 0.30$.

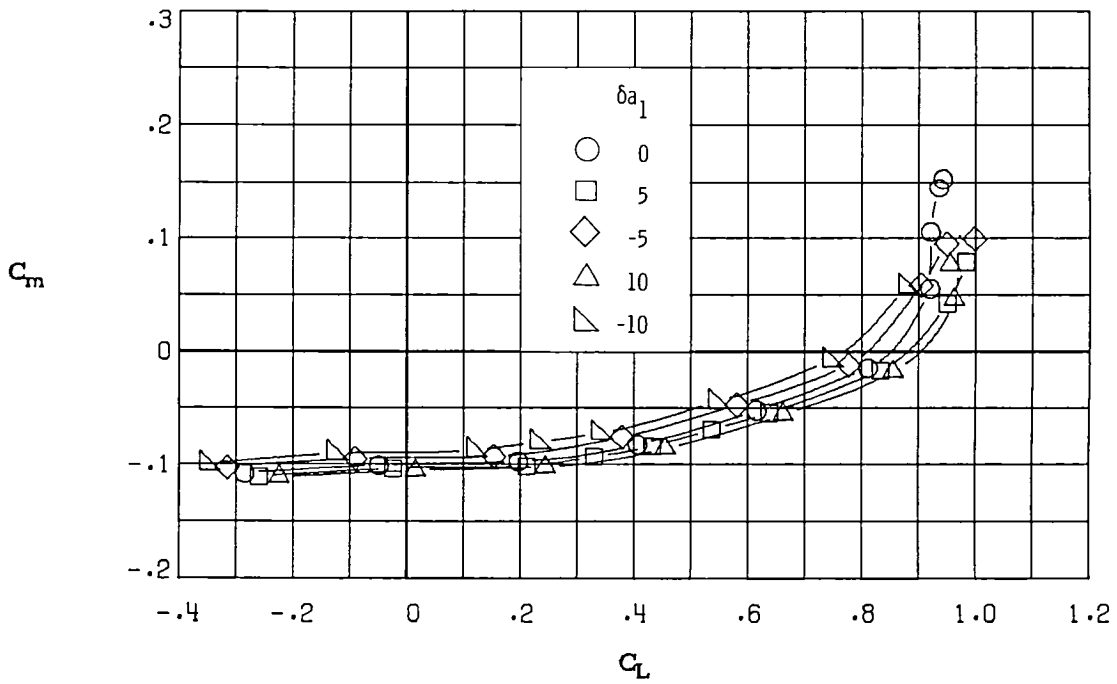

(b) $M_\infty = 0.60$.

Figure 29.- Variation of pitching-moment coefficient with lift coefficient for deflections of aileron 1 (δa_1 in degrees). $\delta a_2 = 0°$; $\delta a_3 = 0°$.

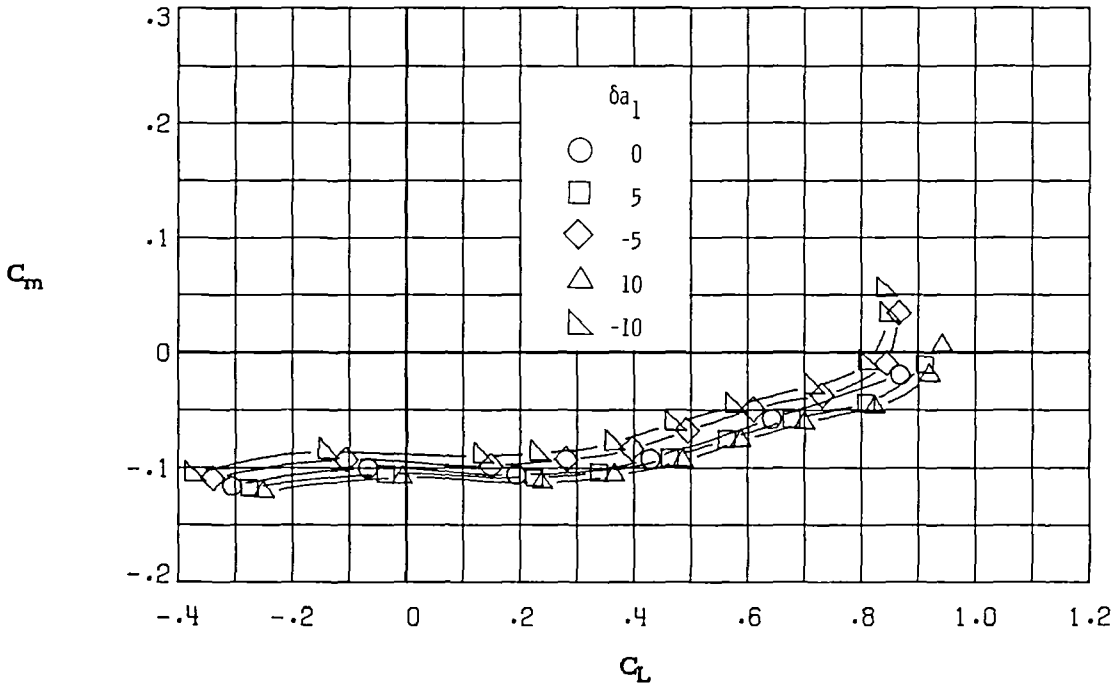

(c) $M_\infty = 0.70$.

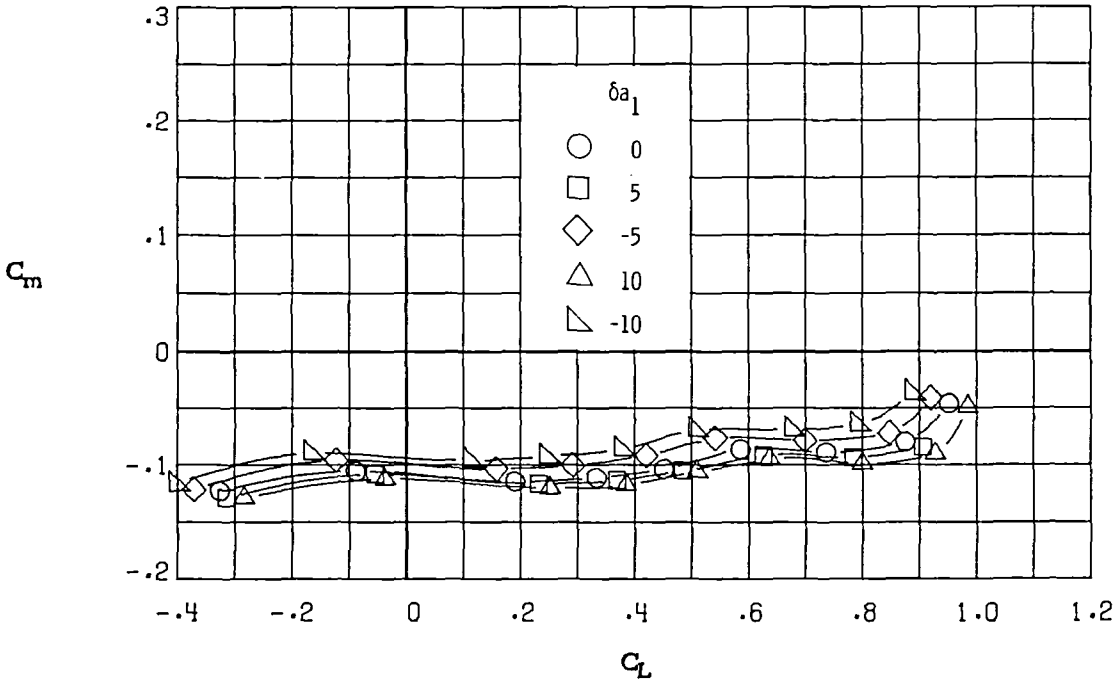

(d) $M_\infty = 0.77$.

Figure 29.- Continued.

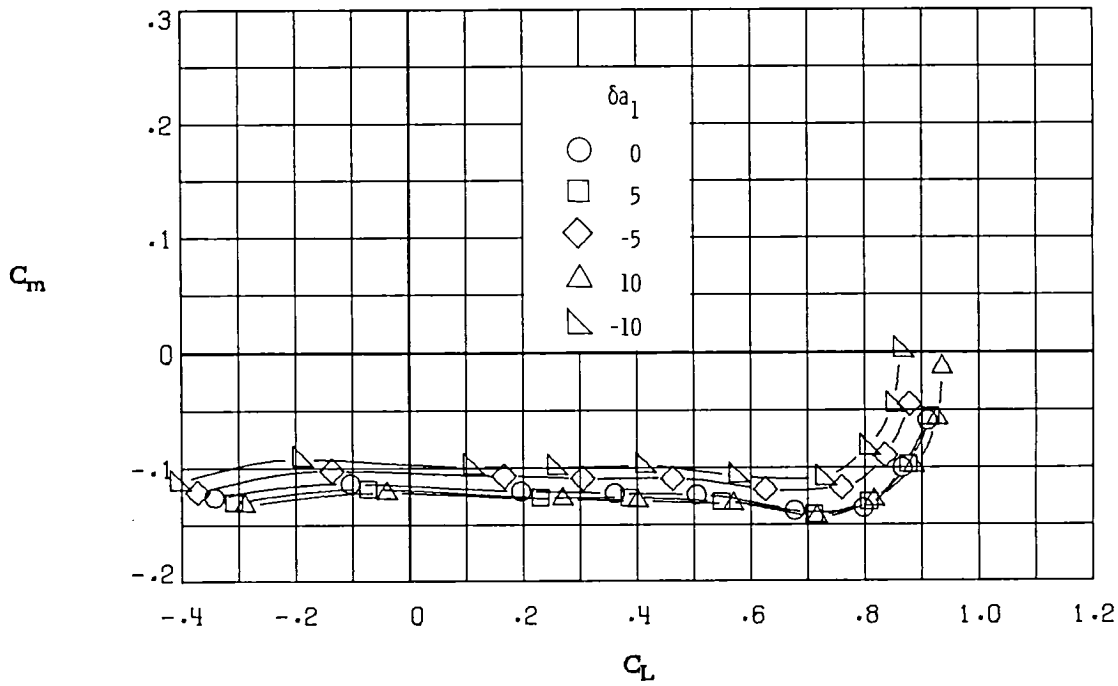

(e) $M_\infty = 0.81$.

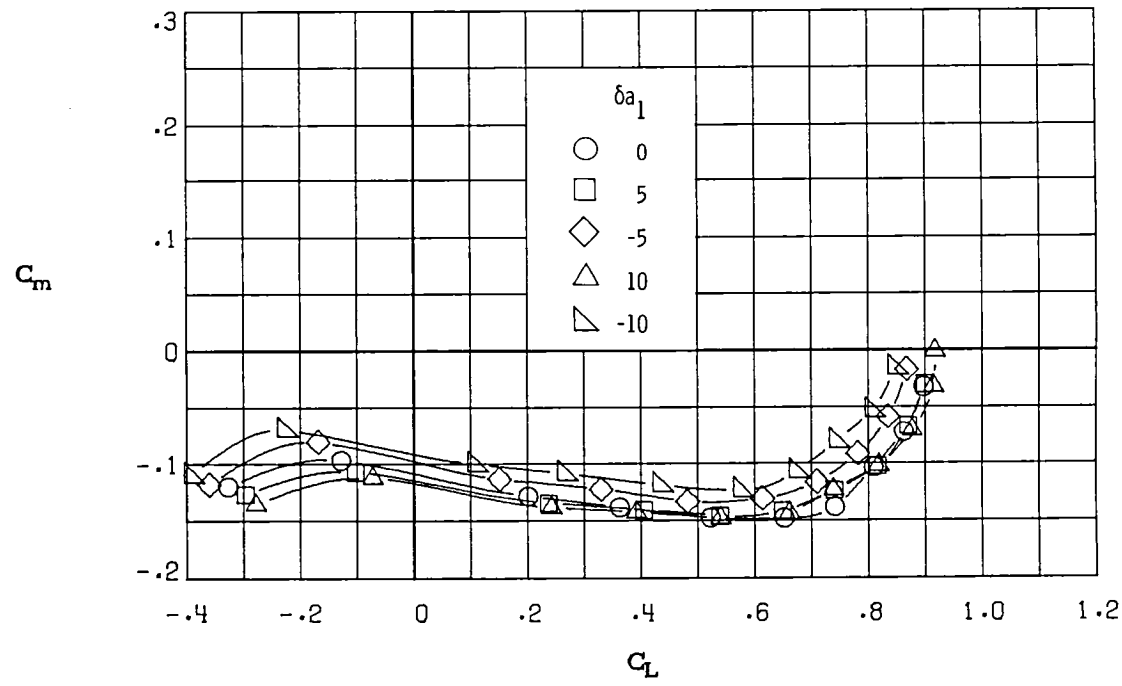

(f) $M_\infty = 0.84$.

Figure 29.- Continued.

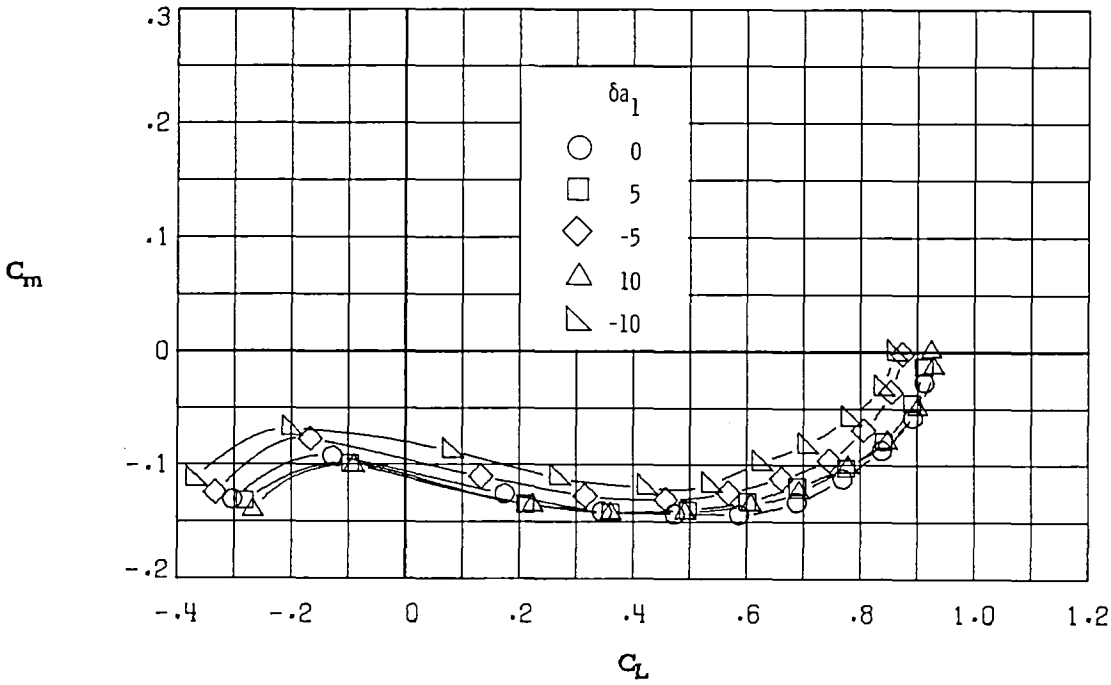

(g) $M_\infty = 0.86$.

Figure 29.- Concluded.

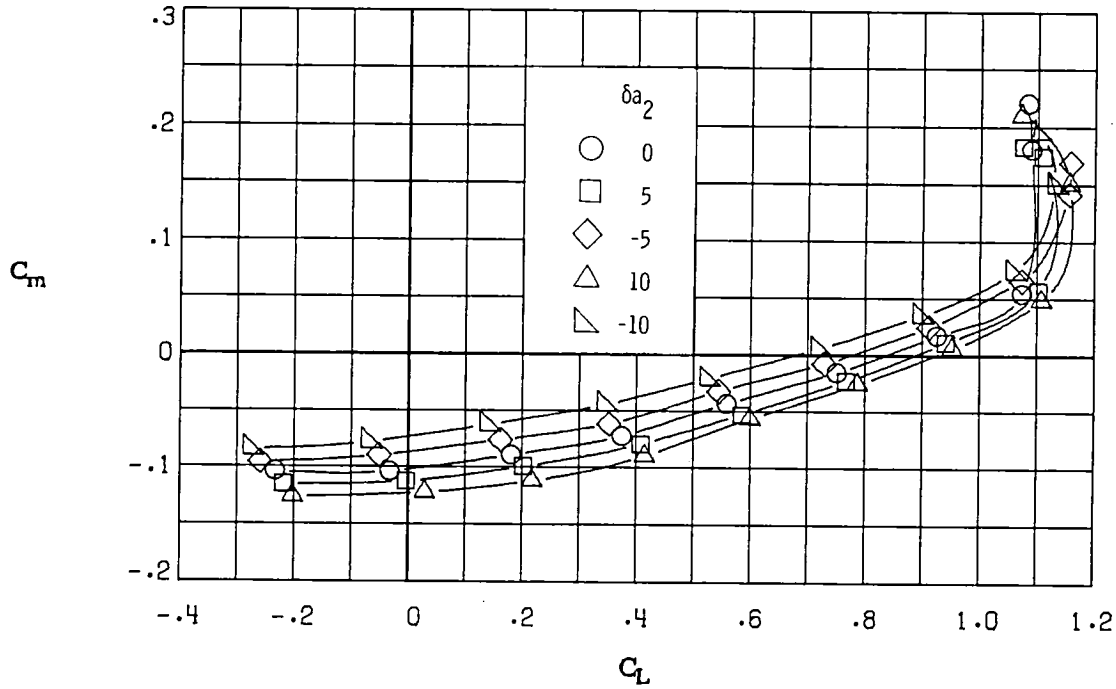

(a) $M_\infty = 0.30$.

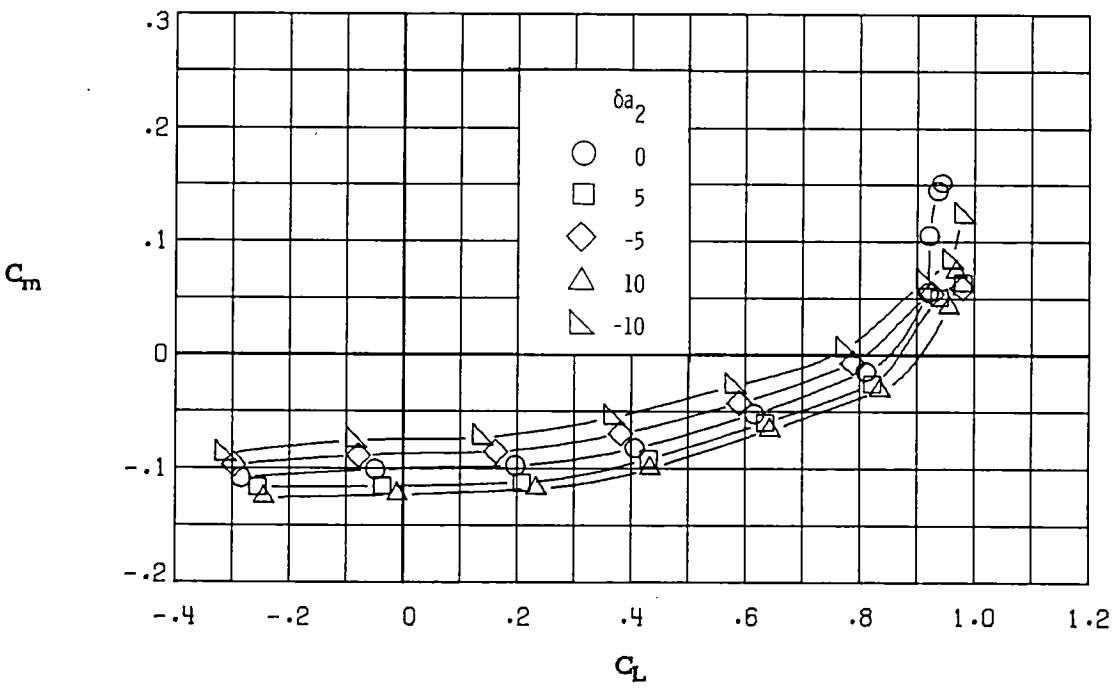

(b) $M_\infty = 0.60$.

Figure 30.- Variation of pitching-moment coefficient with lift coefficient for deflections of aileron 2 (δa_2 in degrees). $\delta a_1 = 0°$; $\delta a_3 = 0°$.

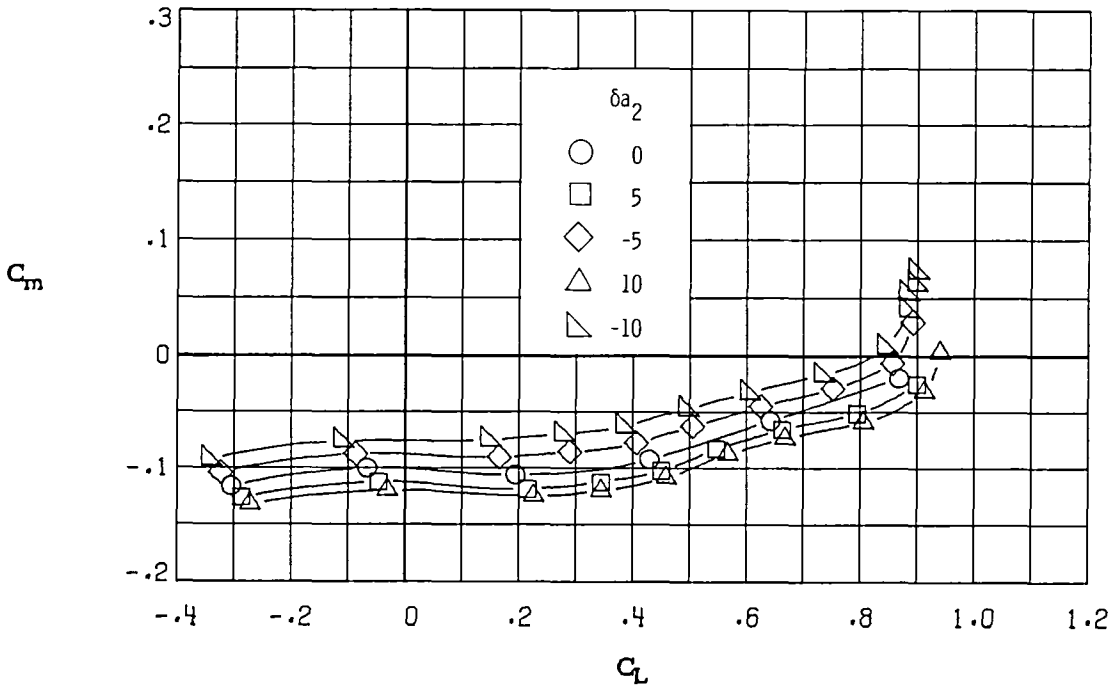

(c) $M_\infty = 0.70$.

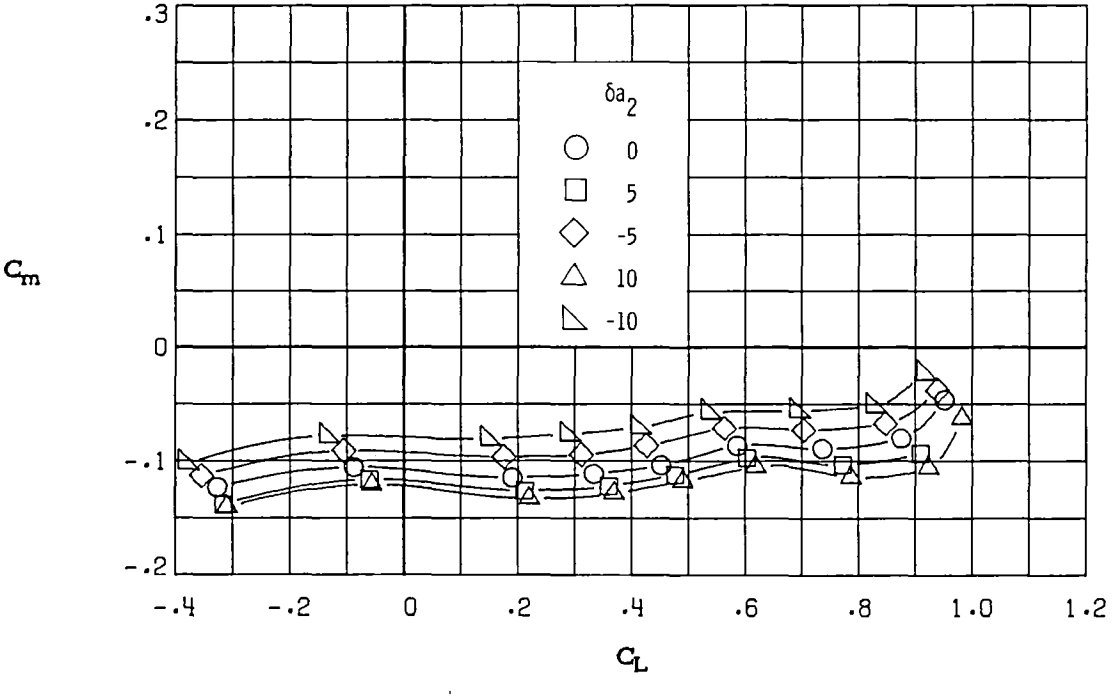

(d) $M_\infty = 0.77$.

Figure 30.- Continued.

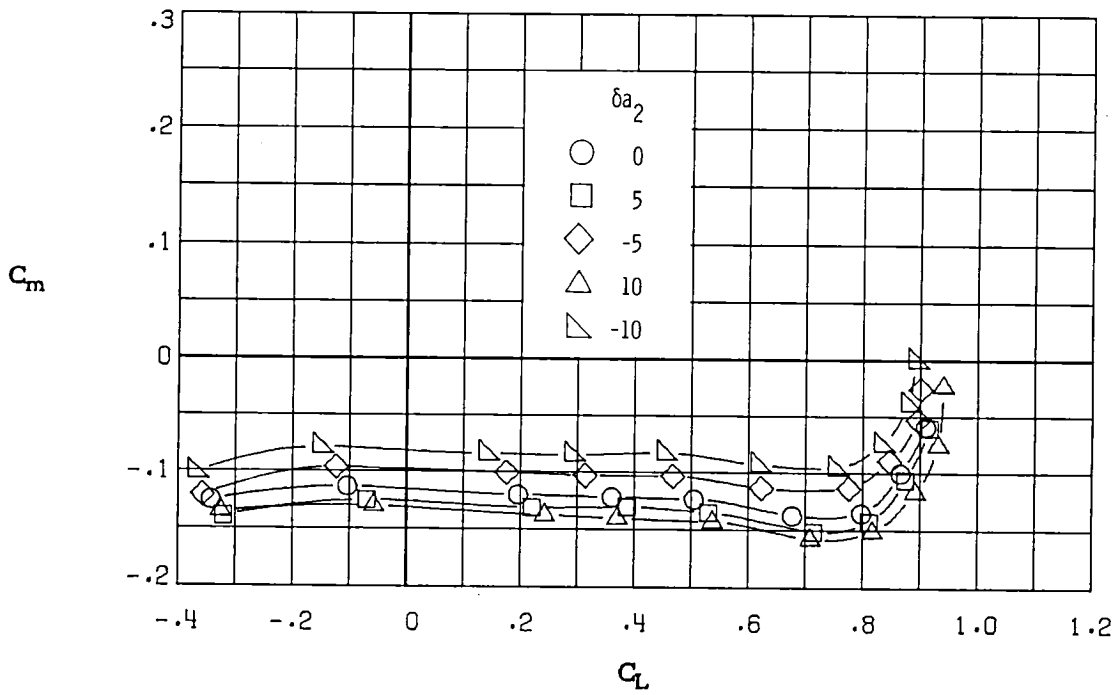

(e) $M_\infty = 0.81$.

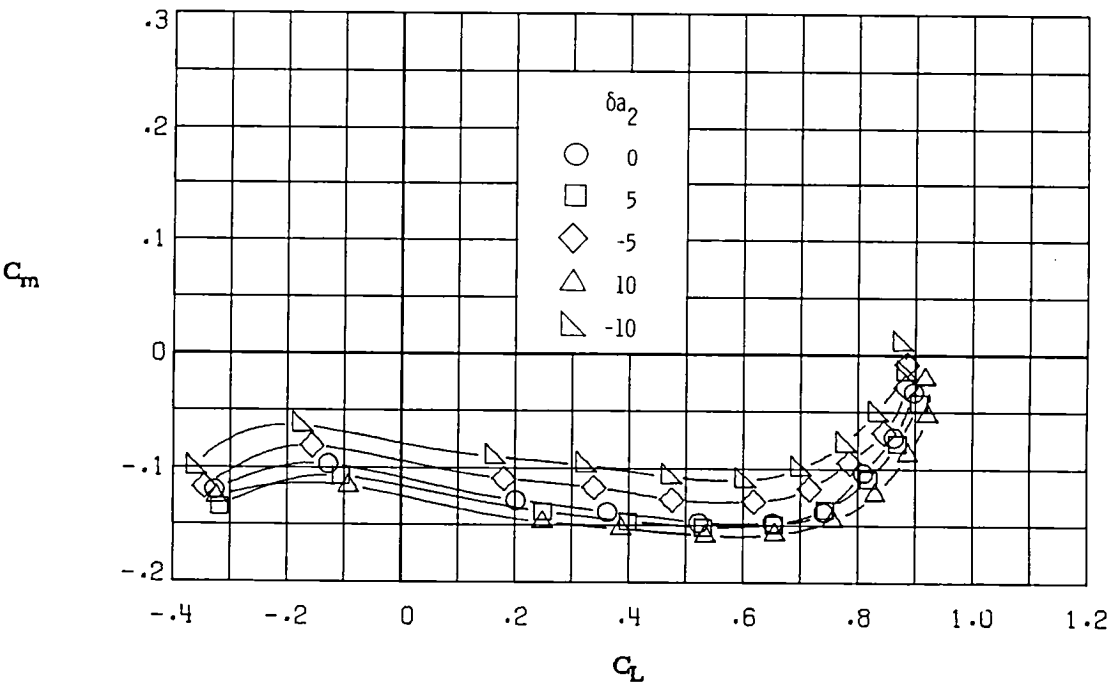

(f) $M_\infty = 0.84$.

Figure 30.- Continued.

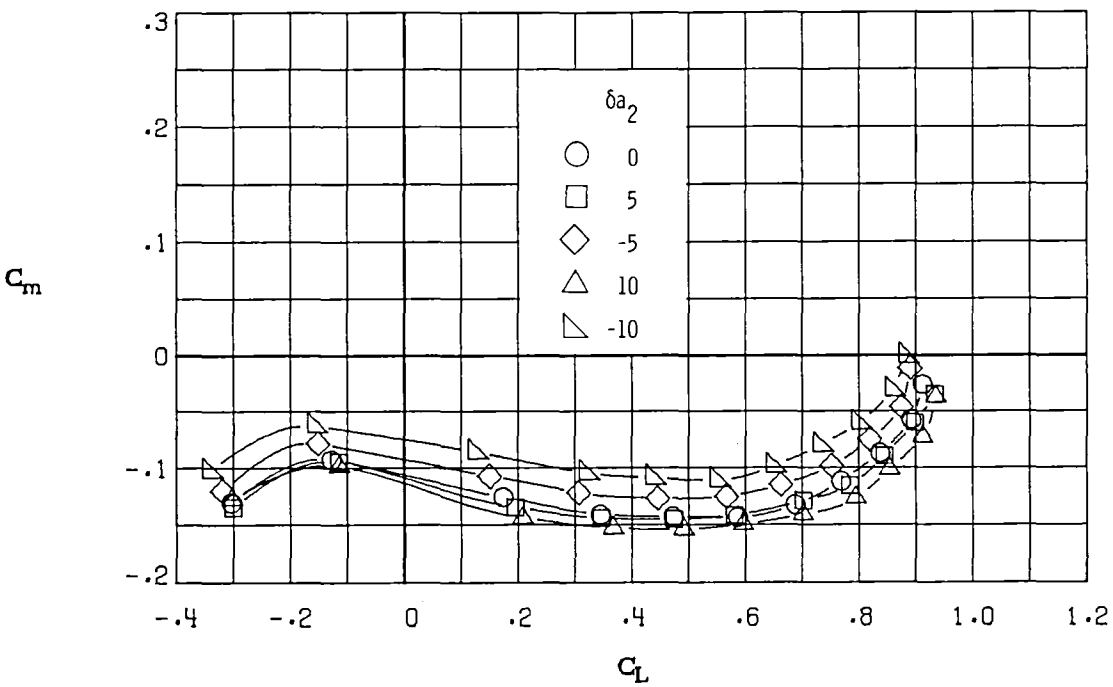

(g) $M_\infty = 0.86$.

Figure 30.- Concluded.

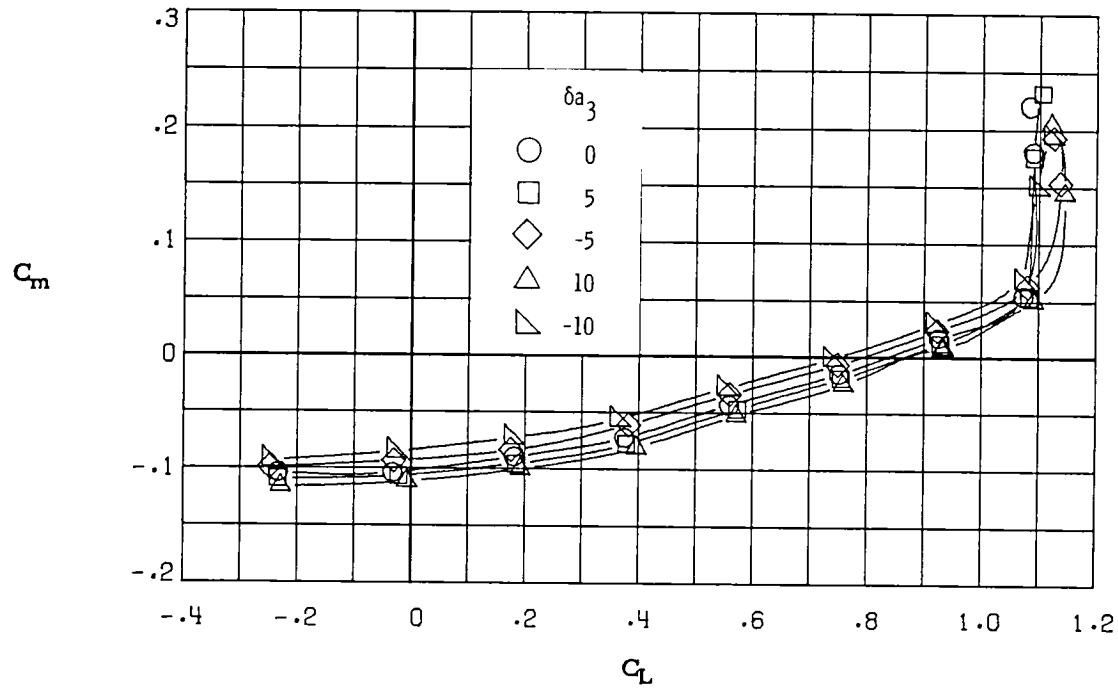

(a) $M_\infty = 0.30$

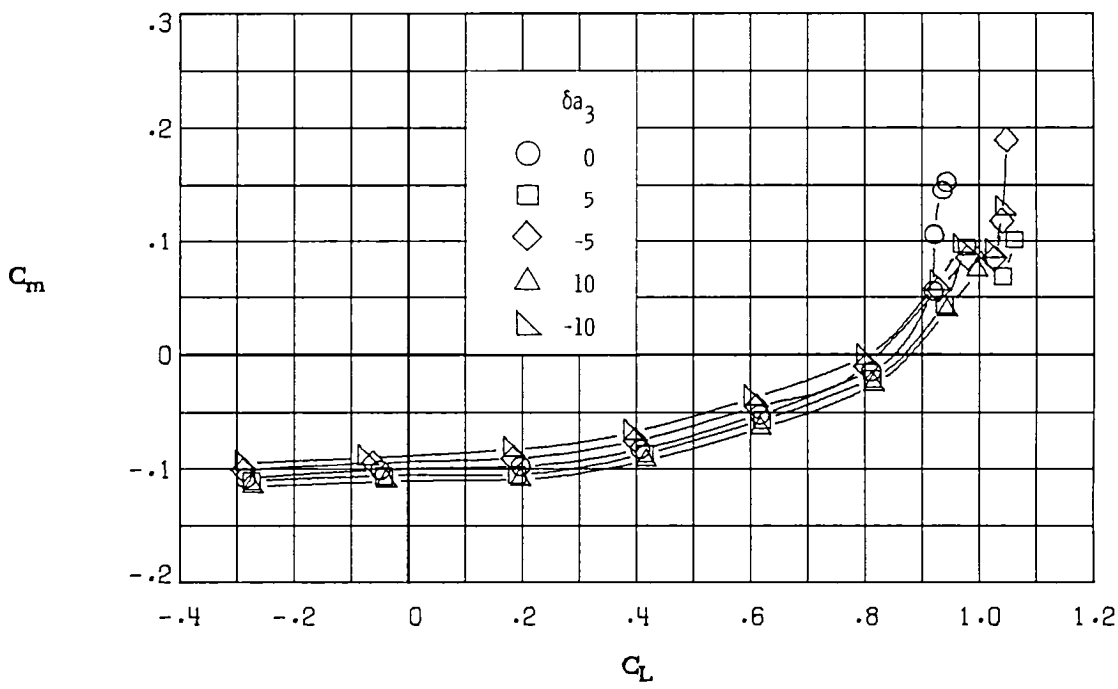

(b) $M_\infty = 0.60$.

Figure 31.- Variation of pitching-moment coefficient with lift coefficient for deflections of aileron 3 (δa_3 in degrees). $\delta a_1 = 0°$; $\delta a_2 = 0°$.

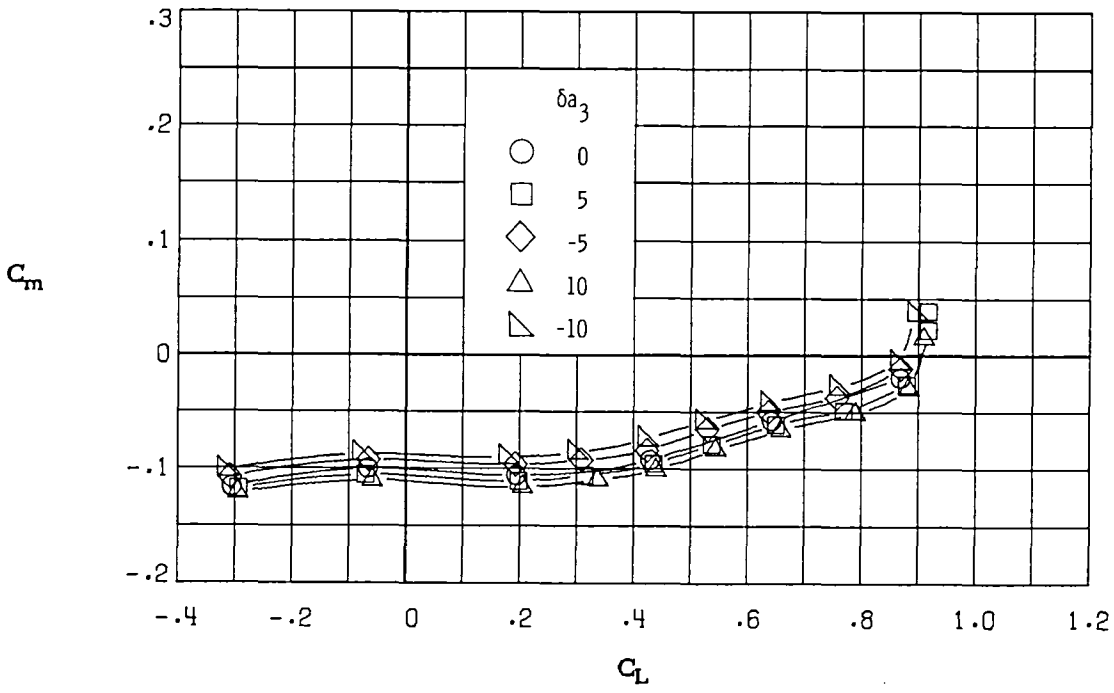

(c) $M_\infty = 0.70$.

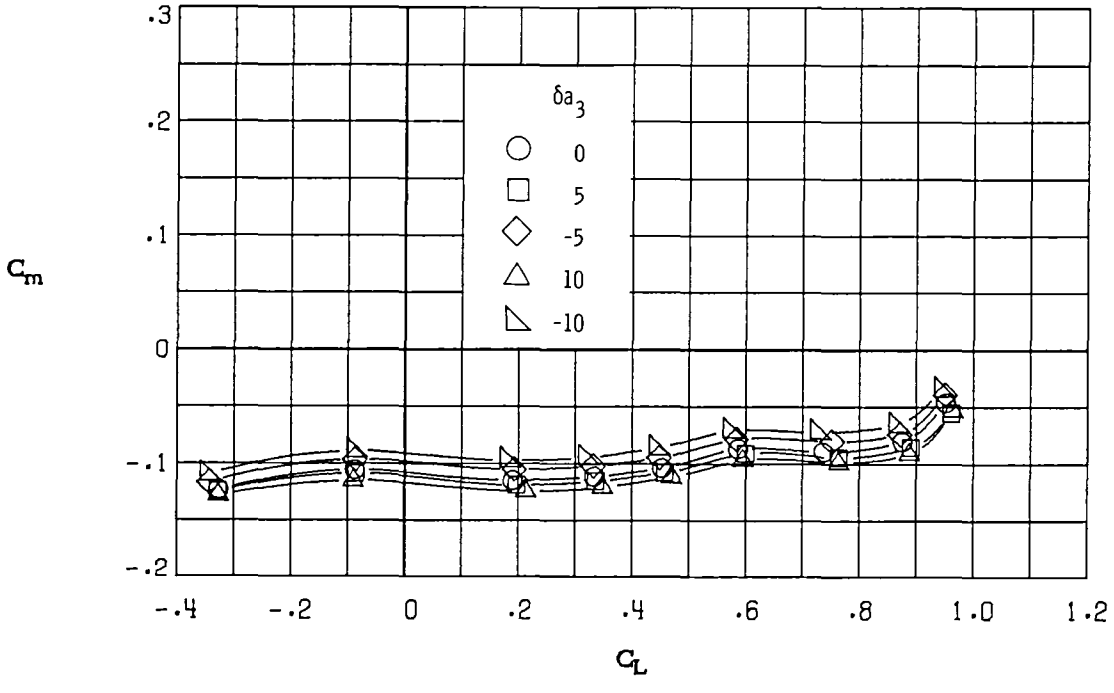

(d) $M_\infty = 0.77$.

Figure 31.- Continued.

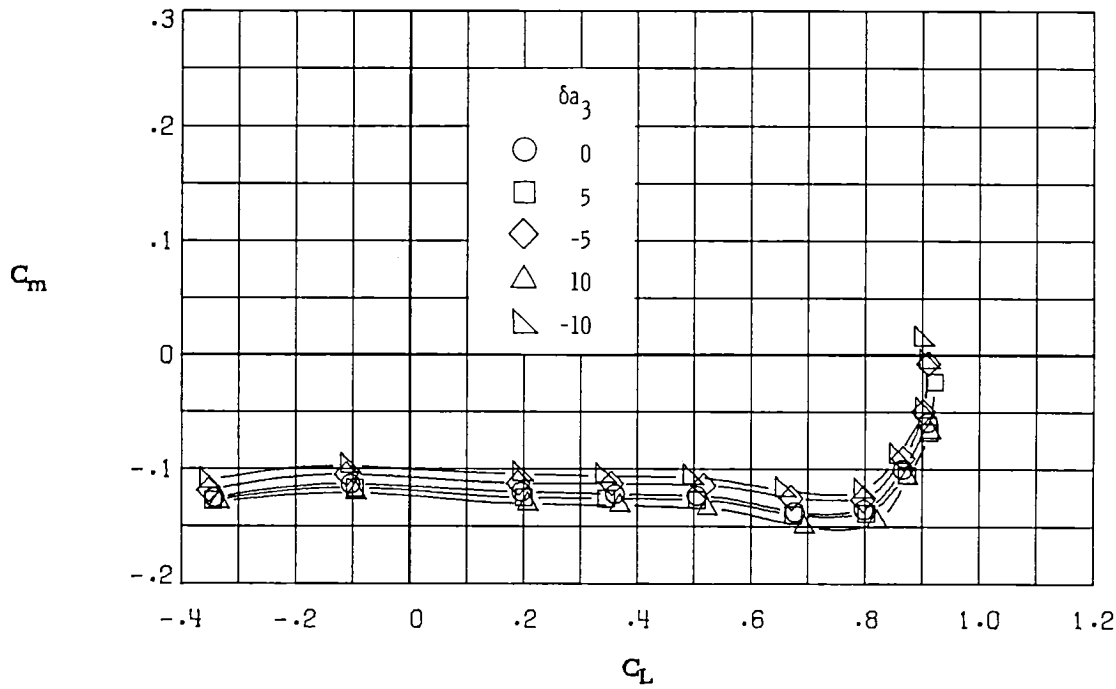

(e) $M_\infty = 0.81$.

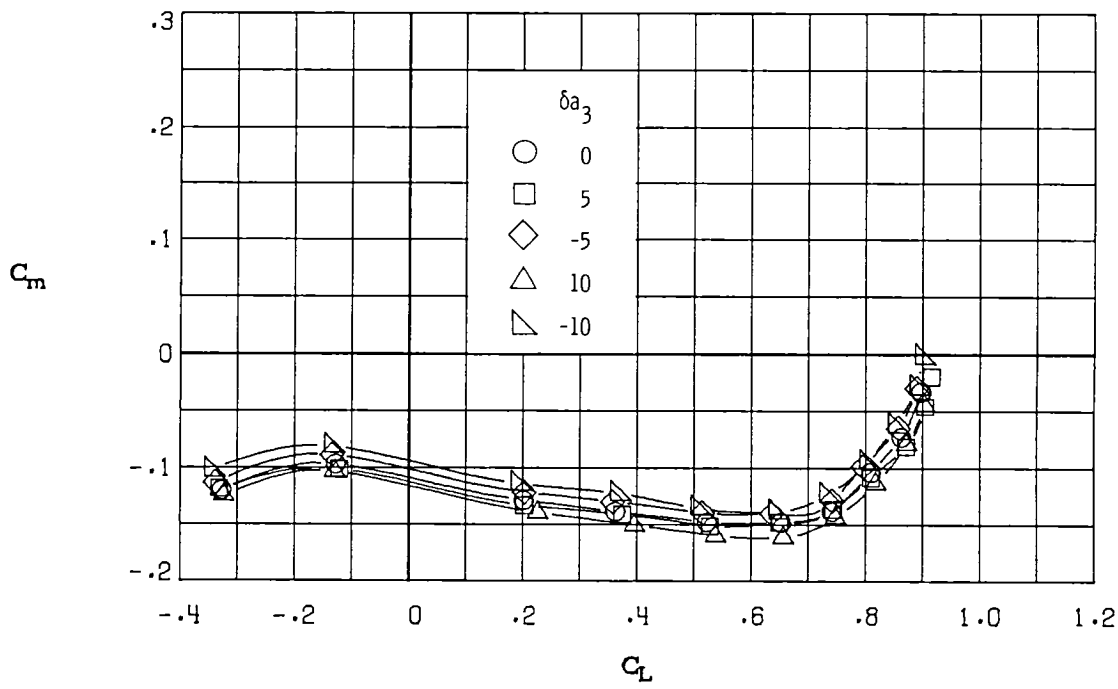

(f) $M_\infty = 0.84$.

Figure 31.- Continued.

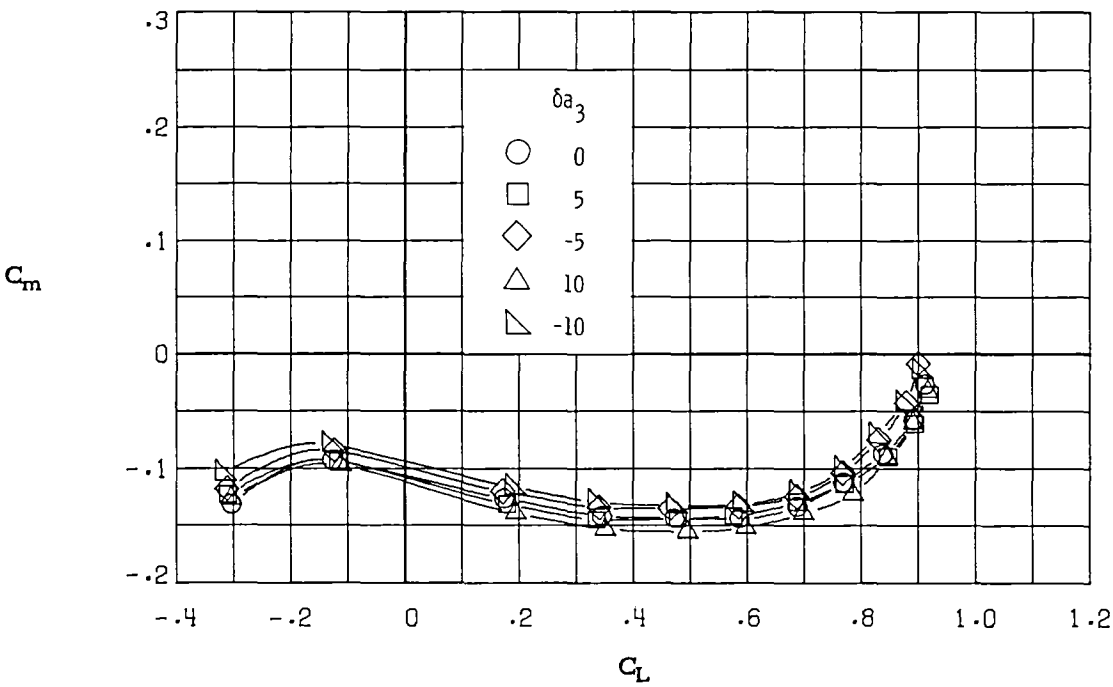

(g) $M_\infty = 0.86$.

Figure 31.- Concluded.

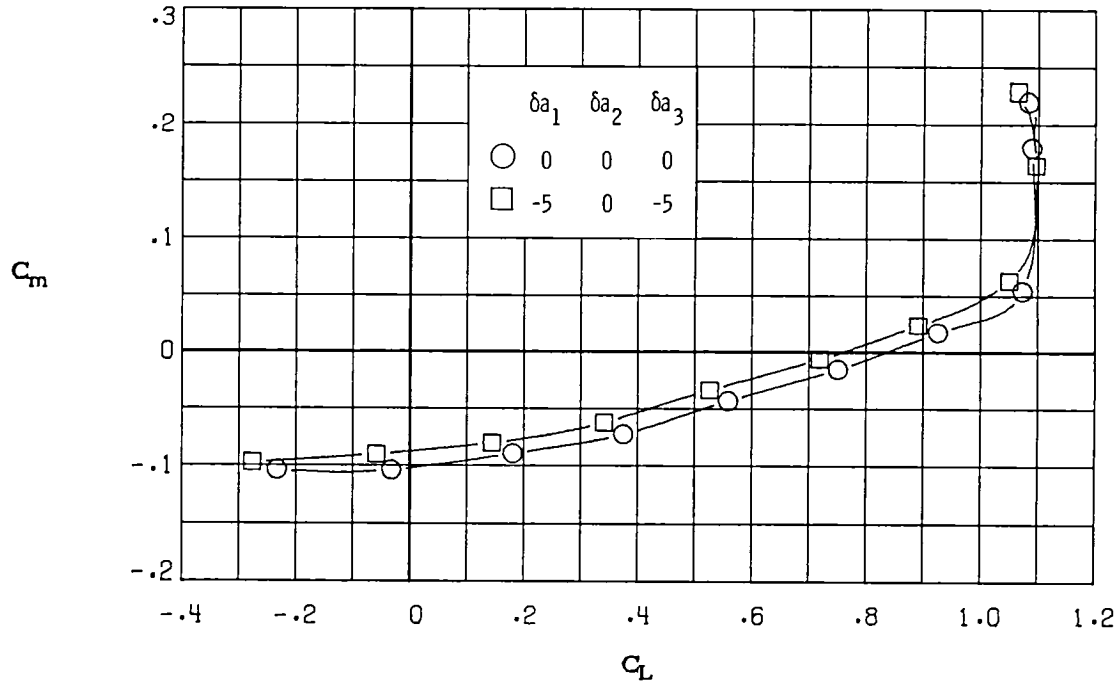

(a) $M_\infty = 0.30$.

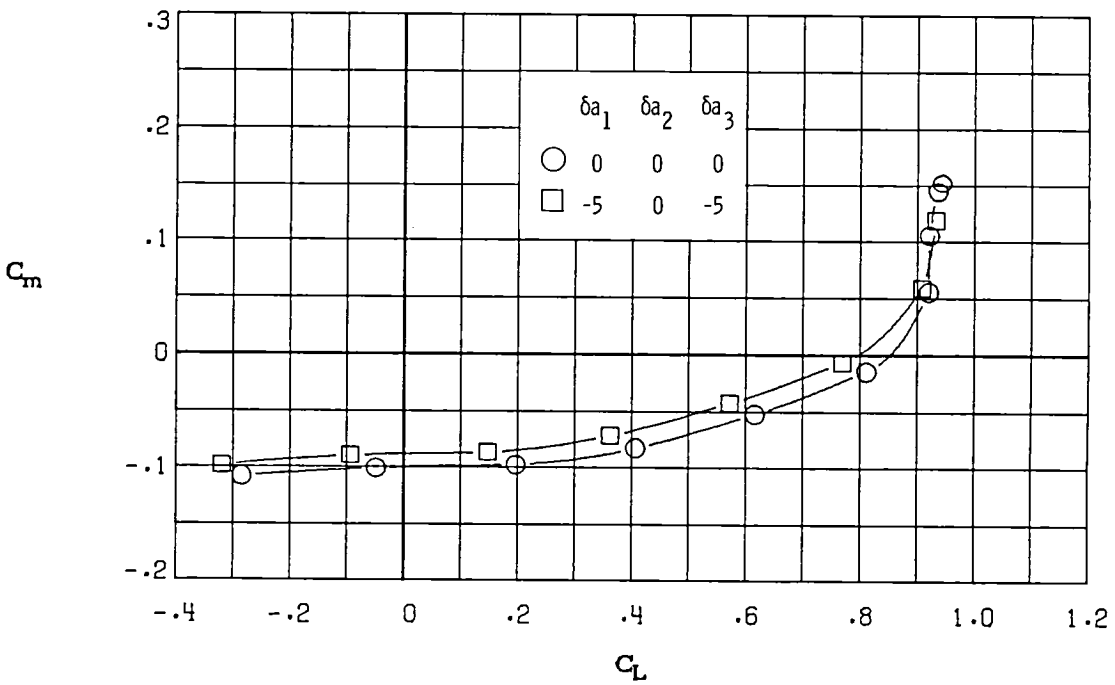

(b) $M_\infty = 0.60$.

Figure 32.- Variation of pitching-moment coefficient with lift coefficient for $\delta a_1 = -5°$, $\delta a_2 = 0°$, $\delta a_3 = -5°$.

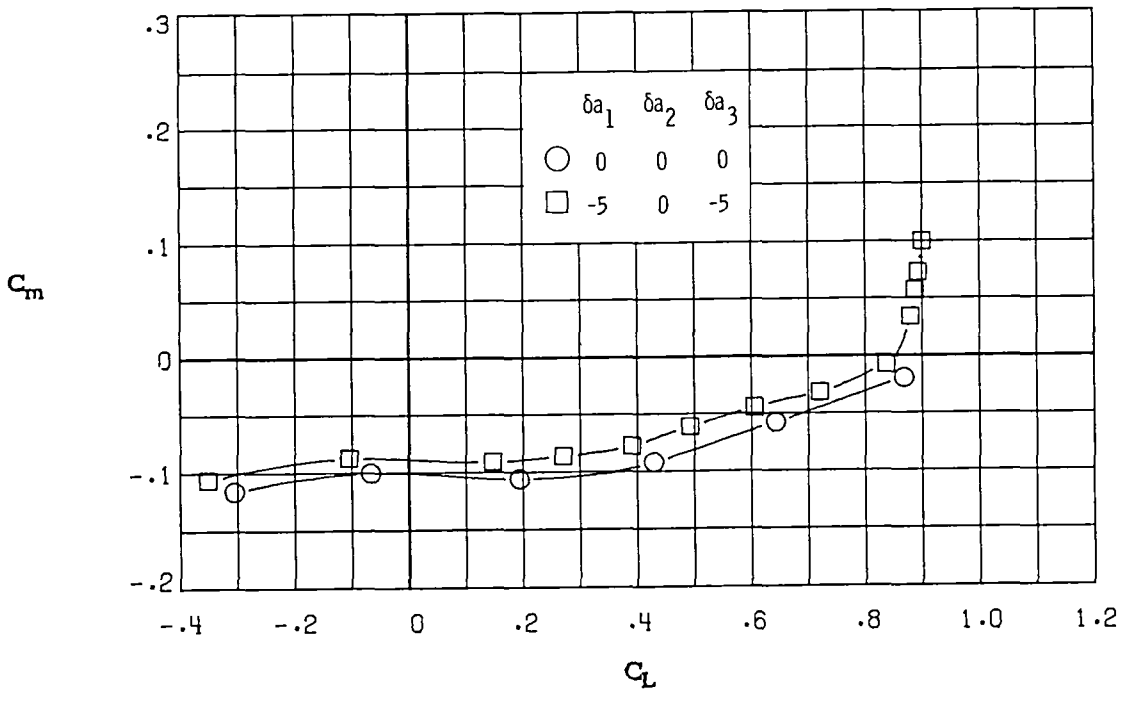

(c) $M_\infty = 0.70$.

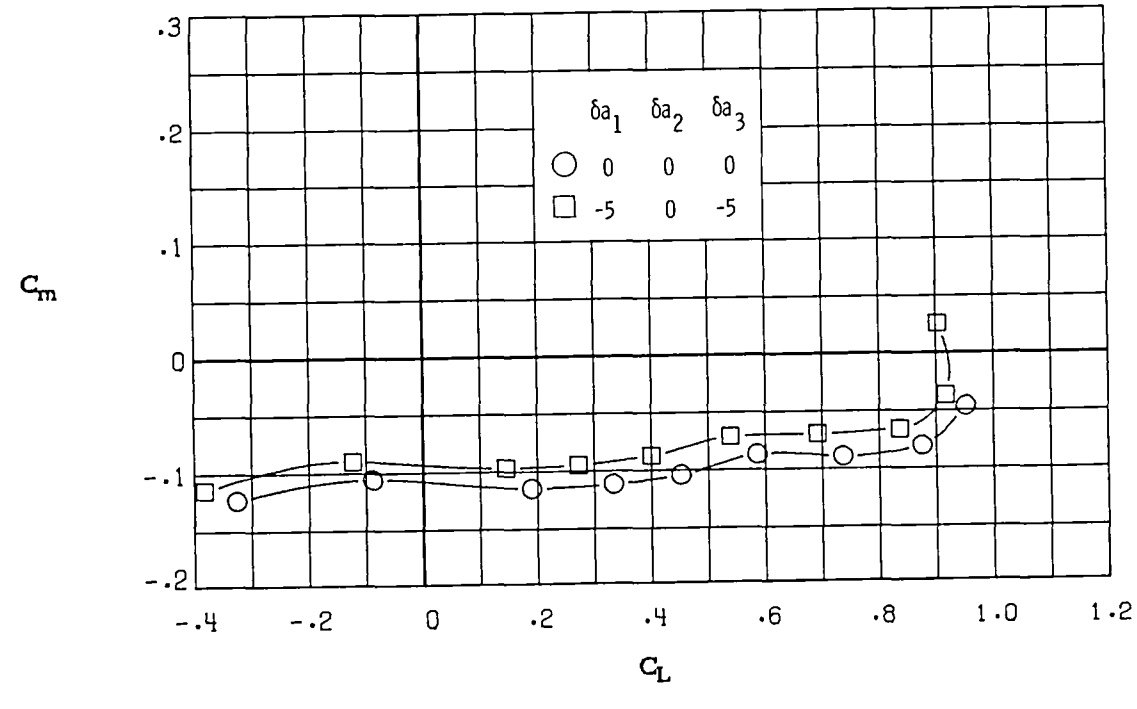

(d) $M_\infty = 0.77$.

Figure 32.- Continued.

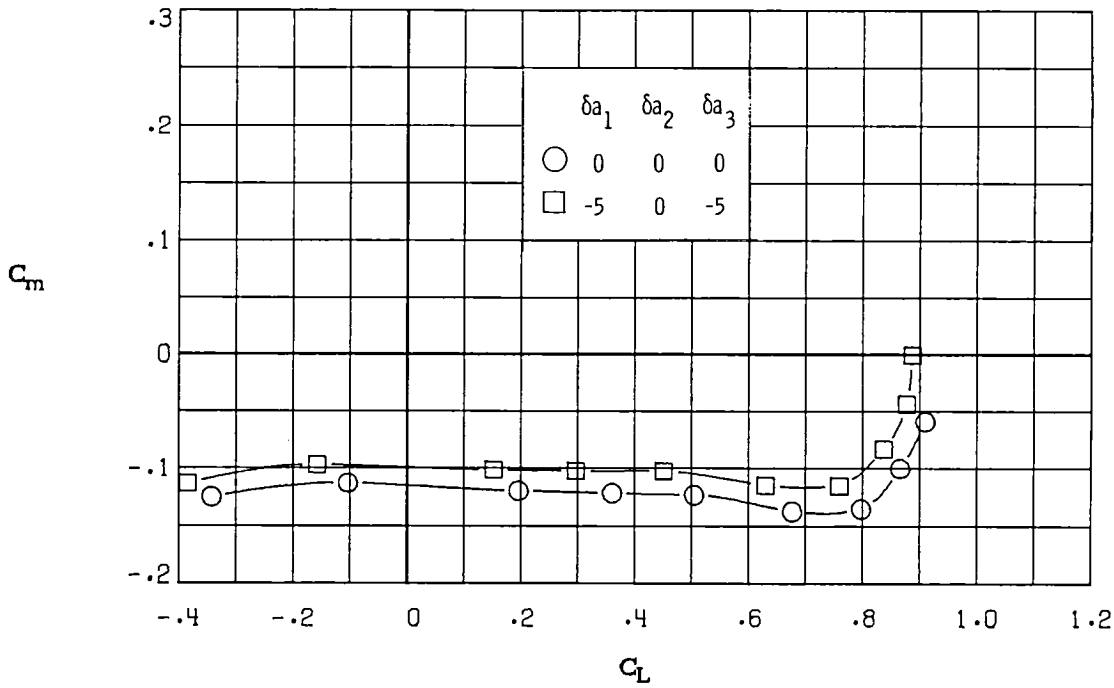

(e) $M_\infty = 0.81$.

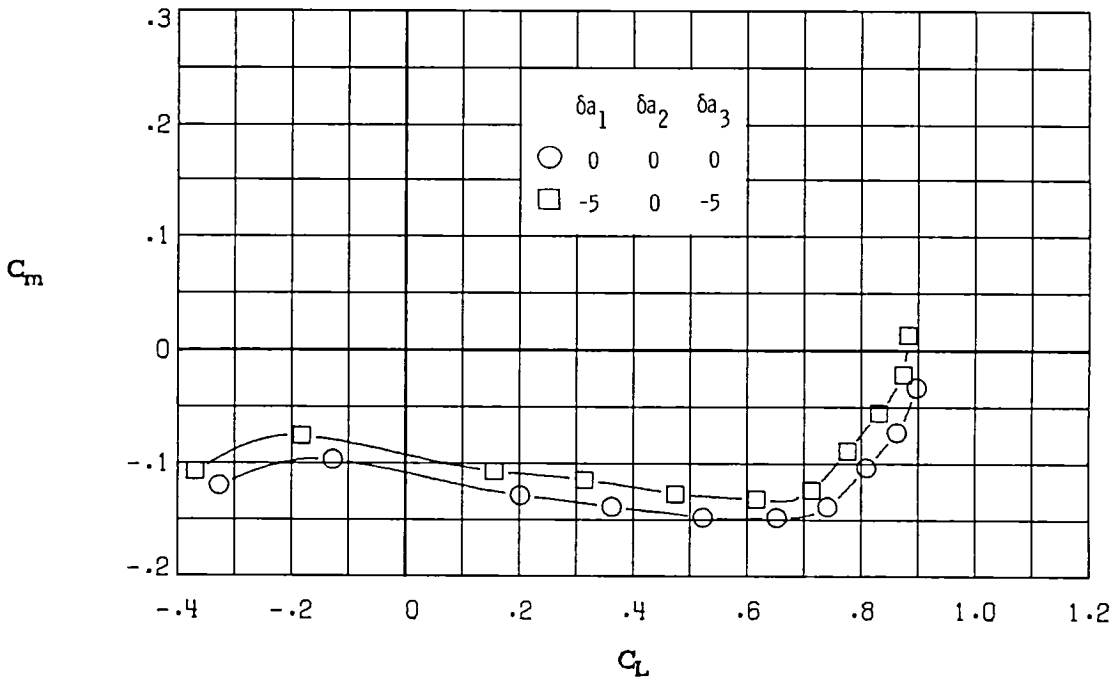

(f) $M_\infty = 0.84$.

Figure 32.- Continued.

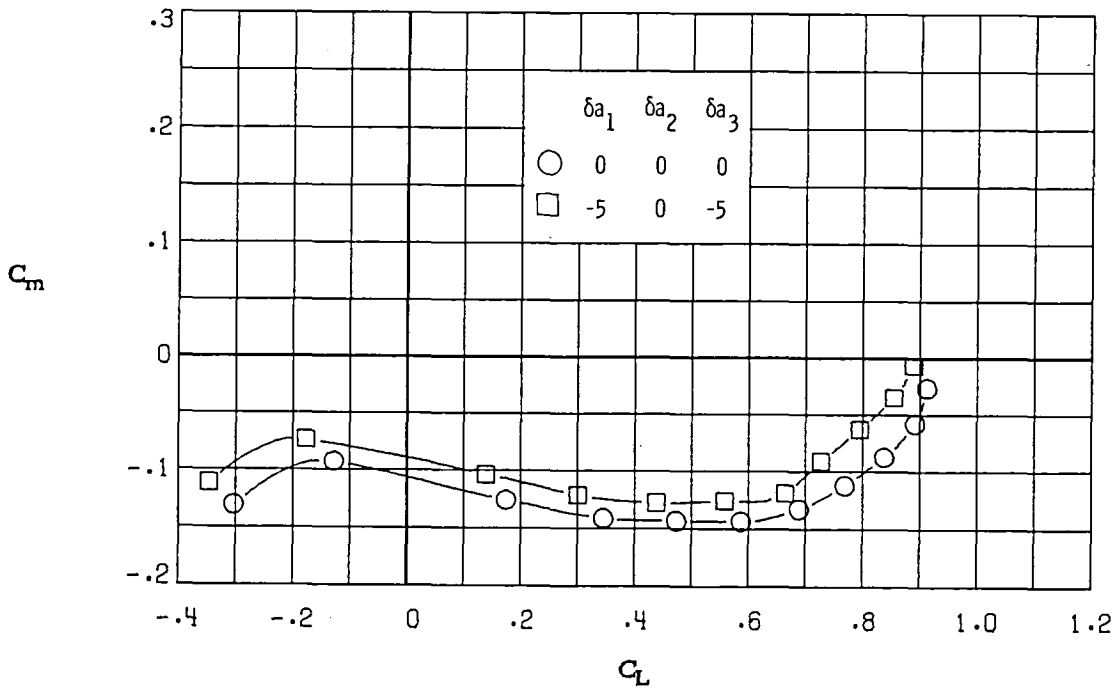

(g) $M_\infty = 0.86$.

Figure 32.- Concluded.

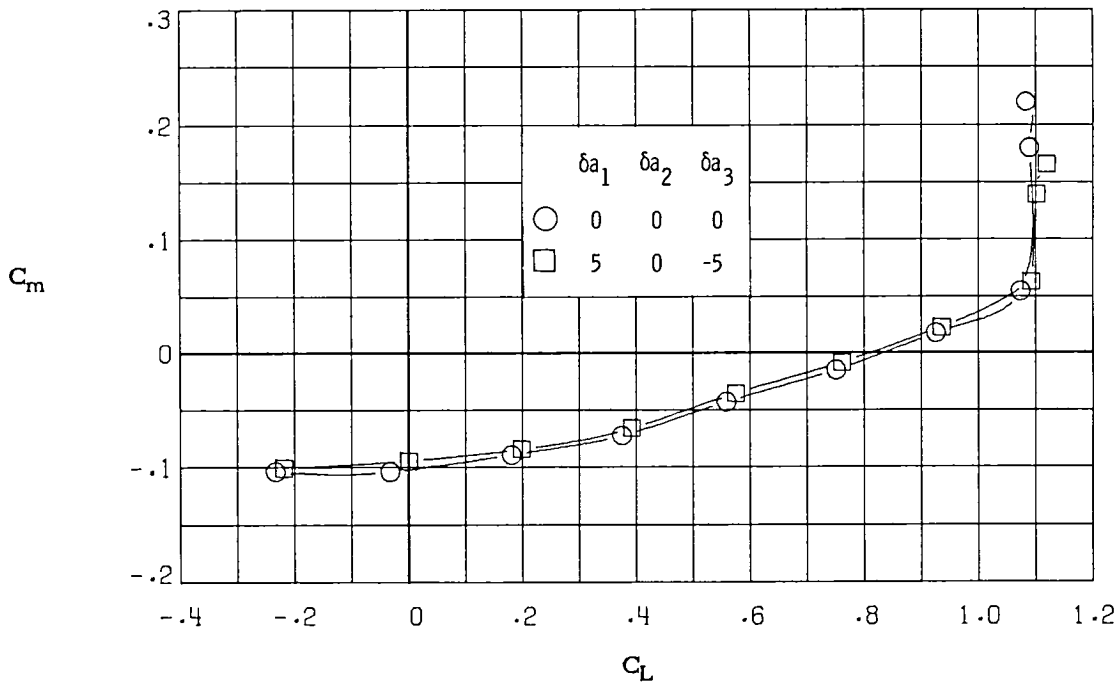

(a) $M_\infty = 0.30$.

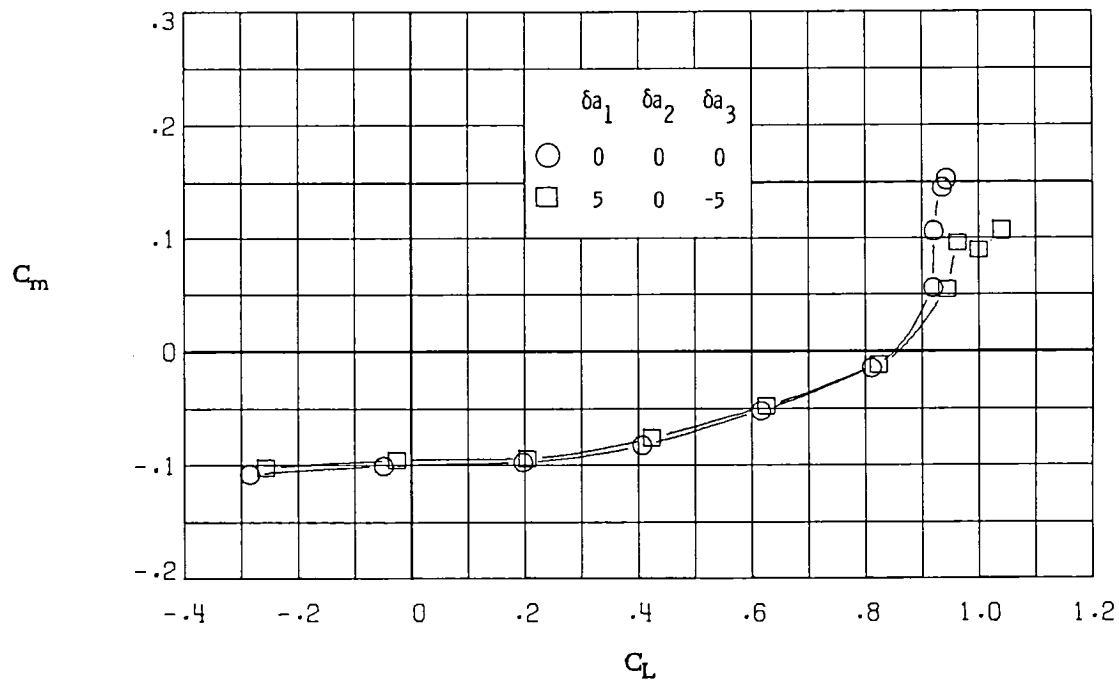

(b) $M_\infty = 0.60$.

Figure 33.- Variation of pitching-moment coefficient with lift coefficient for $\delta a_1 = 5°$, $\delta a_2 = 0°$, $\delta a_3 = -5°$.

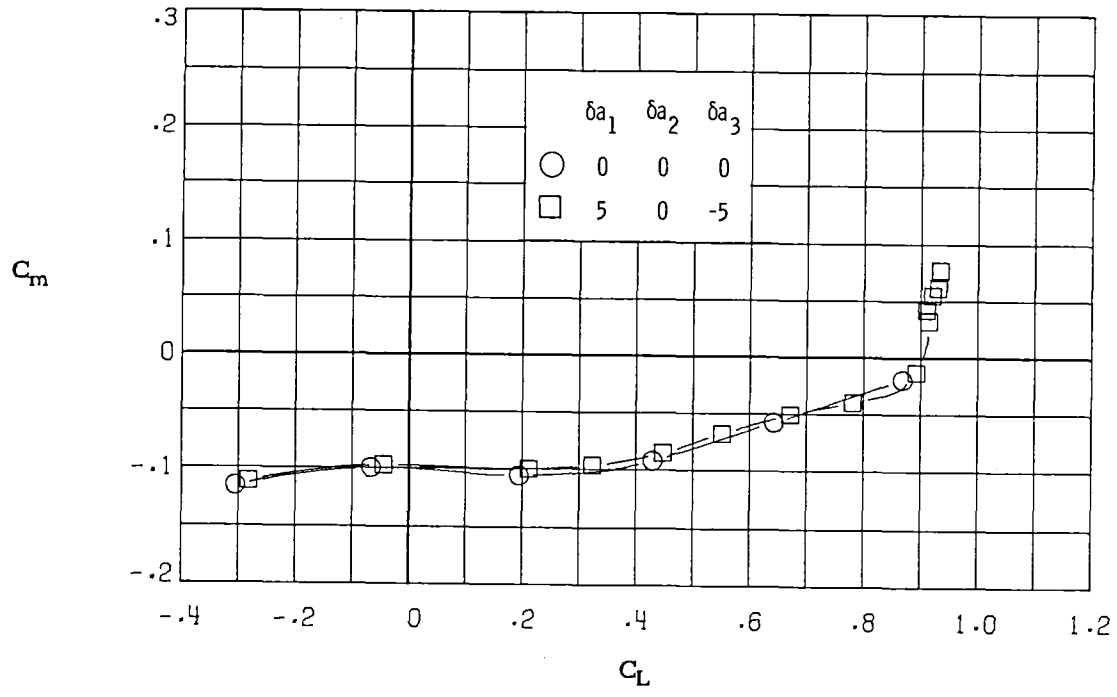

(c) $M_\infty = 0.70$.

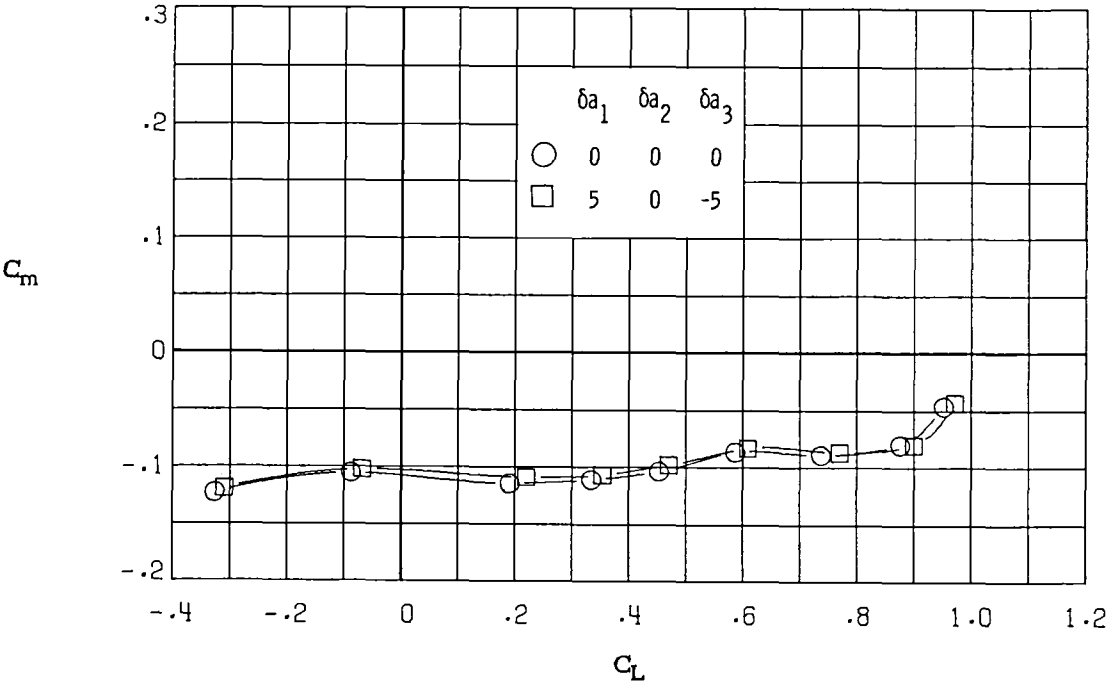

(d) $M_\infty = 0.77$.

Figure 33.- Continued.

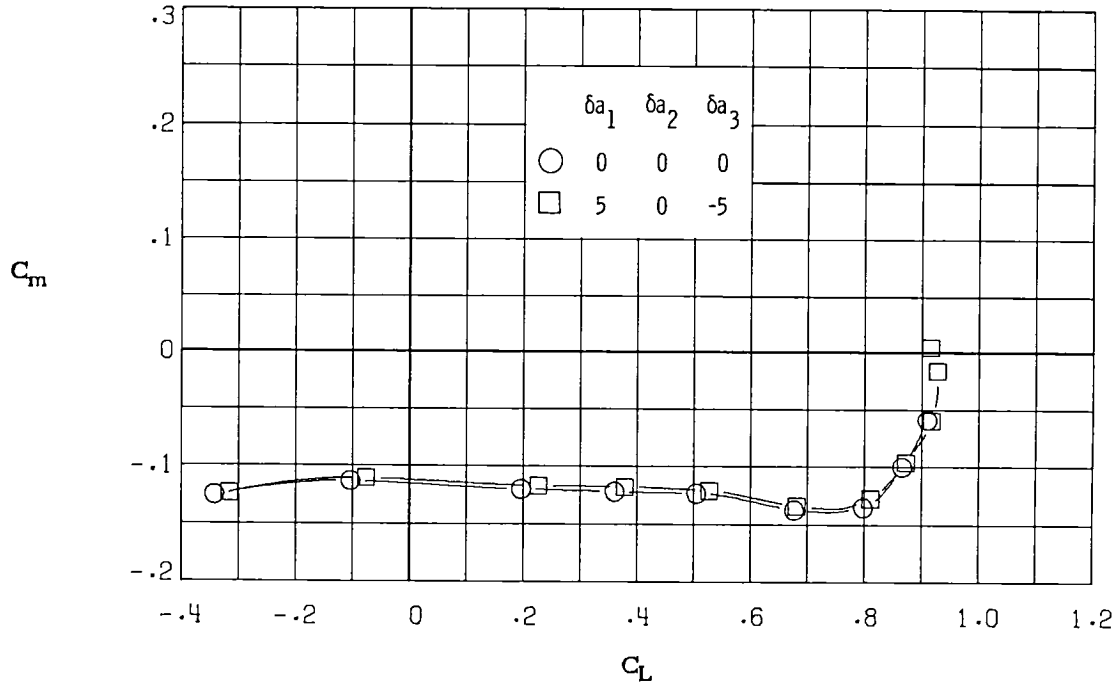

(e) $M_\infty = 0.81$.

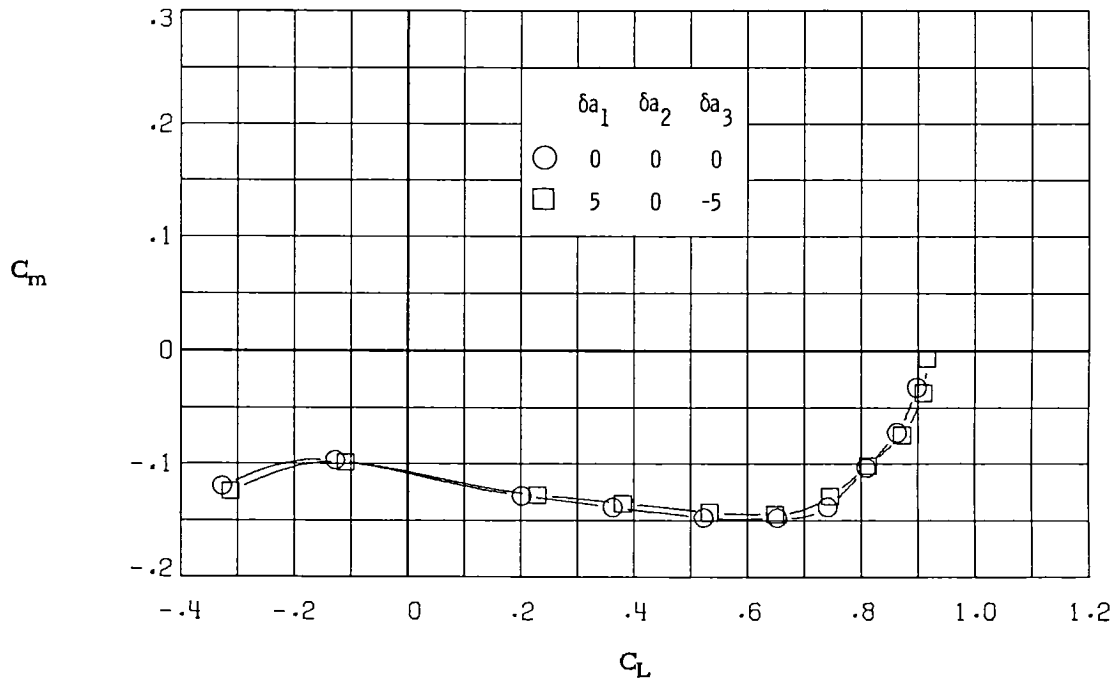

(f) $M_\infty = 0.84$.

Figure 33.- Continued.

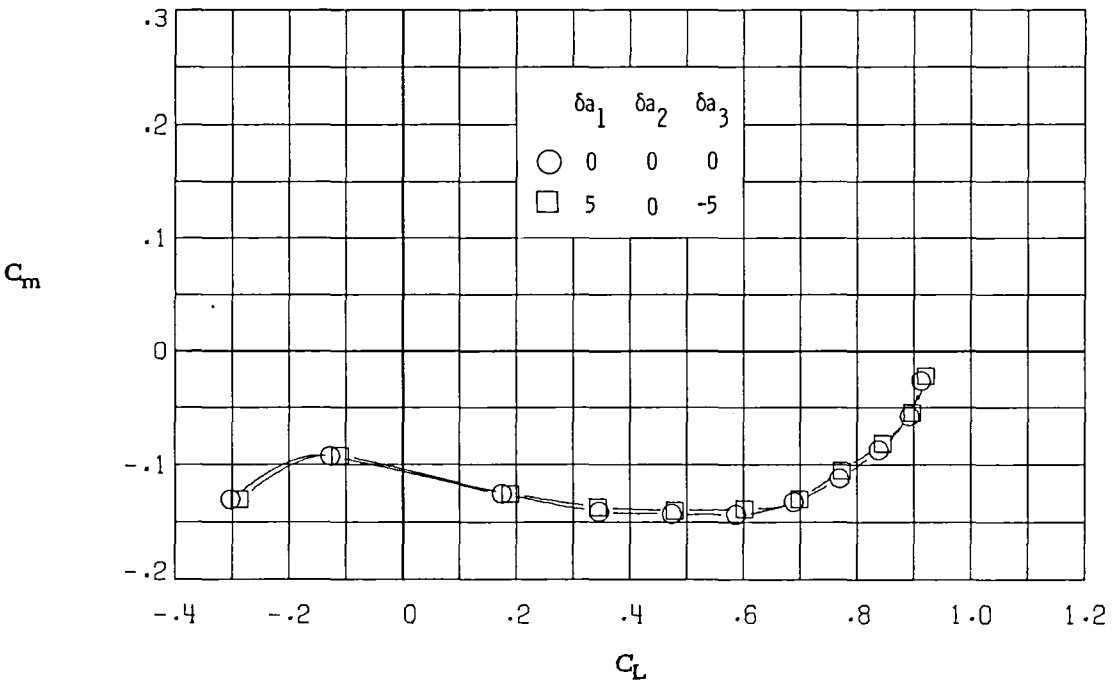

(g) $M_\infty = 0.86$.

Figure 33.- Concluded.

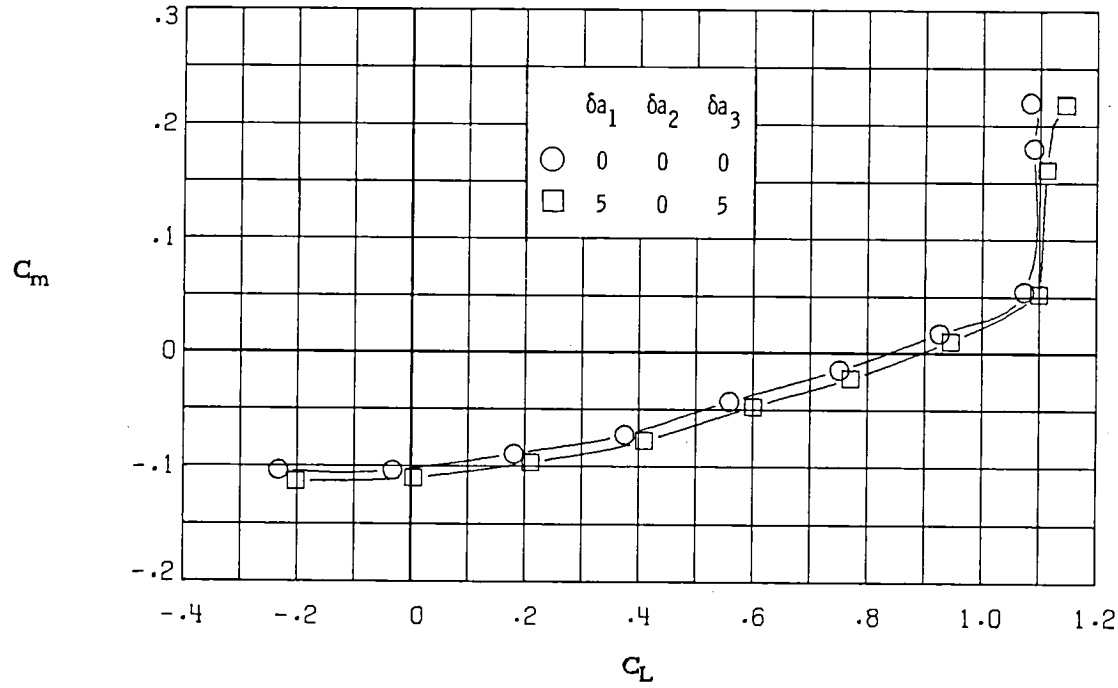

(a) $M_\infty = 0.30$.

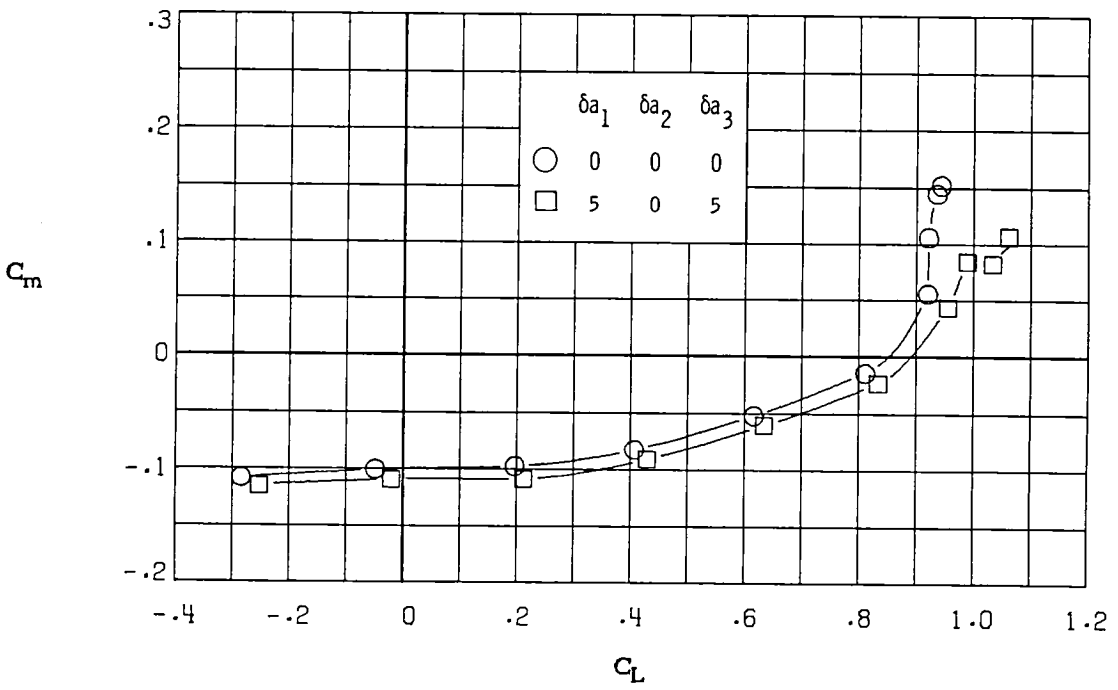

(b) $M_\infty = 0.60$.

Figure 34.- Variation of pitching-moment coefficient with lift coefficient for $\delta a_1 = 5°$, $\delta a_2 = 0°$, $\delta a_3 = 5°$.

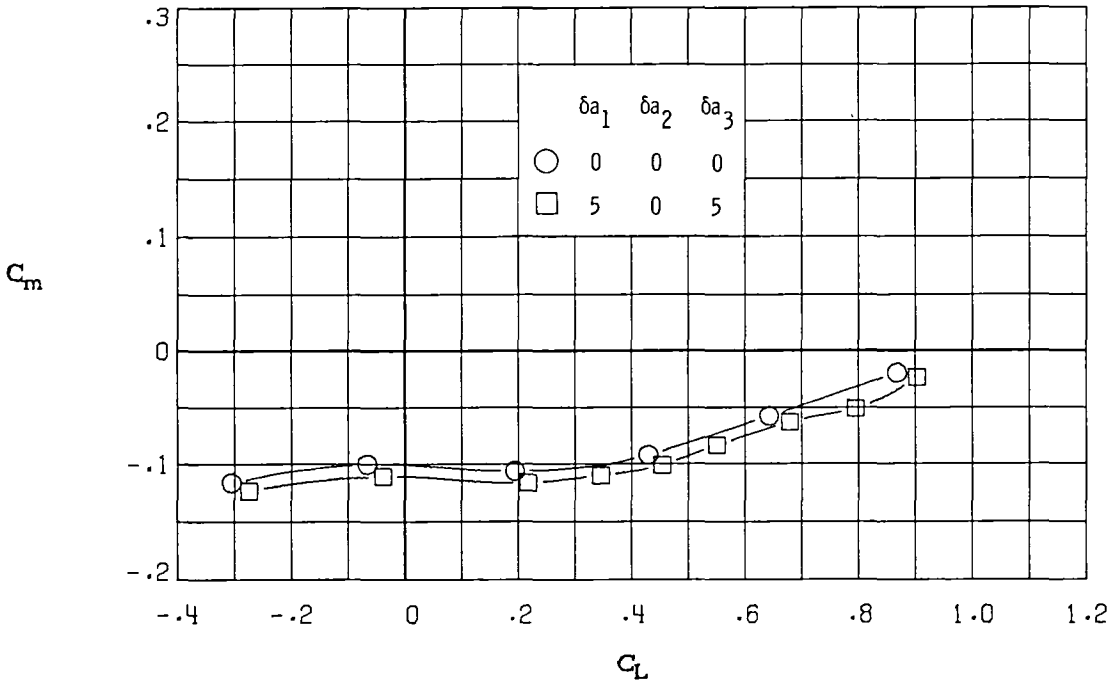

(c) $M_\infty = 0.70$.

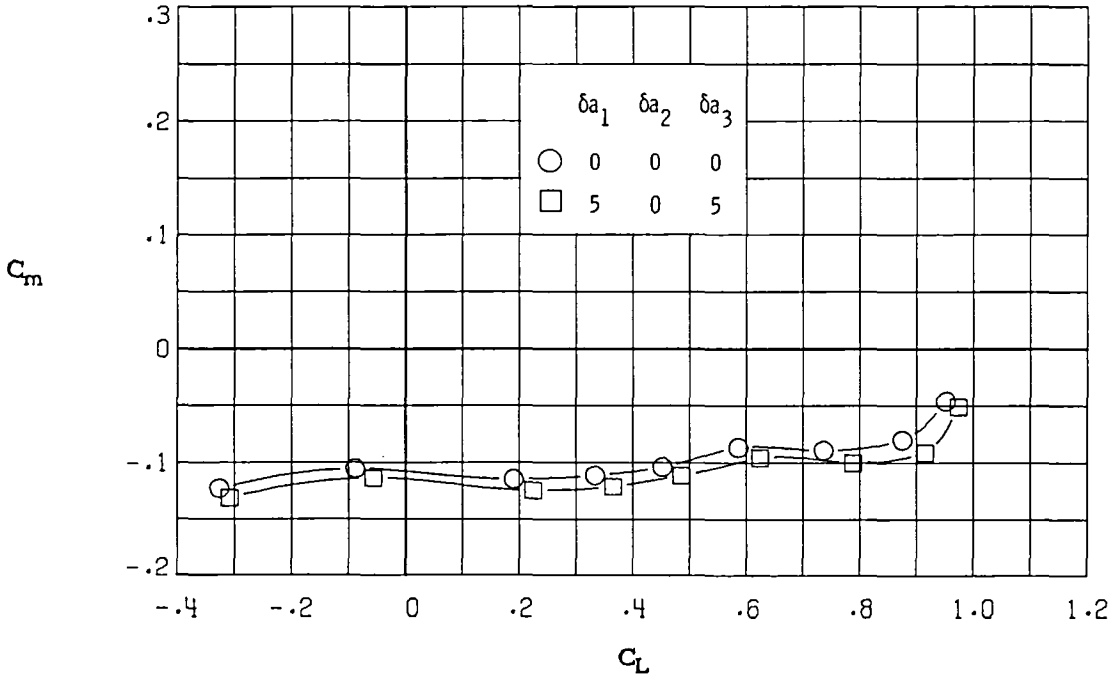

(d) $M_\infty = 0.77$.

Figure 34.- Continued.

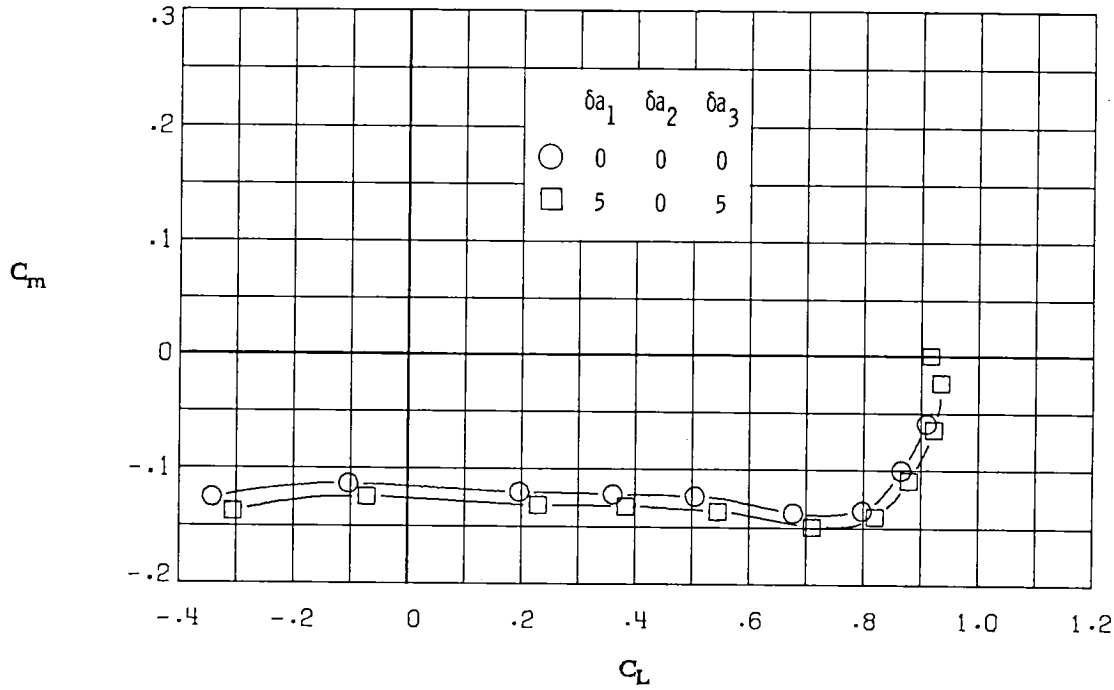

(e) $M_\infty = 0.81$.

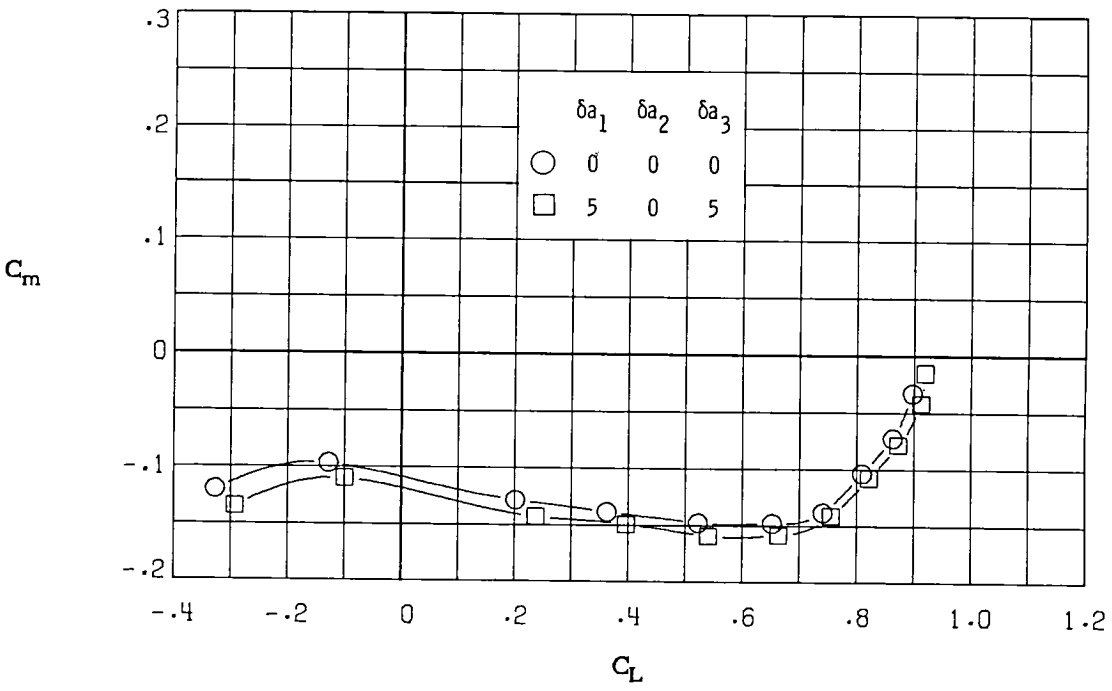

(f) $M_\infty = 0.84$.

Figure 34.- Continued.

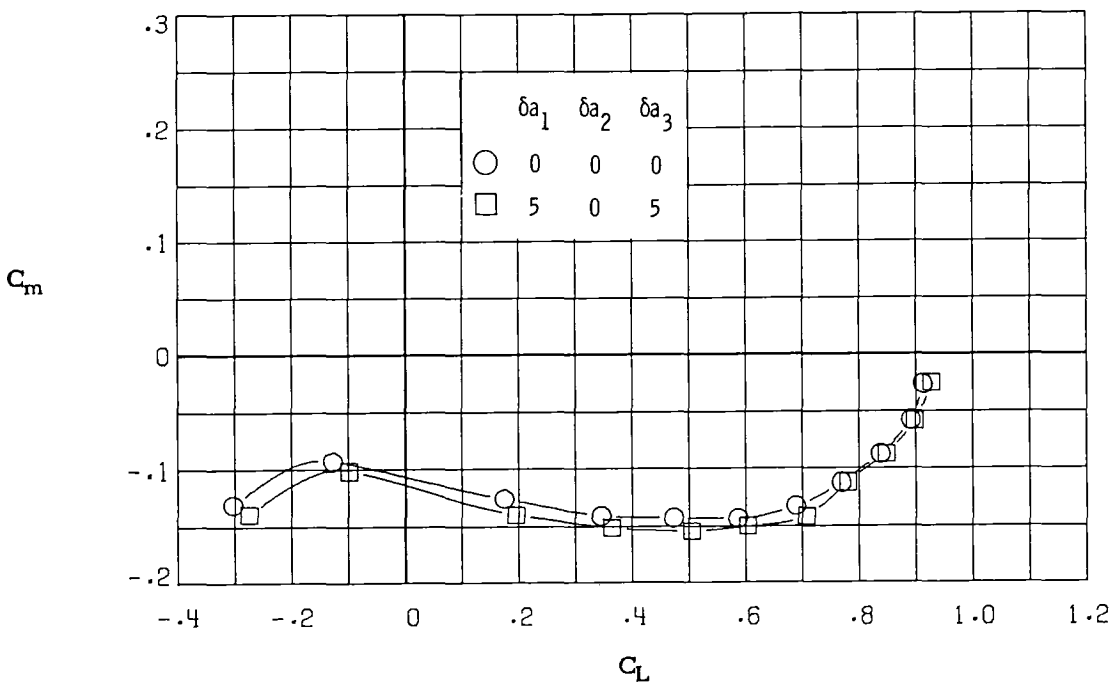

(g) $M_\infty = 0.86$.

Figure 34.- Concluded.

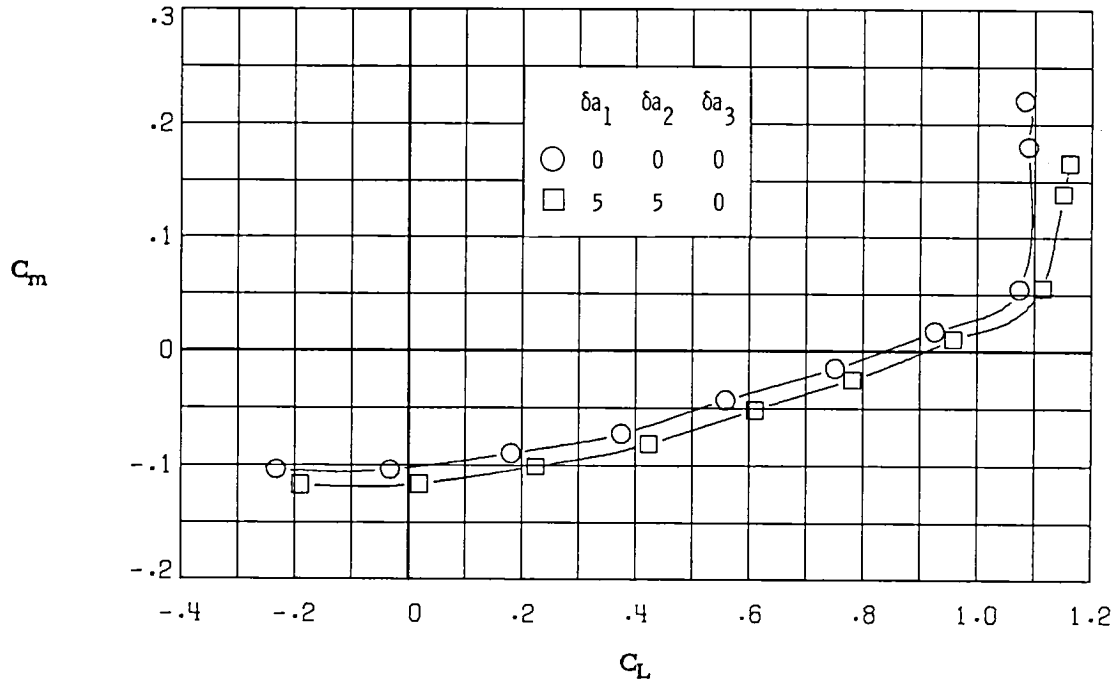

(a) $M_\infty = 0.30$.

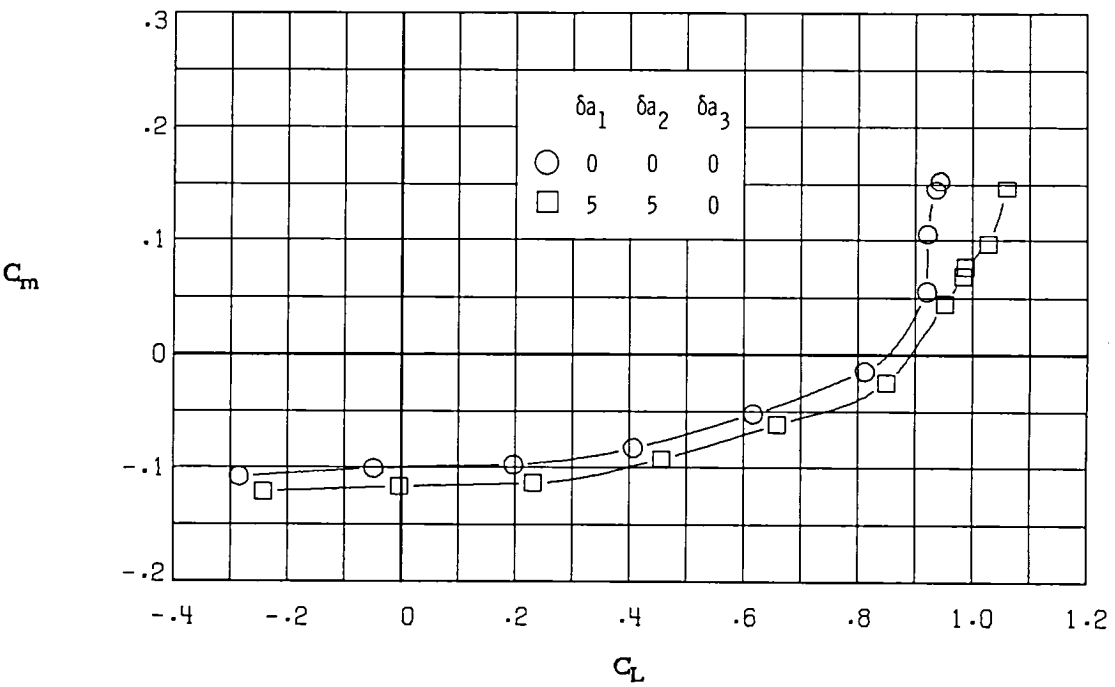

(b) $M_\infty = 0.60$.

Figure 35.- Variation of pitching-moment coefficient with lift coefficient for $\delta a_1 = 5°$, $\delta a_2 = 5°$, $\delta a_3 = 0°$.

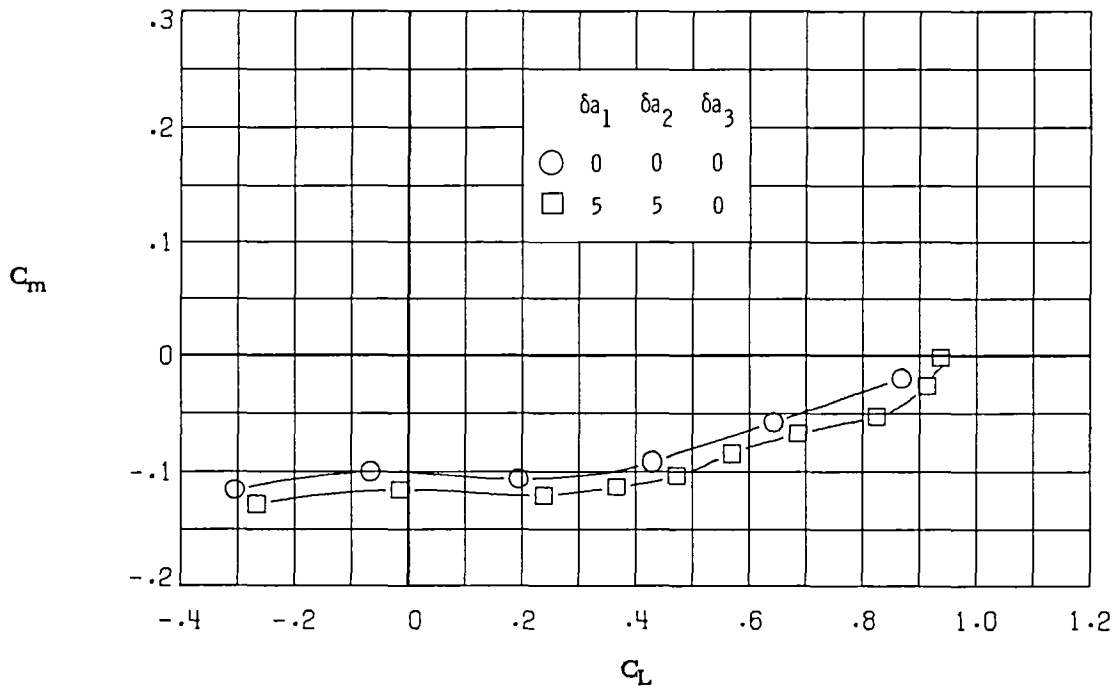

(c) $M_\infty = 0.70$.

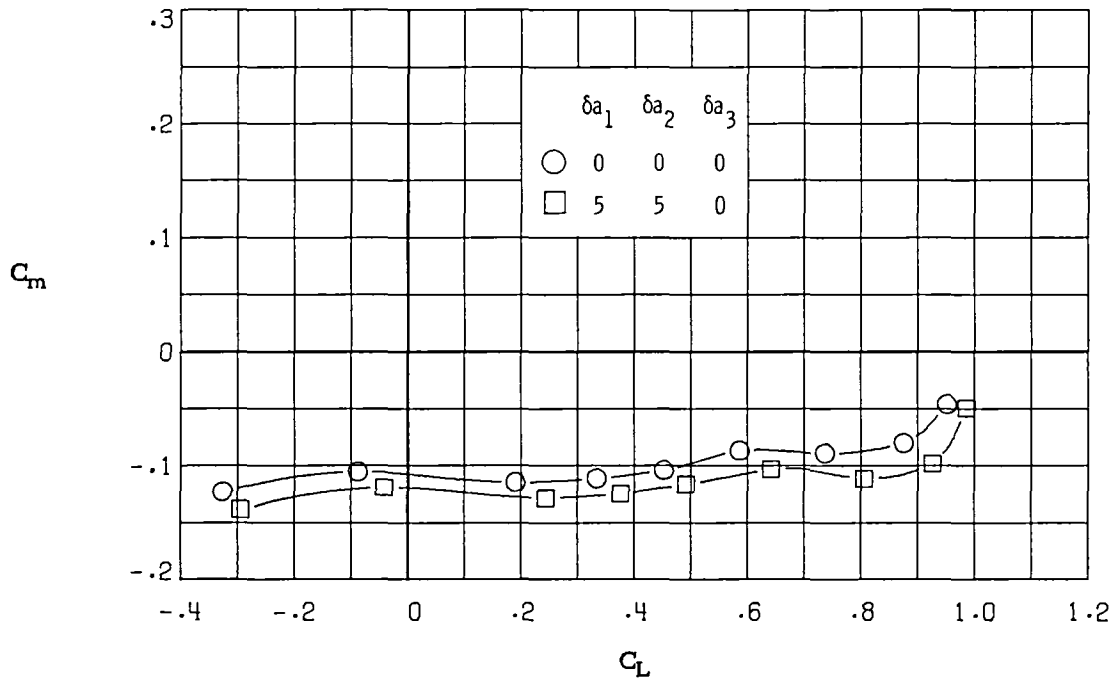

(d) $M_\infty = 0.77$.

Figure 35.- Continued.

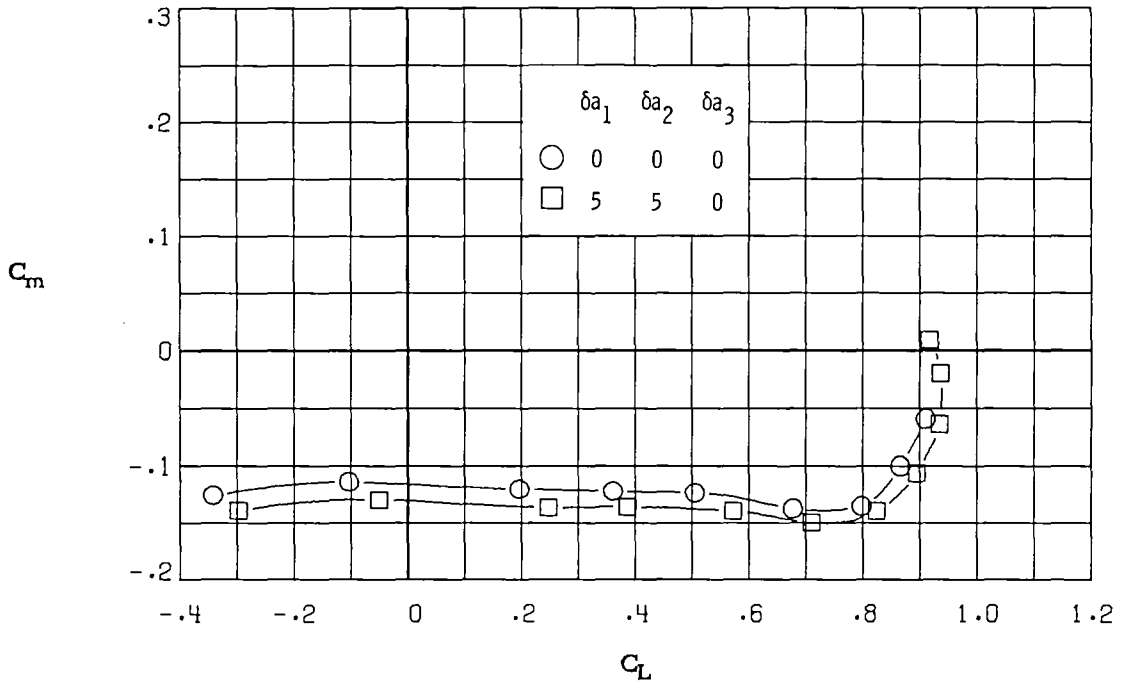

(e) $M_\infty = 0.81$.

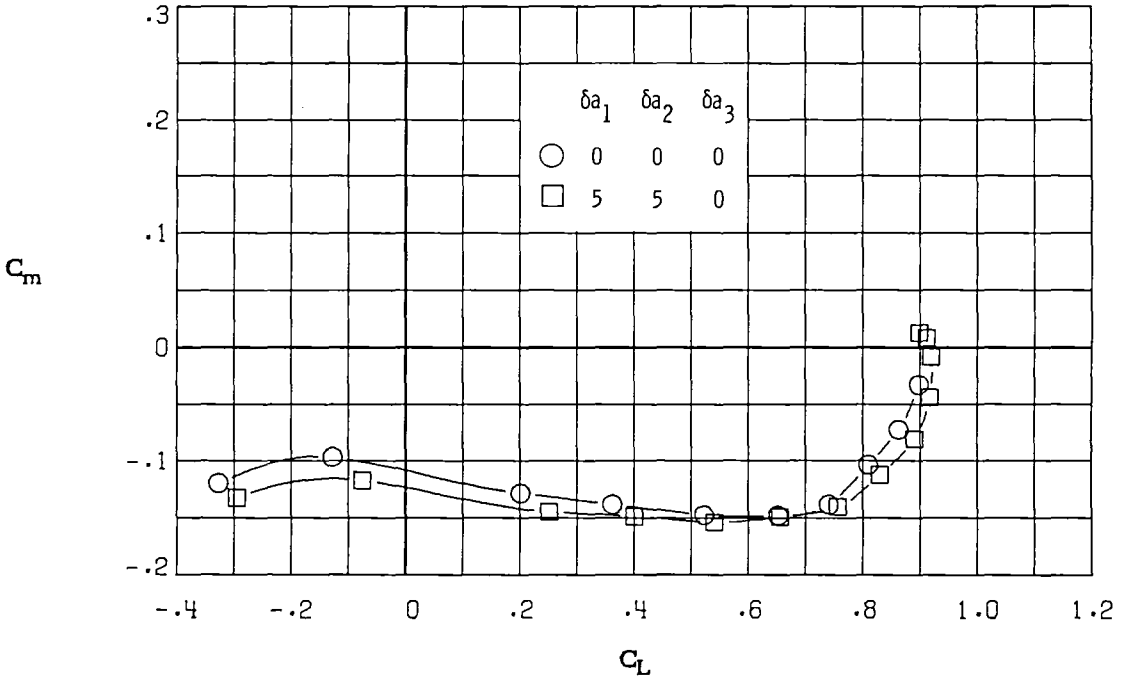

(f) $M_\infty = 0.84$.

Figure 35.- Continued.

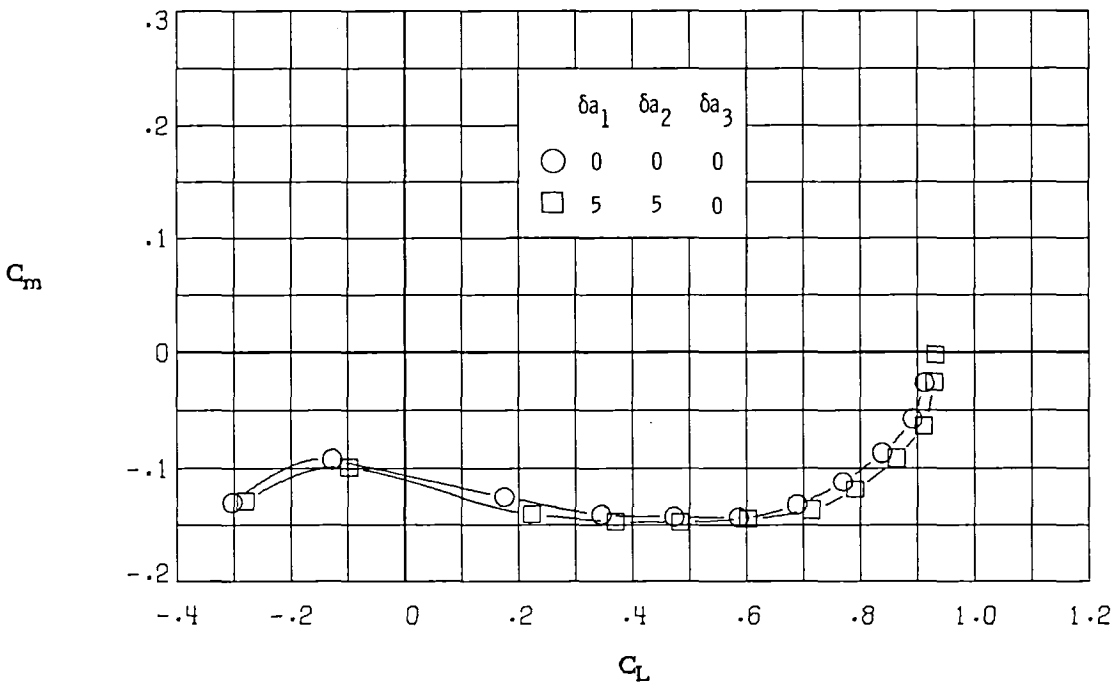

(g) $M_\infty = 0.86$.

Figure 35.- Concluded.

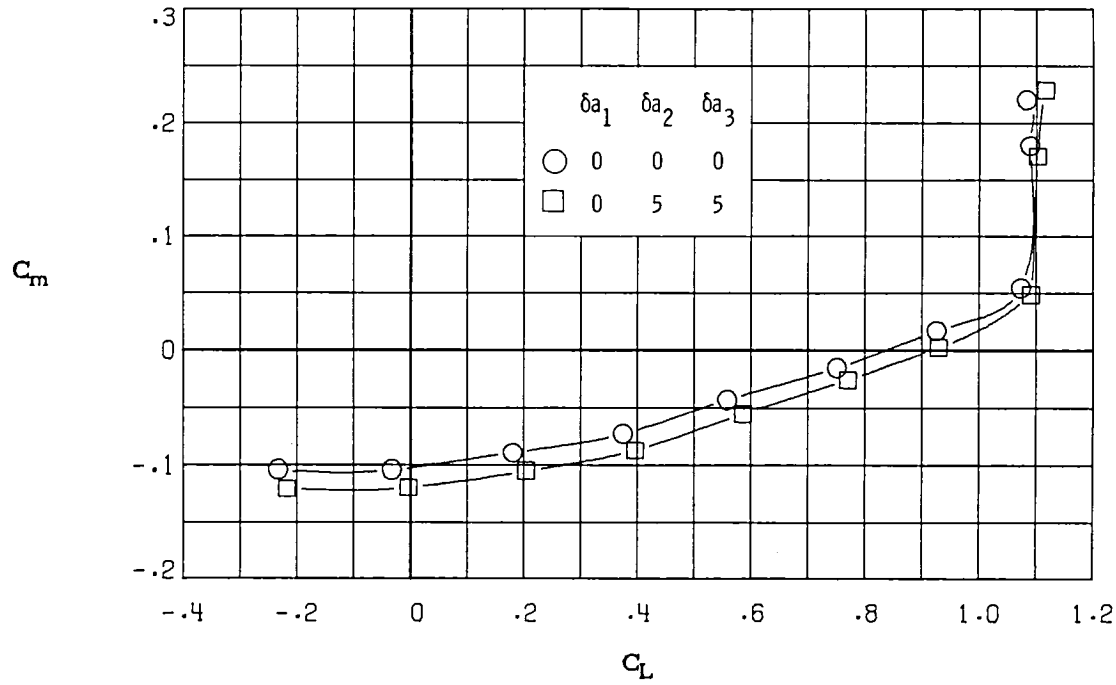

(a) $M_\infty = 0.30$.

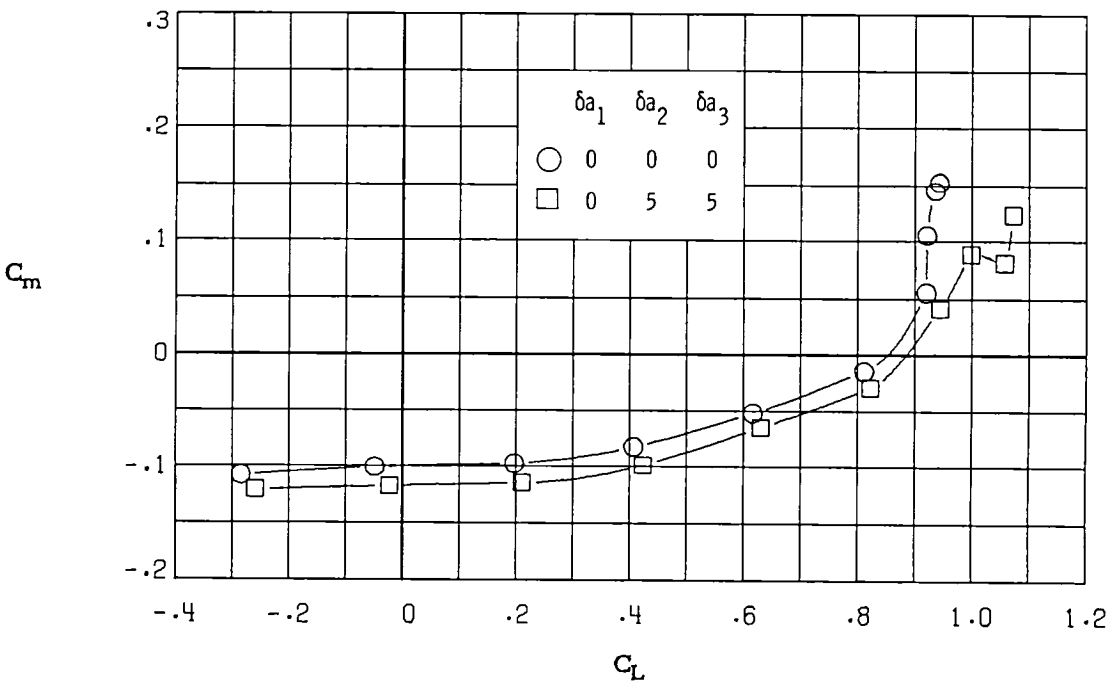

(b) $M_\infty = 0.60$.

Figure 36.- Variation of pitching-moment coefficient with lift coefficient for $\delta a_1 = 0°$, $\delta a_2 = 5°$, $\delta a_3 = 5°$.

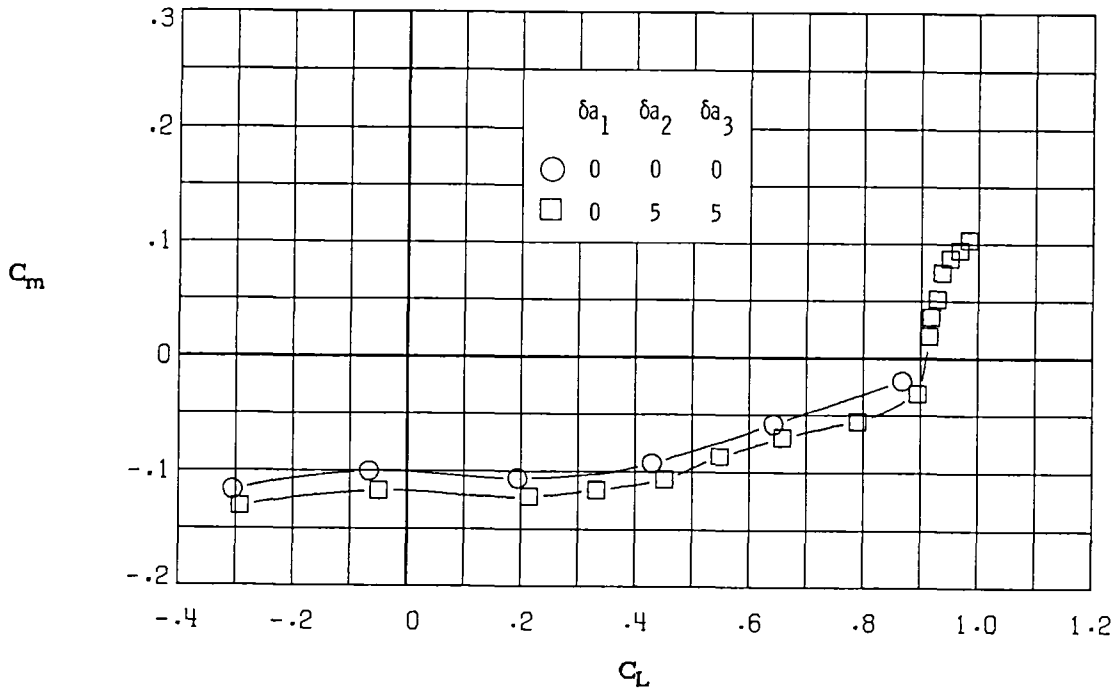

(c) $M_\infty = 0.70$.

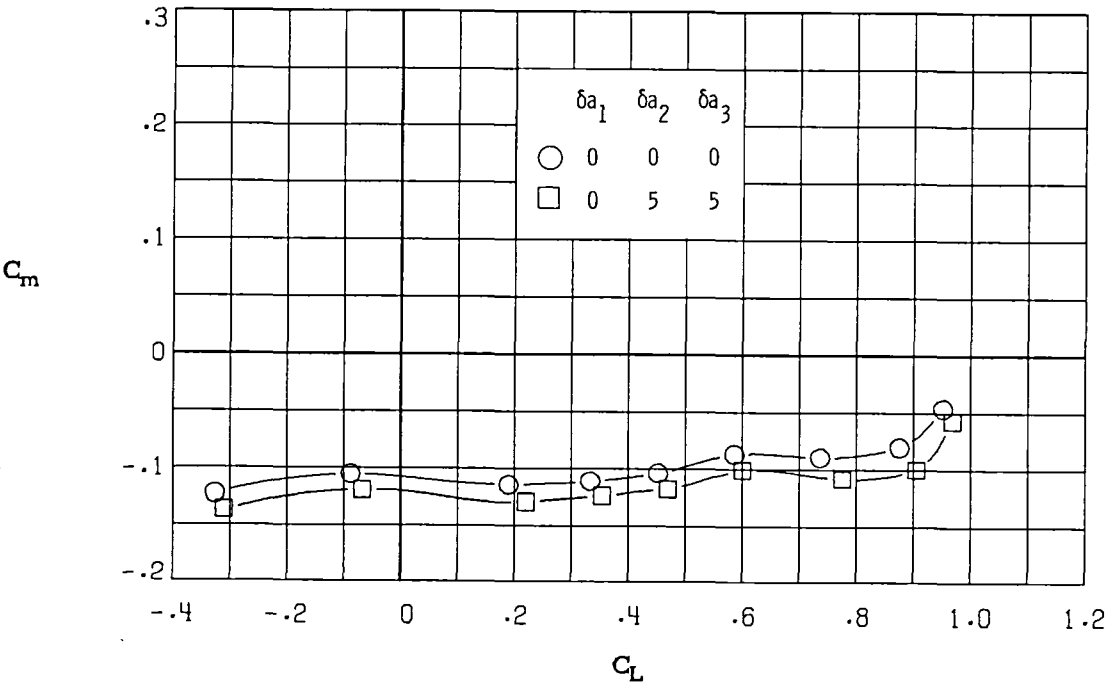

(d) $M_\infty = 0.77$.

Figure 36.- Continued.

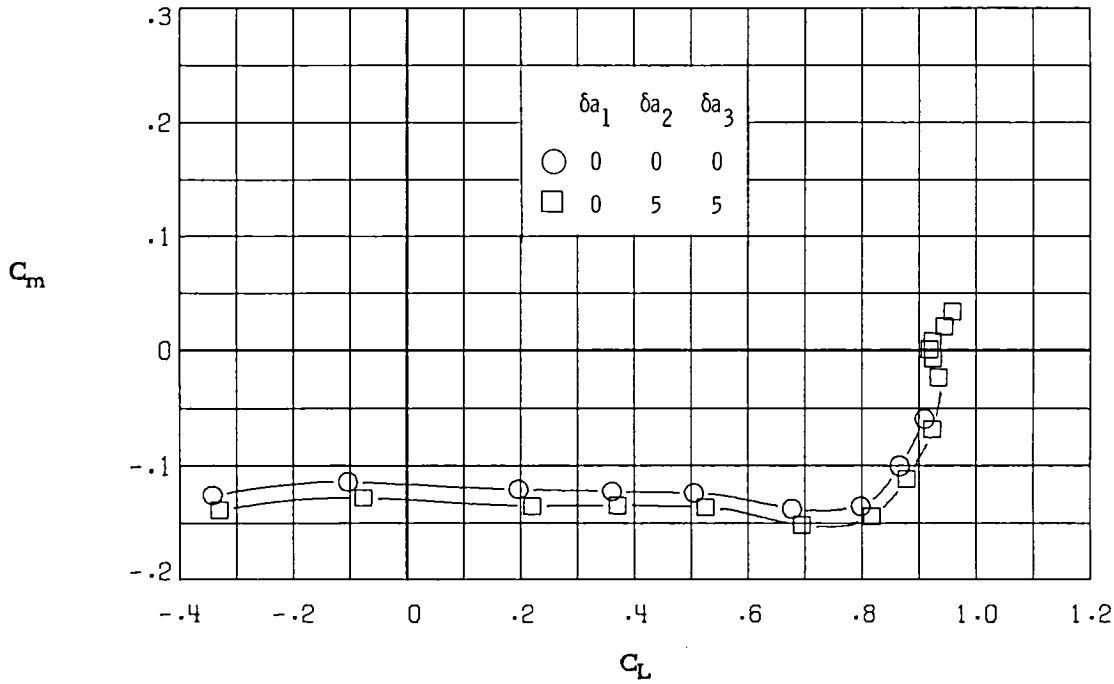

(e) $M_\infty = 0.81$.

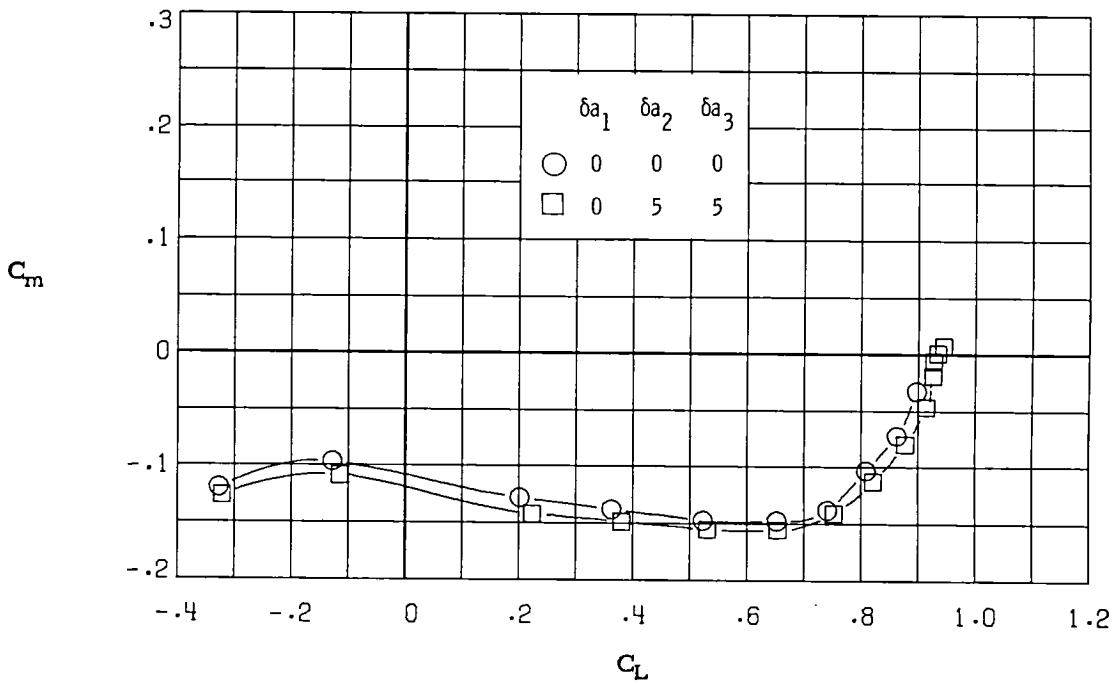

(f) $M_\infty = 0.84$.

Figure 36.- Continued.

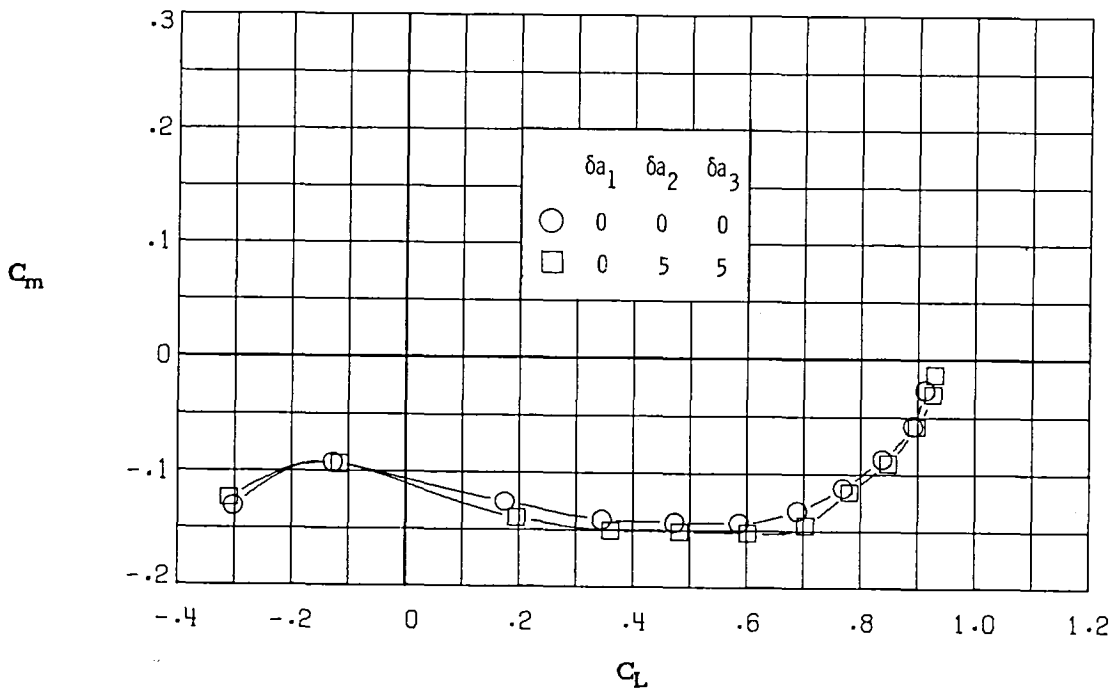

(g) $M_\infty = 0.86$.

Figure 36.- Concluded.

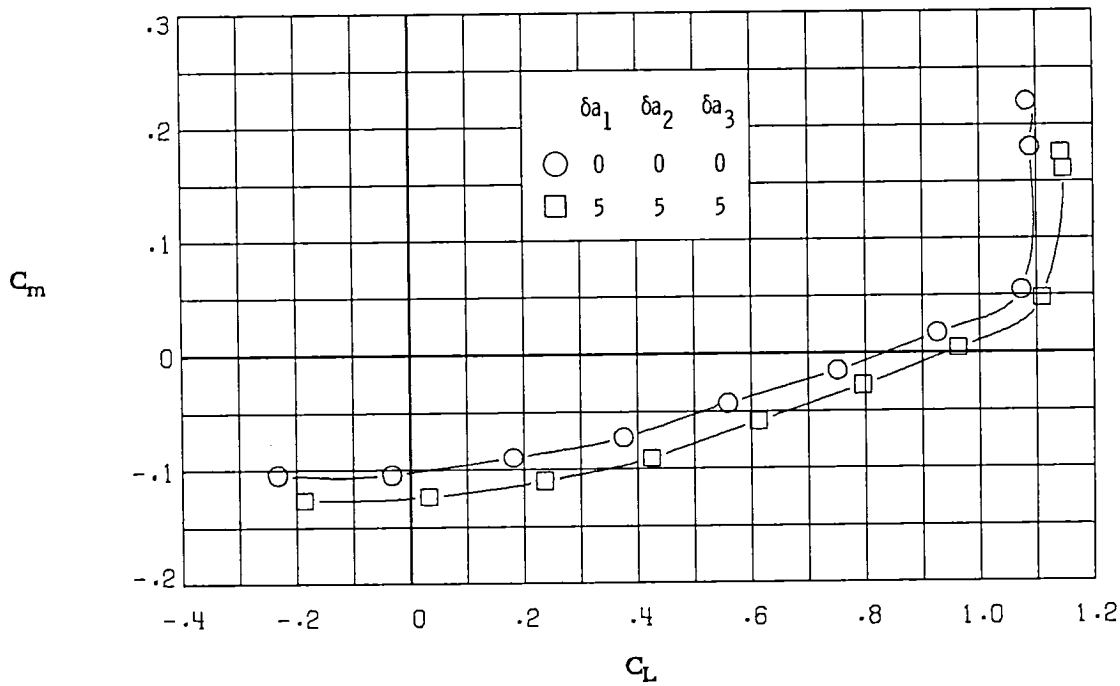

(a) $M_\infty = 0.30$.

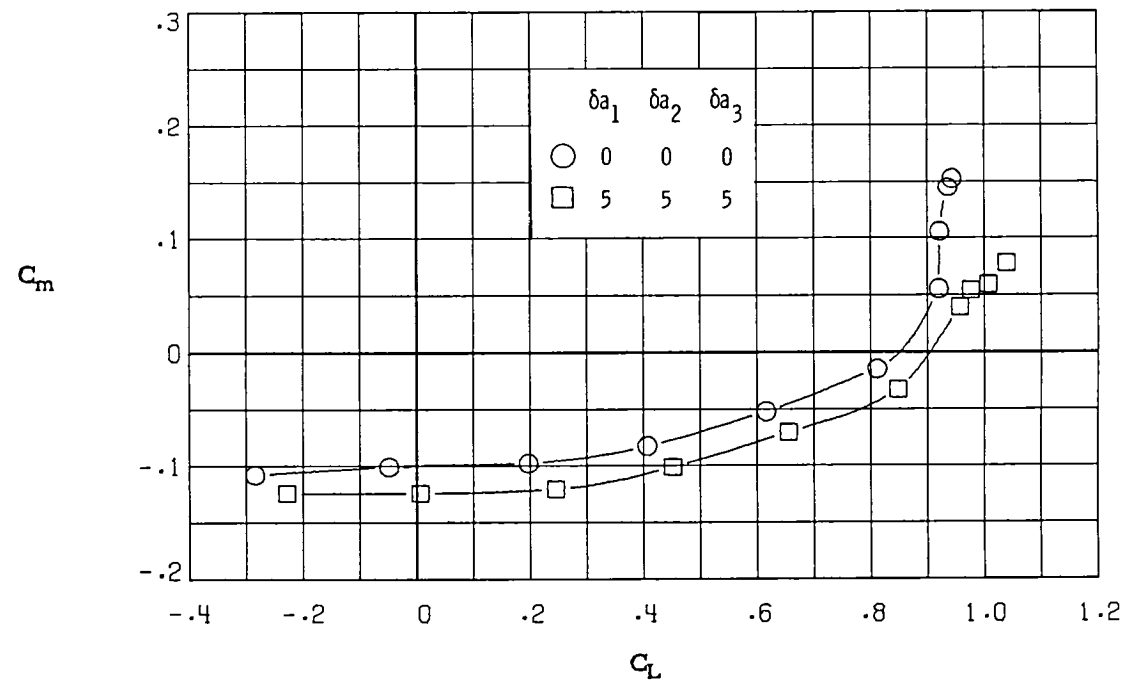

(b) $M_\infty = 0.60$.

Figure 37.- Variation of pitching-moment coefficient with lift coefficient for $\delta a_1 = 5°$, $\delta a_2 = 5°$, $\delta a_3 = 5°$.

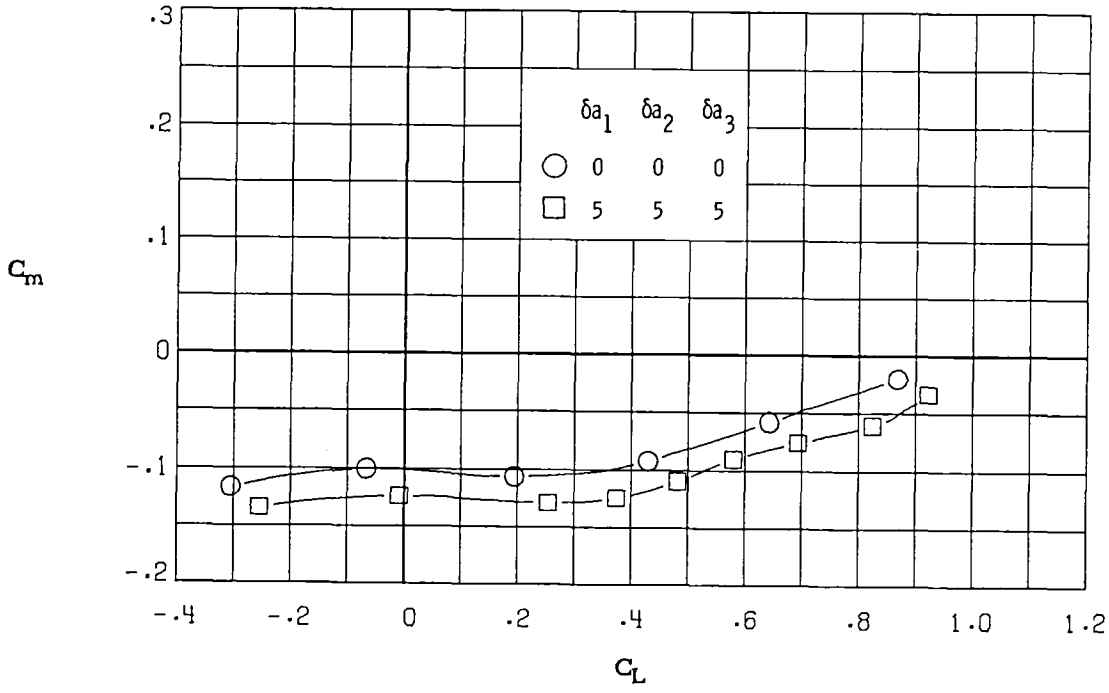

(c) $M_\infty = 0.70$.

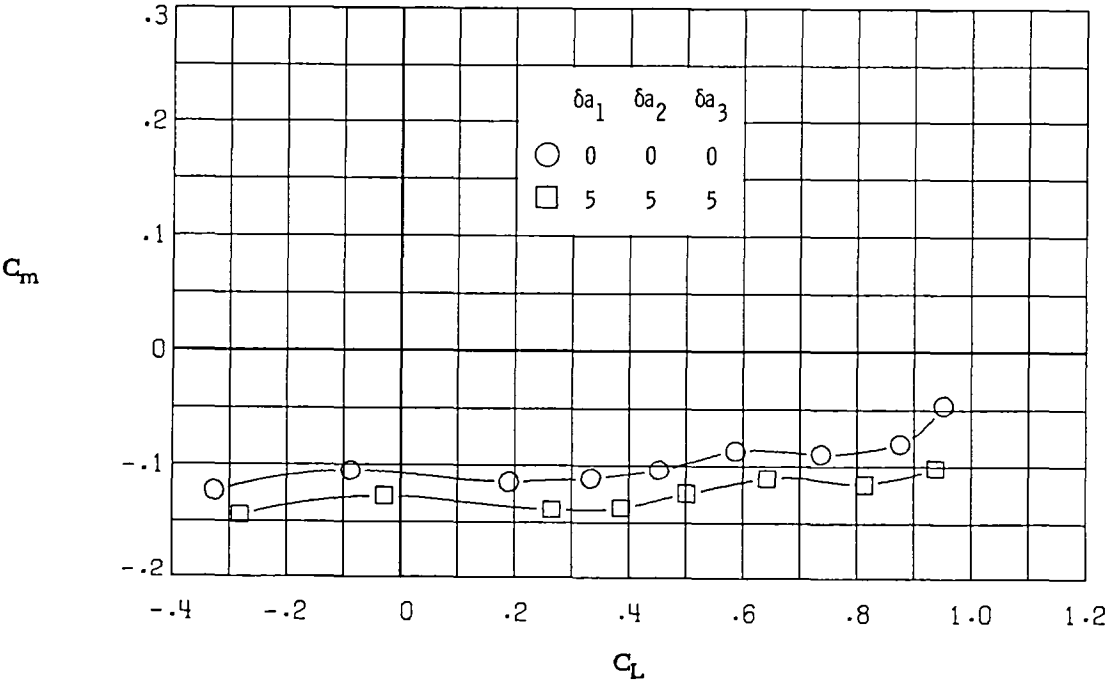

(d) $M_\infty = 0.77$.

Figure 37.- Continued.

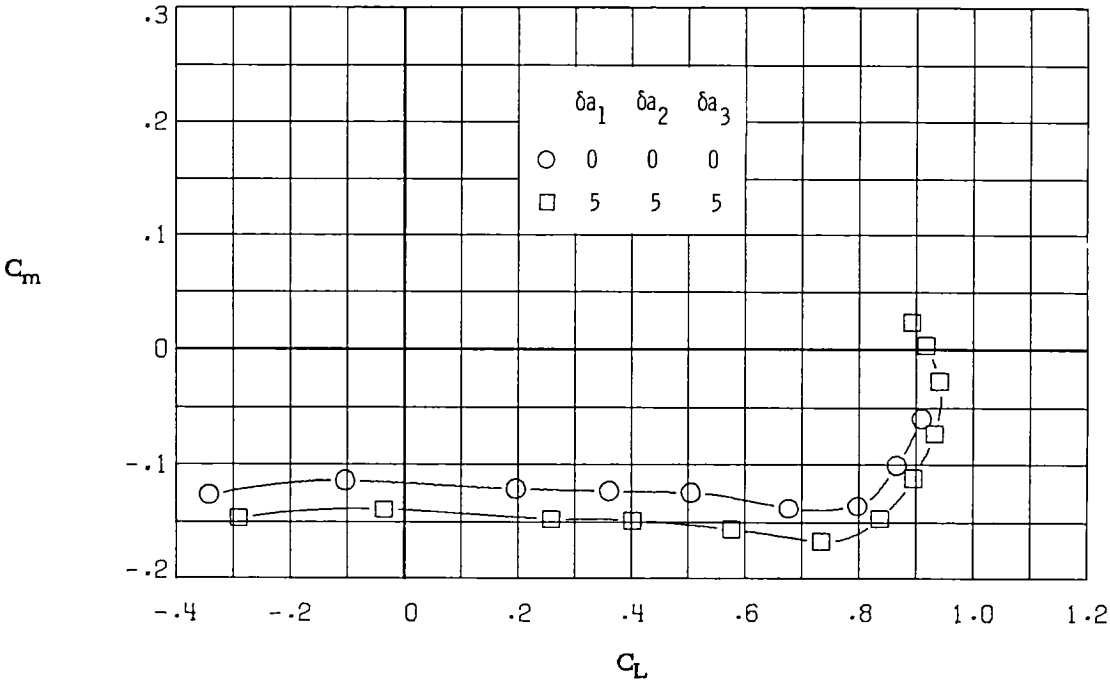

(e) $M_\infty = 0.81$.

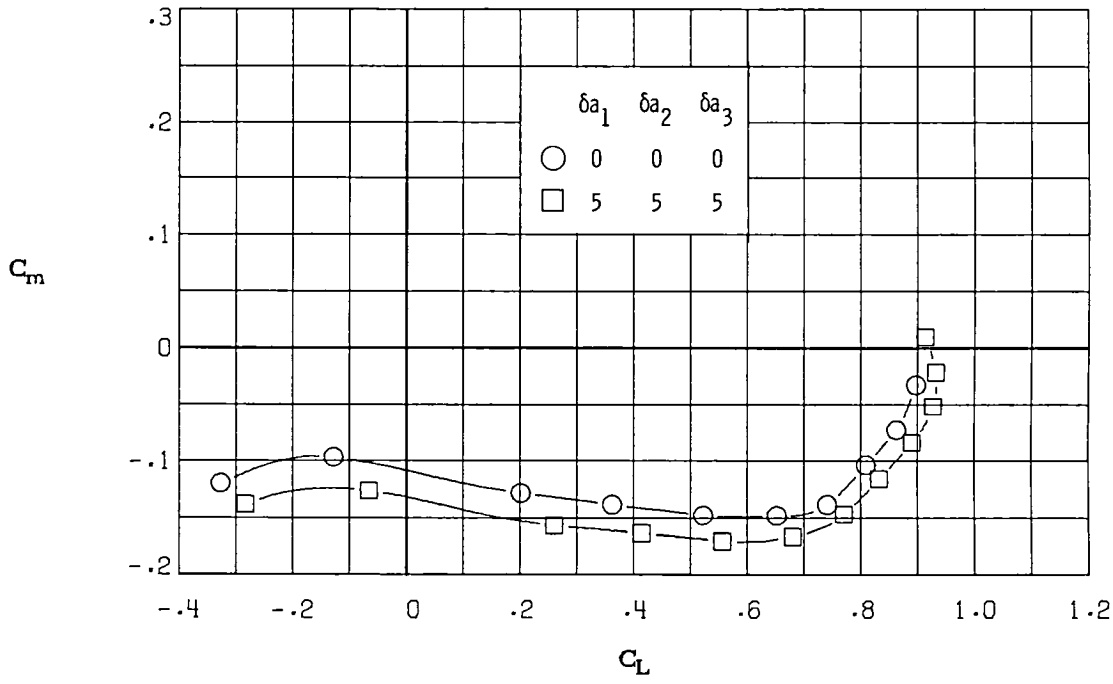

(f) $M_\infty = 0.84$.

Figure 37.- Continued.

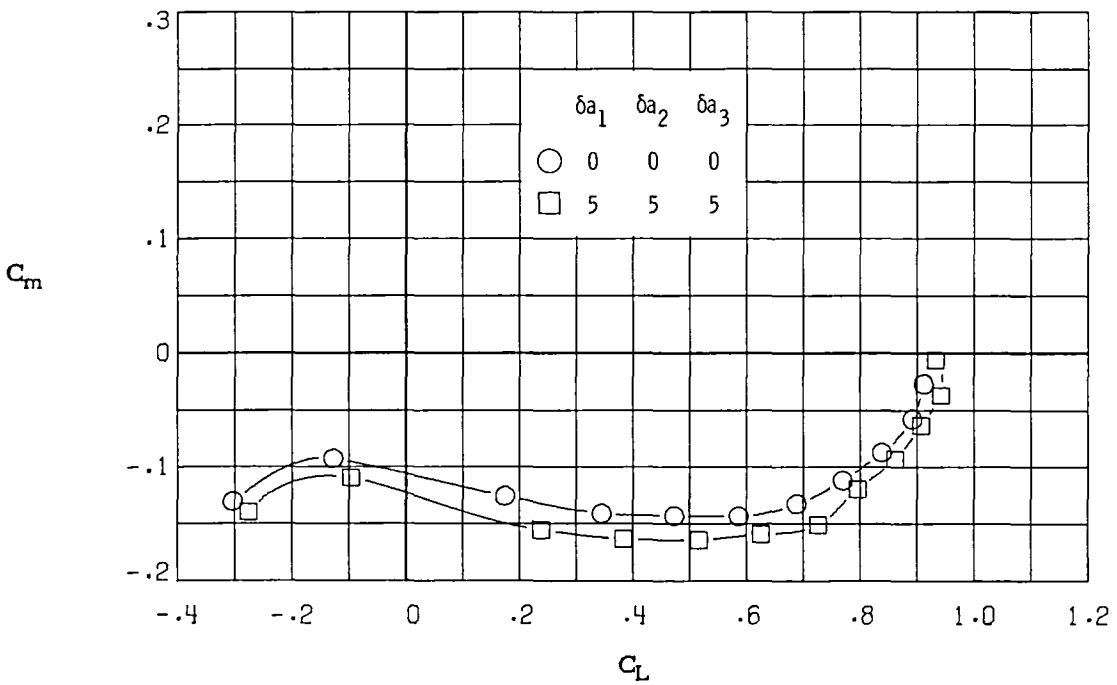

(g) $M_\infty = 0.86$.

Figure 37.- Concluded.

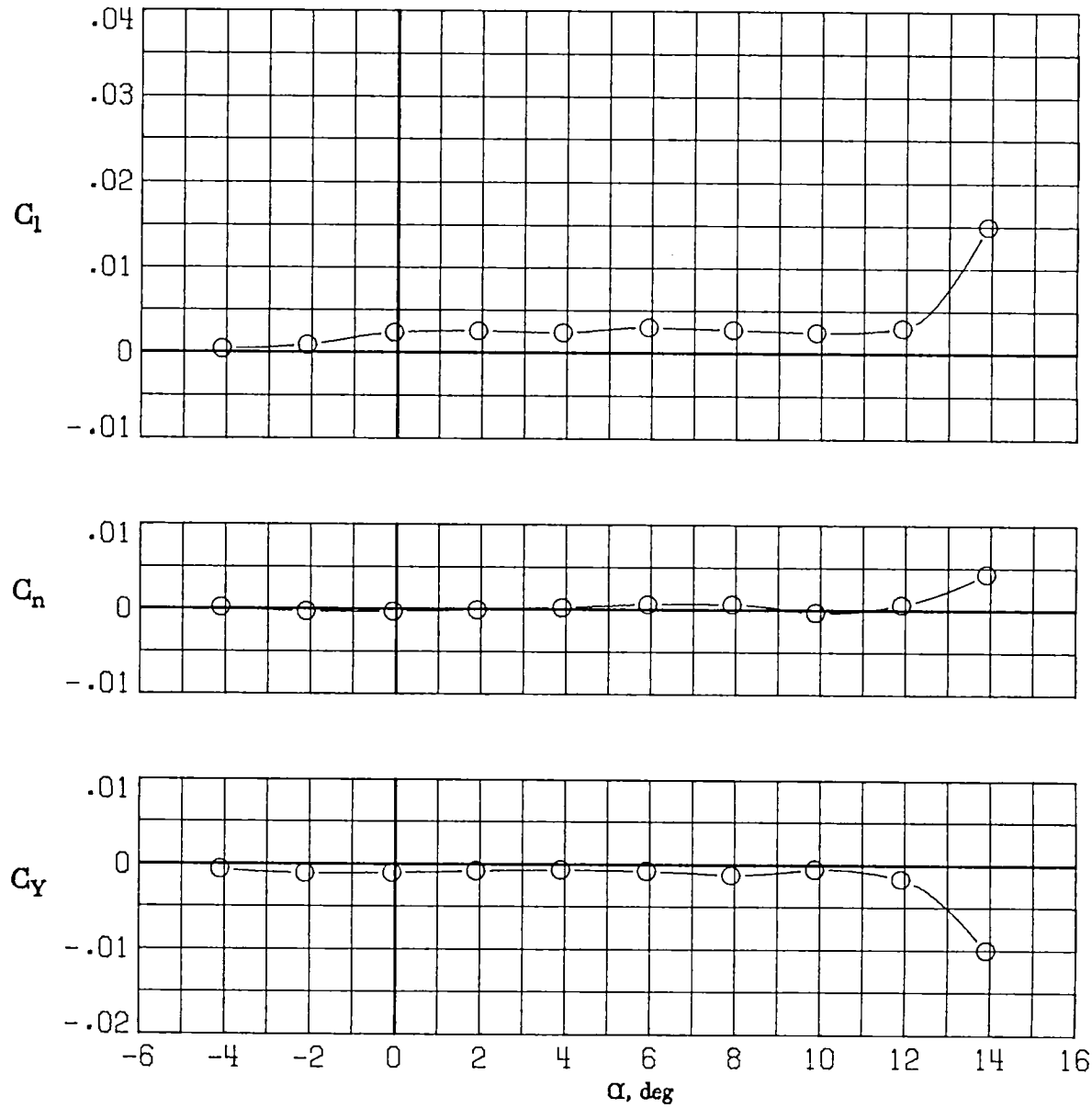

(a) $M_\infty = 0.30$.

Figure 38.- Variation of rolling-moment, yawing-moment, and side-force coefficients with angle of attack for the baseline configuration ($\delta a_1 = 0°$; $\delta a_2 = 0°$; $\delta a_3 = 0°$).

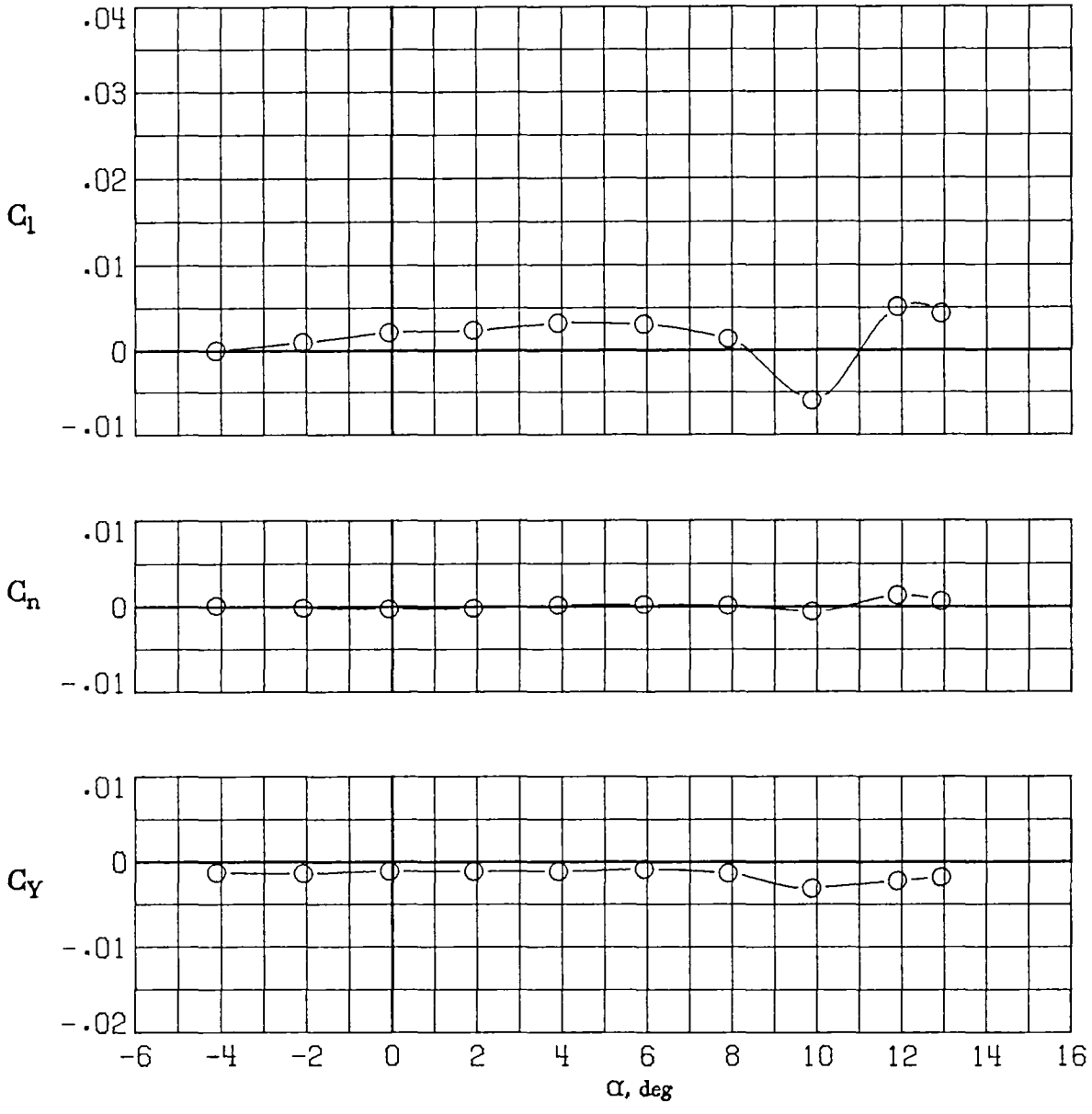

(b) $M_\infty = 0.60$.

Figure 38.- Continued.

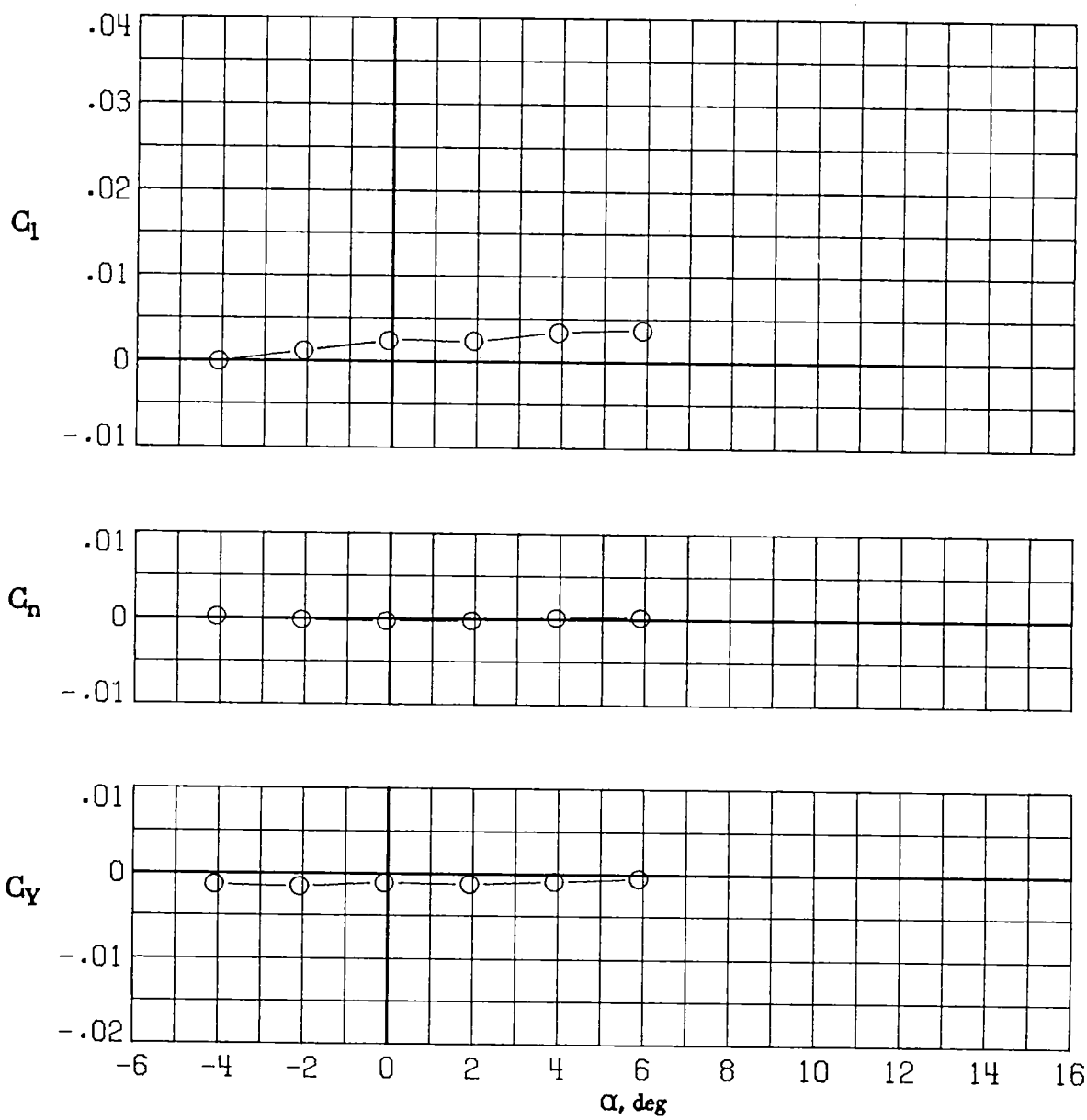

(c) $M_\infty = 0.70$.

Figure 38.- Continued.

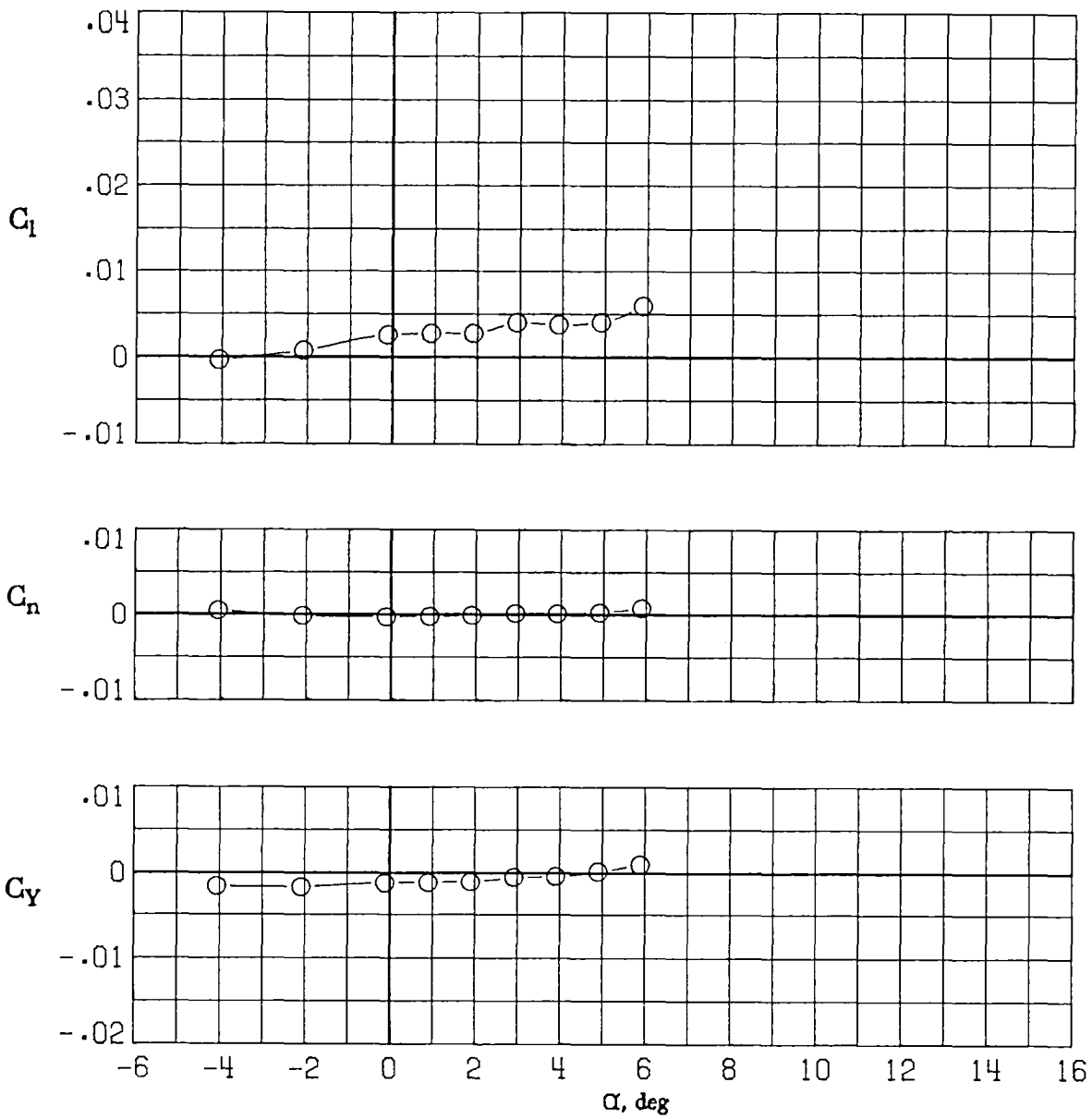

(d) $M_\infty = 0.77$.

Figure 38.- Continued.

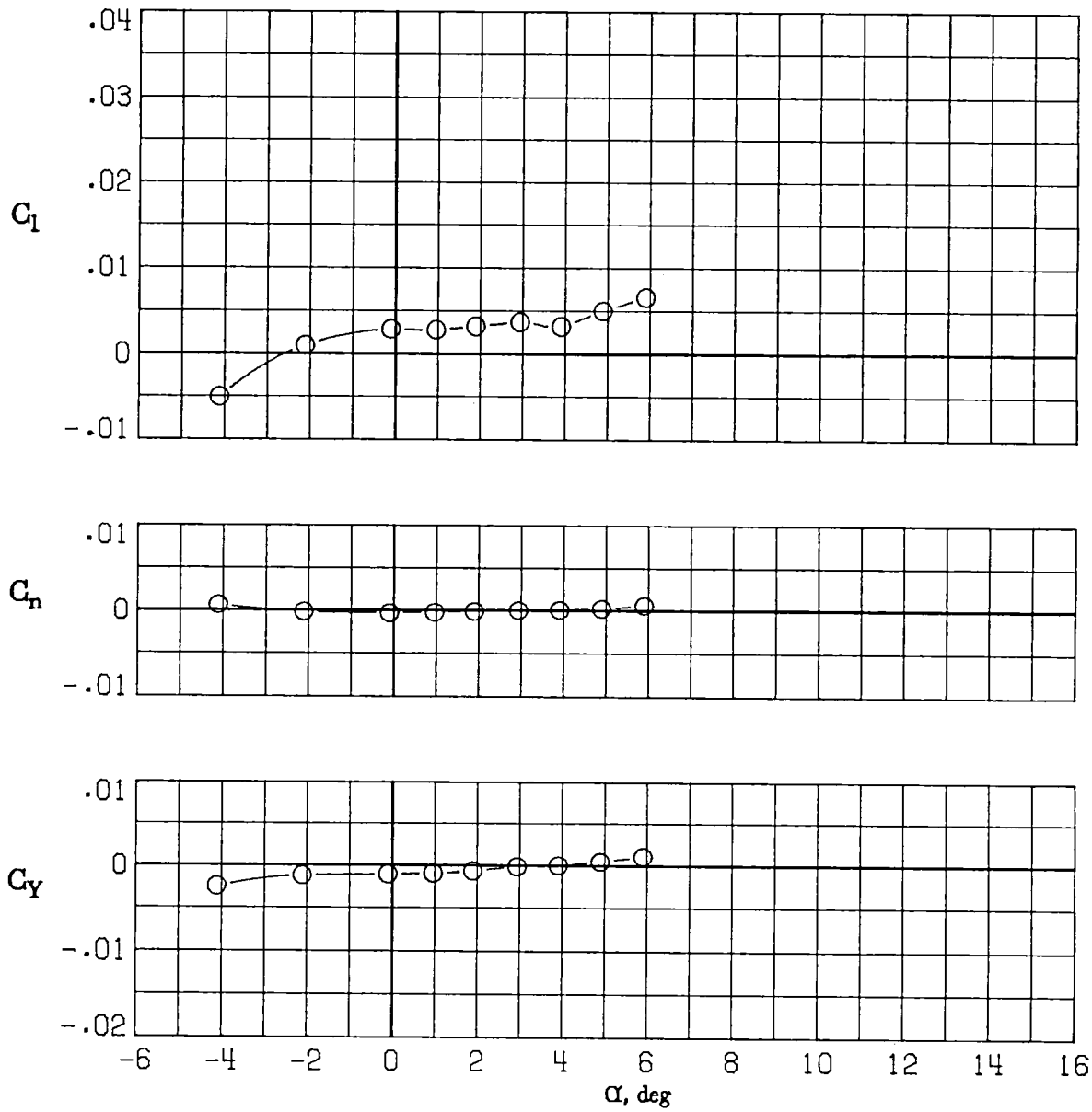

(e) $M_\infty = 0.81$.

Figure 38.- Continued.

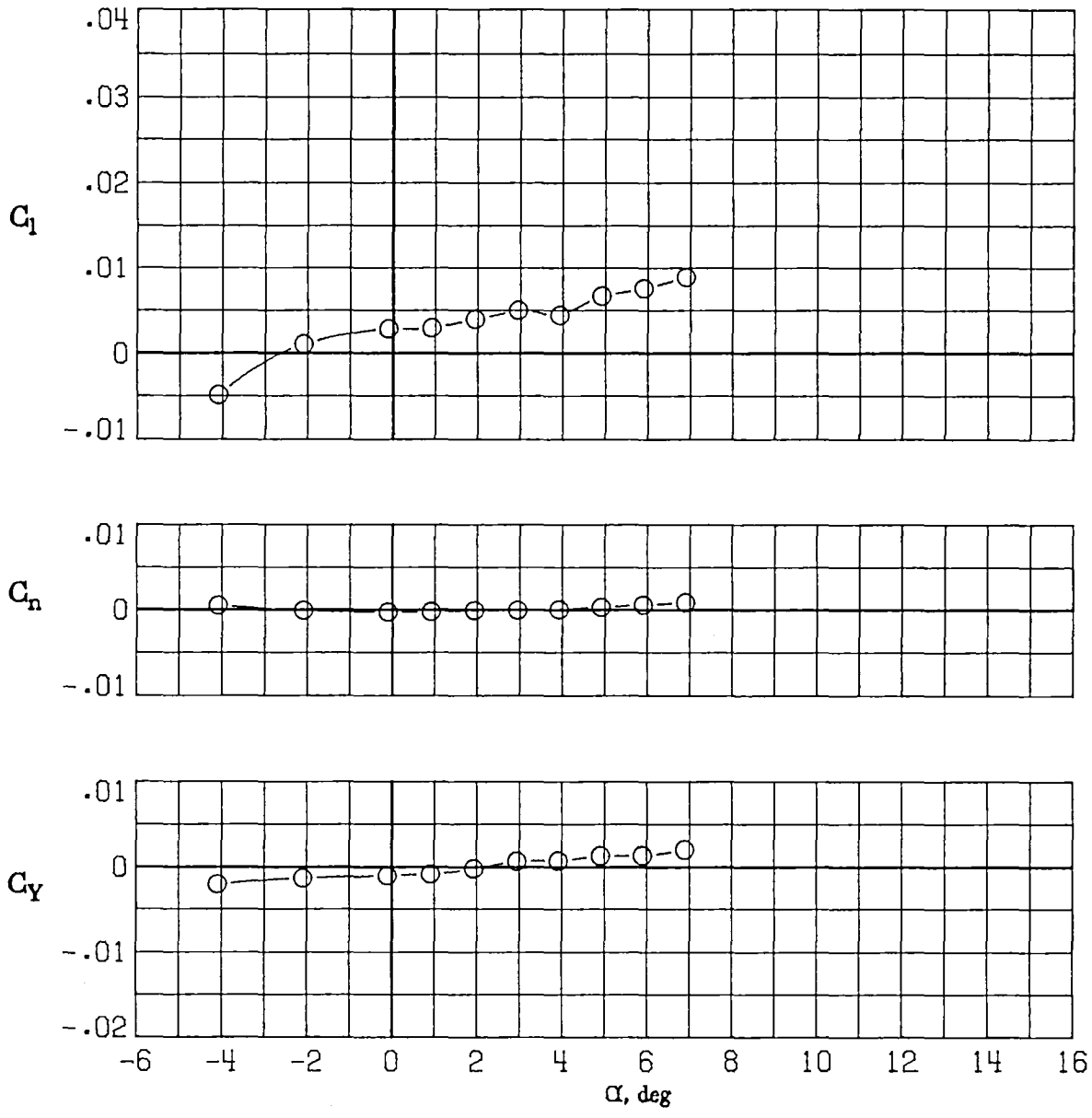

(f) $M_\infty = 0.84$.

Figure 38.- Continued.

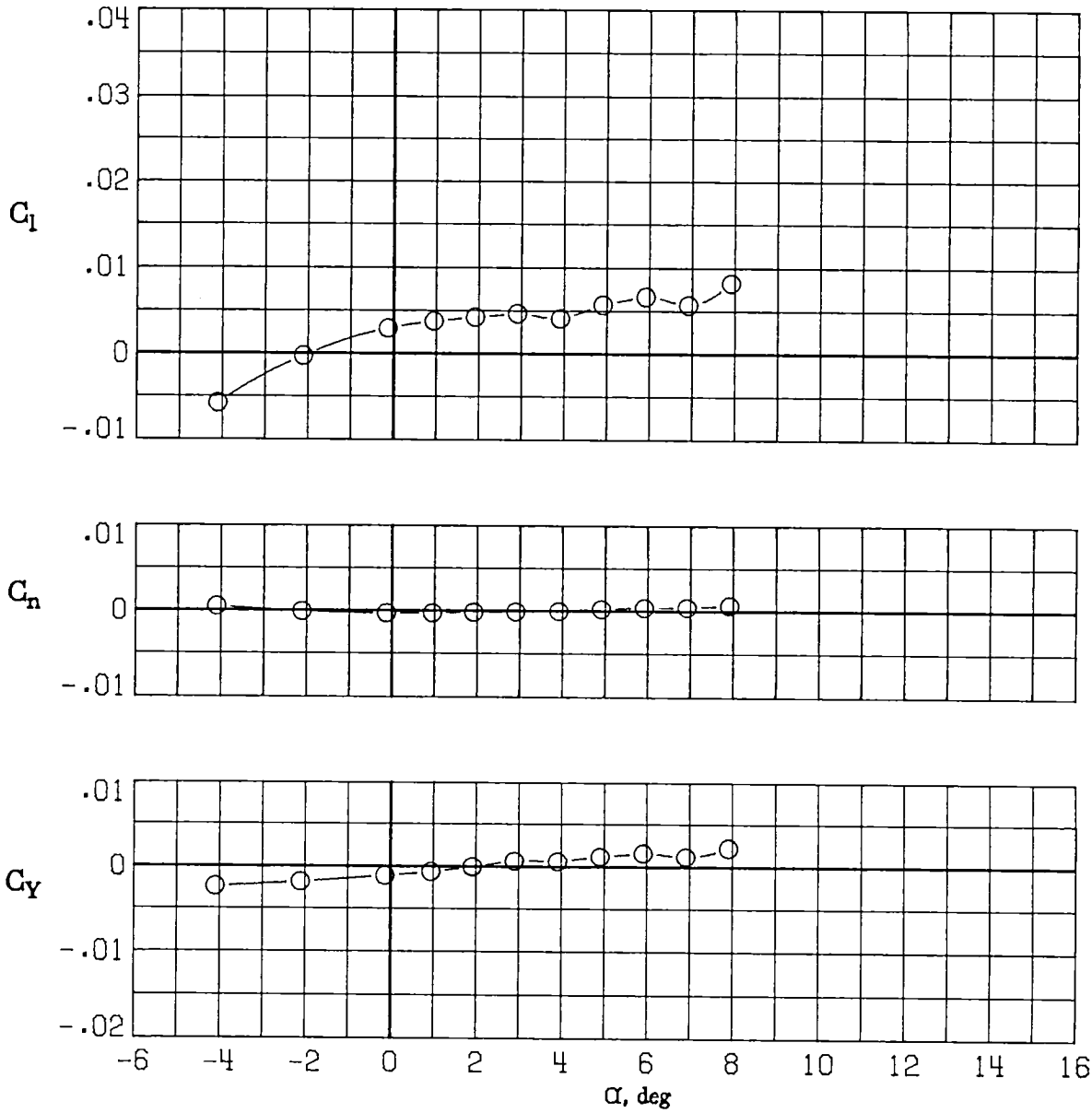

(g) $M_\infty = 0.86$.

Figure 38.- Concluded.

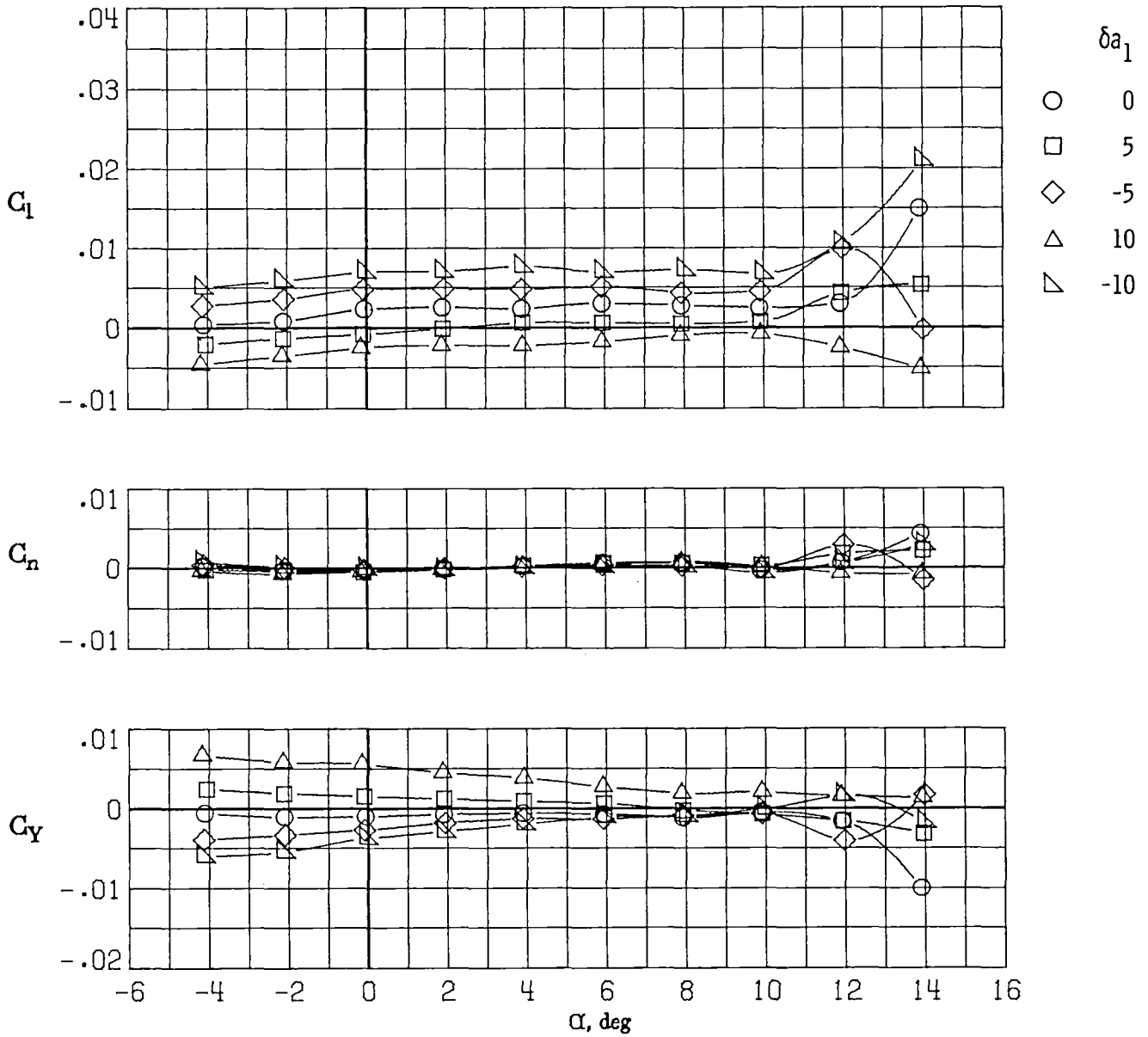

(a) $M_\infty = 0.30$.

Figure 39.- Variation of rolling-moment, yawing-moment, and side-force coefficients with angle of attack for deflections of aileron 1 (δa_1 in degrees). $\delta a_2 = 0°$; $\delta a_3 = 0°$.

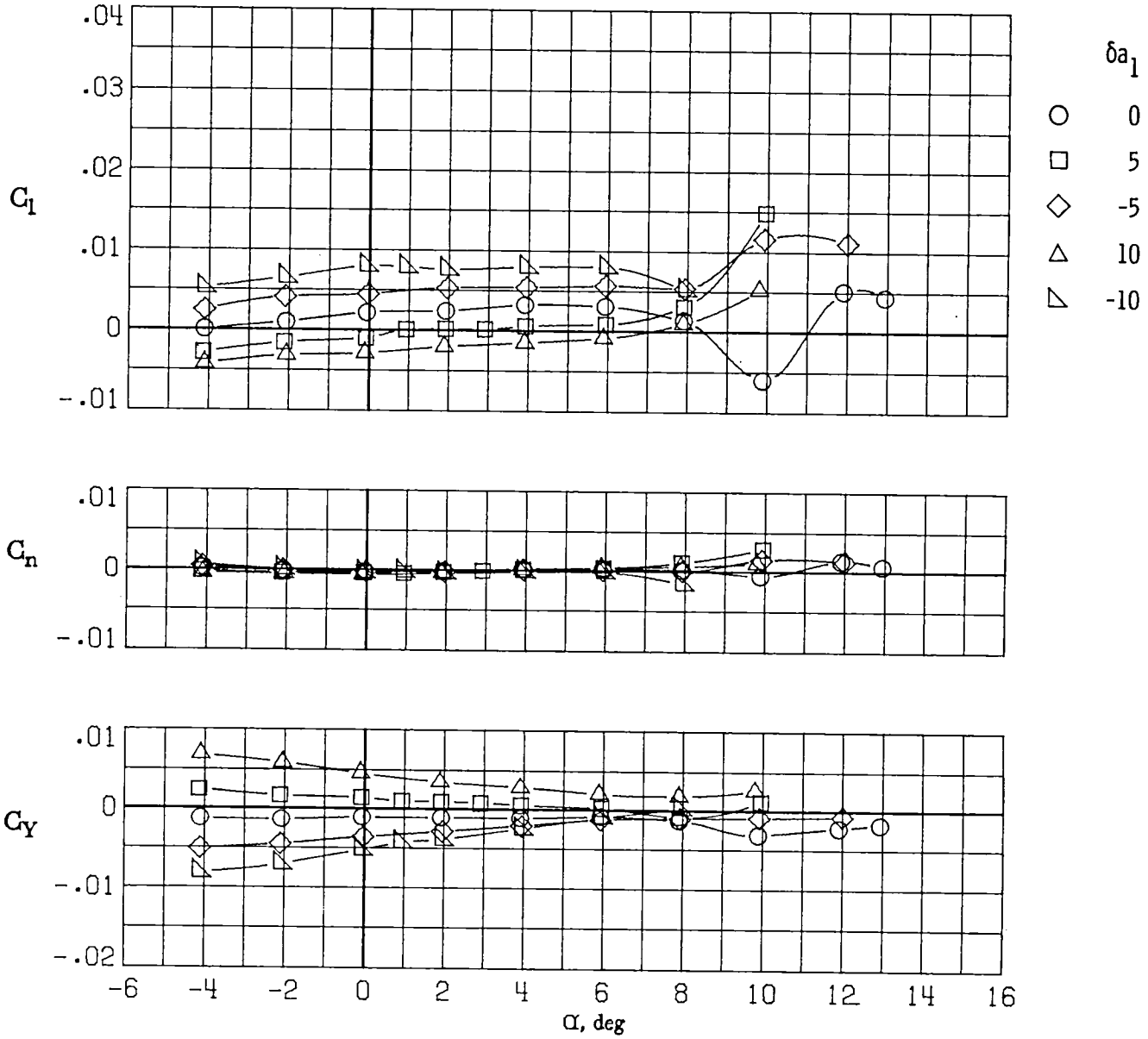

(b) $M_\infty = 0.60$.

Figure 39.- Continued.

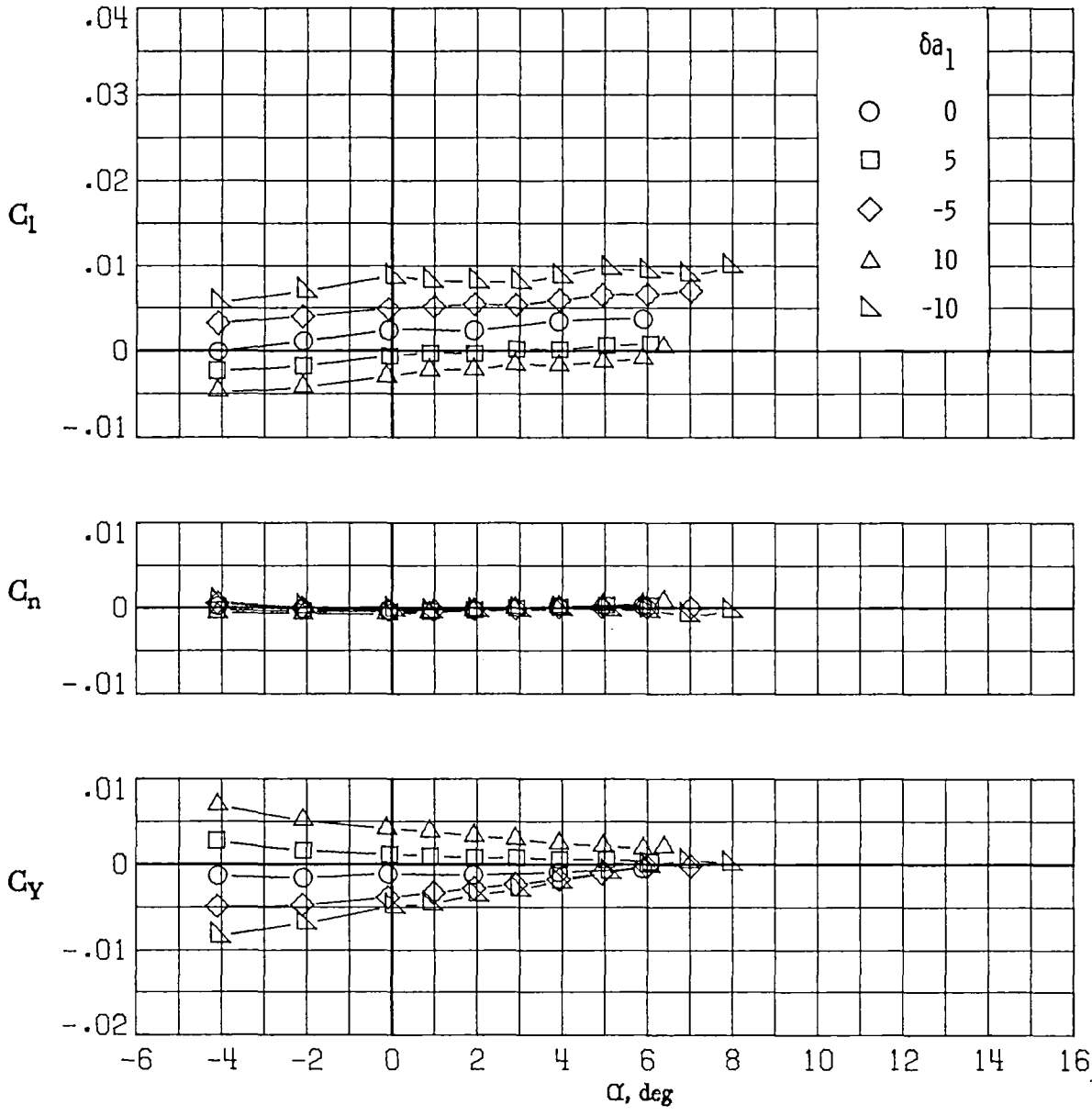

(c) $M_\infty = 0.70$.

Figure 39.- Continued.

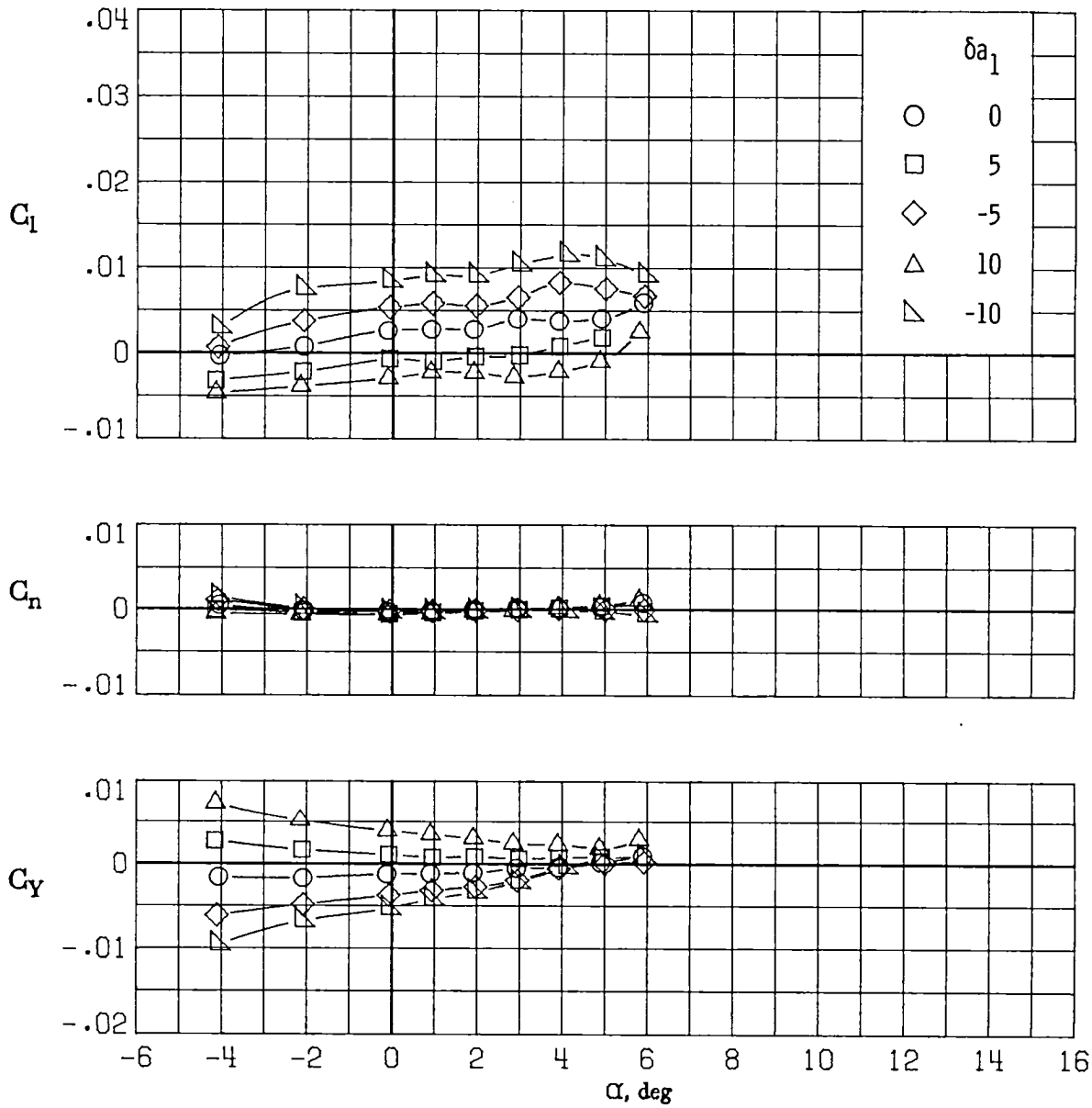

(d) $M_\infty = 0.77$.

Figure 39.- Continued.

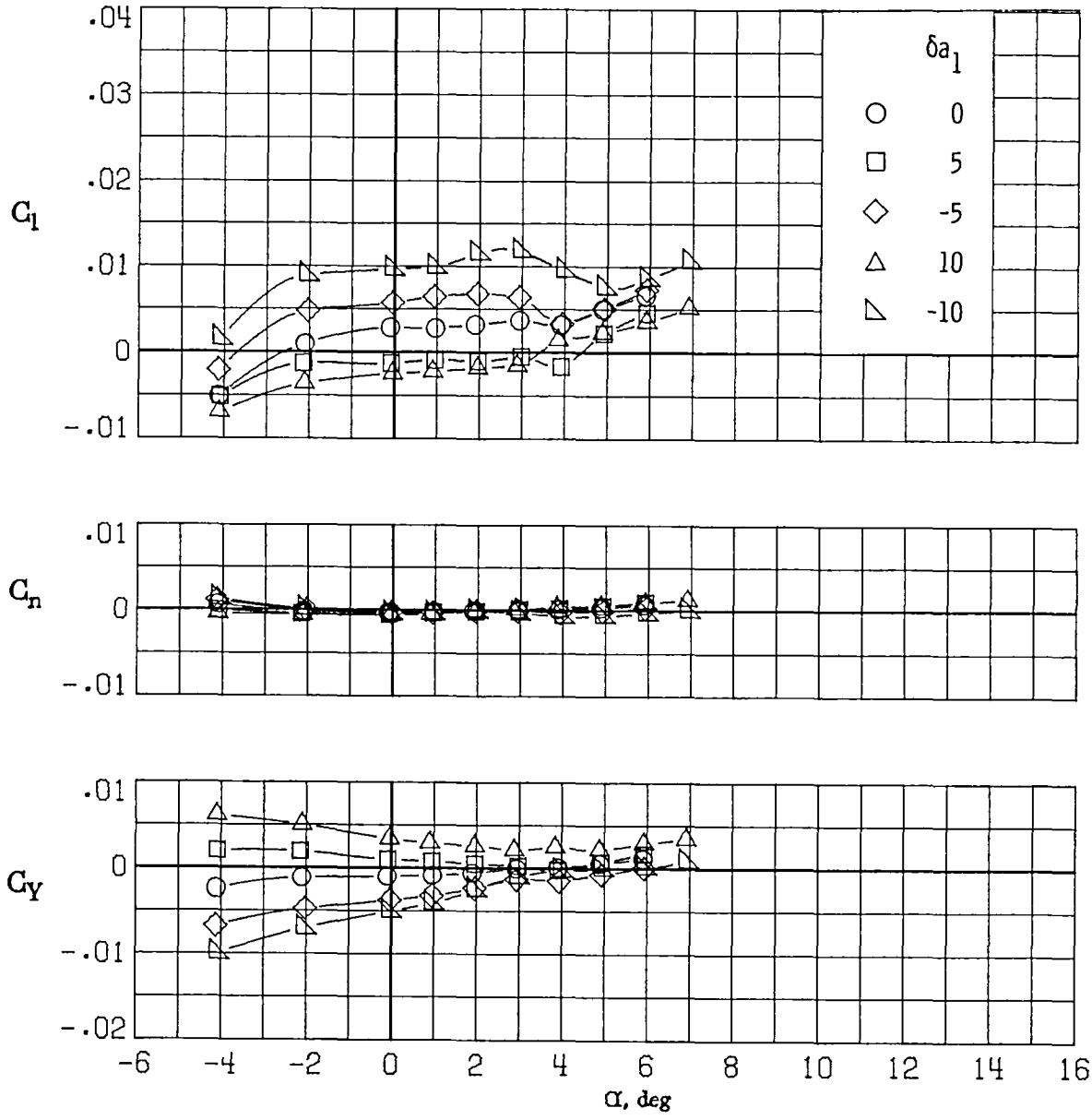

(e) $M_\infty = 0.81$.

Figure 39.- Continued.

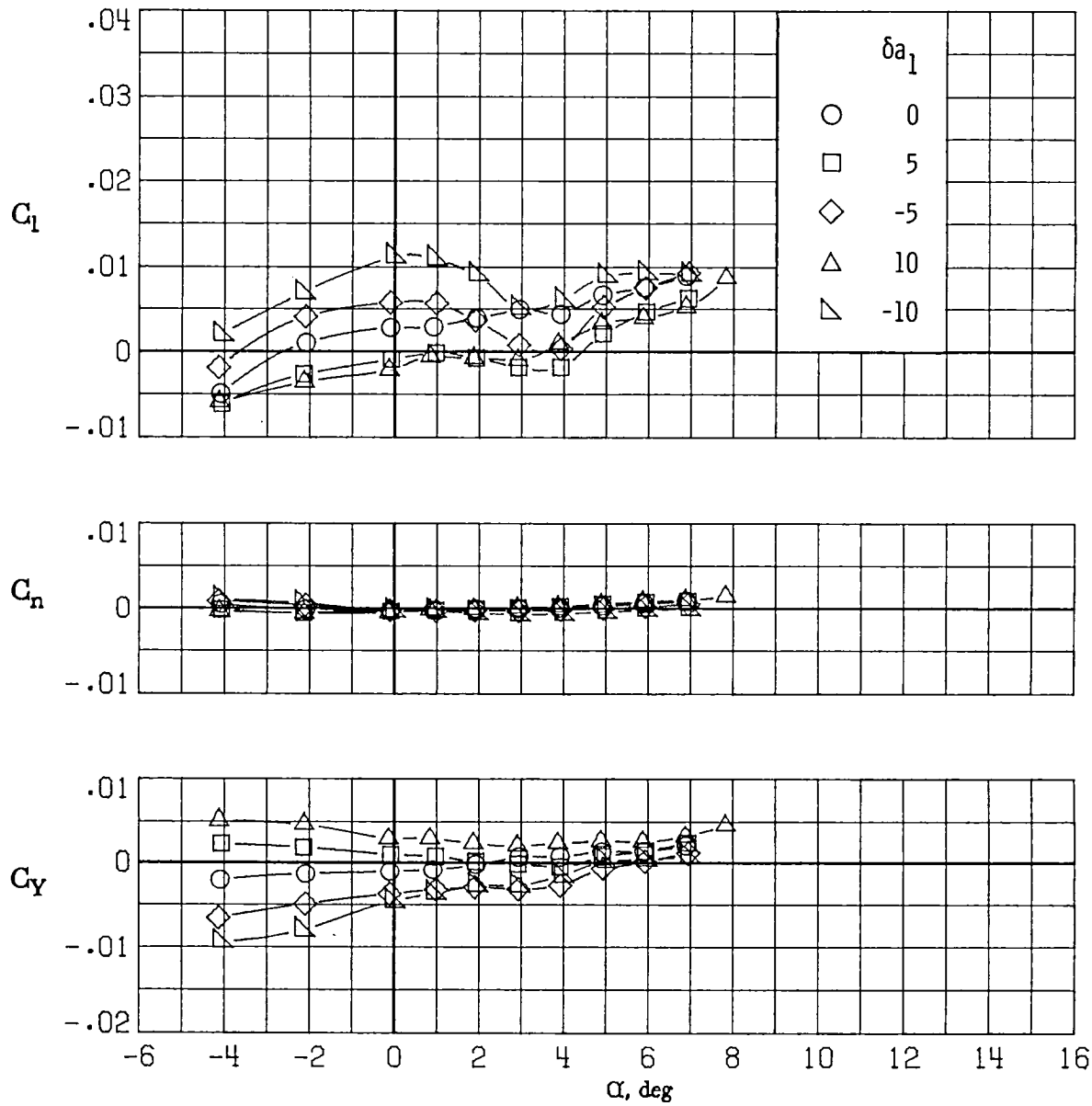

(f) $M_\infty = 0.84$.

Figure 39.- Continued.

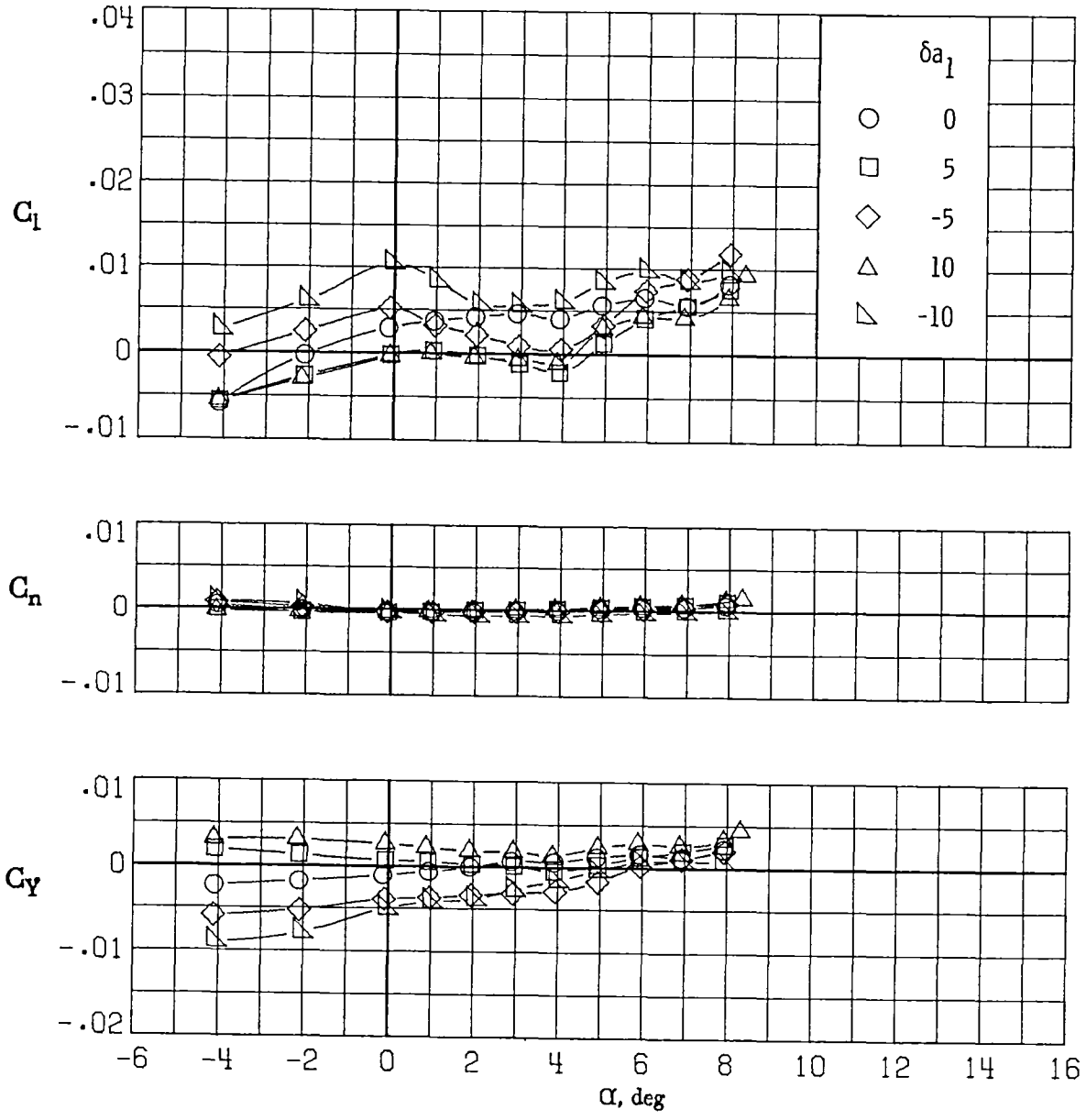

(g) $M_\infty = 0.86$.

Figure 39.- Concluded.

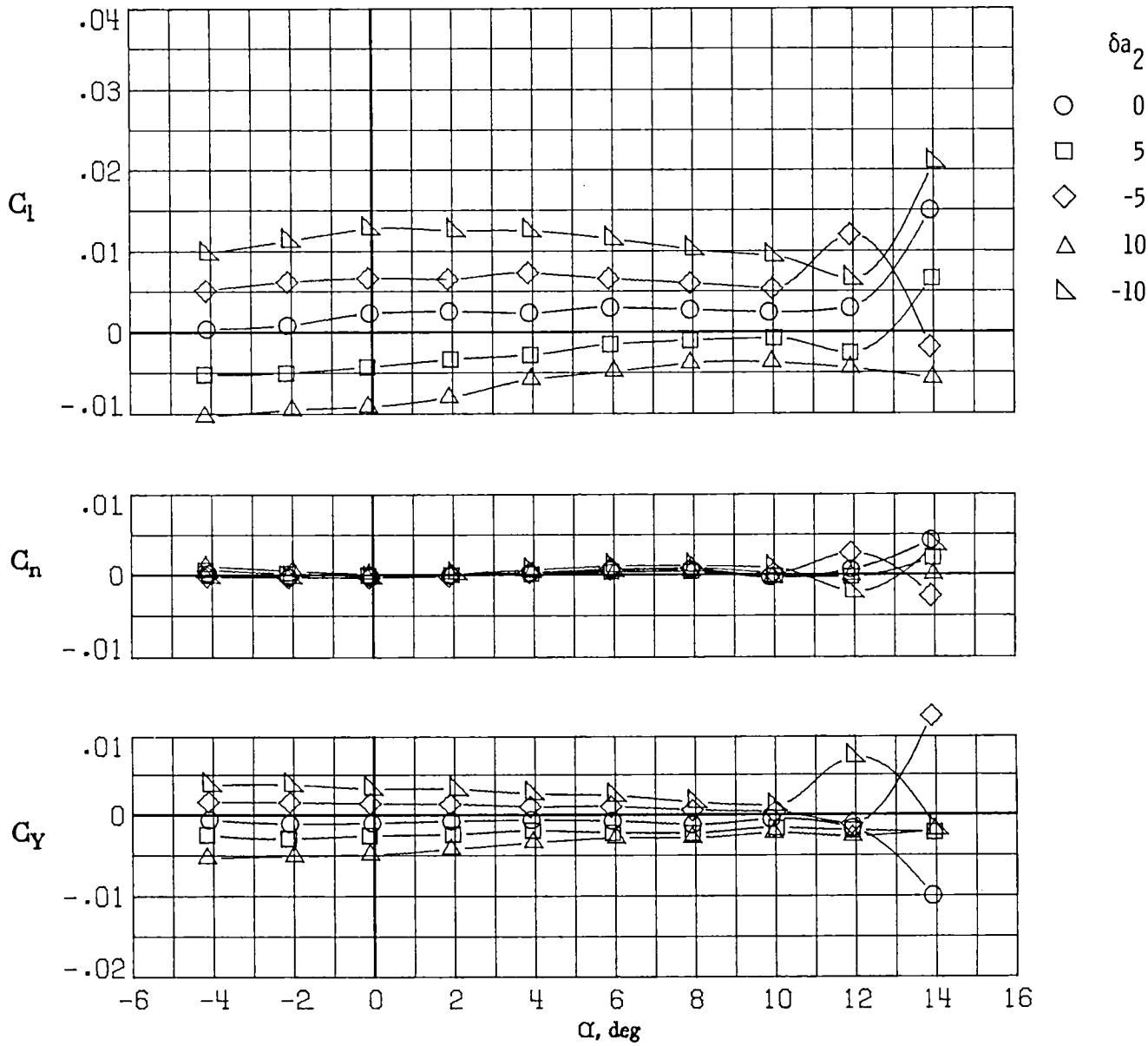

(a) $M_\infty = 0.30$.

Figure 40.- Variation of rolling-moment, yawing-moment, and side-force coefficients with angle of attack for deflections of aileron 2 (δa_2 in degrees). $\delta a_1 = 0°$; $\delta a_3 = 0°$.

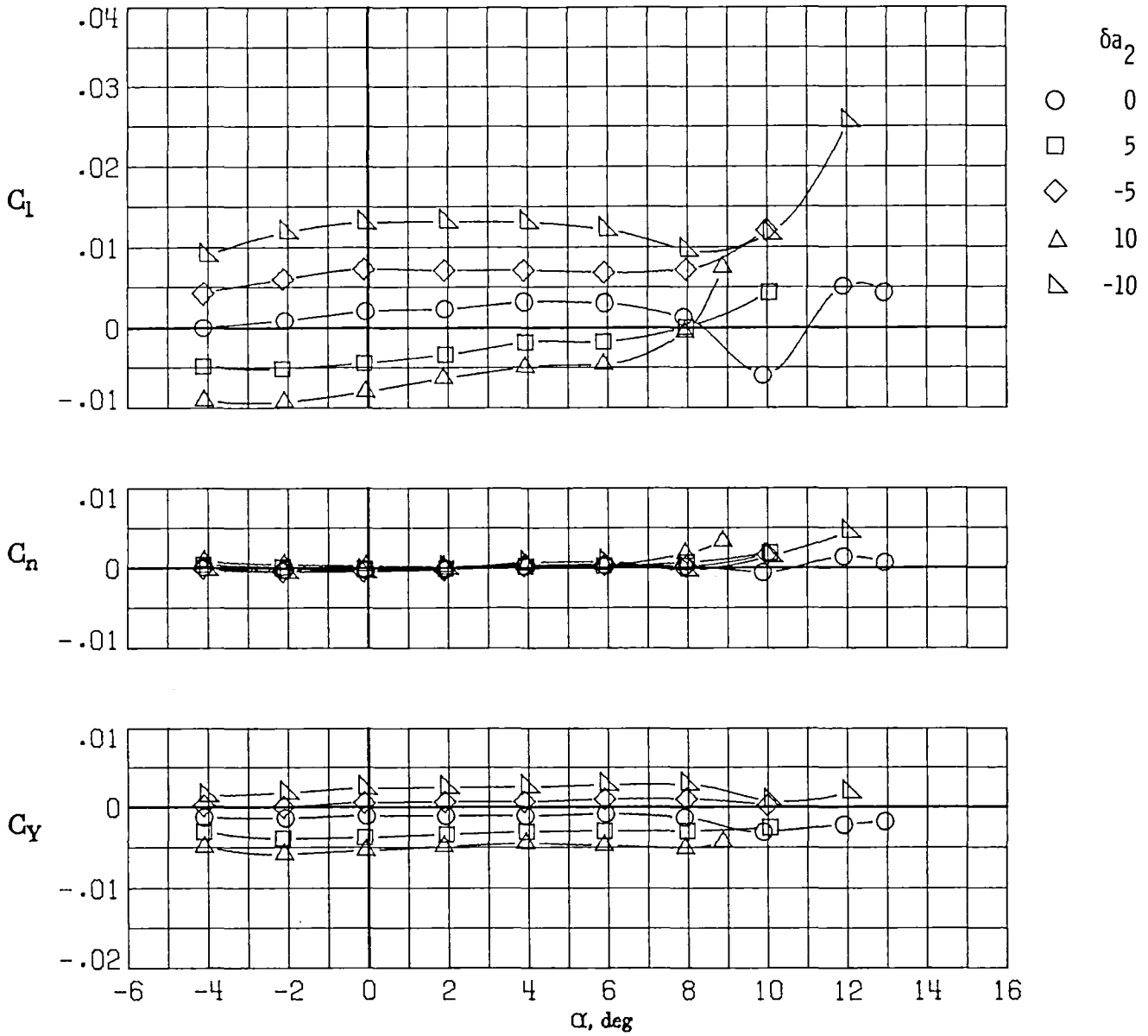

(b) $M_\infty = 0.60$.

Figure 40.- Continued.

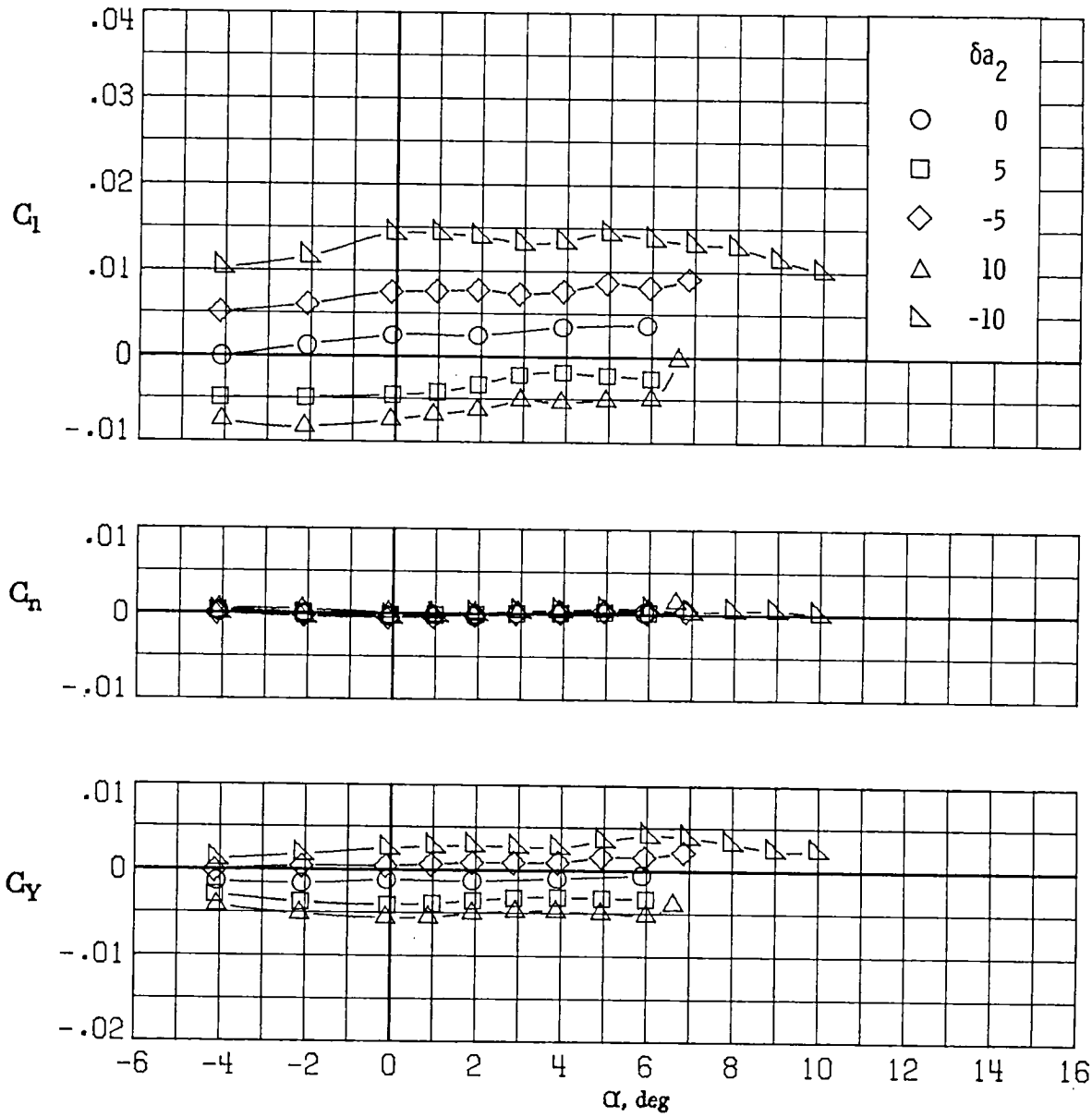

(c) $M_\infty = 0.70$.

Figure 40.- Continued.

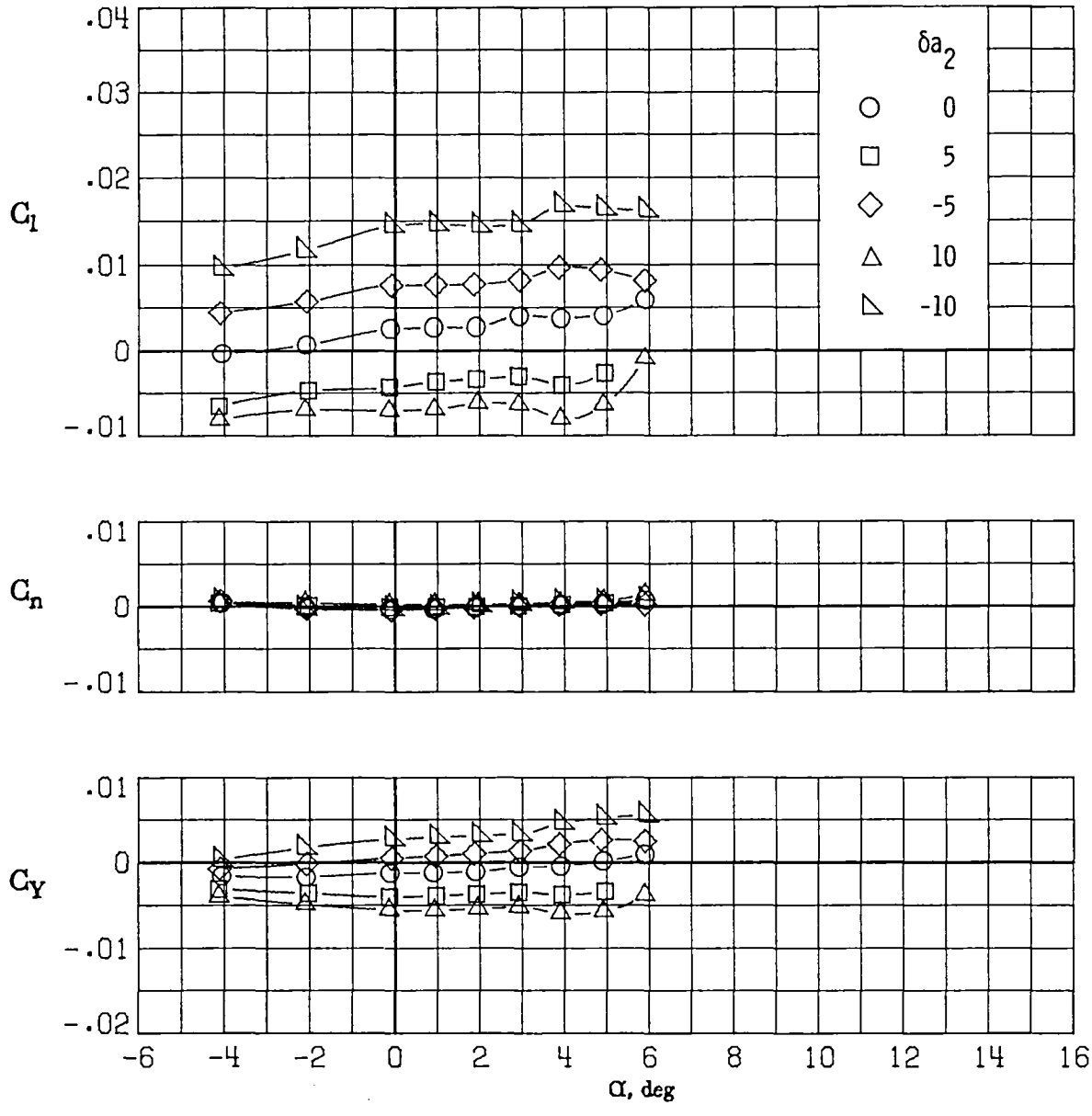

(d) $M_\infty = 0.77$.

Figure 40.- Continued.

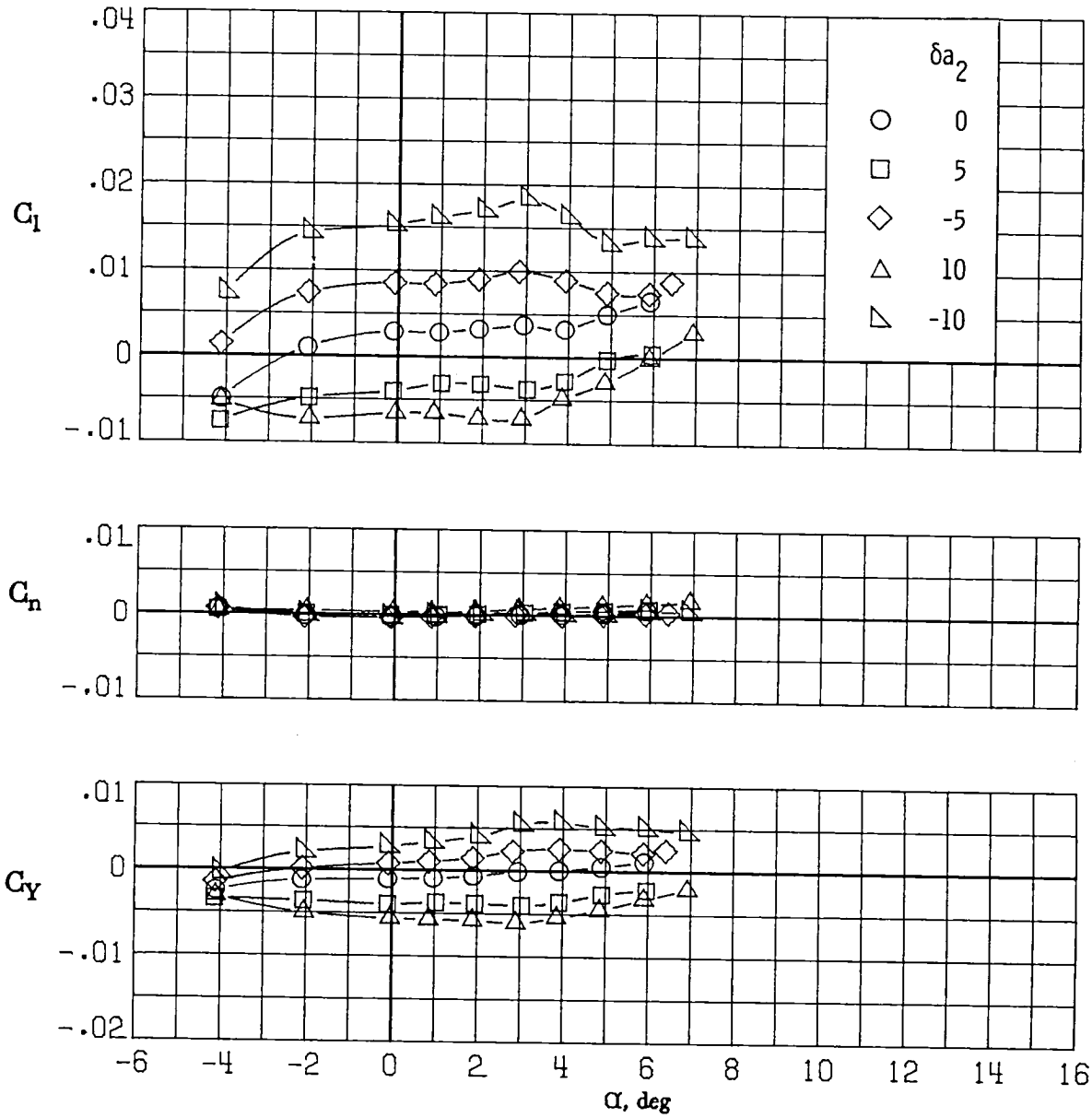

(e) $M_\infty = 0.81$.

Figure 40.- Continued.

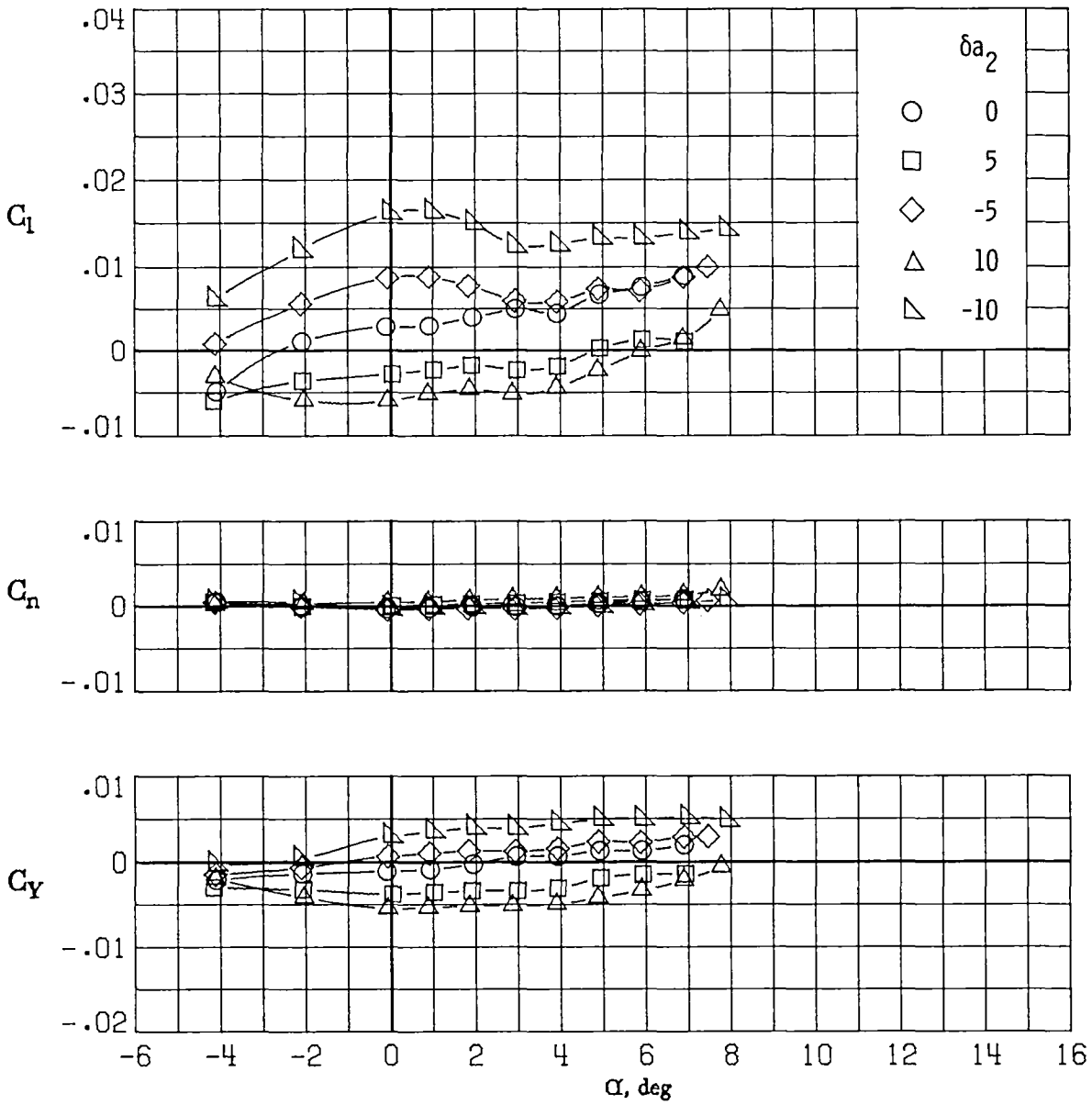

(f) $M_\infty = 0.84$.

Figure 40.- Continued.

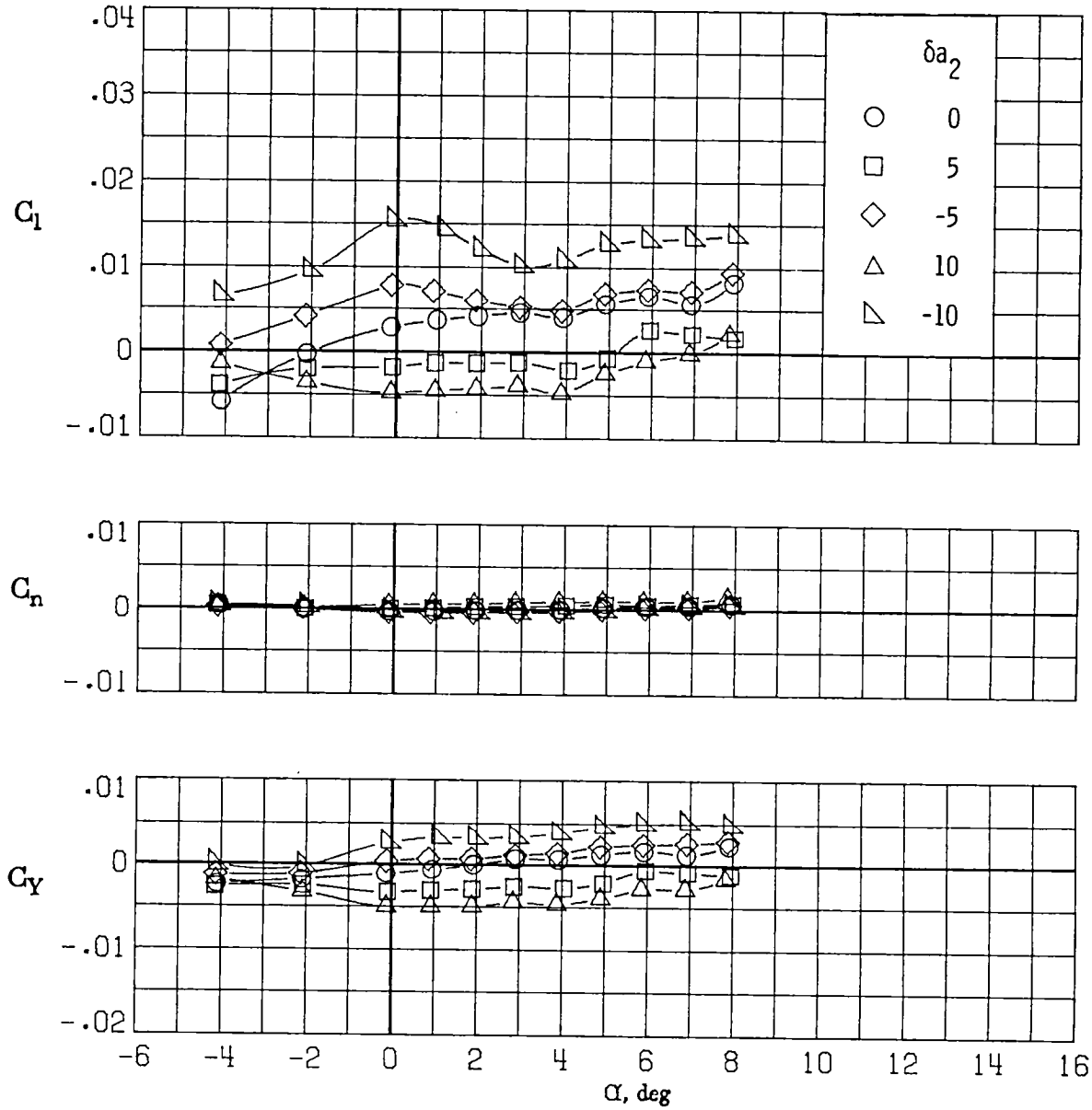

(g) $M_\infty = 0.86$.

Figure 40.- Concluded.

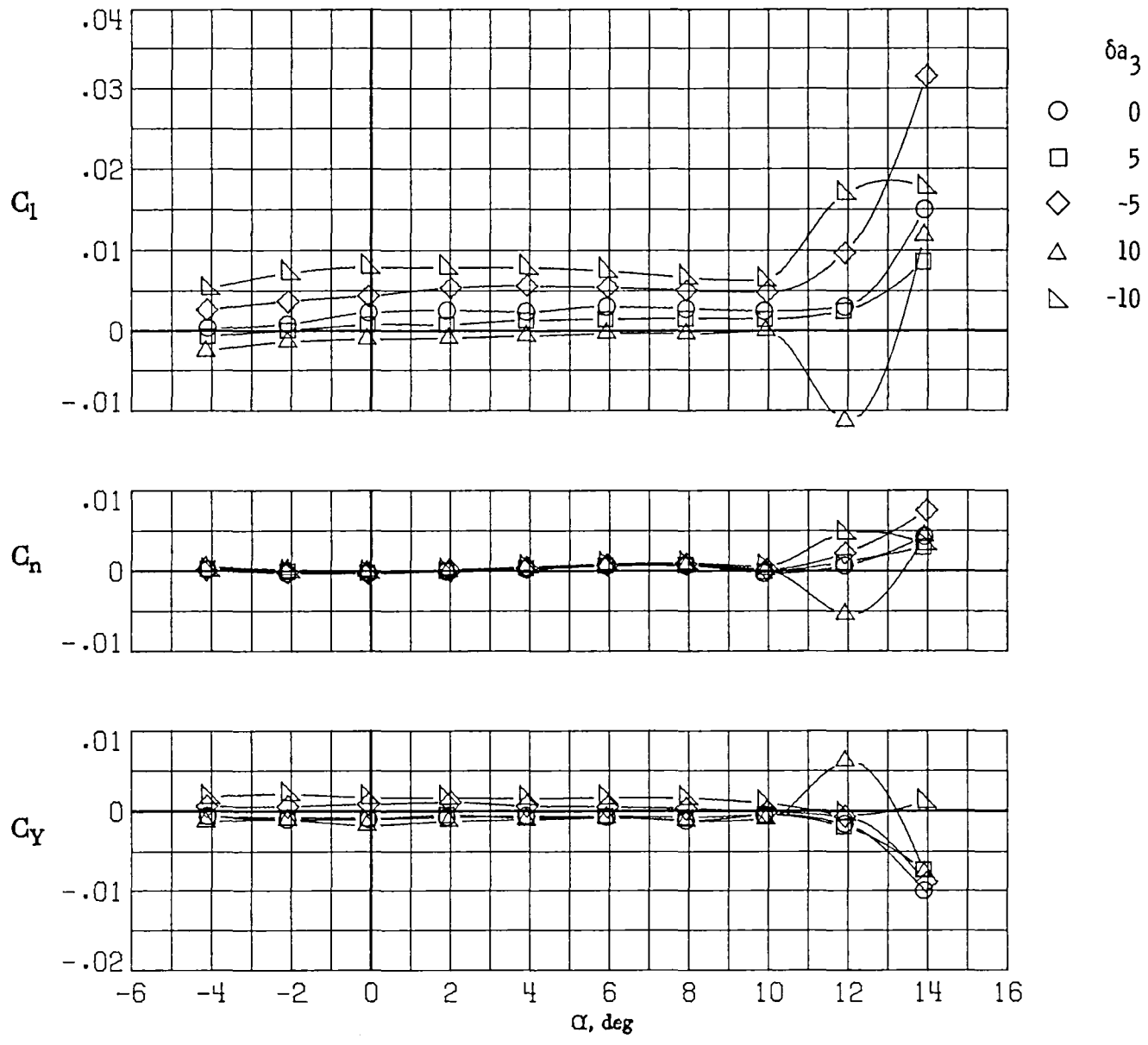

(a) $M_\infty = 0.30$.

Figure 41.- Variation of rolling-moment, yawing-moment, and side-force coefficients with angle of attack for deflections of aileron 3 (δa_3 in degrees). $\delta a_1 = 0°$; $\delta a_2 = 0°$.

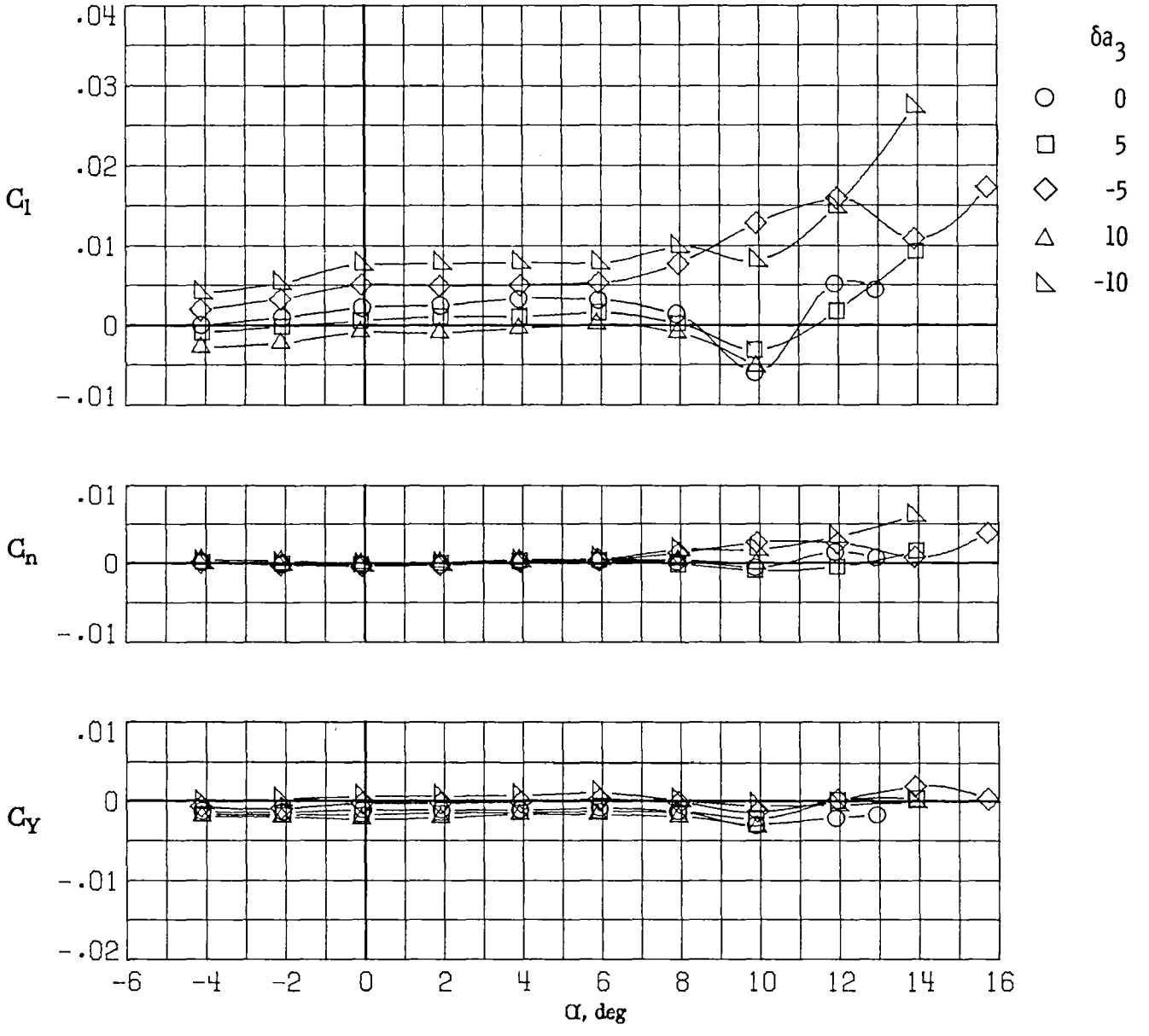

(b) $M_\infty = 0.60$.

Figure 41.- Continued.

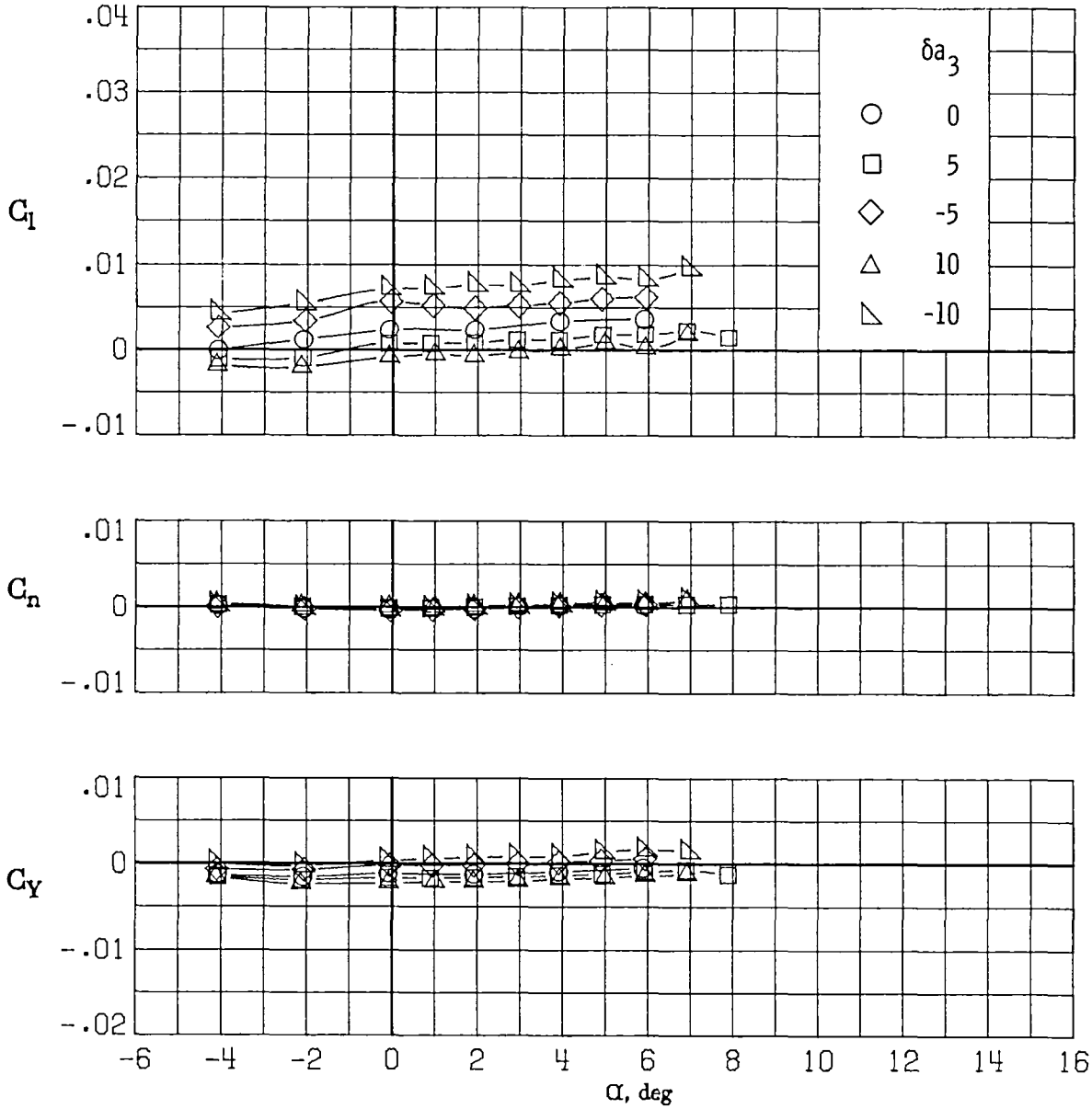

(c) $M_\infty = 0.70$.

Figure 41.- Continued.

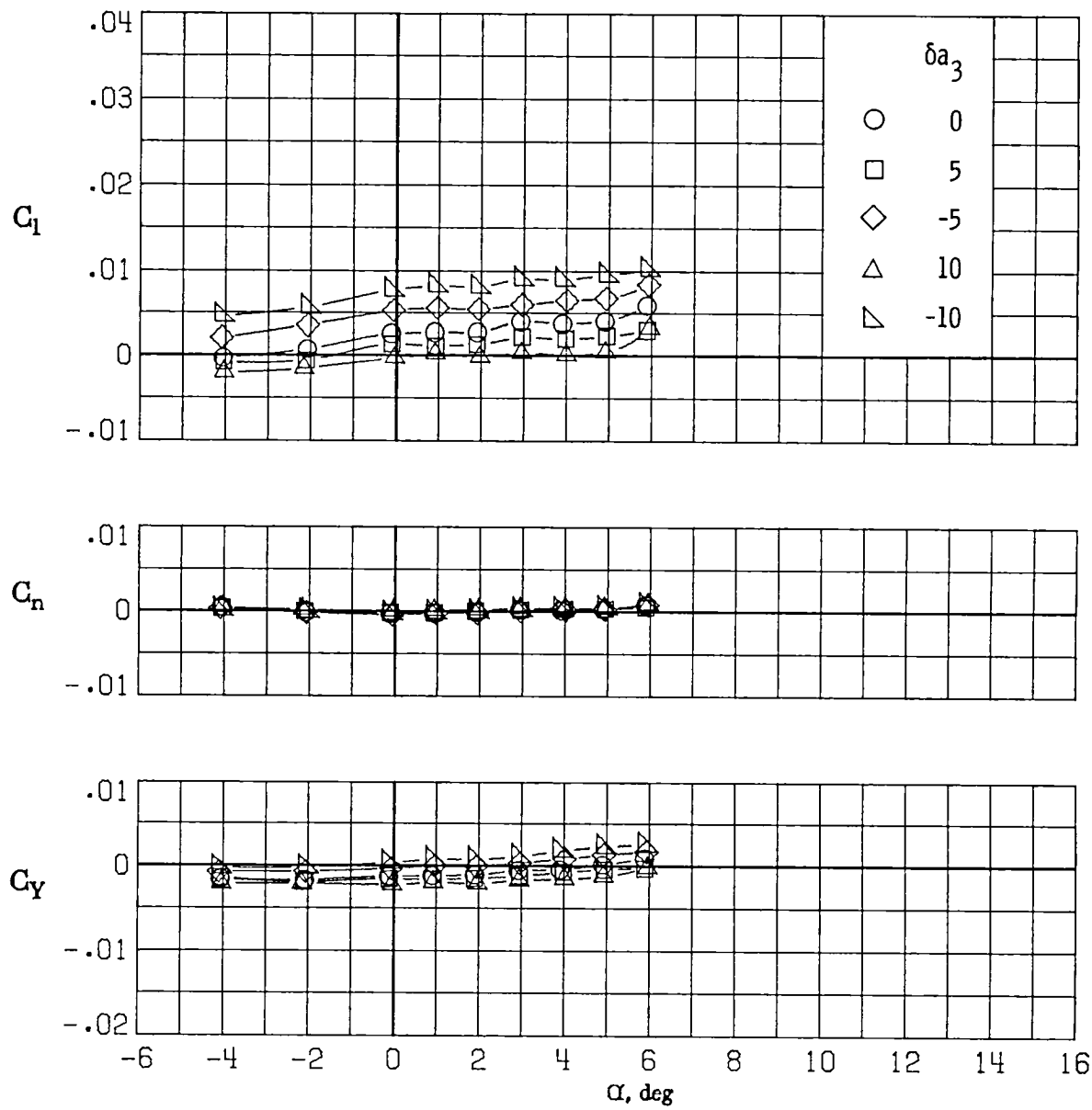

(d) $M_\infty = 0.77$.

Figure 41.- Continued.

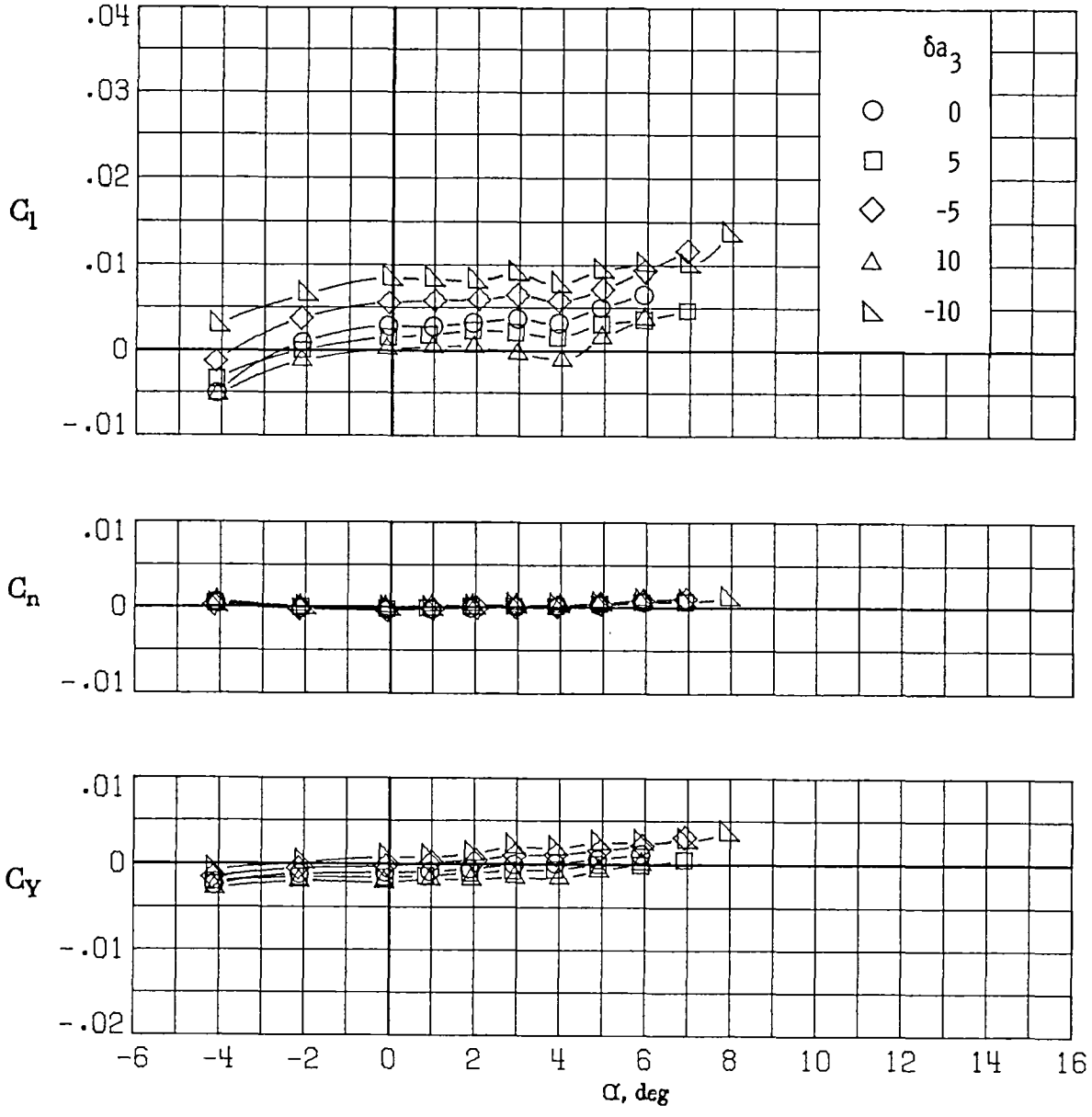

(e) $M_\infty = 0.81$.

Figure 41.- Continued.

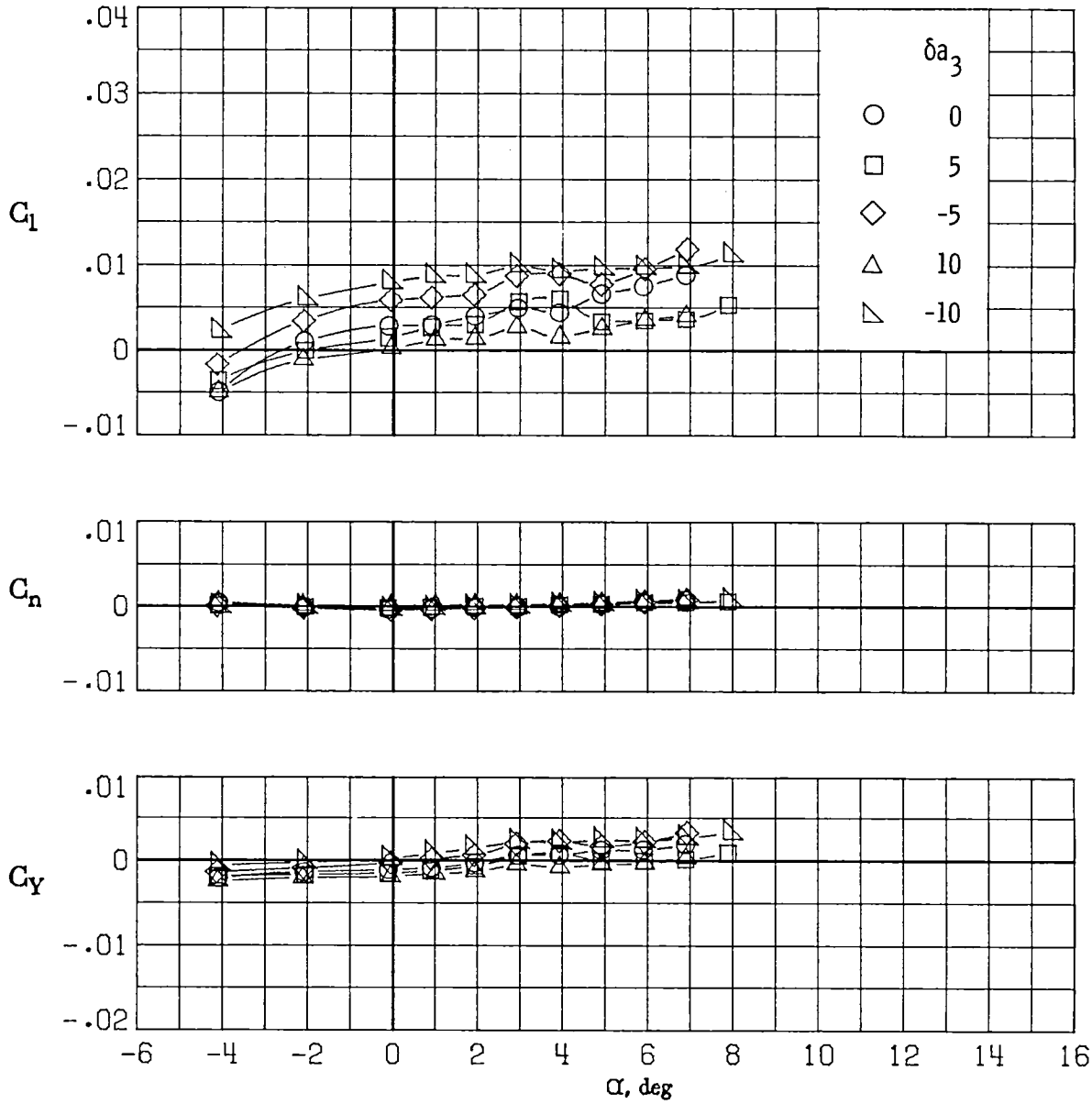

(f) $M_\infty = 0.84$.

Figure 41.- Continued.

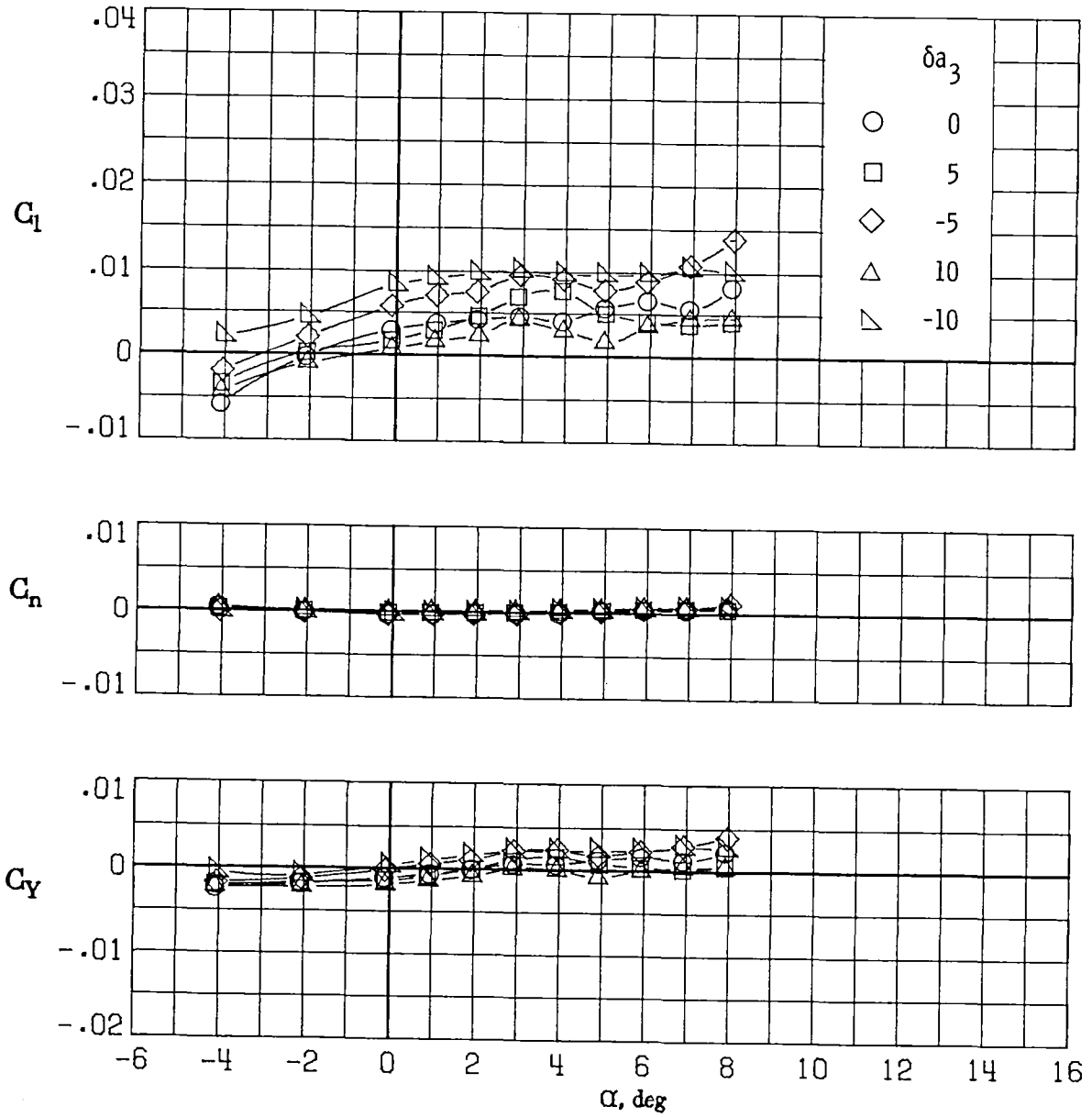

(g) $M_\infty = 0.86$.

Figure 41.- Concluded.

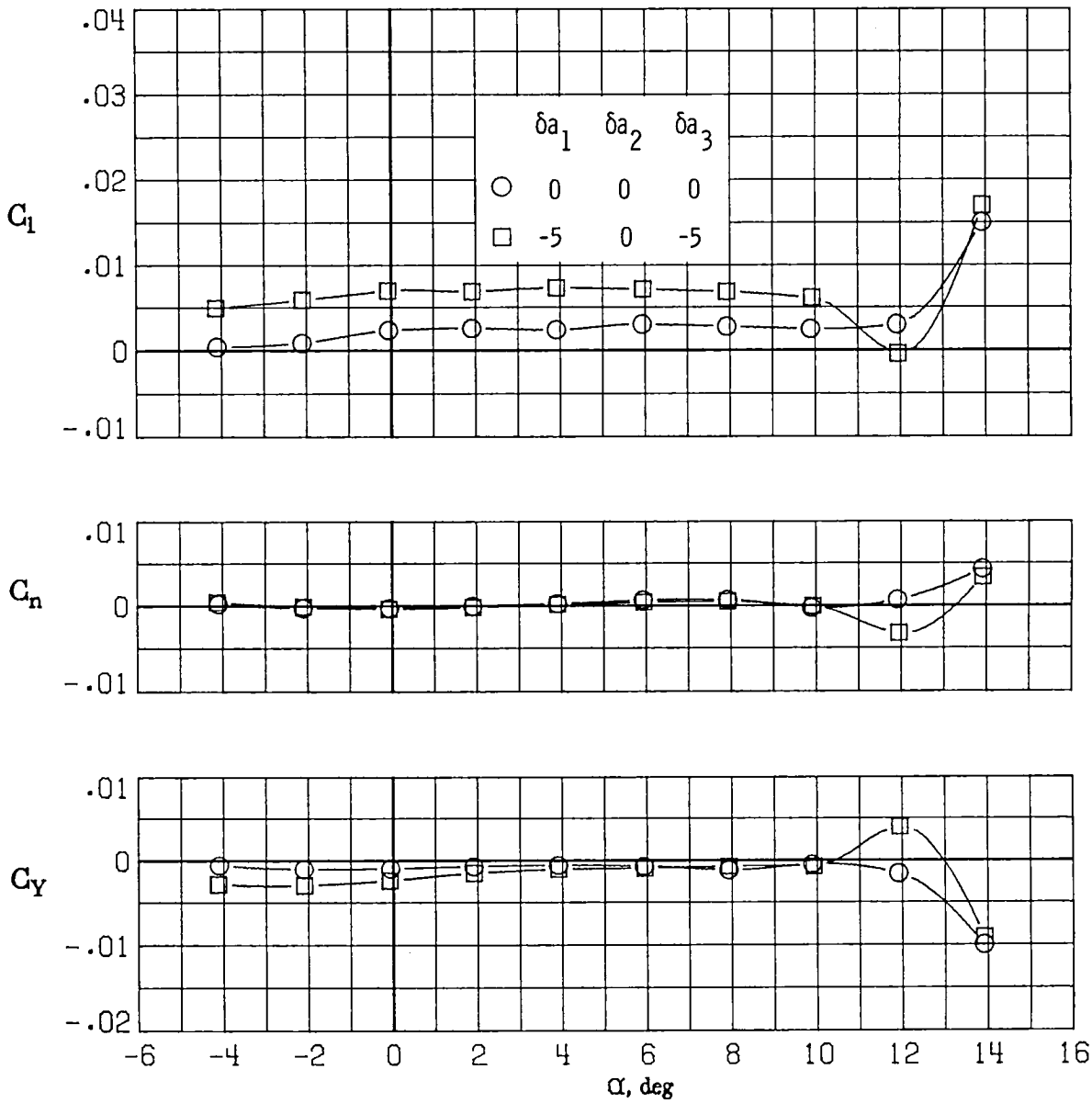

(a) $M_\infty = 0.30$.

Figure 42.- Variation of rolling-moment, yawing-moment, and side-force coefficients with angle of attack for $\delta a_1 = -5°$, $\delta a_2 = 0°$, $\delta a_3 = -5°$.

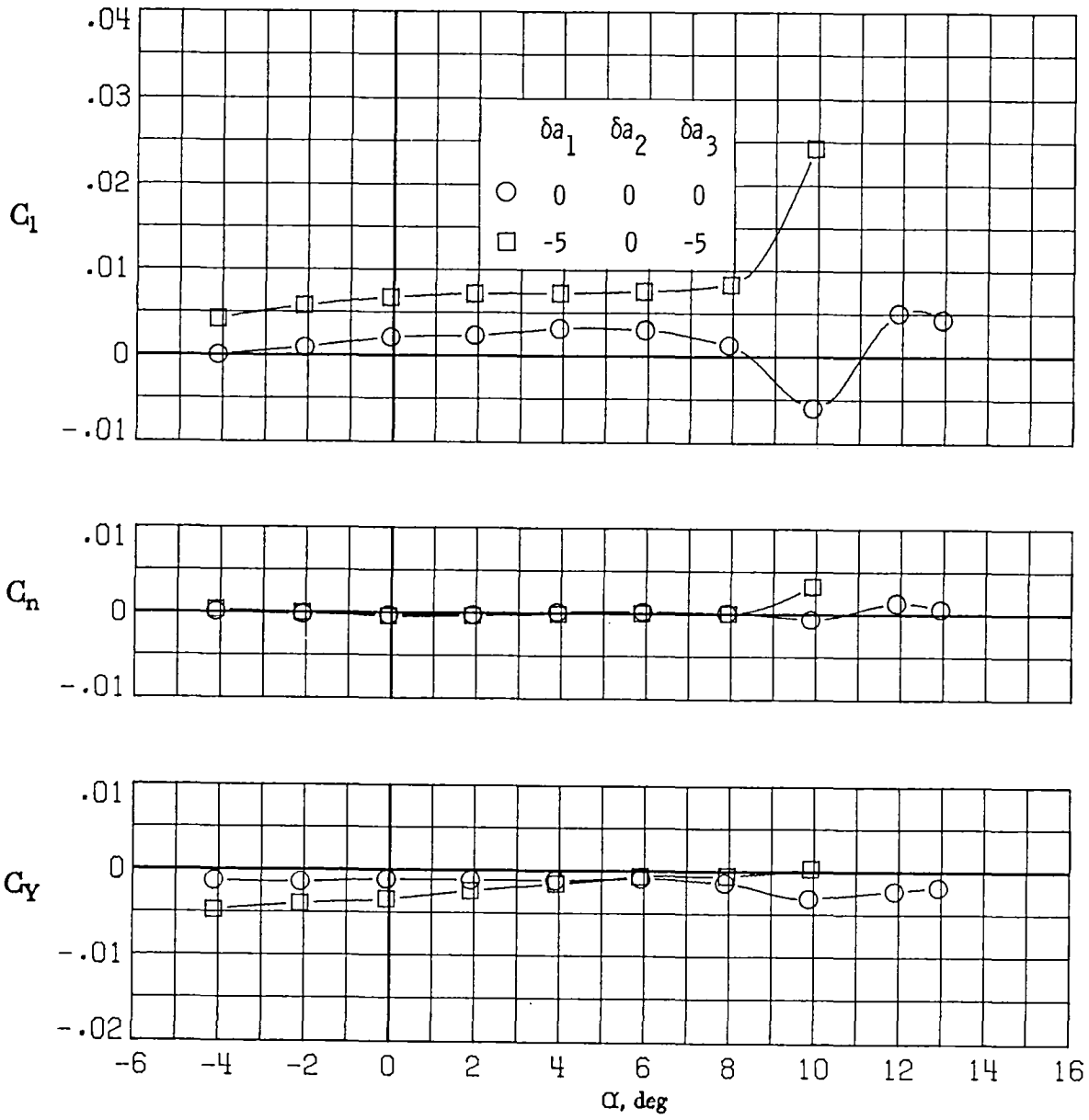

(b) $M_\infty = 0.60$.

Figure 42.- Continued.

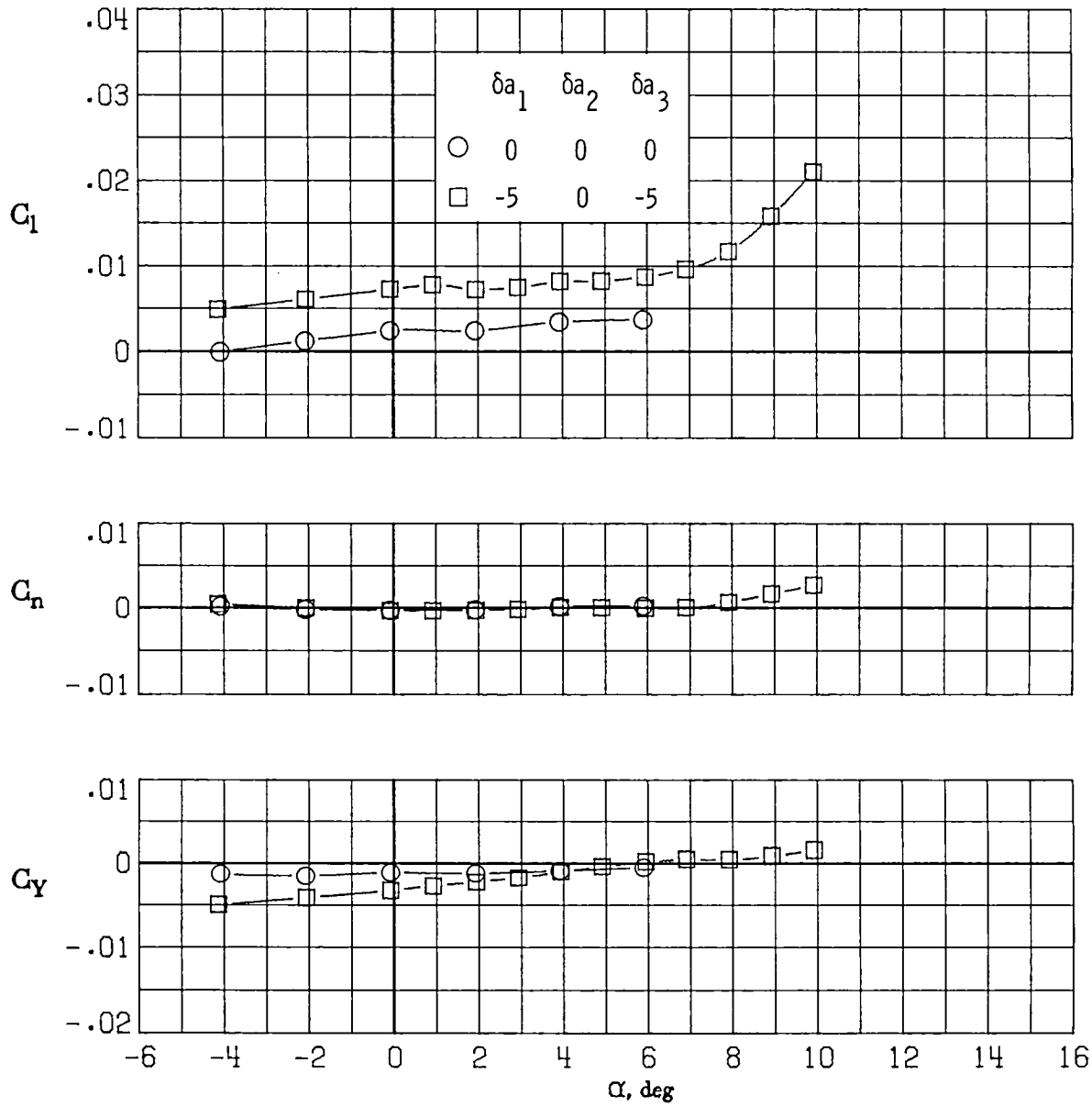

(c) $M_\infty = 0.70$.

Figure 42.- Continued.

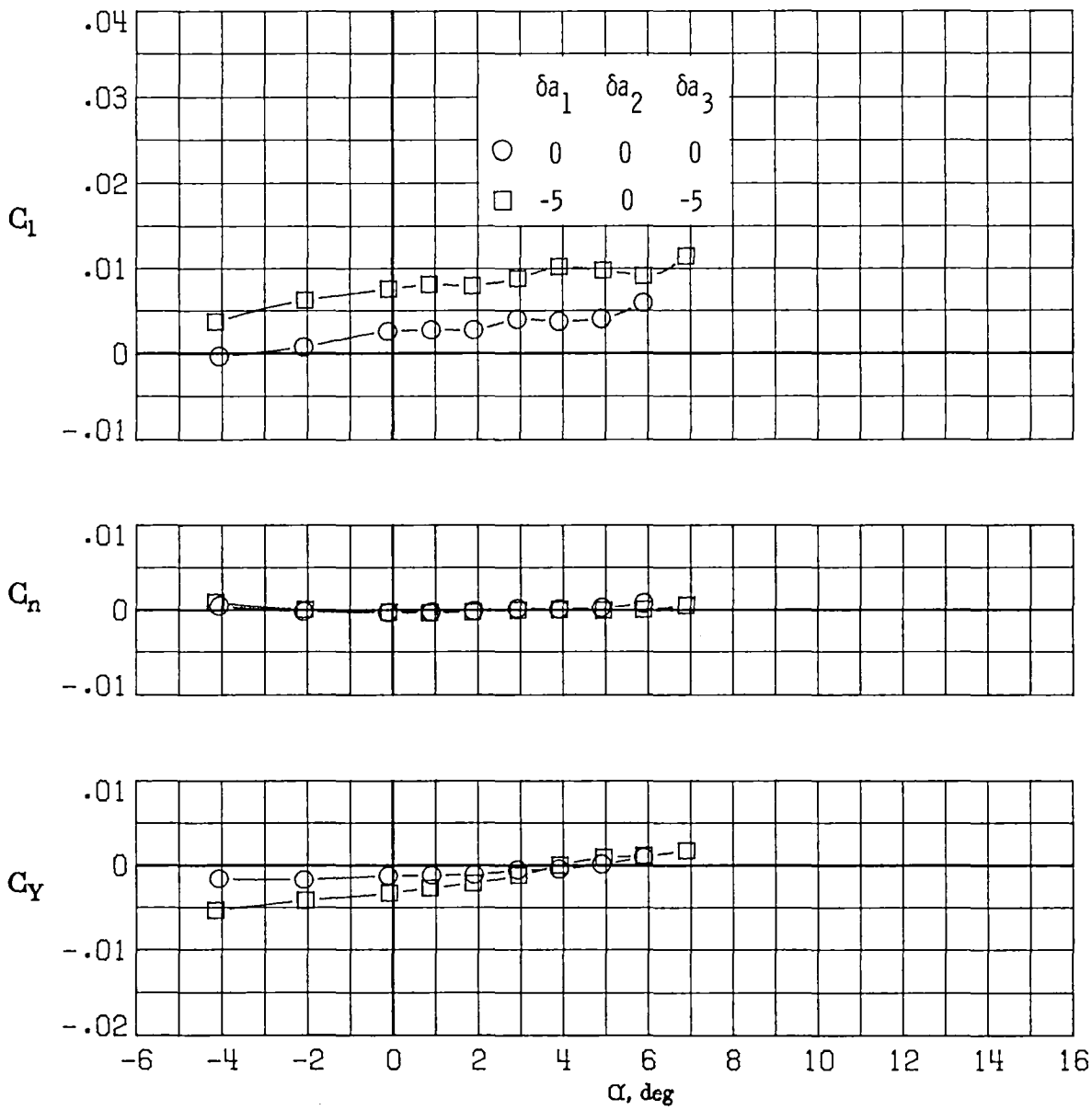

(d) $M_\infty = 0.77$.

Figure 42.- Continued.

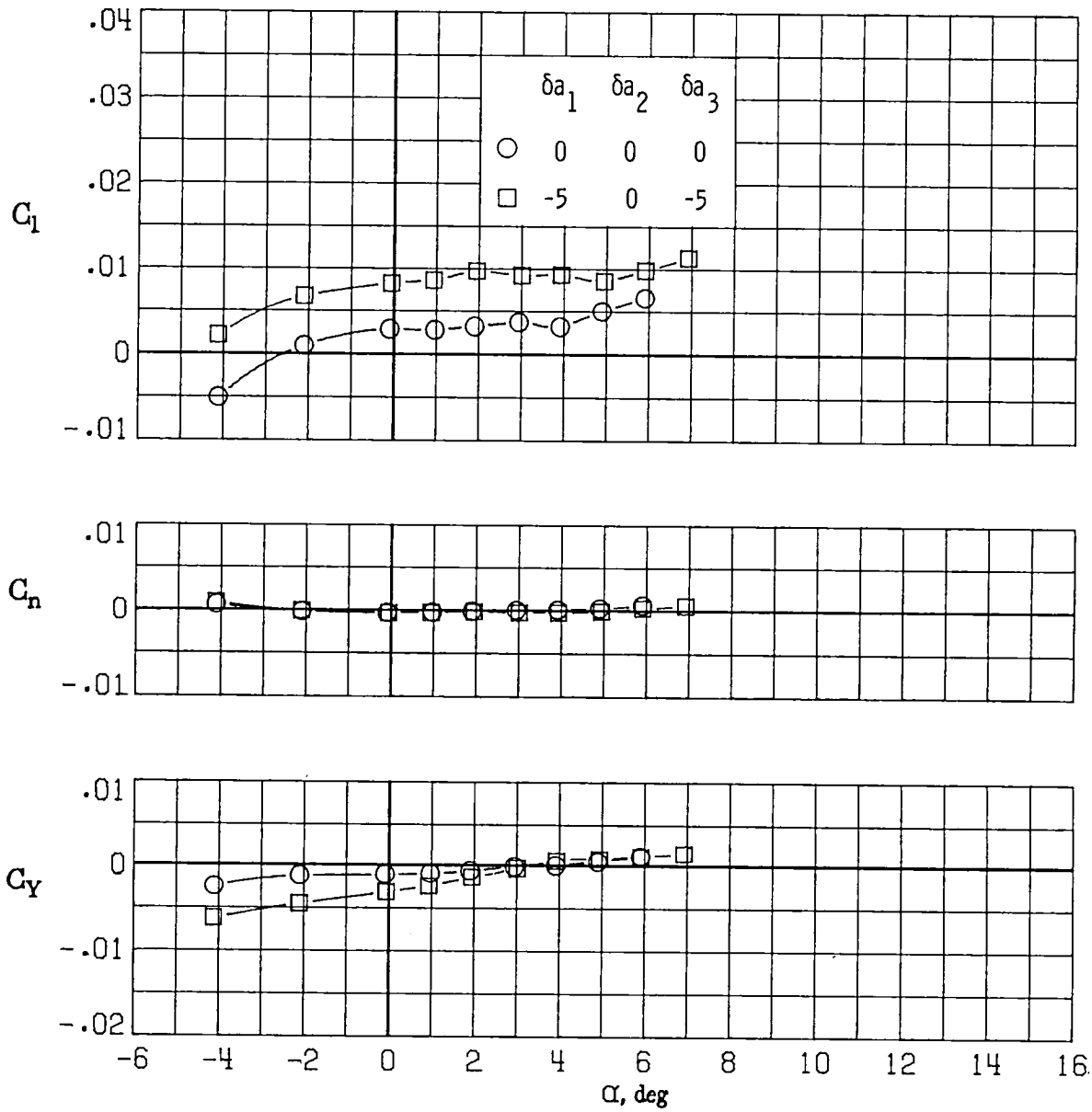

(e) $M_\infty = 0.81$.

Figure 42.- Continued.

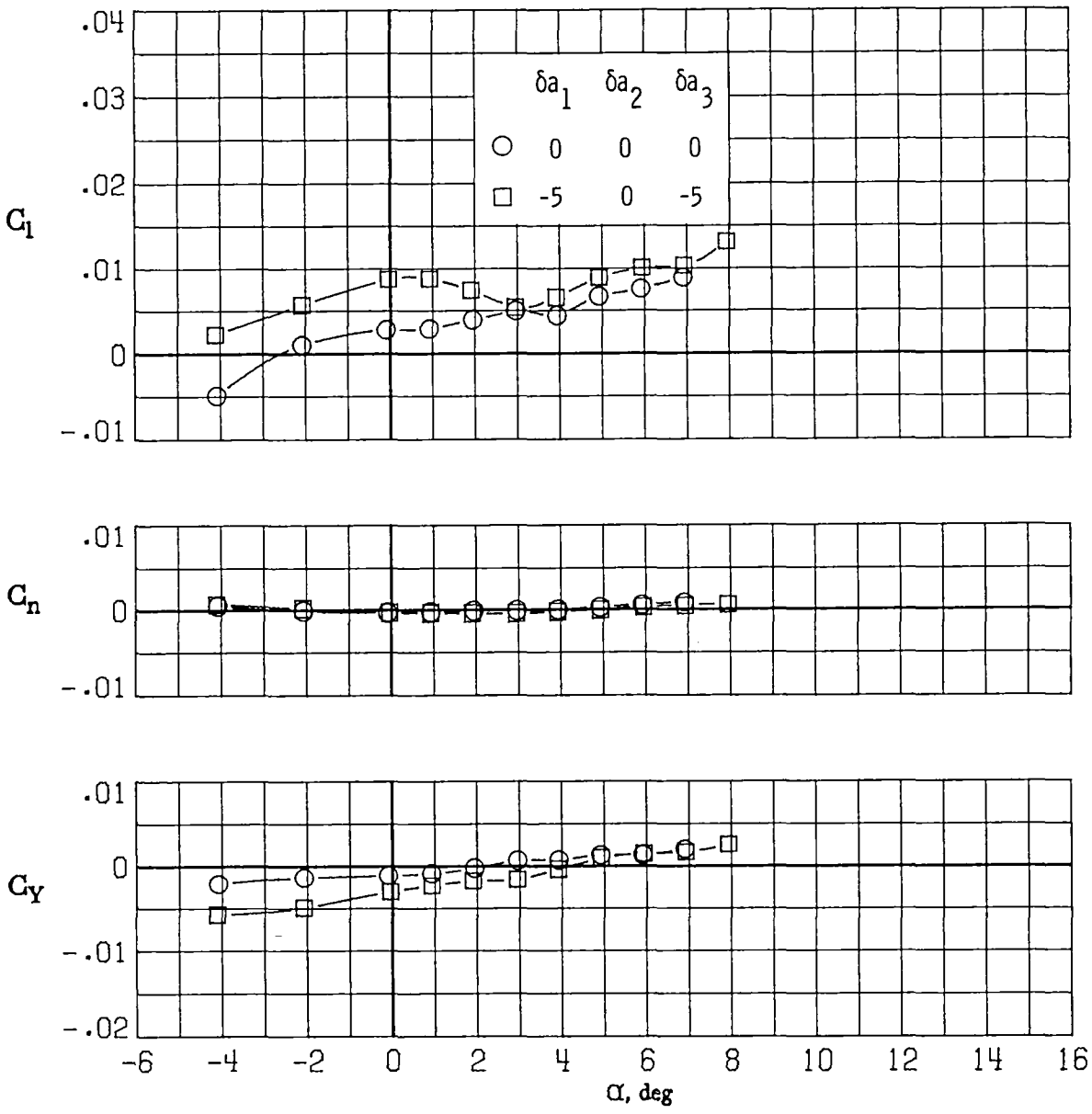

(f) $M_\infty = 0.84$.

Figure 42.- Continued.

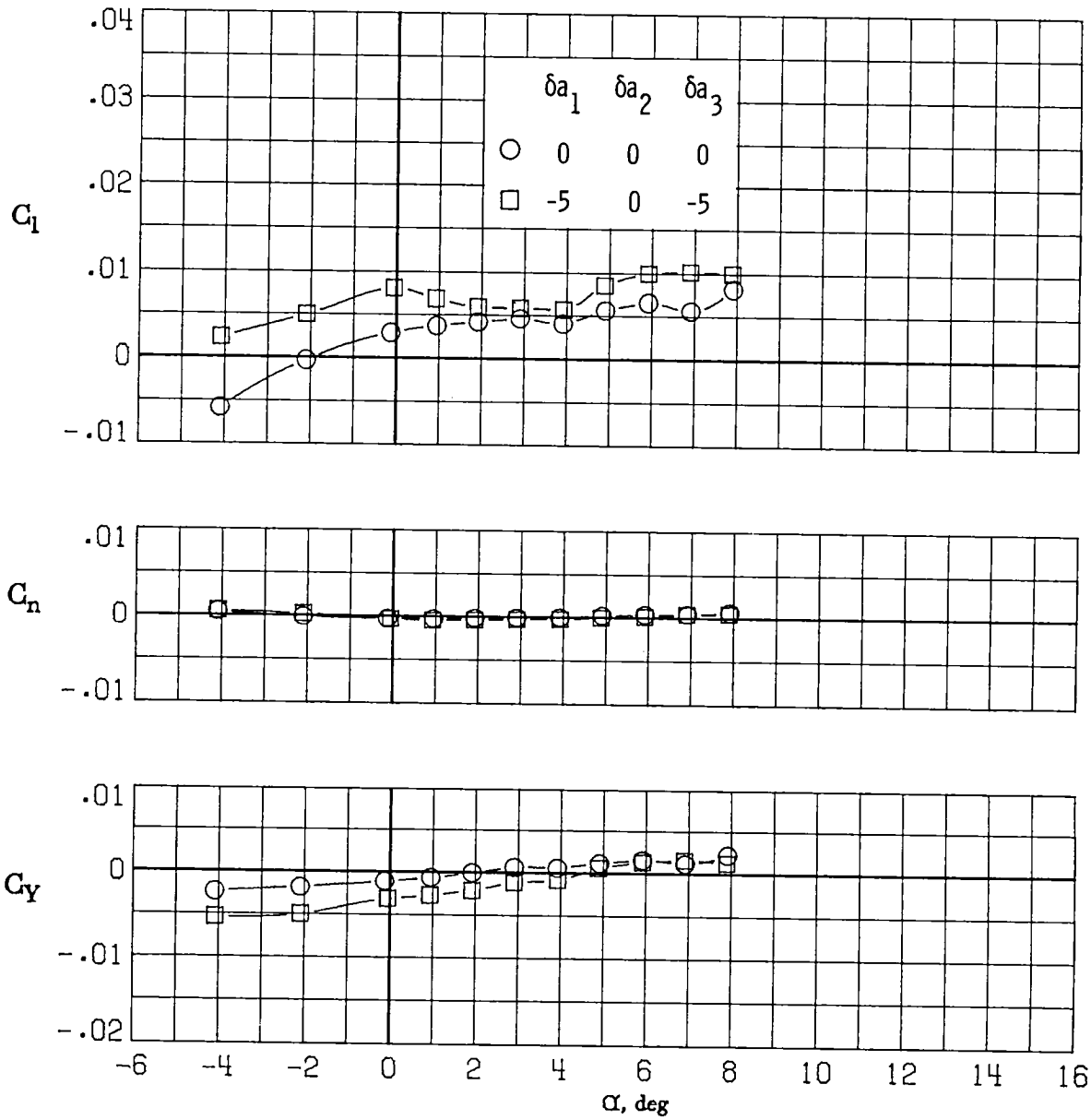

(g) $M_\infty = 0.86$.

Figure 42.- Concluded.

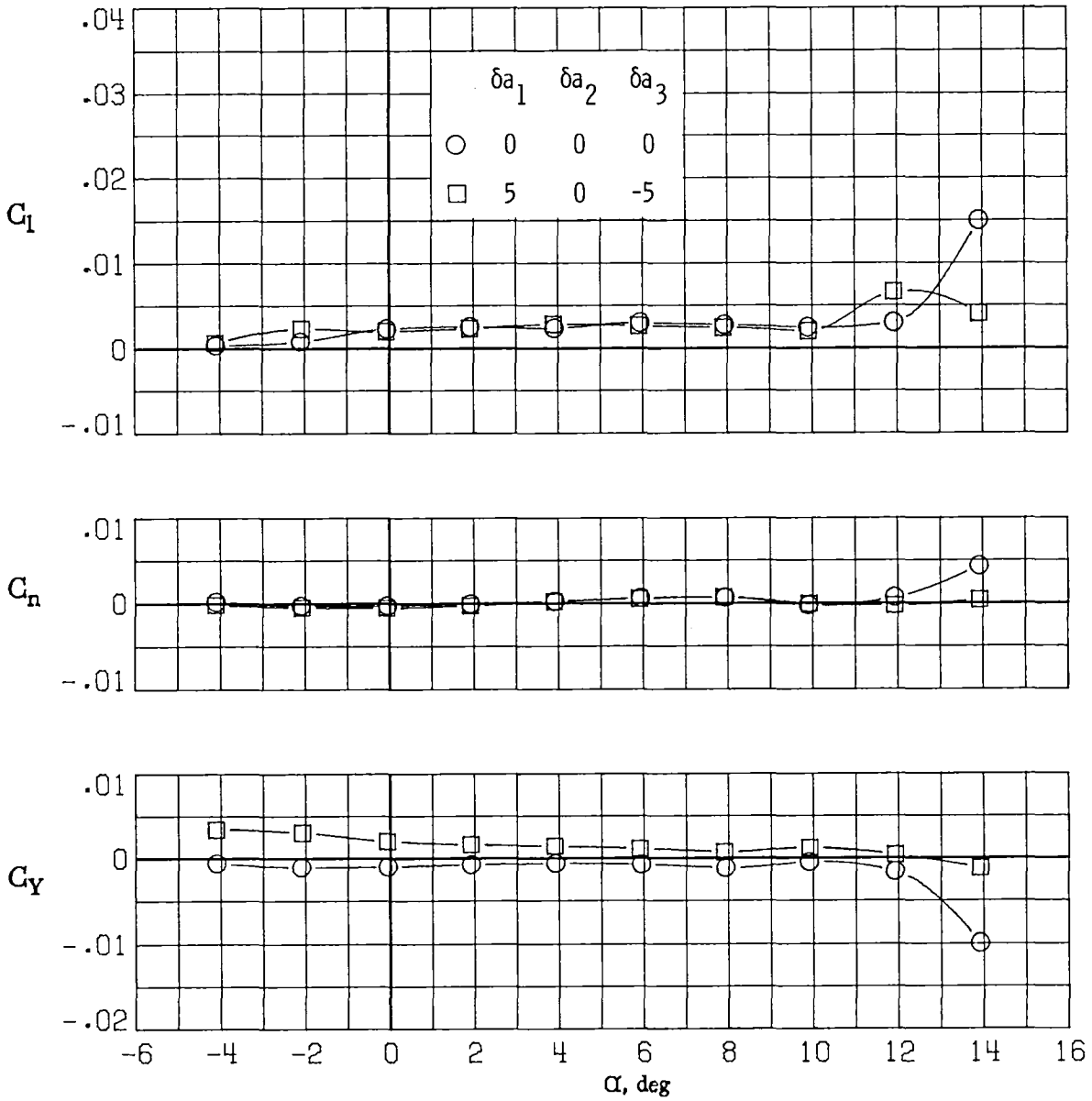

(a) $M_\infty = 0.30$.

Figure 43.- Variation of rolling-moment, yawing-moment, and side-force coefficients with angle of attack for $\delta a_1 = 5°$, $\delta a_2 = 0°$, $\delta a_3 = -5°$.

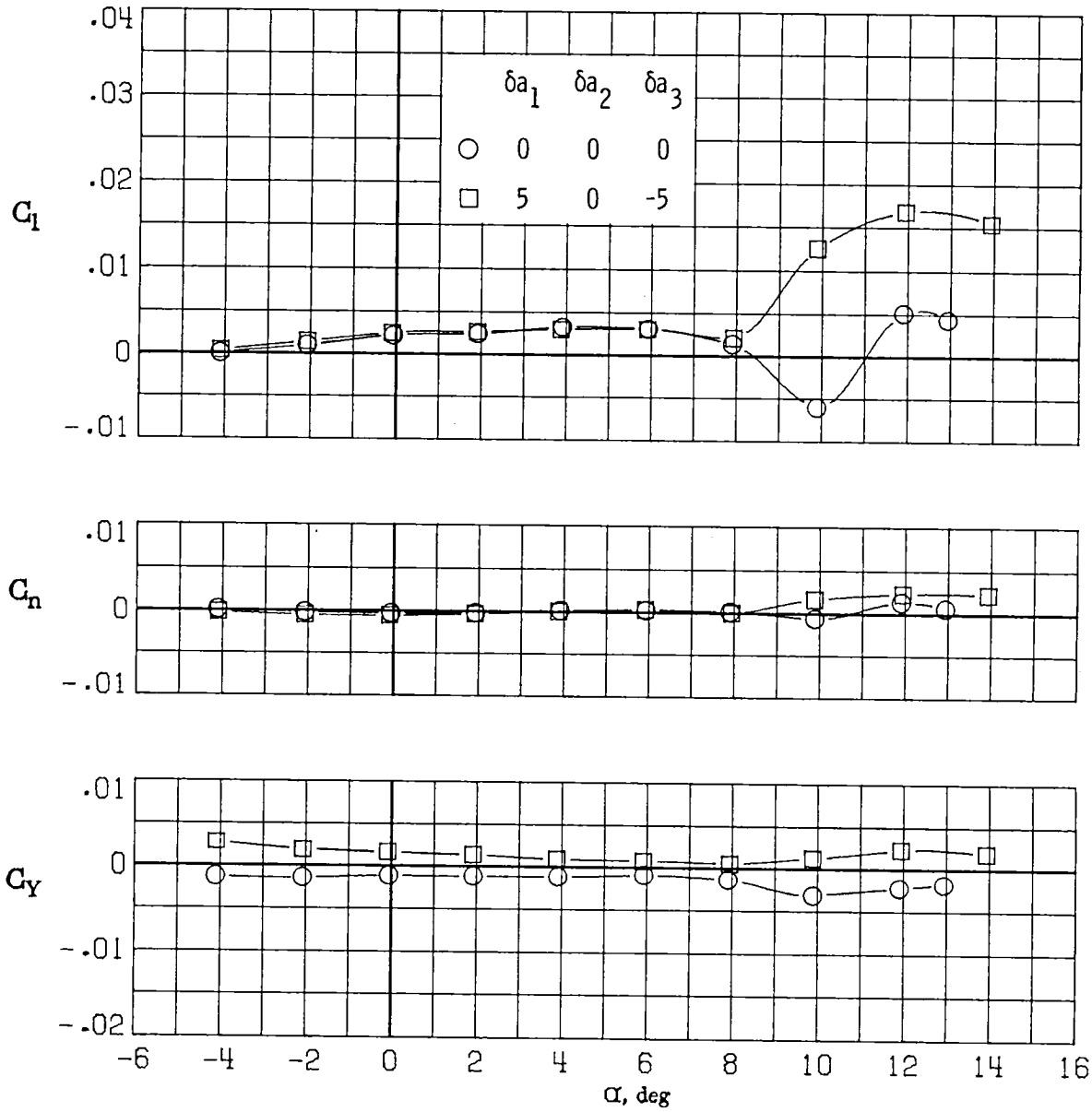

(b) $M_\infty = 0.60$.

Figure 43.- Continued.

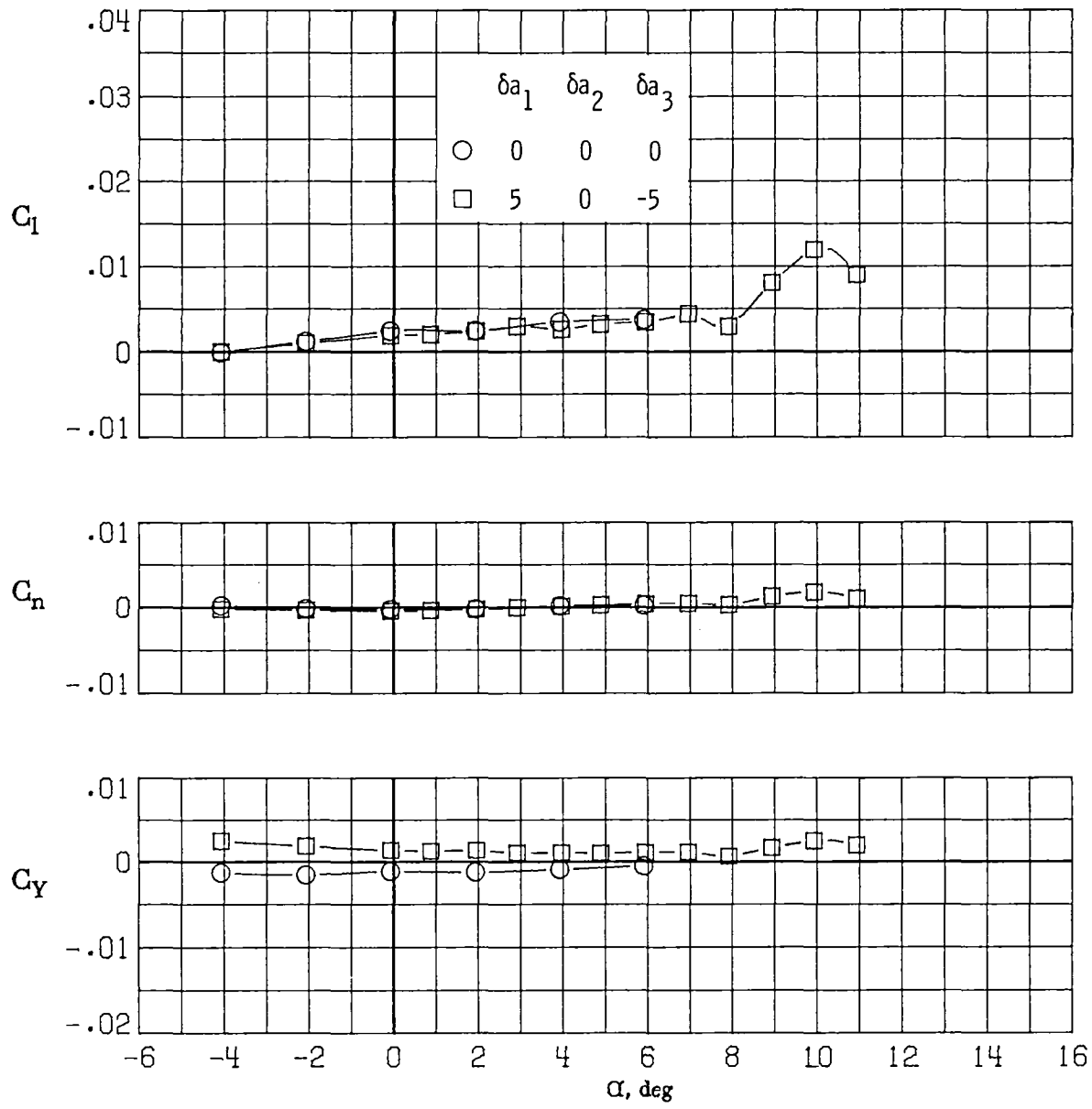

(c) $M_\infty = 0.70$.

Figure 43.- Continued.

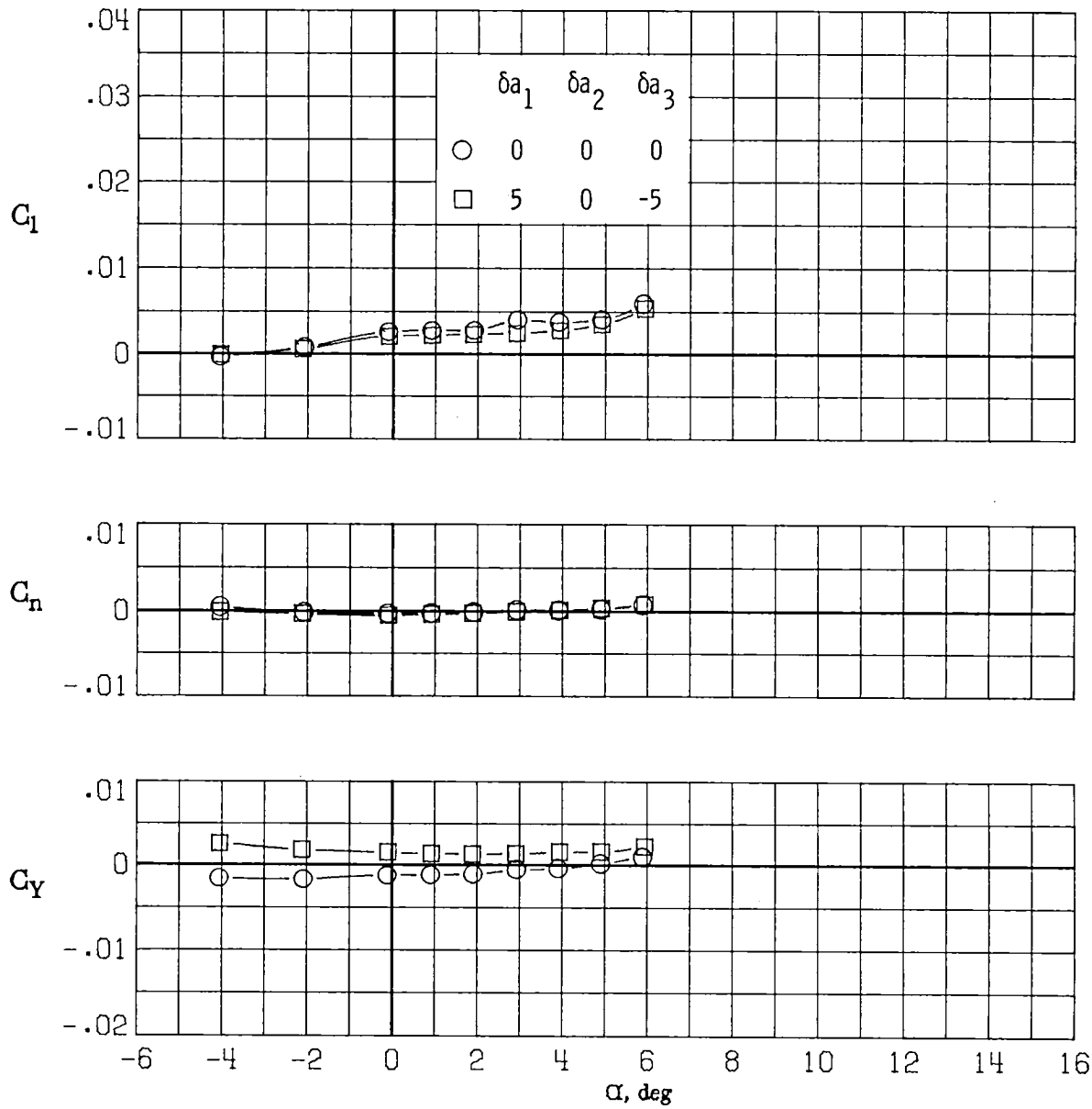

(d) $M_\infty = 0.77$.

Figure 43.- Continued.

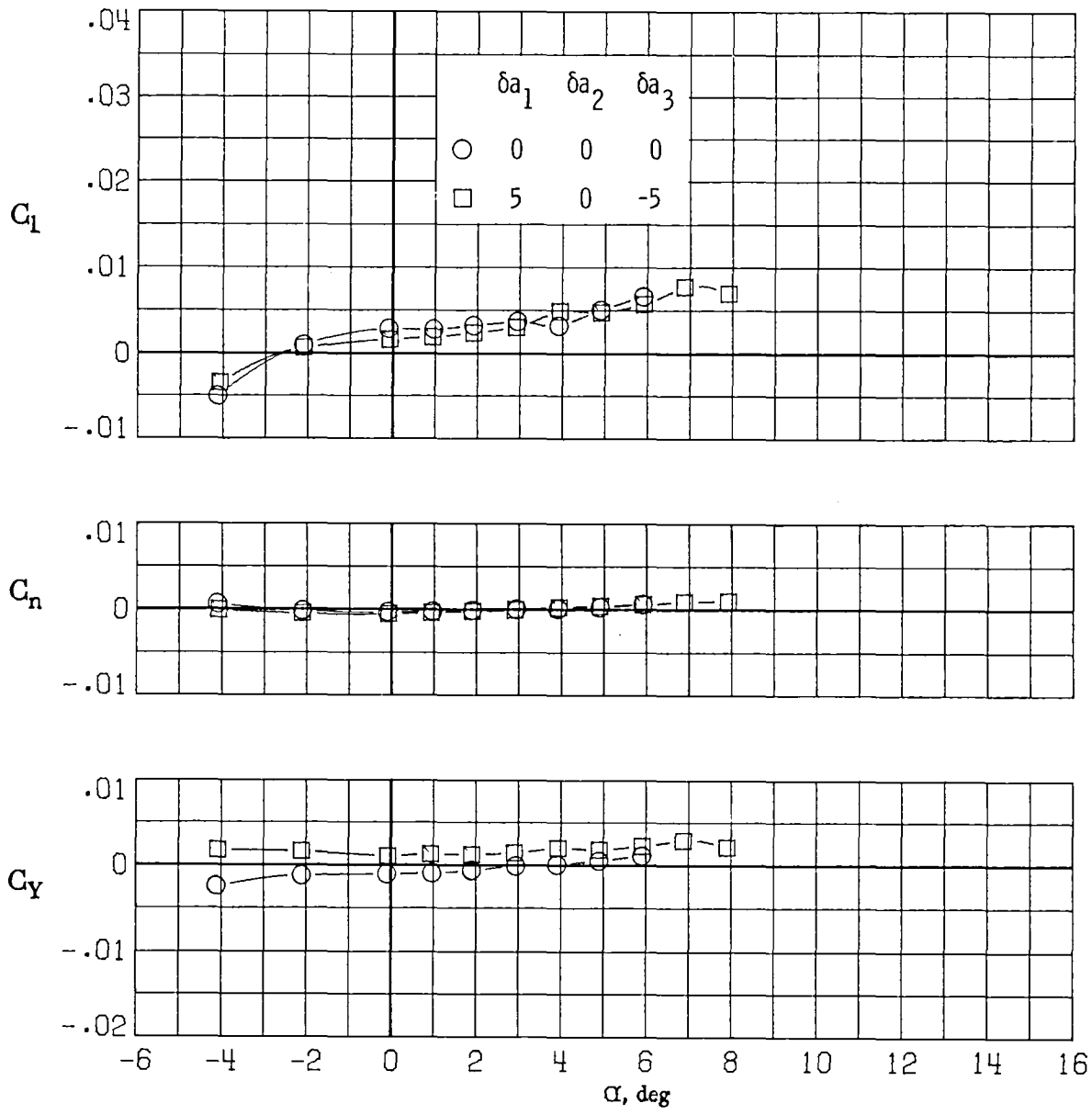

(e) $M_\infty = 0.81$.

Figure 43.- Continued.

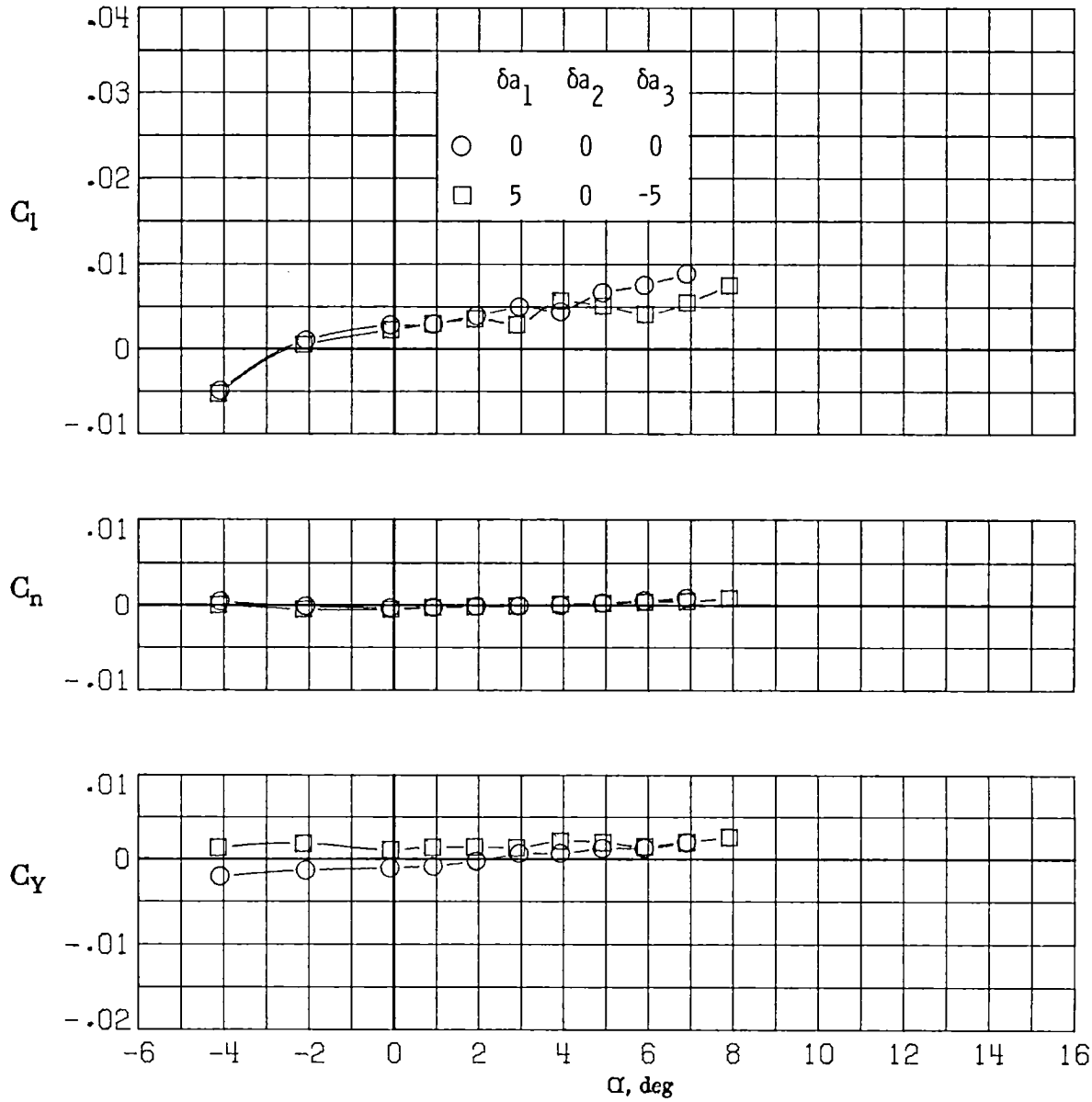

(f) $M_\infty = 0.84$.

Figure 43.- Continued.

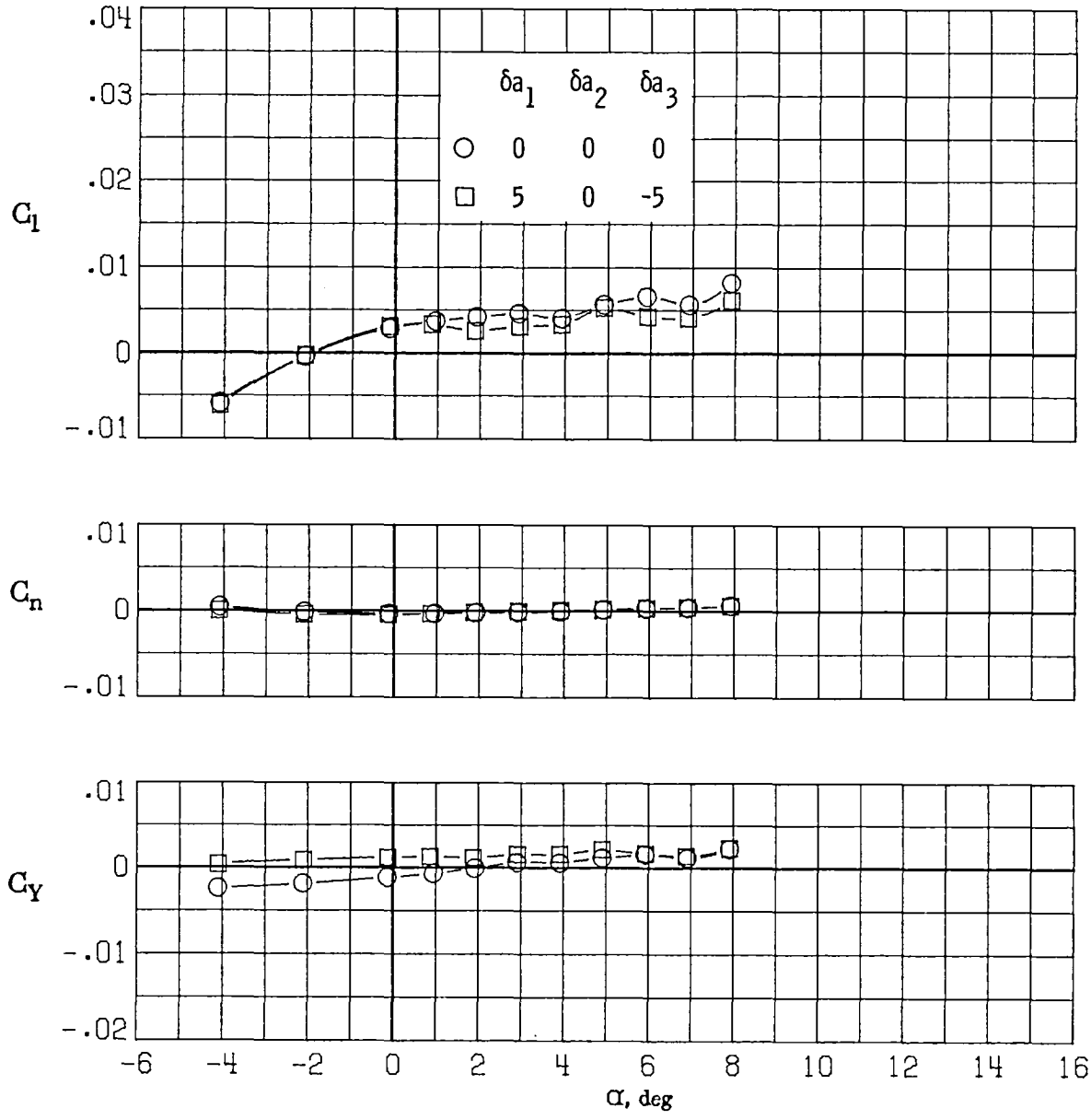

(g) $M_\infty = 0.86$.

Figure 43.- Concluded.

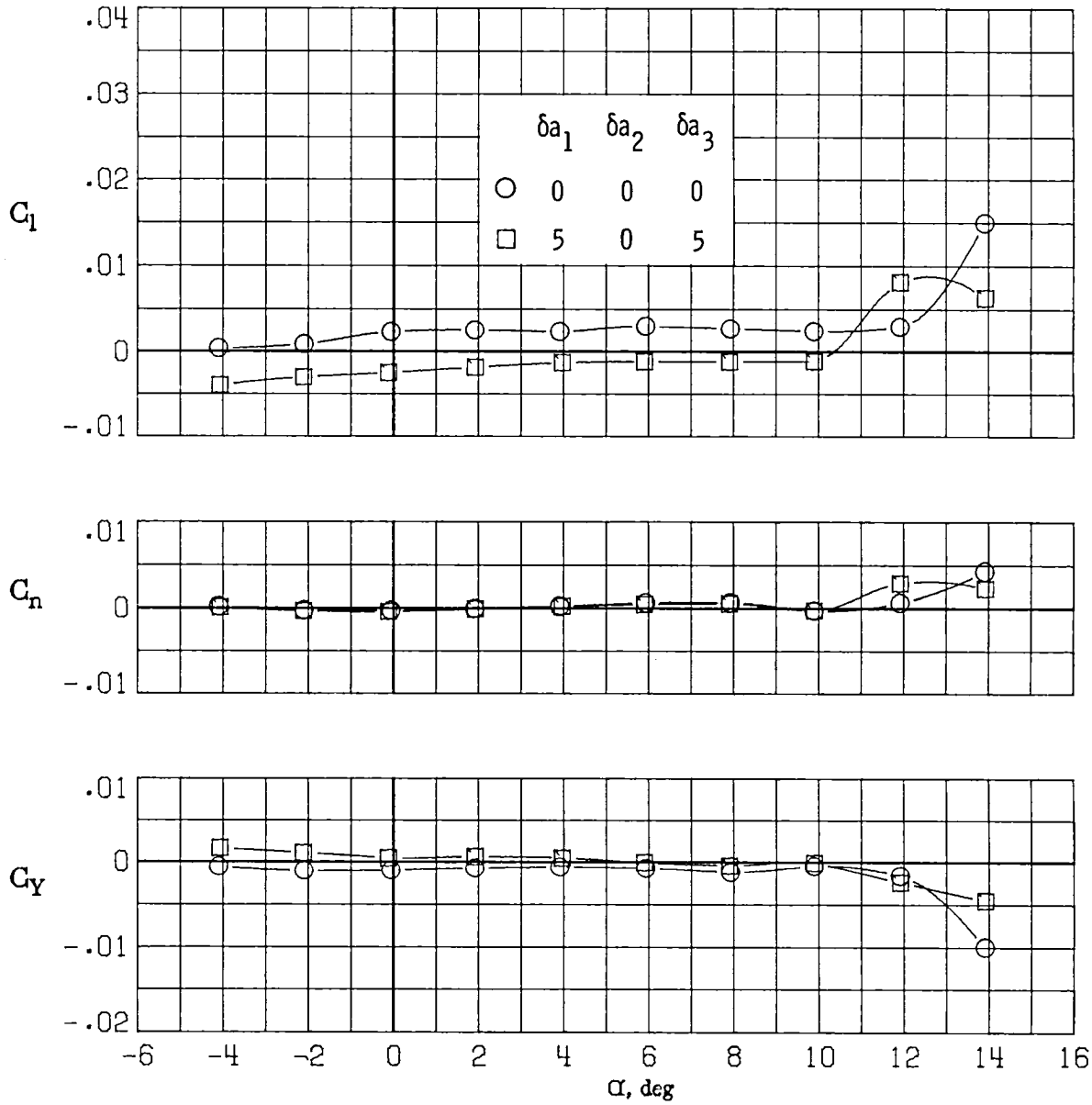

(a) $M_\infty = 0.30$.

Figure 44.- Variation of rolling-moment, yawing-moment, and side-force coefficients with angle of attack for $\delta a_1 = 5°$, $\delta a_2 = 0°$, $\delta a_3 = 5°$.

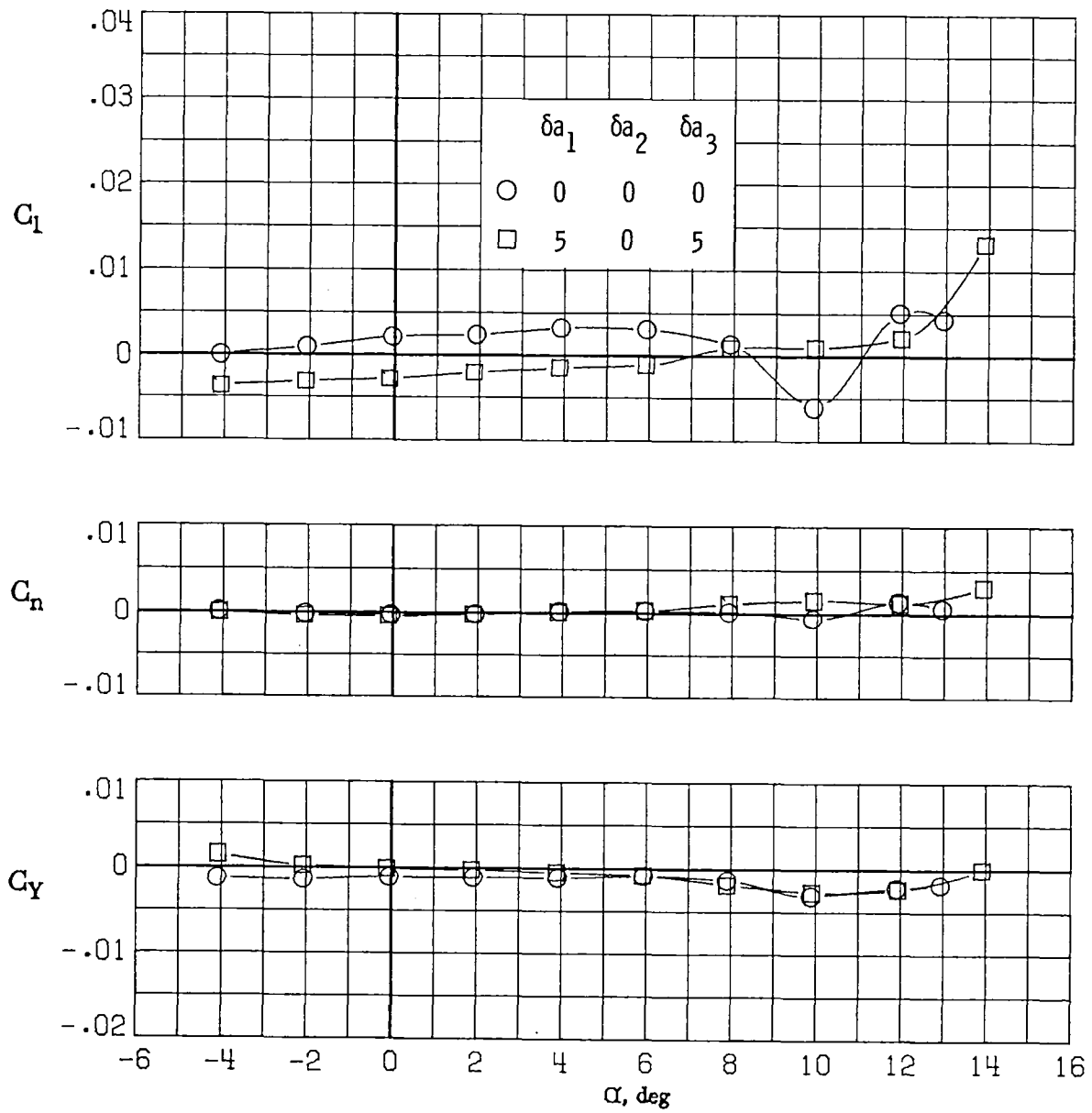

(b) $M_\infty = 0.60$.

Figure 44.- Continued.

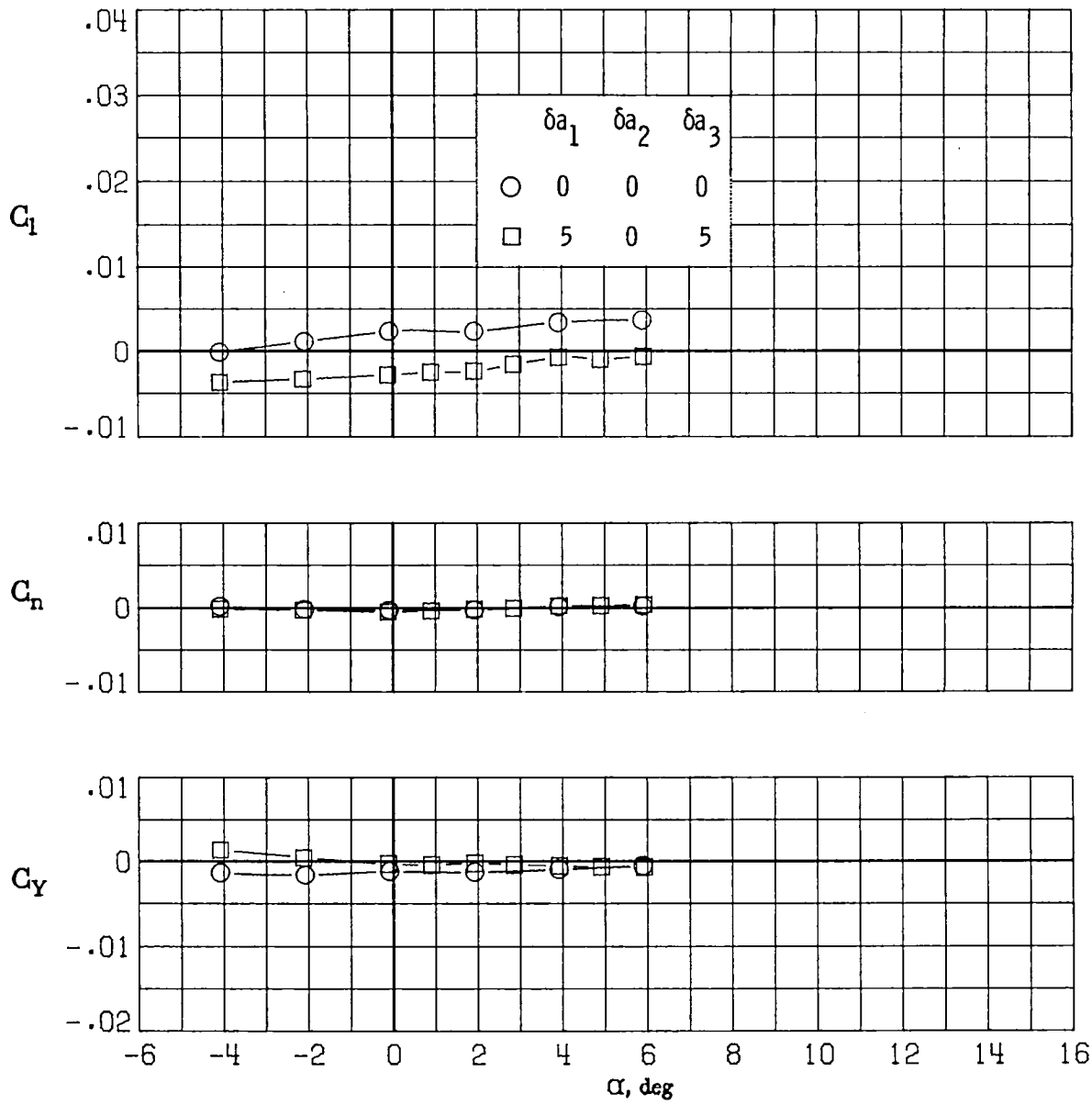

(c) $M_\infty = 0.70$.

Figure 44.- Continued.

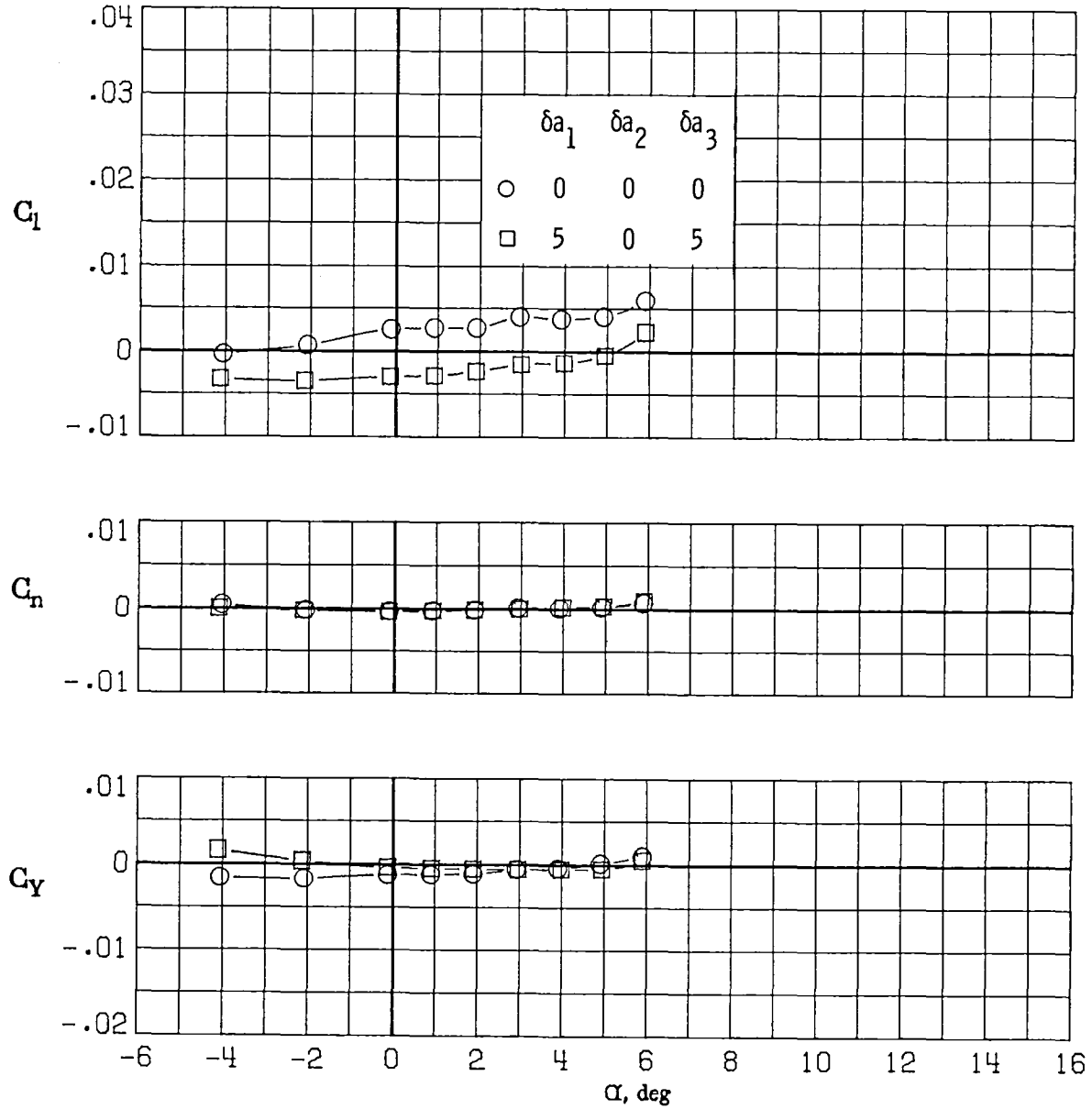

(d) $M_\infty = 0.77$.

Figure 44.- Continued.

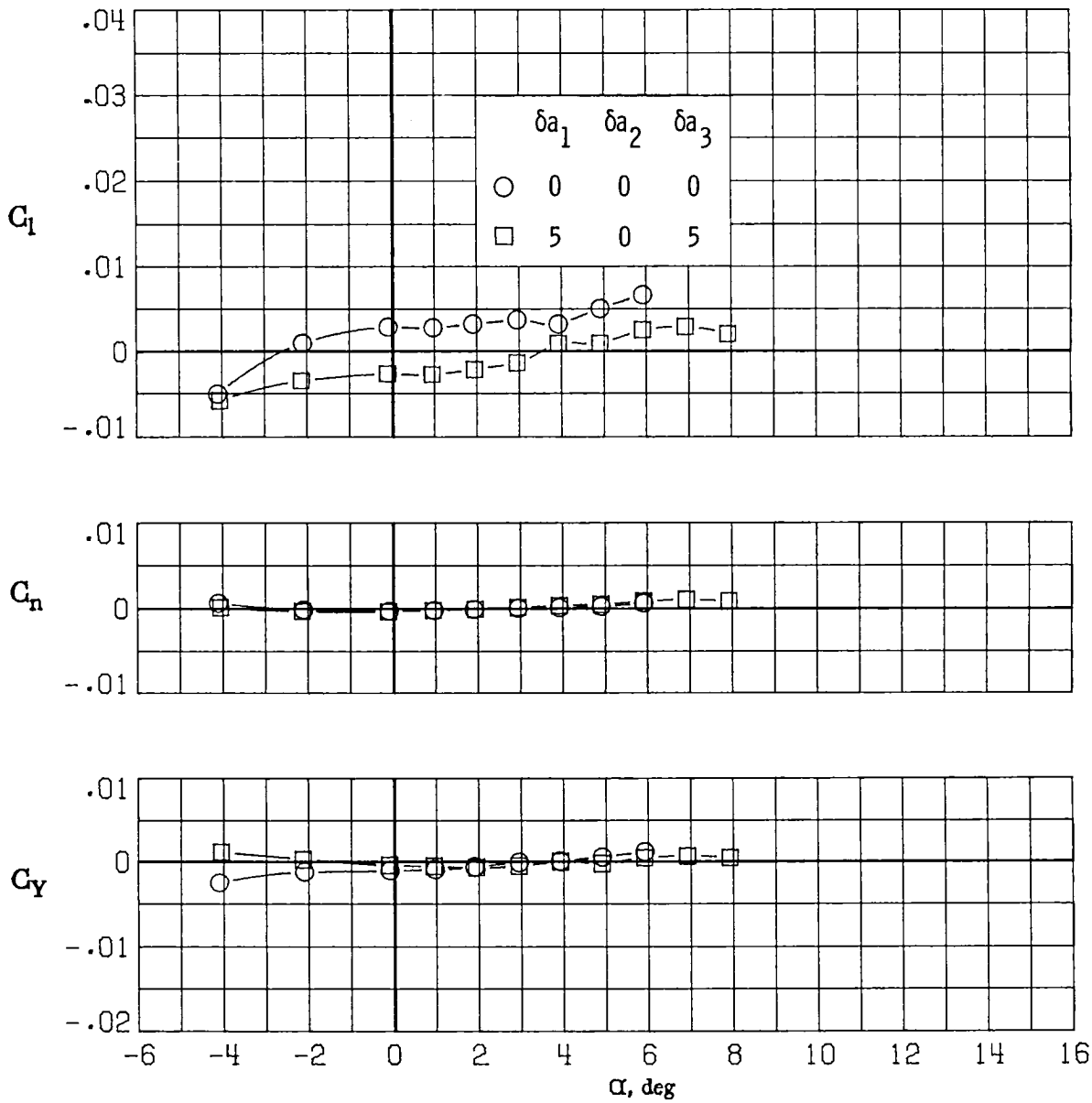

(e) $M_\infty = 0.81$.

Figure 44.- Continued.

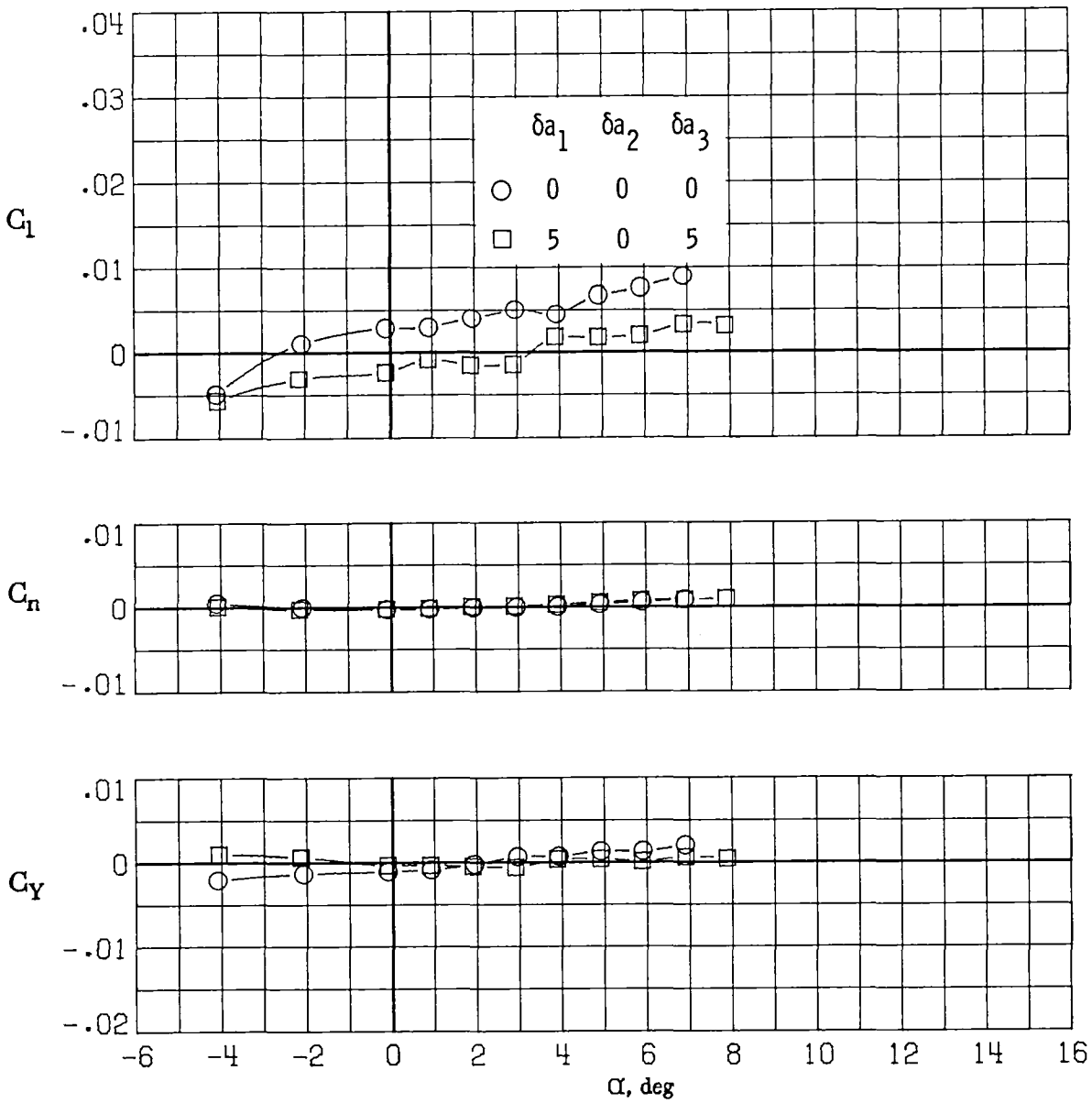

(f) $M_\infty = 0.84$.

Figure 44.- Continued.

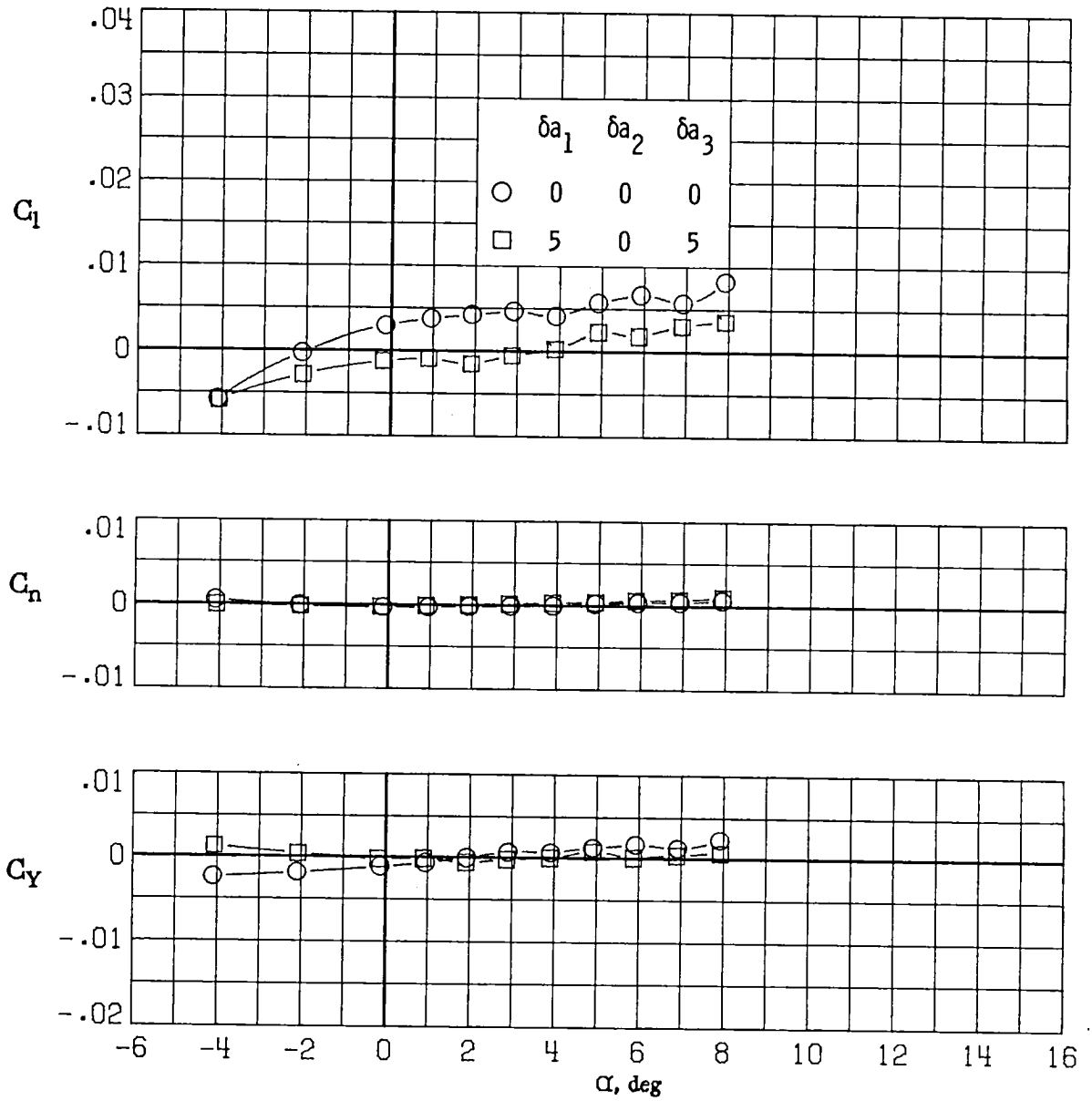

(g) $M_\infty = 0.86$.

Figure 44.- Concluded.

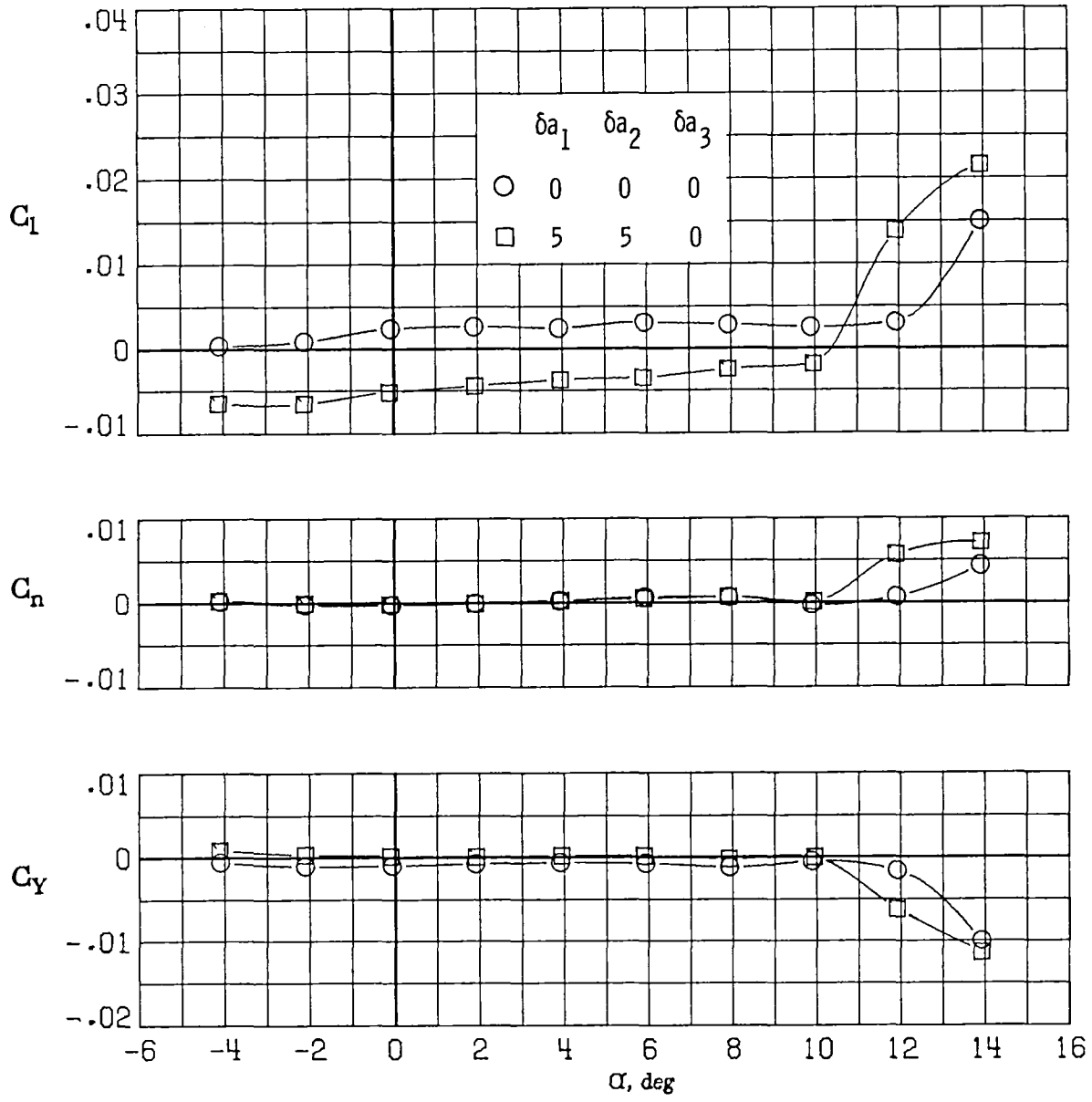

(a) $M_\infty = 0.30$.

Figure 45.- Variation of rolling-moment, yawing-moment, and side-force coefficients with angle of attack for $\delta a_1 = 5°$, $\delta a_2 = 5°$, $\delta a_3 = 0°$.

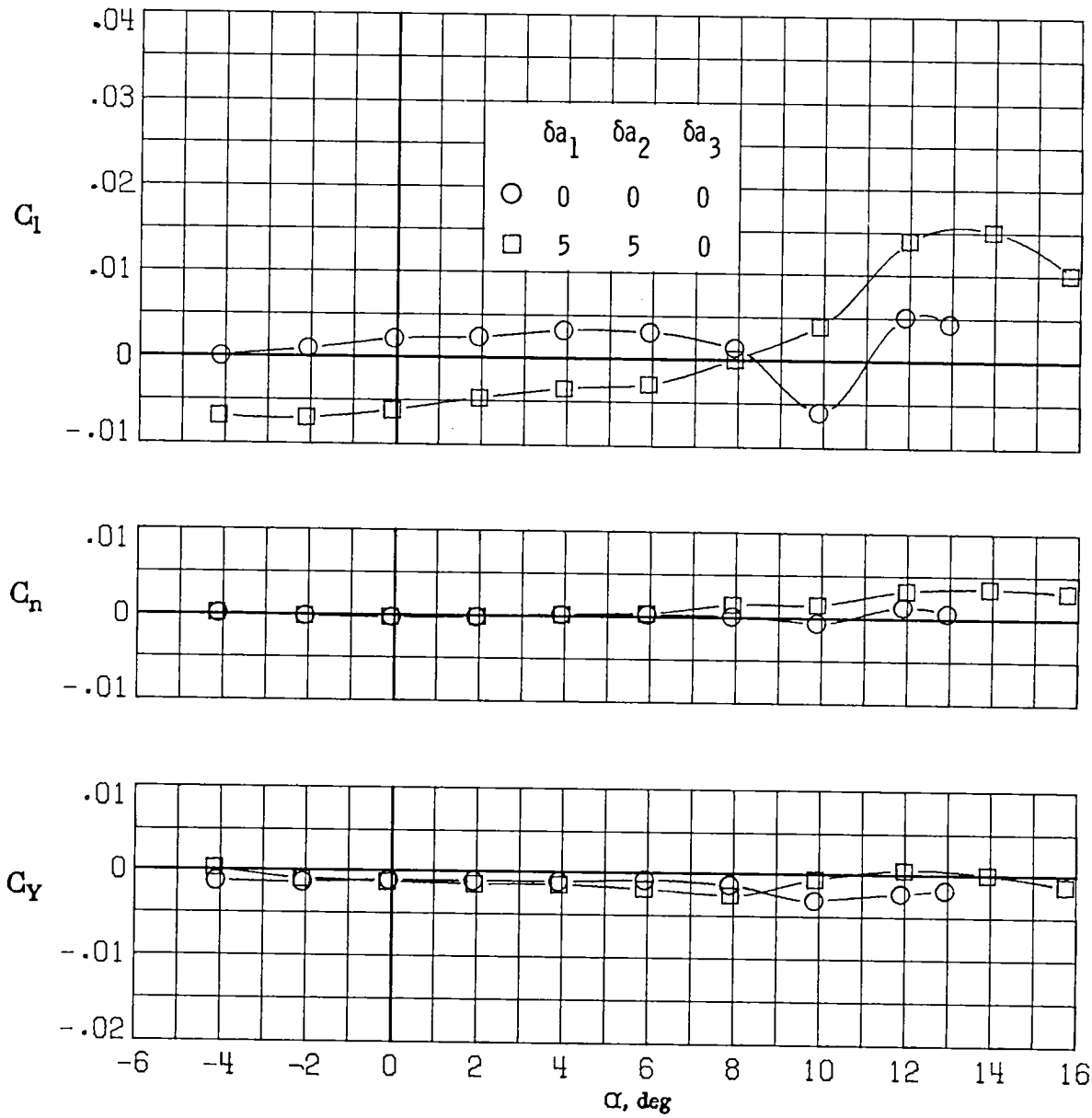

(b) $M_\infty = 0.60$.

Figure 45- Continued.

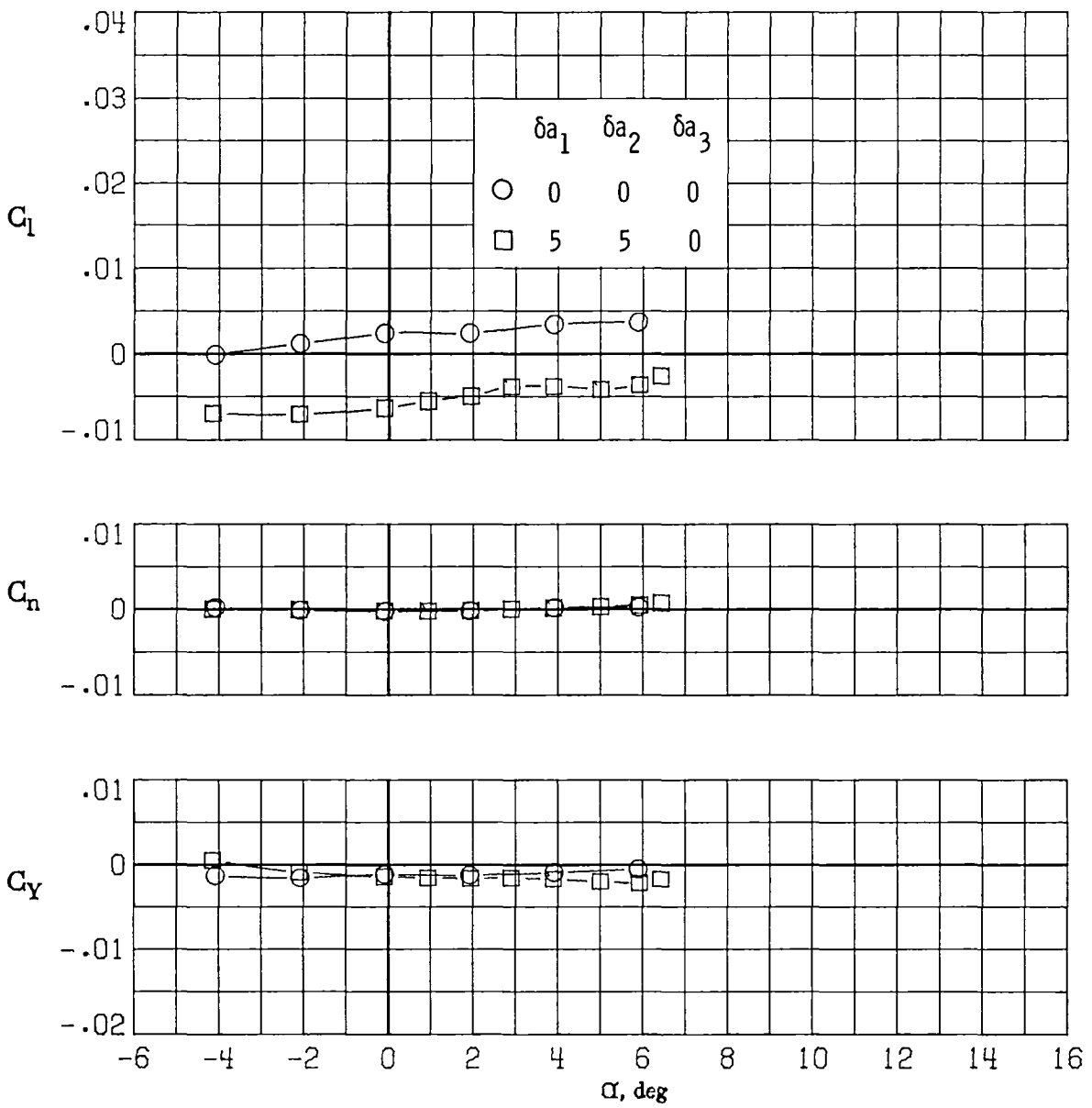

(c) $M_\infty = 0.70$.

Figure 45.- Continued.

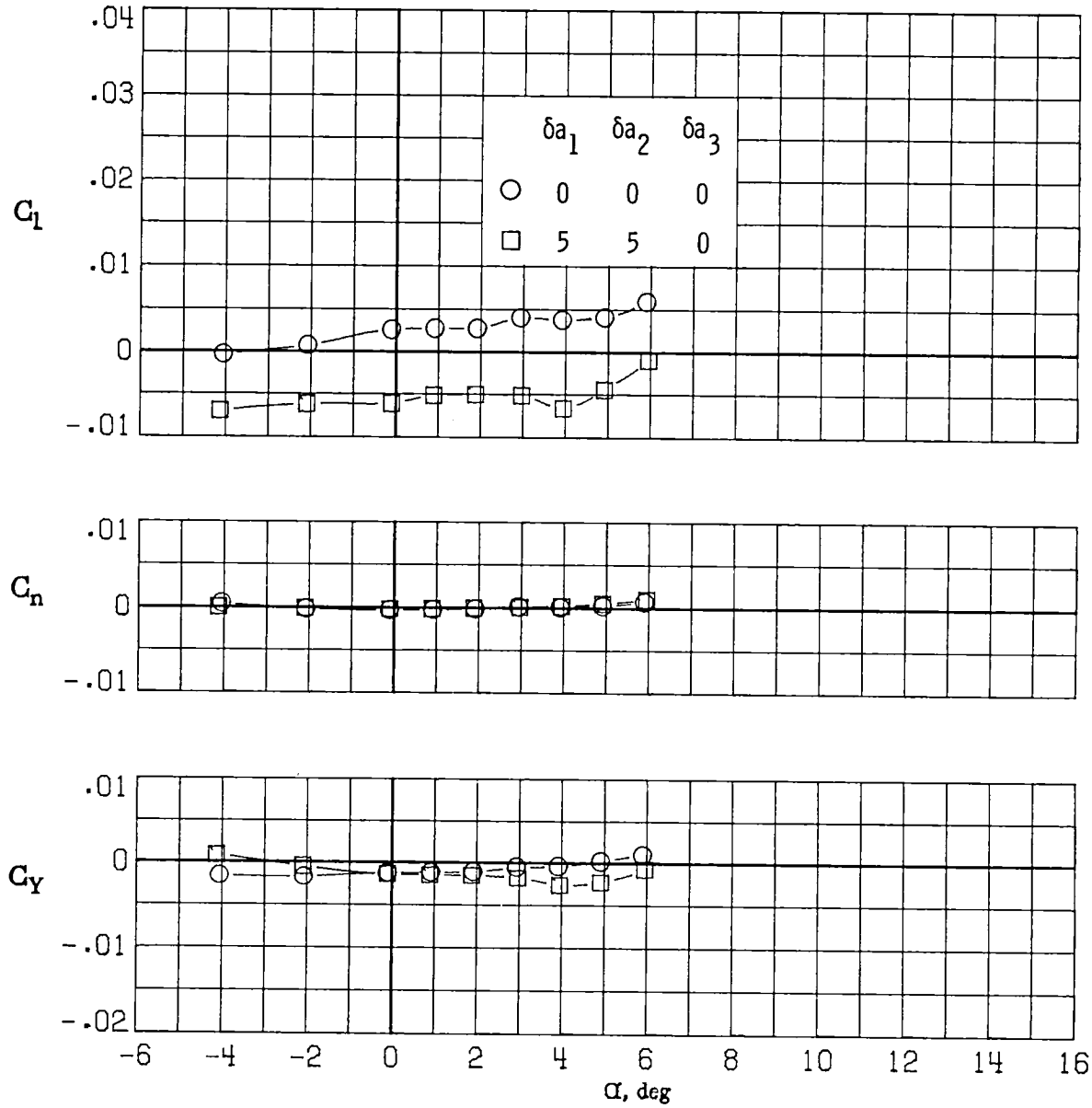

(d) $M_\infty = 0.77$.

Figure 45.- Continued.

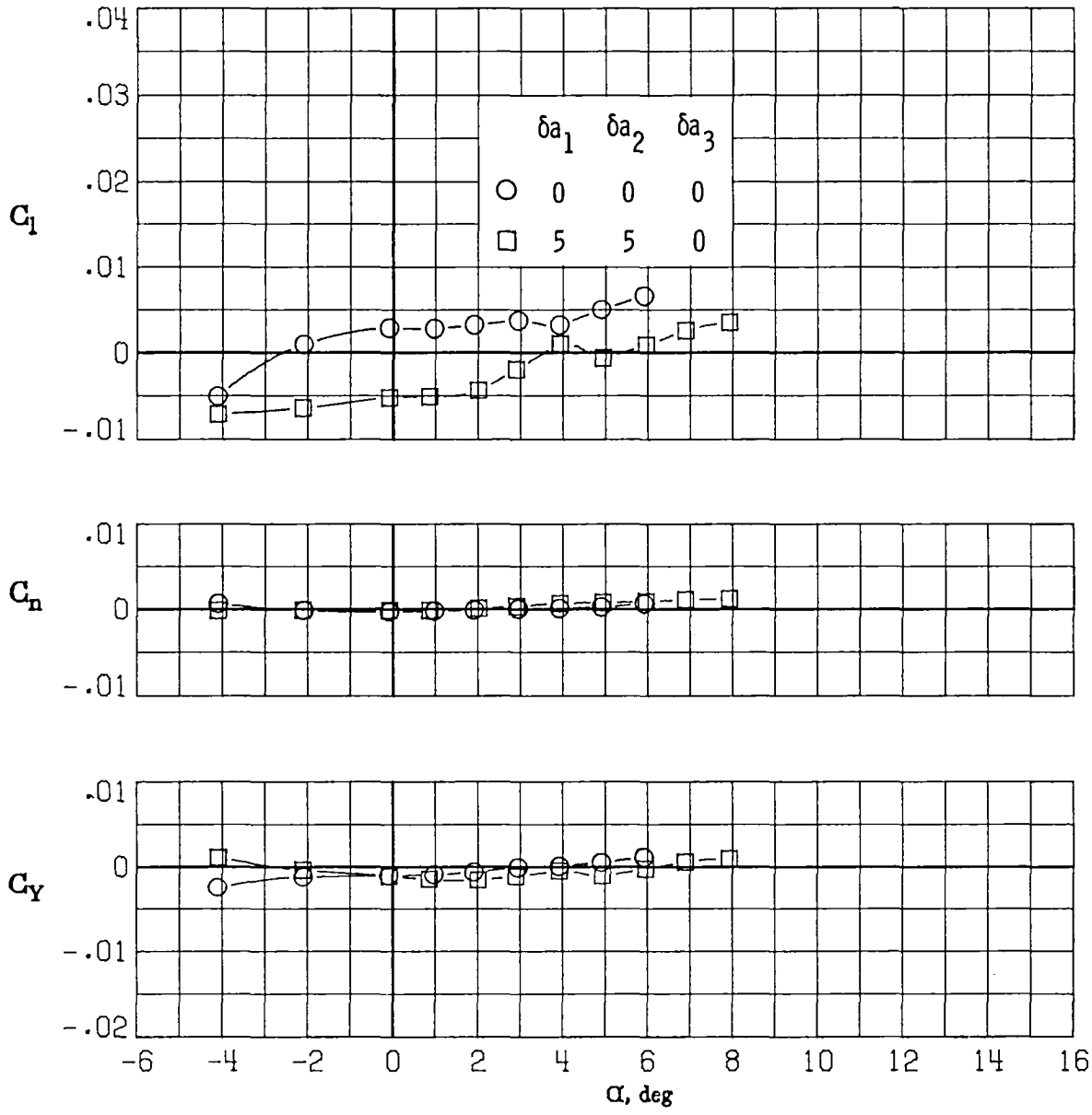

(e) $M_\infty = 0.81$.

Figure 45.- Continued.

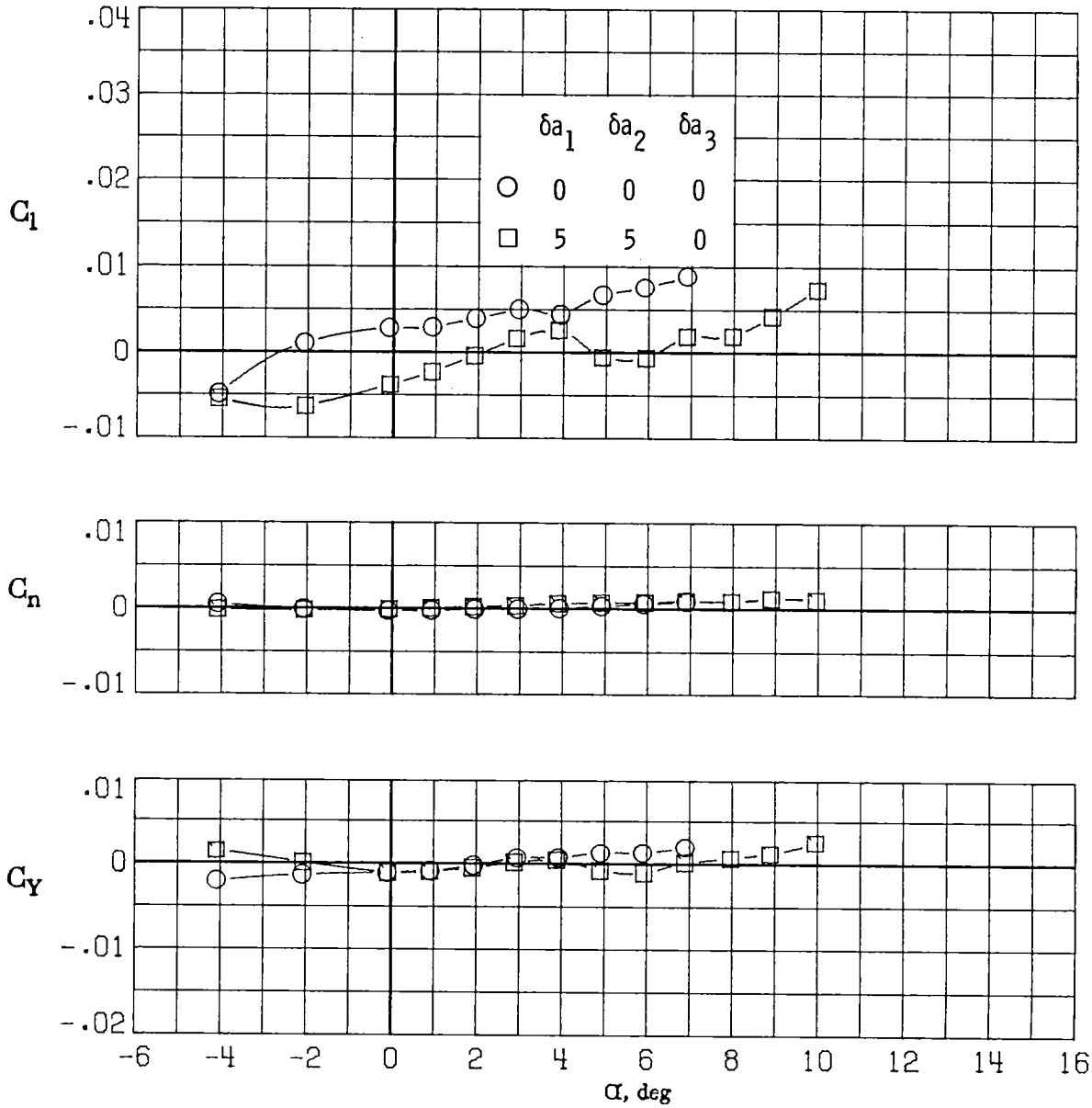

(f) $M_\infty = 0.84$.

Figure 45.- Continued.

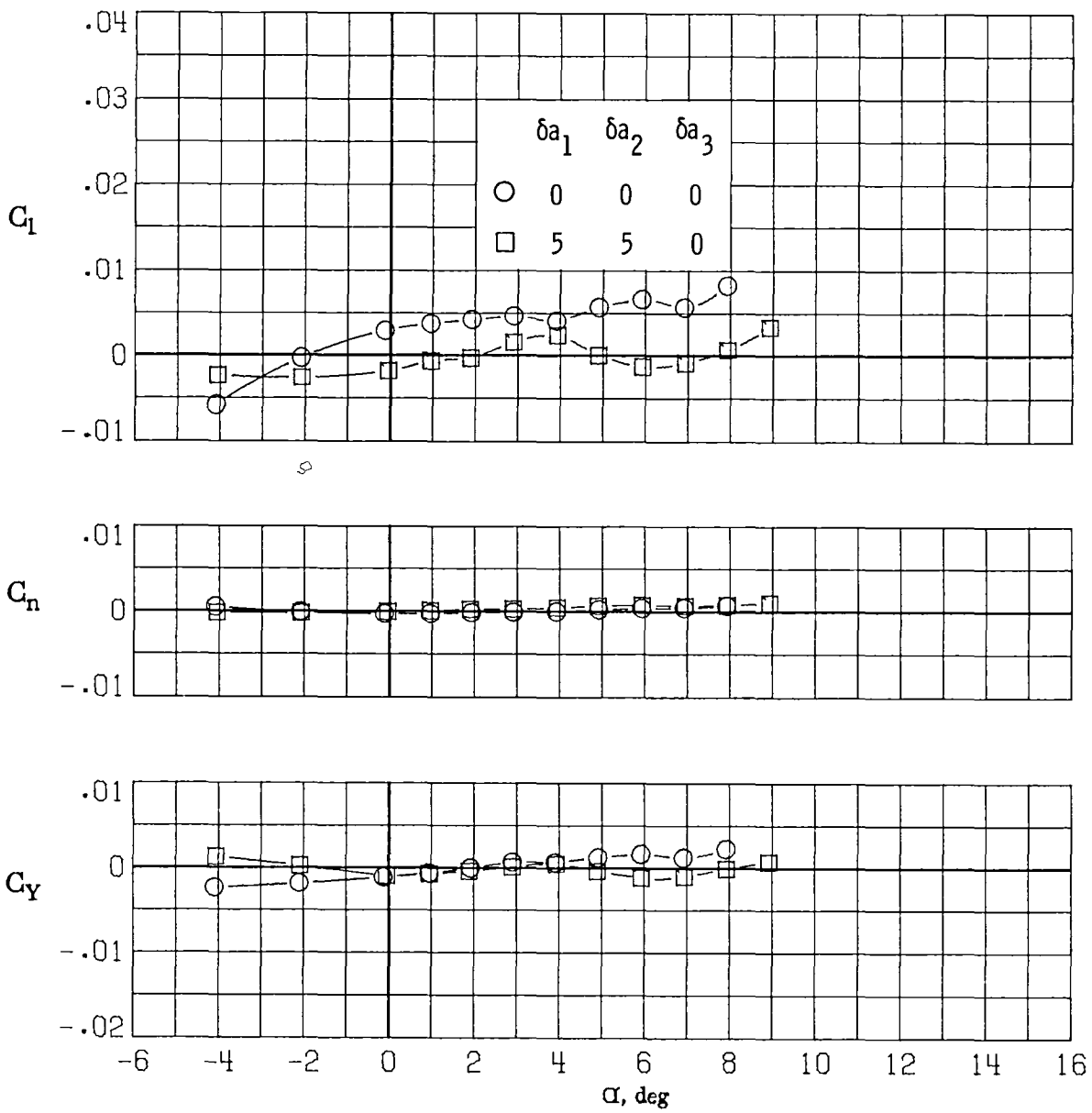

(g) $M_\infty = 0.86$.

Figure 45.- Concluded.

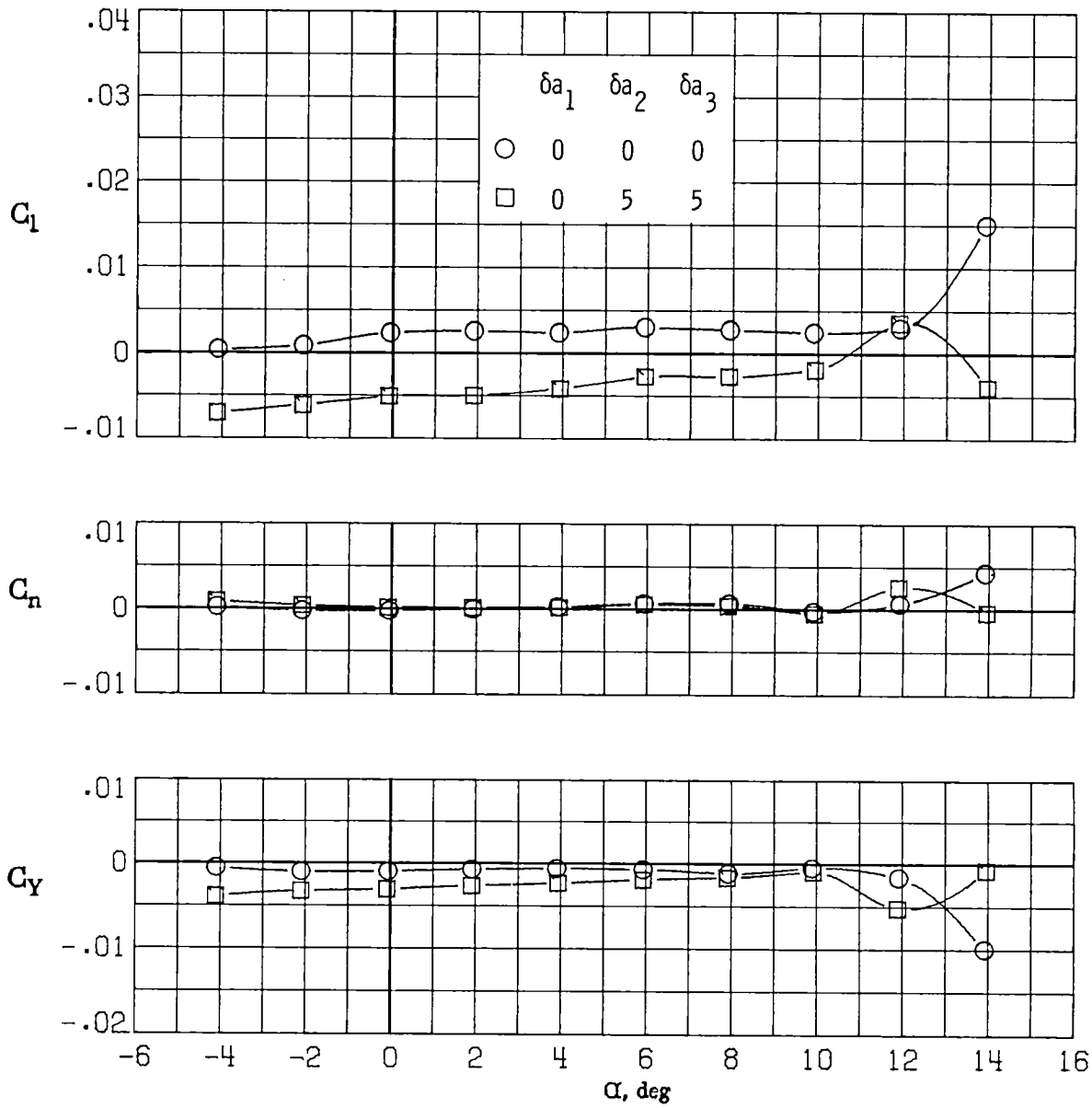

(a) $M_\infty = 0.30$.

Figure 46.- Variation of rolling-moment, yawing-moment, and side-force coefficients with angle of attack for $\delta a_1 = 0°$, $\delta a_2 = 5°$, $\delta a_3 = 5°$.

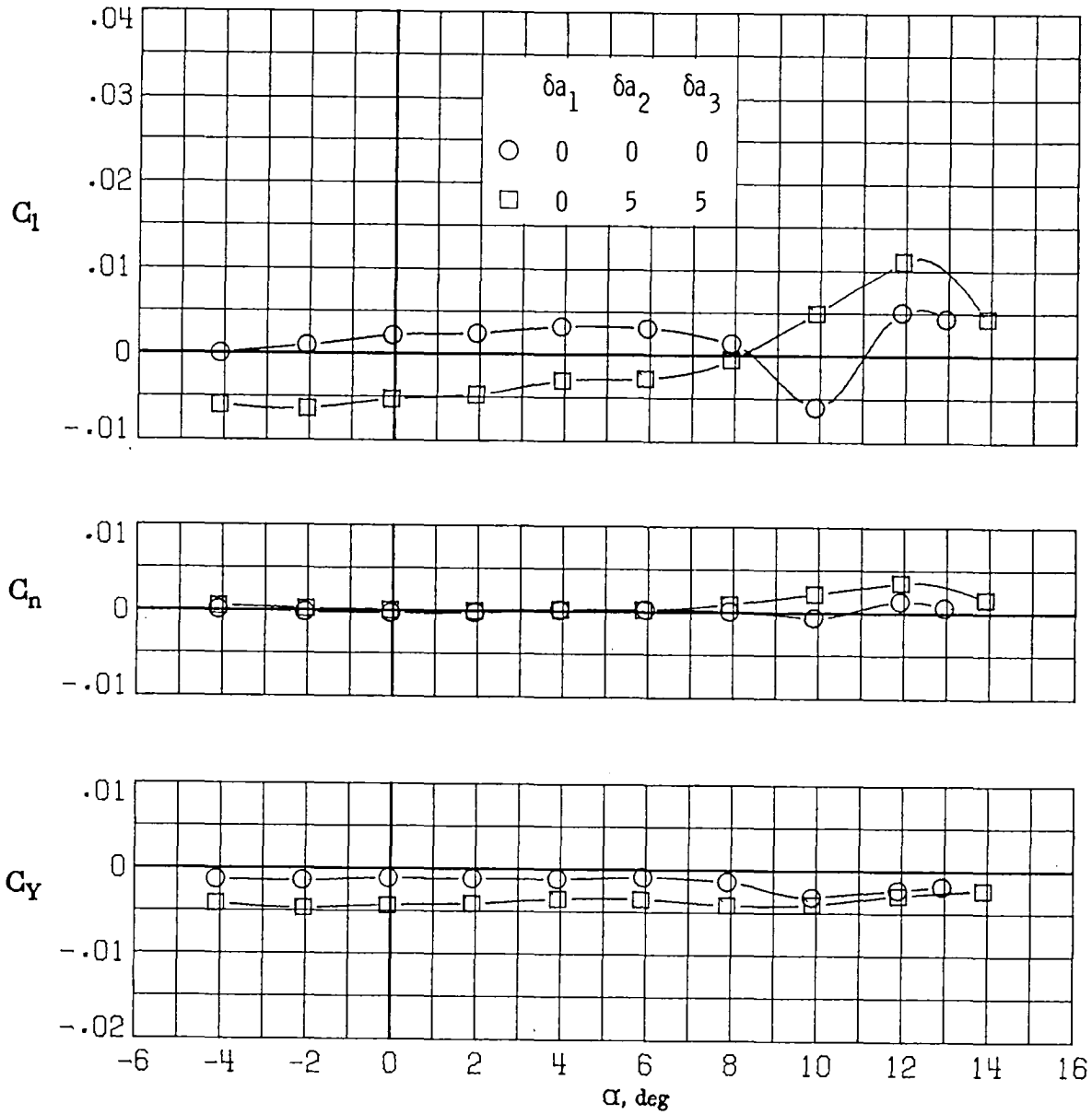

(b) $M_\infty = 0.60$.

Figure 46.- Continued.

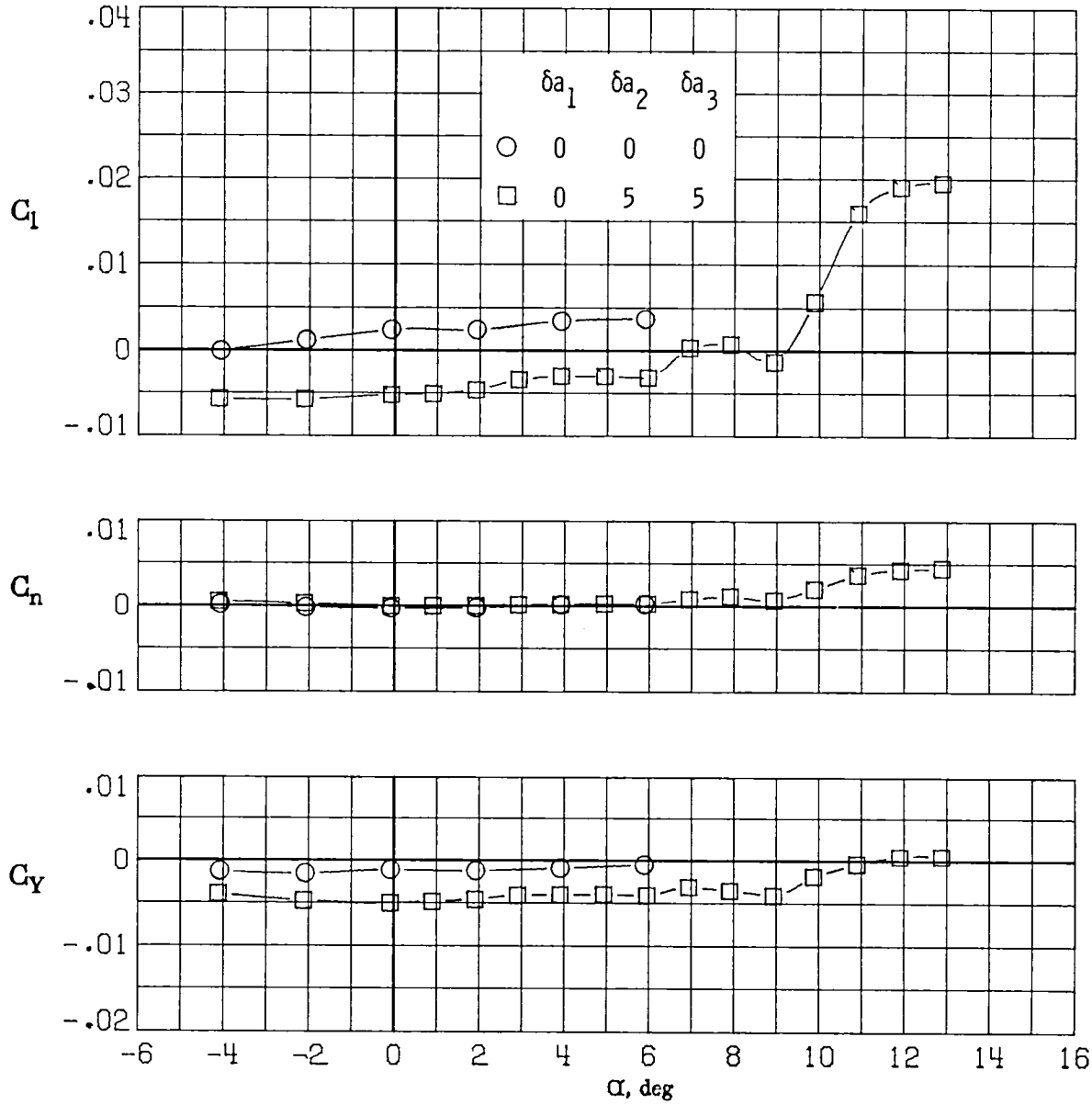

(c) $M_\infty = 0.70$.

Figure 46.- Continued.

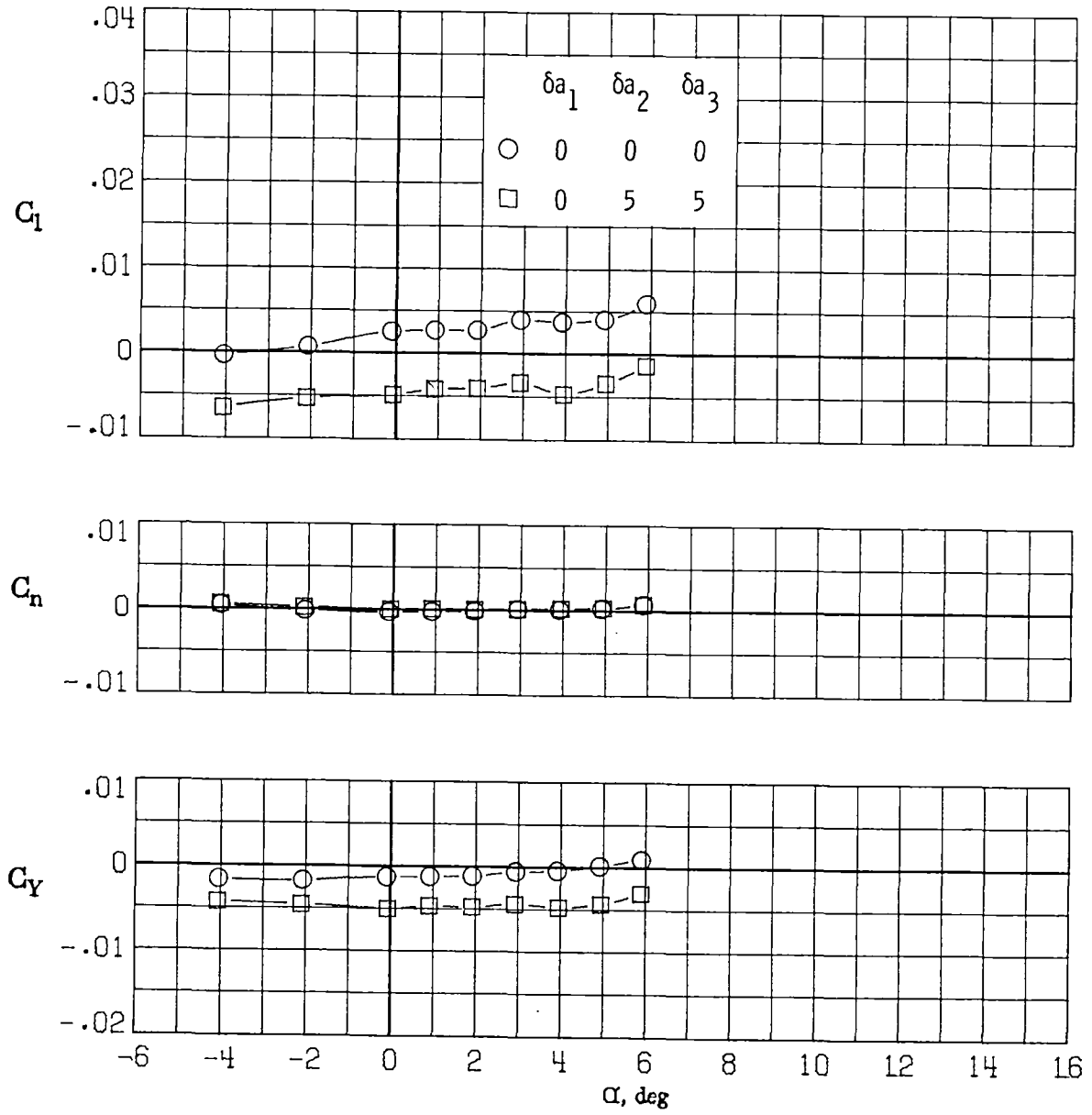

(d) $M_\infty = 0.77$.

Figure 46.- Continued.

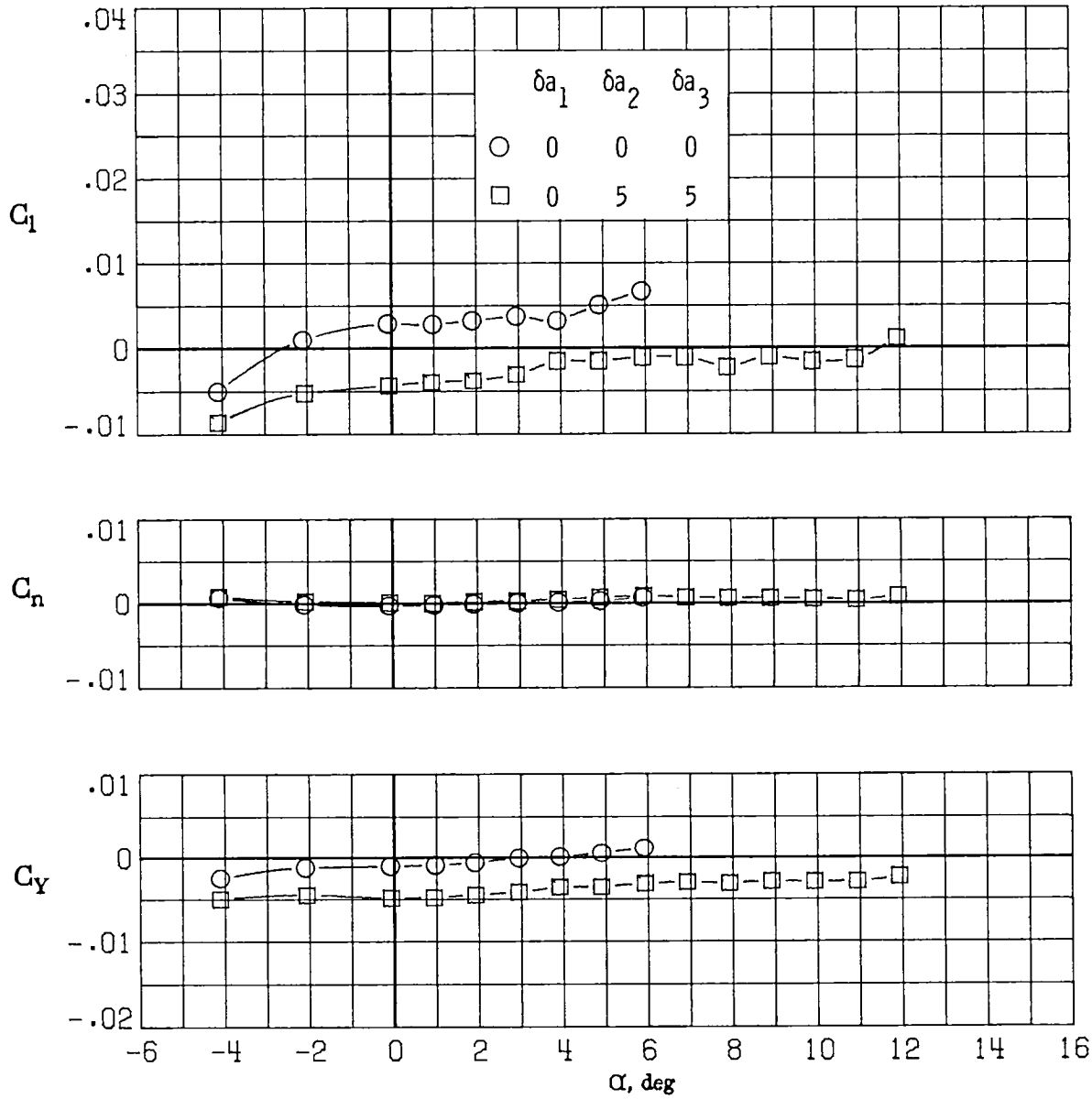

(e) $M_\infty = 0.81$.

Figure 46.- Continued.

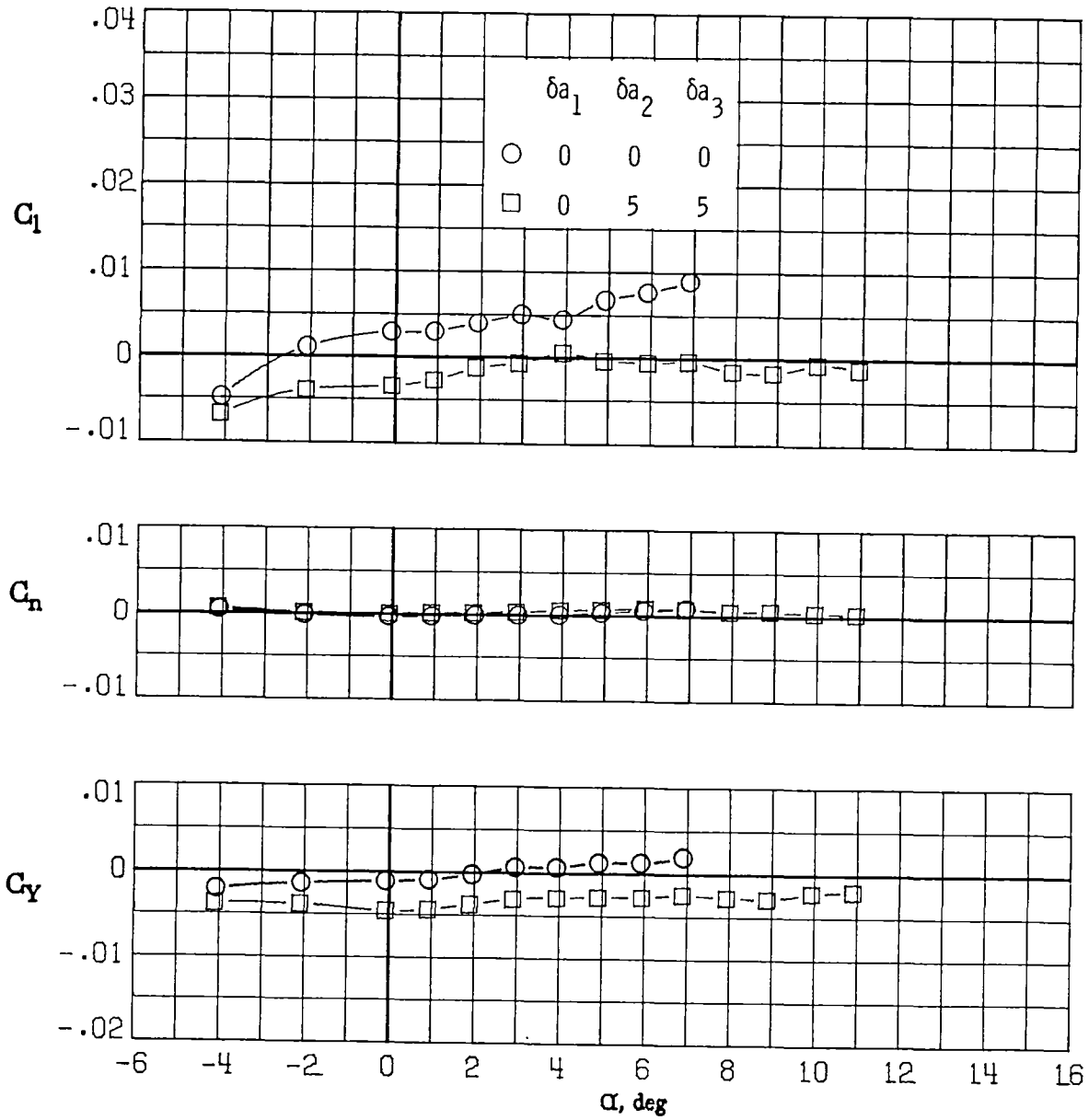

(f) $M_\infty = 0.84$.

Figure 46.- Continued.

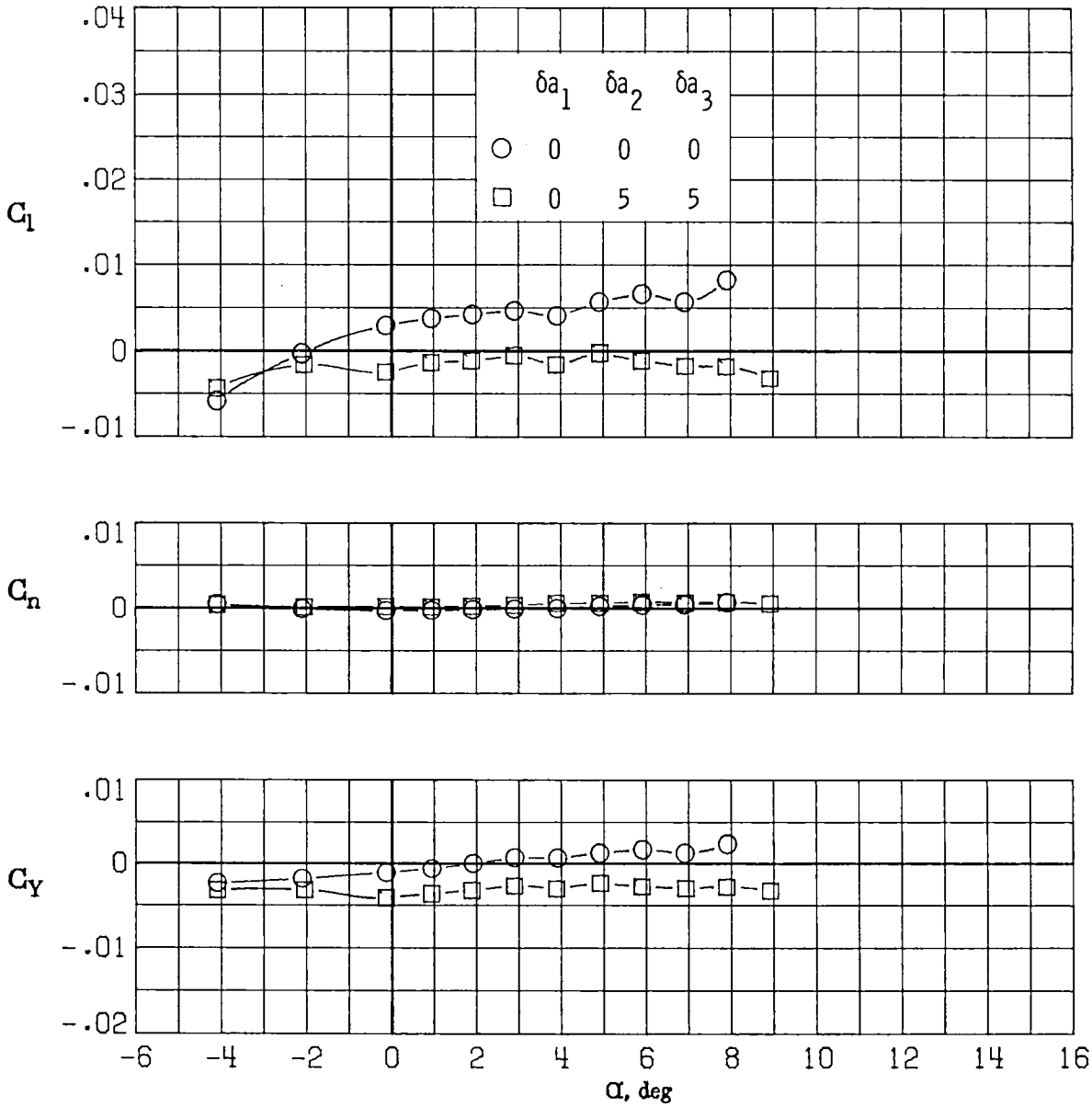

(g) $M_\infty = 0.86$.

Figure 46.- Concluded.

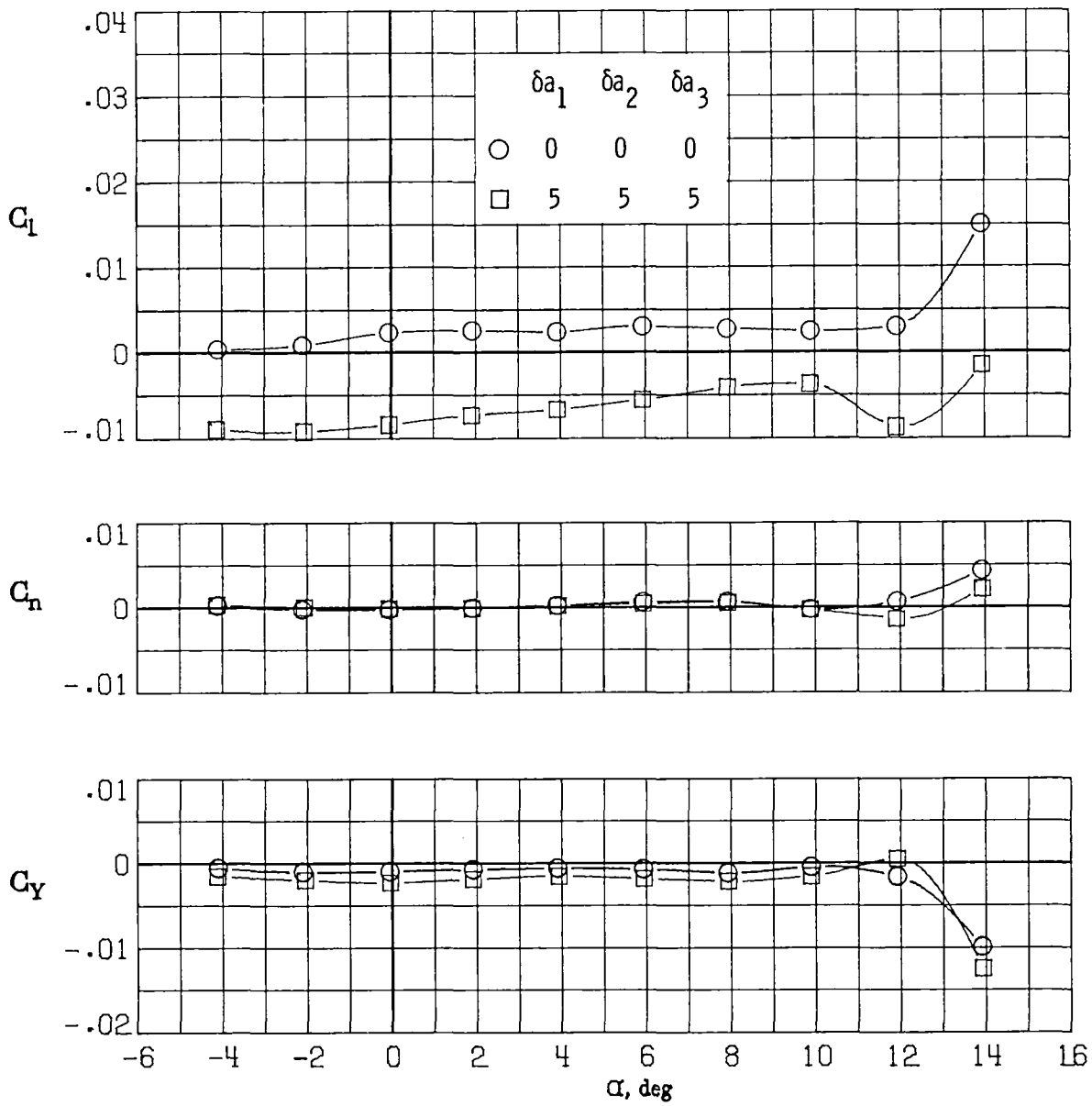

(a) $M_\infty = 0.30$.

Figure 47.- Variation of rolling-moment, yawing-moment, and side-force coefficients with angle of attack for $\delta a_1 = 5°$, $\delta a_2 = 5°$, $\delta a_3 = 5°$.

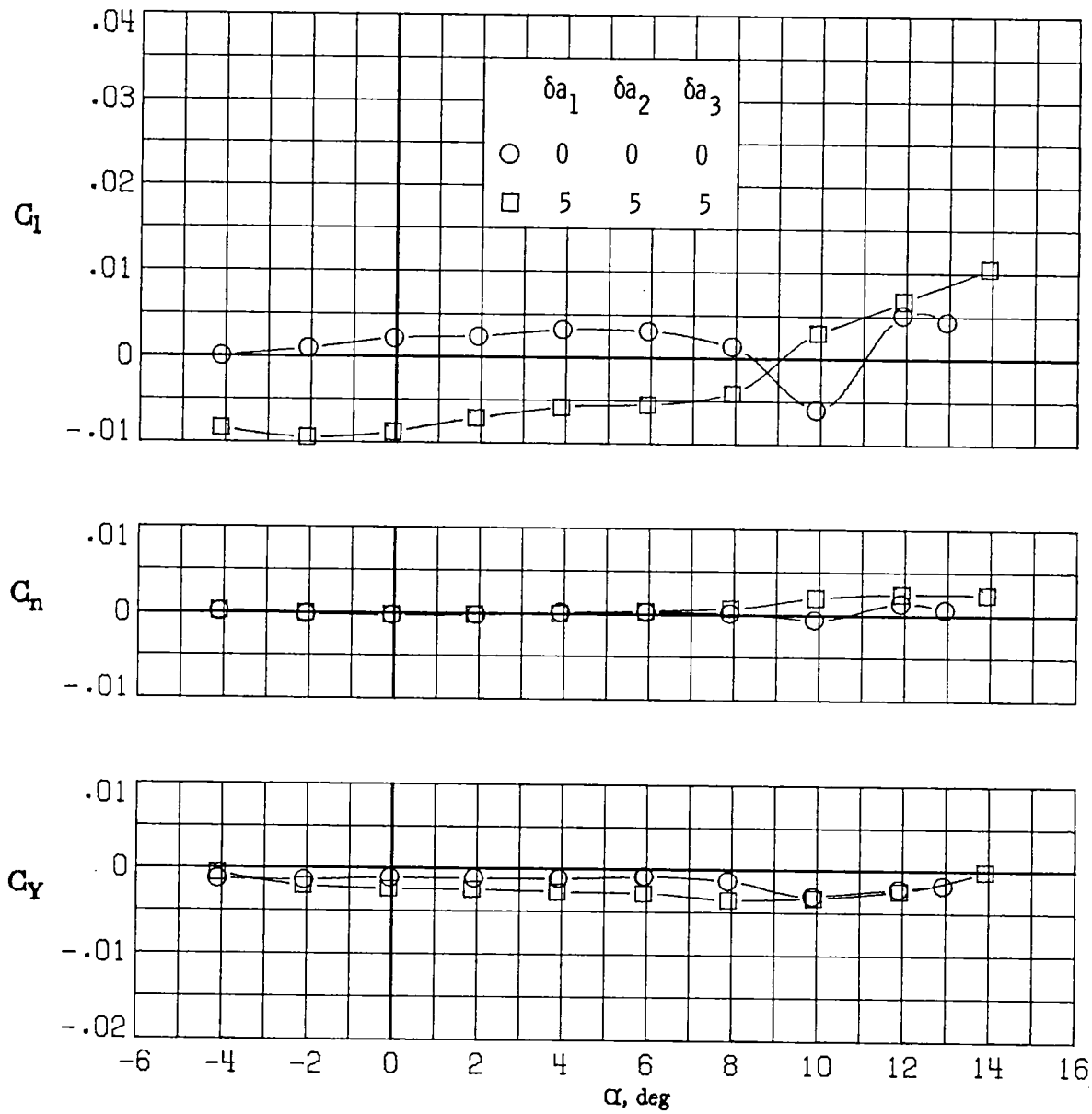

(b) $M_\infty = 0.60$.

Figure 47.- Continued.

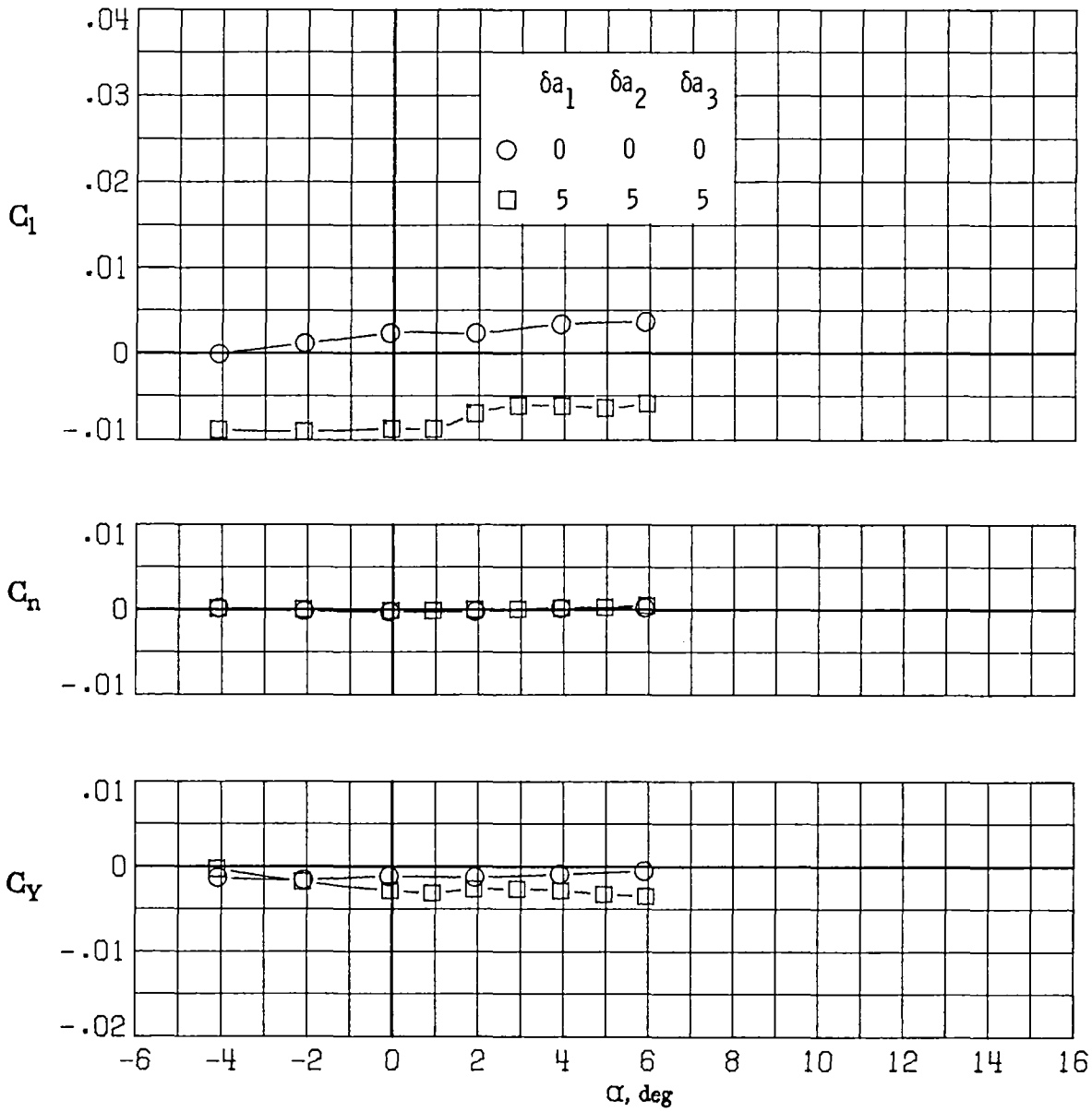

(c) $M_\infty = 0.70$.

Figure 47.- Continued.

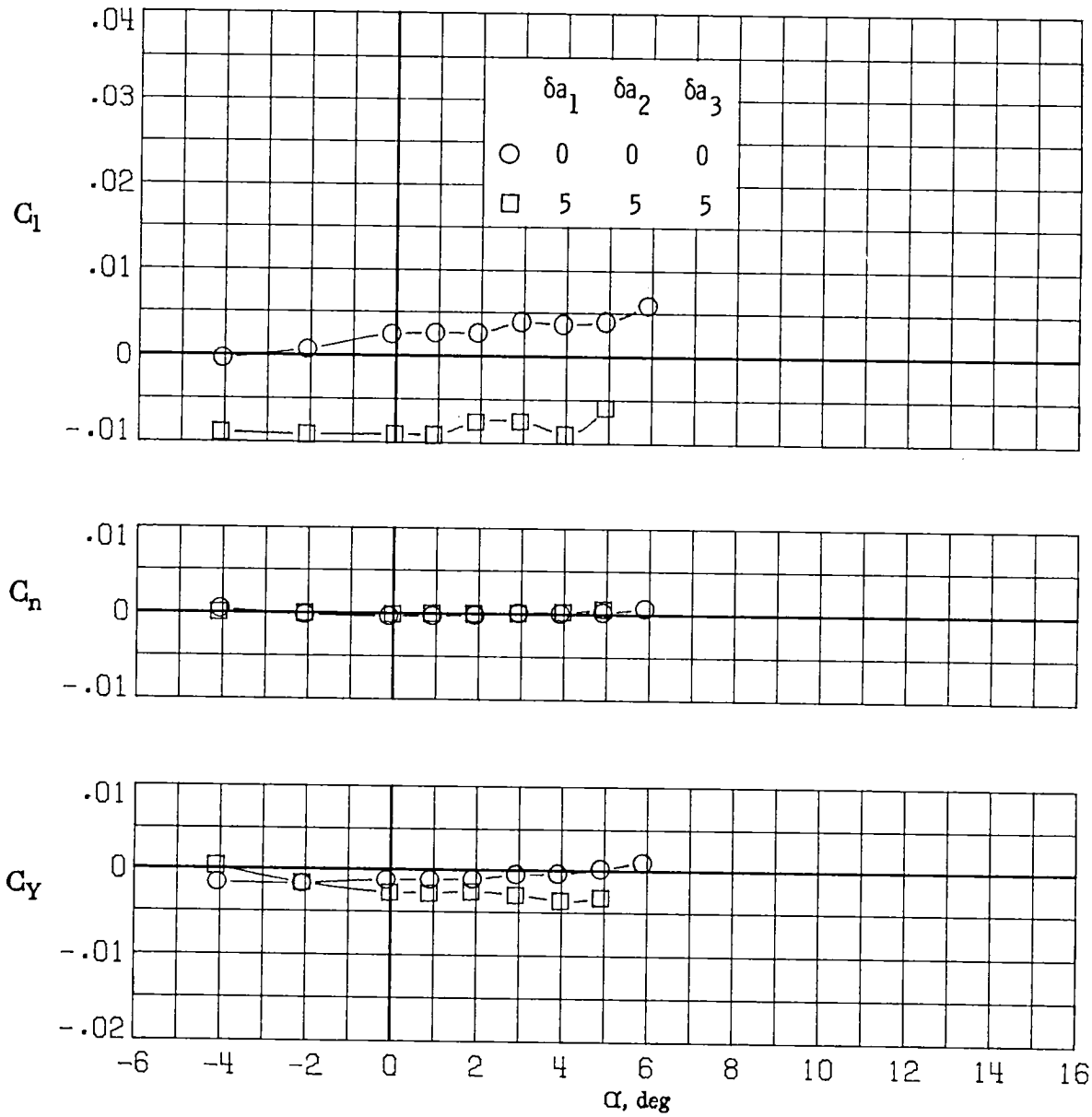

(d) $M_\infty = 0.77$.

Figure 47.- Continued.

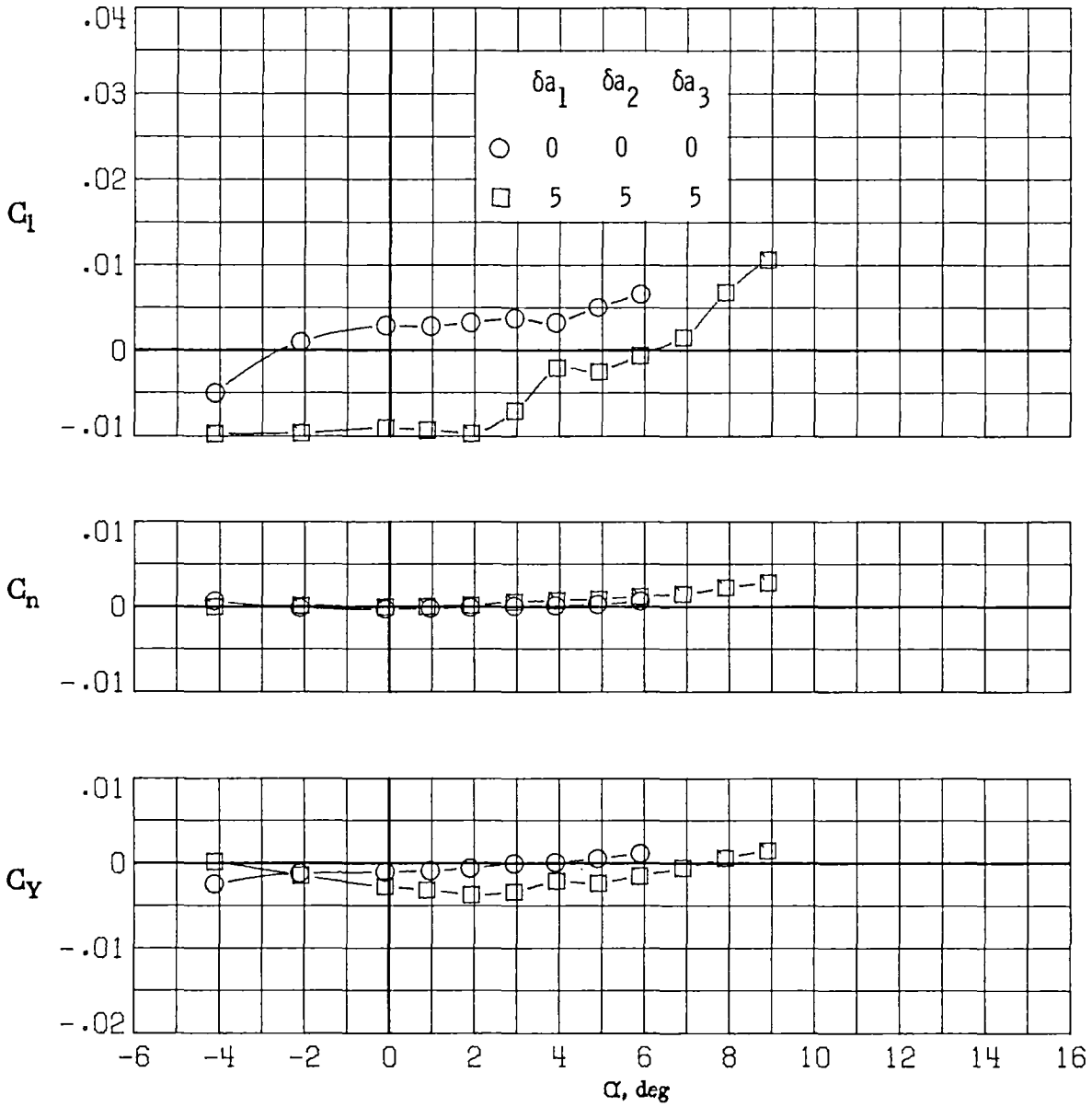

(e) $M_\infty = 0.81$.

Figure 47.- Continued.

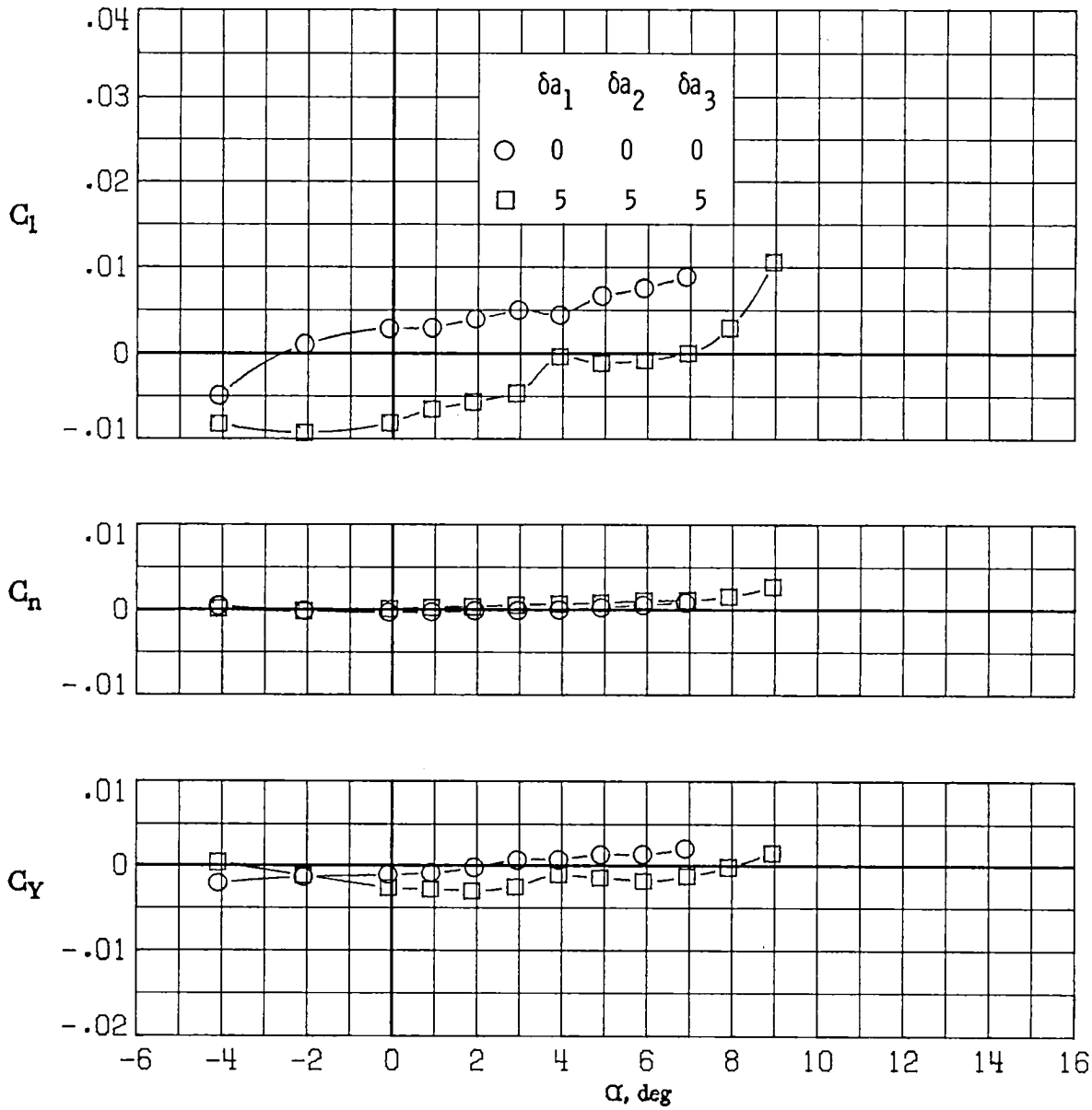

(f) $M_\infty = 0.84$.

Figure 47.- Continued.

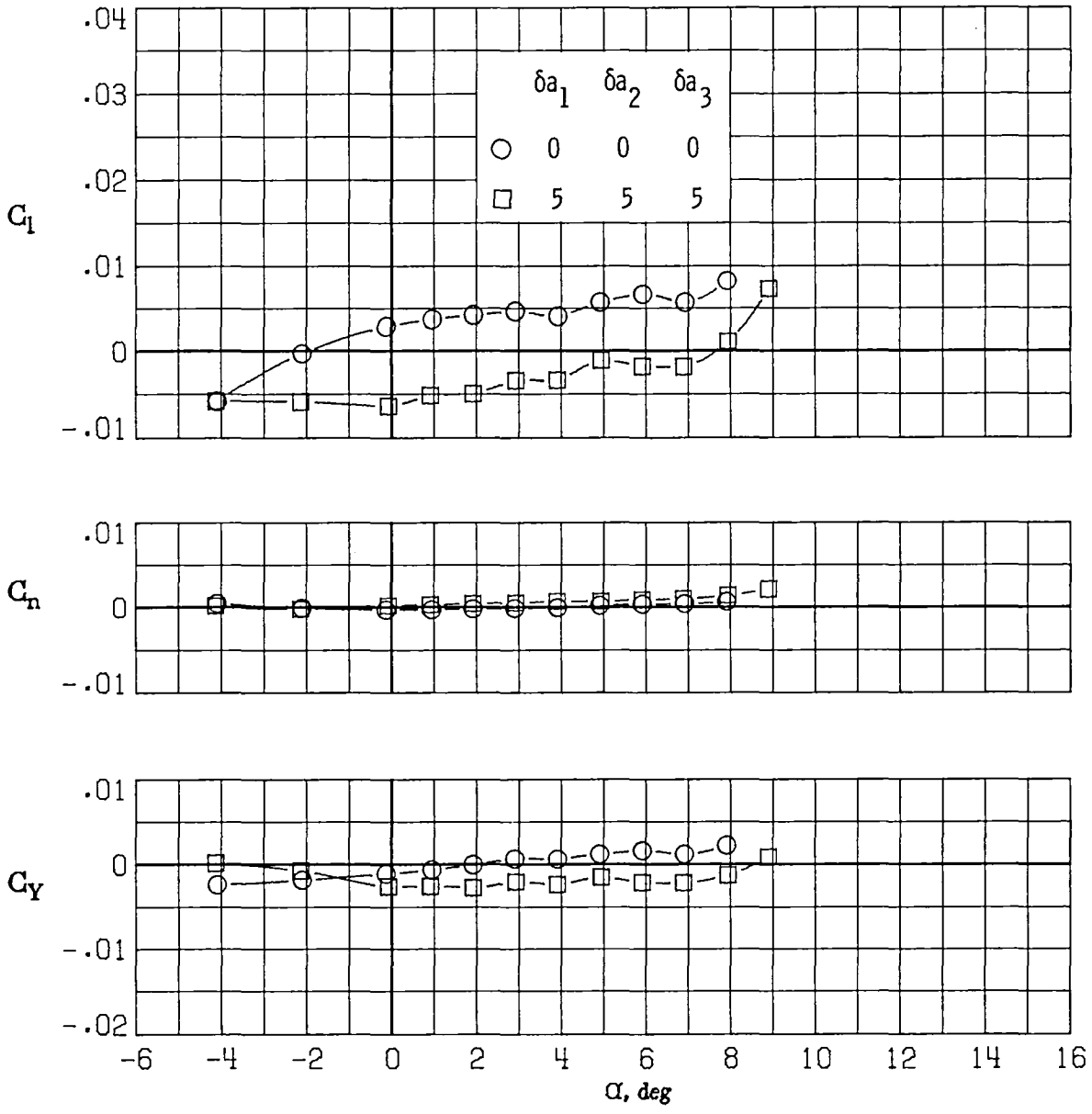

(g) $M_\infty = 0.86$.

Figure 47.- Concluded.

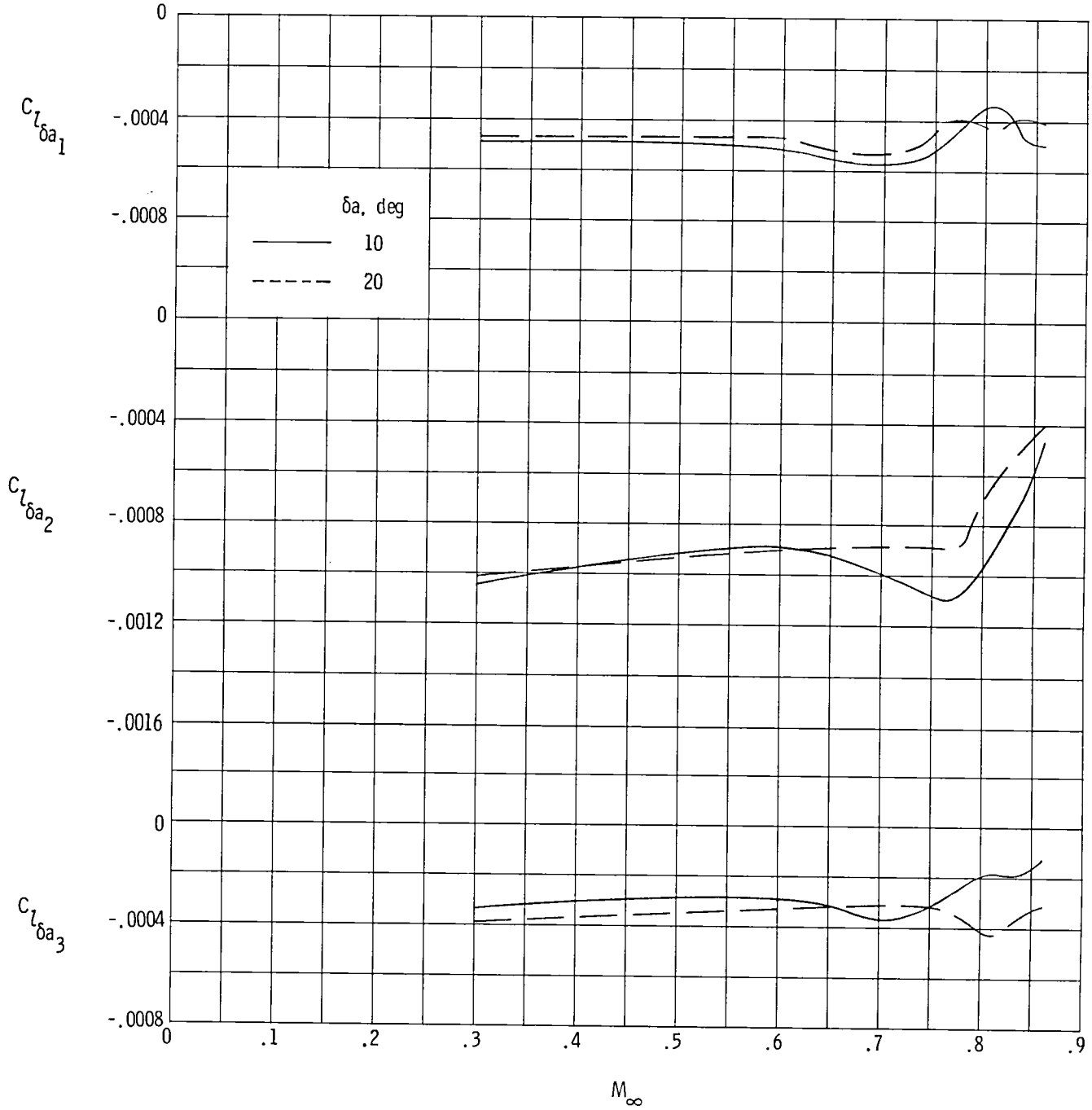

(a) $\alpha = -4°$.

Figure 48.- Variation of control-effectiveness parameter with Mach number.

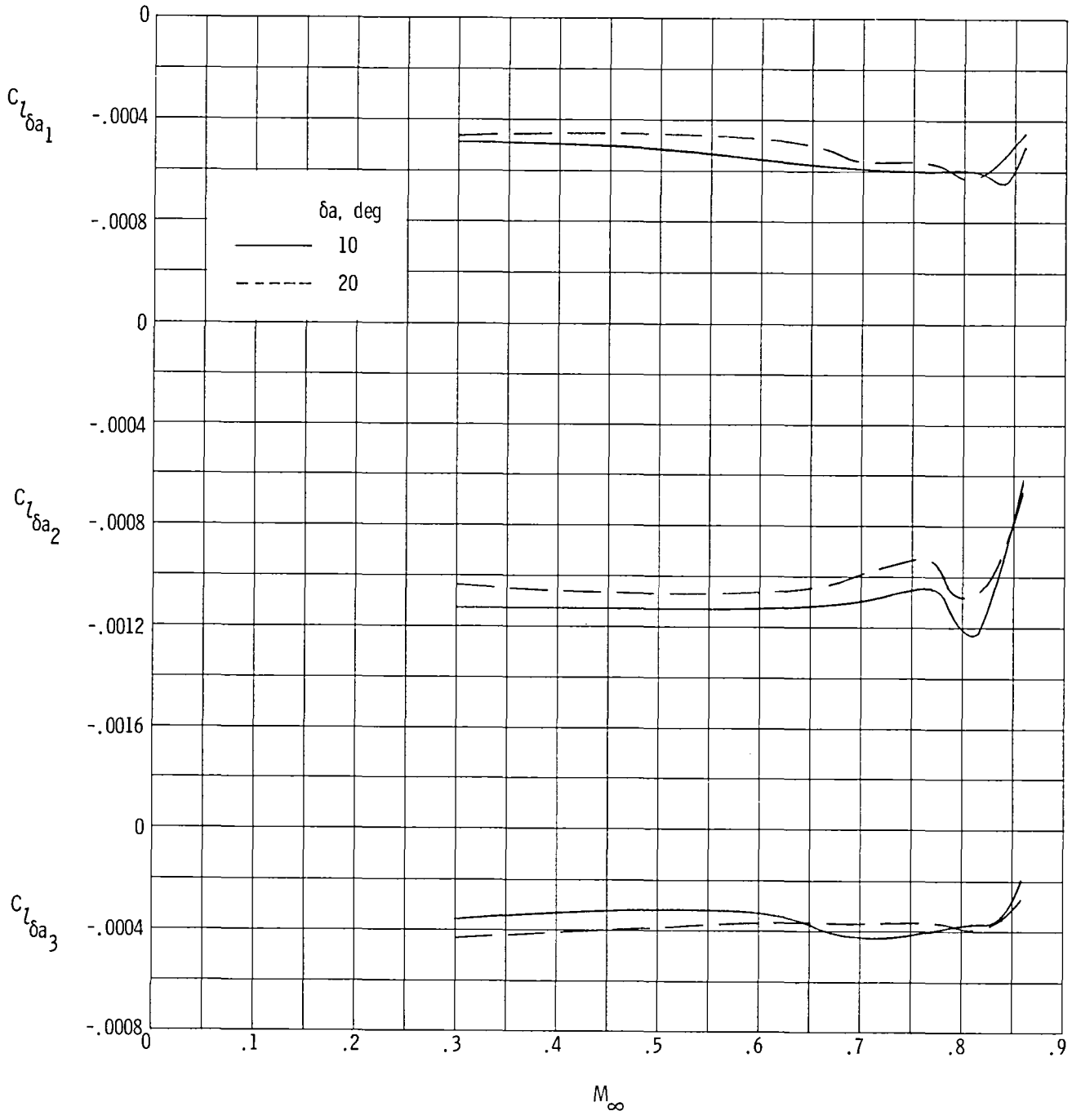

(b) $\alpha = -2°$.

Figure 48.- Continued.

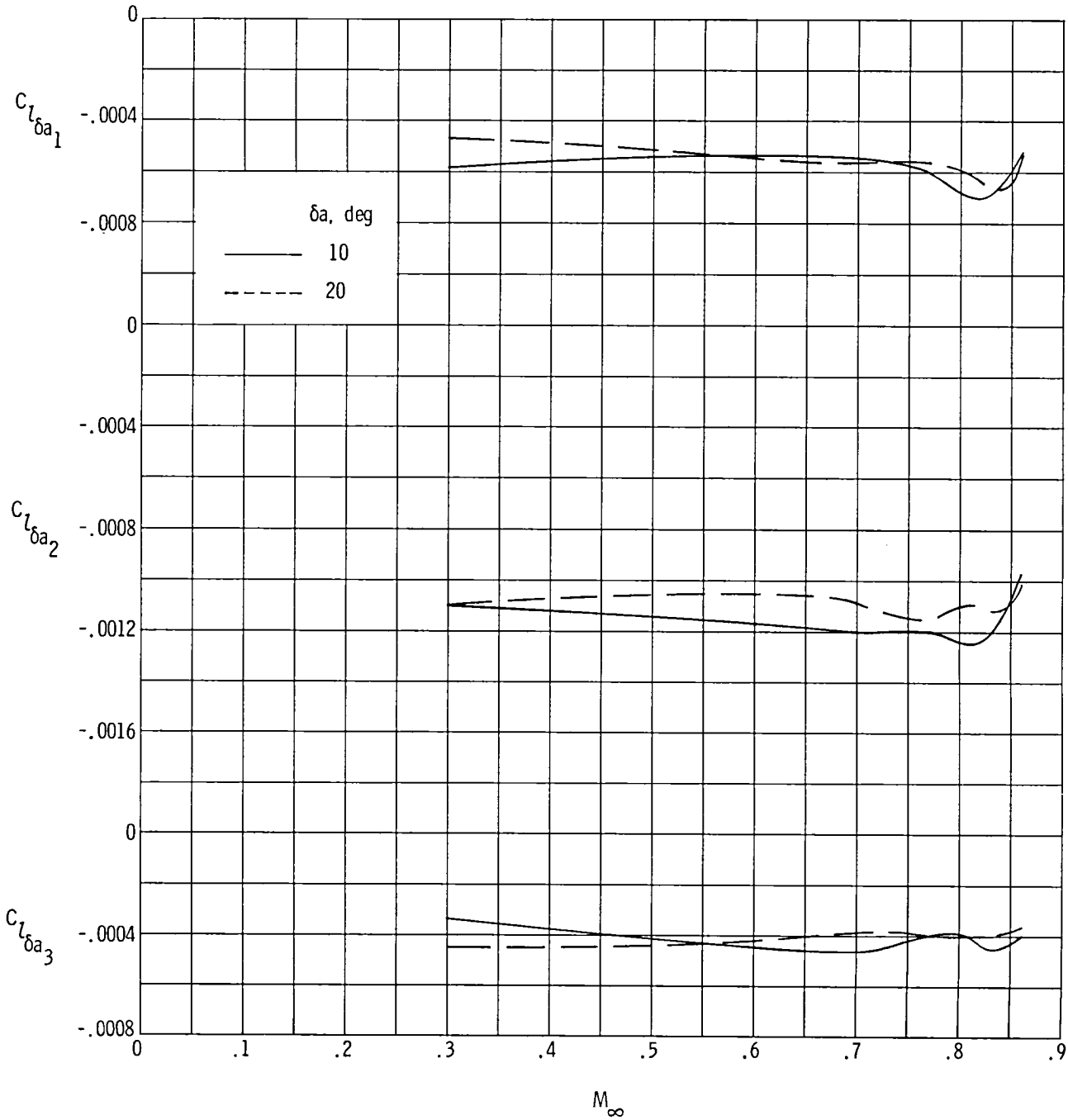

(c) $\alpha = 0°$.

Figure 48.- Continued.

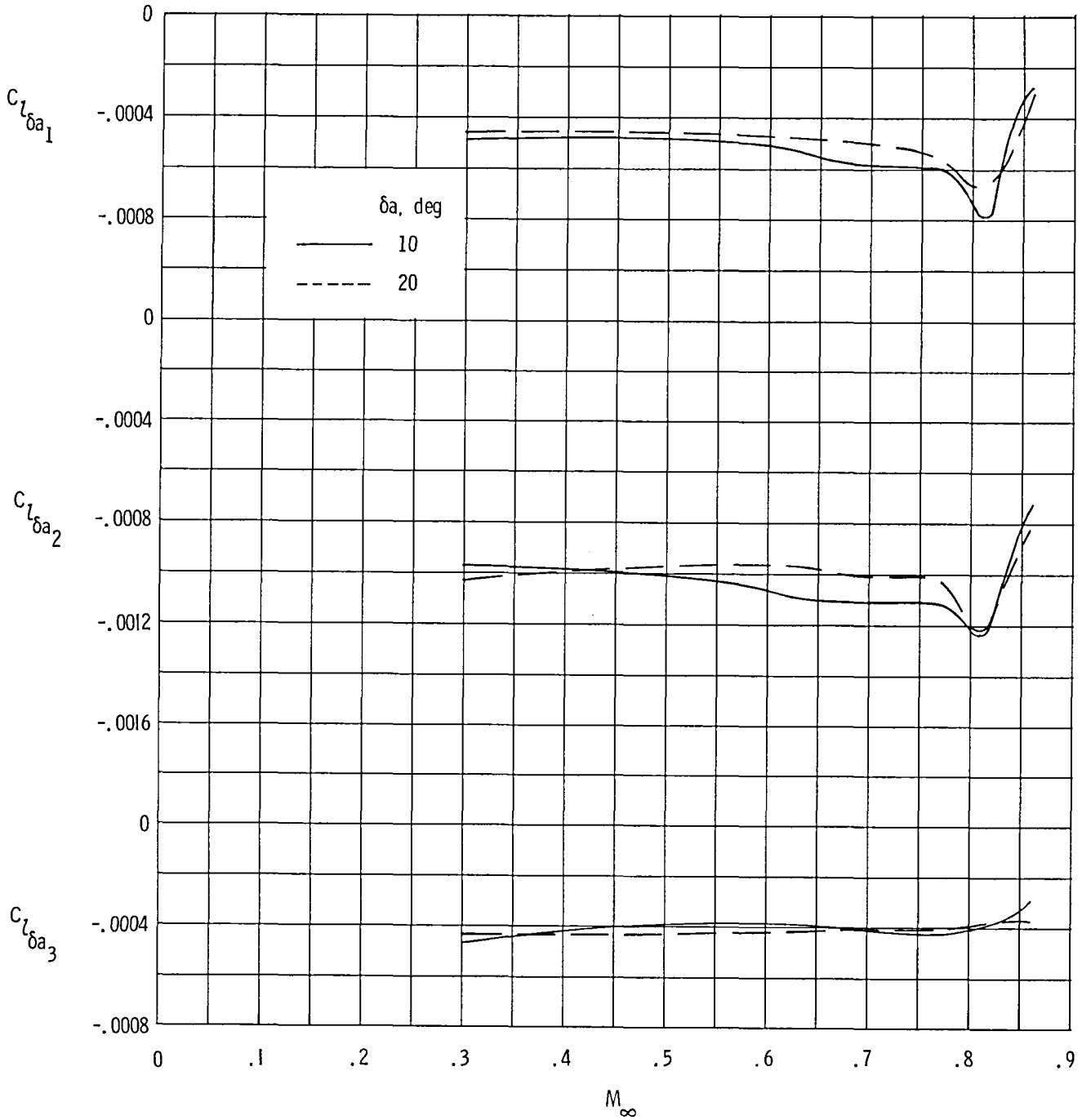

(d) $\alpha = 2°$.

Figure 48.- Continued.

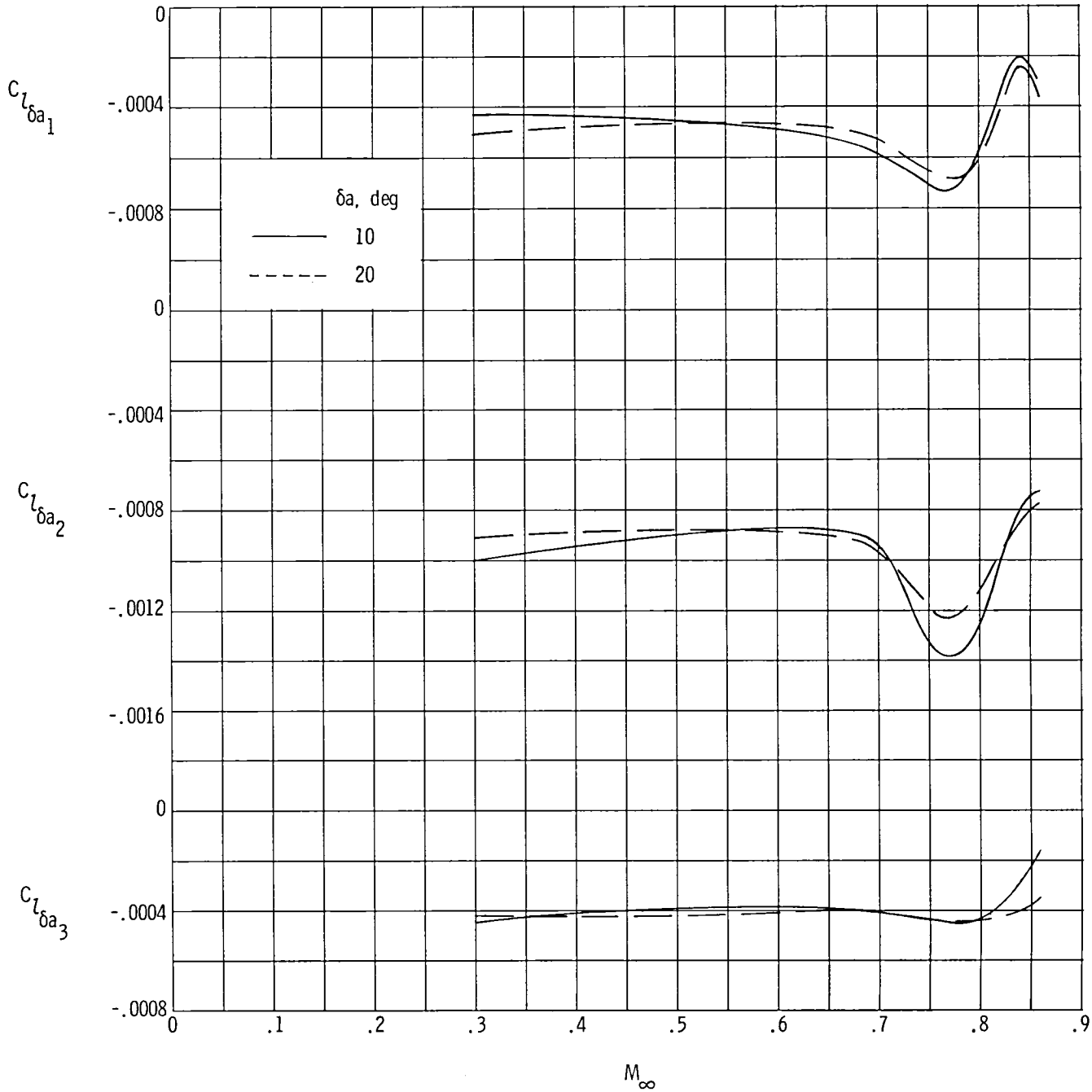

(e) $\alpha = 4°$.

Figure 48.- Concluded.

1. Report No.	2. Government Accession No.	3. Recipient's Catalog No.
NASA TM-85674		

4. Title and Subtitle	5. Report Date
AILERON EFFECTIVENESS FOR A SUBSONIC TRANSPORT MODEL WITH A HIGH-ASPECT-RATIO SUPERCRITICAL WING	December 1983
	6. Performing Organization Code: 505-31-23-07

7. Author(s)	8. Performing Organization Report No.
Peter F. Jacobs	L-15646
	10. Work Unit No.

9. Performing Organization Name and Address	11. Contract or Grant No.
NASA Langley Research Center Hampton, VA 23665	

12. Sponsoring Agency Name and Address	13. Type of Report and Period Covered
National Aeronautics and Space Administration Washington, DC 20546	Technical Memorandum
	14. Sponsoring Agency Code

15. Supplementary Notes

16. Abstract

An investigation to determine aileron effectiveness for a subsonic energy-efficient transport (EET) model with a high-aspect-ratio supercritical wing was conducted in the Langley 8-Foot Transonic Pressure Tunnel. Data were taken over a Mach number (M_∞) range of 0.30 to 0.86. The Reynolds number was 3.0×10^6 per foot for $M_\infty = 0.30$ and 5.0×10^6 per foot for the other Mach numbers. Data are presented for ailerons located at three positions along the wing span. The ailerons were designed as a preliminary active-control concept with gust-load alleviation, maneuver-load alleviation, and flutter-suppression systems. The data indicate a linear variation of rolling-moment coefficient with angle of attack for individual and multiple aileron deflections at Mach numbers up to 0.81. For Mach numbers greater than 0.81, the rolling-moment-coefficient data become nonlinear with increasing angle of attack. At Mach numbers near the design value ($M_\infty = 0.81$), increased aileron effectiveness resulted from aft transition locations, which produced relatively thin boundary layers (higher effective Reynolds number) and greater effective aileron deflections. Individual aileron deflections on the right wing panel produced only small effects on yawing-moment and side-force coefficients.

17. Key Words (Suggested by Author(s))	18. Distribution Statement
Ailerons Control effectiveness Supercritical wing Lateral stability Active controls	~~FEDD Distribution~~ Subject Category 02

19. Security Classif. (of this report)	20. Security Classif. (of this page)	21. No. of Pages	22. Price
Unclassified	Unclassified	275	

Available: NASA's Industrial Applications Centers

NASA-Langley, 1983